KATHOLIEKE UNIVERSITEIT
LEUVEN

Arenberg Doctoral School of Science, Engineering & Technology
Faculty of Science
Department of Earth and Environmental Sciences

STRESS-STATE EVOLUTION OF THE BRITTLE UPPER CRUST DURING EARLY VARISCAN TECTONIC INVERSION

AS DEFINED BY SUCCESSIVE QUARTZ VEIN TYPES IN THE HIGH-ARDENNE SLATE BELT, GERMANY

Koen VAN NOTEN

Dissertation presented in partial fulfilment
of the requirements for the degree of
Doctor of Science, Geology

May 2011

STRESS-STATE EVOLUTION OF THE BRITTLE UPPER CRUST DURING EARLY VARISCAN TECTONIC INVERSION

AS DEFINED BY SUCCESSIVE QUARTZ VEIN TYPES IN THE HIGH-ARDENNE SLATE BELT, GERMANY

Koen Van Noten

Supervisors:
Prof. dr. Manuel Sintubin
Prof. dr. Philippe Muchez

Members of the Examination Committee:
dr. Johannes H. P. de Bresser
PD. dr. Christoph Hilgers
Prof. dr. Rudy Swennen
Prof. dr. Noël Vandenberghe
Prof. dr. Jan Hertogen

Dissertation presented in partial
fulfilment of the requirements
for the degree of
Doctor of Science, Geology

May 2011

© 2011 Katholieke Universiteit Leuven, Groep Wetenschap & Technologie, Arenberg Doctoraatsschool,
W. de Croylaan 6, 3001 Heverlee, België

Alle rechten voorbehouden. Niets uit deze uitgave mag worden vermenigvuldigd en/of openbaar gemaakt worden door middel van druk, fotokopie, microfilm, elektronisch of op welke andere wijze ook zonder voorafgaandelijke schriftelijke toestemming van de uitgever.

All rights reserved. No part of the publication may be reproduced in any form by print, photoprint, microfilm, electronic or any other means without written permission from the publisher.

ISBN 978-90-8649-408-8
D/2011/10.705/26
ISSN 0250-7803
Aardkundige Mededelingen 28

Dankwoord & Acknowledgements

Het is af! Na zes (en een beetje) wondermooie jaren ligt hier eindelijk een werk klaar dat me heeft geïntrigeerd, geëmotioneerd en me ook motiveert om hierna verder te doen met al wat met geologie te maken heeft. Naast alle leuke activiteiten die je tijdens het maken van een doctoraat kan doen, kostte dit doctoraat echter ook moeite, veel moeite om op het punt te geraken waar ik nu sta. Ondanks het feit dat je naam eenzaam op de voorkaft staat, maak je een doctoraat niet alleen, om een doctoraat te maken heb, buiten véél muziek, je vrienden nodig, maar ook collega's die langzaamaan vrienden zijn geworden, promotoren waar ik misschien eerst schrik van had maar die zijn veranderd in toffe, begrijpbare wetenschappers, andere professoren die vanuit hun geïsoleerde groene of oranje toren afdaalden tot fijne collega's, maar bovenal heb je je familie nodig. Lieve mensen, dit woordje van dank is gericht aan jullie allen.

Toen ik aan de UGent afstudeerde lag er na mijn studies een open toekomst voor me. Ik had geen echte gemotiveerde vooruitzichten om verder te gaan in de bijzondere wereld van Chitinozoa en *soft-sediment* vervorming in het Brabant Massief, ondanks een zeer goede begeleiding van prof. Verniers, maar ook geen echte motivatie om het bedrijfswereldje zonder wetenschap in te stappen. Totdat er plots een voltijdse vacature voor een zesjarig mandaat als assistent in de Structurele Geologie aan de K.U.Leuven verscheen bij de onderzoeksgroep van (de voor mij toen nog onbekende) prof. Manuel Sintubin, en dit alles gecombineerd met de voorbereiding van een doctoraat. Een uitgelezen kans om zowel structureel veldwerk te gaan uitvoeren in de Duitse Noordelijke Eifel en in de Ardennen, Geologie van België sprak mij immers als student altijd al aan, als studenten te gaan begeleiden gedurende hun opleiding. Dat het onderwerp van het doctoraat over kwartsaders ging, deed er voor mij niet echt toe, gewoon toehappen. Het is in dit laatste aspect dat ik vooral Manuel, mijn promotor, wens te bedanken voor zijn vertrouwen. Want initieel had ik geen kaas gegeten van structurele geologie, maar door zijn enthousiasme over de geologie van de Ardennen, met in het bijzonder zijn liefde voor de mullions – of veranderen we het in 'bullions' in de toekomst – vreemde regionale worstachtige structuren, werd ik er onmiddellijk ingesmeten en groeide mijn eigen interesse in het wereldje van adervorming. Het is ook dankzij de vrijheid die ik van hem in het onderzoek kreeg, dat dit werk zo'n verregaande conclusies heeft. Manuel kwam geregeld met nieuwe (in mijn ogen soms absurde) ideeën af, maar gepaard gaande met mijn eigen zoektocht, die soms tot ver buiten het onderzoeksgebied liep, vormden we gewoon een bijzonder goed en aanvullend (soms Antwerps) team. Hij spoorde me dan ook telkens aan om onze onderzoeksgroep te vertegenwoordigen op talrijke congressen, wat leidde tot een intussen sterk uitgebreide internationale wetenschappelijke kennissenkring, maar ook om alles steeds te publiceren ondanks dat ik nog twijfelde of het onderzoek al klaar was. Manuel, merci voor de leuke begeleidde jaren, de vlotte communicatie, de talrijke discussies en de uren en dagen gevuld met, al dan niet nuttig, gezever over onderzoek en onderwijs.

Het was pas vanaf dat ik een weg insloeg naar de karakterisatie van de paleo-vloeistoffen waaruit de bestudeerde aders gevormd zijn, dat ik nauw contact kwam met mijn co-promotor prof. Philippe Muchez. Philippe is zowaar nog enthousiaster dan Manuel over alles dat met vloeistoffen te maken heeft, ongeacht of ze oppervlakkig zijn of op grote diepte zitten, of ze economisch relevant zijn of niet, of ze lekker zijn of niet. Door zijn klare en ongelooflijk gedetailleerde kijk op de zaak en zijn uitgebreide en uitermate nauwkeurig bijgehouden kennis van referenties, spoorde hij me telkens aan om elke deelaspect van het onderzoek gedetailleerd uit te werken. Ondanks dat ik geregeld op die fluids heb gevloekt, maakte dit het onderzoek uiteindelijk nog interessanter en breder dan oorspronkelijk gepland was. Philippe wil ik verder zeker bedanken omdat hij vanop zijn sabbatical in Barcelona in de eindfase van het doctoraat alles gedetailleerd en aan een ongelooflijk tempo nalas. Het was een geruststelling om zijn verbeteringen terug te krijgen en dankzij zijn aansporing zijn alle deadlines gehaald. Uiteindelijk leverde het werken onder Manuel en Philippe mooie resultaten op die hopelijk niet het einde vormen, maar eerder het begin voor een leuke verdere samenwerking!

Apart from the input of the supervisors, I would like to acknowledge the members of the jury for reading this PhD and for their scientific input which greatly improved the quality of this work. Initially and at the end, there was prof. Chris Hilgers. I particularly remember our first fieldtrip to the Eifel many years ago and our discussions with nothing but a pencil and some raw field sketches. Chris, you thaught me how to perform a 'paper'-research. This method of working formed the base of the first publication! Daarnaast wens ik ook dr. de Bresser van harte te bedanken voor zijn bijdrage in dit werk. Doordat hij op de hoogte was van dr. Van Baelen zijn werk in Herbeumont, was hij het perfecte jurylid om ons werk in de Ardennen en Eifel te bewonderen en te becommentariëren. De microstructuren en de ISA's hebben geen geheimen meer. Prof. Hertogen en prof. Swennen wens ik te bedanken voor hun input, de discussies op de talrijke doctoraatsweekends de voorbije jaren en voor de aangename losse sfeer op de groene gang omdat een grapje er steeds af kon. Maar natuurlijk was er ook prof. Vandenberghe die me aanspoorde om de Duitse stratigrafie volledig uit te pluizen en de link met België te leggen. De honderden practica en excursies die ik voor hem heb gegeven gaf me de kans om een beter all-round geoloog te worden, los van dit specifiek structureel onderzoek. Bedankt voor de vlotte communicatie en het plezierige beklag over de soms hoofdpijnbezorgende studenten.

Het meeste plezier had ik met mijn trouwe bureaugenoten Hervé en Isaac. Ging het nu over aders, onderzoek of over het leven errond, dit derde deel van onze trilogie over de kwartsaders (weliswaar in een verkeerde geologische volgorde) zou er nooit geweest zijn zonder hun input, discussies en commentaren. Het was een enorme verrijking dat de één nieuwe zaken las die eigenlijk enkel de ander kon gebruiken, zo verruimden we vlotjes onze kennis. Tot op vandaag merci Hervé voor je doordacht half jaartje uitstel van je licentiaatthesis want anders had ik dit doctoraatsonderzoek nooit gehad. Het gaat jullie goed! Op het einde van de trilogie kwam Tom. Ik benijdde het hem niet dat hij in een stressbureau terecht kwam met drie afwerkende doctoraatstudenten, maar zoals hij is, ging hij daar vlot mee om en wringde zich op een vrolijke manier in ons structureel groepke. De basis van "de structurele" werd echter gelegd door Ilse, Tim, Michiel en Dominique, mijn oud-collega's van in de Redingen. Allen op hun eigen manier leerde ze me in het begin ongelooflijk veel bij en ook nadien heb ik daar erg veel aan gehad. Ilse met haar gedreven enthousiasme over onderzoek en 'haar mullions', wetenschappelijk was het vechten om uit haar sporen te treden. Tim (oef, die kwam ook van Gent) en Michiel introduceerden mij in het zalige wereldje van congressen, onze veelal accidentrijke uitstapjes gingen gepaard met de nodige discussies over onderzoek maar gelukkig ook over alles daarbuiten. Ook na Michiel's vlucht naar Engeland, bleef het steeds een plezier om met hen beide bij te babbelen met Engelse pot and pint. *But the most memorable trip I had with Louis during his first Congolese visit to the U.K. to the TSG meeting at Birmingham (this time with a valid visa). Entering the U.K. with Louis, was like entering a toy store with a child. He enjoyed and impressed the TSG community by his work and it was a pleasure guiding him. I'm glad you're almost back! At this point I would also like to thank many people I met at numerous TSG meetings: a special thanks to Richard Walker for being my personal grammatical dictionary but more importantly for lots of fun in the past years together with the other members of the La Roche-en-Ardenne gang, Steve & Dave. Also a warm thanks to Sian & Barbara for the talkable breaks and fieldtrips during these conferences!*

Het draaide natuurlijk niet alleen rond structurele geologie. Samen met Luk en Peter maakten we als '*the last of the assistants'* de studenten het dikwijls lastig, de ene keer als hydrogeoloog, vulkanoloog of ertsdeskundige, een gelukkig zeldzame andere keer als paleontoloog. We gaven excursies en practica aan jan en alleman in de wetenschappen, moge diegene die niet door ons hebben lesgekregen nu hun diploma teruggeven, het zullen er niet veel zijn; van Aywaille en Dinant tot in Luxemburg en de Eifel gidsten we studenten hun bachelorjaren door. Mannen, het was een plezier om met jullie de laatste assistenten te mogen zijn. Ook een leuke dank aan de uitgebreide rest van assistenten waarmee ik door de jaren heen heb samengewerkt: de oude Swennengarde met Liesbeth, Ben en Koen, de nieuwere Swennengarde met Eva, die me vlotjes in 4 jaar voorbijstak, spacingman Carl en dolo-Julie, de Muchez supporters Hamdy en Maarten, de mannen van den bouw Gilles, Lieven en Ruben, lerares Marian en marathonman Gert. Maar plots was daar ook die overweldigende nieuwe garde met Rieko, Bene, Koen, enz.: merci voor de gezwinde overname van al het practica- en excursieleed wanneer ik op het einde al met mijn hoofd al in dit boek zat. Ook de leuke intermezzos met treinbuddies Els, Dennis, Femke en de Annen vergeet ik niet, *and a warm thank you to so many people I here may forget*! Daarbuiten bedankt aan de moeder van alle koffiepauzes Marijke omdat het haar toch maar lukte iedereen erbij te lappen om taart te moeten trakteren voor welke dubieuze reden ook. Tenslotte Friso, merci voor de ontelbare practical jokes en het plezier tijdens het logement als ik niet meer terug in Antwerpen geraakte, hopelijk zag je er niet teveel van af… Er zijn er ook zij die de praktische kant van het doctoreren gemakkelijker maken. Eerst is er den Herman, je ging niet zomaar 'eventjes' langs zijn labo voor een paar slijpplakkes en wafers, nee, een bezoekje ging steeds gepaard met een goeie babbel vol sappige verhalen, en Dirk die deed rustig mee. Er was onze ambitieuze laborante Elvira met al haar machines die gerust meer gebruikt mogen worden. Administratief wil ik Ria en Sofie bedanken om de vlotte manier waarmee zij elke financiële kwestie oplosten en natuurlijk Hilda voor al het lokaal- en practicumgeregel. Uren stond ik aan haar balie met nog maar eens een vraagske. En ik weet ook niet hoe computers het weten, maar als er gestrest wordt, dan crashen ze en doen ze niks meer. Gelukkig waren er Johan, Greet en Hilde om mij te ontlasten van alle die soft- en hardwarefrustraties.

Natuurlijk is er meer dan het leven en werken in Leuven, elke avond keerde ik terug naar Antwerpen en daar lag de ontspanning, de geruststelling van de vele vrienden die me ondersteunde en vroegen '*wat doet gij nu weer al*', een vraag die langzaam veranderde in '*wanneer zijt ge nu klaar*' of in de finale fase '*wanneer zien we u nog eens terug*'. Onmiskenbaar was natuurlijk de LO-crew Mark, Jelle, Stijn, Toon en Robin, de mannen van Deurne Kris en Jan, en Karen en Michelle die natuurlijk niet wilden onderdoen voor de gasten. Ook al begrepen ze allen dikwijls niet waar ik mee bezig was, ze probeerden het toch en dat was belangrijk genoeg voor mij! Ze wisten dat ontspanning nodig was en trokken me van het werk weg, overdag maar vooral 's nachts. Het was ook zalig om tijdens de klimverlofkes in de Alpen met Dieter, Jelle, Jan en Thomas mijn enthousiasme over geologie aan hen over te proberen brengen. Muzikaal intermezzo was er met *Newt*, onze band waarmee er elke donderdag een stevige lap op werd gegeven, met versterkers ingeplugd en volumeknop op maximum viel alles van me af, thanks guys en Wouter, we did it! Op maandagochtend nam ik de lift: dit door de vrienden van de SAC. Zij snapten maar al te goed dat ik op zondag alle weekfrustraties wegwerkte op bal en tegenstander. Kampioenen waren we niet, maar wel masters van de derde helft waardoor iedereen nog steeds bang is van FC SAC! Ook een warme groet aan alle geologiecopains van Gent die bijna allemaal naar het buitenland vertrokken en elkaar blijven impressioneren met hun avonturen.

De grootste dank gaat echter uit naar ons gezin. Ons mama en papa gaven ons Griet, Tim en mij een fantastische onbezorgde jeugd en onze talrijke trips naar de Alpen in Oostenrijk waren voor mij dé drijfveer om uiteindelijk voor geologie te kiezen. Als 'der kleine' heb ik me dit nooit beklaagd. Mama en papa, merci om mij de kans te geven om in Gent te studeren, het nodige zetje erachter, en de jaren van onvoorwaardelijke steun!! Griet en Tom, die het wetenschappelijke wereldje uit ervaring snapten, waren super in het motiveren van hun klein broerke tijdens zijn eindsprint. Naar de onbezorgdheid en frivoliteit van Big Bro Tim en zijn Imelda, die nu hun avontuur beleven in de Cevennen, keek ik op. Zij waren de trigger om zoveel mogelijk fun uit mijn avontuur te halen. Het meeste heb ik gelachen met mijn neefjes en nichtjes: bedachtzame Sten, zotte Noor en Mona, stoere Raven en dartele Merin, voor hen was mijn onderzoek zo klaar als een klontje, als *doctor van de Ardennen* onderzocht ik gewoon de stenen in de bergen, wat is daar nu niet aan te snappen? Met Isabelle en met Peter, die me steeds volledig uitvroeg over de aarde, had ik twee ouders bij die steeds geïnteresseerd waren. Ook kleine zus Tess deed een duit in het zakje, succes met je komende studententijd! Tot slot een warme dank aan alle nonkels, tantes, neven en nichten in alle vier families voor hun honderden vragen en jaren van steun. En de bomma en yiayia die vroegen niks, maar die zagen dat het goed was.

Maar laten we tenslotte eerlijk zijn, eigenlijk is er maar één vrouw die heel de rit mee heeft uitgelopen, die blindelings mee in dit 6-jarig project stapte en zelfs meer vertrouwen in me had dan dat ik zelf had, eentje uit de duizend om haar bezorgdheid, haar geduld als ik mijn presentaties even wou inoefenen, haar veldkookkunsten in de Eifel, eentje die me geruststelde als ik weer te laat en overstrest thuiskwam, zij die de eenvoudige dingen des levens zo speciaal maakt en die maar al te graag onze onbekende toekomst mee induikt. Lieve Kim, weldra zijn we niet meer met twee want er komt een kleintje bij, deze periode is nu afgesloten en een heel nieuwe staat voor de deur, eentje waar ik bijzonder naar uitkijk! Daarom schat, dit boek is voor jou.

Abstract

In the recent decade, there is an increased interest in the processes active at the base of the seismogenic crust, with a particular focus on the evolution and characterisation of elevated fluid pressures that could possibly drive fault rupturing and initiate major earthquakes. The base of the seismogenic zone, however, is not directly accessible. One of the possibilities to overcome this research problem is the study of natural fossil analogues to pursue a better understanding of the formation and evolution of these overpressured fluids at relatively great depths. Within the broad framework of natural analogues, vein studies provide an important insight in the characterisation of fluids and the role of fluid pressure during a complete deformation cycle. In vein analysis, an extensive interdisciplinary approach is required in order to determine a fluid-assisted deformation during orogeny.

This research project focuses on overpressured fluids that are generated in a sedimentary basin during late burial that is affected by an incipient tectonic shortening at the onset of orogeny. Quartz veins that result from the overpressures in sedimentary basins preserve valuable information on the metamorphic fluids which were present during burial and subsequent orogenic deformation. A detailed geometric and kinematic structural analysis of several successive quartz vein types has been performed to allow constraining a geometric evolutionary model of the emplacement of these different, successive veins with respect to structural features such as bedding, cleavage, folds and faults. This model is refined by means of a pervasive microstructural and microthermometric analysis of the vein infill in order to implement physico-chemical parameters such as formation temperature and pore-fluid pressure. Ultimately, this study aims at understanding why, how and when fluids become overpressured and how they subsequently evolve at the onset of orogeny.

More specifically, the study focuses on Lower Devonian multilayer siliciclastic metasediments that were deposited in the Ardenne-Eifel basin. This basin formed part of the northern passive margin of the short-lived Rhenohercynian Ocean which was closed during the Variscan orogeny. These metasediments are currently exposed in the High-Ardenne slate belt (Belgium, France, Luxemburg & Germany), which belongs to the central part of the Rhenohercynian foreland fold-and-thrust belt in the northern extremity of the Central European Variscan belt. The rocks, in which quartz veins frequently occur, are studied in the north-eastern part of the High-Ardenne slate belt (Rursee, Urftsee; North Eifel; Germany) and are affected by a very low-grade metamorphism, which is considered to have a burial origin, pre- to early synkinematic with the prograding Variscan deformation. This metamorphism documents the peak of subsidence and sediment accumulation (~7 km) prior to the main Variscan contraction of the basin.

The analysis focuses on two successive quartz vein types, oriented normal and parallel to bedding respectively, in which the very low-grade metamorphism is reflected. A first vein type consists of several generations of bedding-normal veins that remain perpendicular to bedding around the characteristic, NW-verging, upright to overturned folds of the North Eifel, thereby clearly predating the main Variscan contraction and fold-and-cleavage development of the slate belt. The planar to lensoid veins are mostly restricted to competent sandstone layers, although they sometimes continue into the adjacent incompetent layers, refracting at the competent-incompetent interface, similar to cleavage. The fabric of the bedding-normal veins predominantly shows a fibrous to elongate-blocky vein infill in which the fibres or the elongated crystals are oriented at high angle to the vein walls. Both syntaxial and ataxial growth morphologies are recognised. Repetition of host-rock inclusion bands internally in the vein quartz reflects episodic opening of the vein by the crack-seal mechanism. Pseudosecondary fluid-inclusion planes, oriented at high angle to the crystal fibre walls and reflecting intracrystal healed microcracks, confirm that crystal growth occurred by incremental crack-seal steps.

The specific orientation of fluid-inclusion planes and host-rock inclusion bands indicate that the veins are extension veins which originally grew in Mode I fractures in a rock that was already significantly reduced in porosity during burial. The fluid-inclusion planes have been particularly useful as a microstructural marker to reconstruct the stress state in the basin at the time of vein formation. In this respect, the maximum principal stress (σ_1) was still vertical, corresponding with load of the overburden (σ_V) and the veins opened parallel to the least principal stress (σ_3), that roughly indicate the extension direction in the basin. The propagation of fractures during vein formation occured in the σ_1 - σ_2 plane. Secondary inclusion planes, corresponding to post-veining transcrystal microcracks oriented parallel to the vein walls, evidence that microcracks still developed after opening of the extension veins but still in a similar stress regime as the pseudosecondary inclusion planes.

The consistent pre-folding orientation of bedding-normal veins in the North Eifel corresponds to the pre-folding orientation of intermullion quartz veins in the central part of the High-Ardenne slate belt (Ardennes, Belgium) highlighting that this veining event occurred regionally. The (micro)structural analysis of bedding-normal veins eventually shows that these veins developed at low differential stress during the latest stage of the extensional stress regime and reflect a regional NW-SE opening of the Ardenne-Eifel basin. A structural change of the pre-folding vein orientation from NW-SE (Ardennes) to NNW-SSE (Eifel) is probably related to a post-veining oroclinal bending of the slate belt during the main Variscan contraction due to the presence of the rigid Brabant basement in the north. Apart from the orientation analysis, the spatial distribution of these bedding-normal quartz veins in the High-Ardenne slate belt is investigated in order to determine the effect of the layer thickness to vein spacing. The results show a quasi linear relationship between vein spacing and layer thickness in thin (<40 cm) competent sandstone layers and a non-linear relationship in thicker sandstone layers (>40 cm). Vein spacing tends to increase to a maximum value becoming more or less independent of layer thickness. The resemblance of vein spacing with regularly spaced fractures that result from saturation during fracture development, suggests that in an unfractured rock, the host rock can get saturated by the presence of initial veins in which the veins subsequently either grow by progressive extension or that new cross-cutting veins develop in case the regional stress field changes relatively with respect to the existing veins.

In the North Eifel, bedding-parallel quartz veins cross-cut, truncate and offset the bedding-normal veins and are continuously present around fold hinges. Bedding-parallel veins occur interbedded between two contrasting lithologies, as well as intrabedded in the competent and incompetent sequences. Macroscopically, the veins show a composite internal fabric consisting of several distinct generations of quartz laminae, often marked by slickenlines, intercalated with thin pelitic wall-rock inclusion seams. Microscopically, the variety in microstructures is indicative of different combined mechanisms of vein growth and mineral infill, reflecting a complex vein formation. Repeated crack-seal inclusion bands that are oriented parallel to the vein wall, and thus parallel to bedding, reflect bedding-normal opening of crack-seal quartz laminae. This mechanism also is also evidenced by the alignment of pseudosecondary fluid-inclusion planes internally in the fibres. The presence of blocky laminae reflects crystal growth in an open cavity during bedding-normal uplift. Bedding-parallel stylolites in often occur in these blocky laminae and represent pressure-dissolution during bedding-normal collapse. The occurrence of shear laminae, in which small quartz crystals are dynamically recrystallised during the main phase of the Variscan contraction, has, on the other hand, been used as indicator of bedding-parallel shear events.

The pronounced bedding-parallel fabric is interpreted to form during several alternating phases of bedding-normal uplift and bedding-parallel shearing taking place at the onset of folding. Based on the microstructural analysis, the bedding-parallel veins are classified as extension veins to extensional-shear veins that formed at low differential stress. This vein type is the brittle expression of the first phases of the compressional stress regime affecting the siliciclastic metasediments of the Ardenne-Eifel basin at the onset of Variscan shortening. In this configuration, the bedding-parallel veins demonstrate a particular stress-state in the basin at the time of vein formation in which the maximum principal stress (σ_1) was oriented parallel to a NW-SE-oriented tectonic compression (σ_T) and the minimum principal stress (σ_3) corresponded to the vertical load of the overburden. The succession of bedding-normal to bedding-parallel extension quartz veins thus materialises the transition from extension to compression at the onset of Variscan orogeny and is interpreted to have formed during early orogenic compressional tectonic inversion.

A petrographic and micro-thermometric analysis of fluid inclusions within the vein quartz has further helped to constrain the kinematic and pressure-temperature trapping conditions of both vein types, allowing the reconstruction of the fluid pressure and stress-state evolution during tectonic inversion. The method used for defining the trapping conditions involves cross-cutting isochores, calculated from the salinity and homogenisation temperatures representative of both vein types, with an independent vitrinite reflectance geothermometer that defines the maximum temperature of 250°C at the time of vein formation. The results demonstrate that the bedding-normal extension veins are trapped from a low salinity (3.5-8 eq.wt.% NaCl) H_2O-NaCl fluid at near-lithostatic fluid pressures prior to inversion. After the tectonic inversion, bedding-parallel veins formed from a low salinity (4-7 eq.wt.% NaCl) H_2O-NaCl fluid at lithostatic to supra-lithostatic fluid pressures during the early stages of the compressional stress regime. Subsequently, during progressive Variscan contraction both vein types were passively folded within characteristic, NW-verging, upright to overturned folds of the North Eifel. In contrast to both extensive veining events that characterise the tectonic inversion, quartz veining occurred rather occasionally during the main compression stage of orogeny.

This kinematic history eventually shows a clear relationship between fluid-pressure evolution and the stress-state changes in the basin and exemplifies that (supra-)lithostatic overpressures are easier to maintain during compressional tectonic inversion at the onset of orogeny, than during the main phase of compression. This intimate relationship during the stress-state evolution from extension to compression is illustrated by plotting the changing differential stress (σ_1-σ_3) against the vertical effective stress and the fluid-pressure evolution in a 2D brittle failure mode plot. The results show that the two vein types, which are induced at elevated to (supra-)lithostatic fluid pressures, can only form at low differential stress closely related in time to the tectonic switch. The tectonic setting and the localised stress state in the basin are thus both crucial to determine whether the lithostatic fluid overpressure can be sustained by a rock prior to failure at depth. These 2D brittle failure mode plots are moreover very useful to visualise the influence of rock parameters such as the tensile strength of rock on the maximum overpressures that can be built up during the transition between two stress regimes. This regional aspect of fluid redistribution within overpressured fluid reservoirs contrasts with the more localised fluid flow along fault systems caused by fault-valving.

The 3D aspect of stress transitions during tectonic inversion of a crust is, however, much more complex than represented in a 2D brittle failure mode plot. The tectonic switch, illustrated in these brittle failure mode plots, occurs at a specific isotropic stress state in which the three principal stresses are equal and $\sigma_1 - \sigma_3 = 0$. The chance that a stress state in the Earth’s crust equals an isotropic pressure state is, however, highly improbable. The 2D stress-state evolution visualised in the brittle failure mode plots is therefore an oversimplification of the actual 3D stress-state evolution in the Earth’s crust. To discuss the 3D aspects of stress transitions and to illustrate the complexity of triaxial stress transitions during inversion of Andersonian stress regimes, possible 3D stress-state evolutions are reconstructed based on the bedding-normal and bedding-parallel veins reflecting the early Variscan tectonic inversion. From these 3D stress-state reconstructions is concluded that, no matter what orientation of basin geometry or shortening, a transitional wrench tectonic regime should always occur between extension and compression. This transitional stage should contribute to the permeability enhancement during tectonic inversion, although structures that are related to this transitional stage have not yet been reported in a shortened basin affected by tectonic inversion at low differential stress. Ideally, a transitional ‘wrench’ tectonic regime should be implemented in brittle mode plots at the tectonic inversion.

It has been concluded from this research that the naturally fractured Ardenne-Eifel basin can serve a possible analogue to the present upper crust by its regional extent of overpressuring, but more importantly by demonstrating that a tectonic inversion from extension to compression at the onset of orogeny is the crucial timing during which maximum (lithostatic) overpressures can be sustained.

Keywords: tectonic stress inversion, fluid redistribution, late burial, early tectonic, quartz veins, overpressured basin, fractured reservoir, Variscan orogeny, Ardenne-Eifel basin

Samenvatting

Het afgelopen decennium is er een sterk toegenomen belangstelling in de processen die actief zijn aan de basis van de seismogene korst, met een bijzondere aandacht voor de vorming en karakterisering van verhoogde vloeistofdrukken die mogelijk aanleiding kunnen geven tot activiteit langs grote breuken en daarbij aardbevingen in de aardkorst kunnen veroorzaken. De basis van deze seismogene zone is echter niet rechtstreeks toegankelijk. Een van de mogelijkheden om dit probleem op te lossen en om tot een beter inzicht te komen van de vorming en de evolutie van deze verhoogde vloeistofdrukken op relatief grote diepte, is de studie van fossiele, natuurlijk gefractureerde bekkens. Binnen het brede gamma van deze natuurlijke analogieën kan het bestuderen van mineraalafzettingen en adersystemen leiden tot een belangrijk inzicht in de karakterisering van de vloeistoffen en de rol die de vloeistofdruk speelde tijdens gebergtevorming. In deze studie van mineraalafzettingen is een uitgebreide interdisciplinaire benadering noodzakelijk om deze vloeistofgerelateerde vervorming te kunnen bepalen.

Dit onderzoeksproject spitst zich toe op de bepaling van de vloeistofoverdrukken die worden gegenereerd op het einde van de begraving van een sedimentair bekken, dat wordt beïnvloed door een tektonische verkorting bij de aanvang van gebergtevorming. Aders die gevormd zijn door verhoogde vloeistofdrukken in sedimentaire bekkens bevatten waardevolle informatie over de metamorfe vloeistoffen die aanwezig waren op het einde van de begraving en bij de aanvang van de daaropvolgende gebergtevorming. Het onderzoek bestaat daarom uit een gedetailleerde geometrische en kinematische structurele analyse van twee opeenvolgende kwartsadertypes waarin de relatie met structurele kenmerken zoals gelaagdheid, splijting, plooien en breuken wordt onderzocht. Dit laat toe een geometrisch evolutionair model op te stellen dat de vorming van beide adertypes relatief plaatst ten opzichte van deze structurele kenmerken. Dit model werd verder verfijnd door middel van een doorgedreven microstructurele en microthermometrische analyse van de kwartsopvulling in de aders om fysico-chemische parameters zoals vormingstemperatuur, samenstelling van het fluïdum waaruit de aders vormden en de poriënvloeistofdruk te bepalen. Het onderzoek richt zich op het begrijpen waarom, hoe en wanneer vloeistoffen in overdruk gaan en hoe ze vervolgens evolueren tijdens gebergtevorming.

De studie richt zich meerbepaald op siliciklastische gesteenten die tijdens het Onder Devoon in het Ardennen-Eifel bekken werden afgezet. Dit bekken maakte deel uit van de noordelijke passieve rand van de kortstondige Rhenohercynische Oceaan, welke sloot tijdens de Variscische orogenese. De gesteenten zijn momenteel te bestuderen in de Hoge-Ardennenleisteengordel, welke zich uitstrekt in België, Frankrijk, Luxemburg en Duitsland. Deze leisteengordel maakt deel uit van de Rhenohercynische voorland plooi-en-breukgordel in de noordelijke frontzone van de Centraal-Europese Varisciden. De onderzochte ontsluitingen in deze studie bevinden zich rondom de Rursee en Urftsee stuwmeren in de noordelijke Eifel in Duitsland en behoren tot het noordoostelijke deel van de Hoge-Ardennenleisteengordel. De gesteenten waarin de bestudeerde aders vaak voorkomen zijn vervormd onder een zeer laaggradig metamorfisme, welke met een maximum begraving van 7 km van het Ardennen-Eifel bekken in het bestudeerde deel wordt gerelateerd. Het metamorfisme was gedeeltelijk vroeg-kinematisch en vond plaats tijdens de voortschrijdende Variscische vervorming van het Ardennen-Eifel bekken.

De analyse focust zich op twee opeenvolgende kwartsadertypes. Het eerste adertype doorsnijdt de gelaagdheid onder grote hoek en het tweede, daaropvolgende adertype is parallel aan de gelaagdheid georiënteerd. Het eerste adertype bestaat uit verschillende generaties die steeds onder grote hoek met de gelaagdheid georiënteerd blijven in de hoofdzakelijk overhellende plooien die de noordelijke Eifel karakteriseren. Dit toont duidelijk aan dat hun vorming de plooi- en splijtingsvorming van de

Variscische compressie voorafgaat. De rechte tot lensvormige kwartsaders zijn meestal beperkt tot zandsteenlagen, hoewel ze soms doorlopen in de aangrenzende incompetente siltsteenlagen. Aan de laagcontacten refracteren deze laatste aders op een zelfde manier als de splijting. Een microstructurele analyse van de kwartsopvulling van de laagnormale aders toont een voornamelijk dominantie van vezelige tot langwerpige en blokkige kwartskristallen aan waarbij de vezelige en langwerpige kristallen onder grote hoek met de aderwanden zijn georiënteerd. De kristallen werden gevormd door zowel syntaxiale als ataxiale groeimechanismen. Intern in de kristallen weerspiegelt een herhaaldelijk voorkomen van microscopische banden van het gastgesteente een episodische opening van de aders, typisch voor kristallen die gevormd zijn door het ‘crack-seal’ mechanisme. Pseudosecundaire vloeibare insluitsels komen voor onder grote hoek ten opzichte van de vezelige kristallen en zijn het gevolg van het insluiten van vloeistof in microspleten. Deze specifieke oriëntatie van de pseudosecundaire ‘trails’ bevestigt enerzijds dat kristalgroei gebeurde in kleine ‘crack-seal’ stappen en anderzijds dat de laagnormale aders kunnen worden gedefinieerd als extensie aders die ontwikkelden tijdens lage differentiaalspanningen en oorspronkelijk groeiden in Mode I spleten. Dit gebeurde in een gesteente waarin de porositeit al aanzienlijk gereduceerd was tijdens de begraving. De oriëntatie van de vloeibare insluitsels is bijgevolg bijzonder nuttig om de spanningstoestand in het Ardennen-Eifel bekken ten tijde van laagnormale adervorming te reconstrueren. Ze tonen aan dat de maximale hoofdspanning (σ_1) verticaal was en werd veroorzaakt door het gewicht van de bovenliggende lagen. De aders openden zich parallel aan de kleinste horizontale spanningsrichting (σ_3) en tonen daarbij de extensierichting van het Ardennen-Eifel bekken aan. De verdere ontwikkeling van de aders gebeurde in het vlak van de maximale (σ_1) en intermediaire (σ_2) hoofdspanningsrichting. Ook na de adervorming bleven kleine microspleten zich in het gesteente ontwikkelen met als resultaat de vorming van secundaire vloeibare insluitsels in hetzelfde spanningsveld als de pseudosecundaire insluitsels.

De consistente oorspronkelijke oriëntatie van de laagnormale aders in de noordelijke Eifel, komt overeen met de oriëntatie van de kwartsaders die voorkomen tussen mullions in the centrale deel van de Hoge-Ardennenleisteengordel in België. Deze correlatie benadrukt dat deze adervorming regionaal is. Door (micro)structurele analyse kon uiteindelijk afgeleid worden dat laagnormale aders zich ontwikkelden tijdens lage differentiaalspanningen die karakteristiek zijn voor de NW-SE richting waarin het Ardennen-Eifel bekken opende tijdens de laatste fase van een extensieregime. Een structurele verandering van de oriëntatie van de aders van NW-SE in de Ardennen naar NNW-SSE in de noordelijke Eifel kan verklaard worden doordat na de adervorming de Ardennen als het ware rond het Brabant Massief in het noorden gedrapeerd werden tijdens de Variscische vervorming. Naast deze oriëntatie-analyse is de spatiëring van de aders in de zandsteenbanken onderzocht om de relatie tussen de aderafstand en de laagdikte waarin ze gevormd zijn te bepalen. De resultaten tonen aan dat een er een quasi lineair verband bestaat tussen de spatiëring van de aders en de laagdikte in dunne (<40 cm) zandsteenlagen, maar dat deze relatie niet meer lineair is naarmate de laagdikte van de zandsteenbanken (> 40 cm) toeneemt. In de dikke zandsteenlagen lijkt de laagdikte geen invloed meer te hebben op de spatiëring van de aders. Dit patroon lijkt op de spatiëring van spleten die het gevolg zijn van een verzadiging aan spleetontwikkeling in het gastgesteente. Dit suggereert dat tijdens de initiële vorming van aders het gesteente verzadigd kan geraken aan de aanwezigheid van spleten en enkel een aangroei van de ader zal optreden tijdens verdere extensie, tenzij het regionaal spanningsveld verandert en nieuwe adergeneraties worden gevormd die de vorige doorsnijden.

In de noordelijke Eifel komen vervolgens laagparallelle kwartsaders voor die de laagnormale aders doorsnijden en ze ook verplaatsen. Laagparallelle aders zijn bovendien continu in de kernen van de plooien aanwezig zonder daarbij in dikte te veranderen. Laagparallelle aders komen zowel voor in zandsteen- en siltsteenlagen, als aan laagcontacten tussen beide gesteentesoorten. Macroscopisch zijn de aders gekenmerkt door een gelamineerd uiterlijk, welke bestaat uit een afwisseling van verschillende generaties kwartslamellen, waarop dikwijls wrijfkrassen worden waargenomen, en dunne fragmenten van het gastgesteente. Een verscheidenheid in microstructuren wijst op verschillende mechanismen van opvulling en complexe adergroei. Enerzijds komen afgescheurde banden van het gastgesteente voor, die parallel aan de aderwand en dus de gelaagdheid zijn georiënteerd. Dit wijst op het openen van de ader onder grote hoek met de gelaagdheid. Dit openingsmechanisme wordt bevestigd door de aanwezigheid van pseudosecundaire vloeibare insluitsels in de kwartskristallen. Ook de aanwezigheid van blokkige lamellen in de aders, welke een kristalgroei in een open holte weerspiegelen, is indicatief voor een aderopening bijna loodrecht op de gelaagdheid. Verder zijn deze lamellen gekarakteriseerd door laag-parallelle stylolieten die drukoplossing in periodes tussen de kristalvorming aantonen. Anderzijds komen ook lamellen voor die ontwikkeld zijn tijdens laagparallelle schuifbewegingen tijdens de aanvang van de plooiing. De kwartskristallen in deze schuiflamellen zijn tijdens de algemene vervorming later dynamisch gerekristalliseerd.

Het uitgesproken gelamineerd karakter van de laagparallelle aders is dus te wijten aan een adervorming gedurende meerdere afwisselende fasen van laagnormale opheffing en laagparallelle schuifbewegingen. Op basis van deze microstructuren, kunnen deze laagparallelle aders gedefinieerd worden als extensie aders en extensie-schuifvervormingsaders die beiden ontstaan bij relatief lage differentiaalspanningen. Dit adertype is het brosse resultaat van de eerste vervormingsfasen van de Variscische verkorting tijdens het compressieve spanningsregime en toont een regionaal spanningsveld aan ten tijde van vorming, waarin de maximale hoofdspanning (σ_1) nu horizontaal gelegen is en overeenkomt met een NW-SE georiënteerde tektonische compressie (σ_T). De minimale spanningsrichting (σ_3) kwam in deze configuratie overeen met de verticale begravingsspanning, die ten opzichte van de vorming van de laagnormale aders in grootte niet veranderd is. De evolutie van de vorming van laagnormale naar laagparallelle aders wijst op de overgang van extensie (rek) naar compressie bij het begin van de Variscische orogenese en weerspiegelt de vroeg-orogenetische compressieve tektonische inversie.

Een petrografische en microthermometrische analyse van vloeibare insluitsels in de aderkwarts heeft vervolgens bijgedragen tot de bepaling van de druk- and temperatuursomstandigheden aanwezig tijdens de adervorming van beide types. Dit liet toe om veranderingen in de vloeistofdruk te koppelen aan de spanningsevolutie tijdens de tektonische inversie. De gebruikte methode hiervoor houdt in om op een druk-temperatuursdiagram de isochoren, berekend op basis van het zoutgehalte en de homogenisatietemperaturen van de vloeibare insluitsels, te laten snijden met een onafhankelijke geothermometer. In deze studie is aan de hand van de reflectiviteit van vitrinieten een maximale begravingstemperatuur van 250°C aangetoond. De microthermometrische resultaten geven aan dat de laagnormale extensie aders zijn gevormd uit een waterig fluidum met een laag zoutgehalte (3,5-8 eq.wt.% NaCl) en dat bijna-lithostatische tot lithostatische vloeistofdrukken de tektonische inversie voorafgaan. Na de tektonische inversie, zijn de laagparallelle aders eveneens uit een waterig fluïdum met een laag zoutgehalte (4-7 eq.wt.% NaCl) gevormd, maar onder lithostatische tot supralithostatische vloeistofdrukken en dit tijdens de vroege stadia van het compressieve stress regime. Na de tektonische inversie werden beide adertypes passief vervormd in de NW-overhellende plooien tijdens de hoofdfase van de Variscische orogenese. In tegenstelling tot de uitgebreide aderontwikkeling tijdens de tektonische inversie, trad adervorming enkel lokaal op tijdens de hoofdfase van de Variscische vervorming en is deze enkel gerelateerd aan lokale vervorming.

Deze kinematische geschiedenis toont uiteindelijk een belangrijke relatie aan tussen veranderingen in de vloeistofdruk enerzijds en spanningsveranderingen in het bekken anderzijds. Bovendien werd aangetoond dat vloeistofoverdrukken gemakkelijker aanwezig zullen blijven tijdens een compressieve tektonische inversie aan het begin van een gebergtevorming, dan tijdens de daaropvolgende plooi-en-splijtingsvorming gerelateerd aan de verkortingsgedomineerde hoofdfase van een orogenese. Deze relatie kan worden geïllustreerd in een tweedimensionale ‘brittle failure mode plot’. In dit diagram wordt de spanningsevolutie tijdens de tektonische inversie uitgewerkt door het weergeven van de veranderende differentiaalspanning ($\sigma_1 - \sigma_3$) ten opzichte van de verticale effectieve spanning en de evolutie van de vloeistofdruk. Een dergelijk diagram werd opgesteld voor de twee tijdstippen van adervorming, namelijk voor en na de inversie. Ze toont aan dat de aders, die worden geïnduceerd bij verhoogde tot (supra)lithostatische vloeistofdrukken, enkel gevormd kunnen worden bij lage differentiaalspanningen die in de tijd gerelateerd zijn aan de tektonische inversie. Zowel het tektonisch kader als de regionale spanningsevolutie in een bekken zijn dus van cruciaal belang om te bepalen of vloeistofoverdrukken kunnen aanwezig blijven tijdens de overgang van spanningsregimes alvorens de gesteenten breken. Een dergelijk tweedimensionaal ‘brittle failure mode plot’ is bovendien erg nuttig om de invloed van de gesteenteparameters te visualiseren. Zo bepaalt bijvoorbeeld de treksterkte van het gesteente de maximale overdruk die wordt opgebouwd tijdens een tektonische inversie. Dit regionale aspect van vloeistofherverdeling in bekkens onder hoge vloeistofdruk contrasteert sterk met de meer gelokaliseerde vloeistofherverdeling die langs breuksystemen gebeurt tijdens breukactiviteit.

Het 3D aspect van spanningsverandering tijdens de tektonische inversies van de bovenkorst is echter complexer dan wordt geïllustreerd in het 2D ‘brittle failure mode plot’. In dit diagram gebeurt de tektonische omschakeling tussen twee spanningsregimes bij isotrope spanningstoestand waarin de drie belangrijkste hoofdspanningen gelijk zijn en waarbij $\sigma_1 - \sigma_3 = 0$. De kans dat een spanningstoestand in de aardkorst gelijk is aan een isotrope spanningstoestand is echter zeer onwaarschijnlijk. De spanningsevolutie gevisualiseerd in het 2D ‘brittle failure mode plot’ is daarom een vereenvoudiging van de werkelijke 3D spanningsevolutie in de aardkorst. Om dit probleem en de complexiteit van drie-assige spanningsveranderingen in een Andersoniaans spanningsregime te behandelen, werden 3D spanningsreconstructies van de vroeg-Variscische compressieve tektonische inversie opgesteld waarin de twee bestudeerde adertypes als eindtermen dienden. Uit deze 3D spanningsreconstructies werd besloten dat, ongeacht de oriëntatie van het bekken of verkortingsrichting, tijdens de overgang van extensie (rek) naar compressie er altijd een kortstondig schuifvervormingsregime wordt voorspeld. Dit overgangsregime draagt bij aan de verhoogde permeabiliteit tijdens een tektonische inversie. Hoewel schuifvervormingsstructuren gerelateerd aan deze overgangsfase nog niet werden vermeld in bekkens die onderworpen zijn aan een tektonische inversie bij een lage differentiaalspanning, zou dit overgangsregime toch geïmplementeerd moeten worden in het 2D ‘brittle failure mode plot’ op het punt van de tektonische inversie.

Uiteindelijk werd er uit dit onderzoek geconcludeerd dat het gefractureerde Ardennen-Eifel bekken kan dienen als een natuurlijk analoog voor de bovenkorst door het regionaal voorkomen van overdrukken. De belangrijkste conclusie is echter dat de tektonische omschakeling van extensie naar compressie tijdens de aanvang van een orogenese het cruciale tijdsmoment is om maximale overdrukken te genereren en te onderhouden.

Trefwoorden: tektonische spanningsinversie, vloeistofherverdeling, begravingsgerelateerde en vroeg-tektonische kwartsaders, overdrukken, gefractureerd reservoir, Variscische gebergtevorming, Ardennen-Eifel bekken

Table of contents

LIST OF BOXES

CHAPTER 1 Introduction

1.1 The role of fluid overpressures in the Earth’s crust

In the recent decade, there is an increased interest in the processes active at the base of the seismogenic crust, with a particular focus on the evolution and characterisation of elevated fluid pressures that could possibly drive fault rupturing and initiate major earthquakes. In a continental context, the base of seismogenic zone - or the **brittle upper crust** - is situated in a depth range of 7 km to 15 km (cf. Sibson 1983), above which overburden pressure ranges from ~180 MPa to ~400 MPa and ambient temperature from ~200°C to ~400°C. Primarily due to the ongoing low grade metamorphism, the production of fluids commonly leads to sustained fluid overpressures, *i.e.* suprahydrostatic, in this low-permeability environment. In a number of particular cases of major earthquakes within the upper crust (*e.g.* L’Aquila 2009, Apennine Mountains, Italy), studies have shown a direct link between the fore- and aftershocks and the presence of overpressured fluids at the base of the main earthquake rupture (Miller *et al.* 2004, Pio Lucente *et al.* 2010, Savage 2010, Terekawa *et al.* 2010). It is clear from these studies that overpressured fluids play an important role in seismogenesis, however, it is currently far from understood in which particular period of the seismic cycle these high fluid pressures play an important role. The base of the seismogenic crust, however, is not directly accessible. One of the possibilities to overcome this research problem is the study of natural fossil analogues to pursue a better understanding of the formation, evolution and characterisation of overpressured fluids at relatively great depths in the crust.

In the recent decade, there is an increased interest in the processes active at the base of the seismogenic crust, with a particular focus on the evolution and characterisation of elevated fluid pressures that could possibly drive fault rupturing and initiate major earthquakes. The base of the seismogenic zone, however, is not directly accessible. One of the possibilities to overcome this research problem is the study of natural fossil analogues to pursue a better understanding of the formation, evolution and characterisation of elevated to lithostatic fluid overpressures at relatively great depths.

Within the broad framework of natural analogues, vein and fracture studies provide an important insight in the role of the fluid pressure and the characterisation of fluids during a complete orogenic deformation cycle. These deformation cycles represent the changes in tectonic stress regimes from basin subsidence to orogeny and to subsequent orogenic collapse. Basin inversion might be caused by a variety of mechanisms ranging from continent-continent to arc-continent collision resulting in compression, orogeny, uplift or fault reactivation. Sibson (1998, 2000, 2004) has numerously demonstrated by means of theoretical models that low differential stresses, related to a period of tectonic inversion, allow the build-up of high to supra-lithostatic fluid overpressures, which may give rise to extensional fracturing and extension veins. In the light of basin inversion, the tectonic switch from extensional to compressional Andersonian stress regimes, defined as a positive compressional tectonic inversion, has, however, only been studied from the point of view of the reactivation of normal faults in sedimentary basins as reverse faults during later compression (*e.g.* Cooper *et al.* 1989, Glen *et al.* 2005, Hayward & Graham 1989, Williams *et al.* 1989). This reactivation takes place at elevated differential stress during protracted compression (Sibson 1995) but does not provide insight in processes such as fracturing and veining that accompany the actual switch in stress regimes. The aspect of the generation of high fluid pressures during tectonic inversion has not been handled in these basin inversion studies.

Although veins related to overpressured fluids existing in the Earth's crust during orogenic deformation have been recognised in various recent (*e.g.* Savage 2010, Terekawa *et al.* 2010) and ancient (*e.g.* Brems *et al.* 2009, Cox 1995, Hilgers *et al.* 2006b, Kenis *et al.* 2002a, Nielsen *et al.* 1998, Rodrigues *et al.* 2009, Sibson & Scott 1998) tectonic settings, the link with changes in tectonic stress regimes has been undervalued. Focusing more closely on deformation structures related in time to the actual tectonic switch between stress regimes allows determining the processes active during the incipient shortening of sedimentary basins. The kinematics and composition of syntectonic veins, which have been studied frequently in orogens (*e.g.* Hilgers & Urai 2002, Schultz *et al.* 2002, Urai *et al.* 1991), cannot provide the necessary information to determine the link between overpressuring and stress-state changes during inversion. It is therefore important to actively seek for proper structures that reflect the incipient shortening phase of a deformation cycle. Early pre-tectonic veins, which form prior to folding and cleavage development and which can have an important impact on the palaeorheology of rock (*e.g.* Kenis *et al.* 2002a, 2004), are often neglected in structurally complex systems. If studied carefully, these veins contain, however, key information concerning fluids that are involved during the development and initial deformation of sedimentary basins. Moreover, if these veins result from overpressured fluids at depth, then they can be used to study the geometric and hydraulic properties of fracture networks in the crust that may serve as natural analogues for fractured reservoirs (Gillespie *et al.* 1999, Johnston & McCaffrey 1996, Mazzarini *et al.* 2010, Vermilye & Scholz 1995).

The three key elements for generating veins at depth in the upper crust are a well-defined source of the fluids, subsequent fluid redistribution in a pore network or along secondary features such as fractures and an eventual fluid discharge zone in which crystals or minerals are precipitated from the fluid (Cox *et al.* 2001, Etheridge *et al.* 1984). This research focuses on the last two elements at a relatively small scale. The generation of fluid overpressures can only occur if the permeability of rock remains sufficiently large to allow the captation of fluids. The compaction and lithification, which increase with depth and burial, are important mechanisms that can destroy the porosity and permeability of rock. Lithification and compaction already take place during diagenesis and may continue during low-grade metamorphism (Laubach *et al.* 2010). Siliciclastic basins in which alternating impermeable to low-permeability (*e.g.* shales, pelites) and higher-permeability (*e.g.* sandstones) lithologies occur, are very promising to seal and compartmentalise, respectively, the remaining fluids during compaction. Impermeable layers, such as shales, can compartmentalise the pore fluid system during burial, allowing the pore fluid pressure to rise without any vertical connectivity between the compartmentalised competent units (Gillespie *et al.* 2001, Wangen 2000). As a consequence of compaction and isolation, the fluid pressure in the higher-permeability fluid-saturated compartments will increase and may eventually reach supra-hydrostatic to lithostatic fluid pressures, exerted by the overlying rock-mass but decoupled from the water column in higher levels (van der Pluijm & Marshak 1997).

The main mechanisms considered to be responsible for the built-up of overpressures are disequilibrium compaction, the increase of volume expansion or fluid movements (Hilgers *et al.* 2006c, Swarbrick & Osborne 1998). Faults or large-scale fractures cross-cutting these high-pressure compartments during deformation can drain these fluids to upper levels and can restore the hydrostatic fluid pressure in the compartment (Boullier & Robert 1992, Cox *et al.* 2001). The drainage of deeper burial fluids to higher levels in the upper crust may give rise to mineral precipitation in zones owing to a fluid pressure gradient. Recurrent cyclic fluid pressure built-up and subsequent discharge can eventually create economically interesting mesothermal ore deposits (Bons 2001, Boullier & Robert 1992, Cox 1995, Micklethwaite *et al.* 2010, Sibson & Scott 1998). The cyclic process of discharging fluids and the subsequent rapid fluid pressure drop is classically referred to as 'fault valving' in literature, during which permeability is repeatedly regenerated (Cox 1995, Sibson 1990). This process is related to short-lived and local stress transitions in a consistent remote stress regime (*e.g.* Collettini *et al.* 2006, Foxford *et al.* 2000, Muchez *et al.* 2000, Nielsen *et al.* 1998) and occurs worldwide in the seismogenic mid- to upper crust (Cox 2010), although being spatially restricted to the zone of discharge along the fault(zone).

Overpressures reaching lithostatic values and accumulated within a sedimentary basin can, however, also be favoured by the absence of faults or when faults are oriented unfavourably to allow reactivation during compression (Sibson 1998). In this scenario, drainage of the overpressured compartments cannot occur. As result of the absence of drainage, the interior of these overpressured reservoirs are internally naturally fractured (Bradley & Powley 1994, Gale *et al.* 2007). When fluid pressure is sufficiently large to overcome the rock strength at low differential stress, a process called hydraulic fracturing (Cosgrove 1995a, 1997, 2001), extension to extensional-shear fracturing will occur, giving rise to a transient fracture permeability in which precipitation from the fluid might occur. The outward push of a fluid in a microcrack has the effect of locally creating a tensile stress at the crack tip and as the crack propagates, the volume increases. When new fluids enter the crack, the fluid pressure will decrease afterwards (van der Pluijm & Marshak 1997). Oil engineers commonly use hydraulic fracturing to enhance permeability around a bore hole and to increase the productivity in a well in an oil/gasfield. A better knowledge of the parameters that control hydraulic fracturing, *e.g.* by studying natural examples, can eventually contribute to the understanding of this technique.

A network of hydraulic fractures in alternating sequences developed at low differential stress are termed fault-fracture meshes and typically develop in fluid pressure pulses (Sibson 1996, 2001). Periods in the deformation cycle in which the crust is affected by low differential stresses are those specific moments close to the tectonic switch between stress regimes and thus during tectonic basin inversion (Sibson 2004). Especially the increase in mean stress during compressional tectonic inversion can lead to elevated pressures of fluids captured during burial and compaction in sedimentary basins (cf. Sibson 2000). This suggests that changes in the stress regime, irrespective of the magnitude of the principal stress direction, are coupled to changes in the pore pressure. Elevated fluid pressures have also been demonstrated by in situ borehole pore pressure measurements in shallower environments (*e.g.* Hillis 2003, Van Ruth *et al.* 2003). The tectonic regime and the stress state in the basin are thus both crucial to determine whether the overpressured fluids can be sustained by rock prior to failure. While the transition between tectonic stress regimes is very important in determining the intensity and possibility of fluid redistribution (Sibson 2004), the stress state in the basin (Sibson 2000) and the differential tensile strength of rock in low-permeability alternating sequences (Cosgrove 1995a) will define which types of fractures, and eventually which vein types will develop. Using the orientation of different vein types reflecting the compressional tectonic inversion can therefore be applied as a tool to evaluate the stress-state evolution of a basin during incipient orogenic shortening.

Although a clear relationship between fluid redistribution (vein formation) and stress changes has thus been established theoretically, the evidence of this relationship as preserved in vein systems has not received significant attention. Vein studies, however, provide insights into the role of the fluid pressure and the evolution of P-T conditions during a complete deformation cycle (*e.g.* Boullier *et al.* 1991, Boullier & Robert 1992, Crispini & Frezzotti 1998, Kenis *et al.* 2000). The above shortcoming as reflected in vein studies highlights the needs for further, multi-disciplinary research on veins. This study eventually aims at contributing to this discussion by investigating and correlating the stress-state changes in the Ardenne-Eifel basin at the onset of Variscan orogeny with the changes in pore-fluid pressures during ongoing prograde low-grade metamorphism.

1.2 The High-Ardenne slate belt as research area

1.2.1 Vein development in a low-grade metamorphic terrain

The frontal zone of the central European Variscides, *i.e.* the northern front of the Rhenohercynian fold-and-thrust belt, forms an important area for the study of fluid flow and mineralisation. The High-Ardenne slate belt (HASB), currently cropping out in Belgium, France, Luxemburg and Germany, is one of the areas in this fold-and-thrust belt that partially reflects the Variscan tectonic shortening of the

Lower Devonian Ardenne-Eifel sedimentary basin (see Chapter 2 for a detailed geodynamic setting). This slate belt turns out to be a very suitable study area to tackle the above quoted research questions. Numerous historical, structural and geochemical studies in the anchi- to epizonal metamorphic zone of the Ardenne-Eifel basin have described the formation of pre-kinematic quartz veins relative to the Variscan penetrative deformation, indicating a considerable metamorphic fluid migration accompanied with various gases (Breddin 1930, Breddin & Hellermann 1962, Darimont 1986, Darimont *et al.* 1988, Fielitz 1987, Fielitz 1992, 1995, 1997, Fielitz & Mansy 1999, Jongmans & Cosgrove 1993, Lohest *et al.* 1908, Wünstorf 1943). The veins commonly occur in sandstones and are mostly oriented at high angle to bedding in the typical alternating multilayer sequences of the High-Ardenne slate belt. They are dominantly quartz-rich and reflect the low-grade metamorphism in their mineralogy. In the epizonal part of the slate belt, the veins contain regularly some of the metamorphic minerals found in the adjacent metamorphic rocks (*e.g.* ottrelite, albite, biotite, chlorite, pyrophyllite, garnet, andalusite) suggesting that these host rocks acted as source of fluids that laterally migrated into the fractures (see references in Fielitz & Mansy 1999, Kenis 2004).

Recent (micro)structural and micro-thermometric analysis performed on quartz veins in Lower Devonian metasediments in the central part of the High-Ardenne slate belt (Bertrix-Bastogne-Bütgenbach area, Belgium), revealed that the formation of these well-arranged veins can be attributed to an early, pre-folding, regional extensional fracturing event (Kenis *et al.* 2002a, Kenis 2004, Kenis & Sintubin 2007). This fracturing is exemplified by lenticular, bedding-normal quartz veins organised in parallel arrays (Figure 1.1b), which were formed by the mechanism of hydraulic fracturing at low differential stress in regionally occurring high fluid-pressure compartments at the latest stages of the burial history (Kenis *et al.* 2002a, Urai *et al.* 2001). Prior to these studies, Darimont *et al.* (1988) already assumed that hydraulic fracturing caused the formation of lensoid veins, based on pioneering fluid inclusion studies on lensoid veins in Bastogne (Belgium). Owing to the occurrence of high fluid pressures at the moment of veining, the Lower Devonian Ardenne-Eifel basin can be considered as an exposed a 340 million-year-old fractured reservoir (Hilgers *et al.* 2000, Hilgers *et al.* 2006a, Kenis & Sintubin 2007).

1.2.2 Mullion occurrence and rheology

In the High-Ardenne slate belt, particular cuspate-lobate structures, defined as mullions, occur between the extension veins. In general, irrespective of the presence of veins, mullions are a specific type of concentric folding typical for interlayered competent and incompetent beds with a given relationship of layer thickness and viscosity contrast (Smith 1977). In literature, the occurrence and the development of these specific mullions in the High-Ardenne slate belt have been the subject of a century long discussion (see historical discussions in Kenis *et al.* 2002a, Kenis 2004, Kenis & Sintubin 2007, Sintubin 2008). The discussion was primarily based on the conflicting coexistence of extensional (veins) and compressional (mullions) structures. It remained a controversy as to whether the mullions were formed by the process of layer-parallel extension (boudinage) or purely by shortening (mullion formation). Although these structures originally were described as the classical rectangular boudins (Lohest *et al.* 1908), recent independent studies (Kenis *et al.* 2002a, Kenis 2004, Urai *et al.* 2001) have determined that these structures are in fact mullions developed during a two-phased, brittle-ductile history: in a first brittle phase, extension veins developed during progressive burial in a basin in which the maximum principal stress σ_1 was vertical, corresponding to the load of the overburden (Figure 1.1b). Subsequently, extension veining was followed by layer-parallel shortening at the onset of Variscan orogeny in which the quartz veins became more competent than the sandstone in which they are confined in. As result of the veins acting as mechanical boundaries, a cuspate-lobate geometry of the pelite-psammite interface (mullions) formed ductilely during layer-parallel shortening (Figure 1.1c). In particular, the unusual high aspect ratio of mullions in the High-Ardenne slate belt versus the low aspect ratio of classical boudins caused a questioning of boudinage as a mechanism for veining. Kenis (2004) determined that shortening leading to mullion formation occurred after the compressional tectonic inversion at the early stages of the Variscan orogeny, in a basin with a specific stress state in which maximum principal stress σ_1 was oriented horizontally at that time. In a final stage, these mullions folded passively around the characteristic north-verging folds in the southern part of the High-Ardenne slate belt (Figure 1.1d).

With respect to the occurrence of these mullions, *e.g.* published in Pilger & Schmidt (1957), Sippli (1981), Spaeth (1986) and Kenis (2004), two different areas can be distinguished within the High-Ardenne slate belt: a central part (cHASB), characterised by the presence of mullions pinned by bedding-normal lensoid veins, is outlined from Bertrix - Bastogne - Bütgenbach (Ardennes, Belgium) to Dedenborn (North Eifel, Germany). For the description of these specific outcrops in Belgium and Germany, it is referred to Kenis (2004) and Urai *et al*. (2001) respectively. On the geological maps in the geodynamic setting (Chapter 2), the occurrence of mullions and thus the cHASB will be indicated by a grey semi-transparent overlay. In the North Eifel, mullions have also been reported in the south-eastern Gedinnian cover of the Lower Palaeozoic Stavelot-Venn inlier (Spaeth 1986). The occurrence of mullions more or less corresponds to the occurrence of the Monschau shear zone and epizonal metamorphic conditions. Refolded mullions indicate that mullion formation predates the minor folds in the Monschau shear zone (Fielitz 1992).

Secondly, a peripheral part situated in the northeastern part of the High-Ardenne slate belt (pHASB, North Eifel, Germany) is defined in which planar quartz veins occur in ‘undeformed’ segments which do not show the mullion morphology (cf. Van Noten *et al.* 2008). The Pragian/Siegenian to Emsian alternating metasediments of the pHASB expose a higher structural level of the Ardenne-Eifel basin than the Lochkovian/Gedinnian to Pragian/Siegenian metasediments in the cHASB. Several German historical studies report that quartz veins are ubiquitous in these Lower Devonian sequences of the pHASB. Contrary to the regionally well-arranged vein set in the central part, quartz veins (‘*Milchquarzgänge*‘) are reported to be much less consistent in orientation (Baum 1955,

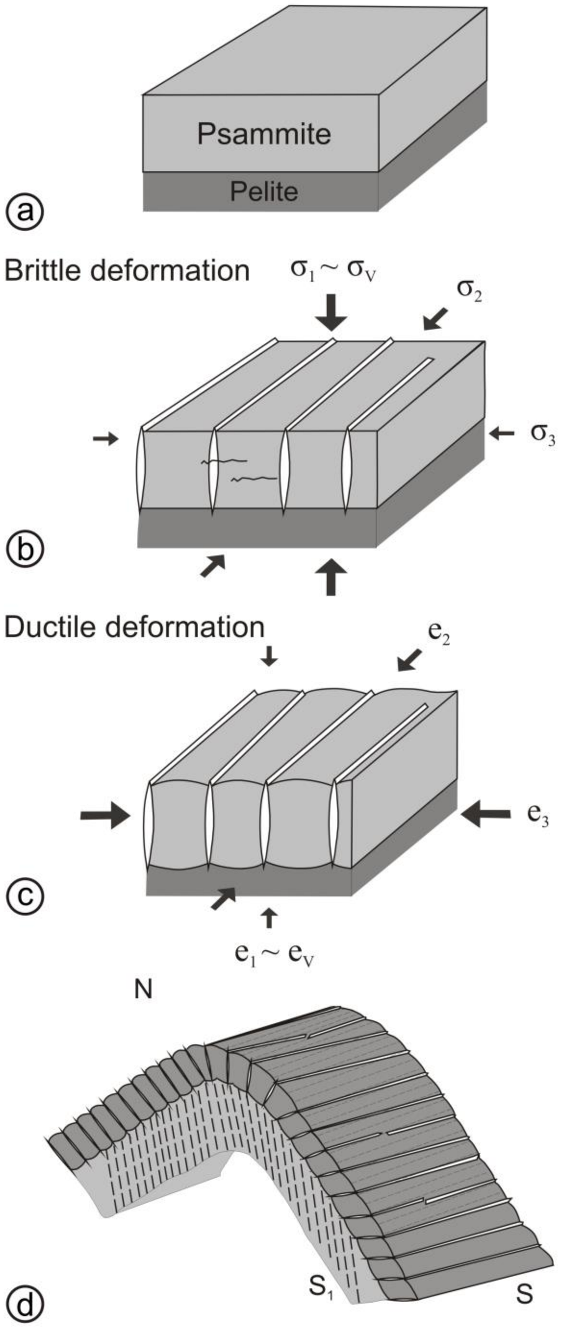

Figure 1.1: Evolutionary model developed by Kenis (2004) as explanation of mullion structures in the High-Ardenne slate belt. **(a)** Undeformed alternating rock sequences during burial. **(b)** Formation of extension veins exemplifying the particular stress state in the basin at the time of vein formation. **(c)** Layer-parallel shortening causing the formation of double-sided mullions after compressional inversion. **(d)** Passive folding of mullions into characteristic north-verging folds of the cHASB. (σ_1; σ_2; σ_3 are maximum, intermediate and minimum principal stress respectively; e_1; e_2; e_3 are maximum, intermediate and minimum stretch directions respectively).

Breddin 1930, Breddin & Hellermann 1962, Hoffmann 1961, Zier & Kuhl 1999). The occurrence of several cross-cutting quartz-vein generations (Breddin & Hellermann 1962) might indicate a more complex fracturing and veining history than in the cHASB. Moreover, the absence of mullions associated with pre-tectonic quartz veins suggests that incipient Variscan shortening must have been expressed differently in the peripheral part. In these historical studies, quartz veins have been explained to form by various mechanisms ranging from mineral infill in an already existing regional fracture system (Breddin & Hellermann 1962) to a relationship with the cleavage planes (Breddin 1930). To date, however, a detailed (micro)structural analysis of the quartz veins in the pHASB is still lacking, although the information from such an analysis of these veins might explain the differences between veining in mid-crustal levels and in upper-crustal levels as reflected in the cHASB and the pHASB respectively. The peripheral part of the High-Ardenne slate in the North Eifel forms therefore a suitable study area for this research.

1.2.3 Bedding-parallel veins in the North Eifel

Besides the absence of mullions, the peripheral part of the High-Ardenne slate belt is characterised by the presence of numerous quartz veins oriented parallel to bedding, clearly a different vein type than the (intermullion) bedding-normal veins (Baum 1955, Hilgers *et al.* 2000, 2006a). In the overall part of the cHASB, however, these veins have not been reported. Only locally in one quarry at Bastogne, a bedding-parallel vein has been observed (Vanbrabant & Dejonghe 2006), although it has not been studied and its fabric and its formation are unknown. To the west of the pHASB, in other parts of the Rhenish Massif, quartz-rich bedding-parallel veins have also been recognised (de Roo & Weber 1992, Weber 1980, Weber 1981). In a tentative study, Hilgers *et al.* (2000, 2006a) suggested by studying the microfabric of one of these bedding-parallel veins, that this vein type might be formed during Variscan contraction and might be related to overpressuring in the Ardenne-Eifel basin. However, despite this study, to date bedding-parallel veins in the North Eifel have been studied insufficiently and their regional significance might be underestimated. These veins can, however, provide important insights into the early structural evolution of fold-and-thrust belts, even though some growth features within the veins might be obscured by subsequent reactivation or recrystallisation of the vein during orogeny (Séjourné *et al.* 2005). The lack of knowledge on the regional significance of the bedding-parallel veins in the pHASB thus highlights the needs for a thorough (micro)structural analysis of these veins.

In the past decade, bedding-parallel veins have caused a considerable debate in literature. They occur worldwide varying from various sedimentary basins to complex structural mountain ranges. It has been demonstrated in these studies that the formation of bedding-parallel veins may originate from gravitational sliding in sedimentary basin (*e.g.* Fitches *et al.* 1986), pure uplift during burial stages (*e.g.* Henderson *et al.* 1990), thrusting during early orogenic compression (*e.g.* Jessell *et al.* 1994), flexural-slip folding (*e.g.* Tanner 1989) or could have a post-folding origin. Although an extensive amount of studies on bedding-parallel veins exists worldwide, there are several limitations in these different models. Often only the structural development of these veins is explained without implementing the combined role of fluid pressure and tectonic stress-state changes. The independent model that is developed in this work and that explains the formation of bedding-parallel veins in the North Eifel will contribute to the general understanding of bedding-parallel veins, but more importantly it can be used as the solely model in which fluid pressure and stress-state changes are implemented and are demonstrated to be crucial to form bedding-parallel veins. The specific approach in this work will be a major improvement with respect to the previous models presented in literature. The constructed model may eventually form a base for a reconsideration of some of these models.

1.2.4 North Variscan front zone

Veins are not only restricted to the High-Ardenne slate belt. The northern front of the Rhenohercynian fold-and-thrust belt, more specifically the North Variscan front zone, forms an important area for the study of fluid flow and mineralisation. Several vein systems at the northern front have been exploited for their economically interesting minerals enclosed in the veins (*e.g.* Muchez *et al.* 1995 1998, 2000, Nielsen *et al.* 1998, Sindern *et al.* 2007). It has been demonstrated that during late Variscan tectonic compressional deformation, large-scale fluid flow and fluid migration has occurred along the major North Variscan (Aachen-Midi) thrust fault(s) (see Chapter 2 for geodynamic setting). Relative hot fluids, which were not in equilibrium with the host-rock conditions characteristic of the front zone, are driven upwards causing thermal anomalies (Lünenschloss *et al.* 1997, 2008, Meere 1995b, Meere & Banks 1997, Schroyen & Muchez 2000, Wagner & Boyce 2003). Furthermore, the area between the North Variscan front zone and the southern hinterland has been the subject of many structural reconstructions of the inverted Rhenohercynian Basin (DEKORP 1991, Oncken *et al.* 1999, 2000, von Winterfeld & Walter 1993, von Winterfeld 1994). Despite this large interest in Variscan tectonics and fluid flow in the frontal zone of the Rhenohercynian fold-and-thrust belt, the interaction and link between changes in the tectonic stress regime, fluid pressure changes and fluid migration has never been investigated in detail. However, Sibson (2004) and Cox (2010) have demonstrated that this interaction is important for the genesis of ore deposits. A better knowledge of the link between mountain building processes and ore genesis could have major economic implications (cf. Blundell 2002). The overpressured compartments in the High-Ardenne slate belt form therefore an excellent research area to investigate this interaction.

Kenis (2004) already demonstrated by the bedding-normal vein in the cHASB, that veins are particularly useful to reconstruct the stress state in the basin at the time of vein formation. Different vein types, moreover, can be used to determine changes or transitions in the stress state in a basin during progressive deformation (Boullier & Robert 1992, Laubach & Diaz-Tushman 2009). Van Baelen (2010) recently postulated that the fluids present in these overpressured compartments of the Ardenne-Eifel basin, currently exposed as veins in the High-Ardenne slate belt, might form the fluid reservoir from which fluids were expulsed towards higher structural levels in the orogen. An analogue of the High-Ardenne slate belt might have been the source of the fluid discharge zone in the Variscan front. Although the missing link between a source as overpressured compartments and the sink in upper levels has not been demonstrated, late Variscan discordant quartz veins studied in the Herbeumont-Bertrix area (Belgium) by Van Baelen (2010), evidence an important fluid permeability enhancement during the late Variscan destabilisation of the Variscan orogen. This work of Van Baelen (2010) demonstrates the importance of the late Variscan tectonic inversion and corroborates the importance of the interaction between fluid flow, fluid pressure changes and changes in the tectonic stress field.

1.3 Objectives

In a more general context, this work aims at providing a better understanding of the intimate coupling between fluid flow, pore-fluid pressure changes and stress-state evolution of sedimentary basins evolving into orogens during early tectonic, fluid-assisted compressional tectonic inversion. The peripheral part of the High-Ardenne slate belt forms the ideal study area to perform this research.

Although Kenis (2004) was able to deduce both the stress state in the basin at the time of bedding-normal vein formation prior to compressional tectonic inversion and the presence of high fluid pressures in the central part of the High-Ardenne slate belt, the regional control on the stress-state in the basin, as well as the dimensions of this overpressured Ardenne-Eifel reservoir are to date unknown. Estimations of the dimensions of such an overpressured reservoir could have implications as analogue to the present overpressured upper crust. This work aims at extending previous research in the Ardennes towards the North Eifel in order to estimate the dimensions of this fractured reservoir and at deducing whether the stress state in the basin at the time of bedding-normal vein formation was consistent in the whole Ardenne-Eifel area. Describing the differences in vein formation between the central and the peripheral part of the slate belt will define how similar geodynamic constraints are expressed differently at different structural levels in a developing slate belt. This research will be performed by means of a multidisciplinary research on the different quartz vein generations that have been reported in the pHASB. A pervasive structural analysis on the veins should above all clarify the relationship of the veins with other structural features.

It is further aimed to deduce the stress-state evolution of the Ardenne-Eifel basin during progressive Variscan deformation. Although mullions, which represent a ductile deformation of the host rock below the brittle-ductile transition, reflect Variscan shortening after the compressional tectonic inversion and are valuable palaeorheological tools, they are insufficient to deduce directly the stress field orientation after tectonic inversion. A structural and microthermometrical analysis of the reported successive quartz veins in the pHASB, which might reflect a more brittle deformation in the higher structural levels of the High-Ardenne slate belt, will infer an insight in the changing stress-state and characterise pore-fluid composition and pressures during inversion. Veins are therefore suitable gauges to deduce the stress state in the basin during vein formation.

Ultimately, this study will not only provide an insight on the coupling between fluid pressure and stress-state changes, but will also discuss the 3D complexity of stress transitions during inversion. Despite the presence of 3D structures, the changes in stress state have generally been considered in 2D. It is aimed to develop a general 3D geometric stress-state model to illustrate the complexity of stress changes during inversion. The development of such stress-state reconstructions allows defining the basic parameters that have an influence on 3D stress-state changes, irrespective of regional parameters. Such a general stress-state model may eventually have a wide range of implications with respect to the evolution of dynamic permeability during tectonic inversion.

1.4 Research strategy and structure of the thesis

In order to achieve the main objectives of this research, it is called upon a structural-geometrical and physico-chemical analysis. Such a combined, multidisciplinary research strategy is in line with the expertise achieved within the *Geodynamics and Geofluids Research Group* at the Katholieke Universiteit Leuven. During the last decades, this research group has gained an international reputation on specific research topics in which the interaction between small-scale to large-scale fluid flow and geodynamic processes during the development of sedimentary basins and subsequent orogeny have been studied. New research techniques were implemented through the years to built an own expertise and strengthen the research facilities. The research strategy of this work specifically relies on the experience within *Geodynamics and Geofluids Research Group* gained during detailed field-based structural analyses and microstructural investigations of vein occurrences in Palaeozoic slate belts (Belgium, Germany, Luxemburg, France), foreland fold-and-thrust belts (Belgium, Italy, Albania, Mexico) and in ore deposits in Neo- to Mesoproterozoic terrains in Central Africa (DRC, Zambia, Rwanda). Moreover, several mineralogical studies focused on the characterisation and microthermometric analysis of fluid inclusions and demonstrated that this is a very useful technique to deduce pressure and temperature conditions during vein emplacement. Apart from this expertise, an independent knowledge concerning vein geometry and vein kinematics has been developed.

Prior to the description of the detailed structural analysis that has been performed on the selected study area, **Chapter 2** presents a complete overview of the geological framework relevant to this study in which the geodynamic evolution of the Rhenohercynian Ocean will be elaborated with a particular focus on the role of the Ardenne-Eifel basin development. Also the different lithostratigraphic units cropping out in the study area and in surrounding areas, as well as the Variscan tectonometamorphic evolution of the North Eifel will be described. This geodynamic chapter provides a useful state-of-the-art on what has been published on the geodynamics of the Ardenne-Eifel area and to which can be referred in following chapters of this work.

Chapters 3 to 8 incorporate the main parts of this work. In **Chapter 3** a detailed structural analysis is presented in order to frame the different vein types which are observed in the Eifel area. Based on four selected outcrop areas that are localised at the Rursee, *i.e.* the

Wildenhof, Eschaulerberg, Hubertus-Höhe and Schwammenauel sections, the geometry and kinematics of the different vein types are described. It is specifically focused on the interaction of veins with structural features such as bedding, cleavage and folds in order to deduce the relative time of vein formation with respect to these structural features. Throughout the description of these outcrops, a considerable effort has been put in the orientation analysis and characteristics of the veins in order to set up a relative chronology of the different vein types. This allows reconstructing the complex fracturing/veining history in the periphery of the High-Ardenne slate belt. At the end of Chapter 3, the overall structural architecture of the Rursee and Urftsee is summarised and a regional geometric evolutionary model, based on macroscopical observations, is constructed. This model is compared to the vein and deformation features that have been studied previously in the central part of the High-Ardenne slate belt. Some of the kinematic analyses in the Chapter 3 result from a published manuscript in Geologica Belgica (Van Noten *et al.* 2008).

In order to understand the vein development in a developing slate belt during Variscan orogeny, a detailed petrographic and microstructural analysis of the veins is needed to refine the geometric evolutionary model. The aim of the presented microstructural fabric analysis in **Chapter 4** is to characterise the mineralogy of the host rock and to deduce the progressive steps of mineral infill during the formation of the different vein types. In the detailed petrographical analysis it is also focused on distinguishing different fluid-inclusion types and their specific orientation within the veins. This eventually contributes to the understanding of successive vein formation. By a subsequent microthermometric analysis of properly selected fluid inclusions, the composition of the fluids from which the veins precipitated, as well as the homogenisation temperatures of the inclusions are reported in **Chapter 5**. Based on a specific method of cross-cutting the calculated isochores with an independent geothermometer, trapping pressures and temperatures are eventually deduced. Further correlation of the deduced trapping temperatures with regional metamorphic conditions of the North Eifel allowed validating the obtained results.

In **Chapter 6**, the specific trapping conditions of the different vein types are integrated in a brittle failure mode plot. Plotting the changes in pore-fluid pressure versus the stress changes during inversion of stress regimes, allows extrapolating the results to a broader context, irrespective of the regional constraints. Chapter 5 and Chapter 6 result from a published manuscript in the Journal of Geological Society, London (Van Noten *et al.* 2011).

The veins studied occur regionally in the High-Ardenne slate belt and often display parallel, evenly spaced arrays. To deduce the local stresses internally in a layer, the regionally examined vein spacing patterns are reported in **Chapter 7**. The results of this analysis are published in a manuscript in the Journal of Structural Geology (Van Noten & Sintubin 2010). Furthermore, although the reconstruction of the brittle failure mode plot is very useful to visualise the trapping conditions during orogenic shortening, its two-dimensional layout is still a simplification of the true 3D stresses in the Earth's crust. Therefore several 3D stress-state reconstructions are developed to illustrate the complexity of 3D stress changes during tectonic inversion and are presented in **Chapter 8**. This chapter results from a manuscript that has been accepted for publication in the special publications(1) of the Geological Society of London (Van Noten *et al.* accepted).

Eventually, the main goals and perspectives which are described in the introduction will be re-evaluated in the final **Chapter 9**. It will also be discussed if the general results of this research concerning the stress-state evolution of the upper crust during compressional tectonic inversion, obtained by analysing successive vein types, can serve as a natural analogue of different settings in other parts of the world.

---

(1) This special publication of the Geological Society of London results from the presentations and discussions at the Anderson Conference (Glasgow, U.K., September 2010) and has been compiled to commemorate the work of E.M. Anderson (1877-1960), one of the most influential structural geologists. His profound insights into stress development in the brittle crust are still commonly used and accepted.

CHAPTER 2 Geodynamic setting

2.1 Rhenohercynian basin development

From a geodynamic point of view, this research focuses on fracturing and subsequent vein formation in Lower Devonian deposits in the north-eastern peripheral part of the High-Ardenne slate belt, which forms a central part of the Rhenohercynian foreland fold-and-thrust belt in the northern extremity of the Central European Variscan belt (Oncken *et al.* 1999). The Central European Variscan belt is a complex zone of terrane accretion which comprises several old parts of oceanic and continental lithosphere being telescoped together during the Variscan orogeny. In a broader context, the Central European Variscides forms part of the Trans-European Suture Zone (Pharaoh 1999) which defines a broad and complex amalgamation of Lower and Upper Palaeozoic terranes. Within the Trans-European Suture Zone, the northern extremity of the Central European Variscides corresponds to the southern border of early Palaeozoic accreted terranes, such as the parautochthon Anglo-Brabant Deformation Belt. This border, *i.e.* the North Variscan thrust front (Figure 2.1), defines the most northern front to which the Variscan nappes have been overthrusted on the previously accreted Lower Palaeozoic terranes during late Variscan convergence.

The Central-European Variscides have been divided in three segments with different tectono-metamorphic histories (Kossmat 1927 in Dittmar *et al.* 1994). In the nineties, several basin reconstructions (Matte 1991, Oncken *et al.* 1999, Pharaoh 1999, von Winterfeld 1994) have shown that each segment was a terrane with Upper Palaeozoic sedimentation. It is referred to Servais & Sintubin (2009) for the correct terminology of continents, plates and terranes. Along a cross-section from the North Eifel (Germany) to south France, three distinct zones can be distinguished, *i.e.* the Rhenohercynian Zone, forming the external Variscides, and the Saxothuringian and Moldanubian Zones, forming part of the Variscan internides (Figure 2.1). These zones were successively accreted during Early Devonian to late Carboniferous times involving SE-directed subduction of minor intervening ocean basins (Plesch & Oncken 1999). The Rhenohercynian Zone forms the northern external zone of the Variscides and represents an external foreland fold-and-thrust belt, in which the Palaeozoic sequences in Devon and Cornwall (Cornubian Massif, south-western U.K.), the Ardennes (Belgium, France, Luxemburg and Germany), the Rhenish Massif (western Germany) and the Harz Mountains (central Germany) (Holder & Leveridge 1986 and references therein) are comprised. The Rhenohercynian Zone is separated from the Saxothuringian Zone by the Rheic Suture (Pharaoh 1999). The latter is defined in the Rhenish Massif at the contact of the Northern Phyllite Zone and the Lower Palaeozoic Giessen allochthon with the Mid-German Crystalline High, which formed during SE-directed subduction of the Rhenohercynian basin beneath the Saxothuringian Zone in late Silurian - Early Devonian times (Franke 2000). This subduction caused the formation of a flysh accretional wedge and the evolution of a magmatic arc in the upper plate, *i.e.* the Mid-German Crystalline High (Oncken *et al.* 2000, Weber 1981), which acted as a rigid body during Variscan collision. The Saxothuringian Zone is correlated with North and Central Armorica and the northern Bohemian Massif and is referred to as the Armorica microplate (Matte 2001). Because Palaeozoic rocks are in most places covered by younger strata, the Saxothuringian Zone is not everywhere visible at the surface and it has been difficult to correlate it in the Central European mosaic (Franke 2000). To the Moldanubian Zone belong several Gondwana-sourced terranes such as the southern part of the Bohemian Massif, the main part of the Black Forest and the Vosges, the northern Central Massif and a small south-eastern part of the Armorican Massif

(Franke 2000). South of the Moldanubian Zone, the orogenic front of the Alpine-Carpathian orogen (cf. Pharaoh 1999) defines the southern border of the Central-European Variscides and represents the Oligocene Alpine emplacement superimposed on the Variscan accreted terranes.

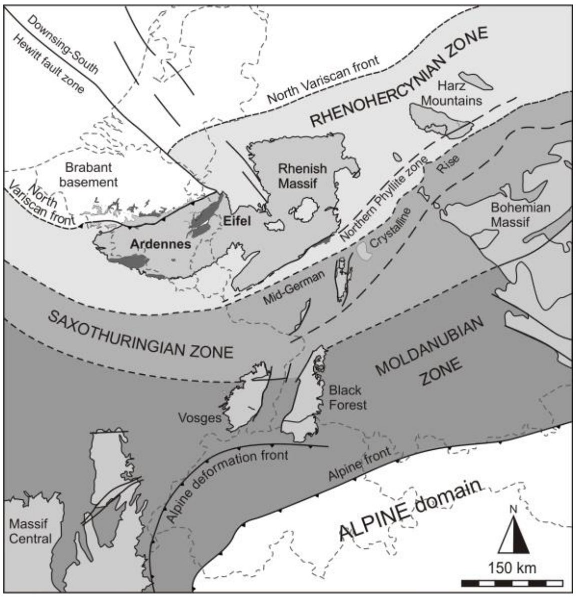

Figure 2.1: Tectonic map of the Central European Variscides showing the distribution of Variscan massifs within their corresponding tectonic zones. Map modified after Pharaoh (1999) and Franke (2000).

Because of the particular interest in the Ardennes and the Rhenish Massif, which are fully incorporated in the Rhenohercynian Zone, only the evolutionary development of the Rhenohercynian basin into the Rhenohercynian fold-and-thrust belt is further elaborated. The evolutionary development and deformation of the southern Saxothuringian and Moldanubian basins into their orogenic belts lies beyond the scope of this research.

In the Ardennes, the onset of crustal extension of the Rhenohercynian basin started at late Silurian times (late Pridoli, *c.* 420 Ma, Sintubin *et al.* 2009) on a basement constituted of Caledonian overprinted Lower Palaeozoic sediments. The incipient development of the Rhenohercynian basin occurred simultaneously with the long-lived Brabantian deformation phase which inverted and deformed a part of the Avalonian microplate assemblage into the Anglo-Brabant Deformation Belt, north of the Variscan front. This orogeny occurred in several phases from the Middle Ordovicium until the early Middle Devonian (Debacker *et al.* 2005, Sintubin *et al.* 2009, Verniers *et al.* 2002). The Brabantian deformation phase expresses the final collision of a part of the Avalonian microplate with a southern part of the Midlands microcraton. During this deformation phase a southwards-directed subduction caused metamorphism, cleavage development and folding of the Brabant Massif, in the south-eastern part of the Anglo-Brabant Deformation Belt (Van Grootel *et al.* 1997). The anticlockwise rotation of the Midlands microcraton has been proposed as the driving mechanism of the opening of the Rhenohercynian basin (Sintubin *et al.* 2009, Woodcock *et al.* 2007). During progressive continental rifting the microplate, on which the Rhenohercynian basin developed, drifted northwards. During this drift, the Rhenohercynian basin developed from an incipient basin on a passive continental margin into the Rhenohercynian Ocean (Plesch & Oncken 1999). Weber (1981) disputed the existence of the development from a basin to a real ocean due to the absence of clear ocean-floor spreading characteristics in Devono-Carboniferous tholeiitic basalts. Dittmar *et al.* (1994), however, report that some metabasalts in the Hunsrück have been identified as oceanic MORB-basalts and confirms the oceanic stage of the Rhenohercynian basin. The thick Lower Devonian sequences, *e.g.* cropping out in the Ardennes and the Rhenish Massif, reflect the rapid syn-rift subsidence of the basin, particularly active during the Pragian. These sequences originate from sediments derived from the Old Red Sandstone continent, which was situated in the north and consists of an amalgamation of Baltica, Laurussia and Avalonia. The high subsidence rate active during Rhenohercynian basin development enhanced the formation of synsedimentary faults and had a maximum activity at the termination of the continental rifting in the early Emsian (Oncken *et al.* 1999). Subsequently, a Middle Devonian post-rift carbonate platform developed on the northern passive margin of the Rhenohercynian basin associated with diminished subsidence and sedimentation.

Contraction and inversion of the thinned Rhenohercynian continental margin started at the most south-eastern boundary of the Rhenish Massif in the Late Devonian (Engel & Franke

1983 in Fielitz & Mansy 1999). Subsequent closure of the Rhenohercynian basin is related to the northwards displacement of the Saxothuringian and Moldanubian terranes, which have been inverted from Middle to Late Devonian (Franke 2000). Further migration of the Variscan internides caused a southwards-directed subduction of the crust at the southern margin of the current Rhenohercynian Zone. The northern part of the Northern Phyllite Zone, *i.e.* currently exposed in the southern part of the Rhenish Massif (Figure 2.1), was hereby partly subducted. The subduction-related and pressure-dominated metamorphism of the Northern Phyllite Zone contrasts with the regional low-grade, burial-related metamorphism in the main part of the Rhenish Massif (Weber 1981). Subsequent contraction of the Variscan externides resulted in the formation of the Rhenohercynian foreland fold-and-thrust belt (Fielitz & Mansy 1999, Oncken *et al.* 1999). This contraction eventually resulted in an allochthonous fold-and-thrust belt overthrusting the autochthonous Brabantian foreland at the North Variscan thrust front. Variscan deformation propagated with a mean shortening rate of *c.* 14 mm/a from south to north through the basin, starting from *c.* 325 Ma, until it reached the Variscan front in the late Carboniferous at *c.* 300 Ma (Ahrendt *et al.* 1983, Oncken *et al.* 1999). By means of palinspastic restorations of several balanced cross-sections through the Rhenish Massif, Oncken *et al.* (1999) calculated that the Rhenohercynian fold-and-thrust belt developed on a 350 km wide passive continental margin and was shortened subsequently during Variscan contraction by some 50 %, up to 180 km. Late orogenic molasse sediments, deposited in a paralic environment during the latest Carboniferous to Early Permian, mark the gravitational collapse of the thickened orogenic wedge and reflect the end of Variscan deformation (Dittmar *et al.* 1994).

2.2 Ardenne-Eifel basin

As outlined above, the Ardennes and the Rhenish Massif forms a central part of the external Rhenohercynian fold-and-thrust belt in the northern extremity of the Central European Variscan belt (Figure 2.1). The Ardennes are defined as the outcrop area of Palaeozoic rocks in northern France, Belgium, Luxemburg and Germany. In this framework, the northern frontal parts of the Rhenohercynian fold-and-thrust belt are characterised by the presence of a major allochthonous domain, the Ardenne allochthon, which thrusted over its foreland, the Brabant parautochthon, during the latest, Asturian, stage of the Variscan orogeny (cf. Mansy & Lacquement 2003, Meilliez & Mansy 1990). This thrusting occurred along the North Variscan Midi - Aachen thrust front, on top of the Upper Namurian-Westphalian coal-bearing cover of the Brabant Massif, formerly known as the Namur Synclinorium. The Ardenne allochthon can further be subdivided into the Dinant fold-and-thrust belt in the north and the High-Ardenne slate belt in the south (Figure 2.2). The deformation within the Dinant fold-and-thrust belt, formerly called the Dinant Synclinorium, is mainly controlled by alternating Middle to Upper Devonian and Carboniferous, mostly competent, sedimentary sequences of which the Upper Devonian, Famennian psammites form ridges in the topography and the Carboniferous alternating limestone and pelitic sequences determine the depressions in the region. The High-Ardenne slate belt consists of mainly Lower Devonian siliciclastic, predominantly argillaceous sequences intercalated with competent quartzite and sandstone layers. The dominant structural feature is a slaty cleavage which formed during the Sudetic stage (*c.* 325 Ma) of the Variscan orogeny (Fielitz & Mansy 1999). Within the High-Ardenne slate belt, the major Troisvierges-Malsbenden backthrust (cf. Breddin 1963) separates the Ardenne culmination from the Eifel depression, in which the former forms a pop-up structure on top of the latter (Figure 2.3a). Within the Ardenne allochthon, four Cambro-Ordovicium basement inliers, *i.e.* the Stavelot-Venn, Rocroi, Givonne and Serpont inliers (Figure 2.2), record the early Palaeozoic basin development on the southern margin of the Peri-Gondwanan microcontinent of Avalonia (Sintubin *et al.* 2009, Verniers *et al.* 2002). The different Ardennian unconformities hence represent a contact of Lower Palaeozoic basement rocks with the diachronous, unconformably overlying upper Silurian to Lower Devonian deposits. These unconformities, which are overprinted by a pervasive Variscan deformation (*e.g.* Van Baelen & Sintubin 2008), reflect a time hiatus during which the Ardennian deformation phase

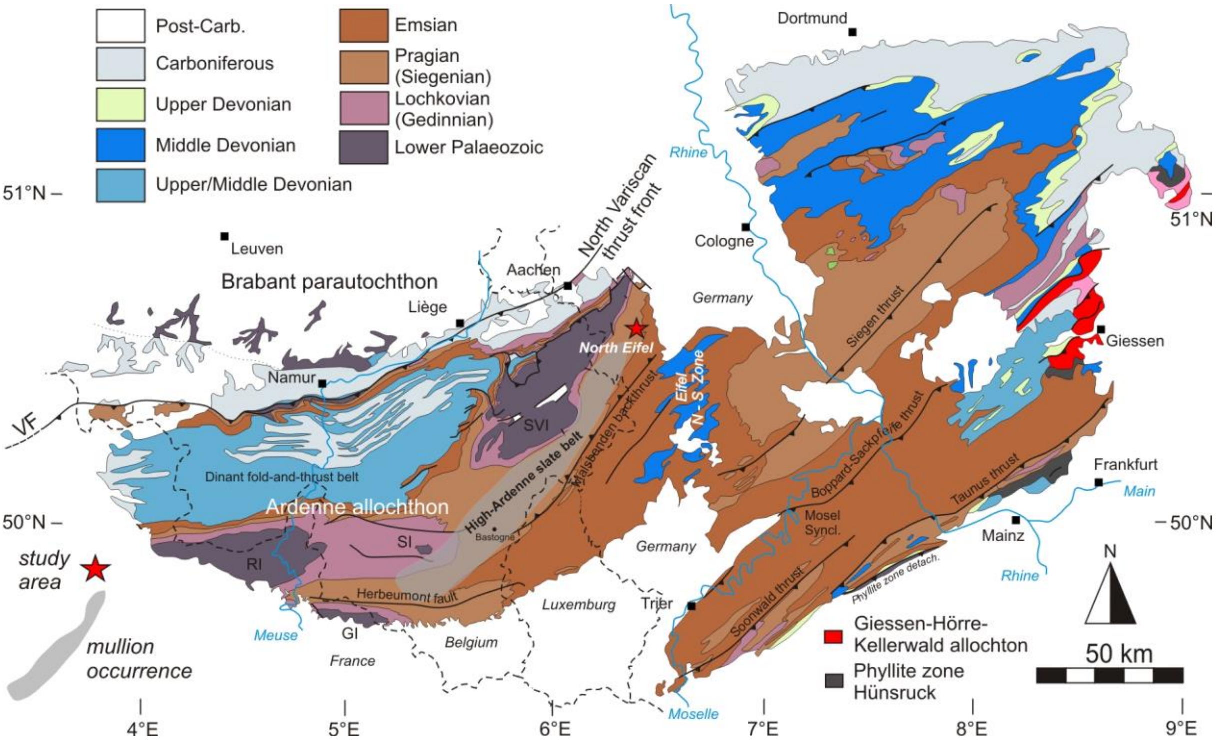

Figure 2.2: Geological compilation of Palaeozoic deposits present in the Ardennes and in the Rhenish Massif modified after Asselberghs (1946) and Oncken *et al.* (2000). The Lower Palaeozoic inliers and the most important thrusts and backthrusts are shown. The occurrence of mullions in the High-Ardenne slate belt is indicated in transparent grey. SVI: Stavelot-Venn inlier, RI: Rocroi inlier; GI: Givonne inlier; SI: Serpont inlier; VF: North Variscan thrust front.

may have taken place. Van Baelen & Sintubin (2008) and Sintubin *et al.* (2009), however, dispute the existence of an Ardennian tectono-metamorphic event and suggest that the angular unconformities, which are observed north of the Rocroi and Stavelot-Venn Massifs, can very well be related to Early Devonian basin dynamics instead of a pervasive Ardennian deformation phase.

The north-eastern to eastern part of the High-Ardenne slate belt, situated in Germany, corresponds to the western part of the Rhenish Massif. Due to the existence of the Cenozoic Rhine graben, the Rhenish Massif has been subdivided in a western and an eastern part, referred to in German literature as ‘Linksrheinisches’ and ‘Rechtsrheinisches Schiefergebirge’ respectively (Walter 1992). From the north-western foreland of the Stavelot-Venn inlier to the southern suture with the Saxothuringian microplate, several structural zones are distinguished within the western Rhenish Massif based on the different deformation styles within each zone (DEKORP 1991, Dittmar *et al.* 1994, von Winterfeld 1994); *i.e.* the North Eifel foreland, the North Eifel, the Eifel North-South Zone, the Mosel Synclinorium, including the Hunsrück Nappe, and the Northern Phyllite Zone at the southern margin of the Rhenohercynian fold-and-thrust belt (Figure 2.2). These zones are further shortly elaborated

NW of the Stavelot-Venn inlier, a predominantly thin-skinned deformation corresponds to the North Eifel foreland, and is separated from the Brabant parautochthon at its northern border by the Aachen thrust. This part is further subdivided in the Würm depression, Aachen culmination and the Inde depression (Oncken *et al.* 2000), equivalents of the Vesdre nappe in the Ardennes. To the south of the North Eifel foreland, the North Eifel is defined as the combination of early Palaeozoic deposits of the north-eastern part of the Stavelot-Venn inlier and Lower Devonian deposits of the north-eastern, peripheral (cf. Van Noten *et al.* 2008) part of the High-Ardenne slate belt. The Eifel N-S Zone, SE of the North Eifel, is a zone of axial depression which is characterised by Mesozoic and Cenozoic sediments resting unconformably on alternating Emsian and Middle Devonian platform sediments. Further

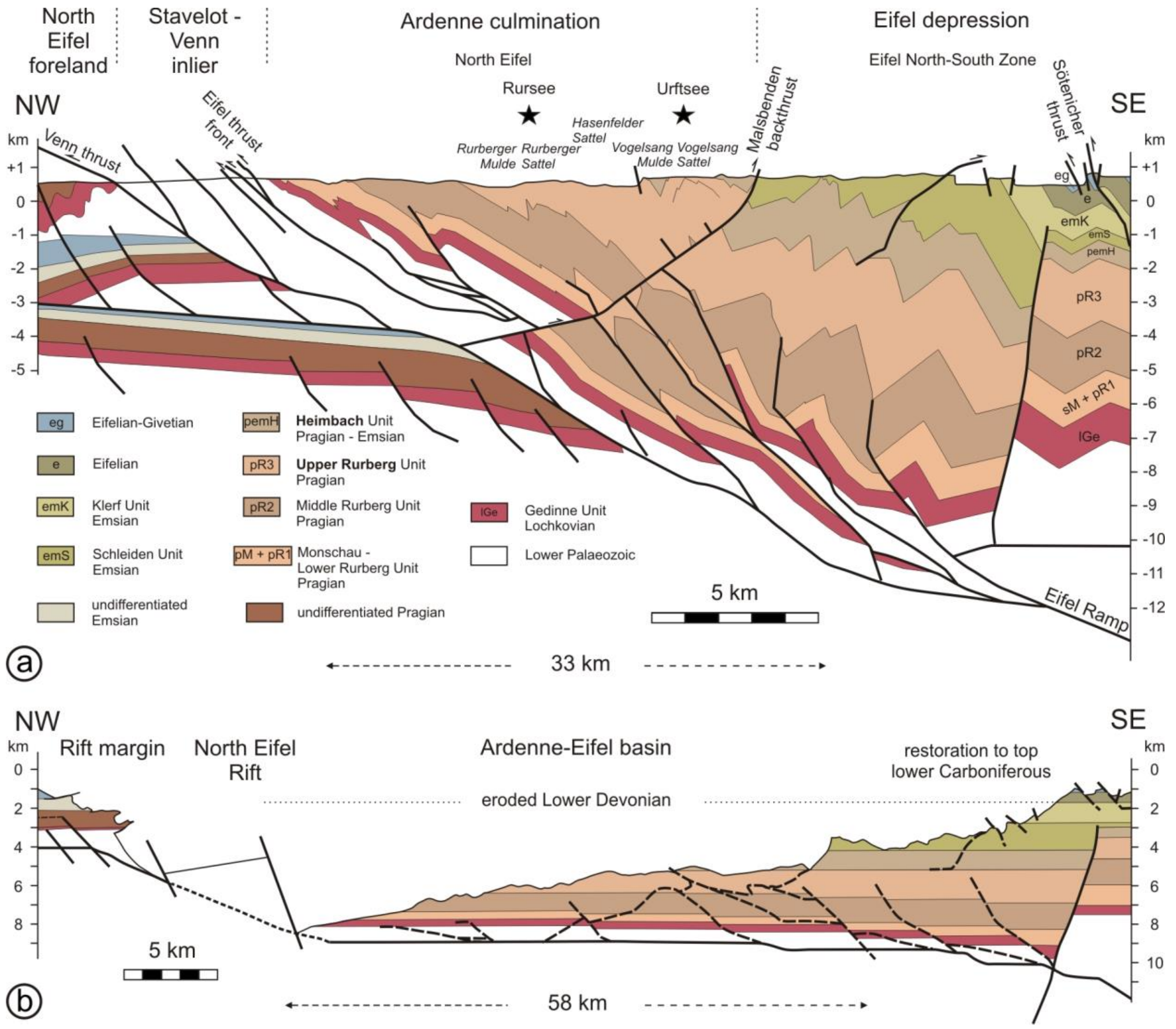

Figure 2.3: (a) Balanced cross-section through the north-eastern part of the Stavelot-Venn inlier and the Eifel cover showing the different structural units within the High-Ardenne slate belt. The black stars localise the study area. **(b)** Palinspastic reconstruction of the cross-section in **(a)** demonstrating the Ardenne-Eifel basin morphology during the lower Carboniferous. Cross-sections modified after von Winterfeld (1994) and Oncken *et al*. (2000).

to the south, the presence of thick sequences in the Mosel Synclinorium marks the existence of a small depocentre of the Rhenohercynian basin, active during the Emsian (Littke *et al*. 2000). The southern border of the Mosel Synclinorium is separated from Northern Phyllite Zone by the Hunsrück-Taunus Boundary Fault, a steep and upright fault zone (Oncken *et al*. 2000), which has been repeatedly active since the late Carboniferous (Littke *et al*. 2000).

Recently published palinspastic restorations of balanced cross-sections, west of the Rhine river (Oncken *et al*. 1999, Oncken *et al*. 2000, von Winterfeld 1994), show that the previously described structural domains correspond to several smaller basins, such as the Ardenne-Eifel basin or the Mosel graben, that were active during Rhenohercynian basin development. Within this broad context, the Ardenne-Eifel basin thus forms a narrow depocentre on the northern passive margin of the developing Rhenohercynian Ocean.

In the palinspastic reconstruction (Figure 2.3b) of the cross-section through the North Eifel and Eifel N-S Zone (Figure 2.3a), two different units show up which are defined by a prominent rift margin fault; to the NW of the Lower Palaeozoic Stavelot-Venn inlier a thin post-rift-related Devonian platform is separated from the thick Ardenne-Eifel basin fill to the SE of the Stavelot-Venn inlier. The margin fault that borders these units represents Lower Devonian crustal stretching during Rhenohercynian basin development and separates the nearly unextended crust to the NW from the strongly attenuated crust in the SE (Heinen 1996, von Winterfeld & Walter 1993). Together with the Eifel basement ramp (cf. von Winterfeld 1994) (Figure 2.3) the rift margin fault played an important role as thrust fault during the syntectonic inversion of the Ardenne-Eifel basin (Oncken *et al.* 1999). Also, the foreland facing thrusts recognised in the balanced cross-section tend to branch off near the intersections of the basement-cover interface with earlier normal faults.

During the Pragian, extensional normal faults, such as the previously described margin fault, began to develop during rapid rifting and subsidence of the Ardenne-Eifel basin. Thermomechanical basin modelling of the syn-rift crustal thinning during the Early Devonian revealed an average lower-crustal thickness of 19 km below the detachment in the North Eifel and a decrease in thickness to 12 km below the detachment in the depocentre of the Mosel graben (Heinen 1996). This exemplifies the slightly asymmetric rift of the Rhenohercynian basin deepening towards its southern margin. In the North Eifel, syn-rift crustal thinning was accompanied with an increased heat flow up to 95 mW/m^2 at the end of the early Emsian (Heinen 1996, Littke *et al.* 2000). In this period, the activity of extensional normal faults reached a maximum. Subsequently, a decrease in heat flow to common values between 50 and 60 mW/m^2, related to post-rift thermal relaxation, occurred during decreased subsidence and Middle Devonian platform development. Restoration of the Moho depth to uniform thickness below the whole Variscides and its foreland is believed to have occur within 20 Ma after final convergence in the frontal zone by the end of the Carboniferous (Henk 1999).

2.3 North Eifel lithostratigraphy

The rapid syn-rift Ardenne-Eifel basin fill during the Lower Devonian Lochkovian-Pragian-Emsian is currently comprised in the High-Ardenne slate belt as thick sequences. In the North Eifel, the overall NNE-SSW Lower Devonian metasedimentary rocks rest unconformably on the SE-dipping limb of the NE-plunging Lower Palaeozoic Stavelot-Venn inlier in the NW (see cross-sections in Figure 2.6) and are covered by the slightly NE-dipping, Permo-Triassic deposits in the east. The Lower Devonian sediments are younging to the SE and will further be discussed separately.

Before referring properly to the literature on the regional litho- and chronostratigraphy, the stratigraphic approach has to be explained. The International Commission on Stratigraphy (IUGS) is developing worldwide a (chrono)stratigraphic terminology to unify the regional nomenclature on a global data base. This coordinated effort is necessary as others use regional and chronostratigraphic terminologies which could have different significance elsewhere.

Regarding the Lower Devonian rocks, the subject of this work, the subdivision into Lochkovian, Pragian and Emsian Stages has been accepted by the IUGS (Bassett 1985), with each stage defined by a physical GSSP at its base, irrespective of any chronostratigraphic biozonation. It is preferred to use this chronostratigraphic terminology in a broad way to allow global correlation between different settings. The historical development of the stratigraphy of the units at the northern border of the Rhenohercynian Basin has resulted in a standard regional subdivision of the Lower Devonian into the stages Gedinnian, Siegenian and Emsian. These stages were introduced by Asselberghs (1946) during his work on the characterisation of the Lower Devonian in southern Belgium and in surrounding areas. These stages have also been used in the Lower Devonian subdivision of the Rhenish Massif (Walter 1992, Weber 1981). In the international Lower Devonian subdivision, the base of the Pragian correlates with the base of the *Eognatodus sulcatus* Conodont Zone (Oliver & Chlupáč 1991). However, as shallow marine biostratigraphic markers are unsuitable for a correlation with international biomarkers, these regional stages were abandoned in the international subdivision.

In practice, the nomenclature and definitions of regional Lower Devonian lithostratigraphic units are defined by national stratigraphic commissions. In this study the vein formation in Lower Devonian units in both German and Belgian part of the High-Ardenne slate belt is compared. As result of this correlation, both German and Belgian nomenclature had to be dealt with. For the units of the North Eifel, correlation of the defined lithostratigraphic units with the internationally chronostratigraphic subdivisions is difficult. In the lithostratigraphic lexicon of the *Deutsche Stratigraphische Kommission* (DNK), the old regional lithostratigraphic stages Gedinnian and Siegenian are still used for the North Eifel units, while for the Lower Devonian lithostratigraphical units defined in the Dinant fold-and-thrust belt and the Vesdre Nappe the old lithostratigraphical units have been correlated with the international stratigraphic nomenclature (Bultynck & Dejonghe 2001). When it is referred to literature during the description of the formations in the North Eifel in this study, both regional and IUGS chronostratigraphy will be used such as in the reference. This prevents misunderstanding of literature.

Because of the scarcity of fossils proper biozones in shallow marine Lower Devonian deposits, the internationally stages cannot directly be correlated with the old lithostratigraphic subdivisions in the Ardennes and the Rhenish Massif (see Bultynck *et al.* 2000). The international Lower Devonian stage boundaries can therefore not precisely be located. It is, however, appropriate in this work to strive to continue using the international stratigraphic nomenclature Lochkovian, Pragian and Emsian defined by their GSSP’s in such way that the deviation from the former chronostratigraphic boundaries Gedinnian, Siegenian and Emsian remain minimal (Noël Vandenberge, pers. comm.). In general, based on spores in the Ardennes (Steemans 1989), the Lochkovian-Pragian boundary is slightly younger than the old Gedinnian-Siegenian boundary, while the Pragian-Emsian is slightly older than the old Siegenian-Emsian boundary (see Figure 2.4). Also the old and new border between the Emsian and Eifelian (former Couvinian in Belgium), and the border between Eifelian and Givetian do not entirely correlate (Bultynck & Dejonghe 2001).

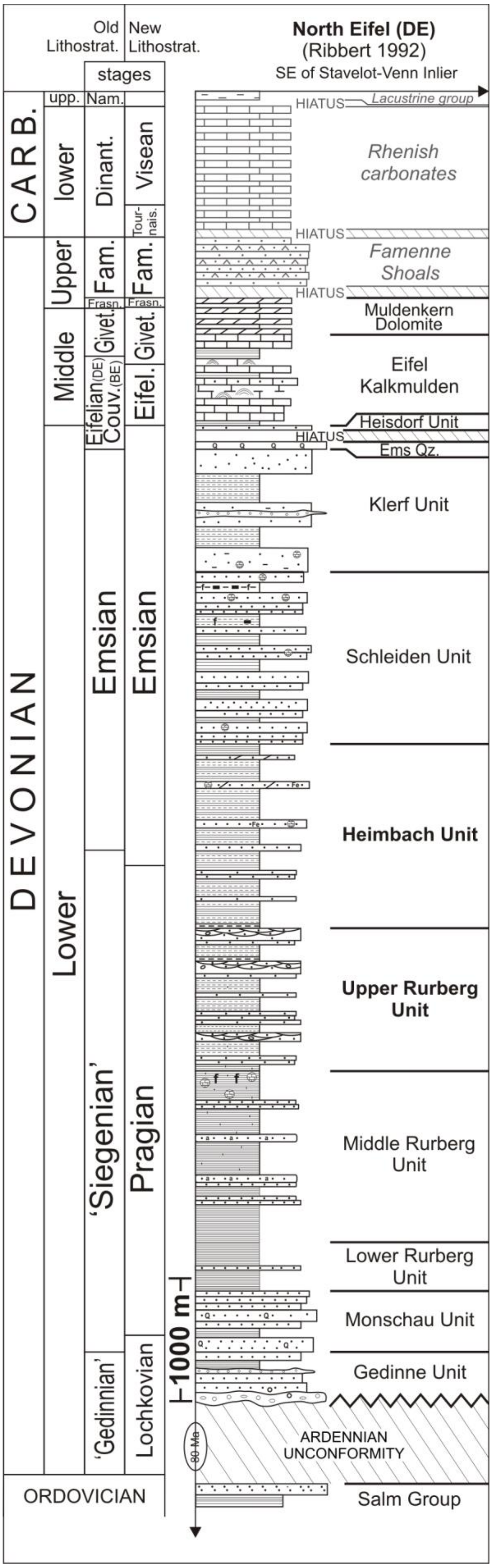

Figure 2.4 (right)**:** Lower Palaeozoic lithostratigraphic units in the North Eifel and Eifel North-South Zone. The gray units correspond to eroded depositional units. Correlation of the old ‘Rhenish’ lithostratigraphic stages with the new Lower Devonian subdivisions is adapted from Bultynck *et al.* (2000).

Owing to the northwards transgression of the Rhenohercynian Ocean in the Early Devonian, sediments in the North Eifel, of which equivalents can be found in the Rhenish Massif, are diachronous with respect to the sediments in the Ardennes (Belgium). The base of the Gedinnian beds, which lie unconformably on top of the Lower Palaeozoic inliers in the High-Ardenne slate belt, is diachronous from the west towards the east (Bultynck *et al.* 2000, Meilliez *et al.* 1991, Steemans 1989). The Lower Devonian deposits in the Ardenne culmination progressively young up from the central part of the High-Ardenne slate belt (Bertrix-Bastogne-Bütgenbach area; Figure 2.2) towards its north-eastern part, *i.e.* the North Eifel, respectively evolving from Gedinnian-Siegenian to Siegenian-Emsian. Litho-stratigraphical correlation between Lower Devonian lithostratigraphical units of the Ardennes and the North Eifel might, however, be difficult owing to this diachronism (Figure 2.5). Nevertheless, based on a correlation of the old lithostratigraphic units on the old geological maps of Wünstorf (1943), Breddin (1963), Knapp (1980) and Ribbert (1992) with units in the Belgo-Luxemburg area Gouvy-Sankt-Vith-Elsenborn region (Vandenven 1990 in Ribbert 1992) and between the latter region and lithostratigraphic units defined in the Dinant Synclinorium (Bultynck *et al.* 2000), correlation is possible (see Figure 2.4) and will be described in the lithostratigraphical description. Furthermore, Kenis (2004) applied the reviewed lithostratigraphy of Bultynck & Dejonghe (2001) for the Lower Devonian lithostratigraphy of Asselberghs (1946) in the central part of the High-Ardenne slate belt. The correlation of lithostratigraphic units of these three areas (Figure 2.5) is illustrated by the cumulative thickness of the units.

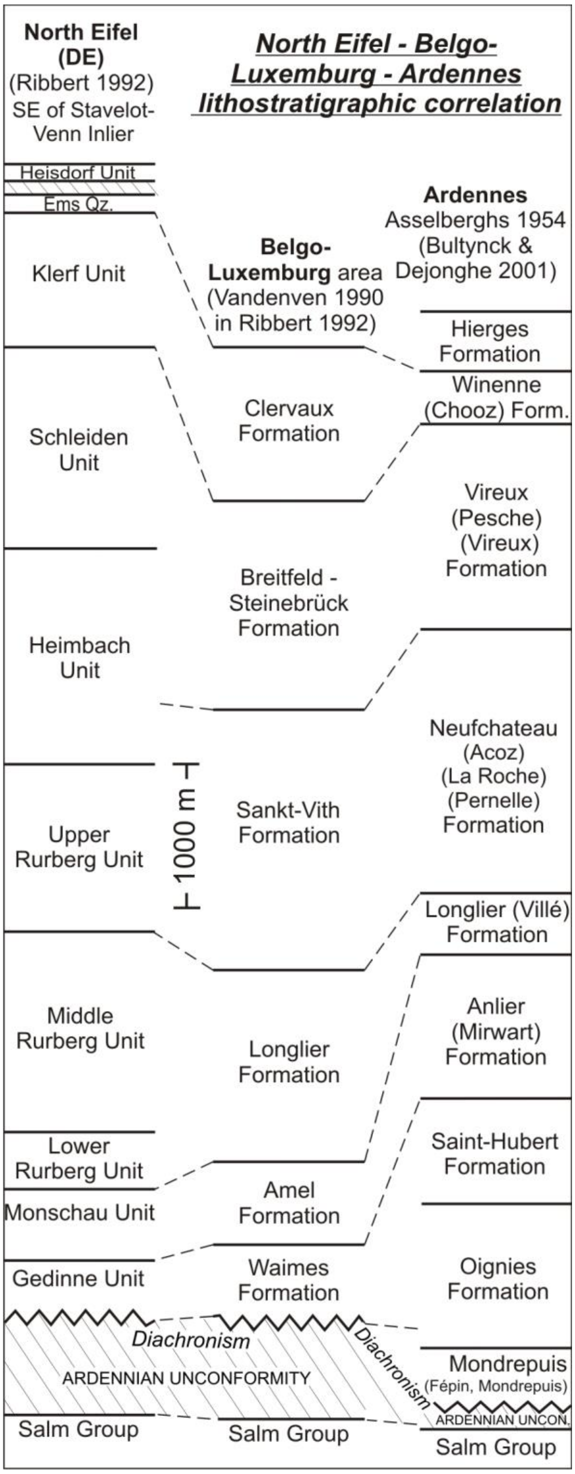

Figure 2.5: Correlation of the Lower Devonian lithostratigraphic units in the North Eifel and Eifel North-South Zone with the formations in the Belgo-Luxemburg area (Vandenven 1990 in Ribbert 1992) and the old (Asselberghs 1946) and new (Bultynck & Dejonghe 2001) Lower Devonian litho-stratigraphical units in the Ardennes. Each area is illustrated by the cumulative thickness of the lithostratigraphic units.

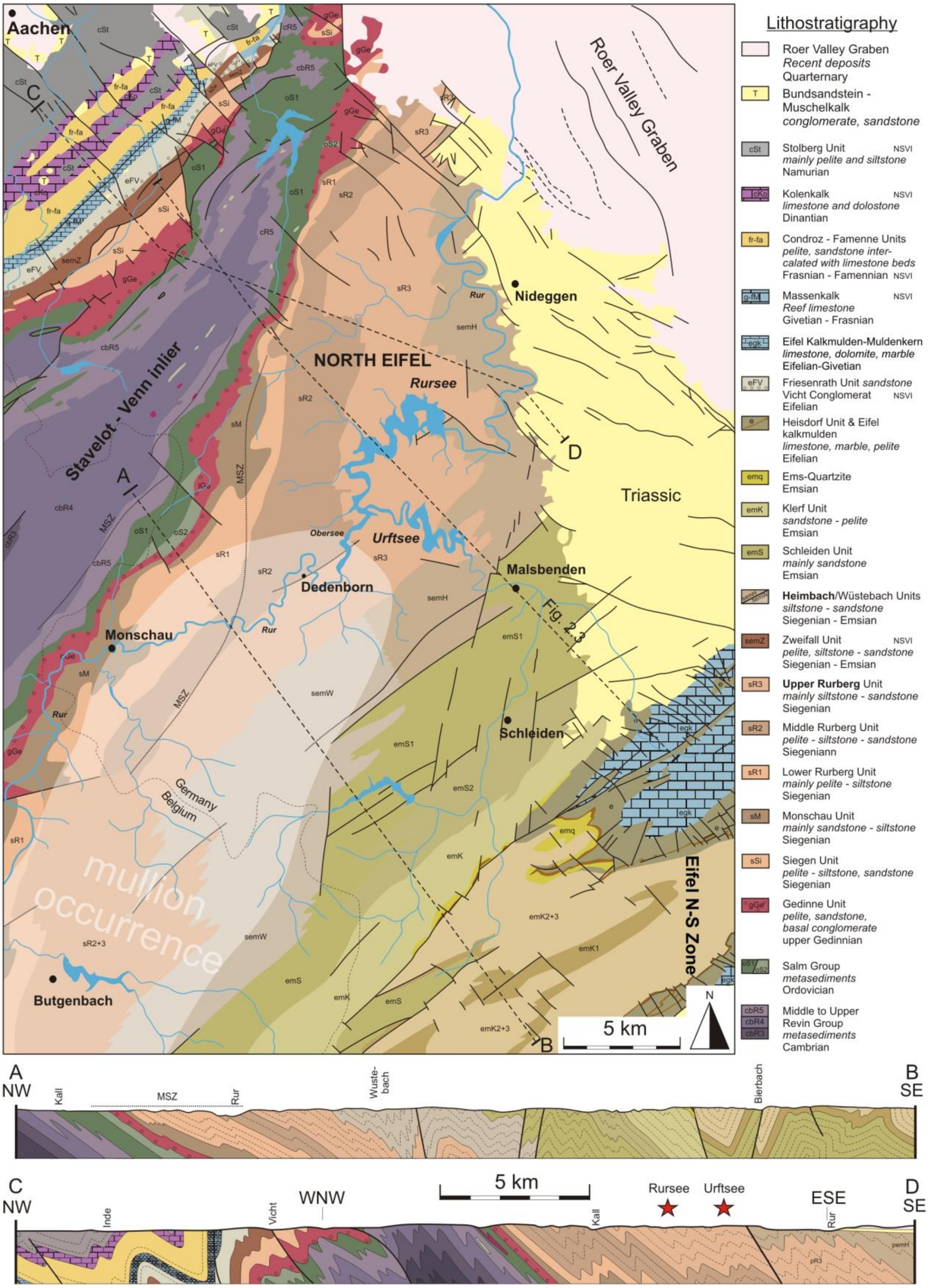

Figure 2.6: Lithostratigraphic map of the North Eifel, bordered by the Stavelot-Venn inlier in the NW and the Triassic cover in the east (modified after Ribbert 1992). A-B and C-D represent two conceptual cross-sections through the North Eifel showing a typical upright to NW-verging fold style towards the Stavelot-Venn inlier. The star in cross-section C-D localises approximately the outcrops at the Rursee. NSVI: lithostratigraphic units north of the Stavelot-Venn inlier; MSZ: Monschau shear zone (Fielitz 1992).

2.3.1 Gedinnian

The oldest cover rocks directly above the unconformity at the southern border of the north-eastern part of the Stavelot-Venn inlier are of late Lochkovian age. This leaves a time hiatus of approximately 70 Ma to 80 Ma with the underlying lower part of the Ordovician Salm Group (oS1 in Figure 2.6) (Jalhay Formation in Verniers *et al.* 2001). Only locally, at the NE of Monschau, the Gedinnian rocks are in contact with a younger and middle part of the Salmian Group (oS2) (Geukens 1999, Ribbert 1992), which is defined as the Ottré Formation in Verniers *et al.* (2001).

The Gedinnian **Gedinne Unit (**gGe**)** has been subdivided in four different parts (Wünstorf 1931, 1943); at the base the unit exists of a discordant basal, fluvial conglomerate with a maximum local thickness of 30 m. The basal conglomerate is succeeded by the Arkose of Waimes, which is characterised by a large amount of brachiopods (Knapp 1980) within an alternation of sandstones, fine-grained conglomerates and arkose. Above the arkose, the Gedinnian consists of alternating red to gray-green siltstones and pelites with inclusions of fine-grained sandstones and quartz-rich conglomerates (250 to 300 m). The overlying pelitic upper part of the Gedinnian mainly contains red-coloured pelites with limestone pebbles included and varies in thickness between 150 and 200 m. The total thickness of the Gedinnian varies around 400 m (Knapp 1980), but may locally increase up to 500 m (Asselberghs 1946). Towards the Belgian part of the High-Ardenne slate belt, the Gedinne beds may correspond to the Oignies Formation (G2b, Wünstorf 1943) and with the Marteau Formation north of the Stavelot-Venn inlier (Bultynck & Dejonghe 2001) (Figure 2.5).

2.3.2 Siegenian

The Siegenian south of the Stavelot-Venn inlier is characterised by the large thickness of the different successive units, which reflect the rapid subsidence of the Ardenne-Eifel basin. The Siegenian deposits start with the **Monschau Unit** (sM) that still may have a late Lochkovian to early Pragian age in the new chronostratigraphy. This unit mainly consists of gray, quartzitic, sandstone layers, with inclusions of small pelitic pebbles internally, intercalated with pelites and dark gray siltstones (Fielitz 1987, Knapp 1980, Wünstorf 1932). Numerous sedimentary structures within the sandstones indicate deposition by strong currents in an energetic, shallow marine, deltaic environment (Schmidt 1956). Thickness of the Monschau unit varies strongly laterally from 100 m in the north of the North Eifel, up to 1500 m at Monschau. von Winterfeld (1994) estimated a thickness of 500 m in the Rursee and Urftsee area. The Monschau Unit may correspond to the Amel Formation in the Belgo-Luxemburg area (Vandenven 1990 in Ribbert 1992) and to the Mirwart Formation in the central part of the High-Ardenne slate belt (Bultynck & Dejonghe 2001) (Figure 2.5).

The **Rurberg Units** succeed the Monschau Unit and are classically subdivided in three units in which the sand-clay ratio increases from the Lower-, over the Middle-, to the Upper Rurberg Unit (Ribbert 2007, Schmidt 1956, Wünstorf 1931, 1936). Differences between the units are further based on the expression of different sandstone layers and the initial colour of the pelites. Stratigraphical borders between the units are rather vague due to the gradual change of the sandy content to the upper units. Fossils, such as phytofossils and brachiopods which are rarely found in these units, are representative of a shallow marine depositional environment in which incursions of fresh water often occurred (Knapp 1980). The **Lower Rurberg Unit** (sR1) is characterised by green-gray to blue-gray pelites. Metre-thick, poorly sorted sandstone layers only locally occur. This mainly pelitic character has made this unit favourable to mine and several smaller quarries are still present around Monschau. The thickness of the unit increases from the NW towards the SE and is estimated to be 400 m in the Rursee area (von Winterfeld 1994). A further subdivision into lower or middle Siegenian is not possible due to the absence of fossils suitable for a detailed biostratigraphy. The **Middle Rurberg Unit** (sR2) resembles the lower unit in such way that it is mainly built of a pelitic lithology, sometimes intercalated with sandstones and arkose. Limestone pebbles within the pelitic sequences occur towards the top of the unit. Plant fossils found in the upper part of the unit classify the unit to the middle to upper Siegenian (Wünstorf 1936). Thickness changes from 300 m to 800 m (Knapp 1980) but increase up to 1400 m in the Rursee area (von Winterfeld 1994). According to Ribbert (1992), the Lower to Middle Rurberg Units may correspond laterally with the Longlier Formation in the central part of the High-Ardenne slate belt and with the Villé Formation in the Dinant fold-and-thrust belt (Bultynck & Dejonghe 2001). The youngest unit of the Rurberg Units, *i.e.* the **Upper Rurberg Unit** (sR3), is exposed in the region nearby the Rursee and Urftsee water reservoirs and is of interest for this research. This unit comprises an alternation of predominantly siltstones with fine-grained sandstones intercalated with coarse-grained sandstones that contain many sedimentary structures (see section 2.4). Petrological investigations report the presence of particles of phyllades and quartzophyllades within the coarse-grained sandstones, which could define them as a greywacke (Knapp 1962). In the pelites, sometimes iron-rich carbonate concretions with a red-coloured weathered rim occur (Wünstorf 1931, 1943). Schmidt & Schröder (1962) report the presence of some brachiopods and phytofossils, *i.e.* early land plants, within the Upper Rurberg Unit. Estimation of the thickness is very difficult due to the diachronous character of the unit and to synsedimentary faulting within the unit (Oncken *et al.* 1999). Knapp (1980) and Ribbert (1992) estimated a range between 600 m and 2000 m with a local thickness of 1160 m in the Rursee area (Richter 1967, von Winterfeld 1994). The Upper Rurberg Unit could correspond to the transition between the Longlier and Sankt-Vith Formation in the Belgo-Luxemburg area (Vandenven 1990 in Ribbert 1992) and to the transition of the Longlier and Neufchâteau Formation in the central part of the High-Ardenne slate belt (Kenis 2004) (Figure 2.5).

2.3.3 Emsian

Likewise the Siegenian units, the Emsian units are subdivided into several units based on their lithological content. Although these units are well defined, stratigraphical borders also gradually change into each other. Towards the east of the study area (Figure 2.6), the Upper Rurberg Unit gradually changes into the younger **Heimbach Unit** (semH), which has an upper Pragian to lower Emsian age (biozonation in Richter 1967 and references therein). The unit consists of dark- to blue-grey pelites and siltstones intercalated with thin sandstone layers and therefore resembles the Upper Rurberg Unit. The Heimbach Unit differs from the Upper Rurberg unit by its smaller amount of sandstones layers and the small dolomitic content within the fine-grained layers. Wünstorf (1931, 1943) reports the presence of iron-rich carbonate concretions within the pelites, of which the concretions consist of 4 % dolomite. In exposure, the upper twenty metres of the Upper Rurberg and the Heimbach Units are often red coloured due to surface weathering of the overlying Triassic Bundsandstein deposits (Breddin 1963). Thickness of the unit varies up to 1500 m in the study area (von Winterfeld 1994) although this estimation is highly uncertain because of the uncertain fault throw of the Malsbenden backthrust in the SE and the overlying Triassic deposits in the east (Knapp 1980, Richter 1967). South of Dedenborn (see Figure 2.6), the Upper Rurberg Unit gradually continues into the **Wüstebach Unit** (semW), which is the lateral equivalent of the Heimbach Unit (Asselberghs *et al.* 1936), although it has a slightly older age (upper Siegenian to lower Emsian) (Knapp 1980). This unit (thickness ~1000 m) is built of dark blue to grey pelites consistently with a minor amount of fine-grained sandstone layers. The transition between Wüstebach and Heimbach is only gradually characterised (Wünstorf in Asselberghs *et al.* 1936). Due to its fine-grained character and the very low carbonate content, the Wüstebach Unit has been exploited in the past as rooftop slates, *i.e.* the *Wüstebach Schiefer* (Knapp 1980). Both the Heimbach and Wüstebach Units may correspond to the transition of the Sankt-Vith to Breitfeld-Steinebrück Formation (Vandenven 1990 in Ribbert 1992) and with the transition of the Neufchâteau and Vireux Formation in the central part of the High-Ardenne slate belt (Kenis 2004) (Figure 2.5).

The overlying lower Emsian **Schleiden Unit** (emS) predominantly consists of sandstones which occur in thick monotone sequences alternating with blue-gray pelites (Wünstorf 1931). Based on the presence of coalificated plant fossils in bituminous shales (*brändschiefer*) in the upper part of the unit, Ribbert (1992) further differentiated a lower (emS1) and an upper member (emS2; Figure 2.6) locally around Schleiden. In contrast to the unclear borders between the previously described Siegenian units, the Emsian lithostratigraphical borders are easy to distinguish in such way that the Schleiden Unit differs from the underlying Heimbach/Wüstebach units by its typical higher carbonate content in the sandstones, increasing from the bottom to the top of the unit (Ribbert 1992). In the overall part of the North Eifel (Figure 2.6), the Malsbenden backthrust separates the Heimbach and Wüstebach Units from the Schleiden Unit, also differentiating the Ardenne culmination from the Eifel depression (Figure 2.3). Due to Malsbenden backthrust, the base of the Schleiden Unit is not observed, which makes thickness estimations highly variable changing from 600 m near Bütgenbach up to 1400 m at Schleiden (von Winterfeld 1994). This unit may correspond to the Vireux Formation in the central part of the High-Ardenne slate belt (Bultynck & Dejonghe 2001) (Figure 2.5).

A relatively sharp border differentiates the Schleiden Unit from the lower Emsian **Klerf Unit** (emK**)**. This unit contains metre-thick, poorly sorted, fine-grained sandstone layers and green-, red- to violet coloured pelites and siltstones (Knapp 1980). Schmidt (1956) furthermore reports the presence of thin levels of conglomerates in the sandstones and defines it as the *Gemünd Konglomerat*. Ribbert (1992) has separated this unit into a lower (emK1) and a middle to upper member (emK2+3) based on the carbonate content of the sandstones in the lower member and the increase in sandy content towards the middle and upper member. The Klerf Unit corresponds to the Clervaux Formation (Vandenven 1990 in Ribbert 1992) in the Belgo-Luxemburg area and with the Winenne Formation in the central part of the High-Ardenne slate belt (Kenis 2004). A thickness variation between 1000 m (von Winterfeld 1994) and 1300 m (Knapp 1980) is characteristic of the Klerf Unit.

The overlying **Ems-Quartzite** (emQ) is a thin, up to 75 m thick unit that consists of a fine-grained, quartz-rich sandstone and a strong, white quartzite that due to its glassy appearance has been described as a *glasswacke* (Knapp 1980). The Ems-quartzite reflects a decrease in clastic input in the Rhenohercynian Ocean at the end of the rapid syn-rift subsidence. At the beginning of the upper Emsian, a new palaeogeographic configuration sets in with the development of a number of relatively small subsiding basins (Meyer & Stets 1980). From then on, there is a strong contrast between the high subsidence and sedimentation rates in the Siegenian and lower Emsian and the development of Middle Devonian carbonate platform sedimentation in these smaller basins (Oncken *et al.* 1999). After a short absence of sedimentation, marking the transition from high to low subsidence rates in the Ardenne-Eifel basin (Figure 2.4) (Knapp 1980), the sandy **Heisdorf Unit** (e) is deposited in the upper Emsian and introduces the Middle Devonian Eifel *Kalkmulden*. The sedimentary hiatus in the upper Emsian (see Figure 2.4) is widespread and has also been observed in the siliciclastic facies of the Rhenish Massif (Stets & Schafer 2009).

2.3.4 Middle Devonian to upper Carboniferous

The **Eifel *Kalkmulden*** (e and egk in Figure 2.6), which are exposed in the Eifel North-South Zone, comprise several thinner units deposited in the Eifelian and Givetian (see further subdivision in Ribbert 1992). They consist of successions of pelites, fossil-rich calcarenites and partially dolomitised limestones that contain biostromes, corals and stromatopores. These lithologies reflect a classical rhythmic build-up of reef mounds which are typically developed in the shallow waters on the carbonate platform during the Middle Devonian (Schmidt 1956). Total thickness of the Eifel Kalkmulden is estimated to be about 740 m (Meyer & Stets 1980, von Winterfeld 1994). The overlying, 300 m thick **Muldenkern Dolomite** marks the end of the Givetian deposition and consists of a stromatopore-rich limestone, possibly dolomitised during post-Variscan influx of hot fluids along Triassic normal faults (Richter 1985). In the Eifel Nord-South Zone, this dolomite continues into the Frasnian. The upper border is characterised by a reworked eroded surface exemplifying another sedimentary hiatus in the Frasnian (Richter 1974 in von Winterfeld 1994). Due to variation in this erosional surface, minimum thickness of this unit has been estimated to 300 m but may increase up to 500 m (Richter 1974 in von Winterfeld 1994).

The deposits after this Frasnian hiatus are of middle Famennian age and consist of subaerial to submarine sediments. In contrast to the Condroz and Famenne Units north of the Stavelot-Venn inlier (see Figure 2.6) and the thick sequences in the Dinant fold-and-thrust belt (Bultynck & Dejonghe 2001), middle Famennian psammites are not preserved in the Eifel area (Paproth *et al.* 1986) but could have reached a thickness of 400 m (von Winterfeld 1994). In the late Famennian, a regional regression and the late Variscan uplift of some tectonic blocks in the Ardennes (Ardennian Shoal in Paproth *et al.* 1986) and Rhenish Massif (Piecha 2002) caused a new hiatus in sedimentation in the Eifel area (Figure 2.4). Further post-Devonian sedimentation is limited to the Dinantian and Namurian with a hiatus in sedimentation from the late Visean to the early Namurian (Yilmaz *et al.* 1996). In his palaeogeographic reconstructions, Ziegler (1990) reports a thickness variation of 200 m to 2000 m for the Dinantian carbonates in the western Rhenish Massif. Although the Dinantian in the Eifel area is currently fully eroded, a thickness estimation of 1000 m is probably more realistic (von Winterfeld 1994). Finally, Namurian continental to lacustrine sediments with a maximum thickness of 50 m are the youngest Upper Palaeozoic rocks deposited in the Eifel area (Yilmaz *et al.* 1996). During the subsequent Westphalian, the Rhenohercynian Zone was uplifted and acted as a source for the Westphalian deposits in the Namur and Campine basin, north of the Variscan front (Yilmaz *et al.* 1996, Ziegler 1990).

2.3.5 Total thickness

To conclude, in order to estimate the total thickness of all units which are deposited in the North Eifel and eventually to estimate the depth of burial, the described thicknesses of the units in the region of the Rursee and Urftsee have been summed. This sum amounts approximately 10.3 km and reflects the total thickness of Upper Palaeozoic deposits above the Ordovician Salm Group. The outcrops studied around the Rursee and Urftsee, of which the structural characteristics will be described in detail in Chapter 3, all belong to the middle to upper part of the Upper Rurberg Unit and locally to the lower part of the Heimbach Unit (Figure 2.4 and Figure 2.6). Thickness of units above the middle part of the Rurberg Unit amounts approximately **~7 km**. As the exact stratigraphic position of the sequences studied within the Upper Rurberg Unit is unknown, an error of ± **0.1 km** has been estimated. This depth will be later used in order to validate the maximum burial temperature during vein formation (see Chapter 5) .

2.4 Depositional environment of the Upper Rurberg Unit

As good index fossils are rare in the thick Siegenian pile and as a detailed biostratigraphy is lacking, the environmental conditions during Siegenian deposition can only be derived from sedimentological observations. Based on representative Lower Devonian cross-sections, several palaeoenvironmental reconstructions have been composed in the past (*e.g.* Goemaere & Dejonghe 2005, Stets & Schafer 2009) and represent very well the sedimentary processes active during deposition. In what follows, field observations at the Rursee will be compared with the some of these palaeoreconstructions in order to show the variability in sedimentary structures of some outcrops.

2.4.1 Sedimentological observations

The observed outcrops of the Upper Rurberg Unit predominantly consist of silty and clay-rich sediments intercalated with decimetre-thick fine-grained to metre-thick coarse-grained sandy beds (Figure 2.7a). Grain sizes have been estimated roughly in the field. The silty beds, monotone grey in colour, are characterised by an intense cleavage development but sedimentary structures are rare. The fine-grained sandstones are often distributed in centimetre-thick wavy to parallel laminations (Figure 2.7b) with locally sandballs incorporated. Coarse-grained beds change from thin, well sorted sands to decimetre-scale channels (gullies) filled up with laminated to cross-bedded sandy layers which are separated from each other by thin millimetre pelitic laminae (Figure 2.7b). At the top of thin beds ripple marks often occur (Figure 2.7c). Biological activity in the coarse-grained sands is only found as bioturbations disturbing the primary bedding structures. On large outcrops, asymmetric, metre-scale point bars are apparent and represent larger channel fills (Figure 2.7e). Besides these sedimentary structures, small-scale synsedimentary deformation such as convolutions and load-cast occurs at the base of the fine-grained sandstones (Figure 2.7d). At the base of the coarse-grained beds, plant remains and shell fragments are only rarely found. Coarsening-upwards sequences evolving from silty to sandy have been observed and are expressed by the pervasive cleavage which gradually changes in nature from a slaty cleavage in the siltstone to a spaced cleavage in the competent fine-grained sandstones. At the top of the sequences cleavage refracts at high angles to competent-incompetent interface reflecting the abrupt change of a coarse-grained unit into a fine-grained unit.

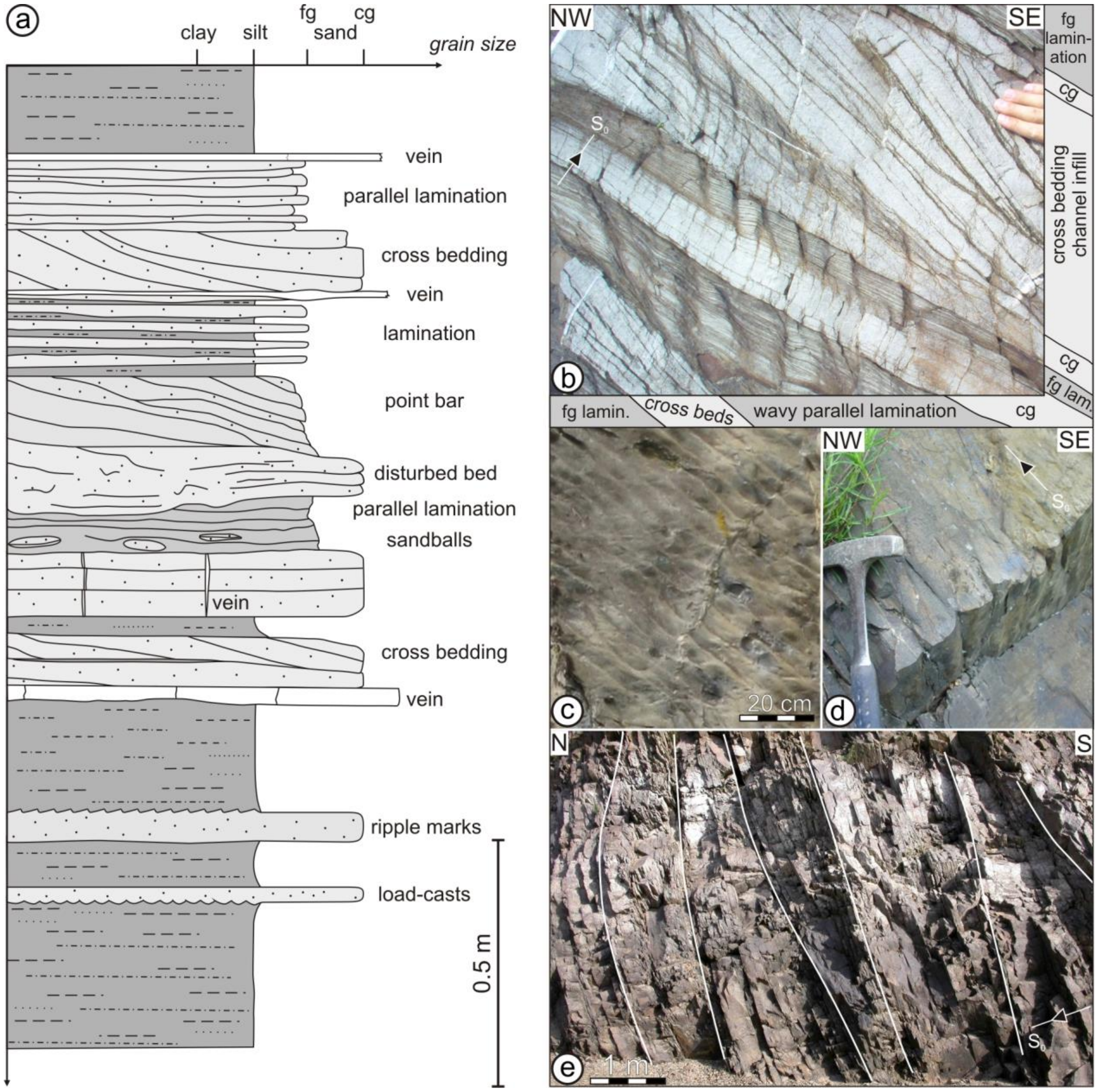

Figure 2.7: Sedimentological observations. See Figure 3.1 and Appendix B for localisation of the outcrops. **(a)** Sedimentological profile showing the nature of shallow marine deposits of the Upper Rurberg Unit. fg: fine-grained sands; cg: coarse-grained sands (Wildenhof section, outcrop 27). **(b)** Intercalation of fine-grained parallel laminations with coarse-grained cross-beds. Stratigraphic younging indicated (Wildenhof section, outcrop 27). **(c)** Bedding surface with ripple marks (Wildenhof section, outcrop 18). **(d)** Load-casts at the base of a fine-grained bed. Stratigraphic younging indicated (Schwammenauel S section, outcrop 119). **(e)** Heimbach beds with reverse structural and stratigraphical polarity showing metre-scale point bars and an alternation of silt- and sandstone beds (Schwammenauel S section, outcrop 153).

2.4.2 Depositional model

The variation in sedimentary structures and grain sizes are related to varying energetic conditions during deposition, rather than to regional sea level changes. Small-scale sedimentary structures, such as ripple marks and cross-beds within channel structures, are representative of an energetic, shallow marine depositional environment. An evolution from parallel laminations to cross-bedding within the sandstones may reflect an increase in current speed while the silty sequences reflect muddy deposition in slowly flowing waters. In the Siegenian Normal facies of the Rhenish Massif (cf. Meyer & Stets 1980), the above described sedimentary structures are representative of large distal meandering fluvial systems existing in a low-relief mud and floodplain environment. These fluvial systems could gradually change into a subaerial delta platform (Meyer & Stets 1980, Stets & Schafer 2002). While the coarse-grained beds reflect the infill of distributary channels running through the flood plain, the fine-grained to silty sediments can be related to mud planes flooded by low-current waters. These Lower Devonian environments were widespread and covered most areas along the northern margin of the Rhenohercynian basin (Stets & Schafer 2009).

Importantly, in order to maintain the very thick Siegenian sequences, the basin subsidence, detritical input and sediment supply had to be in balance nearly all the time during the Siegenian. The rivers brought huge volumes of siliciclastic sediments from the Old Red Sandstone Continent towards the shallow marine basin of which the depth of the basin remained constant due to the activity of extensional synsedimentary faults (Goemaere & Dejonghe 2005, Stets & Schafer 2009). The structures observed in the Upper Rurberg Unit also correspond very well to the Lochkovian Mirwart Formation in the central part of the High-Ardenne slate belt despite the differences in age of both units. This shows the consistency in time and place of the regional Siegenian deltaic system (cf. Meyer & Stets 1980).

2.5 Metamorphism and Variscan deformation in the High-Ardenne slate belt

In the High-Ardenne slate belt, in which the slaty cleavage is the dominant structural feature, the Lower Devonian siliciclastic, predominantly argillaceous sequences underwent a very low- (anchizonal) to low-grade (epizonal) metamorphism (Figure 2.8). In the Ardennes, anchizonal conditions correspond to temperatures of 250°C - 300°C, while epizonal conditions start at 300°C and may increase locally up to 450°C. Only in the SE of the Eifel depression metamorphism did not exceed diagenetic conditions. The highest metamorphic grades are associated with the rocks at the southern limbs of the Lower Palaeozoic Rocroi and Serpont basement inliers and correspond to increased metamorphism due to nappe stacking along inverted Lower Devonian synsedimentary fault zones (Beugnies 1986, Fielitz 1992, 1997). The metamorphism in the High-Ardenne slate belt is considered to have a burial origin, formerly termed as ‘diastathermal’ metamorphism (Fielitz 1995, Robinson 1987 in Fielitz & Mansy 1999), and the metamorphic temperatures correlate very well with the age and thickness of the Lower Devonian sedimentary sequences. It is believed to be pre- to early synkinematic with respect to the prograding Variscan deformation, thereby documenting the peak of subsidence and sediment accumulation in the Ardenne-Eifel basin (Fielitz & Mansy 1999). In the Dinant fold-and-thrust belt, north of the High-Ardenne slate belt, the initial burial-related diagenetic conditions are overprinted by an anchizonal/beginning epizonal synorogenic metamorphism (Figure 2.8) related to nappe stacking of the advancing orogenic front during Variscan deformation (von Winterfeld 1994).

In the Eifel area, the sigmoidal shape of quartz overgrowth of metamorphic porphyroblasts (pyrite) in the pelites of the Monschau Unit is a clear indication for the pre- to synkinematic metamorphism (Fielitz 1992, Spaeth 1979). At the southern border of the Stavelot-Venn inlier, this metamorphism shows typical peak metamorphic conditions corresponding to the upper epizone with temperatures of 400°C - 450°C and pressures of 100 MPa to 300 MPa (Fransolet 1978, Kramm & Buhl 1985). These epizonal conditions, however, only occur in the Monschau shear zone (Fielitz 1992). To the SE of this high-strain zone, the rocks in the Eifel area are affected by a high-temperature, low-pressure metamorphism, similar to the metasediments in the Rhenish Massif in which temperature did not exceed 350°C (Weber 1981). The metamorphic grade corresponds to anchizonal conditions in the North Eifel and diagenetic conditions in the Eifel North-South Zone (Figure 2.6). The age of this metamorphism must be younger than some magmatic intrusions in the Stavelot-Venn inlier which are affected by cleavage development and which are dated at 381 Ma (Kramm & Buhl 1985 in Fielitz & Mansy 1999, Han *et al.* 2003), but older than 326 ± 7 Ma based on K/Ar-datation of recrystallised phyllosilicates in Gedinnian rocks (Piqué et al. 1984 in Kenis 2004).

During late Carboniferous Variscan shortening of the Rhenohercynian belt, different fold styles are created throughout the High-Ardenne slate belt. The overall structural architecture changes from NW-verging and slightly NE-plunging, upright to overturned NE-SW-trending fold trains in the North Eifel (Pilger & Schmidt 1957, Wünstorf 1931, 1936) into slightly north-verging, upright east-west-trending folds in the western part of the High-Ardenne slate belt (Hance *et al.* 1999, Kenis 2004). The transition of the overturned fold style in the North Eifel into upright folds in the western part of the High-Ardenne slate belt occurs gradually (Hance *et al.* 1999). Concomitant with the variation in fold style, also the dominant, penetrative slaty cleavage in the slate belt changes from moderately SE-dipping to steeply south-dipping respectively. Most folds are hectometre in scale and seem to be largely synchronous with Variscan cleavage development as evidenced by the parallelism of the cleavage with the axial planes of the folds in the slate belt. Both Fielitz (1992) and Spaeth (1979) argue that this major structural change in fold- and cleavage orientation of the two areas, is probably related to an oroclinal Variscan overprint over the southern border of the pre-Variscan subsurface basement high in the foreland, *i.e.* the Brabant basement.

Similar as to the major part of the Rhenish Massif, the structural development of the North Eifel is characterised by a strong NW vergence (Weber 1981). Folds gradually change from hectometre-scale, upright folds in the Malsbenden-Schleiden area in the SE (Figure 2.6; SE of cross-section A-B) into overturned, NW-verging folds in the Rursee study area (Figure 2.6; NW of cross-section A-B and SE of cross-section C-D). Towards the south-western border of the Stavelot-Venn Inlier, small decametre-scale folds characterise the Monschau shear zone. This zone contains NNW-verging, east-plunging folds (Fielitz 1992, Spaeth 1969, 1979), a trend which differs distinctively from the general NE-SW trend of the major hectometre folds. These minor folds, moreover, exemplify an intense shortening and stretching lineation along the southern border of the Stavelot-Venn inlier (Ribbert 1992) in which the abnormal orientation of the folds can be explained by rotation of the original folds around an ENE-plunging rotational axis during basement-parallel shear (Hoffmann 1961, Spaeth 1979). Concomitant with the varying fold styles, an intensification of the slaty cleavage exists from the SE towards the NW in the North Eifel. Cleavage is largely parallel to the axial planes of the folds and varies from an almost vertical spaced cleavage in the Malsbenden-Schleiden area, over a slaty SE-dipping (60° SE) cleavage in the Rursee study area, towards a gently inclined (30° SE) slaty or continuous cleavage in the intensely deformed and metamorphosed SE-limb of the Stavelot-Venn Inlier (Hoffmann 1961, Knapp 1980, Wünstorf 1936). Similar as to the metamorphic grade, the intensity of the deformation thus decreases towards the SE.

The major NW-dipping Malsbenden backthrust, which is locally characterised by several separated north-dipping backthrusts (Breddin 1963), does not only separate the Siegenian and Emsian Lower Devonian Units (see Figure 2.6), but also forms a clear border in deformation style. South of this fault, structures are southerly backtilted, resulting in a locally steep to even north-dipping, weakly developed cleavage which contrasts with the steep SE-dipping continuous slaty cleavage north of the fault (Ribbert 1992, von Winterfeld 1994). Furtak (1965) observed a similar pattern between the cleavage attitude and the north-dipping Troisvierges fault at the Belgian-Luxemburg border and proposed to extend the smaller backthrusting faults at Malsbenden with the Troisvierges fault into the major Malsbenden-Troisvierges backthrust. The North

Eifel is furthermore characterised by SE-dipping faults and by listric thrust faults (Fielitz 1987, Weber 1981), of which some are interpreted as inverted, pre-shortening synsedimentary faults (Oncken *et al.* 1999). By taking up a large part of the overall shortening, these thrust faults have played a major role during the late stage of Variscan contraction (Spaeth 1979).

In general, the Variscan shortening started in the early Visean (335 Ma to 330 Ma) (Oncken *et al.* 1999) and intensified during the northwards propagation of Variscan deformation front from 325 Ma to 300 Ma (Ahrendt *et al.* 1983). Cleavage development and folding occurred between 325 Ma and 310 Ma ago. The age of the penetrative deformation in the North Eifel ranges from 327 Ma in the SE to 305 Ma in the NW (Ahrendt *et al.* 1983).

Locally in the Herbeumont-Bertrix area, the late Variscan destabilisation of the High-Ardenne slate belt is expressed by the emplacement of discordant quartz veins which cross-cut the Variscan cleavage and which developed in the extensional stress regime after the late Variscan tectonic inversion. These quartz veins developed from planar extension veins that subsequently underwent shape modification during progressive late-orogenic extension. Afterwards, the deformation of cleavage planes into kink bands and reactivation of cleavage as low-angle normal faults mark the final stages of the Variscan orogeny (Van Baelen 2010). Late Variscan kink bands have been recognised in the Eifel area, but their geometrics have never been studied and hence the kinematic significance of these kink bands remains enigmatic.

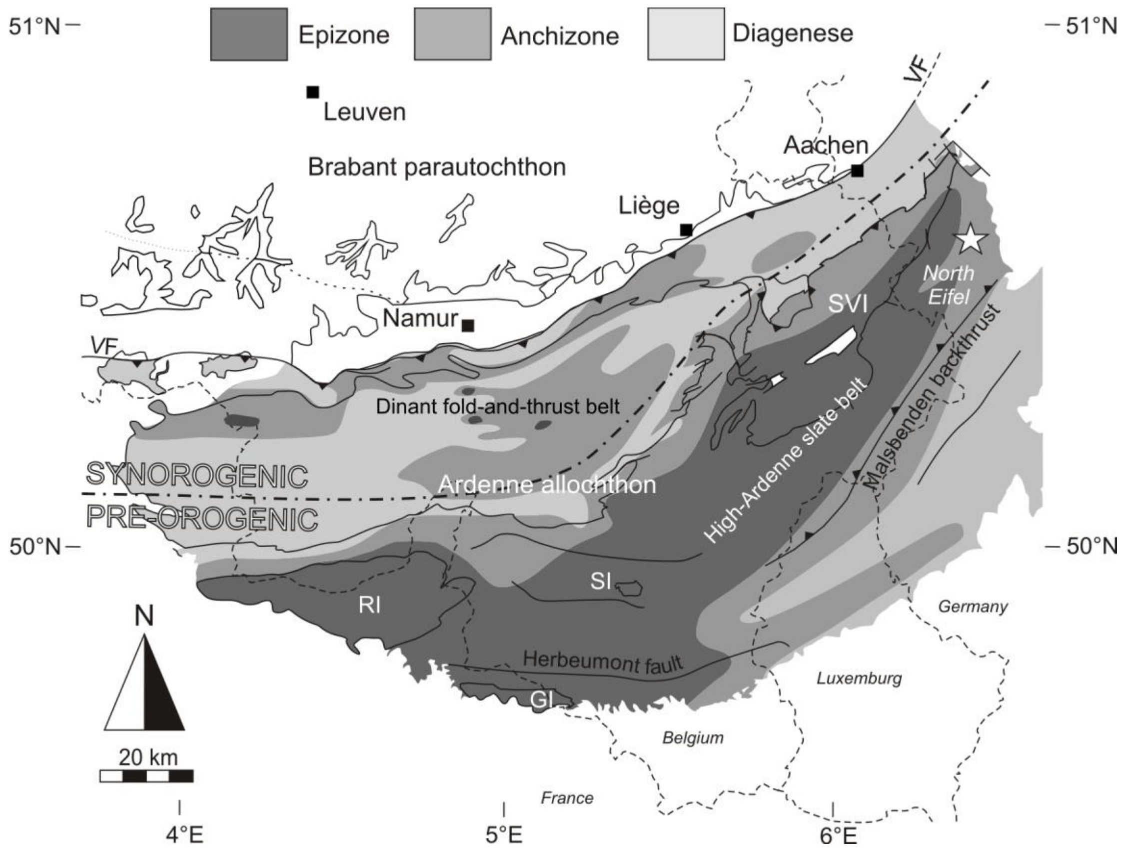

Figure 2.8: Very low-grade to low-grade metamorphic zonation in the Ardenne allochthon compiled from the metamorphic data in Fielitz & Mansy (1999). Besides the different metamorphic zones, also the transition zone between pre-orogenic (burial-related) and synorogenic metamorphism is indicated. The study area (white star) is localised in the anchizonal part of the High-Ardenne slate belt. VF: North Variscan thrust front; SVI: Stavelot-Venn inlier, RI: Rocroi inlier; GI: Givonne inlier; SI: Serpont inlier.

2.6 Post-Variscan development

The late Carboniferous Variscan deformation was followed by Permian and early Triassic erosion and peneplanation of the Variscan chain. During the Mesozoic, a long period of tectonic quiescence existed, which is followed by uplift (doming), erosion and post-orogenic faulting. Uplift of the Ardennes, Eifel and Rhenish Massif started in the Upper Cretaceous and was followed by a phase of large-scale tilting in the Palaeocene. This is for instance exemplified by steeply west-dipping Variscan folds in Lower Devonian sequences at the western border of the Stavelot-Venn inlier (Sintubin & Mathijs 1998). Subsequently, major doming occurred during the late Oligocene and continued until recent times (Garcia-Castellanos *et al.* 2000, Walter 1992). The uplift of the North Eifel occurred largely parallel to the subsidence of the Lower Rhine Graben and the Roer Valley Graben along large N-S- to NW-SE faults that were formed or might have been reactivated during subsidence (Meyer & Stets 2002). Currently the Stavelot-Venn inlier and the unconformably lying Lower Devonian deposits are situated on the riftshoulders of the Roer Valley Graben. The activity along these faults has caused block rotation within the North Eifel, as is evidenced by the large fold-plunge variability in the Heimbach area (Baum 1955). Compared to the North Eifel, the rate of uplift of the Eifel North-South Zone was lower and currently forms an area of axial depression in the landscape (Meyer & Stets 2002).

2.7 Synthesis

In this chapter, the geology of the High-Ardenne slate belt and surroundings have been presented with an emphasis on the late Palaeozoic geodynamic evolution of Rhenohercynian basin and the regional lithostratigraphical units deposited in the Ardenne-Eifel basin. Concomitant with burial, the metamorphic grade of the Lower Devonian sediments in the peripheral part of High-Ardenne slate belt increased up to the anchizone. The main phase of the Variscan contraction of these units caused a specific deformation style in the study area in the North Eifel with NW-verging overturned folds and a spaced SE-dipping axial planar cleavage. In the next chapter a detailed structural analysis of different structural features such as folds, cleavage and faults is presented in order to frame the different vein types within the overall structural architecture to be able to determine the temporal evolution of a late basin that is shortened during progressive Variscan deformation. An analysis of the occurrence and orientation of quartz veins relative to these structural features forms the base of this study and allows determining the relative timing of vein emplacement in a progressive deformation history. The reconstruction of this deformation history starts from a macroscopic field description of the veins (Chapter 3) and is refined by a microstructural analysis of the veins and host rock (Chapter 4) in order to construct the ultimate geodynamic model.

CHAPTER 3 Structural analysis

3.1 Introduction

The aim of this structural analysis is to frame different types of quartz veins within the overall architecture of the study area by a detailed, field-based geometric analysis. A large effort has been put into determining the relative chronology of different vein types with respect to primary and secondary structural elements. The study area is located at ~30 km ESE of Aachen and 15 km NE of Monschau (Germany). Lower Devonian alternating sequences classified to the Upper Rurberg, Heimbach and Schleiden Units are present in excellent outcrops, which are continuous for several hundreds of metres along hiking paths and along the shores of the Rursee and Urftsee water reservoirs. The good quality of outcrops is preserved due to seasonal water fluctuations of the reservoirs (autumn and winter are the best seasons to have maximum outcrop capacity, see Appendix B) which keep the outcrops along the shores free of any surface weathering.

Although the folded and faulted Lower Devonian rocks at the Rursee have been reported in several mapping theses of a number of students of the *Rheinisch-Westfälische Technische Höchschule* (RWTH) Aachen (*e.g.* Glasmacher *et al.* 1989 in Kukla *et al.* 2008, Vinzelberg 2002, Zier & Kuhl 1999), the Rursee and Urftsee have been chosen to be remapped during several field seasons in order to have a more detailed overview of all structural features and of the overall architecture. Based on the good outcrop exposure, three different sections of the eastern part of the Rursee have been chosen to study in detail: Wildenhof, Eschaulerberg, and Hubertus Höhe - Schwammenauel (see localisation on structural map of Figure 3.1). In order to have a regional idea about the consistency of vein patterns, the veins at the Rursee are subsequently compared with selected outcrops at the northern shore of the Urftsee (see field data of the mapping in Appendix A).

This chapter is divided in several subchapters in which the different sections studied along the Rursee and Urftsee water reservoirs are discussed. In order to refer properly to a certain outcrop, all outcrops are grouped in different zones, of which each zone corresponds to a single fold limb. Apart from the localisation of the outcrops, in each section an extensive orientation analysis of all structural linear and planar elements such as bedding (S_0), cleavage (S_1), bedding-cleavage intersection lineation (L_i), folds and fold hinge lines. The fold hinge line (FHL) is a field term and is used for the line measured at the fold hinge, while the fold axis will be used as the constructed intersection of two fold limbs on stereographic projection. Apart from these structural elements, a detailed geometric description and orientation analysis of different vein types (V) are given. These field observations are summarised in several tables representative of each section. In this work, the orientation of planar features (bedding, cleavage, veins, faults) is written as dip direction/dip in azimuth convention (*e.g.* 045/85 for a plane dipping 85° to the NE) and the orientation of linear features (intersections, fold hinge lines) is written as trend/plunge (*e.g.* 045/85 for a line plunging 85° to the NE). The bedding-cleavage intersection lineation is measured in the field and is crosschecked afterwards for its regional attitude by merging bedding and cleavage data in a lower-hemisphere, equal-area stereographic projection (see Table 3.1, Table 3.2 and Table 3.3 for summary of data). The poles to planar elements, as well as linear elements, are plotted in two orientation analysis programs: *GEOrient 9.2* (Holcombe 2004) and *StereoNett 2.46* (Duyster 2000) in order to perform a structural orientation analysis. The average orientations and maximum density of measurements are automatically determined in these programs. Throughout the geometric description, the data mentioned are mostly the mean values of several measurements on a certain outcrop, unless specifically mentioned.

Also several rotation exercises have been performed for each section studied to deduce the original orientation of the veins prior to fold-and-cleavage development. At the end of this chapter a synthesis of the overall structural architecture of the North Eifel, based on the sections studied, and a summary of all vein types will be given to constrain an evolutionary geodynamic structural model that can be discussed with respect to several models in literature. The nomenclature used for the description of the veins, will be introduced in BOX I and BOX II in the first case study. In the regional context, the Rursee study area is located between the *Rurberger Mulde* and the *Hasenfelder Sattel*, *i.e.* a local depression and culmination respectively corresponding with a large scale, first-order syncline-anticline fold train (Ribbert 1992, von Winterfeld 1994) (Figure 2.3a). The Urftsee outcrops are localised between the *Vogelsang Mulde* and the *Vogelsang Sattel*, respectively corresponding to a larger scale syncline-anticline fold train (Figure 2.3a).

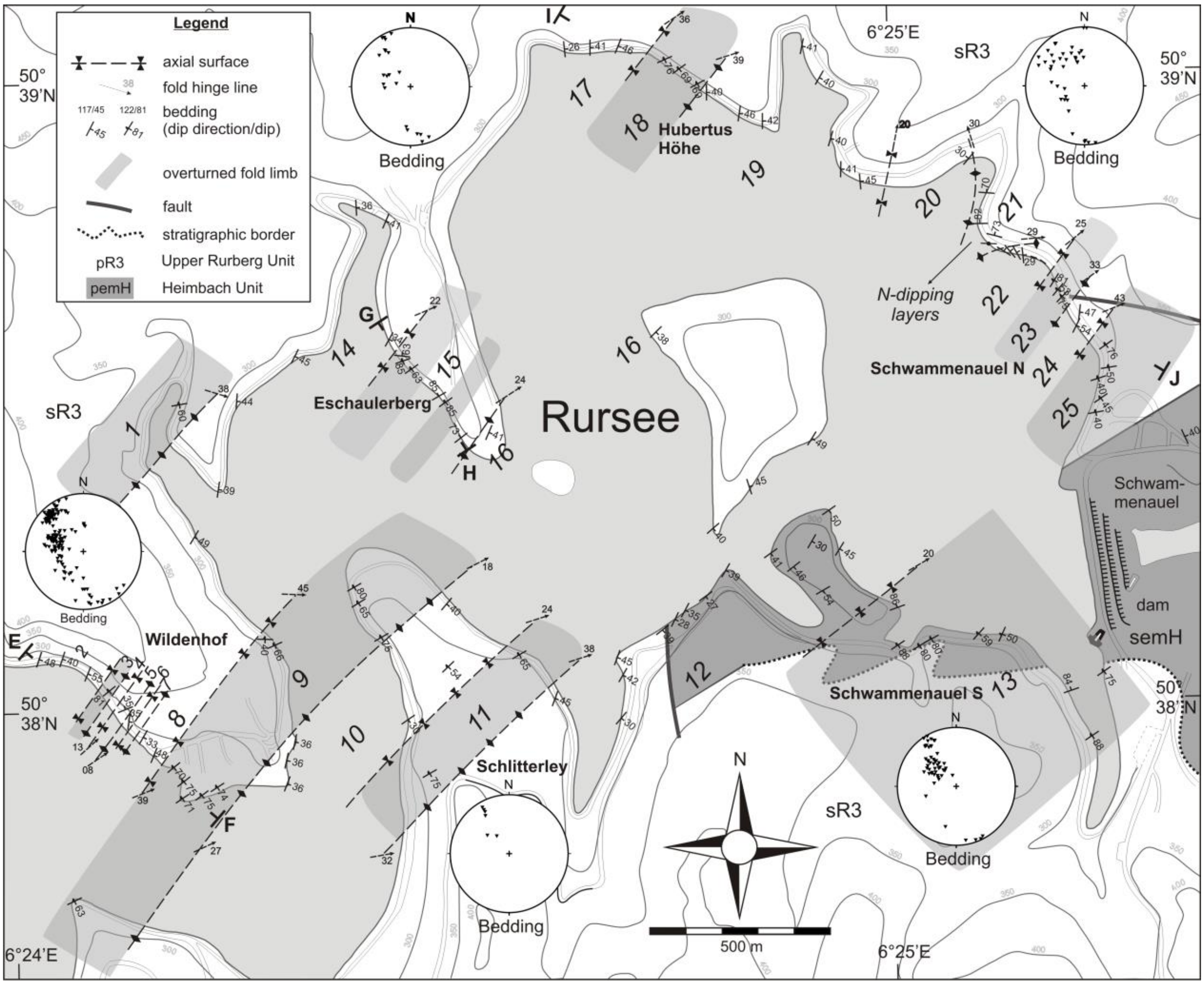

Figure 3.1: Structural map of the eastern part of the Rursee (modified after Van Noten *et al.* 2008). Cross-section E-F (Figure 3.3), G-H (Figure 3.21) and I-J (Figure 3.30) represent the outcrops studied in the Wildenhof, Eschaulerberg and Hubertus Höhe - Schwammenauel sections, respectively. Due to the general fold dip towards the NE, the outcrops in the NE of the map are situated on a higher stratigraphical and structural level. The stratigraphical contact between the Upper Rurberg and Heimbach Unit are modified after Ribbert (1992). See Table 3.1, Table 3.2, Table 3.3 for the specific field data of fold limbs 1 to 25.

3.2 Case I: Wildenhof section

3.2.1 Localisation

The outcrops studied in the Wildenhof section are situated in the south-western part of the Rursee study area, approximately 1.5 km NE of the little village Woffelsbach. A water level of 270 m NN[2] is used as reference level in Figure 3.3 and corresponds to the water level during autumn and winter. The outcrops at the shores provide a useful correlation with the structures along the road section. The largest outcrops are located along a NW-SE road section and along the shores beneath this road level, of which the accessibility is highly dependent on the seasonally fluctuating water level (see Appendix B). A few hundred meters to the SE, the road section continues along the shores at the Wildenhof campsite, *i.e.* the *Wassersportstätte 'Wildenhof'*, property of RWTH Aachen. The outcrops at the road section and along the shores are referred to as the Wildenhof section throughout this work. In order to deduce some key sections, in which different vein types can be observed that possibly reflect the regional occurrence of quartz veins, the Wildenhof section is subjected to a detailed geometric analysis. The exact position of the discussed outcrops is indicated on the scale-bar below the Wildenhof cross-section in Figure 3.3. Zones 1 to 10 correspond to the different fold limbs observed in this section, of which zone 9 and 10 can be correlated with the outcrops at the southern shores across the Rursee at Schlitterley, continuing in zones 11 and 12 (Figure 3.1; Table 3.1).

3.2.2 Geometric analysis

As described in section 2.4.1, the rocks observed in the Wildenhof section belong to the Upper Rurberg Unit and display an alternation of coarse-grained sandstones with intercalated fine-grained, laminated sandstones and silty sequences. For over 430 meter (cross-section E-F in Figure 3.1 and Figure 3.3), the Wildenhof and Schlitterley sections show syncleavage, NW-verging, upright to overturned folds, with subangular to rounded fold hinges and moderately SE-dipping (50° to 60°) axial surfaces (Figure 3.2; Figure 3.3). Bedding changes throughout the Wildenhof cross-section from a normal SE-dipping attitude (zones 2, 4, 6 and 8) to a normal NW-dipping attitude (zones 5 and 7) in upright folds, or from a normal SE-dipping attitude to an overturned SE-dipping attitude (zones 3 and 9) in overturned folds. The SE-dipping fold limbs with a normal (S_0~112/43) and overturned (S_0~140/73) structural polarity are exemplified on the stereographic projection (Figure 3.2) by a high concentration of bedding poles in two clusters, which is characteristic of subangular folds (Twiss & Moores 1992). These NW-verging overturned folds (*e.g.* zone 4) commonly have interlimb angles of 40° which classifies them as tight folds. Stereographic analysis of bedding in the NW-verging upright folds (*e.g.* transition between zones 5 and 6, or zones 7 and 8), characterised by SE-dipping (S_0~112/43) and NW-dipping (S_0~350/72) fold limbs, shows a scattered pattern of bedding poles along the mean girdle, being representative of cylindrical folds (Twiss & Moores 1992). The NW-verging attitude of the both fold styles corroborates the regional Variscan tectonic grain in the North Eifel. Axial surfaces are exemplified by a pronounced overall SE-dipping axial planar cleavage, which has a constant attitude (S_1~126/55) in the Wildenhof section (Figure 3.2b; Table 3.1). The main tectonic foliation is a distinct pervasive cleavage. Whereas the silty or sometimes pelitic sequences are characterised by a slaty cleavage, a weak or spaced cleavage exists in the competent sandstone beds. Opposing senses of cleavage refraction, indicative of the structural polarity, can be observed in the normal SE-dipping limbs with respect to the normal NW-dipping or overturned SE-dipping fold limbs.

The bedding-cleavage intersection lineation is the most prominent linear feature and can be used as a tool to predict or confirm the orientation of the local fold hinge line. The intersection lineation varies from upright to moderately, NE- to east-plunging (Figure 3.2). In contrast to the constant cleavage attitude, the bedding-cleavage intersection lineation shows a considerable variability throughout the outcrops. This variability can be explained by the variable sedimentology of the Upper Rurberg Unit.

---

[2] NN: Normalnull: German zero sea level point equal to the NAP (Normaal Amsterdams Peil)

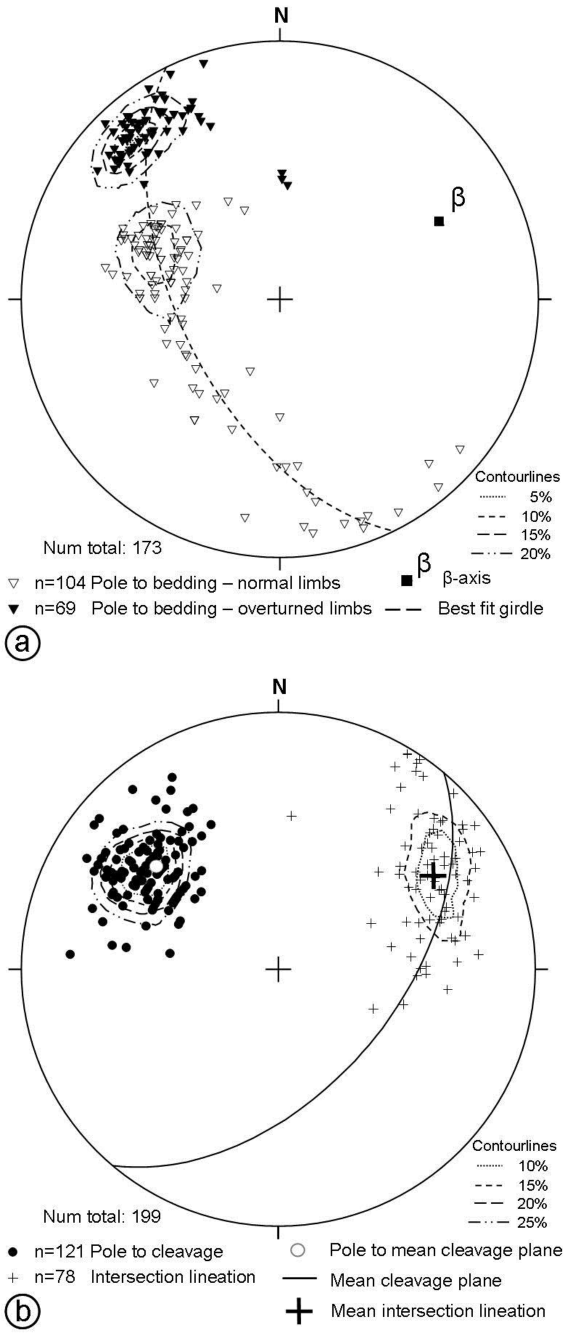

Figure 3.2: Lower-hemisphere, equal-area stereographic projection of measured structures at the Wildenhof section. **(a)** Poles to bedding. **(b)** Measured bedding-cleavage intersection lineation and poles to cleavage.

Because of the presence of small-scale gullies and larger-scale point-bars (see description in section 2.4.1) bedding surfaces have often a wavy character while cleavage attitude remains constant. Because of this, the bedding-cleavage intersection may slightly differ from bed to bed. Also, smaller folds are sometimes present in larger fold limbs. If these smaller folds occur in rather silty sequences, than they are not influenced by surrounding competent beds and the intersection lineation can vary. Despite this variability, the β-axis, *i.e.* the pole to the best fit girdle around which the bedding poles are arranged on the stereographic projection (Figure 3.2) and which has a value of β~063/32, corresponds well with the mean value of the measured intersection lineation (L_i~059/29) or with the merged bedding-cleavage intersection lineation. Both the mean intersection lineation and the β-axis support the presence of gently NE-plunging folds that have moderately to steeply inclined axial surfaces at the Wildenhof section. The southern overturned limb at Wildenhof (zone 9) can be connected with the northern extremity of the Schlitterley promontory across the Rursee (Figure 3.1). Hence, the NW-SE Wildenhof fold train, described in this section, continues at Schlitterley towards the SE.

The fold limbs and hinge zones of both upright and overturned folds are cross-cut by faults. At m60 and m90 (Figure 3.3; Figure 3.4a), two such major fault zones are present. The absence of any correlation of beds in the footwall with beds in the hanging wall, suggests that both faults must have displacements of at least a few tens of metres. The fault zones, with a maximum width of 0.5 metre, are characterised by an internally strongly disrupted, clayey fault gouge, indicative of a localised shear zone, and are surrounded by a damage zone with reworked host-rock fragments (Figure 3.4b and c). The orientation of these moderately to steeply SE-dipping fault zones is largely parallel with the orientation of the axial surfaces of the overturned folds. Other small-scale faults have a similar SE-dipping orientation and show a minor reverse displacement (*e.g.* m235 in Figure 3.3, reverse faults cross-cutting the synclinal hinge). Based on both the orientation of these minor faults with respect to the horizontal plane (> 30°) and on the displacement direction along the fault plane, these faults can be classified as reverse faults and not as thrust faults. However, small thrust faults are observed near some synclinal fold hinges in which faulting has caused duplication of the layers in the hinge.

An example of a thrust fault is visible between the syncline-anticline couple at m112 (Figure 3.5a) in which fault displacement occurred along out-of-syncline thrust towards the adjacent anticline.

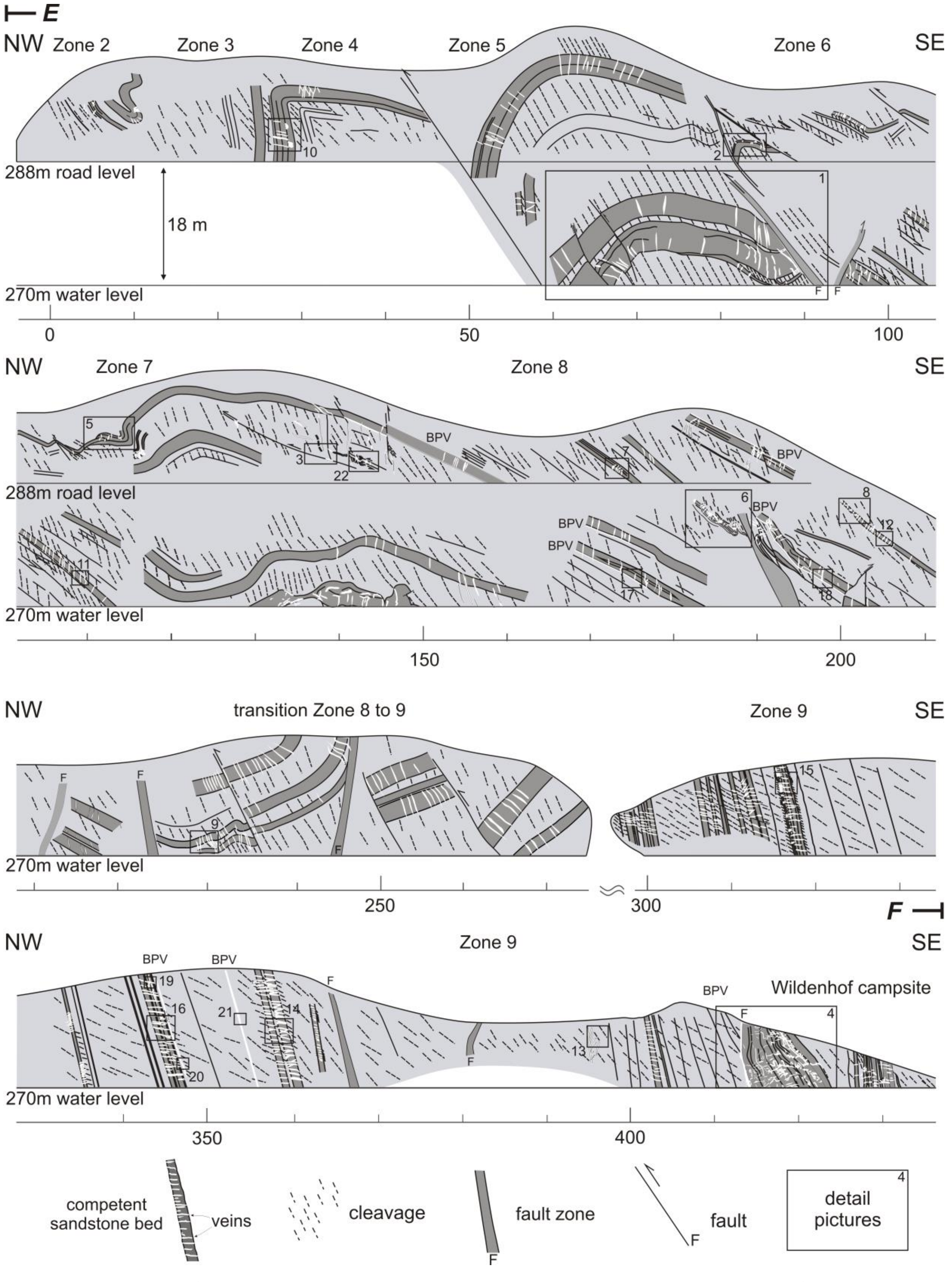

Figure 3.3: Wildenhof structural cross-section (E - F in Figure 3.1) constructed by means of photographs and field drawings showing bedding, cleavage, folds, faults and veins (modified after Van Noten *et al.* 2008). For over 430 meter, the cross-section contains hectometre-scale, NW-verging, upright to overturned folds with an apparent axial planar cleavage. Mind the gap of 30 m between m270 and m300. Location of photographs: (1) Figure 3.4a and Figure 3.7a; (2-4) Figure 3.4; (5-7) Figure 3.5; (8) Figure 3.6; (9-13) Figure 3.7; (14-16) Figure 3.8; (17-21) Figure 3.13; (22) Figure 3.19.

Table 3.1: Bedding and cleavage data of the investigated zones at the Wildenhof-Schlitterley section. See Figure 3.1 for localisation of the fold limbs (zone 1 to 12). The number of measurements is given in brackets. Grey zones represent the data specific for an overturned limb. - : not observed or suspicious data.

Outcrop	**Bedding (S_0)**	**β - axis of bedding**	**Cleavage (S_1)**	**S_0/S_1 L_i (measured)**	**S_0/S_1 L_i (merged)**
Zone ***1***	170/60 (2)	-	160/40 (1)	090/44 (1)	085/08 (3)
Zone ***2***	105/46 (24)	057/32	121/56 (15)	059/32 (11)	061/37 (36)
Zone ***3***	139/78 (7)	063/42	126/63 (6)	058/42 (3)	058/36 (13)
Zone ***4***	133/45 (2)	-	145/65 (1)	033/34 (3)	065/21 (3)
Zone ***5***	353/74 (9)	061/36	138/62 (2)	064/57 (1)	071/36 (11)
Zone ***5 - 6*** *: transition*	064/42 (7)	-	113/66 (4)	026/44 (3)	045/40 (11)
Zone ***6***	069/32 (5)	090/30	119/55 (8)	066/32 (2)	054/31 (13)
Zone ***7***	145/90 (10)	-	135/35 (2)	051/19 (2)	055/07 (12)
Zone ***8***	108/43 (31)	-	128/54 (16)	059/27 (12)	070/37 (47)
Zone ***8 - 9*** *: transition*	345/75 (8)	022/64	122/66 (5)	066/32 (2)	059/46 (10)
Zone ***9*** *- Wildenhof*	144/72 (54)	214/37	127/53 (43)	059/26 (26)	066/33 (81)
Zone ***9*** *- Schlitterley*	149/73 (4)	-	133/45 (3)	068/20 (1)	066/21 (5)
Zone ***10*** *- Wildenhof*	104/40 (5)	028/12	139/59 (10)	073/33 (7)	075/36 (15)
Zone ***10*** *- Schlitterley*	138/35 (2)	-	152/60 (1)	080/27 (1)	071/15 (3)
Zone ***11*** *- Schlitterley*	150/70 (2)	-	130/40 (2)	073/34 (2)	068/21 (4)
Zone ***12*** *- Schlitterley*	157/45 (1)	-	150/50 (1)	065/35 (1)	-
Zone ***1 - 10***	Best fit girdle:		Mean value:	Mean value:	Mean value:
Wildenhof fold train	243/58 (164)	063/32	126/55 (114)	059/29 (73)	064/31 (255)
Zone ***9 - 12***	Best fit girdle:		Mean value:	Mean value:	Mean value:
Schlitterley fold train	247/70 (9)	067/20	139/46 (7)	072/27 (5)	068/19 (12)

These out-of-syncline thrusts cross-cut bedding and duplicate the sandstone layer in the hinge zone. They primarily form because of an increase in bed curvature and they solve the accommodation problem in the fold core (cf. Mitra 2002). Parallel to the fault, thick quartz veins locally occur. These veins are marked by slickenlines, presumably tracking the out-of-syncline fault movement. The slates just below the synclinal hinge are characterised by a well developed cleavage, which gradually changes from gently dipping just below the hinge zone (Figure 3.5a) into its regional, moderately SE-dipping orientation. From the road level towards the water level (m125), this complex syncline-anticline-syncline fold train evolves into a single open syncline (Figure 3.3). At m90 and m200, two NW-dipping faults occur antithetic to larger SE-dipping fault zone. These SE- and NW-dipping faults seem to be genetically related and can be interpreted as a pop-up structure causing an upwards displacement of the sequences between both fault types, notwithstanding the fact that a reverse displacement along the SE-dipping faults has not been observed. In contrast to the antithetic fault at m90, the displacement along the NW-dipping fault at m200 could be observed and measures one metre.

Based on its gently-dipping orientation with respect to the horizontal plane, another gently SE-dipping thrust fault can be observed in the silty sequences at m140 (road level, zone 8; Figure 3.4d). This fault is oriented parallel to bedding and its fault plane is marked by quartz precipitation, giving rise to a bedding-parallel fault vein which laterally varies in thickness. Such a local thickening of the vein is interpreted as an asymmetric dilational jog that represents local shearing along the fault plane (Figure 3.4d). The fault vein is moreover marked by slickenlines at its upper and lower vein wall, of which a direction of fault movement towards the anticlinal hinge to the NW can be deduced. Observations indicate that this gently SE-dipping thrust fault is approximately 20 metre long and dies out in the silty sequences close to the anticlinal hinge between zone 7 and zone 8. A temporal relationship between folding and thrusting could, however, not been established due to the

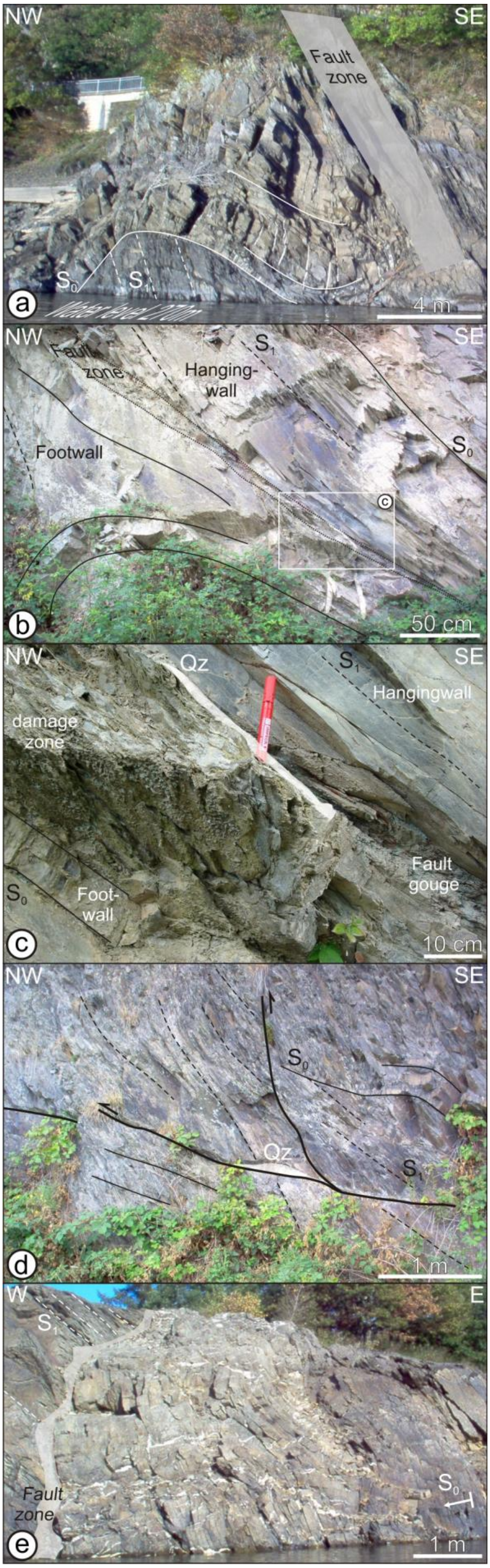

absence of observation of the thrust fault cross-cutting the anticlinal fold hinge. This thrust fault, moreover, locally bifurcates into steeply-dipping reverse faults branching off from the thrust plane causing minor, decimetre displacements of an overlying sandstone layer (Figure 3.4d). The fault planes of these minor bifurcations are also characterised by quartz precipitation.

At m190, a metre-scale, higher order fold is developed in a sandstone layer that occurs interbedded in silty sequences (Figure 3.5b and c). The S-shaped fold has a NW-verging asymmetry and is developed in the SE-dipping limb of zone 8. Around the anticlinal fold hinge, a cleavage fanning can be observed in the silty sequences. Also other synclinal hinges show a clear divergent cleavage fanning in the hinge zone of the fold. Two reverse faults, marked by quartz with irregular geometries in the fault plane, cross-cut the folded sandstone layer and displace it over a couple of decimetres. Below the folded and thrusted sandstone, the reverse faults can be traced where they cross-cut the silty sequences, but after 0.5 metre both reverse faults disappear into the bedding planes of the underlying siltstones. A substantial amount of displacement of these minor faults has thus taken place parallel to the bedding planes of the siltstones. Both small-scale faults that displace the folded sandstone layer seem to be formed during a similar NW-directed deformation as the folding of the layer. Shortening accommodated by this folding and thrusting of the sandstone layers is estimated to be 40%, which is deduced from the difference in original versus shortened length.

Figure 3.4 (left)**:** Fault zones observed at the Wildenhof cross-section. **(a)** Anticline-syncline fold train cross-cut by a SE-dipping (reverse) fault zone (m65-90). **(b)** Bedding-parallel fault zone above a synclinal hinge. (m85, zone 6). **(c)** Detail of the fault gouge in (b). Bedding-parallel quartz vein at the top of the fault zone. **(d)** Bedding-parallel reverse faulting in silty sequences in a SE-dipping limb. A dilational jog filled with quartz associated with the fault movement (m140, zone 8). **(e)** Chaotically fractured sandstone sequence below a bedding-parallel fault zone in the overturned SE-dipping limb at Wildenhof camping (m420, zone 9). Structural and stratigraphic younging inficated. For location, see Figure 3.3.

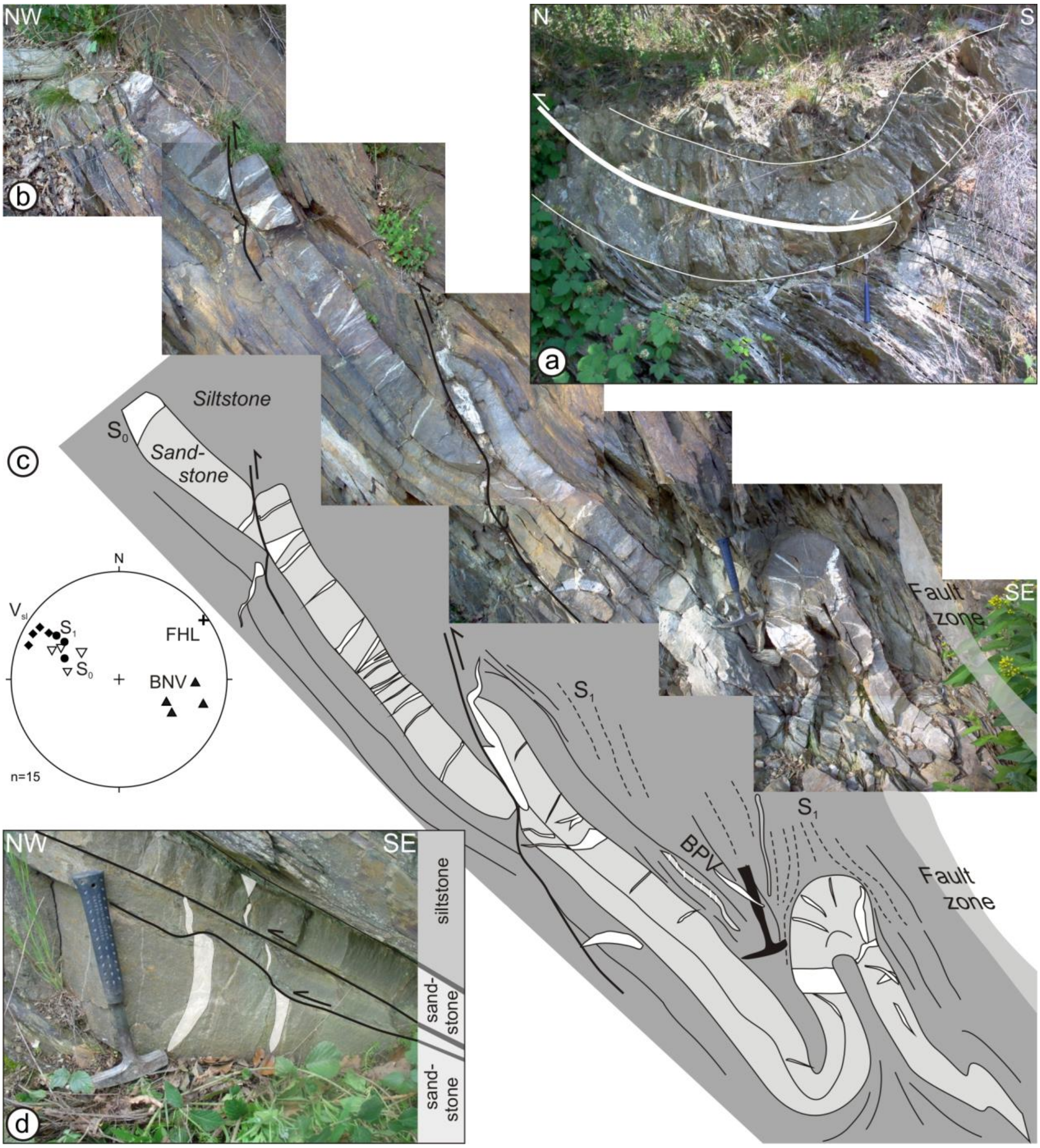

Figure 3.5: Small-scale deformation structures observed at the Wildenhof cross-section (modified after Van Noten *et al.* 2008). Hammer (~32 cm) for scale. For location see Figure 3.3. **(a)** Out-of-syncline thrust fault between two thick competent sandstone layers (m110; zone 7). **(b)** Silty sequences with a NW-verging asymmetric, metre-scale folded sandstone layer and reverse faults with a minor displacement (m185; zone 8). **(c)** Field drawing of (b) and lower-hemisphere equal-area stereographic projection of bedding, cleavage, fold-hinge line (FHL). Orientation of bedding-normal veins (BNV) and veins in the silty sequences (V_{sl}) are also plotted. **(d)** Bed to bed movements as exemplified by displaced bedding-normal quartz veins. Displacement occurs in the thin pelitic interlayer in a direction in agreement with the flexural-slip mechanism (m170, zone 8).

To the SE of the folded layer, a 0.5 meter-wide, steeply SE-dipping fault zone cuts the prolongation of this layer (Figure 3.5b and c). These thicker fault zones are commonly characterised by a clayey fault gouge with internally disrupted wall-rock fragments and are often characterised by a red-coloured, weathered appearance. Similar wide fault zones with associated fault gouges and unknown fault displacements have also been recognised between m210 and m250 (Figure 3.3) cross-cutting the wide, open synclinal hinge zone. In contrast to the planar reverse fault in this synclinal hinge, it remains unclear whether the cross-cutting fault zones have a reverse or normal fault displacement. The wide syncline forms a second-order fold transition from the mainly, gently SE-dipping layers (m0 to m250) to a long fold limb (zone 9) with a consistent overturned polarity (S_0 ~144/72), which is exposed at the Wildenhof campsite (m300 to m430). This overturned limb shows SE-dipping beds with a mean orientation of S_0~144/72. Cleavage dips less steeply than bedding (S_1~127/53), indicative of the overturned orientation. The sandstone layers within this overturned limb are densely fractured by several bedding-normal and bedding-parallel quartz veins, which are further investigated in section 3.2.3 and section 3.2.4. Also at m420 a sequence of coarse-grained sandstones is densely fractured. The omnipresent siltstones and slates are interrupted by coarse-grained sandstones, mostly characterised by the occurrence of numerous quartz veins. Apart from the common bedding-normal and bedding-parallel veins, also quartz veins with an irregular geometry are present within this chaotic zone. The top of this complex zone is bordered by a 20 cm-wide bedding-parallel fault zone. This complex zone has not been studied in detail as the vein patterns seem to have a local origin controlled by the faults that occur between the sandstones. The veins might be indicative of local fluid releases along small-scale faults and might not relate to the regional vein formation that forms the subject of this work.

A few outcrops show a local subparallelism of cleavage and bedding attitude (*e.g.* m200, zone 8). As result of this subparallelism, boudinage of the competent sandstones has taken place (Figure 3.6), possibly due to pure flattening or thinning of the layers related to the cleavage development (cf. Price & Cosgrove 1990, Van Baelen & Sintubin 2008). According to the boudinage classification of Goscombe *et al.* (2004), these boudins can be classified as single-layered, slightly asymmetric torn-boudins with quartz veins present between the separated blocks. Furthermore, small layer-to-layer displacements have been observed internally within the boudinaged competent sandstone layer, as exemplified by millimetre offsets of hairline-thin, bedding-normal quartz veins (Figure 3.6b). These decimetre-scale bed-on-bed movements are wide-spread and are more obvious in sequences in which sandstones are separated by thin pelitic interlayers (Figure 3.5c) that form a location for movement horizons or slip planes during flexural-slip folding. The amount of displacement can sometimes be measured by means of displaced bedding-normal quartz veins (Figure 3.5c). In this case, the displacement represents a top-to-northwest bedding-parallel displacement as result of flexural slip in the SE-dipping limb during folding.

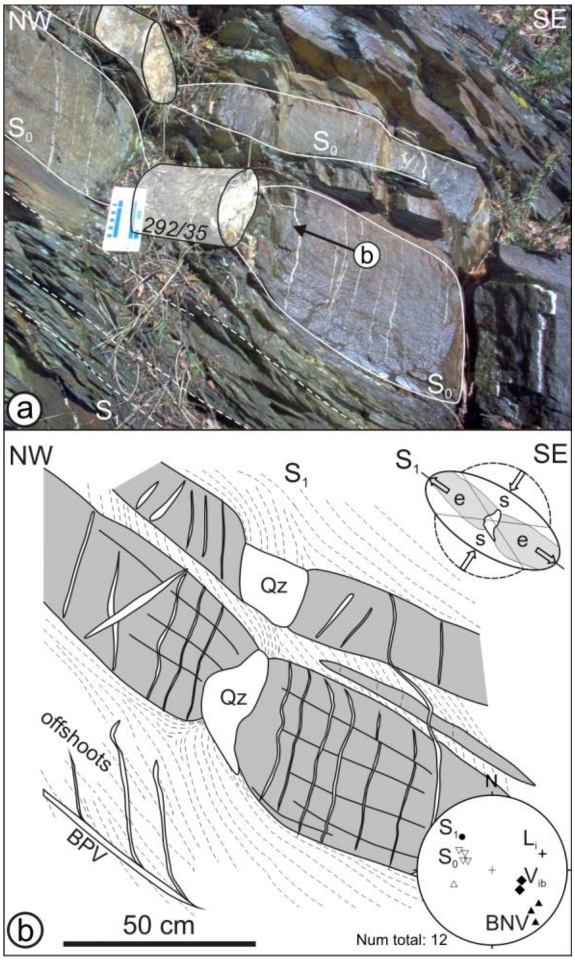

Figure 3.6: (a) Photograph of boudinaged sandstone layer with local subparallelism of bedding and cleavage (m200, zone 8); **(b)** Field drawing of **(a)** oriented normal to the vein-bedding intersection lineation. Within the sandstone hairline-thin, bedding-normal quartz veins (BNV, full triangles) occur. In the silty part (white), a laminated bedding-parallel vein (BPV, white triangle) occurs. The strain ellipse shows shortening parallel to cleavage. e: elongation; s: shortening; V_{ib} = orientation interboudin vein (diamond).

3.2.3 Bedding-normal veins

3.2.3.1 Geometric description

BOX I - Terminology used in the geometric description of bedding-normal veins (BNVs)

Natural vein arrays are common in sedimentary and low-grade metamorphic layered rocks. In order to carefully describe the veins that occur in the studied Upper Rurberg and Heimbach layered sequences, the terminology that is used in the geometric description of the bedding-normal veins (**BNVs**) is explained in detail in this box. This terminology is partly adapted from the description that is used to describe fracture arrays.

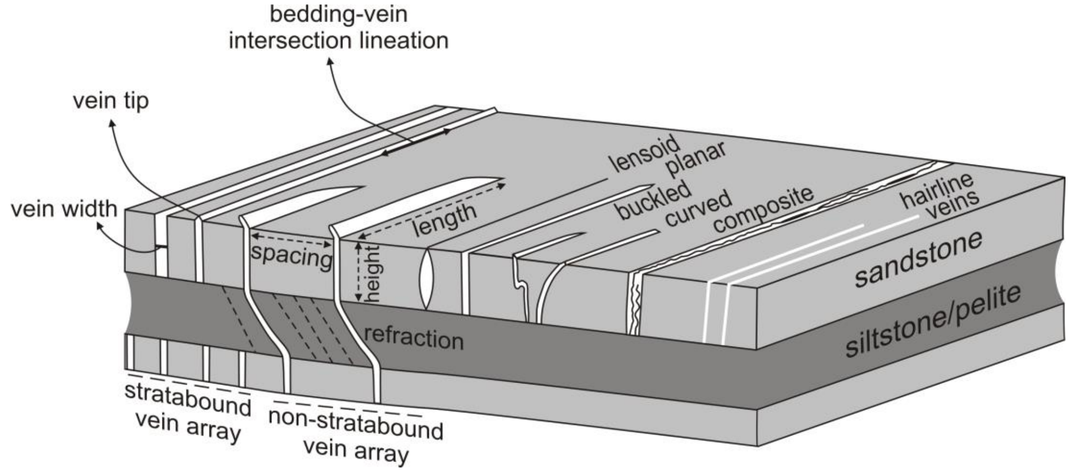

In this study, a **fracture** refers to any non-mineralised opening crack, across which host-rock minerals have been broken either with or without any measurable displacement. A fracture is therefore a surface that exists of two **fracture planes**, along which the material has lost cohesion and strength (van der Pluijm & Marshak 1997). If a lateral displacement parallel to the fracture planes is absent, the fracture opened as a Mode I extension fracture and is called a **joint**. A **vein** is a mineral-filled fracture or joint that usually forms in **vein arrays**, *i.e.* a group of regularly oriented veins in a layered sequence. Based on the consistent orientation of vein arrays or on mutually cross-cutting relationships, different **vein generations** can be determined. Two different groups of veins, *i.e.* **vein types,** are distinguished with respect to their orientation to bedding; either oriented at high angle to bedding (BOX I) or parallel to bedding (see BOX II). Veins usually originate from precipitation from a fluid that is present in an open fracture that either can be opened continuously during vein formation or that opened and closed repeatedly during several episodes. Depending on this different opening behaviour of the fracture, different vein fabrics will develop. As cohesion is restored again due to mineral-infill of the fracture, the contact between the host rock and the vein is termed the **vein wall** in stead of a fracture plane. The outer ends of the vein, *i.e.* the **vein tips**, are specific zones of the vein in which no deformation of the host rock exists above or below the vein tip. A vein that extends through a layer from one layer boundary to the opposite one in a layered sequence is defined as a **stratabound** vein (cf. Gillespie *et al.* 1999) with the **height** of the vein corresponding to the thickness of the host-rock layer and the **spacing** of the vein corresponding to the distance between two adjacent veins measured perpendicular to the vein walls. If a bedding surface can be observed in outcrop, the **length** of the vein can be measured along the intersection of the vein and the bedding plane.

To the orientation of this intersection is referred to as the **vein-bedding intersection lineation** (L_{V-S_0}). Stratabound veins can also be entirely embedded into a unique layer without reaching the bedding surface. A **non-stratabound** vein refers to a vein that cross-cuts multiple layers in a heterogeneous layered sequence (cf. Gillespie *et al.* 1999). The vein tips of such a non-stratabound vein can extend in the incompetent layer that encompasses the fractured competent layer.

BOX I (continued)

Non-stratabound vein arrays may change in orientation or **refract** at the competent-incompetent interface from an orientation at high angle to bedding in the competent layer to an orientation at lower angle to bedding in the incompetent layer. The **width** or **thickness** of stratabound or non-stratabound veins is measured perpendicular to the vein walls and vary from millimetre-thick **hairline** to thick **composite** veins. Whereas the former refers to thin apertures resulting from a single opening fracture-infill, the latter refers to a vein that has formed as result of multiple fracturing and infill events. **Hairline veins** are defined as narrow spaced stratabound veins. **Offshoots** are small veins that branch off from a larger vein that is emplaced in the same fractured host rock, forming a local network of veins. The veins studied have regular shapes that are planar, curved, buckled or lensoid. **Planar** veins involve all veins that have straight vein walls and have a continuous vein width along the vein height. At the vein tip, the vein thickness of planar veins remains constant. Veins that are continuous in thickness but have bowed vein walls are termed **curved** veins. If minor folding of the vein walls has been observed, the vein is called a **buckled** vein. Finally, **lensoid** veins have (often symmetrical) curved vein walls with opposite directions of curvature. They start from a single point at the vein tip and evolve to a thick vein in the centre part.

A geometric analysis of the quartz veins in the Wildenhof section shows that the majority of the veins studied are oriented at high angle to bedding, between 70° and 90° with respect to the bedding plane. This bedding-normal attitude remains continuous in the fold limbs and around the fold hinges (Figure 3.7a). In the core of the fold hinges (*e.g.* synclinal hinge at m230 in Figure 3.3, Figure 3.7b), axial planar cleavage hardly refracts through the competent sandstone due to the specific orientation of bedding perpendicular to the fold axis in the fold core. In the folds limbs, cleavage is more refracted in the competent units than compared to refraction in the fold core. If veins are continuous through a composite layer, composed of an alternation of fine to coarse-grained sandstone layers intercalated with thin pelitic interlayers, non-stratabound veins show a change in orientation in the pelitic layer while it is oriented at higher angle to bedding in the sandstone layer (Figure 3.7d and e; BOX I). They thus refract at the competent-incompetent interface giving the veins a sigmoidal appearance (Figure 3.7c). The curvature of the vein at the competent-incompetent interface strongly depends on the thickness of the silty layer. It is thus observed that the bedding-normal veins have a similar behaviour as cleavage in such way that non-stratabound veins also refract at the incompetent-competent interface in a similar way as cleavage. In the fold limbs this refraction of the veins is obvious, while in the fold hinges barely refraction occurs (*e.g.* Figure 3.7b). Most bedding-normal veins are, however, restricted to the competent sandstone layers (Figure 3.7g), *i.e.* stratabound veins, in which their thickness dimensions vary considerably from hairline-thick veins (Figure 3.7f) to centimetre-thick composite veins (Figure 3.7h). On the one hand, thin hairline veins with narrow apertures are mostly present in thin sandstone beds and are closely spaced. Thicker veins, on the other hand, are mostly present in thicker units and seem to be more widely spaced. Macroscopically, the thin veins comprise fibrous quartz crystals, whereas the thick composite veins contain blocky quartz crystals, separated by several pelitic host-rock inclusions, which are more or less parallel to the vein wall. If host-rock inclusions are absent, sometimes a clear syntaxial growth can be observed macroscopically in which the veins are filled with fibrous quartz crystals (Figure 3.7g). Observations on the bedding surface, hardly ever exposed, reveal that stratabound veins have a consistent orientation within the layer and are rather limited in length, maximum up to some metres (Figure 3.7i). Composite stratabound veins may vary from a clear planar shape into a slightly buckled or curved shape.

Veins also occur in silty sequences in which cleavage is the most prominent feature. In this lithology, veins are irregular in shape and they are refracted by cleavage which gives the vein a fractured appearance (Figure 3.7j and k). Veins in slates or in silty sequences, moreover, often branch off from a central vein into several smaller hairline veins, possibly due to the absence of a competent bedding surface and can be distributed in an en-echelon configuration.


NW
SE
Water level 207m
2 m
a
N
S
S$_0$
S$_1$
20 cm
b
NW
SE
S$_0$
Vein refraction
c
NW
SE
S$_1$
d
NW
SE
S$_1$
S$_0$
e
NW
SE
S$_0$
S$_0$
f
NW
SE
S$_0$
g
S$_0$
h
NW
S$_0$
Vein length
SE
i
SE
S$_1$
NW
j
S$_1$
k

Figure 3.7 (previous page)**:** Characteristics of bedding-normal quartz veins observed at the Wildenhof section. **(a)** Veins at high angle to bedding in the fold hinge (m80). **(b)** Veins in the hinge zone of a synclinal hinge (m230). **(c)** Vein refraction of two different vein generations at the competent-incompetent interface (m30). **(d)** Stratabound vein at high angle to a SE-dipping laminated fine-grained sandstone layer (m170). **(e)** Vein deformation in agreement with flexural-slip folding (m185). **(f)** Narrow-spaced hairline veins (zone 2). **(g)** Planar bedding-normal vein in a thin competent unit. The sketch shows two different phases of syntaxial quartz growth (zone2). **(h)** Composite vein which comprises several quartz laminae and thin host-rock inclusion seams (m360). **(i)** Vein length on the bedding plane (zone 10). **(j-k)** Cleavage refracting through irregular-shaped quartz veins in a pelitic sequence (m395). For location see Figure 3.3. Hammer (~32 cm), fingernail (~1.3 cm) and pencil (~14 cm) to scale.

3.2.3.2 Orientation analysis

In order to determine if different vein events have occurred through time, a considerable effort has been put in an orientation analysis of the veins. Based on cross-cutting relationships of veins, and on different orientation of vein arrays, several vein generations are recognised (Figure 3.8). Especially in the well exposed overturned limb at Wildenhof (zone 9; Figure 3.3) several distinct quartz vein generations are observed. In what follows, first the orientation of these different vein generations within this single fold limb is described. Afterwards, the orientation of the veins in the overturned limb is compared to the veins in other fold limbs at the Wildenhof section to try deducing a local chronology in quartz veining events.

The best outcrops to study cross-cutting relationships are those situated at m320 (Figure 3.8d), m345 (Figure 3.8c), m360 (Figure 3.8b), m362 and m405 in the overturned limb (S_0~144/72; zone 9) of the Wildenhof section (Figure 3.3). A first and oldest generation V_A (V_A~357/78; Figure 3.10a) has only locally been observed in the approximately one metre thick layer on the m345-outcrop and comprises millimetre-thin, single-opening non-stratabound veins that are limited in height to maximum 30 cm (Figure 3.8d). A second, steeply dipping generation V_B cross-cuts generation V_A and is consistent in orientation along the entire Wildenhof overturned limb (V_B~053/64; Figure 3.10a). This prominent generation V_B mostly comprises composite veins that are composed of several quartz laminae intercalated with host-rock inclusion seams (Figure 3.7h; Figure 3.8b, c and d). However, also single opening veins have been observed in generation V_B. In contrast to generation V_A, which is rather limited in length in a single layer, generation V_B mostly contains stratabound veins cross-cutting the entire sandstone layer. The veins have a mean thickness of one to two centimetres, although vein thickness up to five centimetres has been observed in the m345-outcrop (Figure 3.8d). They are furthermore not always planar in shape; also curved veins (Figure 3.8b) oriented at high angle to bedding are present in some sandstone layers. In fine-grained laminated sandstones (*e.g.* Figure 3.8c), the veins have a more tortuous pattern due to the laminated character of the layer. Small, millimetre displacements of the veins occur in the more silty parts. In thinner beds, a higher fracture density is apparent than in thicker beds.

A third generation V_C is less consistent in orientation than generation V_B (V_C~038/34; Figure 3.10a) and comprises planar to slightly buckled stratabound and non-stratabound veins without any host-rock inclusions (Figure 3.8b). Generation V_C either cross-cuts generation V_B or changes in orientation to a parallel orientation in the direct vicinity of generation V_B, suggesting that already a competence contrast must have existed at time of vein formation of generation V_C. Moreover, due to the existence of generation V_B, generation V_C varies in orientation and shows a larger spread in a single bed than normally would be the case in an unfractured layer.

These three vein generations have been described in the Wildenhof overturned limb (zone 9). In order to evaluate if these vein generations are also present and consistent in orientation in other fold limbs along the Wildenhof section, the three vein generations are compared to veins in the other fold limbs. The easiest way to start this correlation is to compare the veins in the overturned limb of zone 9 with another overturned limb with similar steeply dipping bedding such as present at m30 (S_0~139/78, zone 3; Figure 3.7c) which also contains several consistent sets of veins.

Although the veins on this outcrop at m30 do not mutually cross-cut, two separate generations are recognised, of which one is gently dipping and the other steeply. Both non-stratabound vein generations refract at the competent-incompetent interface in a similar way as cleavage refracts (Figure 3.7c). Based on their orientation with respect to the horizontal plane, these two generations of zone 3 can be compared with vein generations V_B and V_C in zone 9 in such way that the steeply dipping veins and the gently dipping veins correspond in orientation to generation V_B and V_C respectively (Figure 3.10a and d). Due to the slightly different bedding orientations of both outcrops, *i.e.* S_0~144/72 (zone 9) versus S_0~162/85 (m30 in zone3), the orientation of both vein generations V_B and V_C slightly differ from zone 3 to zone 9. This correlation indicates that the two latest vein generations V_B and V_C are continuously present in the overturned limbs. Subsequently, these generations in the overturned limbs can be compared to the veins in the SE-dipping normal limbs and in NW-dipping limbs.

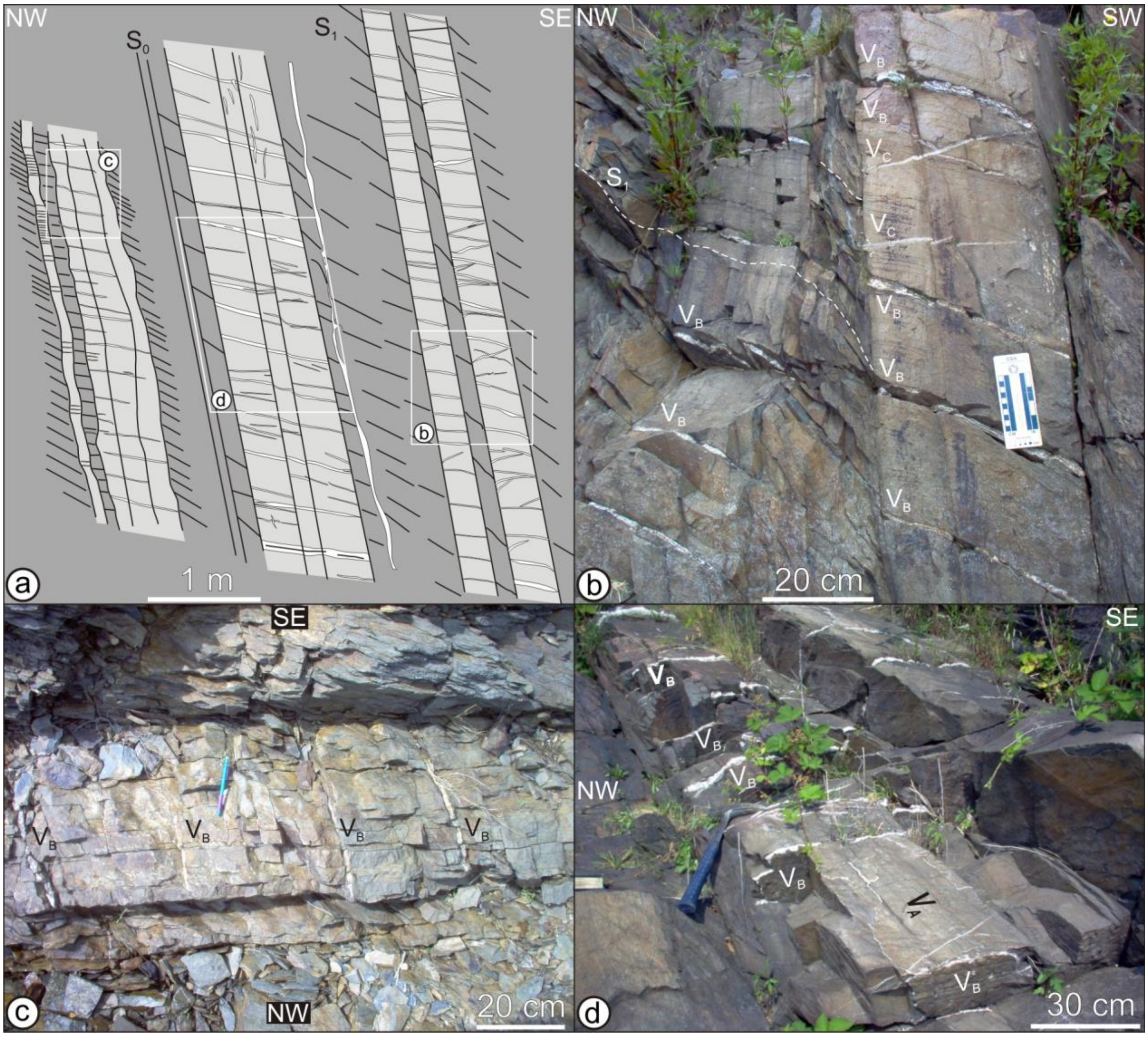

Figure 3.8: Cross-cutting quartz vein generations in the Wildenhof overturned limb (zone 9). See Appendix B for outcrop location. **(a)** Compiled field drawings of three sandstone layers exemplifying the local distribution of quartz veins. **(b)** Generation V_C cross-cutting generation V_B (m360; Wildenhof 44). **(c)** Consistent orientation of generation V_B in a fine-grained laminated sandstone layer (m320; Wildenhof 40). **(d)** Generation V_B cross-cutting generation V_A (m345; Wildenhof 42).

In the competent beds along the normal SE-dipping limb (*e.g.* m100 to m110 and m170 to m180; zone 8; Figure 3.3), several stratabound veins with a composite nature are recognised (*e.g.* Figure 3.7d). Cross-cutting relationships are absent, but based on the different orientations of the veins, two vein generations can be recognised (V~289/75 and V~315/76; Figure 3.10g).

Furthermore, the competent sandstones in the NW-dipping folds limbs in the upright folds (*e.g.* zone 5, zone 7 and transition of zone 8 to 9, Figure 3.7b), comprise several quartz vein generations that are consistent in orientation on a single outcrop, but differ in orientation along the fold limb due to the curvature of bedding in the upright folds (*e.g.* curved bedding in zone 5, Figure 3.3). The veins measured in the NW-dipping fold limbs, show a large spread in orientation on the stereographic projection because of these different bedding orientations (Figure 3.10j). It is thus not useful to calculate an average vein orientation for the veins in different fold limbs with varying bedding orientation.

In their present orientation, the quartz veins measured in the three types of fold limbs have thus similar orientations within a single fold limb, but vary in orientation between the different fold limbs. One common characteristic feature is that the veins remain (sub)-perpendicular to bedding in the fold hinges and around the fold hinges, such as for example in the anticlinal fold at m60. This observation suggests that vein formation occurred prior to the formation of folds. In order to evaluate the original vein orientation, the vein-hosting beds need to be restored to their original horizontal orientation prior to folding. Such a restoration (*e.g.* Jackson 1991) can be performed in two steps (Figure 3.9). First, owing to the fact that the folds in the Wildenhof section have gently, NE-plunging fold hinges, indicated by the average bedding-cleavage intersection lineation (L_i~056/29), the local plunge of the fold needs to be removed by rotation around a virtual axis perpendicular to the fold hinge line. Because of this first step, the effect of regional tilting, which resulted from post-folding regional block faulting (see section 2.6), is removed. Second, after untilting of the fold, the different fold limbs have to be unfolded to the horizontal plane around the untilted local fold hinge line, which is oriented perpendicular to the strike of bedding (cf. Debacker *et al.* 2009). This method is evaluated by refolding the beds along the local intersection lineation in order to see if the original vein orientation could be restored (see also Van Noten *et al.* 2008). The error between both methods is estimated to be less than 5°. If the local fold hinge line is absent, also the local bedding-cleavage intersection lineation, oriented parallel to the local fold hinge line, can be used as an alternative to undo the effect of the fold plunge. To evaluate if similar vein generations are present in different fold limbs, each fold limb has been restored to the horizontal plane. Afterwards, the vein orientations in the gently SE-dipping layers (zone 8), the NW-dipping layers (zones 5, 7 and 8 to 9) and the overturned limbs (zone 3 and 9) can be compared.

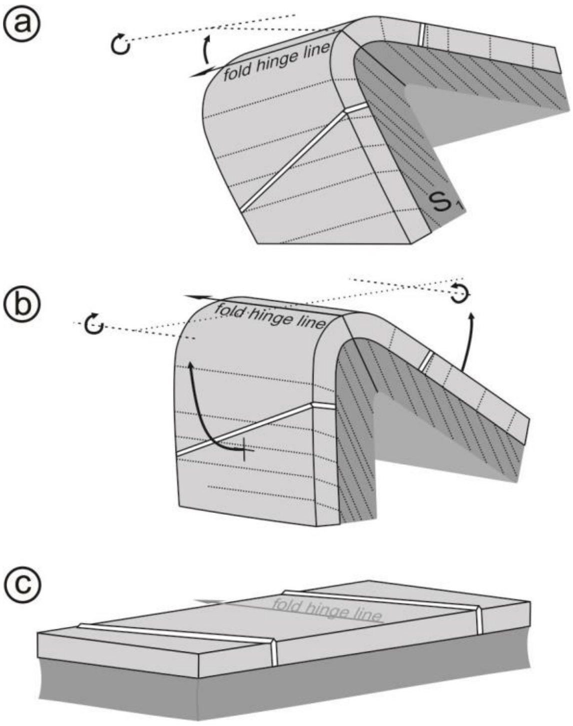

Figure 3.9: Example of an unfolding exercise illustrating the two different steps necessary to restore the beds to their original horizontal orientation at the time of vein formation. **(a)** Present fold orientation. Removing the effect of the plunge of the fold occurs by rotation along an axis normal to the fold hinge line. **(b)** Unfolding of the fold limbs towards the horizontal along the untilted fold hinge line. **(c)** Reconstructed vein orientation prior to folding.

As result of this unfolding exercise, subsequent data (Figure 3.10) shows the pre-folding orientation of the veins at the time of fracturing and infill of the veins.

After restoration of the beds of the Wildenhof overturned limb (zone 9; Figure 3.10b), three different vein generations with different original vein orientations are deduced. The vein array of the oldest generation V_A, which only has been observed locally in a single sandstone layer (m345), has an original E-W orientation (V_A~359/78). Vein generation V_B cross-cuts V_A at an almost perpendicular angle and has an average, original NNE-SSW orientation (V_B~281/76). Generation V_B is cross-cut by generation V_C which has an original NE-SW orientation (V_C~314/81). After unfolding, the three vein generations are oriented at high angle to bedding, although not entirely perpendicular, with the angle between veins and bedding ranging between 68° and 90°. The rotation exercise shows variability in dip direction with V_A dipping to the north, V_B to the west and V_C to the NW. The veins in the unfolded overturned limb of zone 3 (Figure 3.10e) shows a quasi similar orientation for V_B after unfolding (V_B~106/86), although the dip direction of the original veins is oriented to the ESE, in an opposite direction as V_B in the unfolded overturned limb of zone 9. V_C in zone 3 (V_C~332/84) has the same dip as V_C in zone 9 but shows a small difference in dip direction. Notwithstanding these small differences, it can be concluded that after unfolding of both overturned fold limbs, vein generations V_B and V_C remain comparable in their current and original orientation after unfolding, so that this method is properly used.

In their present orientation, the beds in the SE-dipping normal limb (zone 8) contain two different vein generations (Figure 3.10g) which are both characterised by a composite nature but which are mutually not distinguishable due to the absence of cross-cutting relationships. However, based on the orientation of these veins after unfolding (Figure 3.10h) and based on a comparison of the veins in the unfolded SE-dipping normal limb (Figure 3.10g) with those of V_B and V_C in the overturned limb (Figure 3.10b), it can be concluded that the original N-S veins (V_B~094/65) and the original NE-SW veins (V_C~133/58) correspond to V_B and V_C of the Wildenhof overturned limb respectively. Although the veins in both compared fold limbs have thus similar strikes, the vein generations in the unfolded normal limb dip to the east (V_B) or the NE (V_C) after unfolding (Figure 3.10h) which is the opposite direction compared to the veins in the overturned limb (Figure 3.10b).

Furthermore, the different vein generations in the NW-dipping limbs (zones 5, 7 and 8 to 9) are mutually not distinguishable, but are determined to be consistent in orientation after restoration of the beds towards the horizontal (see Figure 3.10k). Generation V_B shows a large spread in orientation and ranges from N-S- to NE-SW (V_B~309/77) while generation V_C has a much more consistent E-W orientation (V_C~353/74). These vein generations dip towards the west (V_B) and to the NW (V_C), similar to the restored veins of the overturned limb.

It can be concluded from the rotation exercises that two of the three described vein generations are consistent in orientation along the Wildenhof section independent of the position of bedding along the folds and in their current as well as in their original orientation. Vein generation V_A is only distributed locally.

Figure 3.10 (next page)**:** Lower-hemisphere, equal-area stereographic projection of bedding-normal quartz veins in selected outcrops at the Wildenhof section. Grey arrows show the unfolding direction. V_A (circle); V_B (triangle); V_C (square). **(a-c)** Generations V_A, V_B and V_C in the SE-dipping overturned limb (zone 9) (a) in their present orientation and (b) after unfolding. (c) Bedding-vein intersection lineation. **(d-f)** Veins in the SE-dipping overturned limb at m30 (zone 3) (d) in their present orientation and (e) after unfolding. (f) Bedding-vein intersection lineation reoriented into S_0~130/72. **(g-i)** Veins in the SE-dipping normal limbs (zone 8) (g) in their present orientation and (h) after unfolding. (i) Bedding-vein intersection lineation reoriented into S_0~130/72. **(j-l)** Veins in the NW-dipping fold limbs (zones 5, 7 and 8 to 9) in their (j) present orientation and (k) after unfolding. (l) Bedding-vein intersection lineation reoriented into S_0~130/72.

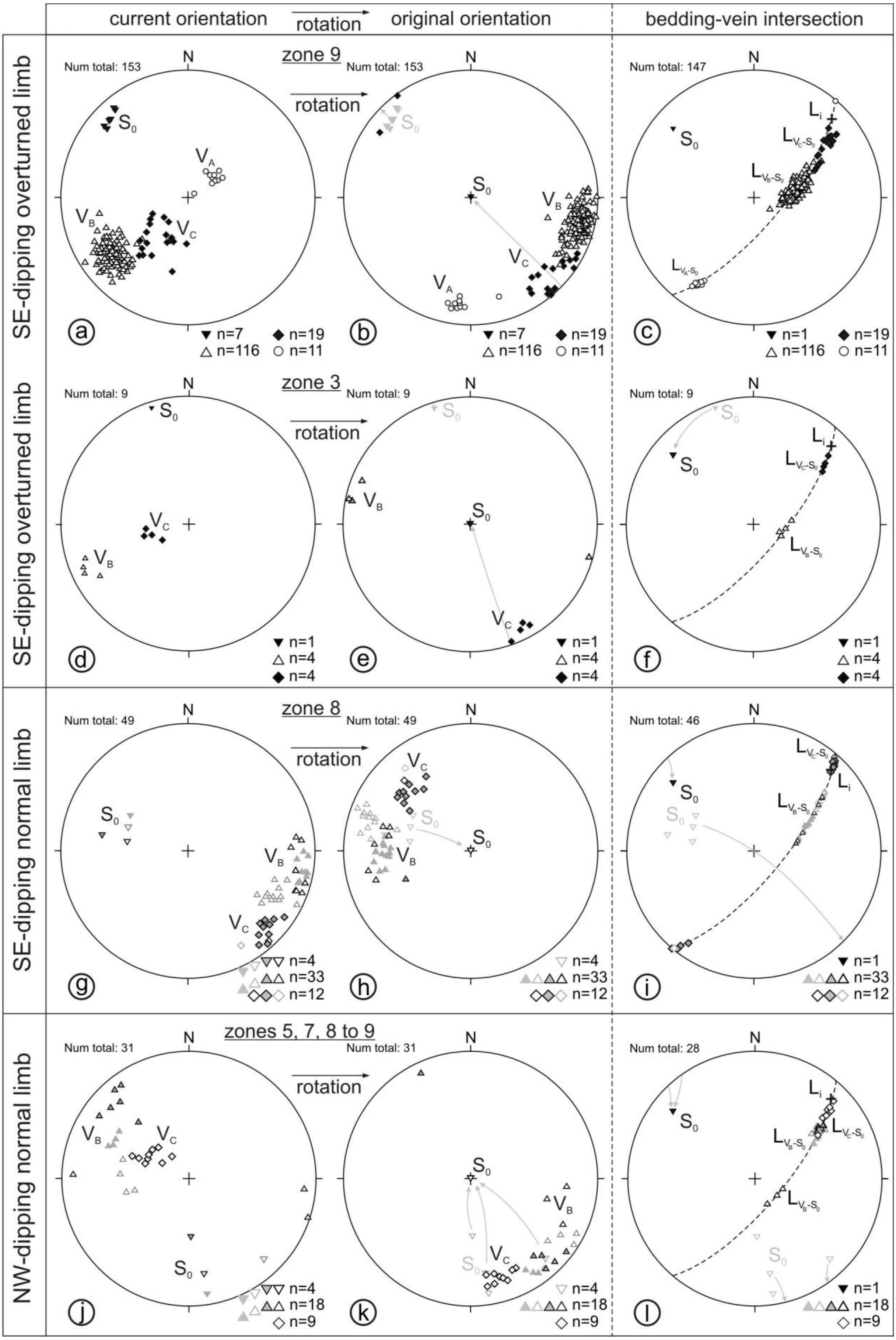
current orientation
rotation
original orientation
bedding-vein intersection
SE-dipping overturned limb
zone 9
Num total: 153
Num total: 153
Num total: 147
N
S0
VA
VB
VC
Li
LVC-S0
LVB-S0
LVA-S0
a
b
c
▼ n=7 ◆ n=19
△ n=116 ○ n=11
▼ n=1 ◆ n=19
△ n=116 ○ n=11
SE-dipping overturned limb
zone 3
Num total: 9
d
e
f
▼ n=1
△ n=4
◆ n=4
SE-dipping normal limb
zone 8
Num total: 49
Num total: 46
g
h
i
n=4
n=33
n=12
▼ n=1
NW-dipping normal limb
zones 5, 7, 8 to 9
Num total: 31
Num total: 28
j
k
l
n=4
n=18
◇ n=9
▼ n=1

In addition to the unfolding excises, the consistency of the veins with respect to the orientation of the folds is checked by an additional rotation exercise. On the bedding planes the intersection of the veins with bedding can be observed. As veins are consistent at a single outcrop, the bedding-vein intersection lineation (L_{V-S_0}) should also be consistent. In order to check this consistency, the angle between the local bedding-cleavage intersection lineation (L_i) and the bedding-vein intersection lineation has been measured or has been calculated if the bedding plane could not be observed. In the Wildenhof overturned limb (Figure 3.10c) the intersection lineation of V_A with bedding has been observed in the m345-outcrop and is oriented anticlockwise at 35° to 45° to the local bedding-cleavage intersection. The intersection of generation V_B with bedding $(L_{V_B-S_0})$ has a large, clockwise angle (~40° to 70°) with the local L_i, whereas the intersection of generation V_C with bedding $(L_{V_C-S_0})$ occurs at lower angle (5° to 20°) with respect to L_i (Figure 3.11).

This angle between L_i and the intersection of bedding and veins is confirmed in the overturned limb of zone 3 (Figure 3.10f) in which the intersection of the steeply dipping V_B and the gently dipping V_C are also orientated clockwise at high and low angle to the local L_i respectively. In order to compare the consistency of this angle in the different fold limbs studied, an additional rotation exercise has been performed in which the bedding of the different fold limbs are rotated into the bedding of the m360-outcrop in the overturned limb (S_0~130/72). This rotation occurs along the mathematical intersection of the two bedding planes. Results show that rotation of the bedding of the m30-outcrop (S_0~162/85) into the bedding of the m360-outcrop (S_0~130/72) shows a positive correlation of the angle between L_{V-S_0} of the two vein generations V_B and V_C and the local Li in zone 3 and zone 9 (see Figure 3.10f versus Figure 3.10c).

Rotation of the beds in the normal SE-dipping fold limb (zone 8) into the overturned bedding orientation of the m360-outcrop (Figure 3.10i) shows that $L_{V_C-S_0}$ and $L_{V_B-S_0}$ are oriented at low angle to the local L_i, although V_C (5°-30°) oriented in an anticlockwise sense and V_B (10°-50°) in a clockwise sense with respect to L_i.

Also the angle between $L_{V_B-S_0}$ and $L_{V_C-S_0}$ is narrower in the normal SE-dipping limb than in the overturned SE-dipping limb.

Rotation of the beds in the NW-dipping limb into the overturned bedding orientation of the m360-outcrop (Figure 3.10l) shows that $L_{V_C-S_0}$ is oriented at low angle to L_i (5°-10°) in a clockwise sense and $L_{V_B-S_0}$ at a larger angle (15-30°), and also in a clockwise sense.

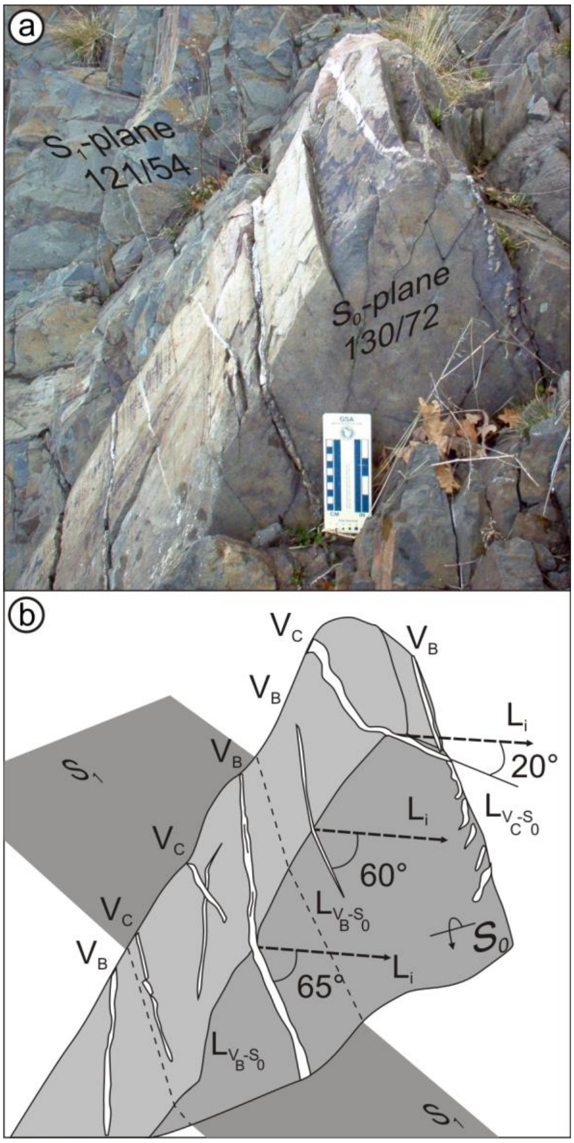

Figure 3.11: **(a)** Photograph of an overturned SE-dipping sandstone layer (m360; zone 9) showing two vein generations V_B and V_C. GSA-bar for scale. **(b)** Angle between bedding-cleavage intersection lineation (L_i) and bedding-vein intersection lineation of $V_B\,(L_{V_B-S_0})$ oriented at high angle to L_i and $V_C\,(L_{V_C-S_0})$ oriented at lower angle to L_i.

Eventually, this comparison demonstrated that in the different folds V_B and V_C are oriented consistently with respect to the local fold hinge.

In the Wildenhof section, quartz veins are furthermore present in the incompetent silty or pelitic layers in the different fold limbs in which they are cross-cut by cleavage (Figure 3.7k). In this lithology, however, the veins show a less consistent vein orientation than in the competent units (Figure 3.12a). In order to check if these veins formed prior to folding and can be compared with the orientation of those in the competent units, veins have been unfolded in a similar way as the method illustrated in Figure 3.9. The result of this unfolding exercise shows a large range in dip as well as in dip direction of the veins after unfolding (Figure 3.12b). They range in orientation from N-S to E-W and are oriented at high (70°) to low (30°) angle to bedding. This unfolding exercise shows that the quartz veins interbedded in siltstone sequences observed in different fold limbs have similar orientations after unfolding, but are difficult to compare to one of the previously described generations in the competent units. This is possibly due to substantial reorientation of the veins during cleavage development in the silty sequences.

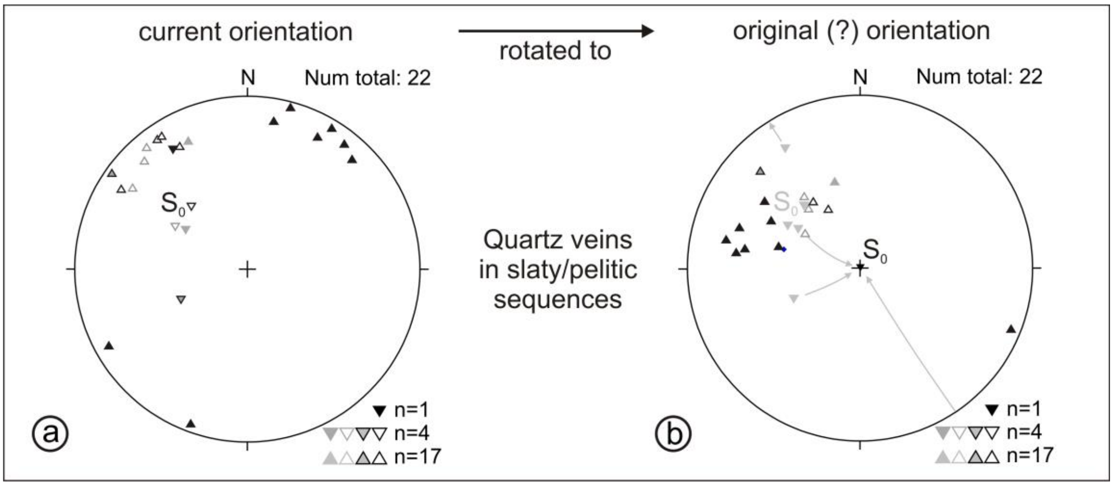

Figure 3.12: Lower-hemisphere, equal-area stereographic projection of irregular-shaped quartz veins in silty or pelitic sequences at the Wildenhof section. **(a)** Veins in their present orientation in the overturned SE-dipping fold limb (m395; Figure 3.7k) and in the SE-dipping fold limb (m170 and m200). **(b)** Veins rotated passively into a horizontal bedding orientation wondering if they resemble bedding-normal veins. Rotation conform the method illustrated in Figure 3.9.

3.2.4 Bedding-parallel veins

3.2.4.1 Geometric description

BOX II - Terminology used in the geometric description of bedding-parallel veins (BPVs)

A bedding-parallel vein (**BPV**) or a bedding-vein (*e.g.* Koehn & Passchier 2000) usually forms in a basin consisting of alternating multilayer sequences, in which the emplacement of several BPVs can easily occur, whatever the process of vein formation might be (*e.g.* Cosgrove 1993, Fitches *et al.* 1986, Fowler 1996, Jessell *et al.* 1994). The formation of BPVs, which is discussed in this work, has caused considerable debate. In order to describe the veins properly and independently from the different models published, the terminology that is used in the geometric description of this vein-type is explained in detail in this box.

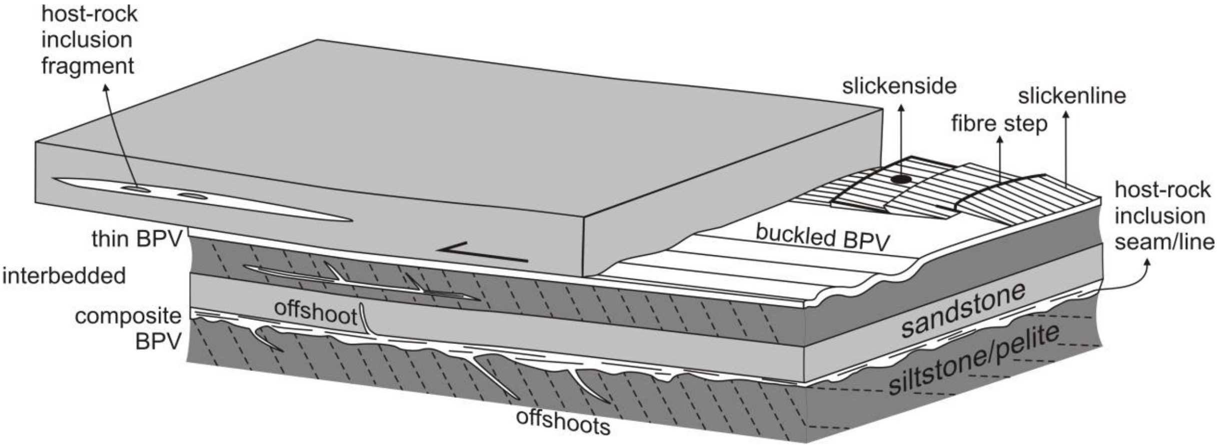

In this study, a BPV refers to a vein that either occurs **interbedded** between two contrasting lithologies, or **intrabedded** within the incompetent or competent lithology. Depending on the thickness and internal complexity of the vein, a single laminated or composite vein can be distinguished. The **thin** veins, on the one hand, are characterised by an apparent single laminated quartz growth without any host-rock inclusions in the vein quartz. They are millimetre-thick and remain constant in thickness along the vein length. The veins have been assumed to be blocky quartz veins due to the absence of macroscopically visible fibre crystals. **Composite** veins, on the other hand, have a complex internal fabric consisting of macroscopically observable quartz laminae intercalated with very thin, millimetre-size, pelitic of silty host-rock inclusion **seams**, which are seen at the outcrop as host-rock inclusion **lines**. Larger pieces of host rock observed in the composite veins are termed as host-rock inclusion **fragments**. If a thin or composite BPV bifurcates at its upper or lower vein wall, the upper or lower veins are defined as local **offshoots**. The veins can be **planar,** with flat vein wall morphology, or **buckled** if the vein curves along its length. Composite veins have irregularly curved vein walls at the incompetent contact, while they have a flat morphology at the competent contact. Bedding-parallel movements are recorded by several structural features on the vein surfaces. These surfaces may have a polished appearance, known as **slickensides**, and on these surfaces several movement striae or **slickenlines** may be developed parallel to the relative slip between the layers. They thus indicate the direction of shear along the surface (Ramsay & Huber 1987). The relative movement sense between the two blocks separated by the BPV can be tracked by several overlapping **fibre steps**. Although clear fibrous crystals are often not recognisable in these fibre steps, this terminology is used by analogy with fault geometry. Moreover, by analogy, the layer above the vein is referred to as the ‘hangingwall’ of the veins, while the opposite lower layer is referred to as the ‘footwall’ of the veins. The relative sense of direction of the ‘hanging wall’ with respect to the ‘footwall’ is indicated by the overlap direction of the fibre steps (*e.g.* overlap to the left on the figure in this BOX II) or can be traced in the field by feeling a smooth surface in the overlap direction and a ‘sticky’ surface in the opposite direction.

BOX II (continued)

The most common example in which the upper described terminology is used, is flexural-slip folding. This commonly occurs in multilayer sequences and involves the slip of upper beds over lower beds in the fold limbs towards the anticlinal axis during folding (Tanner 1989). Slickenlines found on such flexural-slip surfaces or on thin flexural-slip veins record a net slip vector which is commonly oriented at high angle to the fold hinge in cylindrical folds. The shear sense recorded by the fibre steps on the bedding-parallel veins reverse systematically from one limb to the next (Tanner 1989).

If slickenlines represent flexural-slip folding between the layers in a multilayer sequence, slickenlines should be oriented at a consistent high angle to the local fold hinge line and slip directions or the change in fibre steps should be oriented (sub)-perpendicular to the local fold axis (Tanner 1989, 1990). Furthermore, veins in alternating fold limbs should have opposite directions of fibre steps which should indicate opposite sense of movements towards the hinge zones with the largest bedding-slip at the inflection points in the fold limbs and a decrease to zero at the hinges (Cosgrove 1993). It is important to highlight these flexural-slip features as the bedding-parallel veins of the study area sometimes resemble the characteristics of flexural-slip BPVs. During the geometric and kinematic analysis, it is analysed whether the BPVs of the North Eifel comply with these criteria.

Along the Wildenhof section, several bedding-parallel quartz veins have been observed. Based on their varying position with respect to the surrounding rock-type, four different configurations for the BPVs are defined. The veins either occur interbedded at the interface of beds of contrasting lithology, *e.g.* siltstone-sandstone or sandstone-siltstone without any consistent preference to develop above or below the competent unit, or intrabedded in the incompetent or competent sequences. These different types of BPVs are described on the basis of four cases.

(*case i*) The first case that is described, concerns two BPVs at m175 and m195 in the normal SE-dipping fold limb of zone 8 (Figure 3.3). These BPVs are present between underlying siltstone and overlying coarse-grained sandstone (Figure 3.13a and b). The upper vein wall has a flat morphology and displays a sharp contact with the base of the sandstone. The lower vein wall is characterised by an irregular boundary with the underlying pelites. Due to this irregular shape of the vein wall, the BPV shows a considerable thickness variation along its length ranging from 1 cm to maximum 7 cm. Locally below the BPV in the underlying silty layer, small quartz veins, which are present at high angle to bedding, curve at the contact with the BPV to a parallel position with the BPV (Figure 3.13b). These observations suggest that these small quartz veins in the siltstone and in the sandstone are local offshoots of the BPV. These offshoots are also present in the sandstone above the BPV (Figure 3.13c). At the intersection of the BPV with the offshoot, cross-cutting could not be observed. This intersection can rather be described as a bifurcation of the BPV with the bedding-normal vein branching off from the BPV. Cleavage either refracts through these small offshoots as well as through the BPV. In the SE-dipping normal limb, offshoots occur frequently and have a SE-dipping orientation with a similar strike as the BPV from which they branch off. On a NE-SW outcrop, in which bedding has an apparent horizontal dip (*e.g.* Figure 3.13a), the length of the BPV, situated below a coarse-grained sandstone layer, can be deduced by following this BPV at the m170-outcrop at the water level for over 25 m up to the m150-outcrop at the road level. In general, such a BPV thus extends along its lengths to several tens of metres and its thickness ranges from a few cm up to 10 cm, thereby commonly showing very high aspect ratios. Internally, this type of BPV can be described as a centimetre-thick composite, laminated quartz vein. It has a complex internal fabric consisting of several distinct generations of quartz laminae intercalated with very thin, millimetre-size, pelitic wall-rock seams which vary from very thin pelitic slices, approximately parallel to the vein walls, to pelitic host-rock fragments. The internal lamina-surface and the outer vein walls are often marked by slickenlines.

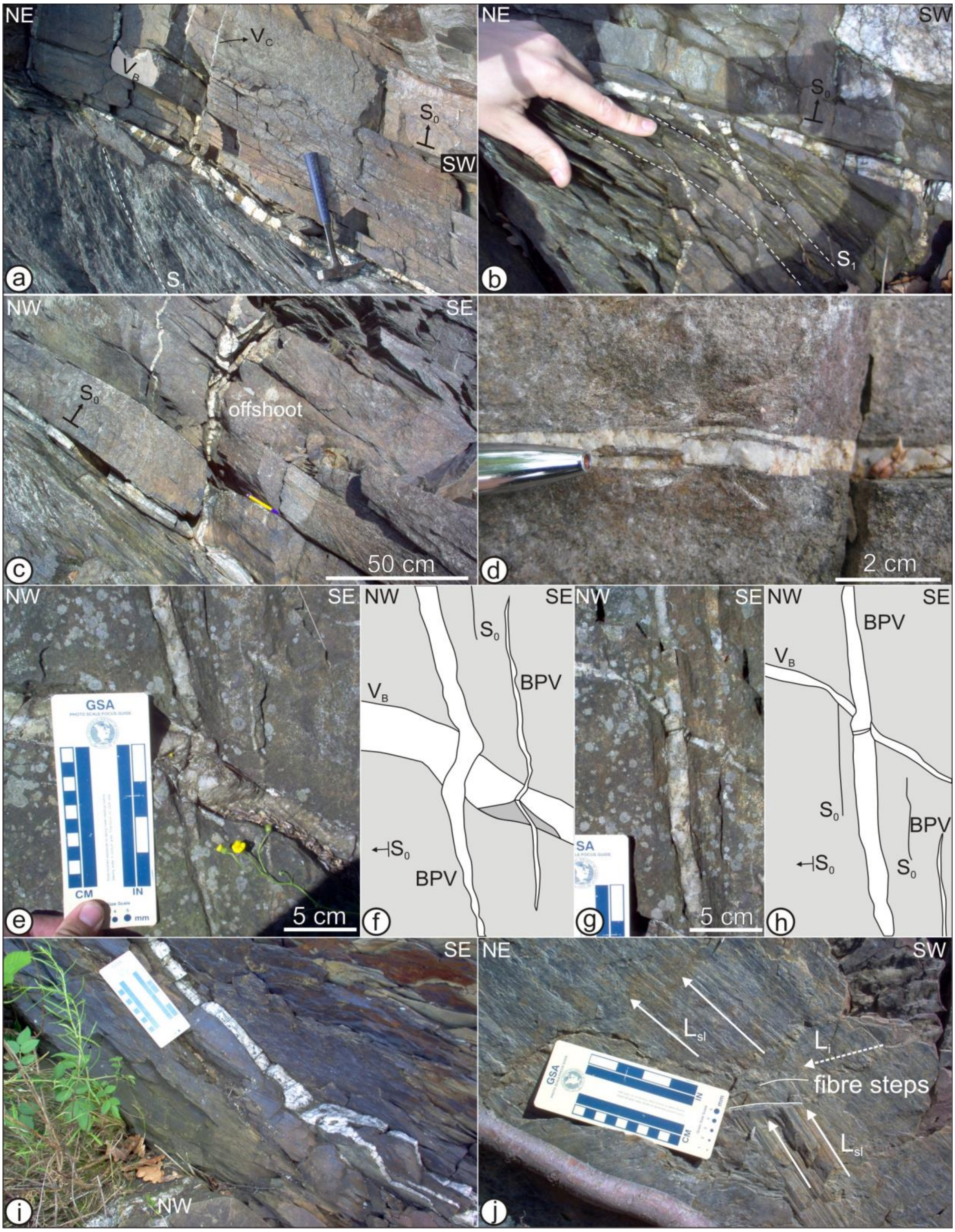

Figure 3.13: Bedding-parallel quartz vein (BPV) characteristics at the Wildenhof section. **(a)** Interbedded BPV with an irregular contact with the underlying siltstone and a sharp contact with the overlying sandstone (m175). **(b)** Small quartz veins overprinted by cleavage and in close relationship with a composite BPV (m175). **(c)** Interbedded composite BPV with bedding-normal quartz vein offshoots (m195). **(d)** Millimetre-thick BPV with several host-rock inclusions in a coarse-grained sandstone layer (m175). **(e-h)** Photographs and detailed sketches of centimetre-thick BPVs cross-cutting bedding-normal vein generation V_B in a coarse-grained sandstone layer (m345). **(i)** Centimetre-thick, composite BPV with a large host-rock fragment. **(j)** Upper side of a thin BPV marked by slickensides with multiple slickenline orientations at high angle to Li (m335). GSA centimetre scale bar, hammer (~32 cm), fingernail (~1.3 cm) and pencil (~14 cm) for scale.

(*case ii*) At the road level (m160 and m195), two other BPVs occur interbedded above a coarse-grained sandstone layer. They are two and three centimetre thick respectively and can be traced along their lengths at the whole outcrop. Locally at the m195-outcrop, the BPV is cross-cut by a SE-dipping normal fault with minor displacement. The SE-dipping cleavage, which is well developed in the silty layers above the BPV refracts through the sandstone layer and either cross-cuts the vein or changes in orientation in the vicinity of the vein to a parallel orientation with the vein. A relative relationship between the BPV and stratabound veins in the sandstones could not be established. The veins consist of milky-white, blocky quartz crystals without any apparent host-rock inclusions.

(*case iii*) A third configuration concerns centimetre-thick BPVs intrabedded in coarse-grained sandstone layers in which they cross-cut stratabound bedding-normal quartz veins (*e.g.* m345; Figure 3.13e-h). When (fibrous) stratabound or non-stratabound BNVs are present within the sandstone layer, the BPVs cross-cut them, independent of the generation to which the BNV belongs. Based on the bedding-normal displacement of the BNVs along the bedding-parallel vein, an opening perpendicular to the bedding-parallel vein wall is suggested. Internally, these veins consist of milky-white, blocky quartz crystals in which millimetre-thick host-rock inclusion fragments are included (Figure 3.13d). Similar to the thick BPVs in (*case i*), these thin BPVs can be traced along their length for several tens of metres.

(*case iv*) Finally, BPVs also occur within silty sequences, in which they range in thickness from millimetre-thick quartz veins to centimetre-thick, composite veins consisting of several laminae of blocky quartz crystals intercalated with pelitic host-rock inclusion fragments (Figure 3.13i). The composite veins have a fractured appearance because of the fact that cleavage cross-cuts the BPV at regular distances (Figure 3.13i). At m180 and m395, several thin quartz veins, oriented at high angle to the BPVs, can be interpreted as local offshoots of the underlying composite BPV (Figure 3.7j and k). The thin, single laminated BPVs contain polished vein walls which are characterised by slickenlines, slickensides and sometimes fibre steps.

3.2.4.2 Orientation analysis

The interbedded BPVs, as well as those within the sandstone and siltstone layers are oriented parallel to bedding. Plotting the orientation of the vein walls on a stereographic projection would give a similar result as bedding plotted in Figure 3.2a, although the scatter along the best fit girdle would be larger due to the irregular vein walls of the composite veins in (i).

Composite interbedded veins (*cases i and ii*) and the thin single laminated veins (*case iv*) are often marked by slickenlines (L_{sl}) which are uniform in trend on the one side of a single lamina, but slightly vary in orientation with those observed on the opposite side of the vein wall or they can change in orientation from lamina to lamina when the BPV consists of multiple laminae. Although slickenlines may be consistent on a single BPV, they often vary in orientation on different BPVs in the same fold limb. In order to check consistency in slickenline orientation on BPVs in different fold limbs, a considerable effort has been put into the orientation analysis of the slickenlines (Figure 3.14). Slickensides and slickenlines have been observed on BPV walls in the normal as well as in the overturned SE-dipping limbs of the Wildenhof section. When they are present, they only occur on the planar vein walls of interbedded composite BPVs, *i.e.* at the contact with the competent sandstone, and are absent at the irregular side of the veins which occur at the interface with the incompetent layer. The slickenlines are furthermore absent on BPVs ‘intrabedded’ in sandstone layers. In the normal fold limbs, *e.g.* zone 8, slickenlines plunge gently to the SE and SSE at a clockwise angle of 50° to 105° with the local intersection lineation (Figure 3.14a). In the overturned limb of zone 9, however, slickenlines on the BPVs plunge steeply to the SW and SSW (Figure 3.14b) at a clockwise angle of 90° to 130° with the local intersection lineation. The variation in slickenline orientation is smaller on the BPVs in the overturned limbs than those observed in the normal limbs (Figure 3.14a and b). Also the plunge of the slickenlines is different in the two fold limbs in such way that slickenlines are oriented at higher angle to the local L_i in the overturned limb than in the normal limb. Although slickenlines are more or less consistent on BPVs in a single fold limb, they clearly differ in orientation in different fold limbs. In order to check whether there would be a parallel slickenline orientation prior to the current tilted bedding orientation, a rotation exercise has been performed (Figure 3.14c). In this exercise, the overturned SE-dipping fold limb of zone 9 has been rotated in different steps over the local intersection lineation into the average bedding orientation of zone 8 (S_0~108/43). The layers in the normal SE-dipping limb have also been rotated to this average bedding orientation in order to compare slickenline orientation properly. After rotation, the largest overlap between the slickenlines on the normal and overturned limb occurred after complete rotation of the overturned limb into the normal limb (Figure 3.14c). However, despite these similar slickenline populations, a large variability in slip striation, as exemplified by the variability in angle (>30°) between the slickenlines and the local L_i, remains present after rotation.

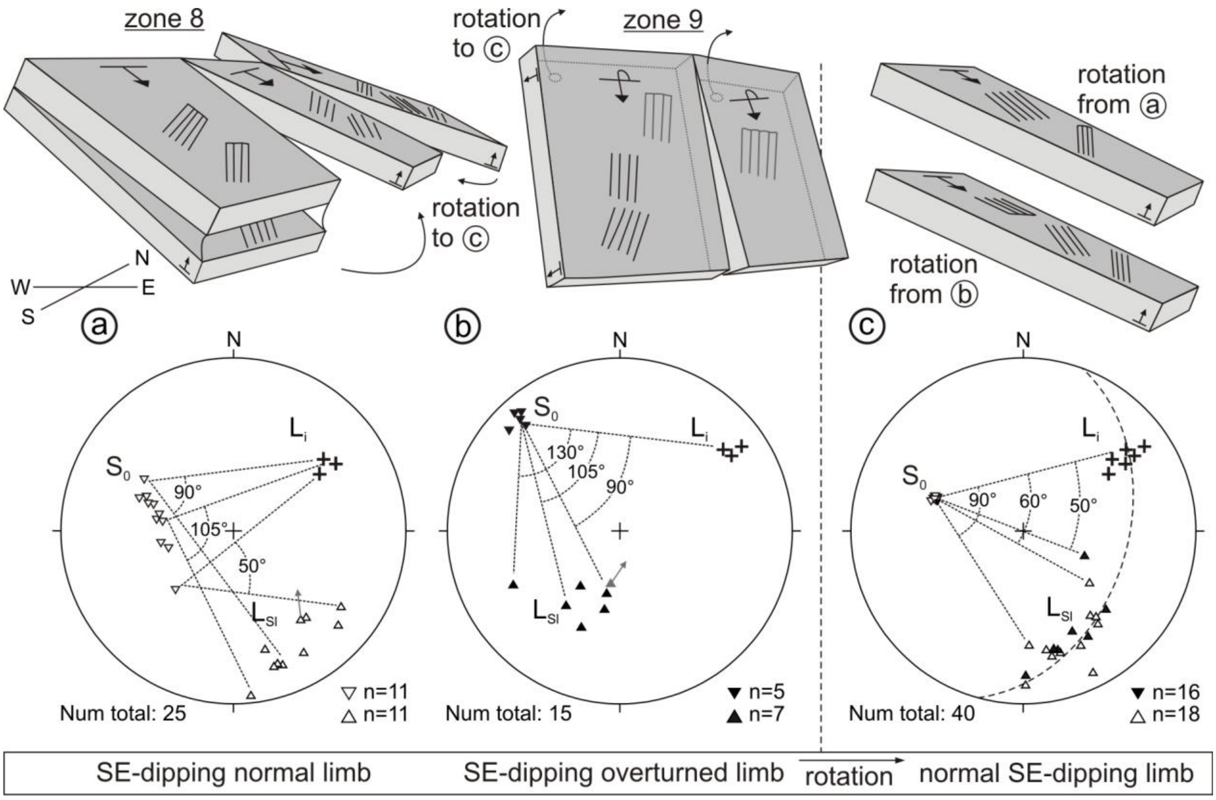

Figure 3.14: Variation in slickenline orientation on BPVs measured in the different fold limbs of the Wildenhof section. **(a)** Slickenlines on the SE-dipping normal limb (examples from zone 8). **(b)** Slickenlines on the overturned SE-dipping limb. **(c)** Slickenlines show a > 30°-variation with respect to the local L_i after reorientation of (a) and after rotation of (b) over the Li into the average bedding orientation of zone 8 (S_0~108/43).

Apart from slickenline orientation, also overlapping fibre steps have been recognised on the veins. If the sense of shear indicated by fibre steps could be determined, it is consistent in orientation on a single vein. The m335-outcrop in the overturned limb (zone 9; Figure 3.13j) can be used as an example to illustrate the shear movement along the BPV that can be deduced from slickensides, slickenline orientation and fibre steps. Slickenlines are oriented at high angle to the local bedding-cleavage intersection lineation (Figure 3.14b) and thus at high angle to the local fold hinge line (Figure 3.13j and Figure 3.14b). The fibre steps, which are present on the slickensides, are oriented subperpendicular or at high angle to the slickenlines and subparallel to the local intersection lineation. The direction of overlapping fibre steps on this BPV thus indicates that the relative sense of movement of the ‘hanging wall’ occurred in an upwards direction with respect to the ‘footwall’, at high angle to the local fold hinge line. Although this relative movement is in agreement with the shear movement expected from flexural-slip folding (Tanner 1989), the overall regional shear along the veins has to be elaborated by means of more examples.

Fibre steps are only observed on the upper vein wall in thin BPVs (Figure 3.13j) in which they indicate an upwards movement of the ‘hanging wall’ with respect to the ‘footwall’ of the BPV. In order to check if the slickenlines are generally formed due to flexural-slip folding, the relative displacements of the layers by means of the orientation of the fibre steps at various locations along a fold need to be known. Unfortunately, the BPV walls are often completely polished in such way that fibre steps could not be determined anymore, thereby preventing to deduce the sense of movement along the BPV. Therefore, the study of slickenline orientation and fibre steps needs to be elaborated to other case studies in which fibre steps are present continuously on a single BPV around a fold. Fibre steps are for instance observed in the synclinal hinge at the m110-outcrop in Wildenhof section and are indicative of local out-of-syncline thrusting. On this outcrop, slickenlines are oriented orthogonal to the fold hinge (Figure 3.5a). In other cases slickenlines on sandstones or on thin bedding-parallel veins can indicate flexural slip between two layers.

3.2.5 Kinematic interpretation

The combination of a detailed geometric analysis of both vein types with features such as cleavage, folds and faults, allows, on the one hand, understanding the structural evolution of these features and, on the other hand, setting up a relative structural chronology of features. It will be elaborated that a progressive deformation history was responsible for the formation and deformation of the different vein types.

3.2.5.1 Bedding-normal veins

From the geometric description of the bedding-normal veins, it is clear that different mechanisms were responsible for vein formation. Based on the width and the macroscopical characteristics of the veins, three different veining mechanisms are identified. These different mechanisms are not restricted to one single vein generation, but occur in the all three different generations V_A, V_B and V_C observed in the Wildenhof section.

A first mechanism, concerns the millimetre-thin, hairline, stratabound veins (*e.g.* Figure 3.7f) that are only observed in thin competent beds. Their macroscopic fabric shows fibrous crystals that are oriented at high angle to the vein walls. This nature of quartz infill indicates rapid or immediate infill of the dilation after fracturing with the precipitation rate exceeding the fracturing rate. The very narrow spacing of these hairline veins moreover suggests that these hairline veins developed from a single opening and a single infill of a fracture which might not been reopened afterwards.

The second mechanism involves milky-white, thicker veins, up to some centimetres in thickness, which are characterised by several phases of infill without the presence of any host-rock inclusion seams. This veining mechanism could initially have been developed from a hairline vein into a thicker vein, although this cannot be determined macroscopically. The observed syntaxial vein fabric in Figure 3.7g indicates a first phase of crystal growth from the vein wall towards the median line of the vein, which is succeeded by a secondary phase of vein growth, clearly separated from the earlier phase. Based on these successive phases and absence of lateral displacement, these veins can be determined as Mode I extension veins.

A third mechanism concerns the composite, centimetre-thick quartz veins that frequently occur in the Wildenhof section. Macroscopically, these composite veins comprise several quartz laminae separated by thin aligned host-rock inclusions oriented parallel to the vein walls (Figure 3.7h; Figure 3.8b-d). This macroscopic fabric indicates that these veins formed due to successive fracture and sealing phases during which small parts of the host rock were separated from the vein wall during fracturing and were incorporated within the veins during sealing (Van Noten *et al.* 2008). Along their vein length, composite veins initially may have grown separately but ultimately became interconnected after successive phases. Such interconnections have for instance been described by Hilgers & Urai (2005). In order to validate these three vein filling mechanisms, the vein fabrics have however, to be elaborated in detail by means of a pervasive microstructural analysis (see Chapter 4).

Based on the geometry of the bedding-normal veins in the Wildenhof section, it is obvious from the following arguments that both stratabound as well as non-stratabound quartz veins predate the Variscan fold-and-cleavage development. The stratabound quartz veins, which are restricted to the competent fine- to coarse-grained sandstone layers, are mostly oriented at high angle to bedding, independent of the bedding orientation and on the position in the fold. As can be seen on the bedding surface of many sandstone layers, these planar veins extend for several metres along their lengths. Throughout the different observed fold types, the veins remain at high angle to bedding in the fold limbs and in the fold hinges. This observation is indicative of pre-folding veining and suggests that vein formation occurred prior to the formation of folds, presumably in (sub)horizontal position during burial. It could also be recognised at many localities that cleavage cross-cuts both the stratabound and the non-stratabound veins. Moreover, if a non-stratabound vein exceeds a competent bed and continues into an incompetent unit, *i.e.* the siltstone or pelitic sequence, it is deformed and refracts at the competent-incompetent interface in the same way as the cleavage does (Figure 3.7c and e). This has been observed in non-stratabound veins that cross-cut several competent and incompetent layers as well as in those non-stratabound veins of which only the vein tips exceed the competent-incompetent interface. These arguments are indicative of pre-cleavage vein formation. As cleavage is observed to be axial planar to the folds in the Wildenhof section and as it refracts in opposite directions through the competent sandstones in opposite fold limbs, it is fair to assume that cleavage developed contemporaneous with the folds, after bedding-normal vein formation. It can also be excluded that the veins result from orthogonal strain in the outer arc of a fold during buckling, during which hinge cracks develop. Consequently, the pre-folding hypothesis suggests that the veins in the inner arc of a fold should be more deformed than in the outer arc of a fold.

It is concluded from the unfolding exercise (Figure 3.10b, h and k) that the NW-dipping fold limbs, as well as both normal and overturned SE-dipping fold limbs in the Wildenhof section contain a consistent vein generation V_B after rotation to the horizontal. The vein generation V_A is only locally observed. Subsequent generation V_B is cross-cut by generation V_C, which is less consistent in orientation due to the presence of V_B, but which can be recognised in the different fold limbs in which it remains cross-cutting V_B. Although both generations are oriented at high angle to bedding, unfolding also revealed that most veins are not perfectly orthogonal to bedding after rotation (Figure 3.10b, h and k). This implies that veins either did not develop perpendicular to bedding and hence that beds were slightly tilted at the time of vein formation or that they initially were oriented perpendicular to bedding but are deformed afterwards into their subperpendicular attitude during subsequent folding. Several arguments are supportive for the latter mechanism. Firstly, the stratabound veins often have a curved shape (*e.g.* Figure 3.8b and c). No matter the fold limb in which the vein is enclosed, the upper vein tip always curves towards the anticlinal hinge zone of the fold. Secondly, the refraction of non-stratabound veins at the competent-incompetent interface always occurs, similar as to cleavage refraction, towards the anticlinal hinge (*e.g.* Figure 3.7e). Thirdly, after unfolding to horizontal bedding, the veins in the normal limbs (Figure 3.10h) dip in an opposite direction than the veins in the overturned (Figure 3.10b) and the NW-dipping limbs (Figure 3.10k), although one would assume that if a single vein generation is formed, it would have a constant orientation with respect to bedding. These three observations are in agreement with a deformation that is expected during fold development in such way that the curved stratabound veins, which dip in opposite directions at the different fold limbs after unfolding, and the refracted non-stratabound veins are indicative of continuous simple shear during flexural-flow folding (Ramsay & Huber 1987).

Based on the geometry of the veins, a kinematic deformation model can be proposed with the aim to sketch the evolutionary fold-and-cleavage development and the resulting deformation of quartz veins (Figure 3.15). The starting point in this model is originally planar stratabound or layer-cross-cutting non-stratabound quartz veins in undeformed horizontal layers that are deformed during progressive folding and contemporaneous cleavage development. The type of post-emplacement deformation of the veins largely depends on the configuration of the host-rock succession.

In multilayer sequences, *i.e.* competent layers separated by incompetent layers (Figure 3.15a), the refraction of non-stratabound veins commonly occurs at the layer interface with veins oriented at high angle to bedding in the competent beds and at lower angle to bedding in the incompetent layer (*e.g.* Kisters 2005, Mamtani *et al.* 2007). The direction of refraction is similar as the curvature of the stratabound veins in the competent beds. Both observations are explained by continuous layer-parallel, simple shear during flexural-flow folding through the fold structure in which the amount of shear is larger in the incompetent unit as in the competent unit (Ramsay & Huber 1987).

In a multilayer sequence that largely consists of a succession of several competent beds, or in a multilayer sequence in which the competent beds are separated by millimetre-thick pelitic layers, non-stratabound veins are often displaced (*e.g.* Figure 3.5d, Figure 3.7a) in such direction that the structurally uppermost layers systematically have moved towards the adjacent anticlinal hinge (Figure 3.15c). The shift of the initially cross-cutting quartz veins is indicative of a discontinuous bedding-parallel slip along the competent layers due to flexural-slip folding (Ramsay & Huber 1987). From all these observations and from the kinematic model, illustrated in Figure 3.15, it is thus plausible that both non-stratabound and stratabound veins were originally planar and are deformed during folding. Remarkably, in some coarse grained-sandstone beds cleavage refraction has a similar curvature as the veins (Figure 3.8b), corroborating the flexural-flow deformation.

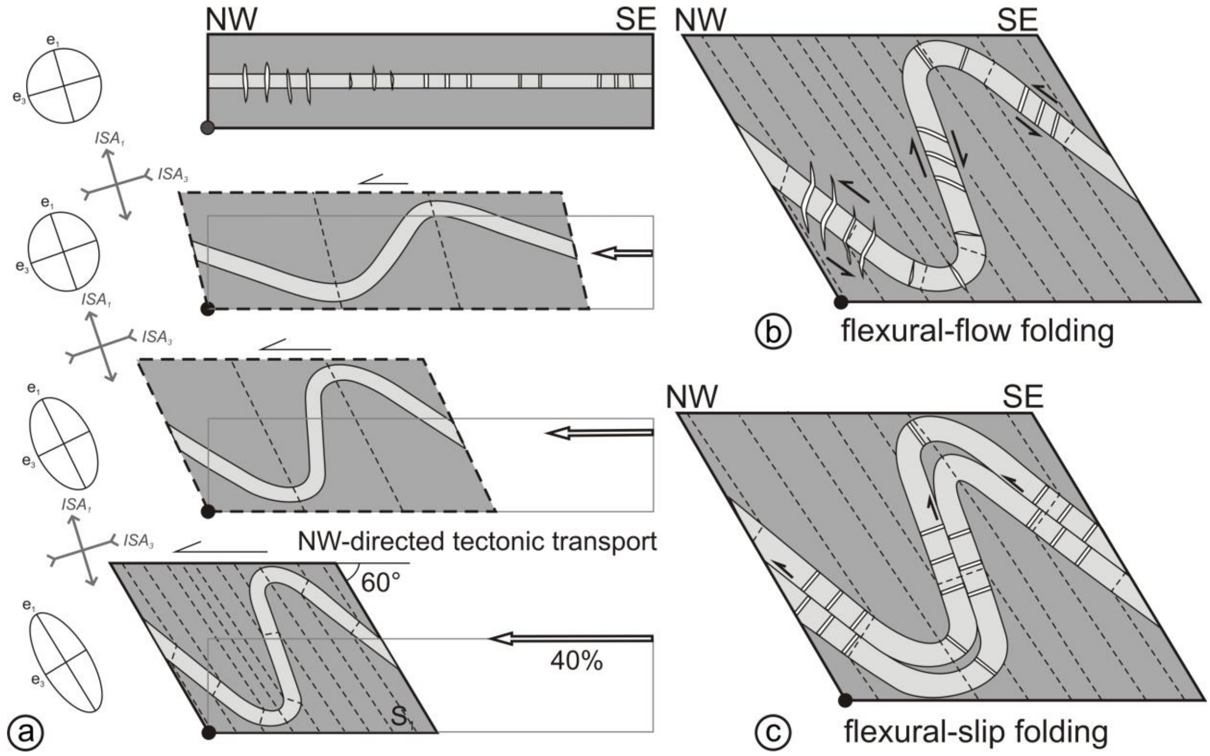

Figure 3.15: **(a)** Kinematic model proposed for the fold-and-cleavage development starting from a horizontal layer with bedding-normal quartz veins, folded into an overturned fold during which volume and line length of the competent layer has been kept constant. For simplicity, the stages of bedding-parallel veining are not illustrated. e$_1$ and e$_2$ are respectively minimum and maximum stretching axes in the incremental strain ellipse. ISA$_1$ and ISA$_3$ are respectively maximum and minimum incremental strain axes. **(b)** Stratabound and non-stratabound vein deformation due to flexural-flow folding of competent and incompetent layers. **(c)** Displaced non-stratabound quartz veins due to flexural slip at the contact between two competent layers after flexural-slip folding.

In the kinematic model, the overturned fold is reconstructed in possible successive steps that illustrate the incremental strain of the deformed competent layer. In this reconstruction, the line length of the competent layer and total volume of the initial rock body (grey box in the reconstruction) has kept constant. Stretching is illustrated by an orthogonal set of incremental strain axes (ISAs) which define maximum (ISA_1) and minimum (ISA_3) values of stretching during deformation (cf. Twiss & Moores 1992). The intermediate incremental stretching axis ISA_2 is oriented perpendicular to ISA_1 and ISA_3, parallel to the finite fold hinge line. In incremental each step, extensional and shortening instantaneous stretching should be parallel to the ISA_1 and ISA_3 respectively (cf. Passchier & Trouw 2005). The incremental deformation of the rock body is illustrated by the changing shape of the different strain ellipses in which the stretching axes (e_1 and e_3) are initially parallel to the ISAs but rotate anticlockwise during subsequent shearing. Furthermore, ISA_1 should be oriented at an angle of > 45° to the horizontal shear plane to allow maximum stretching of the initial rock body. The fact that the deformation can be reconstructed with ISAs that remain constant implies that the veins are deformed during coaxial progressive deformation.

The kinematics of vein deformation proposed in this model, *i.e.* vein deformation due to flexural-slip and flexural-flow folding, is largely based on the geometry of the veins. The refraction of veins cross-cutting multiple layers have been described previously and it thus seems to be plausible to relate them to flexural-flow folding. The curved stratabound veins, however, occur less frequently, although the internal deformation of competent layer during folding is well understood and is illustrated in many textbooks on structural geology. In order to validate this curvature of the veins in a fold limb, the flexural-flow model has been simulated in a line-length balancing program. It was chosen to work with *2DMove* of © Midland Valley because of its possibility to deform objects passively into a given fold structure during which the total line length of the initial object remains constant. The initial starting point is a continuous undeformed competent layer that contains multiple quartz veins oriented perpendicular to bedding (Figure 3.16a). The reasons for this specific initial geometry have been discussed above. Afterwards, an overturned fold geometry has been chosen which is representative of the overturned fold style of the Wildenhof section (Figure 3.16b).

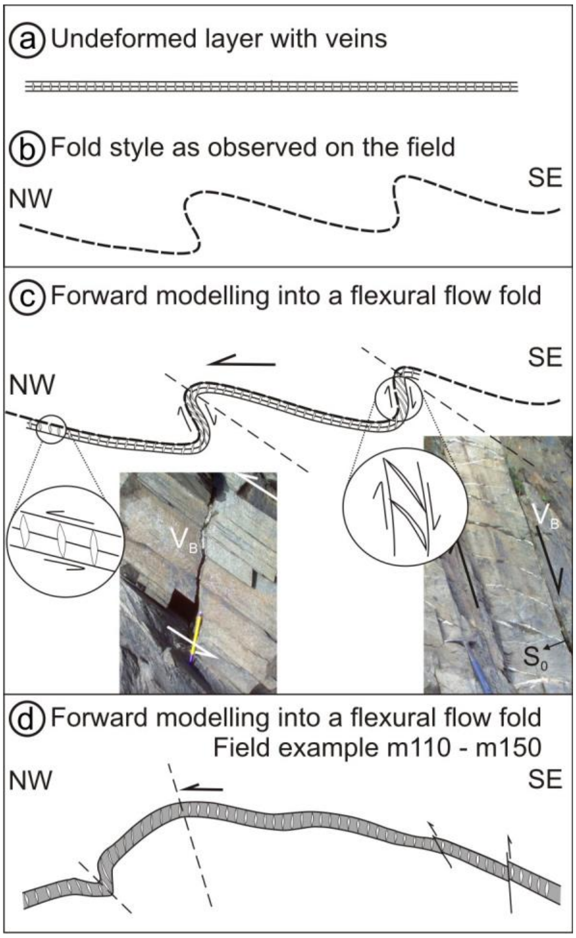

Figure 3.16: Kinematic model for the deformation of originally planar quartz veins, produced by a line-length-balancing program (*2DMove* © Midland Valley). **(a)** Starting point is an undeformed layer with originally planar stratabound bedding-normal quartz veins. **(b)** Overturned fold train representative of the Wildenhof fold train. **(c)** Resulting forward model by using the *flexural-flow unfold tool*, showing curved veins in both fold limbs and corresponding field examples (m110 and m360). **(d)** Forward modelling of the layer in (a) into the upright fold at m110 - m150.

In the *2DMove* program it is possible to apply a forward modelling in which the initial undeformed layer is folded into the overturned fold style by keeping the line-length constant and creating a fold with a uniform layer thickness (class 1B fold in Ramsay's (1967) fold classification). Furthermore, in order to validate the curvature of the veins, the option *flexural-flow mechanism* has been chosen in the program which allows continuous simple shear, localised in the competent layer, during folding. The resulting geometry (Figure 3.16c) shows a strong curvature of the veins in the overturned fold limbs and minor deformation of the veins in the normal fold limbs. On the one hand, the simulated curvature of the veins in the overturned fold limb corresponds well with the geometry observed in the field and the veins proposed in the kinematic model in Figure 3.15b. The vein tips in the upper structural levels of the overturned limb, all point towards the adjacent anticlinal hinge as is expected during flexural-flow folding. In the normal limbs, on the other hand, the observed curvature of the veins in the field only occurs in the fold limbs and not in the region closely towards the fold hinge. Possibly the length of the different folds limbs in the initial fold style (Figure 3.15b) will influence the ultimate vein curvature. Nevertheless, the correspondence of the kinematic model (Figure 3.15) and the field examples with the model produced by the *2DMove* program validates flexural flow in competent units and supports the pre-folding nature of the veins. A second exercise has been performed on a real field example such as the upright fold structure at m110 - m150 (Figure 3.16d) which has been chosen to illustrate the vein deformation in the normal NW-dipping fold limbs. Similar as to the previous case, an undeformed layer with BNVs was folded into a previous chosen fold structure by the *flexural-flow mechanism* in *2DMove*. The resulting forward model (Figure 3.16d) illustrates the absence of any vein deformation in horizontal layers in the middle part of the fold while a reorientation or deformation of the veins occurs towards the anticlinal hinge in the NW-dipping limb, corresponding to the field observations**.**

The overall part of bedding-normal veins is observed in competent layers in which the veins either are restricted to the competent layer or cross-cut a multilayer sequence consisting of an overall competent attitude. Apart from these observations, quartz veins also occur in slaty or silty sequences (Figure 3.7j and k) in which they are orientated at lower angle to bedding than the veins in the competent layers. The timing of these quartz veins remains enigmatic. In order to deduce their possible orientation prior to folding, the host rock has been unfolded towards the horizontal (Figure 3.12). After unfolding, veins range in dip from 30° to 70° with respect to the horizontal and vary in dip direction from N-S to E-W. This broad variation in orientation makes it difficult to group them into a specific vein generation as those observed in the competent layers. Also, the original orientation of these veins, which were formed prior to the formation of folds and cleavage as suggested by cleavage cross-cutting the veins (Figure 3.7j and k), is difficult to determine as they are possibly reoriented due to cleavage development in the slates and siltstones. The possibility that quartz veins can rotate during cleavage development has been illustrated by the deformation of non-stratabound quartz veins during flexural-flow folding. Furthermore, it might still be possible that the veins in slaty sequences could have formed after the BNVs in the competent units, during rotation of the layers during progressive folding, at the onset of cleavage development. The last-mentioned possibility has not been elaborated.

3.2.5.2 Bedding-parallel veins

The varying configurations of the observed bedding-parallel veins with respect to the surrounding host rock possibly indicate several different bedding-parallel veining mechanisms. In order to deduce these mechanisms, the four different configurations, described as *case i* to *iv* in section 3.2.4.1 are discussed separately in this kinematic interpretation. Based on the BPV characteristics, a relative chronology with respect to the BNVs and the regional fold-and-cleavage development can be constrained.

The composite interbedded BPVs, situated both below and above the competent units (*case i* and *ii*), have a complex macroscopical internal fabric consisting of different quartz laminae separated by several pelitic host-rock inclusion lines and fragments. At the contact with the competent unit, the vein wall of these vein types has a flat morphology, while at the contact with the under- or overlying siltstone the vein wall is more irregular causing a considerable thickness variation along the vein length. This variable morphology of the vein wall suggests that the veins are detached from the competent sandstone unit during vein formation, while they are more intimately related with the siltstone, which is exemplified by the siltstone host-rock fragments and inclusion lines incorporated in the veins and the numerous offshoots in the silty layers. This composite layering moreover indicates that these BPVs formed as a result of successive fracturing and sealing phases during bedding-normal uplift during which parts of the incompetent host rock have been incorporated within the vein (Figure 3.17c). The periods of bedding-normal uplift are followed by gravity-driven bedding-normal collapse (Figure 3.17d and f) during which fluids may have been expelled from the cavity from which the veins precipitated.

The varying orientation of the slickenlines, observed on different laminae in the BPVs and which are oriented at high angle to the local fold hinge lines (Figure 3.14), suggests that these composite veins (de)formed during bedding-parallel shear movements. These interbedded composite veins are interpreted to form as a result of bedding-normal uplift (absence of shear and pure extension), combined with bedding-parallel shear that either occurred during quartz precipitation, *i.e.* oblique opening, or between the emplacement of the different laminae. Local fluid release, exemplified as offshoots in the incompetent as well as in the competent units, may have accompanied the shear movements during vein formation (*e.g.* Teixell *et al.* 2000).

These BPVs are cross-cut by a regional axial planar cleavage, which developed contemporaneous with the folds, thereby giving the BPVs a fractured appearance. In order to propose a relative timing of the emplacement of these interbedded BPVs with respect to the regional fold-and-cleavage development, the incremental strain of the rock body during vein formation should be analysed.

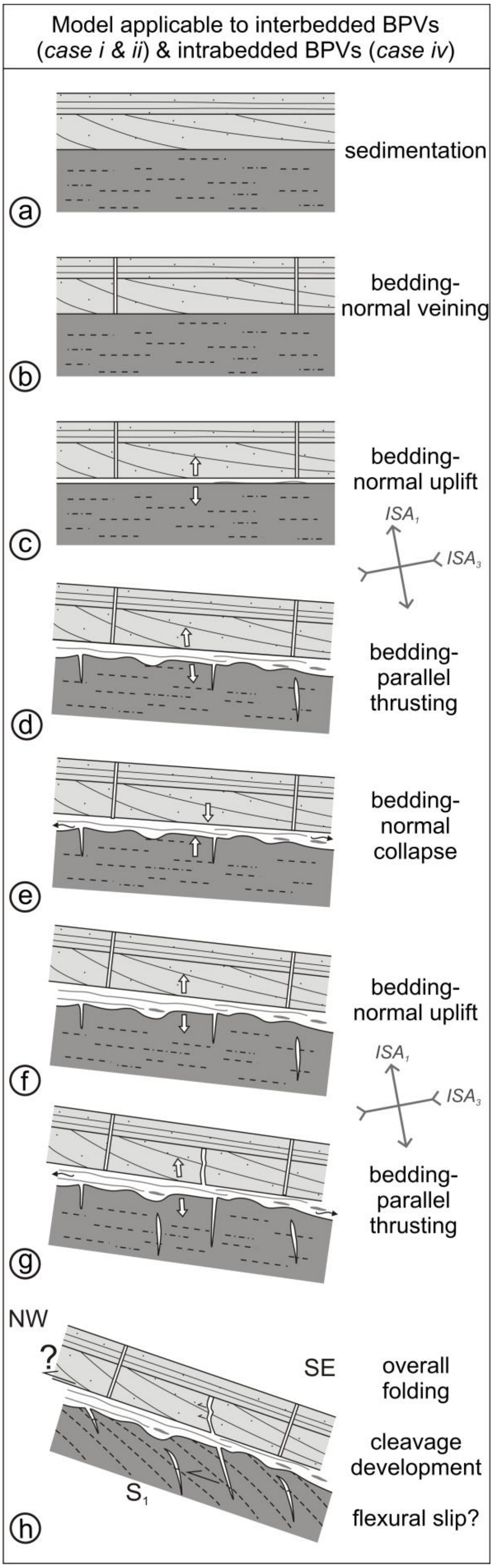

Figure 3.17 (right)**:** Schematic tentative vein mechanism proposed for the interbedded BPVs and the intrabedded veins in siltstone which developed after sedimentation **(a)** and bedding-normal veining **(b)** due to **(c-g)** successive phases of bedding-normal uplift combined with bedding-parallel thrusting. Each incremental phase of uplift might be followed by bedding-normal collapse during which fluids are expelled out of the fracture. Maximum incremental strain axis (ISA$_1$) at high angle to bedding during bedding-parallel shear. For simplicity, the tilting of bedding is exaggerated. **(h)** The resulting BPVs rotated passively during folding and may form a focus to further flexural slip.

It has been demonstrated that a coaxial progressive deformation is responsible for the formation of the regional overturned folds (see Figure 3.15). This implies that also during development of the bedding-parallel veins, the incremental strain axes (ISAs in Figure 3.17 and Figure 3.18) should remain constant in orientation during vein development. During bedding-normal uplift, maximum opening is perpendicular to bedding. Hence, a vertical maximum ISA_1 can define, orthogonal to bedding. However, subsequent oblique opening during bedding-parallel shear cannot develop if maximum stretching (ISA_1) remains perpendicular to the shear plane, *i.e.* the bedding plane (cf. Passchier & Trouw 2005).

Therefore, to solve this problem, a slight rotation of the layers must have been occurred prior to shearing. In this configuration (Figure 3.17c), oblique opening will be possible as the bedding-parallel shear plane is oriented at high angle to the maximum ISA_1. This tilting of the layers can be attributed to the onset of folding in which the layers start to buckle. However, the angle of tilting with respect to horizontal will be minor as the veins are continuous for several tens of metres long. In order to confirm this proposed combined veining mechanism, the quartz microstructures of the composite veins should be investigated in order to determine how uplift and shearing co-occurred (see Chapter 4). One has to keep in mind that during fold-and-cleavage development, some veins may have been reactivated during flexural-slip folding, while other are possibly striated due to bed-parallel movement of the overlying layer (Figure 3.17h).

As described in the geometric description, BPVs intrabedded within the competent sandstone (*case iii*; Figure 3.13d-h) have the least complicated geometry. These relatively short and thin BPVs consist of milky-white blocky quartz crystals and clearly cross-cut the bedding-normal veins, indicating that they post-date bedding-normal vein formation. At the contact between the BPV and the BNV, almost no lateral displacement (Figure 3.13e), or just a few millimetres of lateral displacement (Figure 3.13f) has been measured along the bedding-parallel vein walls. These observations suggest that these BPVs are pure extension veins that are formed during incremental bedding-normal uplift of the overlying rock column in order to create the cavity or fracture necessary to precipitate the vein fill (Figure 3.18a-f). The fact that sometimes clear host-rock inclusions are present in the vein, *e.g.* sandstone fragments in Figure 3.13d, indicates that these intrabedded vein types formed as a result of successive and recurrent phases of fracturing and mineral infill. Unfortunately, no macroscopic observations such as mineral fibres could confirm the extensional opening trajectory during bedding-parallel vein formation.

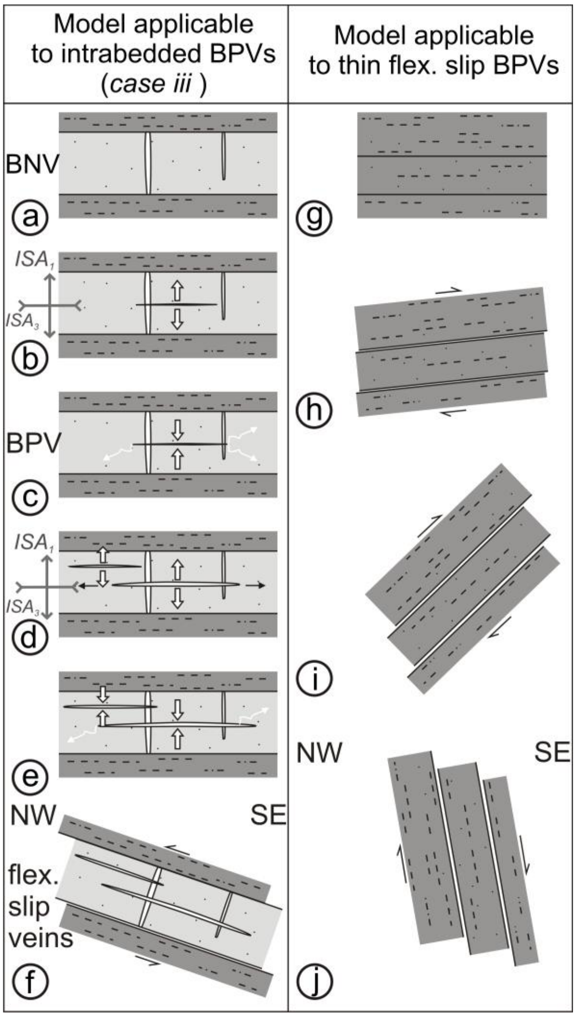

Figure 3.18: Schematic tentative veining mechanisms for the intrabedded BPVs. **(a)** Bedding-normal veining is succeeded by several phases of **(b-e)** bedding-normal uplift and bedding-normal collapse with expulsion of fluids. Fracturing parallel to the minimum incremental strain axis (ISA_3). **(f)** The intrabedded quartz veins are rotated passively during folding whereas BPVs situated at interbedded surfaces may slip during subsequent flexural-slip folding. **(g-j)** Formation of thin intrabedded flexural-slip BPVs in an overturned siltstone sequence due to successive phases and increasing slip during flexural-slip folding.

This necessitates a further detailed microstructural analysis of the veins in order to deduce the fracturing and growth rate of minerals precipitated in the vein and to determine the mechanism responsible for bedding-normal uplift (see Chapter 4).

Similar as to the previous model of the composite interbedded BPVs (Figure 3.17), bedding-normal uplift must have been followed by bedding-normal collapse (Figure 3.18c and e). It is difficult to establish a relative chronology of the veins of *case iii* with respect of overall folding and cleavage development, as cleavage does not cross-cut the coarse-grained sandstone layers and hence does not cross-cut the intrabedded BPVs. However, as lateral displacements are absent and flexural slip only occurs at specific interbedded surfaces, it is suggested that the intrabedded BPVs in the competent units, formed by the proposed mechanism, developed prior to buckling resulting from fold-and-cleavage development and rotated passively during folding together with the coarse-grained sandstone layer.

The fourth type of BPVs, *i.e.* centimetre-thick BPVs interbedded in silty sequences (*case iv*) are characterised by several host-rock fragments internally (Figure 3.13i). It is suggested for these interbedded BPVs that they also formed during several phases of bedding-normal uplift (Figure 3.17) during which the silty host-rock inclusions were incorporated in the veins. Shear-related features are not observed macroscopically but are deduced in the fabric analysis (see Chapter 4).

Finally, the millimetre-thick quartz veins intrabedded in silty sequences should be separated from the four cases as they are formed by a different mechanism. They are mostly characterised by slickensides which contain slickenlines that are oriented consistently on a single quartz lamina but may vary slightly from lamina to lamina. From the orientation analysis, it is clear that this BPV type represents bedding-parallel movements between two layers due to flexural-slip folding (Figure 3.18g-j). Clear shear sense indicators, however, are only locally observed, *e.g.* zone 9 in the SE-dipping overturned limb, in which the fibre steps locally point towards the anticlinal hinges conform to the movement expected during flexural-slip folding (Fowler 1996, Tanner 1989). Flexural-slip veins should, moreover, have opposite fibre steps at the other side of the fold and tapering vein tips towards the fold hinge. Theoretically, flexural-slip veins are absent in a fold hinge due to a decreasing amount of slip towards the hinge and absence of slip at the hinge zone (Cosgrove 1993). Unfortunately, the opposite normal limb of zone 8 did not contain any BPVs that are marked by clear fibre steps or opposite shear senses that could have confirmed this hypothesis, despite the fact that displaced BNVs in this fold limb clearly exemplify flexural slip (Figure 3.5d). Also, the absence of BPVs at the fold hinges of the Wildenhof section does not immediately imply absence of slip at the hinges. The lack of evidence justifies extending the study area to other outcrops around the Rursee to refine the flexural-slip mechanism and the regional implication of this type of BPVs.

3.2.5.3 Folds, syntectonic veins and faults

Along the Wildenhof section a transition from smaller-scale decametre upright folds (zones 2-7; Figure 3.3) into hectometre overturned folds (zones 9-12; Figure 3.1) is observed. Throughout this section, cleavage is largely axial planar with respect to the folds and refracts in opposite directions away from the fold hinges, indicating that cleavage developed contemporaneous with the folds. In addition to the BNVs and BPVs also minor tectonic structures are observed to be associated with quartz veins. Observations collectively suggest that these veins are syntectonic veins related to overall buckling, cleavage development and faulting.

Small-scale folds, such as the folded layers at m5 or m185 (Figure 3.5b and c) in the Wildenhof section (Figure 3.3), contain several quartz-filled, bedding-normal extension cracks in the hinge zones which typically form due to tangential longitudinal strain of the rigid outer part of the hinge zone and are termed as hinge cracks (cf. Ramsay & Huber 1987). In these small-scale folds, additional quartz veins oriented oblique to bedding are also observed in the fold limbs (Figure 3.19a). They do not belong to the early BNVs but instead cross-cut and thus post-date them. Although these oblique veins vary in shape from planar to complex sigmoidal geometries, they can be interpreted as tension gashes that commonly develop in a localised shear zone (Twiss & Moores 1992). The sigmoidal tension gashes are generally S- or Z-shaped depending on the sense of shear along the shear zone. They, moreover, usually form in the competent sandstone layers and are related to internal flexural flow of the competent layer during the formation of smaller-scale folds (cf. Figure 21.12 in Ramsay & Huber 1987).

It depends on the timing of vein initiation with respect to the orientation of bedding whether a planar vein or a sigmoidal vein will develop. In the example illustrated in Figure 3.19, planar vein arrays may have evolved into sigmoidal arrays during progressive folding. In this model, initially tension gashes develop parallel to the minimum ISA$_3$. Subsequently, during progressive tilting and continuous bedding-parallel shear in the fold limb, new tension gashes will develop, whereas the earlier gashes further open during rotation and eventually form sigmoidal patterns. Theoretically, new cross-cutting planar tension gashes, opening parallel to the minimum ISA$_3$, may form during continuous shearing. However, in this particular example the vertical cross-cutting vein can only form if the minimum ISA$_3$ and maximum ISA$_1$ mutually switch (Figure 3.19b). In this configuration the incremental strain axes allow horizontal opening of the vein which must have been formed in a different context.

A few outcrops show a local subparallelism of cleavage and bedding attitude (*e.g.* m200; Figure 3.5c). As result of this subparallelism, boudinage of the competent sandstones has taken place, due to pure flattening or thinning of the layers related to the cleavage development. Associated syntectonic interboudin quartz veins are locally observed in layers in the necks of the boudins. Other syntectonic features such as dilational jogs (m145; Figure 3.4d) are observed in close relationship with bedding-(sub)parallel thrusts. These jogs exemplify progressive opening of a vein that developed parallel to the fault/shear-plane. The origin of the observed jogs are difficult to determine; either they reflect bedding-parallel thrusting early kinematic to folding and are in close relationship with the formation of the BPVs, or they formed cogenetically with syn- or post-folding thrusts such as the small-scale thrusts at m185 (Figure 3.5b and c). The slickenlines which track the fault movement, as well as the observation that the fault bifurcates along its prolongation, supports syn- to post-folding timing of the dilational jog and thrust development.

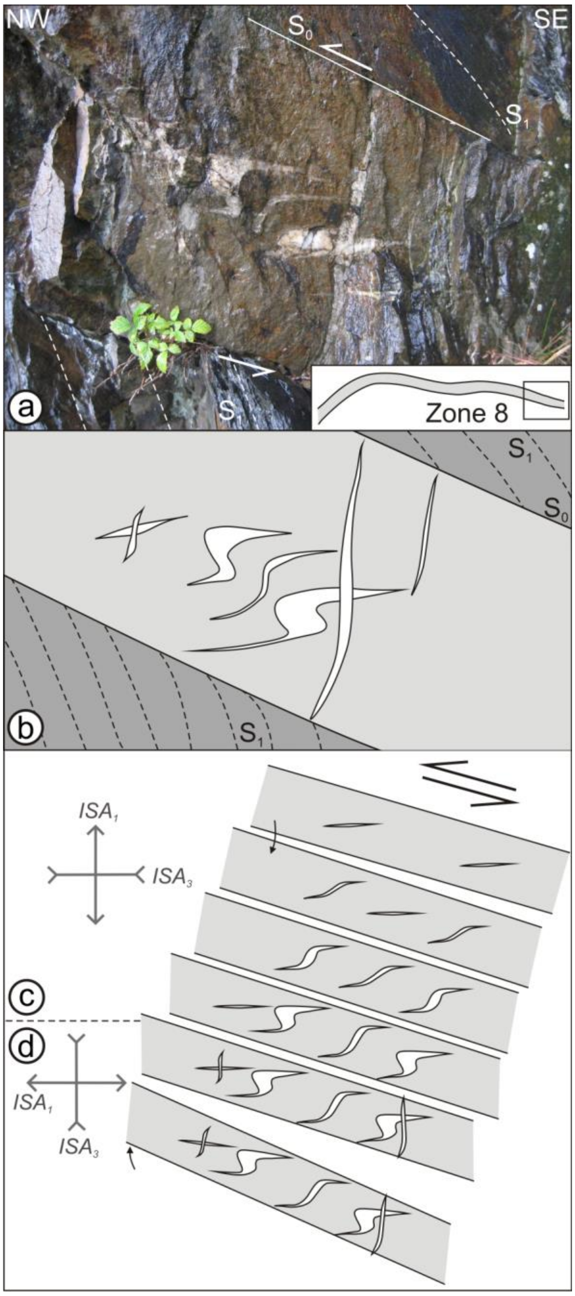

Figure 3.19: Tension gashes in fold limbs. **(a-b)** Photograph and field drawing of sigmoidal tension gashes in a normal SE-dipping limb (m143, zone 8). **(c)** Simplified kinematic model: extension fractures initially develop during shearing of the fold limb during flexural-flow folding (compression). Subsequently, new fractures and sigmoidal gashes develop by continuous shear. Minimum and maximum incremental strain axes (ISAs) remain constant in this stage. **(d)** Cross-cutting veins can only form after reorientation of the ISAs, indicative of extension.

Along the Wildenhof section several steeper fault zones occur (Figure 3.4). Although the displacements are often unknown, the occurrence of metre-scale pop-up structures and associated thrusts suggests that also the larger fault zones are reverse faults. The fact that the orientation of these reverse faults is largely parallel with the axial surfaces of the upright and overturned folds of the Wildenhof section suggests that these faults formed in a similar compressional regime as the folds. According to Holland *et al.* (2006), however, the SE-dipping fault zone at m190 (Figure 3.5c) and a comparable fault zone in the synclinal hinge at m220, are normal faults with a variable fault width. These authors describe these normal fault zones as fault zones with a heterogeneous assemblage of strands of weakly to strongly deformed fault gouge with differently deformed clayey material. They concluded from the thickness of the fault zone, the absence of a clearly developed fault-core damage zone structure and from the absence of mapable offsets in the local geological map that the displacement caused by the faults is less than a few tens of metres. Also their analysis of the clay gouge of the fault at m190 pointed out the porosity of the clay gouge is to be much higher than the porosity of the 'overconsolidated' host rock, *i.e.* siltstones. Therefore Holland *et al.* (2006) suggested that deformation must have taken place in much shallower conditions than during the Variscan deformation and that at the time of faulting, the fault gouge was still deep enough to be isolated from surface weathering but shallow enough to avoid "cooking" of the fault gouge at deeper conditions. Hence, the observed orientation of these fault zones support that they were initiated as a reverse fault during the main Variscan contraction, after the main folding and cleavage development. Subsequently, they are reactivated as a normal fault. Timing of reactivation, however, remains a discussion; either reactivation initiated during late-Variscan extensional phases related to the collapse of the Variscan orogen (cf. Van Baelen 2010), or they represent normal faults during post-Variscan faulting.

3.2.6 Interpretation & synthesis

Based on the outcrops studied along the Wildenhof section exposed at the northeastern shores of the Rursee, a preliminary deformation history of the Pragian Upper Rurberg Unit can be proposed that outlines the chronology of fracturing and veining events, folding, cleavage development and faulting.

Chronologically, after sedimentation and compaction of the alternating sequences of the Upper Rurberg Unit, **bedding-normal quartz veins** formed first. It is concluded from many deformation features such as vein refraction, cleavage cross-cutting the veins, vein deformation due to flexural-slip and flexural-flow folding, that the veins predate the overall fold-and-cleavage development. If bedding is restored into its original horizontal position prior to folding, three observed vein generations V_A, V_B and V_C are determined to be consistent in orientation along the whole Wildenhof section. At the time of bedding-normal vein formation the layers were thus still in a horizontal position. The fibrous infill of the veins and the absence of any displacement parallel to the vein walls, moreover, suggest that the BNVs are extension veins which formed prior to buckling of the layers and presumably in an extensional stress regime. It has been demonstrated in different models in the Wildenhof case study that the incremental strain axes of deformation remain constant during veining and subsequent deformation, indicative of a coaxial progressive deformation. This implies that the orientation of the veins may be used to determine the state of stress during vein formation. If veins, which initiated as fractures, are uniform in trend over a large area, then they can be used as indicators to determine the palaeostress orientations at the time of fracturing or veining (Cox *et al.* 2001, Gillespie *et al.* 2001, Laubach *et al.* 2004a). Veins that display pure extension are classically interpreted to form perpendicular to the minimum principal stress σ_3 and are aligned parallel to the intermediate σ_2 and maximum σ_1 principal stresses in the σ_1 - σ_2 plane (Secor 1965). Due to the fact that veins are formed in a horizontal bedding position, the maximum principal stress σ_1 must have been vertical at the time of vein formation, corresponding to the load of the overburden, and σ_2 can be deduced from the alignment of the veins. This configuration corresponds to the stress state in a sedimentary basin. It is suggested from the results of the rotation exercise (Figure 3.10) that hence the palaeostress evolution can be deduced from the original orientation of V_A

over V_B to V_C. The regional occurrence of V_A is highly uncertain as it is only observed in one fold limb. Hence, this generation is not used for the interpretation of the palaeostress. The transition of V_B to V_C would imply a rotation of the local stress state at Wildenhof from a N-S to NNE-SSW directed $\sigma_1 - \sigma_2$ plane during V_B-emplacement, indicative of **NW-SE extension**, to a NE-SW-directed $\sigma_1 - \sigma_2$ plane at the time of V_C-emplacement (see Figure 3.10). This tentative model of reorientation of the stress field during bedding-normal vein formation is only derived from the orientation of two local quartz vein generations and needs to be further elaborated by investigating the consistency in orientation of these generations over a larger area. Furthermore, also the regional tectonic stress needs to be implemented in this tentative palaeostress-state evolution.

Bedding-parallel quartz veins subsequently cross-cut bedding-normal veins. Depending on the relative position of the BPV with respect to the adjacent host rock, several BPV-types are distinguished of which the intrabedded BPVs in sandstone layers represent **bedding-normal uplift** (Figure 3.18), whereas the composite and laminated interbedded BPVs reflect combined bedding-normal uplift and **bedding-parallel thrusting** (Figure 3.17), both presumably taking place in the compressional regime. Bedding-parallel slip initiated at the onset of folding but predates the main phase of folding and cleavage development. This is evidenced by cleavage cross-cutting the veins and variability of slip orientations on a single BPV, varying from orthogonal to oblique with respect to the local fold hinge line. Forming these BPVs would require (partial) uplift of the rock column above the BPV during veining. There are several mechanisms to explain the bedding-normal uplift, *e.g.* due to internal high pore fluid pressures (Cox 1995, Fitches *et al.* 1986, Rodrigues *et al.* 2009), and the combined bedding-normal uplift and bedding-parallel thrusting (*e.g.* Jessell *et al.* 1994, Koehn & Passchier 2000). This discussion, however, would be more relevant if the regional consistency of BPVs in the North Eifel is understood, rather than discussing it after the first Wildenhof case study. Therefore possible veining mechanisms are discussed after the other case studies in section 3.5.2, in which BPVs are compared to BPVs observed in the Rhenish Massif (Baum 1955, Breddin 1930, de Roo & Weber 1992, Hilgers *et al.* 2006a, Nielsen *et al.* 1998, Weber 1980) and in other mountain belts (*e.g.* Boullier & Robert 1992, Cobbold & Rodrigues 2007, Fitches *et al.* 1986, Hilgers *et al.* 2006b, Jessell *et al.* 1994, Koehn & Passchier 2000, Rodrigues *et al.* 2009).

Subsequent to the formation of the BPVs, as the tectonic deformation continues, overall buckling caused the characteristic NW-verging, upright to overturned folds with associated axial planar cleavage in the Wildenhof study area. Small-scale tectonic features with associated quartz veining such as interboudin veins (Figure 3.6), out-of-syncline fault-related veins (Figure 3.5), sigmoidal tension gashes (Figure 3.19), filled hinge cracks, displaced or deformed bedding-normal veins (Figure 3.15) and thin flexural-slip BPVs (Figure 3.13j) accompany folding. One has to keep in mind, however, that the BPVs might have been reactivated during progressive folding and the possibility exists that BPVs related to early folding and flexural slip BPVs are mutually not exclusive.

The deformation of the Variscan cleavage into kink bands has only locally been observed in pelitic sequences. Although the kink band geometry, which can indicate the maximum principal stress direction at the time of cleavage deformation, has not been studied, kink bands may be attributed to the late Variscan destabilisation of the High-Ardenne slate belt (cf. Van Baelen 2010). Also several large fault zones cross-cut the fold limbs and fold hinges and are observed to post-date the main Variscan fold-and-cleavage development. Most fault zones have similar SE-dipping orientations compared to the axial surfaces of the upright to overturned NW-verging folds and therefore they can be interpreted as syn- to post-folding reverse faults, formed during the compressional stage of the Variscan deformation. Due to the unknown displacements of the large faults, the relative timing of faulting remains enigmatic; either they reflect synfolding, *i.e.* fault-bend-folding or fault-propagation-folding (*e.g.* Dittmar *et al.* 1994), or post-folding, *i.e.* break-thrust folding. Furthermore, these fault zones initiated as reverse faults during the Variscan orogeny, but are later reactivated as normal faults during fault movement (Holland *et al.* 2006), either due to extensional tectonics during orogenic collapse (Van Baelen 2010) or later post-Variscan fault movements.

3.3 Case II: Eschaulerberg section

3.3.1 Localisation

The main reason to have studied the Eschaulerberg section is to check consistency of the different vein types that have been observed at the Wildenhof section. The outcrops exposed at the Eschaulerberg section are situated along the western side of the Eschaulerberg peninsula in the middle part of the Rursee study area (see Figure 3.1), approximately 2 km south of the little village Schmidt. Maximum outcrop capacity is only assured in autumn and winter during decreased water level of the Rursee reservoir (271m NN during the 2009 field work campaign). In these periods, the steep and inaccessible Eschaulerberg cliffs provide an excellent, 500 m long cross-section on which the overall folding structures and veining patterns can be studied. Along a small path that connects the ‘mainland’ with the southern end of the peninsula, the upper parts of the Eschaulerberg cliffs (> 278m) can also be visited in summer at high water level. The lower parts at the shores, however, can only be visited by means of a small boat or can be overlooked on the passengers vessel of the ‘*Rursee-Bahn’* (*Rursee Schifffahrt*) that travels the Rursee several times a day during the tourist season. While the overall structural architecture of the Eschaulerberg section is sketched by means of some important outcrops along the cross-section, the geometry of the veins are mainly discussed by a detailed key-outcrop in the middle part of the cross-section. The exact position of the discussed outcrops is indicated on the scale-bar below the Eschaulerberg cross-section (Figure 3.21).

3.3.2 Geometric analysis

Owing to the overall NE-plunging attitude of the fold hinges in the Rursee area, the outcrops at the Eschaulerberg section are situated on a higher lithostratigraphical and structural level than those observed in the Wildenhof section (Figure 3.1). Similar as to the previous case study, the observed folds in the Eschaulerberg section display a general, moderately NE-plunging attitude, despite a small variation from NNE- to east-plunging (Figure 3.20b). In the overall part of the cross-section, the orientation of bedding-cleavage intersection lineation (L_i~066/30) corresponds to the orientation of locally measured fold axes. For over 500 m (cross-section G-H in Figure 3.1 and Figure 3.21), the Eschaulerberg section consists of a hectometre-scale, NW-verging, upright to slightly overturned fold train, which is characterised by several secondary folds.

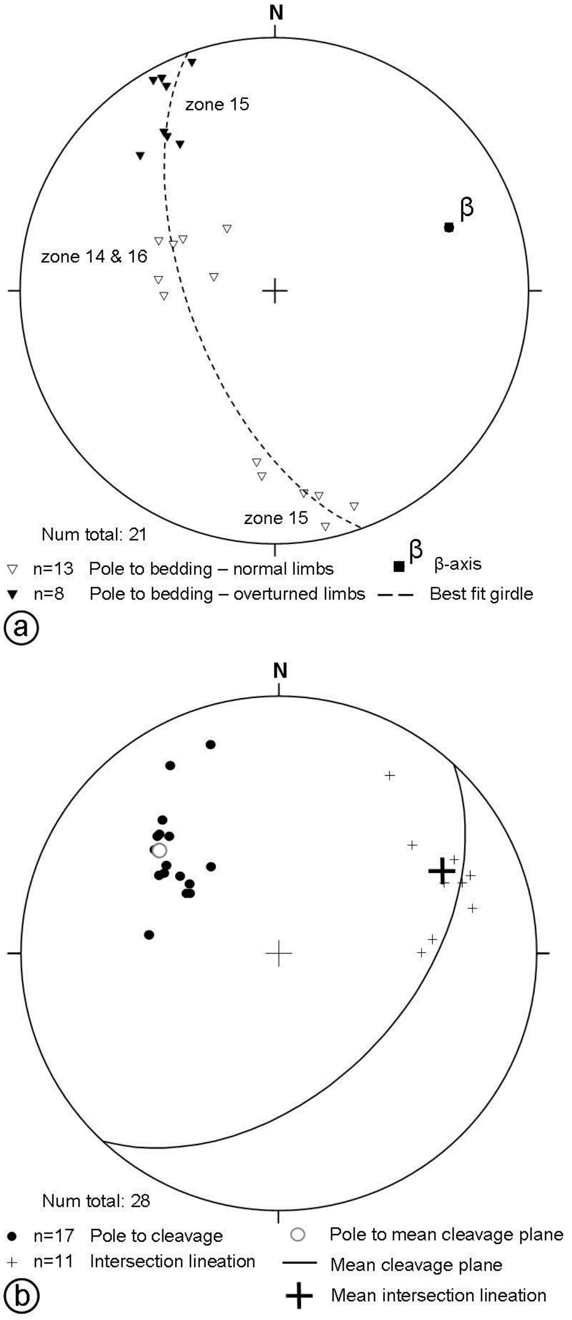

Figure 3.20: Lower-hemisphere, equal-area stereographic projection of measured structures at the Eschaulerberg section. **(a)** Poles to bedding. **(b)** Bedding-cleavage intersection lineation and poles to cleavage.

A pervasive, axial-planar, spaced and slaty cleavage (S_1~133/47) is observed in the coarse-grained sandstones and the fine-grained, laminated sandstones or silty sequences respectively. These lithological units are characteristic in the Siegenian Upper Rurberg Unit (sR3).

Based on the orientation of bedding, three distinct fold limbs are recognised from the NE to the SW along the cross-section. These fold limbs are defined as zone 14 (normal SE-dipping), zone 15 (overturned SE-dipping) and zone 16 (normal SE-dipping) (see Figure 3.1; Figure 3.20a; Table 3.2). The moderately SE-dipping normal limb of zone 14 can be correlated with zone 2 at the north-eastern shores of Wildenhof (case study I), but also to the north-western normal fold limb of zone 17 at the Hubertus Höhe section (case study III), regardless of its higher structural level. The approximately 200 m long zone 14 is characterised by a consistent bedding orientation (S_0~106/38) without the presence of faults or secondary folds. At m20, the transition of zone 14 into zone 15 occurs along an open syncline with an apparent axial planar cleavage. Some outcrops of zone 15 are illustrated in Figure 3.21. The approximately 300 m long fold limb of zone 15 ranges in bedding orientation from steeply NW-dipping with a normal polarity (S_0~348/77) to a vertical attitude and eventually into a steeply overturned SE-dipping limb with an inverse structural polarity (mean S_0~145/73). This alternating bedding attitude has been indicated on the Rursee structural map as transparent grey zones for the overturned bedding and white zones for the normal bedding (see Figure 3.1). Instead of a transition of decametre-scale folds such as observed between zones 2 and 7 in the Wildenhof cross-section (see Figure 3.3), zone 15 is characterised by several higher-order or parasitic, metre-scale folds restricted to the fold limb. Overturned SE-dipping layers have planar bedding surfaces that are continuous at the outcrop. Upright to steeply NW-dipping layers, however, are often buckled (Figure 3.21; Figure 3.22) into buckle folds that may vary from metre-scale bedding undulations (m380) to entire secondary folds with the development of a small, normal SE-dipping limb in the middle of the fold (*e.g.* folds at m150 and m203; Figure 3.21). These secondary folds are very interesting due to the fact that both BNVs and BPVs are continuously distributed around the folds which allows inferring the relative chronology between both veining events and folding. The secondary fold at m150 has been studied in detail and is discussed in section 3.3.3. At the south-eastern end of the Eschaulerberg peninsula, zone 15 continues into the SE-dipping fold limb of zone 16 (S_0~112/48) that can be correlated with the beds at the north-western corner of the island in the Rursee. The overall part of zone 16, however, is covered by water. The buckle folds at the end of the cross-section (see m380; Figure 3.21; Figure 3.22e) are developed in thick coarse-grained competent sandstone layers that are often limited in length and wedge out owing to the sedimentological nature of these beds. These wedges represent metre-scale point bars (see section 2.4.2) and complicate tracing bedding around the buckle folds.

Table 3.2: Bedding and cleavage data of the investigated zones at the Eschaulerberg section. See Figure 3.1 for localisation of the fold limbs (zone 14 to 16). The number of measurements is given in brackets. Grey zones represent the data specific for an overturned fold limb. - : not observed or suspicious data.

Outcrop	**Bedding (S_0)**	**β - axis of bedding**	**Cleavage (S_1)**	**S_0/S_1 L_i (measured)**	**S_0/S_1 L_i (merged)**
Zone ***14***	106/38 (5)	-	125/51 (8)	054/24 (4)	062/29 (13)
Zone ***14 - 15*** *: transition*	358/72 (5)	-	122/58 (2)	082/21 (2)	070/44 (7)
Zone ***15***	145/73 (8)	-	134/46 (5)	082/42 (2)	060/16 (13)
Zone ***16***	112/48 (3)	-	128/51 (2)	061/33 (3)	-
Zone ***14 - 16***	Best fit girdle:		Mean value:	Mean value:	Mean value:
Eschaulerberg fold train	250/62 (21)	070/38	133/47 (17)	066/30 (11)	064/30 (33)

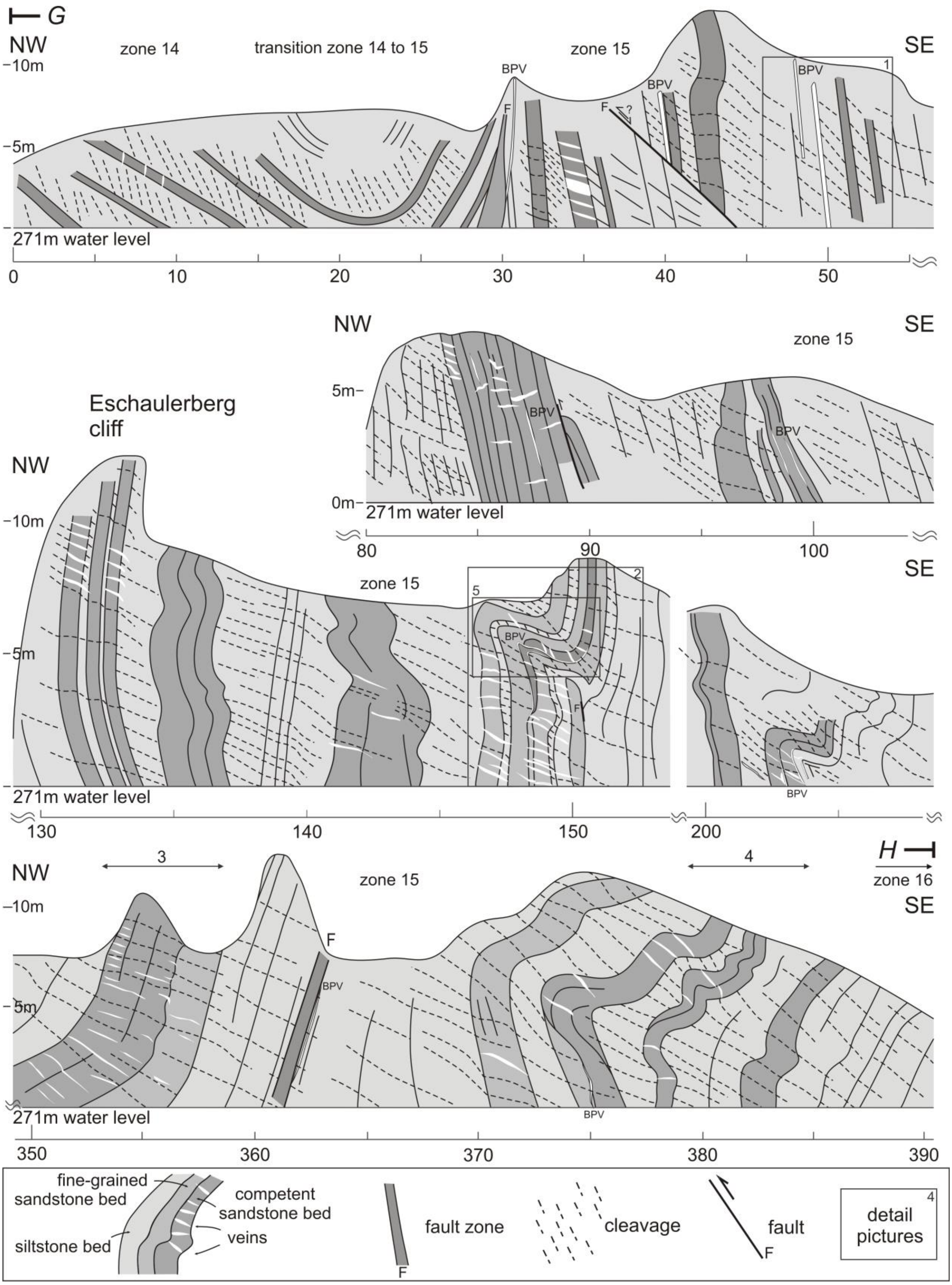

Figure 3.21: Eschaulerberg conceptual structural cross-section constructed by means of field drawings and photographs taken from the water, showing bedding, cleavage, folds, faults and veins. For over 500 meter, the Eschaulerberg cross-section consists of a hectometre-scale, NW-verging, upright to slightly overturned fold sequence characterised by buckle folds and an apparent axial planar cleavage. Mind the gaps between some outcrops and the changes in scale between the different cliffs. Location of photographs: (1-4) Figure 3.22b-e; (5) Figure 3.23.

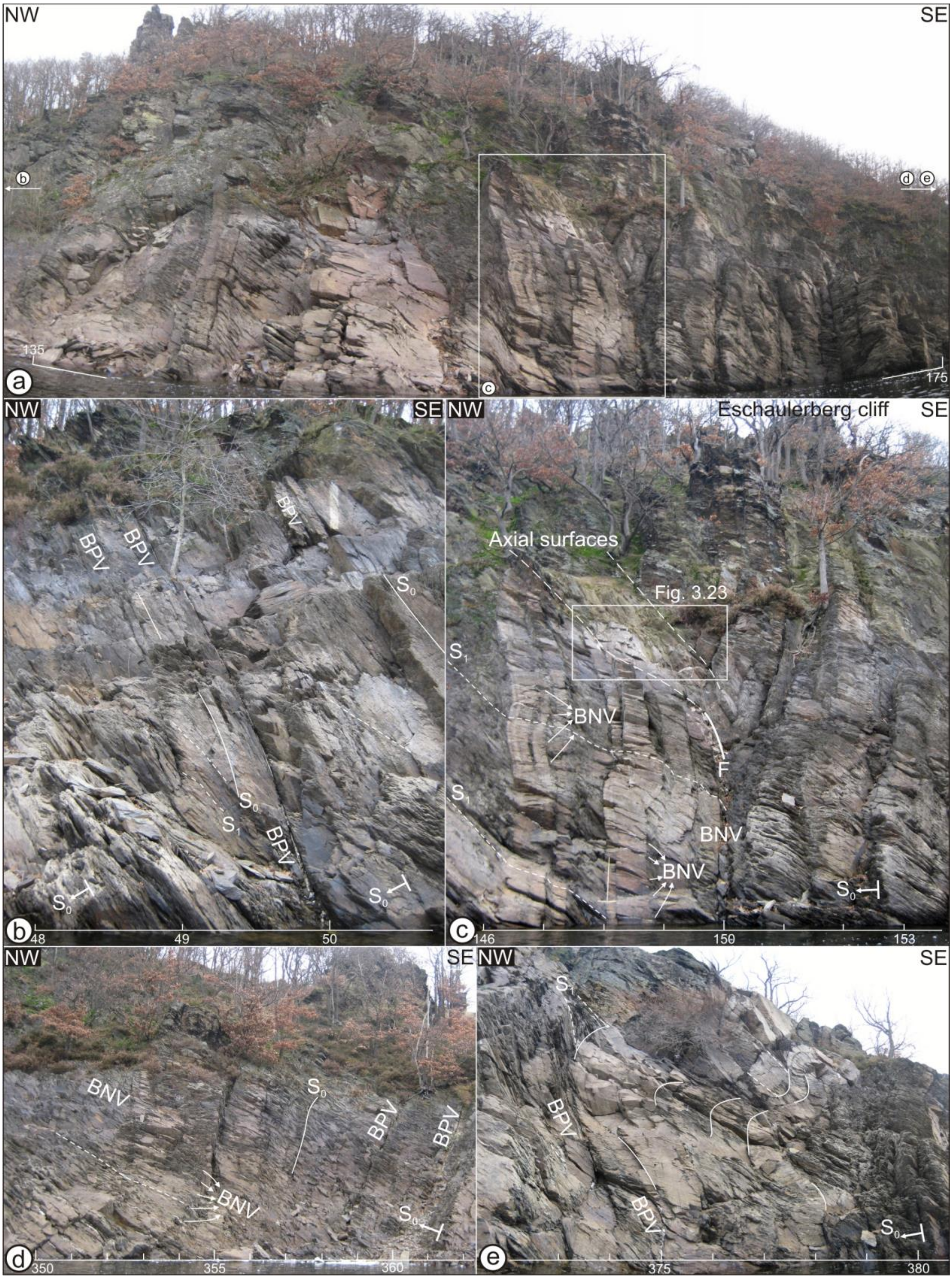

Figure 3.22: Representative parts of the Eschaulerberg cliffs showing deformation within the upright NW-dipping and overturned SE-dipping layers of zone 15. The scale bar (in metre) below each photograph corresponds to the scale bar at Figure 3.21. **(a)** Panorama of the Eschaulerberg cliffs showing upright to slightly overturned Upper Rurberg beds. **(b)** Overturned fold limb characterised by alternating fine-grained sandstone and siltstone containing interbedded BPVs. **(c)** Secondary anticline-syncline fold train in upright to overturned layers. **(d)** SE-dipping overturned layers with bedding-parallel fault zone and interbedded BPVs. **(e)** Buckle folds in NW-dipping competent layers at the end of the Eschaulerberg peninsula. Water level ~271 m.

Locally at m30, a metre-scale fault zone cross-cuts the synclinal hinge between zone 14 and zone 15 Figure 3.21. The fault zone shows a large variation in width, ranging from a few centimetres at the top to approximately 1 m at the base. Absence of correlation of bedding below and above the fault zone hampers deducing the fault offset or determining the nature of the fault as a reverse fault or a normal fault. The fault zone is characterised by a prominent thin clayey fault gouge and has a rather sharp contact with the surrounding host rock. As the fault zone increases in thickness, damaged or disrupted wall-rock fragments and multiple strands of fault gouge become more prominent (cf. Holland *et al.* 2006). The upper fault wall has a constant dip towards the NW, while its base ranges from a vertical orientation at its upper thinnest part, to a SE-dipping orientation (F~185/75) at its thickest part (see m30 at Figure 3.21). At m360 another 0.3m-wide fault zone occurs parallel to bedding. A bedding-parallel vein accompanies the base of this fault. A relationship between BPV and the fault has, however, not been established. Small planar faults, oriented parallel to cleavage and cross-cutting the overturned layers of zone 15 (*e.g.* m40) are sometimes observed. Similar as to the faults with a fault gouge, the sense of displacement has not been determined owing to the absence of correlation of the beds at both sides of the fault.

3.3.3 Eschaulerberg parasitic fold

The geometry of the parasitic fold observed at m148, is of particular interest because it is one of the few outcrops in the area in which several bedding-normal veins (BNVs; see BOX I) and bedding-parallel veins (BPVs; see BOX II) can be observed together. The outcrop has moreover the advantage that both vein types are draped around a fold structure. A geometric analysis of this fold allows constraining a relative chronology between these structural features. In a regional context, this parasitic fold can be identified as a third-order fold in a fold limb of the second-order fold train between zones 14 and 15. First-order folds correspond regionally with the transition of the *Rurberger Mulde* into the *Rurberger Sattel* and *Hasenfelder Sattel* in the Rursee study area, such as shown in Figure 2.3a.

The outcrop displays a 3 metre wide anticline-syncline fold train, marked by a pronounced NW-verging asymmetry and an axial planar cleavage. From NW to SE, the fold train consists of an overturned, steeply (~80-75°) SE-dipping limb, a normal, shallow (~25°) SE-dipping limb and a normal steeply (~70°) NW-dipping limb (Figure 3.23a and b). Based on the interlimb angle of these fold limbs, the fold train can be described as a close anticline (interlimb angle ~56°) followed by an open syncline (interlimb angle ~90°). The bluntness of both folds can be defined as angular and subrounded for the anticlinal and synclinal hinge respectively. The 80 cm thick coarse-grained sandstone layer present in the core of the parasitic fold is characterised by a spaced cleavage, whereas a closely spaced cleavage is observed in the surrounding siltstones. Cleavage refracts at the siltstone-sandstone interface in the fold limbs in such way that it refracts away from the fold hinges, such as expected in a fold created by a progressive fold-and-cleavage development. A divergent cleavage fanning is observed at the outer side of the anticlinal hinge, whereas in the siltstone in the core of the fold, a convergent cleavage fanning is observed.

Actually two fold hinges (FH_1 and FH_2 in Figure 3.23b and c) can be observed in the anticlinal hinge. FH_1, developed in a sandstone layer that seems to wedge out towards the SE, is characterised by BPV_1 that remains constant in thickness around the hinge zone. In the core of this FH_1, a thick irregular, seemingly irregularly folded quartz vein is present. FH_2 occurs above the outwedging sandstone layer and developed in two thinner sandstone layers that continue to the SE into the synclinal hinge. FH_2 contains BPV_2 that developed between these two thinner sandstone layers and is folded around the fold hinge. This fold hinge is, moreover, also characterised by the presence of numerous thin quartz veins. The sigmoidal veins at the top of the upper sandstone layer probably represent local shear in the upper part of the fold. To the SE, BPV_1 continues below the thick sandstone in the synclinal hinge. This part of BPV_1 is marked by NW-SE-trending slickenlines on its upper vein wall. The lower vein wall has an irregular pattern and is intimately related with the lower lying siltstone (Figure 3.23c). A third BPV_3 is present below the outwedging sandstone layer and is folded in the core of FH_1. All three BPVs are marked by macroscopic host-rock inclusions (indicated with black lines in the BPVs in Figure 3.23b).

Due to the numerous thin quartz veins in the core of FH_2 it is difficult to trace bedding of the upper sandstone layers in the fold core. The folded BPV_2 in FH_2, however, shows that these sandstone layers have been folded on top of the out-wedging sandstone layer. In order to reach this position, it is plausible that the upper two sandstone layers, folded in FH_2, must have been thrusted towards the NE, on top of the lower-lying, out-wedging sandstone layer. This is exemplified by slickenlines on the thick BPV_1 in the synclinal hinge (Figure 3.23d). This thrusting thus implies that the sandstones are duplicated. The siltstones above and below the parasitic Eschaulerberg fold do not mark any sign of this duplication. At the upper side of both fold hinges, the siltstone rather seems to be squeezed between FH_2 and FH_1, clearly illustrated by the cleavage that converges towards the cusp of this contact (Figure 3.23c).

The described complex deformation and duplication in the anticlinal hinge is absent in the synclinal hinge, in which bedding remains uniform in thickness around the fold which can be described as a class 1B parallel fold in Ramsay's (1967) classification of folded layers.

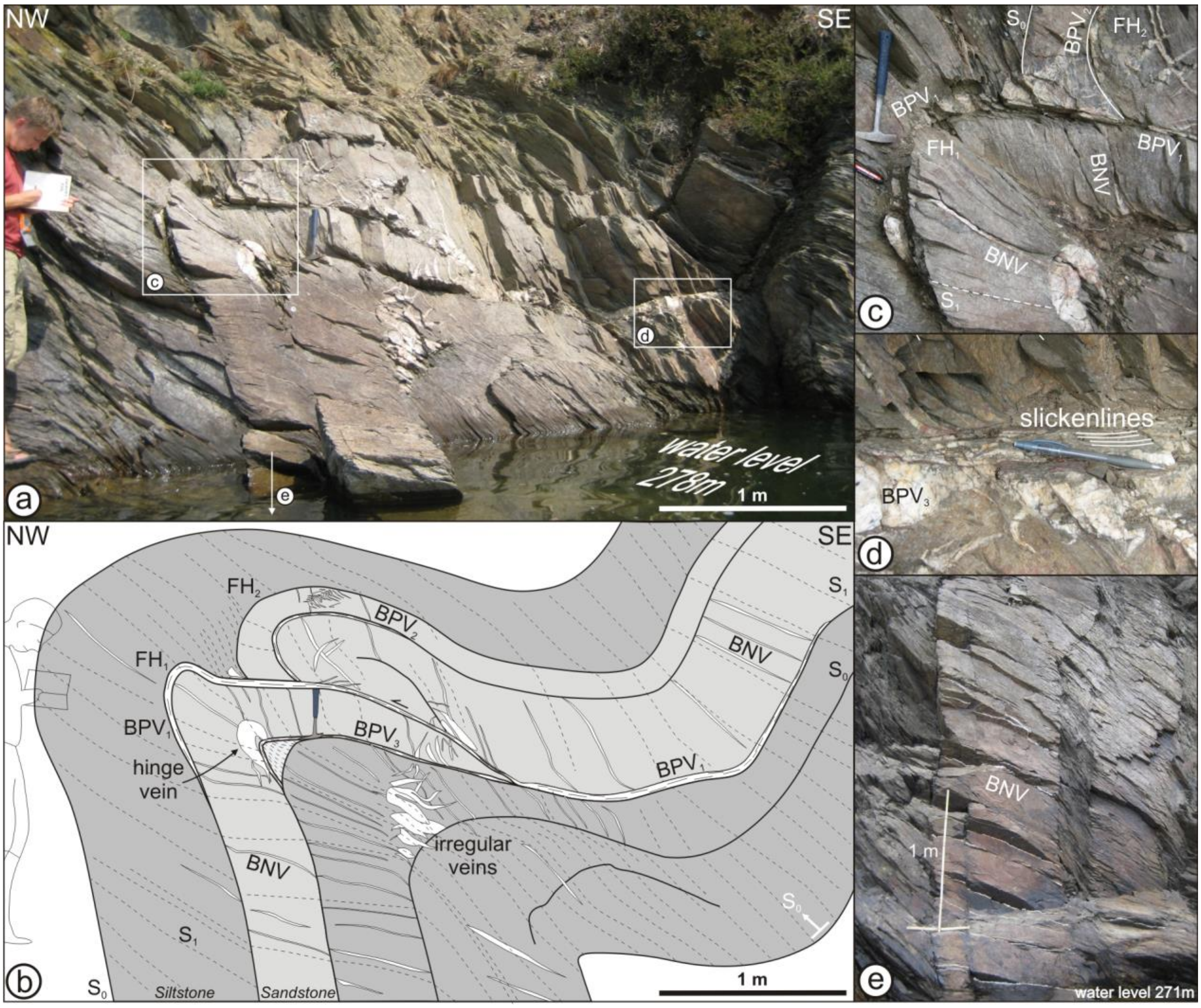

Figure 3.23: Eschaulerberg parasitic fold geometry (m148). **(a)** Photograph and **(b)** field drawing of the fold showing curved BNVs and folded BPVs, which are consistently present around the fold hinges and remain uniform in thickness around the fold. The fold has a regional NW-verging asymmetry and an axial planar cleavage (a and b modified after Van Noten *et al.* 2011). **(c)** BPVs at the outer side of the fold hinge (FH) and a hinge vein at the inner side of the anticlinal fold hinge (hammer~32 cm). **(d)** NW-SE-trending slickenlines on the upper vein wall of the BPV (pencil ~14 cm). **(e)** BNVs are consistently present in the overturned limb in a lower level.

3.3.4 Bedding normal veins

The three fold limbs observed in the parasitic Eschaulerberg fold are similar in orientation as the fold limbs observed in the whole Eschaulerberg section in such way that the orientation of the overturned SE-dipping and the normal NW-dipping limbs correspond to zone 15 and the normal SE-dipping limb corresponds to zone 14. Hence, the orientation of the bedding-normal veins, which are omnipresent in this parasitic fold, can be compared to the orientation of other BNVs observed in the different fold limbs of the Eschaulerberg section. This comparison can be used for determining consistency of vein generations in the whole Eschaulerberg section. In order to do so, firstly, the BNVs in the parasitic fold are described geometrically. Secondly, their orientation is compared in an orientation analysis with other BNVs in the different fold limbs of the Eschaulerberg section.

3.3.4.1 Geometric description

BNVs are present in the folded sandstone layers, as well as in the underlying siltstone layer (Figure 3.23a and b). The veins are uniform in thickness both in the sandstone and siltstone layers and they do not exceed a thickness of 1 cm. Macroscopically, veins consist of milky white quartz with an internal distribution of millimetre-thick host-rock inclusion lines. Veins are more closely spaced in the siltstone than in the sandstone. In the overturned SE-dipping sandstone layer and in the underlying siltstone layer, the veins are continuously present towards lower levels (see m148 - m150 in Figure 3.21; Figure 3.22c; Figure 3.23e). They are moreover oriented oblique to bedding (~70°) and have a curved shape in such way that the upper (structural) vein tip curves towards the anticlinal hinge FH_1 while the lower (structural) vein tip curves away from the hinge zone. Compared to perfectly perpendicular BNVs, they seem to have rotated clockwise. The BNVs in the normal SE-dipping limb have an opposite curved shape than those in the overturned fold limb (Figure 3.23e). Here, the upper (structural) vein tip of the veins curves towards the anticlinal hinge FH_2 whereas the lower tip curves towards the synclinal hinge having rotated anticlockwise. Both in the anticlinal and synclinal hinge, as well as in the NW-dipping limb, the veins are oriented at high angle to bedding and the refracted cleavage is oriented subparallel to the veins (Figure 3.23a and b). All the BNVs observed in this fold are restricted to the host rock and are defined as stratabound veins (see BOX I). Hence, a clear refraction of the veins at the incompetent-competent or competent-incompetent interface, such as was observed for non-stratabound veins in the Wildenhof section has not been observed.

Throughout the fold, the BNVs have a consistent thickness with a mean thickness of one centimetre. Sometimes hairline veins, comprising fibrous quartz crystals, occur between the centimetre-thick veins. Macroscopically, these centimetre-thick BNVs can be classified as composite veins as quartz laminae alternating with pelitic host-rock inclusion lines occur.

3.3.4.2 Orientation analysis

In the Eschaulerberg parasitic fold, bedding-normal veins thus occur at high angle to bedding. Only one vein generation is observed and is folded around the fold hinges. No additional cross-cutting vein generations have been observed. In their present orientation, the veins change in orientation from V_{SE}~079/41 in the overturned limb, V_{SE}~132/80 in the normal SE-dipping limb to V_{NW}~112/51 in the NW-dipping limb. In order to determine if this single bedding-normal vein generation represents a single veining event, an unfolding analysis has been performed on the veins. The strategy followed during unfolding is identical to the unfolding exercise in the Wildenhof case study (see method in Figure 3.9). Firstly, the effect of the plunge of the parasitic fold is removed and secondly, the fold limbs are restored to the horizontal. As result of this exercise (Figure 3.24), it is shown that the veins are nearly vertical in horizontal layers and that they have a similar NE-SW strike in the three different fold limbs. However, despite of their similar trend, the veins have opposite dip directions after unfolding. After unfolding, the veins in the gently SE-dipping fold limb dip towards the NW, while the veins in both the overturned SE-dipping and gently, NW-dipping layers dip towards the SE in their original orientation.

In order to try deducing a local chronology in quartz veining along the whole Eschaulerberg section, the orientation of the single vein generation in the three fold limbs of the parasitic fold is compared with the veins occurring in zone 14 and zone 15. The results of this comparison (see Figure 3.24) shows that the veins in the normal SE-dipping fold limb at zone 14 are similar in orientation as the veins in the same fold limb in the parasitic fold after unfolding, although the strike might slightly change from NNE-SSW to NE-SW respectively. Locally at m50, an outcrop representative of the overturned SE-dipping limb of zone 15, two other cross-cutting vein generations are observed. After unfolding (see Figure 3.24) the overall observed veins (V_{SE}) plot in a similar NE-SW orientation as the veins in the comparable fold limb in the parasitic fold. Moreover, they also dip towards the NW in their original orientation. The NE-SW generation cross-cuts an early E-W generation (circles in Figure 3.24), but is cross-cut by subsequent NW-SE oriented veins (diamonds inFigure 3.24). After unfolding, both steeply dipping vein generations dip to the north and the NE respectively. The cross-cutting generation, however, is absent in the parasitic fold and in other parts of the Eschaulerberg section. The veins in the steeply NW-dipping fold limbs, furthermore, have a NE-SW strike, and dip steeply towards the NW after unfolding. They are comparable to those in the NW-dipping fold limb in the parasitic fold.

To conclude, this comparison shows the existence of one consistent vein orientation along the whole Eschaulerberg section, that is cross-cut by a second and third vein generation locally. In its current orientation, the strike of this consistent, earliest vein generation is oriented parallel to the local fold hinge lines and turns NE-SW after unfolding.

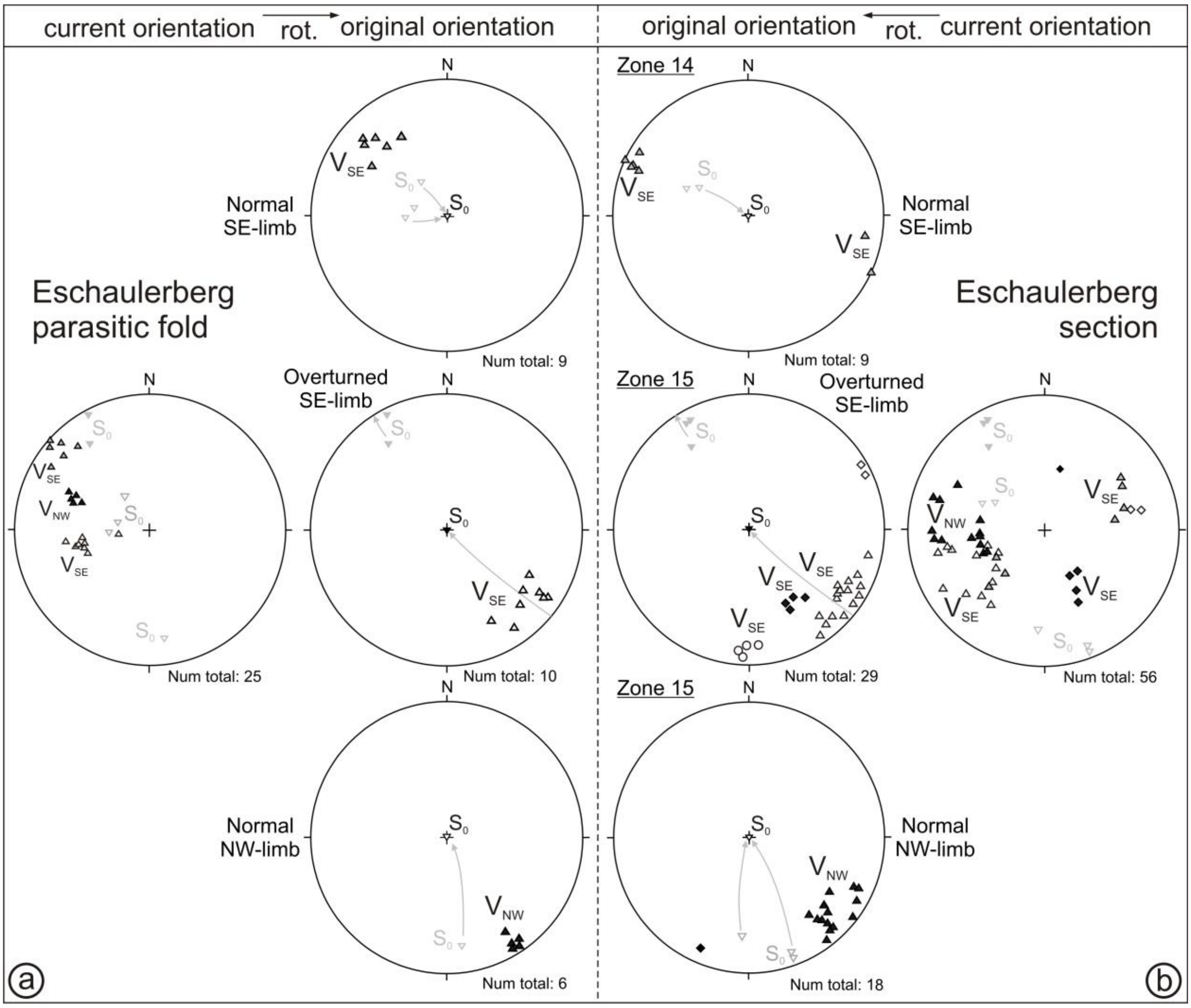

Figure 3.24: Lower-hemisphere, equal-area stereographic projection of BNVs in their current and unfolded (rotated) original orientation in the **(a)** Eschaulerberg parasitic fold, compared to the BNVs in the **(b)** fold limbs (zones 14 and 15) of the Eschaulerberg section. Grey arrows show the unfolding direction. V_{SE}: veins in a normal or overturned SE-dipping limb; V_{NW}: veins in a NW-dipping limb.

3.3.5 Bedding-parallel vein(s)

Bedding-parallel veins are observed numerously within the Eschaulerberg section and can be identified as interbedded veins as they always occur between two contrasting lithologies, namely siltstone and sandstone (*e.g.* m40, m50, m87 in Figure 3.21; Figure 3.22b). Sometimes slickenlines and slickenfibres are observed on the outer vein wall, marking bedding-parallel movements. Often these slickenlines are oriented at high angle to the local fold hinge line. A detailed orientation analysis of the slickenline and slickenfibre orientation has been performed on BPV_1 in the Eschaulerberg parasitic fold (Figure 3.25a-b). This BPV_1 is of particular interest because it occurs in the synclinal hinge and continues towards the anticlinal fold hinge (FH_1). It changes from a, locally 5 to 10 cm-thick, interbedded BPV below the thick, coarse-grained sandstone layer in the syncline to a 5 cm-thick interbedded vein above the thick sandstone layer in the core of the anticlinal fold hinge FH_1. Along its vein length, the upper vein wall has a flat morphology in the synclinal hinge, but is marked by several offshoots in the centre of the fold in which the vein is interbedded between the duplicated sandstones. The lower vein wall or the underside of the vein is characterised by an irregular boundary, with several small offshoots into the underlying siltstone sequence in the syncline, but remarkably, it has a flat morphology in the anticlinal hinge FH_1 at the contact with the underlying sandstone layer. Along its length, the upper vein wall of BPV_1 is also marked by several slickensides with slickenlines (see Figure 3.23d). Slickenlines (L_{sl}) and fibre steps have been measured and analysed in the three fold limbs (Figure 3.25a and b). In the NW-limb, slickenlines are NW-SE (L_{sl}~305/30). In the normal SE-dipping limb, slickenlines trend NNW-SSE (L_{sl}~160/25) and in the overturned limb slickenlines have a SW-plunging, nearly vertical orientation (L_{sl}~228/80). As illustrated on the stereographic projection (Figure 3.25b), the slickenlines are oriented at high angle to the local synclinal and anticlinal fold hinge lines of the parasitic fold. Remarkably, at all three positions the observed fibre steps are similar and are indicative of a top-to-the-NW bedding-parallel shear of the overlying layer. As previously mentioned, the BPV continues around both the anticlinal and synclinal hinge without changing in thickness, which strongly suggests a pre- to early folding origin of the BPV.

To determine this hypothesis, an unfolding exercise has been performed in which the slickenlines of the three fold limbs have been rotated from their current orientation (Figure 3.25b) in the Eschaulerberg parasitic fold into a consistent bedding plane (see (1) in Figure 3.25c).

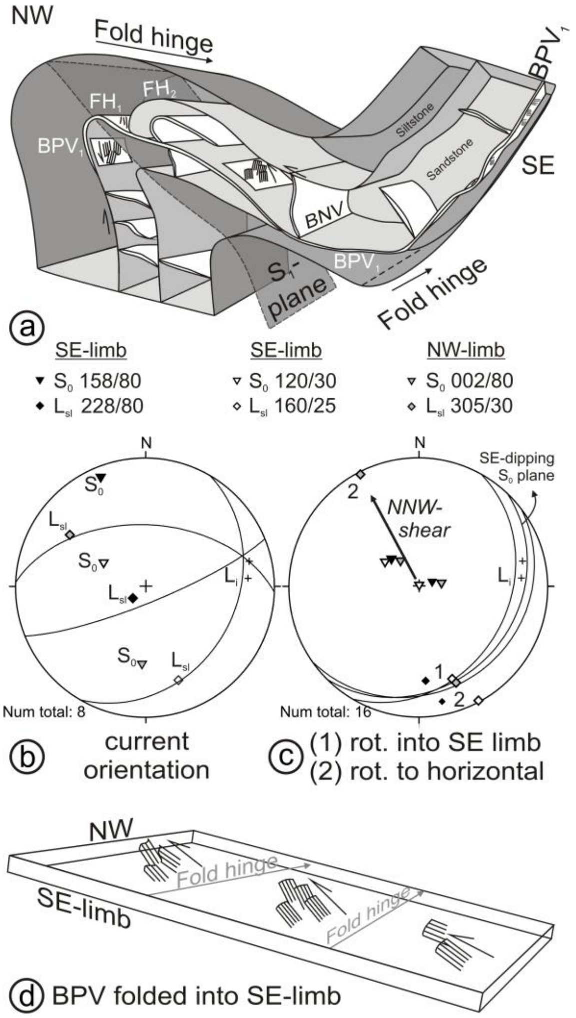

Figure 3.25: (a) 3D fold kinematics of the 'parasitic' fold structure at the Eschaulerberg section showing the consistency of a BPV around the fold hinge, the duplication of the sandstone layers between FH_1 and FH_2 and flexural-flow folding of the BNVs in the fold limbs. Length of the fold train is approximately 4m. **(b)** Orientation of slickenlines (L_{sl}) in their current orientation and **(c)** after unfolding of the whole BPV_1 into (1) a SE-dipping orientation and (2) the original horizontal orientation. **(d)** Slickenline orientation and fibre steps are consistent in orientation after unfolding and mark a NNW-directed shear.

If the slickenlines are similar in trend after unfolding, then the pre-folding hypothesis can be confirmed. For the ease of the exercise and also to avoid additional untilting of the fold hinge, it was chosen to keep the SE-dipping limb constant and to refold the overturned limb and the NW-dipping limb into the orientation of the SE limb. Unfolding has been performed around the anticlinal fold hinge for the overturned limb and around the synclinal hinge for the NW-limb.

The results show that the slickenline orientation and fibre steps are similar for the three different positions on the continuous SE-dipping BPV (Figure 3.25c). This suggests that thrusting and thus bedding-parallel slip occurred in a similar direction along the whole vein at the onset of folding, prior to overall buckling. If the BPV is further unfolded toward the horizontal (see (2) in Figure 3.25c), by untilting the fold hinge line and restoring the SE-dipping orientation into its original horizontal orientation (conform the mechanism in Figure 3.9), a NNW-directed shear can be deduced.

3.3.6 Kinematic interpretation

Based on the geometric description of bedding-normal and bedding-parallel veins with respect to the observed fold geometry, a kinematic evolutionary history can be reconstructed for the deformation features observed at the Eschaulerberg section. In order to constrain this evolutionary model, one has to assume that the buckle folds, for instance at m375-380, and the Eschaulerberg parasitic fold at m148 developed contemporaneously with the larger, second order folds in the area so that all the deformation features described in the parasitic fold can be dated relatively to the fold-and-cleavage development. This assumption is valid for the following reasons and is illustrated by the possible coaxial progressive deformation in Figure 3.26.

When a horizontal layer starts to shorten during the NW-directed tectonic transport related to the overall Variscan shortening, regionally materialised by cleavage, initially the layer will start to fold gently. In a multilayer sequence, in which a sandstone layer is for instance intrabedded in a thick siltstone sequence, the early developed NW-dipping limb can subsequently start to buckle. These secondary buckle folds will develop, possibly at an irregularity, because of the particular orientation of the NW-dipping limb in this incipient fold, oriented at high angle to the tectonic grain.

When shortening continues, the buckle folds can possibly evolve into a parasitic fold structure developed in the overall NW-dipping limb. If tectonic shortening, however, occurs within a multilayer sequence of several closely spaced sandstone layers, the sequence will be impeded by the presence of these competent layers during progressive shortening. Continuous shortening can eventually result in a lock up of the layers due to a lack of space resulting in small-scale harmonic buckle folds (*e.g.* m375-m380; Figure 3.22e).

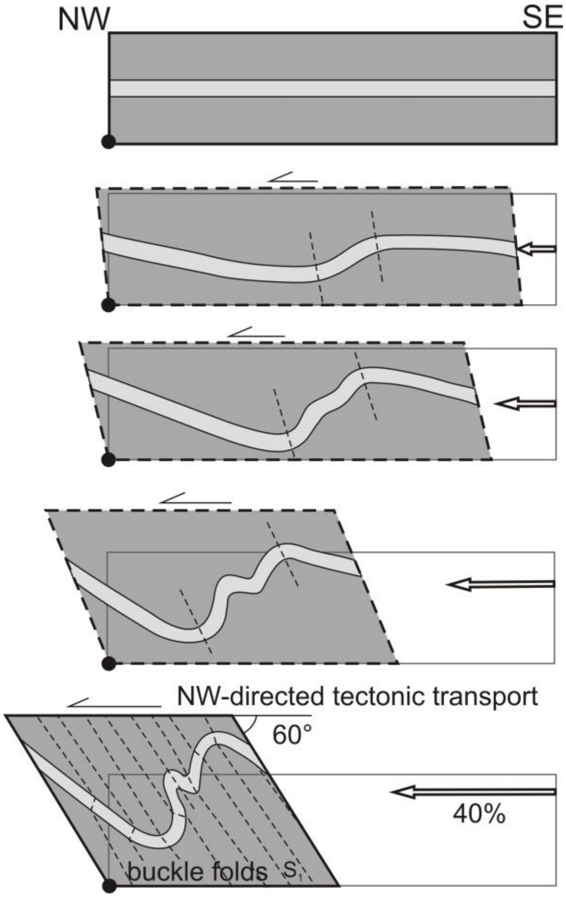

Figure 3.26: Kinematic model proposed for the formation of buckle folds in the NW-dipping limbs of the Eschaulerberg section during progressive fold-and-cleavage development. The intermediate stages may have been different but are meant to illustrate possible progressive steps in buckle fold development.

Along the Eschaulerberg section and in the parasitic fold, one consistent bedding-normal vein generation has been determined. It consists of both hairline veins and centimetre-thick, composite stratabound veins. On the one hand, the macroscopic fabric of the hairline veins shows a fibrous mineral infill reflecting a single opening and fracture infill. The composite veins, on the other hand, consisting of several quartz laminae alternating with host-rock inclusion seams, reflect a veining mechanism in which multiple fracturing and sealing phases are responsible for vein formation. The mineral infill is elaborated in Chapter 4, but from the macroscopic vein infill it can already be concluded that these veins are extension veins which opened in a horizontal bedding configuration prior to folding. It is concluded from the original NE-SW-directed strike of this consistent vein orientation prior to folding (Figure 3.24) that a NW-SE opening was responsible for vein formation along the Eschaulerberg section. Locally, this vein generation is cross-cut by two younger generations, which cannot be correlated to other veins elsewhere in the section. Owing to the limited occurrence of these cross-cutting veins, their implication on the regional development of quartz veins has been ignored, although they could reflect different opening directions after opening of the earliest vein generation. Regardless of the different cross-cutting relationships, it is concluded from the fact that all bedding-normal veins remain perpendicular to bedding in the fold limbs and in the fold hinges, that the BNVs clearly predate the regional fold-and-cleavage development.

In the parasitic fold, several bedding-parallel veins are folded continuously around both the synclinal and anticlinal fold hinge. The thick BPV_1 is of particular interest because of its continuity along the anticline-syncline fold train. Macroscopically, it consists of thick quartz laminae, intercalated irregularly with disrupted host-rock inclusion lines, illustrating a complex formation history of the vein by multiple opening and sealing phases. The different BPVs are continuously present around fold hinges. This observation is incompatible with the flexural-slip mechanism in which slip is absent in the fold hinges. Furthermore, the vein wall is characterised by slickenlines that are uniform in trend along the vein in the anticline-syncline fold train and that are oriented at high angle to the local fold hinge line. Fibre steps on the vein wall all represent a consistent NNW-directed shear. This shear is deduced by unfolding the fold limbs toward the horizontal into one continuous vein (Figure 3.25d). BPV_1 thus suggests that vein formation results from bedding-parallel thrusting related to small, low-angle thrust faults which are interpreted to reflect small ramps that duplicate sandstone layers into doubled sequences (Figure 3.23a and b). In the parasitic fold, this thrusting and duplication is complicated by the seemingly out-wedging sedimentary character of the overturned sandstone layer above which the folded anticlinal hinge FH_2 with incorporated bedding-parallel veins was developed. Nevertheless, BPV_1 represents bedding-parallel veining at the onset of folding during layer-parallel slip. The origin of the interbedded BPV_2, present between the two folded sandstone layers in FH_2, remains enigmatic because of a lack of structural indicators that can reveal its development. It could have been developed by bedding-normal uplift, such as described for the intrabedded BPVs in the Wildenhof section (Figure 3.18a), or it could reflect bedding-parallel thrusting, prior to the formation of BPV_1.

The BNVs have, furthermore, a specific geometry in which the upper vein tip curves towards the anticlinal hinge and the lower vein tip curves towards the synclinal hinge, similar to the refracted cleavage (Figure 3.25a). These observations strongly suggest that this curvature can be attributed to post-veining deformation related to continuous simple shear in the host rock during flexural-flow folding (Ramsay & Huber 1987). This is also visualised in the unfolding exercise (Figure 3.24): the results of unfolding show that the BNVs in the Eschaulerberg section, are not perfectly orthogonal to bedding after rotation of the beds to the horizontal. In their original orientation, the veins in the overturned SE- and normal NW-dipping limbs, dipping to the NW, have opposite dip directions compared to the veins in the unfolded normal SE-dipping limb, dipping to SE. This specific opposite subperpendicular attitude is also a consequence of flexural-flow folding.

Ramping may have been initiated at specific places, at which the multilayers contain an irregular sedimentary architecture, such as large scale gullies or point bars. They may subsequently have played a role at the initial stages of fold development in such way that they influenced the location of fold hinges during progressive horizontal shortening. This is clearly exemplified by the parasitic fold in which such a ramp is folded.

The latest structure observed in the Eschaulerberg section comprise high-angular faults which cross-cut bedding, folds and veins. They vary from faults with a strongly developed fault gouge to planar faults of which the displacement could not be deduced. The mostly upright to SE-dipping orientation of these faults indicate that they developed in a similar compressional regime as the overturned folds in the Eschaulerberg area and that they might have been reactivated afterwards. This reactivation might have occurred either during late-Variscan extensional tectonics or during post-Variscan faulting.

3.3.7 Synthesis

To conclude, based on the geometric observations and kinematic interpretations of the structures and veins studied in the Eschaulerberg section and in the parasitic fold, a preliminary evolutionary history can be proposed that outlines the evolution from veining events to subsequent deformation. **Bedding-normal veins** have been observed in the Eschaulerberg section. They reflect a regional veining event, caused by **NW-SE extension** of the layers, which were at that time in a horizontal position. It is concluded that the BNVs formed in an extensional stress field in which the NE-SW-alignment of the consistent vein generation corresponds to the $\sigma_1 - \sigma_2$ principal plane and the NW-SE opening direction of the veins to σ_3. The two local cross-cutting veins observed in the Eschaulerberg section are probably the reflection of a local change in stress field orientation that may have been developed because of the minor differences in magnitude between σ_2 and σ_3, allowing a short transient stress field in a remote (far-field) stress field.

Subsequently, **bedding-parallel veining** occurred after bedding-normal veining. Bedding-parallel vein formation in the Eschaulerberg section is attributed to small-scale **ramping** and associated bedding-parallel **thrusting** causing duplication of the competent layers at the onset of folding. It is deduced from slickenlines and fibre steps on the vein wall, that this bedding-parallel thrusting reflects local NNW-SSE-directed compression during vein emplacement. In this configuration, the maximum principal stress σ_1 may correspond to the tectonic compression representative of a compressional stress regime. The regional implications of bedding-parallel veins succeeding bedding-normal veins, which indicate a transition of regional stress field orientation, is further discussed in the general discussion of this chapter in section 3.5.

3.4 Case III: Hubertus Höhe - Schwammenauel section

3.4.1 Localisation

Although the Wildenhof case and the Eschaulerberg case already provide a useful geometric evolutionary model in which the successive development of different vein types, folds, cleavage and faults is studied, it was further chosen to investigate the Hubertus Höhe and Schwammenauel sections, not only to check consistency in veins, but also because of a peculiar outcrop situated in zone 21, of which no equivalent exists in the Rursee area. The deformation features observed in this peculiar outcrop will possibly contribute to the present tentative evolutionary geometric model proposed in the discussion of the previous case studies. SE of Hubertus Höhe, the shores at Schwammenauel, both north and south of the Schwammenauel dam, have been investigated. These different sections are further referred to as Schwammenauel N and Schwammenauel S respectively. The beds belong to the Upper Rurberg Unit (Hubertus Höhe; Schwammenauel N) and the Heimbach Unit (Schwammenauel S). Because of the regional NE-plunging fold attitude, outcrops in the Hubertus Höhe - Schwammenauel N section are situated at a higher structural and stratigraphic level than those observed at Schwammenauel S, Wildenhof and Eschaulerberg. This is also the main reason that fold limbs (indicated as different zones on the structural map, see Figure 3.1) do not correspond between Wildenhof, Eschaulerberg and Hubertus Höhe.

3.4.2 Transitional geometries between folds

3.4.2.1 Geometric description

The structural architecture of the outcrops along the NW-SE trending road section at Hubertus Höhe is very consistent and comprises NW-verging, overturned, hectometre-scale folds with close interlimb angles and angular fold hinges (see Figure 3.30). Stereographic analysis of bedding shows that the folds are highly cylindrical. Two separate clusters, representing limbs with a normal (S_0~113/41) and an overturned (S_0~143/69) structural polarity, can clearly be recognised (Figure 3.27a). These overturned folds, which are marked by an associated axial planar cleavage, are similar in style as the overturned folds in the Wildenhof section (Figure 3.30 and Table 3.3). Mean cleavage attitude (S_1~129/53; Figure 3.27b) is highly comparable with that at Wildenhof (S_1~126/55) and Eschaulerberg (S_1~133/47) reflecting the regional attitude of the main tectonic foliation.

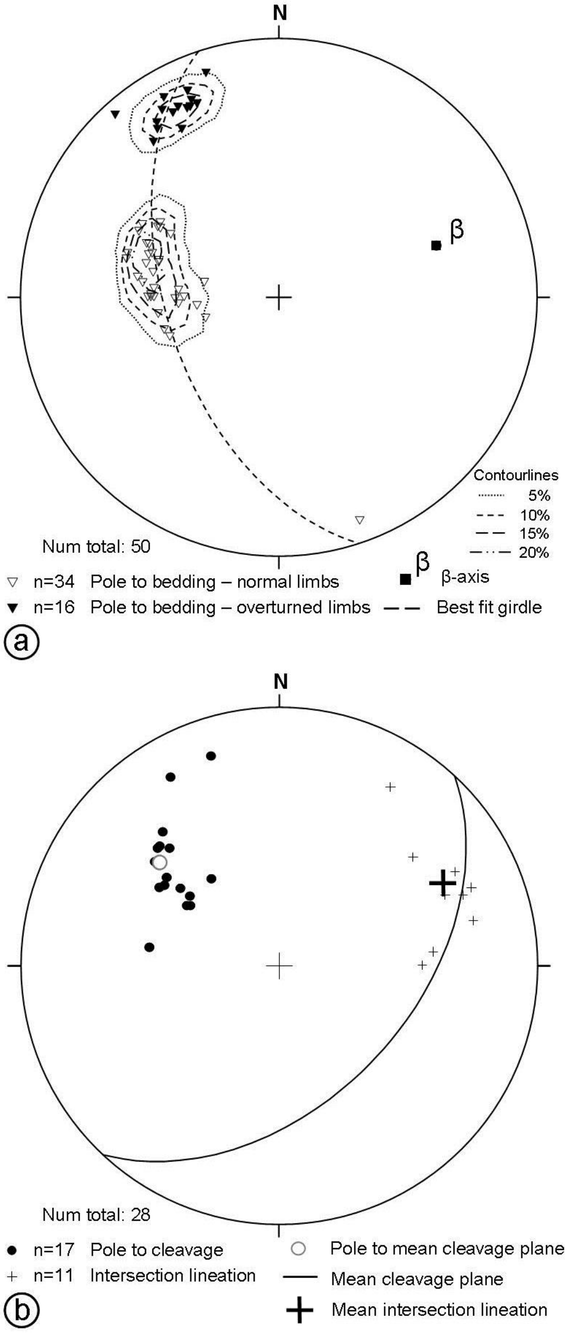

Figure 3.27: Lower-hemisphere, equal-area stereographic projection of measured structures at the Hubertus Höhe section. **(a)** poles to bedding; **(b)** bedding-cleavage intersection lineation and poles to cleavage.

East of this east-dipping limb, bedding changes from east-dipping to a NW dip direction (S_0~318/30; zone 20) giving rise to an open syncline between zones 19 and 20, in which cleavage refracts in the opposite direction in the two fold limbs. Cleavage, however, changes remarkably from SE-dipping (S_1~130/50; zone 19) to west-dipping (S_1~265/75; zone 20), a pattern found nowhere else in the study area.

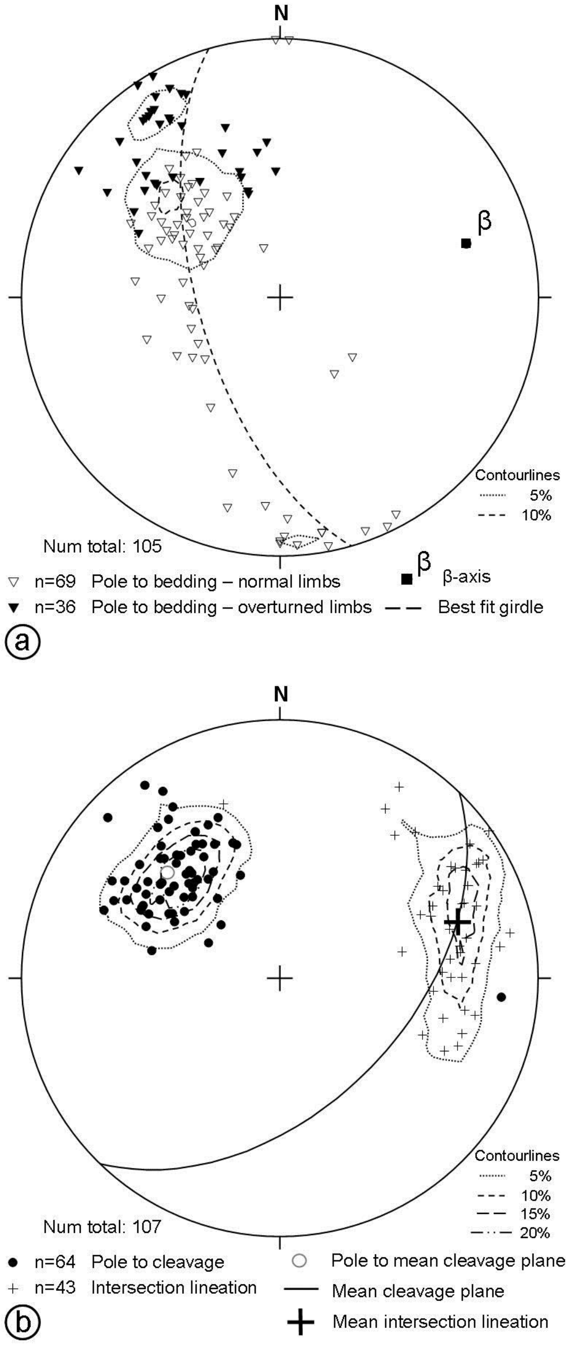

Figure 3.28: Lower-hemisphere, equal-area stereographic projection of measured structures at the Schwammenauel N and S sections. **(a)** Poles to bedding. **(b)** Bedding-cleavage intersection lineation and poles to cleavage.

Further to the SE, the NW-dipping fold limb of zone 20 transforms into the north-dipping fold limb of zone 21 (S_0~000/83) in which the outcrops comprise steep, almost upright layers younging to the north (Figure 3.29a, b and c). Internally in this north-dipping limb, the competent sandstone layers are often folded into metre-scale buckle folds (Figure 3.29b and c).

This peculiar bedding orientation is unique in the study area. Moreover, this attitude does not fit into the model of the regionally observed overturned fold style, in which both normal and overturned limbs usually dip to the SE. These upright, north-dipping layers are exposed for over 100 m to the SE, before bending into gently NE-dipping layers (064/32; zone 22; Figure 3.30). From this normal NE-dipping limb towards the Schwammenauel dam, two other hectometre-scale overturned folds are exposed (zones 23 - 25). These hectometre folds, with associated axial planar cleavage again reflect the regional fold pattern (Figure 3.28a). Analysis of the intersection lineation (L_i~077/32; Figure 3.28b) indicates that the overturned folds at Schwammenauel mainly plunge towards the ESE. The outcrops at Schwammenauel S are situated at a lower structural level than the Schwammenauel N section. They comprise a different fold architecture with one long overturned fold limb (S_0~139/71; zone 13) that turns into a SE-dipping normal limb at zone 12 (S_0~128/41) along a closed syncline, thereby forming the continuation of the Wildenhof-Schlitterley fold train (see Figure 3.1).

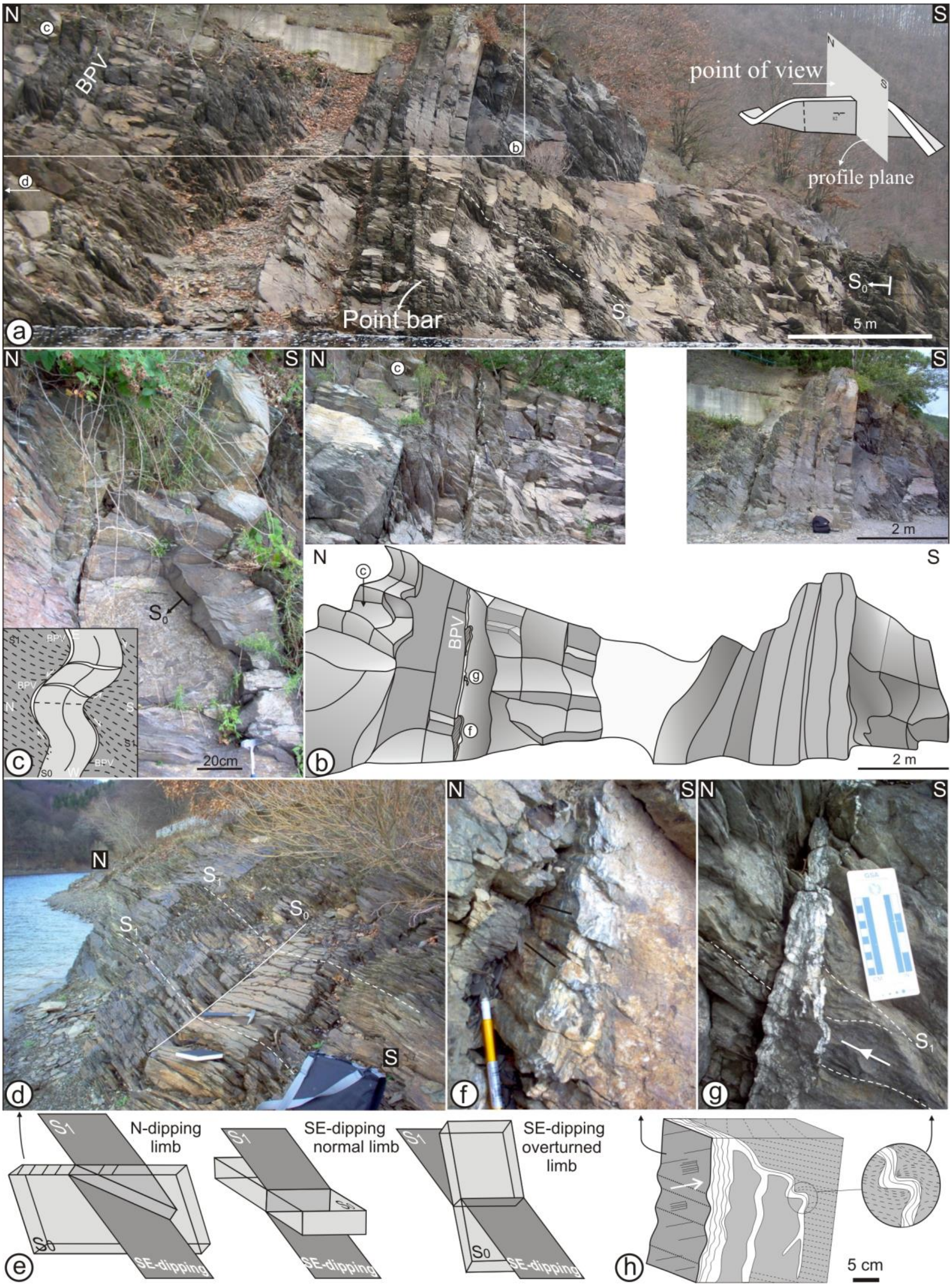

Figure 3.29: Geometric observations of the north-dipping layers in the box fold at the Schwammenauel section (zone 21; Figure 3.1). **(a)** Overview of N-dipping layers and **(b)** interpretation of the outcrop. **(c)** BPVs present in the hinge and cusps of the buckled layers. **(d)** 'Oblique' cleavage refraction in the N-dipping layers. **(e)** 'Oblique' cleavage refraction in the box fold compared to 'normal' cleavage refraction such as observed in the normal and overturned SE-dipping limbs. **(f)** Composite, buckled intrabedded BPV with slickenlines. **(g)** Buckled BPV showing intimate relationship of the vein with the underlying siltstone. **(h)** Illustrative sketch of the deformation features in the buckled BPV in (f) and (g).

3.4.2.2 Kinematic interpretation

Along the Hubertus Höhe - Schwammenauel N section a transition between two fold styles occurs (see Figure 3.30 for interpretation). The NW-verging overturned folds, observed at Hubertus Höhe and near the Schwammenauel dam, are interrupted by NW-dipping layers and by upright, north-dipping layers of zone 20 and zone 21 respectively. These observations give evidence of an upright box fold consisting of two steeply plunging fold hinges and a flat, steeply dipping hinge zone, *i.e.* the north-dipping layers. Only one of the two fold axes of this box fold is exposed (L_i~085/39) and corresponds to the layers bending from a north to a NE dip direction at the transition of zones 21 with 22. The other fold axis can be interpreted being parallel to the local bedding-cleavage intersection lineation (L_i~342/30) of the NW-dipping layers (zone 20). It is likely that this box fold has a local appearance and that it will die out towards the north. Surprisingly, however, cleavage in the north-dipping layers dips to the SE (S_1~118/51) and remains axial planar with respect to the regionally overturned folds, seemingly not influenced by the formation of this box fold. The local bedding-cleavage intersection lineation in the north-dipping layers (L_i~085/36) remains parallel to the intersection lineation in other outcrops along the Hubertus Höhe - Schwammenauel N section, but only changes locally at the two fold hinges of this box fold.

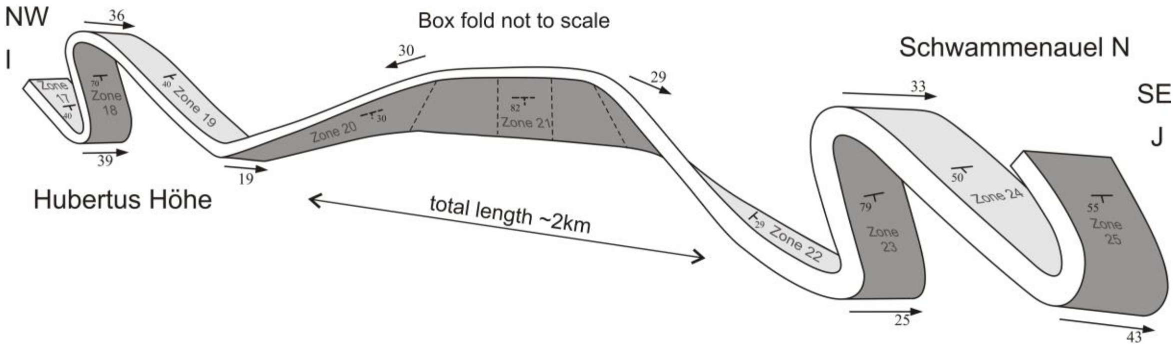

Figure 3.30: Schematic geometric representation of fold geometry between Hubertus Höhe and Schwammenauel S (Cross-section I - J in Figure 3.1). Note that figure is not to scale, but is meant to show how the structure of the box fold fits into the regional fold style. For true dimensions of the north-dipping layers and location see zone 21 in Figure 3.1. Total length of the cross-section is approximately 2 km. See text for discussion on the transition between the common overturned folds and the north-plunging box fold.

The origin of the north-dipping attitude of the beds, however, remains unclear and is further unravelled in this kinematic interpretation. Small-scale observations illustrated in Figure 3.29 and summarised below, suggest that tilting of the layers towards the north actually predates buckling of the competent beds in the box fold and that this tilting occurred at the onset of the pervasive fold-and-cleavage development. The evolutionary history of the particular deformation structures in the north-dipping layers and the formation of the box fold is illustrated in Figure 3.31 and is further explained below.

Firstly, cleavage does not refract as one would expect in the normal or overturned limbs, but rather refracts 'obliquely' through the competent layers in the north-dipping limb. In the normal SE-dipping limbs, cleavage usually refracts steeply through the competent beds, while in the overturned beds, cleavage refraction is mostly shallow dipping to the NW (Figure 3.29d and e). The orientation of the 'oblique' refraction through the north-dipping layers is, however, to the east. Generally, the onset of cleavage development is assumed to occur during layer-parallel shortening prior to folding (Treagus 1983). With ongoing shortening in a progressive deformation, siltstone and sandstone sequences will start to behave differently: the incompetent layers are able to continue shortening during compression due to their large compressibility until the present regional cleavage attitude is formed, whereas sandstones will behave differently and shortening will be accommodated by buckling. The embryonic cleavage development in the sandstone layers will at a certain moment rotate passively during buckling, because further shortening in the layers is prohibited, which eventually leads to cleavage refraction (Treagus 1983, Van Baelen & Sintubin 2008). If this concept of passive rotation of an embryonic cleavage is applied to the ‘oblique’ refraction observed in the north-dipping beds of the box fold, it is fair to assume that beds must already have an exceptional north-dipping attitude at the time of the embryonic cleavage development in the competent sandstone, presumably at the onset of folding.

Secondly, the competent layers, interbedded in siltstone sequences in the north-dipping limb, show a cuspate-lobate morphology (Figure 3.29c). Such layer metre-scale buckling in a single fold limb has been observed previously in the Eschaulerberg case study, although they were situated in a NW-dipping limb. The north-dipping attitude, however, is observed nowhere else which indicates that this is rather exceptional in the study area. The origin of this buckling can be unravelled by means of the orientation of the slaty cleavage in the surrounding siltstone. Theoretically, cleavage formation in the incompetent units is a result of the regional tectonic shortening. Cleavage planes will thus be oriented at high, nearly perpendicular angle to the tectonic grain and can be used as a useful indicator for the supposed shortening. In the north-dipping limb, the regional cleavage attitude is oriented at high angle to the buckled layers indicating a NW-SE-directed shortening (Table 3.3; Figure 3.29c and d). Hence, in order to create these small-scale buckle folds, the layers in the box fold must already have been tilted towards the north, otherwise they would not start to buckle.

Thirdly, a divergent cleavage fanning is present near these small-scale buckle folds (see inlet in Figure 3.29c). Cleavage is squeezed in the cusps, whereas in the lobate parts cleavage diverges towards the cusps, indicating that cleavage development was closely related to buckling of the layers. Moreover, the fold hinges of these buckled folds (FHL~085/45) plunge in the same direction as the local bedding-cleavage intersection lineation (L_i~085/36). These arguments suggest that buckling and cleavage development were contemporaneous (Figure 3.31) and might post-date an early tilting of the layers towards the north (Figure 3.31b).

The peculiar configuration of tilted beds could possibly have a sedimentary origin or it can develop during the incipient development of the regional folds. However, in order to give a conclusive answer to the relative timing of this early north-directed tilting of the layers with respect to all structural features, also the characteristics of the bedding-normal veins and bedding-parallel veins in the north-dipping layers have to be included. If the structural evolution of these veins corresponds to the observation and kinematic interpretations of the veins in other case studies, it will be possible to date tilting relatively to these features. Therefore the geometry of the veins is described first.

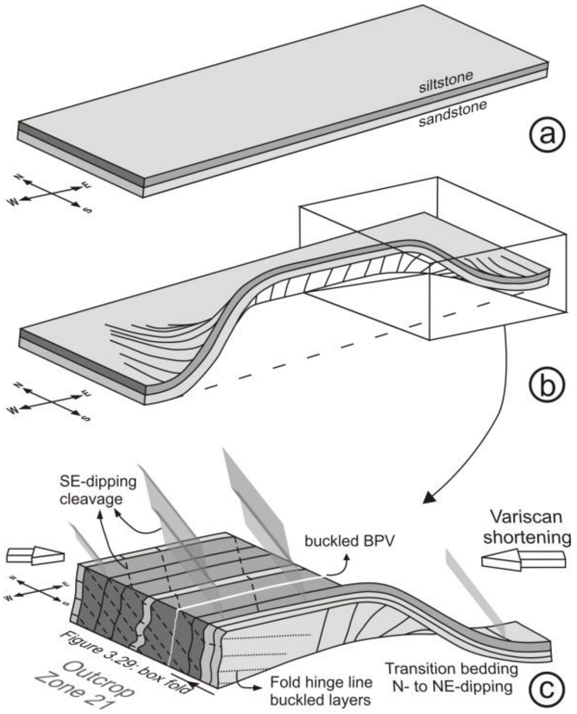

Figure 3.31: Evolutionary sketch of the north-dipping layers and their particular deformation structures in the Schwammenauel section. Figure not to scale. **(Stage a)** Initial stage after sedimentation. **(Stage b)** Incipient development of the box fold due to early tilting of the layers towards the north at the onset of fold development. **(Stage c)** Progressive SE-NW directed Variscan shortening, as represented by the regionally consistent SE-dipping slaty cleavage, causing both buckling of the beds in the box fold and ‘oblique’ cleavage refraction across the competent beds. The formation of bedding-parallel veins predates stage b as they are also buckled in stage c.

Table 3.3: Bedding and cleavage data of the investigated zones at Hubertus Höhe and north and south of the Schwammenauel section. See Figure 3.1 for localisation of the fold limbs (zone 12-13; 17-25). The number of measurements is given in brackets. Grey zones represent the data specific for an overturned limb. Entries in bold correspond to exceptional orientation data that contradict with the overall structural architecture in the Rursee area. - : not observed or suspicious data

Outcrop	**Bedding (S_0)**	**β - axis of bedding**	**Cleavage (S_1)**	**S_0/S_1 L_i (measured)**	**S_0/S_1 L_i (merged)**
Outcrops Hubertus Höhe: zone 17-19					
Zone ***17***	102/41 (14)	043/21	131/58 (10)	067/28 (6)	068/36 (26)
Zone ***18***	151/73 (16)	-	133/51 (12)	074/38 (9)	071/30 (28)
Zone ***19***	096/41 (20)	069/36	128/48 (16)	088/40 (7)	089/41 (36)
Zone ***17 - 19***	Best fit girdle:		Mean value:	Mean value:	Mean value:
Hubertus Höhe fold train	252/54 (50)	072/36	132/51 (38)	076/36 (22)	076/36 (86)
Outcrops Schwammenauel N: zone 21-25					
Zone ***20*** *NW-dipping*	**318/30** (2)	**317/30**	***265/75 !*** (1)	**342/30** (1)	347/27 (3)
Zone ***21*** *N-dipping*	**003/83** (10)	085/39	120/51 (8)	085/36 (6)	089/46 (18)
Zone ***22*** *NE-dipping*	064/32 (9)	077/31	128/58 (5)	082/30 (1)	060/31 (14)
Zone ***23***	128/64 (7)	-	126/44 (6)	036/21 (3)	-
Zone ***24***	123/47 (4)	113/47	116/58 (2)	039/30 (2)	128/51 (6)
Zone ***25***	160/48 (12)	-	136/42 (6)	096/25 (5)	078/15 (18)
Zone ***21 - 25***	Best fit girdle:		Mean value:	Mean value:	Mean value:
Schwammenauel N fold train	265/57 (44)	085/33	125/49 (28)	077/32 (18)	083/36 (66)
Outcrops Schwammenauel S: zone 12-13					
Zone ***12*** *- Schwam S*	128/41 (39)	069/37	133/48 (13)	062/23 (9)	051/08 (29)
Zone ***12 - 13*** *: transition*	344/85 (5)	-	145/45 (2)	069/20 (3)	-
Zone ***13***	139/71 (17)	080/27	145/61 (21)	076/24 (12)	069/23 (60)
Zone ***12 - 13***	Best fit girdle:		Mean value:	Mean value:	Mean value:
Schwammenauel S fold train	246/69 (61)	066/21	142/50 (36)	070/24 (25)	060/16 (89)

3.4.3 Bedding-normal veins

3.4.3.1 Geometric description

Along the Hubertus Höhe - Schwammenauel N and S sections, the numerous bedding-normal quartz veins are mostly stratabound to the competent sandstone beds. The veins vary in geometry and in thickness. Lensoid, centimetre veins (Figure 3.32a), composite and slightly buckled veins (Figure 3.32b and c) and hairline veins with millimetre apertures (Figure 3.32d) have been observed. The composite veins consist of several thin veins which initially grew separately but at the end formed one composite vein (see composite veins in Chapter 4 for explanation). Non-stratabound veins refract at the incompetent-competent layer boundary similar as cleavage, representing post-veining flexural-flow deformation such as interpreted in the Wildenhof case study (Figure 3.32e). The majority of veins are orientated at low angle to the local fold hinge line. However, in the overturned fold limb at Hubertus Höhe (zone 18) a cross-cutting vein generation is oriented at high angle to the local fold hinge and intersection lineation (Figure 3.32f and g). Observations on the bedding plane show that this vein generation has an en-echelon geometry, indicative of shear perpendicular to bedding. The classical interpretation of en-echelon arrays in simple shear parallel to the vein-array in the direction opposite to which the vein tips point (Bons 2000). They, moreover, usually form in brittle-ductile shear zone, in which the host rock is deformed in such way that the en-echelon fractures open first and subsequently crystallise. By continuous shear, en-echelon veins eventually can develop sigmoidal patterns (Ramsay & Huber 1987). The sigmoidal pattern in this en-echelon vein array (Figure 3.32g and i) is, however, related to the linkage of several en-echelon, anastomosing veins during numerous phases of vein growth, rather than related to continuous shear. Macroscopically, the oblique opening of the veins is exemplified by fibres which are oriented oblique to the vein wall (Figure 3.32h) and are curved in a direction that is in agreement with the dextral shear expected from the geometry of the en-echelon arrays. The inlet in Figure 3.32i shows a possible vein growth mechanism. Besides cross-cutting the vein generation at low angle to the local fold hinge line, the observed dextral shear during en-echelon vein formation seems not to have a regional implication because both sinistral and dextral vein arrays have been observed in the overturned fold limb.

Similar vein arrays with slightly buckled geometries have been observed in the north-dipping hinge zone of the box fold (Figure 3.32j). This vein generation is the earliest generation observed in the box fold (1st gen) and is oriented at high angle to the local intersection lineation and to the fold hinge lines of buckle folds. Observations on the bedding plane reveal that these veins can extend in length up to a couple of meter.

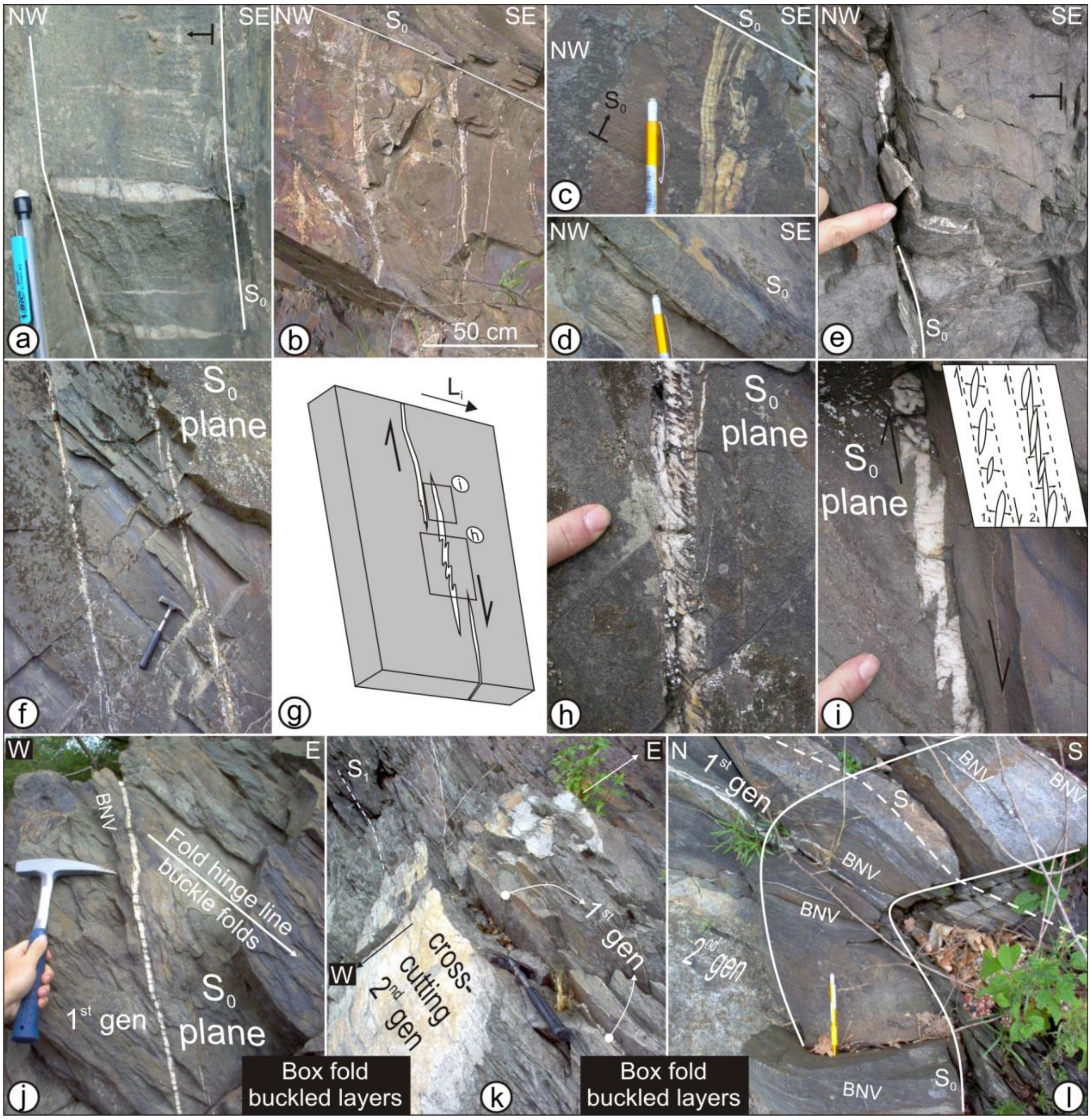

Figure 3.32: Bedding-normal vein characteristics of the Hubertus Höhe - Schwammenauel N & S section. **(a)** Lensoid, **(b-c)** composite and **(d)** hairline veins. **(e)** BNV refracting at competent-incompetent interface. **(f-g)** Photograph and sketch of en-echelon BNVs oriented at high angle to local fold hinge (zone 18). **(h)** Curved fibrous infill obliquely to the vein wall. **(i)** Detail of the en-echelon array. The inlet shows a possible formation model based on vein geometry. **(j)** BNV (1st gen) visible on the bedding-plane of buckle folds (box fold; zone 21). **(k)** 2nd vein generation cross-cutting the early 1st generation. **(l)** BNV (1st gen) continuous around the buckle fold (box fold; zone 21). Hammer ~32 cm, pencil ~14 cm and fingernail ~1.3 cm for scale.

In the small-scale buckle folds, this first generation comprises thin stratabound bedding-normal veins (1st gen in Figure 3.32k) which are continuous in the hinges along their height and refract at the competent-incompetent interface (Figure 3.32l). In this configuration they resemble cleavage refraction in the buckle folds. Non-stratabound veins are sometimes displaced at the competent-incompetent or competent-competent interface in such a direction in agreement with flexural-slip folding. Curved veins owing to flexural-flow folding have not been observed. This early generation is cross-cut by millimetre-thick stratabound veins (2nd gen in Figure 3.32k). However, only a few veins corresponding to this second generation are locally observed.

3.4.3.2 Orientation analysis

Different fold styles characterise the Hubertus Höhe - Schwammenauel section. It can be concluded from the geometry of the bedding-normal veins studied that vein formation occurred prior to regional fold-and-cleavage development. In order to compare vein orientation between the different fold limbs properly, each type of fold limb is rotated to the horizontal, conform to the method illustrated in Figure 3.9. In the unfolding exercise, the normal and overturned limbs of the Hubertus Höhe and Schwammenauel section are unfolded separately (Figure 3.33a-d). Because of its unusual bedding orientation, also the box fold is unfolded separately.

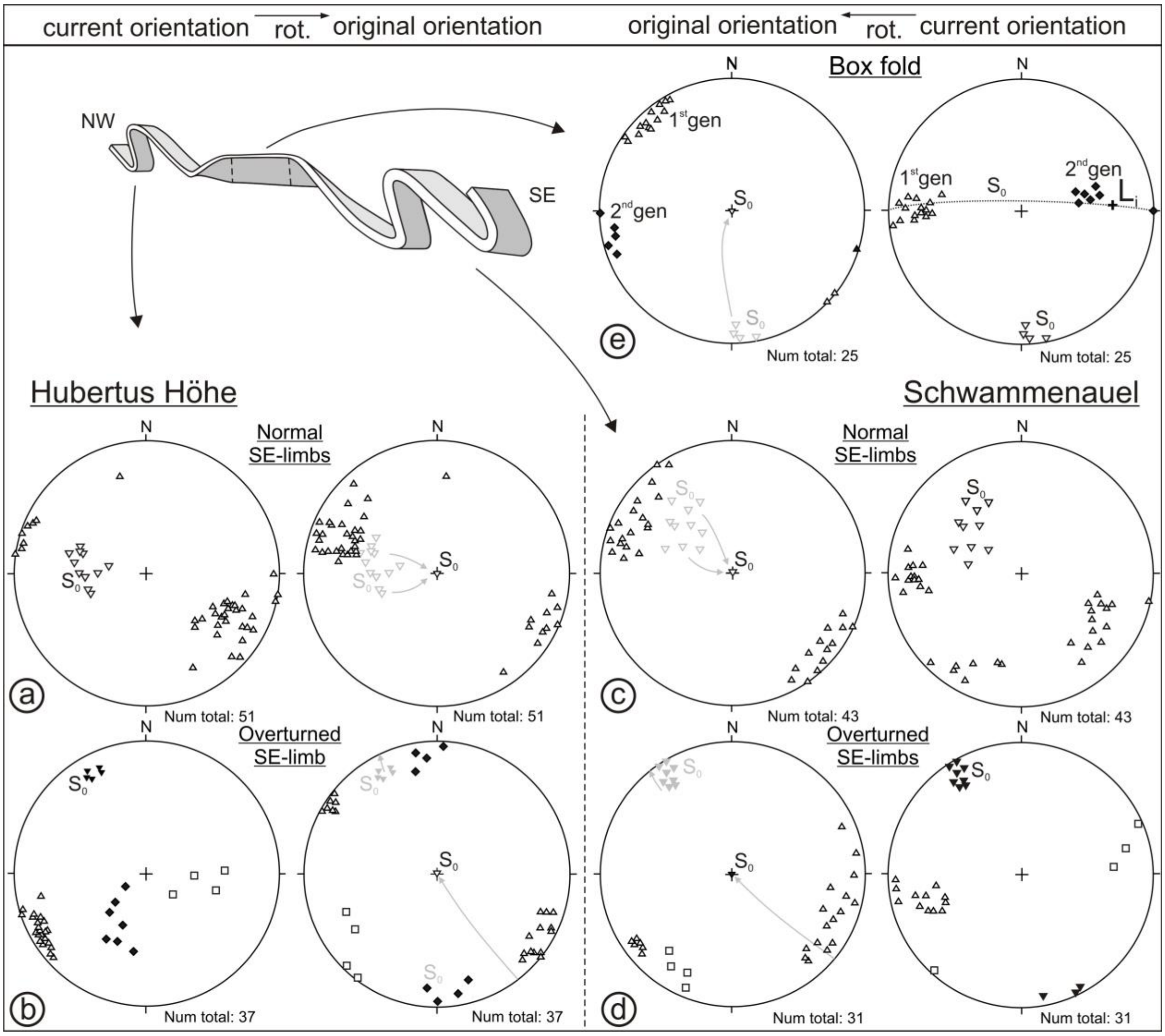

Figure 3.33: Lower-hemisphere, equal-area stereographic projection of BNVs in their current and unfolded (rotated) original orientation at **(a-b)** Hubertus Höhe, **(c-d)** Schwammenauel and **(e)** in the box fold at Schwammenauel N. Diamonds (en-echelon vein) and squares represent cross-cutting generations. Grey arrows show the unfolding direction.

The results of this exercise show that the veins (triangles in Figure 3.33) oriented at low angle to local intersection lineation in both normal and overturned fold limbs of the Hubertus Höhe section, have a consistent NE-SW orientation in their original configuration prior to folding. In their original orientation the veins display a large variation in dip ranging between NW- and SE-dipping. This variation may be an effect of the large plunge variation of the intersection lineation (see Figure 3.27b).

The cross-cutting en-echelon veins (diamonds in Figure 3.33b), oriented at high angle to the local intersection lineation in the overturned fold limb of the Hubertus Höhe section, have an E-W orientation after rotation and are nearly vertical. The rotation exercise further reveals the presence of a third generation in the Hubertus Höhe section although a cross-cutting relationship with another vein generation has not been observed in the field. This third generation (squares in Figure 3.33b) has an NW-SE- orientation after rotation, which corresponds to similar veins in the unfolded overturned layers of the Schwammenauel section. Similar as in the Hubertus Höhe section, however, a cross-cutting relationship has not been observed.

It can be concluded from the unfolding exercise that one consistent vein generation is present in both the Hubertus Höhe and Schwammenauel sections. This consistent generation has an original NE-SW alignment and opened in a NW-SE direction (Figure 3.33). The steeply NW-directed dip of the original veins in the unfolded overturned folds results from flexural-flow folding. The effect of flexural-flow folding is absent in the normal SE-dipping limbs.

Finally, also the north-dipping layers of the box fold are unfolded. This rotation exercise shows that the earliest vein generation (1st gen in Figure 3.32j and k and in Figure 3.33e), which is currently oriented at high angle to the intersection lineation (L_i), was originally NE-SW and becomes nearly vertical after rotation. The subsequent cross-cutting generation (2nd gen in Figure 3.33e) has a nearly north-south original orientation and dips steeply to the north.

If the veins in the different fold limbs at Hubertus Höhe and Schwammenauel section are compared, it can be concluded that one consistent vein generation, with an original NE-SW alignment, remains consistent along the whole Hubertus Höhe - Schwammenauel section. This consistent generation is cross-cut locally by en-echelon vein arrays representing a, possibly local, shear-related deformation. Furthermore, it can be argued that the 2nd vein generation, observed in the box fold, and a third unknown generation observed in the overturned fold limbs might have a local origin as they cannot be correlated to the consistent vein generation in the whole section, or to the en-echelon vein arrays.

3.4.4 Bedding-parallel veins

3.4.4.1 Geometric description

In the Hubertus Höhe, Schwammenauel N and S outcrops many bedding-parallel quartz veins are exposed and are divided in two different groups, based on their macroscopic geometry. A first group comprises thin, millimetre-size (< 1 cm), single laminated BPVs (Figure 3.34a, b and c). They occur interbedded between beds of contrasting lithology or interbedded between two competent beds (Figure 3.34a). Their upper vein wall is always marked by slickenlines and clear fibre steps, of which shear movement and shear direction can be deduced. Veins extend for several tens of metres and aspect ratios are usually very high (Figure 3.34d). In outcrops in which the bedding planes have an irregular pattern owing to the sedimentary architecture, such as in small-scale gullies, these thin BPVs are usually limited in length.

A second group of BPVs is more common and comprises thick (up to 10 cm) composite, laminated veins which are continuous for several tens of metres. The veins are mostly interbedded at the incompetent-competent interface (Figure 3.34e), although intrabedded veins in siltstone sequences also have been observed (Figure 3.34f). When a BPV is interbedded between a sandstone and siltstone, the upper vein wall has a flat morphology, whereas the lower vein wall is intimately related to the underlying siltstone. Thickness of such a BPV varies considerably along its length. Composite veins interbedded between two competent units and intrabedded veins, however, have a consistent thickness along their vein length.

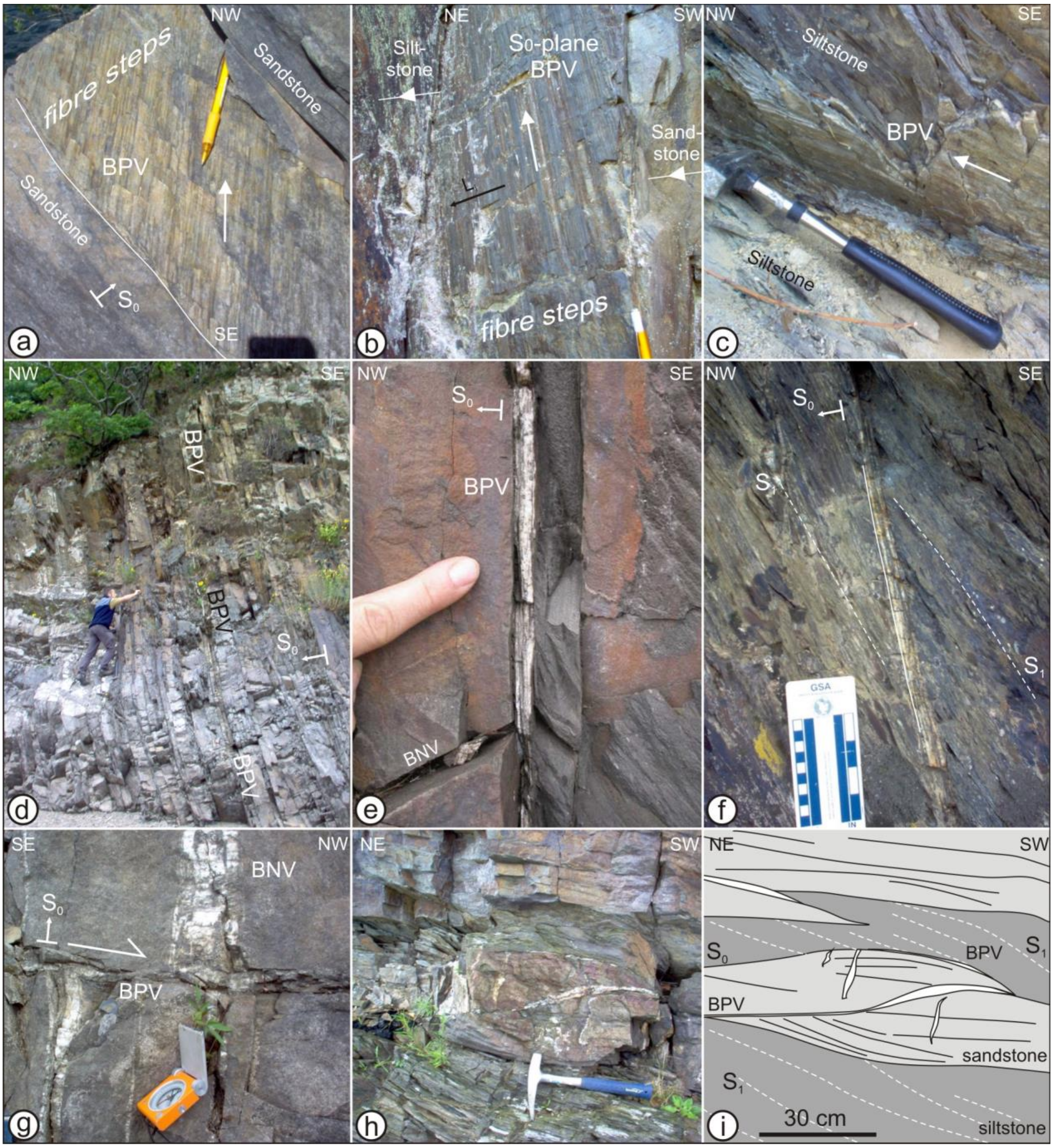

Figure 3.34: Bedding-parallel quartz vein characteristics at the Hubertus Höhe - Schwammenauel section. Fingernail ~1.3 cm, pencil ~14 cm, hammer ~32 cm, compass ~8 cm and GSA cm-scale bar for scale. **(a)** Fibre steps on a thin interbedded flexural-slip BPV with NW-SE-trending slickenlines indicative of NW-directed thrusting. **(b)** Thin interbedded flexural-slip BPV (between silt- and sandstone) on an overturned fold limb. Fibre steps show the sense of displacement (zone 13). **(c)** Interbedded BPV in a normal limb showing NW-directed thrusting (zone 17). **(d)** Interbedded BPV continuous for over 10 m (supervisor for scale; zone 13). **(e)** Interbedded composite BPV (zone 18). **(f)** Composite intrabedded BPV in a siltstone sequence (zone 18). **(g)** Composite BPV cross-cutting and off-setting a non-stratabound BNV. The displacement of the BNV is at about ~6 times the thickness of the vein (zone 12). **(h)** Photograph and **(i)** illustration of a small-scale thrust accompanied by a BPV cross-cutting a coarse-grained sandstone.

Composite BPVs, consisting of several quartz laminae intercalated with macroscopic host-rock inclusion seams, are observed to cross-cut and offset bedding-normal veins, indicating that both types of veining are separate events (Figure 3.34g and h). The vein tips of these composite BPVs are barely exposed. If they are observed, the vein tips occur in small-scale thrusts related to small-scale ramping along which a sandstone sequence is duplicated (Figure 3.34h and i). The BPVs situated in these ramps, cross-cut bedding along low-angle faults. In the example of Figure 3.34i, the vein tip starts at the end of the small-scale thrust and continues towards the NE below the competent sandstone. The profile plane is oriented parallel to the NE-SW strike of the vein, so a thrust direction cannot be observed. However, the displacement of non-stratabound bedding-normal veins (Figure 3.34g) might suggest that thrusting is oriented to the NW. Thrusting is moreover exemplified by slickenlines and slickenfibres that are present on the individual quartz laminae within the composite veins. Slickenlines are uniform in trend on individual quartz laminae but slightly differ in orientation from lamina to lamina. Fibre steps on the slickensides are unfortunately often completely polished so that a shear or thrust direction cannot be determined.

The north-plunging box fold, in which buckled layers are present owing to the abnormal orientation of the layers at the time of cleavage development, contains several bedding-parallel quartz veins, intrabedded between siltstone sequences and interbedded below and above sandstone beds. The BPVs present at the competent-incompetent interface in this box fold are characterised by a buckled nature and an intimate relationship (irregular boundary) with the underlying pelites (Figure 3.29g and h). This relationship is exemplified by small quartz offshoots, branching off from the buckled composite bedding-parallel vein into the underlying pelites (Figure 3.29g and h). Cleavage abuts against the composite vein and seems to be squeezed into the cusps of the curved branch of the bedding-parallel vein (see detailed sketch in Figure 3.29h). It has furthermore been observed that BPVs are present in the cusps as well as in the lobate parts of the small-scale buckle folds developed in the sandstone layers of the box fold (see inlet in Figure 3.29c).

3.4.4.2 Slickenline analysis & interpretation

It has been described in the geometric analysis that both thin and composite thick BPVs are marked by slickenlines, and that sometimes a shear sense could be distinguished from the orientation of the fibre steps. The thin, single laminated BPVs are also present at the interface of a sandstone with an underlying siltstone sequence. According to Tanner (1989, 1990), this specific configuration is the most favoured site for flexural slip and for generating flexural-slip bedding-parallel veins. Theoretically, according to the flexural-slip mechanism, displacement along the bedding planes should be exemplified by slickenlines that are nearly orthogonal to the local fold axis. Shear sense indicators such as fibre steps or cross-cut and displaced bedding-normal veins with an opposite sense of displacement at both sides of the fold, are clear indicators of a flexural-slip origin of veins (Tanner 1989).

In order to check this hypothesis, an orientation analysis of all slickenlines present on the BPVs in the Hubertus Höhe and Schwammenauel N and S outcrops has been performed. The results of this analysis (Figure 3.35) show that slickenline orientation in both normal and overturned fold limbs of the characteristic overturned folds are all oriented at high angle to the local bedding-cleavage intersection lineation and are thus indirectly also nearly orthogonal to the local fold hinge line. In these characteristic overturned folds the slickenlines plot in two different regions, corresponding to the two mean bedding planes of the fold limbs (S_0~139/71 and S_0~128/41 for overturned and normal bedding respectively; Figure 3.35). Through the slickenlines a best fit girdle (263/75) can be constructed of which the pole, the so-called π-axis (Tanner 1989) (here π~083/15) plots in the same region as the mean local intersection lineation (L_i~065/30). This orthogonal attitude of slickenlines with respect to the local intersection lineation has also been demonstrated on thin BPVs in the Wildenhof section (see Figure 3.14), but a clear shear sense is often lacking.

Furthermore, considering the shear sense deduced from the fibre steps in the overturned fold limbs, the fibre steps, often visible at the upper side of the overturned thin BPVs (Figure 3.34b), demonstrate a top-to-the-NW shear sense, characteristic of the upper ‘hangingwall’ layers thrusting on top of the lower ‘footwall’ layers. Fibre steps on the upper vein wall of thin BPVs in the normal, SE-dipping layers indicate a mean shear sense to the NW, indicative of a relative shear sense in which the ‘hangingwall’ layers thrust on top of the underlying ‘footwall’ layers towards the NW. Also, these thin BPVs have never been observed in the hinge zones of the overturned fold, which corroborates the absence of flexural-slip veins in hinge zones (cf. Fowler 1996, Tanner 1989).

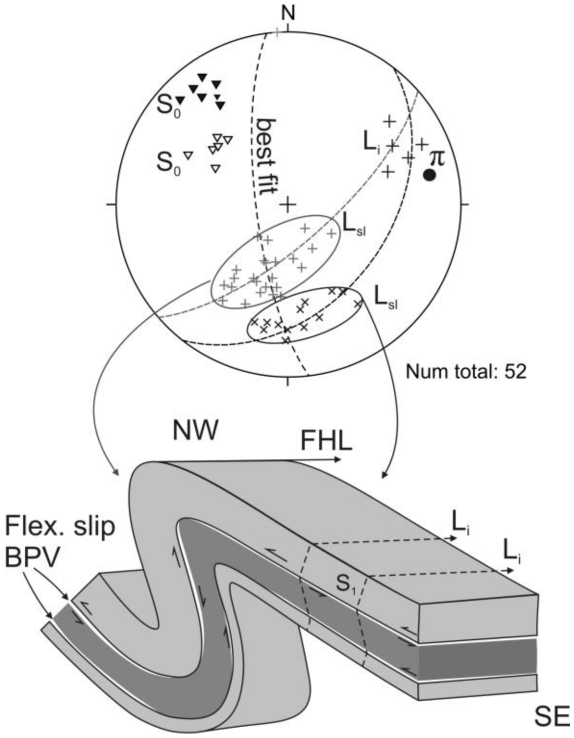

Figure 3.35: Flexural-slip analysis of slickenline orientation on thin bedding-parallel veins of Hubertus Höhe and Schwammenauel N and S outcrops. Lower-hemisphere, equal-area stereographic projection of slickenlines in the normal SE-dipping and overturned SE-dipping fold limbs of the characteristic overturned folds. Slickenlines are oriented nearly orthogonal to the local fold hinge line. The computed π-axis represents the pole of the best fit girdle through the slickenline orientation and is parallel to the intersection lineation.

Contrary to these flexural-slip veins, BPVs continuously present around fold hinges have been observed in the hinge zones of the box fold at Schwammenauel N. In the north-dipping layers, a buckled BPV occurs (Figure 3.29f and g) that is marked by slickenlines that are uniform in trend on individual quartz laminae but slightly differ in orientation from lamina to lamina (Figure 3.29f). Remarkably, although slickenlines observed on several BPVs in the study area are mostly oriented at high angle to the local bedding-cleavage intersection lineation and to the local fold hinge line, the slickenlines measured on the BPV of the north-dipping layers are exceptional because they trend more or less parallel to the local intersection lineation (Figure 3.36a and d). Using fibre steps on the slickensides as a macroscopic shear sense indicator, a westwards directed shear sense is deduced (Figure 3.36a). The above described composite BPV is continuous and can be traced along its vein length without changing in thickness around the fold hinge of the box fold towards the normal, east-dipping limb of zone 22 (Figure 3.36b). The slickenlines present on the same BPV in the normal fold limb are, however, oriented differently and trend to the NNW (Figure 3.36c and d). Constructing a best fit girdle through the slickenlines of both fold limbs on the stereographic projection, gives a π-axis that has a large angle (86°) to the local east-plunging fold hinge line (Figure 3.36d). This analysis indicates that the formation of this composite BPV is incompatible with the flexural-slip mechanism as the π-axis should be oriented parallel to the local fold hinge.

In order to determine the original direction of thrusting, the BPV in the box fold has been rotated to the horizontal. During this exercise, it was precisely observed if during unfolding there would be a specific moment in which the slickenlines at both sides of the fold would overlap. Such a specific orientation of fold limbs could possibly indicate thrusting of the layers that were already slightly folded. Unfortunately, this specific orientation does not exist. Slickenlines of both fold limbs remain at high angle (60°) to each other after unfolding (Figure 3.36e). This indicates that bedding-parallel slip must have occurred at the onset of folding. Moreover, bedding-parallel slip can be attributed to layer-parallel thrusting with variability in shear direction. This is exemplified both on a local scale, by the variability in slip direction on a single composite BPV, in which slickenlines are oriented differently from lamina to lamina (Figure 3.36a) reflecting different stages of fracturation, as well as on a larger decametre scale as demonstrated by the large (60°) slip variation, irrespective of the formation of the box fold, on a single vein that extends for several tens of metres. In some examples the displacement of BNVs has been observed. The displacement of the BVNs is at about ~6 times the thickness of the BPV (Figure 3.34g) and indicates a considerable strain rate during bedding-parallel thrusting.

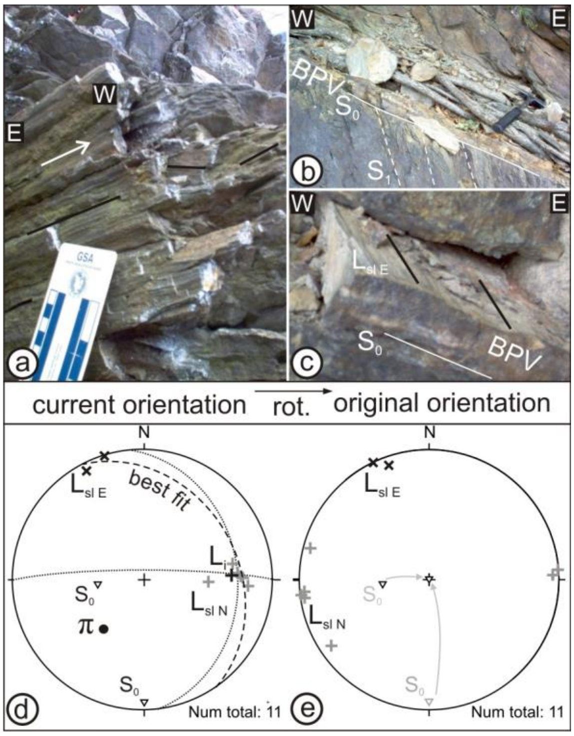

Figure 3.36: Slickenline orientation analysis of slickenlines on the composite BPV continuously present around the fold hinge of the box fold (zone 21-22). **(a)** Composite, intrabedded BPV with different orientations of slickenlines on different quartz laminae (north-dipping hinge). **(b)** Similar BPV and **(c)** slickenlines in the east-dipping fold limb. **(d)** Slickenline orientations in their current orientation and **(e)** in their original orientation after rotation of the limbs towards the horizontal. High angle (60°) between slickenlines remains present after rotation.

3.4.5 Discussion & synthesis

From the various structures observed at the Hubertus Höhe - Schwammenauel section, a relative deformation history can be constructed in which, starting from burial to the main orogenic deformation, bedding-normal quartz veins, bedding-parallel quartz veins, box fold, folds and cleavage are properly placed.

The first deformation structures that are observed are various bedding-normal quartz veins. An unfolding exercise reveals that different, whether or not cross-cutting, vein generations developed in a configuration in which the layers were still in a (sub)horizontal position, as exemplified by veins being oriented at high angle to bedding. Although the veins are various in shape ranging from hairline-thick veins, lensoid fibrous veins to composite, multifractured veins, they all can be considered as extension veins in which opening occurred perpendicular to the vein wall. Only locally based on curved fibres, an oblique opening has been determined in en-echelon vein arrays, related to bedding-normal shear. Extension veins are defined to be particularly useful to determine the orientation of the (regional) stress state. In this configuration, extension veins are aligned in the σ_1 - σ_2 plane and form perpendicular to the minimum principal stress σ_3. If this theory is applied to the veins in the Hubertus Höhe - Schwammenauel section, a specific **NW-SE extension** can be estimated, as exemplified by the overall consistent early vein generation (Figure 3.33). In this stress state during extension, σ_1 corresponds to the vertical load of the overburden while σ_2 is horizontal and oriented NE-SW. The shear-related (cross-cutting) generation might indicate that the stress field rotated subsequently into an E-W orientation with N-S extension. However, because of the fact that this cross-cutting vein generation is locally distributed, it is unclear whether this reflect a regional stress-state or if it only concerns a local phenomenon. Furthermore the veins in the box fold do not correspond to other generations in the Hubertus Höhe section, possibly because of the local complexity of box fold formation.

Bedding-parallel quartz veins cross-cut, truncate and offset BNVs, clearly indicating that both vein types formed during separate events, with BPVs always postdating BNVs. Apart from the thin interbedded BPVs, which are developed during flexural-slip folding, the interbedded and intrabedded composite BPVs can be attributed to bedding-parallel shear related to **bedding-parallel thrusting** in which sandstone sequences are duplicated owing to low angular thrusts. The veins are moreover continuous around fold hinges without changing in thickness and are refracted by cleavage in the fold limbs. These observations are incompatible with the characteristics of flexural-slip BPVs, thus suggesting that bedding-parallel thrusting and accompanied veining occurred at the onset of folding. This thrusting is recorded by various slickenlines present on different laminae in composite BPVs that indicate a large **variability in slip direction**. Locally, at Schwammenauel, the north-dipping layers, forming the flat hinge zone of a hectometre-scale upright box fold, have an atypical orientation compared to other fold limbs in the study area. Internally in this box fold, interbedded BPVs show a buckled morphology whereas in other outcrops they are usually planar along their length. Also in the small-scale buckled sandstone layers, BPVs are present in the cusps as well as in the lobate parts of the fold and bedding-normal veins remain perpendicular to bedding around the fold hinge. These observations give a conclusive answer to the relative timing of the tilting of the layers towards the north, which occurred subsequent to both veining events but preceded the main cleavage development and overall folding.

3.5 Discussion

In this part the results of the macroscopic structural analysis are discussed by comparing the observations and kinematic interpretations of the different case studies. Eventually, a geometric evolutionary model of all observed features can be constructed in which all events are relatively dated This model, including the two different veining events and subsequent deformation in the peripherical part of the High-Ardenne slate belt, are subsequently compared with vein and mullion formation in the central part of the High-Ardenne slate belt in order to illustrate how deformation is expressed differently at different structural levels in a slate belt. This comparison is illustrated in Figure 3.46 as result of this discussion.

3.5.1 Bedding-normal veins as palaeostress indicator

By means of the three different case studies, it has independently been demonstrated that the formation of bedding-normal quartz veins predate the formation of bedding-parallel veins, folds and cleavage. An extensive orientation analysis of the BNVs has resulted in the recognition of different bedding-normal vein generations based on cross-cutting relationships and on the observation that late vein generations are often influenced in their growth due to the presence of previous generations. As veining predates overall folding, it was concluded that all these bedding-normal vein generations formed in a configuration in which the sedimentary layers were still at a (sub)horizontal position. In order to deduce the original vein orientation of each generation prior to folding, several unfolding exercises have been performed. It is now interesting to compare the individual rotation exercises of each case study to determine if different cross-cutting vein generations are consistent at the Rursee study area (Figure 3.37). After this comparison the results can be extrapolated to another area, the Urftsee area, to show if the veins observed at the scale of the Rursee are representative of the North Eifel (Figure 3.40).

It is assumed that each vein generation developed under a certain local or remote stress field. The main reason for determining the original vein orientation is that each generation can be used as independent evidence of the stress field orientation prevalent during its formation. This assumption is based on macrostructural features such as the often fibrous infill of BNVs suggesting that these are primarily extension veins in which the veins opened orthogonal to the vein wall. Extension veins are generally considered to open in the σ_1 - σ_3 plane, parallel to σ_3, and propagate in the σ_1 - σ_2 plane, with the alignment of the veins parallel to σ_2 (Cox *et al.* 1995, Secor 1965). In this configuration σ_1 was still vertical corresponding to the load of the sediments in a setting in which the layers were in a horizontal position. Based on the fact that $\sigma_1 \sim \sigma_v$, it is fair to assume that veining occurred in a sedimentary basin. It has been demonstrated that during subsequent fold-and-cleavage development, vein deformation occurred by flexural-slip and flexural-flow folding, in which the minimum and maximum incremental strain axes remained constant. This indicates that the reconstructed kinematic history occurred during coaxial progressive deformation and that the geometry of the veins can be used to deduce the stress state at the time of vein formation. The specific stress state of $\sigma_1 \sim \sigma_v$ is hence representative of an extensional Andersonian stress regime (Anderson 1951) and illustrates that at the time of bedding-normal veining, the basin was affected by extension.

3.5.1.1 Rursee area

The results of the unfolding exercises performed on the different fold limbs in the three case studies eventually show the original vein orientation of the bedding-normal veins. At Wildenhof, three cross-cutting vein generations V_A, V_B and V_C are defined and are determined to be the oldest, intermediate and youngest generation respectively (Figure 3.37). V_A, however, is only locally distributed in the overturned SE-dipping fold limb of zone 9 and its significance is unclear. It could be argued that, based on a similar orientation, that the orientation of this V_A generation can be correlated with the orientation of other similar early, E-W vein generation in the Eschaulerberg section (Figure 3.36b). The most consistent vein generation that can be correlated between the three case studies is the second vein generation V_B. It slightly changes in orientation from Wildenhof to Eschaulerberg and is more scattered in orientation in the Hubertus Höhe -

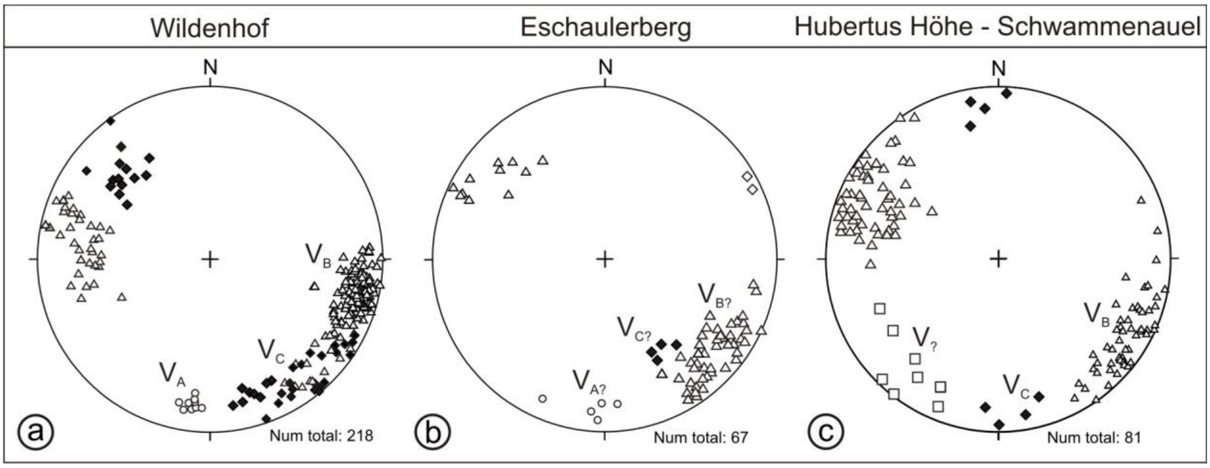

Figure 3.37: Comparison of bedding-normal vein generations in their original orientation of the different case studies at the Rursee area (lower-hemisphere, equal-area stereographic projection). **(a)** 3 distinguished, cross-cutting vein generations V_A, V_B, V_C in the Wildenhof section. **(b)** 2 cross-cutting vein generations that might correlate with V_B and $V_{C.}$ **(c)** 3 different, cross-cutting vein orientations of which 2 generations might be correlated with V_B and V_C. $V_?$: unknown vein generation compared to the other case studies.

Schwammenauel section. Nevertheless, it is observed to be the earliest generation in many outcrops, or it does locally cross-cut V_A. The orientation of this V_B generation varies from NNE-SSW in Wildenhof and NE-SW at Eschaulerberg, to a more scattered orientation at Hubertus Höhe - Schwammenauel with a mean NE-SW orientation. The consistent V_B generation is subsequently cross-cut by a third V_C vein generation that is less consistent than V_B on an individual outcrop because of the presence of V_B affecting fracture propagation of V_C. The orientation of this youngest orientation varies from NW-SE at Wildenhof and Eschaulerberg to E-W at Hubertus Höhe - Schwammenauel. Locally at Hubertus Höhe, the emplacement of V_C is related to bedding-normal shear causing the formation of en-echelon bedding-normal quartz veins (Figure 3.32f and g). It is moreover demonstrated that the opposite dips of the veins after unfolding (Figure 3.37) can be attributed as an effect of subsequent flexural-slip deformation after veining that cannot be undone in the unfolding exercises.

From the orientation of the different vein generations, a tentative evolution in stress field orientation can be proposed. In this evolution the local V_A generation is ignored as it only reflects a local stress state. It is concluded that at the time of bedding-normal vein formation in the Rursee area the layers were still in a horizontal position and that the σ_1 - σ_2 plane of the stress state in the basin evolved from a NE-SW orientation, in which the characteristic and regionally consistent V_B veins formed, to a mean ESE-WNW orientation, in which the sometimes shear-related, cross-cutting V_C generation formed.

3.5.1.2 Urftsee area

The results obtained from the vein orientation in the Rursee can subsequently be correlated with the orientation of other bedding-normal veins in the North Eifel. Another interesting area with full outcrop capacity is situated at the shores of the Urftsee, approximately 5 km south of the Rursee area (see Figure 2.6). It is referred to Appendix A for a detailed structural field map and corresponding structural orientation/field data. This area is characterised by slightly NW-verging folds with associated steeply SE-dipping axial planar cleavage. The fold hinges vary from gently SE-dipping to gently NW-dipping giving rise to upright folds (*e.g.* Figure 3.38a and b; Figure A1 in Appendix A). This fold style slightly differs from the fold style observed in the Rursee area as overturned folds are barely observed in the the Urftsee area (see orientation data in Appendix A). The outcrops studied comprise alternating sandstone and siltstone sequences which correspond to the Upper Rurberg Unit and the Heimbach Unit. They are situated on a higher structural level than the Rursee outcrops, corresponding to first-order folds of the *Vogelsang Sattel* in the SE and *Vogelsang Mulde* in the NW (see Figure 2.3a).

From Malsbenden to the Urftsee dam, bedding-normal veins are ubiquitous present in many outcrops. These BNVs have similar characteristics as the veins described in the Rursee area: they remain orthogonal to the bedding around the characteristic north-verging folds (Figure 3.38a and b), refract at the competent-incompetent interface similar as cleavage (Figure 3.38c and d) and have a lensoid shape with a fibrous infill (Figure 3.38e). On the bedding-planes, the veins can be traced along their length for several metres (Figure 3.39). These observations allow attributing a pre-folding and pre-cleavage origin to these quartz veins.

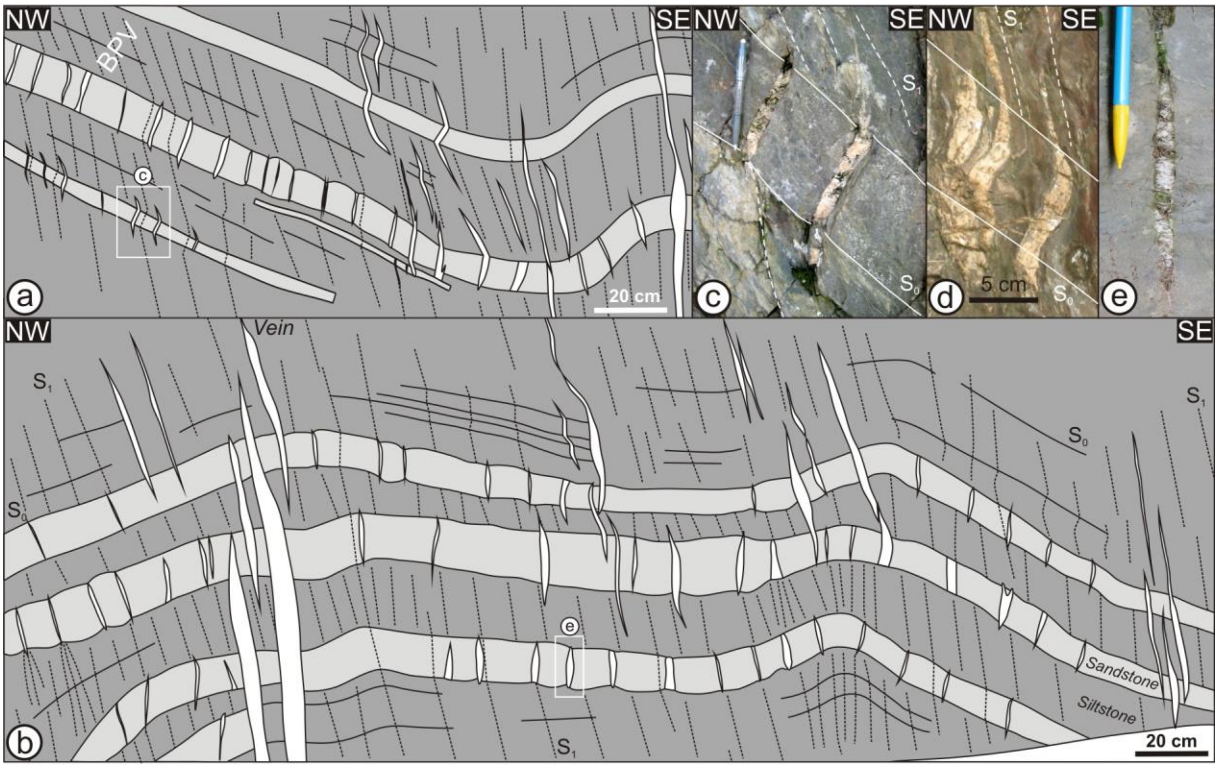

Figure 3.38: Bedding-normal characteristics for a selected outcrop at the shores of the Urftsee (zone 7, Urftsee. See Appendix 1 for localisation of field map). **(a-b)** BNVs distributed around the characteristic open, slightly NW-verging fold with steeply SE-dipping axial planar cleavage, representative of pre-folding veining. **(c-d)** BNVs refracting at the competent-incompetent interface similar to cleavage, representative of a pre-cleavage veining. **(e)** Detail of a lensoid bedding-normal vein wit fibrous infill. Pencil ~14 cm for scale.

As a result of the relative timing of vein formation prior to folding and cleavage development, the original orientation of the veins can, after an unfolding exercise, be compared with those observed at the Rursee area in order to check regional consistency of the veins. A selected outcrop, representative of the Urftsee outcrops, has been chosen to study the vein orientation in detail (situated in zone 7 on the Urftsee structural map, see Appendix A for localisation). This outcrop displays an open fold train in which BNVs are often evenly spaced and continuously present (Figure 3.38a and b). In the rotation exercise, first, the fold hinges are untilted to the horizontal, and second, the fold limbs can be restored to the horizontal over the untilted local fold hinge line, conform to the method illustrated in Figure 3.9. In their original orientation, the BNVs of the selected outcrop (Figure 3.40a) represent a specific stress state in which the alignment of the veins demonstrate that the σ_1 - σ_2 plane was oriented NNE-SSW at the time of vein formation. Veins opened parallel to σ_3, as illustrated by the fibrous infill (Figure 3.38e), that was oriented WNW-ESE. The orientation of BNVs in this representative outcrop of zone 7 is similar to that of other veins in the whole Urftsee area (Figure 3.40b), although locally these veins are cross-cut by a second generation that is orientated nearly ESE-WNW after unfolding. This illustrates that the σ_1 - σ_2 plane of the regional stress field was first oriented NNE-SSW during the formation of the earliest vein generation and subsequently rotated to a nearly ESE-WNW orientation. The stress field orientation deduced from the veins at the Urftsee is similar to that derived from the original orientation of the veins at the Rursee (Figure 3.37).

This comparison eventually shows that the veins studied in the Rursee area are representative of a regional veining event in the North Eifel, in which the σ_1 - σ_2 plane of the regional (far-field) stress field was originally oriented NNE-SSW to NE-SW and subsequently could have changed from the latter orientation towards an E-W orientation. Locally additional cross-cutting vein generations have been observed. The absence of a regional correlation, however, might suggest that these generations are the result of a local transient stress field, rather than additional reorientation of the far-field regional stress field.

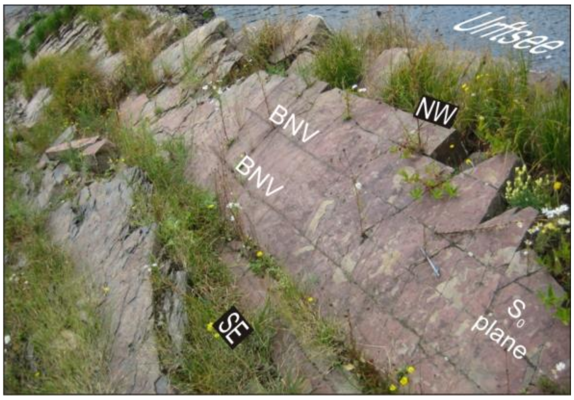

Figure 3.39: Bedding-normal veins continuous for several metres, visible on a bedding-plane in a SE-dipping normal limb (zone 27, Urftsee. See Appendix A for field map and orientation data).

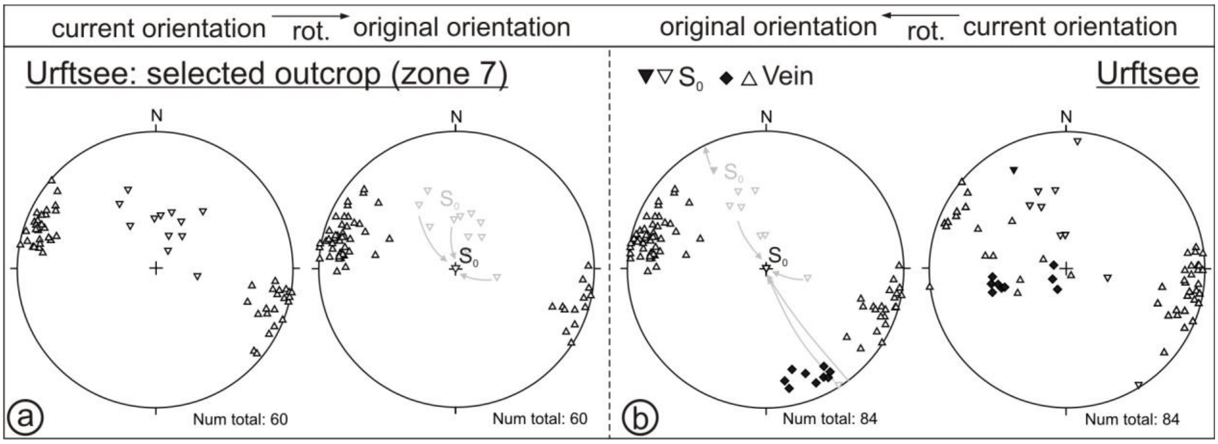

Figure 3.40: Lower-hemisphere, equal area projection of bedding-normal veins in their current and original orientation. Unfolding exercise performed on a selected outcrop (left), representative of the veins in the Urftsee area (right). Data from a selected outcrop (zone 7; Urftsee) at the northern shores of the Urftsee. See Appendix A for structural map, localisation and field data of the outcrop.

3.5.1.3 Central High-Ardenne slate belt

Numerous historical and recent studies have reported the presence of bedding-normal veins in the Lower Devonian sequences in the anchizonal to epizonal, central part of the High-Ardenne slate belt (see references in Darimont 1986, Kenis *et al.* 2002a, Kenis 2004, Kenis & Sintubin 2007). This veining is expressed by the occurrence of a regular and consistent set of lensoid bedding-perpendicular veins with a mullion geometry developed between the veins. The tectonometamorphic history of these features and the development of mullions have been introduced in sections 1.2.1 and 1.2.2. It has been demonstrated by the above mentioned authors that the lenticular veins are developed in well-organised parallel arrays which can be attributed to a regional, pre-folding extensional fracturing event. The regional attitude of this event is illustrated by the orientation of the quartz veins around the central part of the slate belt. To estimate the original orientation of the veins, prior to folding, Kenis (2004) performed an unfolding exercise in which the bedding-normal veins of several study areas in the cHASB were backrotated to the original position (Figure 3.41a). Subsequent orientation data show that the veins were originally nearly vertical and were oriented NE-SW. This orientation is representative of a regional veining event that occurred in an anisotropic stress field with a vertical σ_1 and horizontal σ_2. In this configuration, opening of the veins occurred parallel to σ_3 in a NW-SE direction. Only in one peculiar case at Remagne, an unusual vein orientation has been deduced that does not correlate regionally (Figure 3.41) and might be related to the development of the 'Ourthe zone' (see Hance *et al.* 1999, Kenis 2004).

Towards the peripheral part of the High-Ardenne slate belt, quartz veining is still a regional phenomenon but is expressed differently by several cross-cutting vein generations (Figure 3.41b). It is deduced from the orientation of the consistent vein generation V_B that during extension, the σ_1 - σ_2 orientation of the stress field was oriented NE-SW to NNE-SSW. Based on its orientation prior to folding it can be concluded that this generation corresponds to the regional vein arrays in the cHASB reflecting the regional stress state in the Ardenne-Eifel basin at that time.

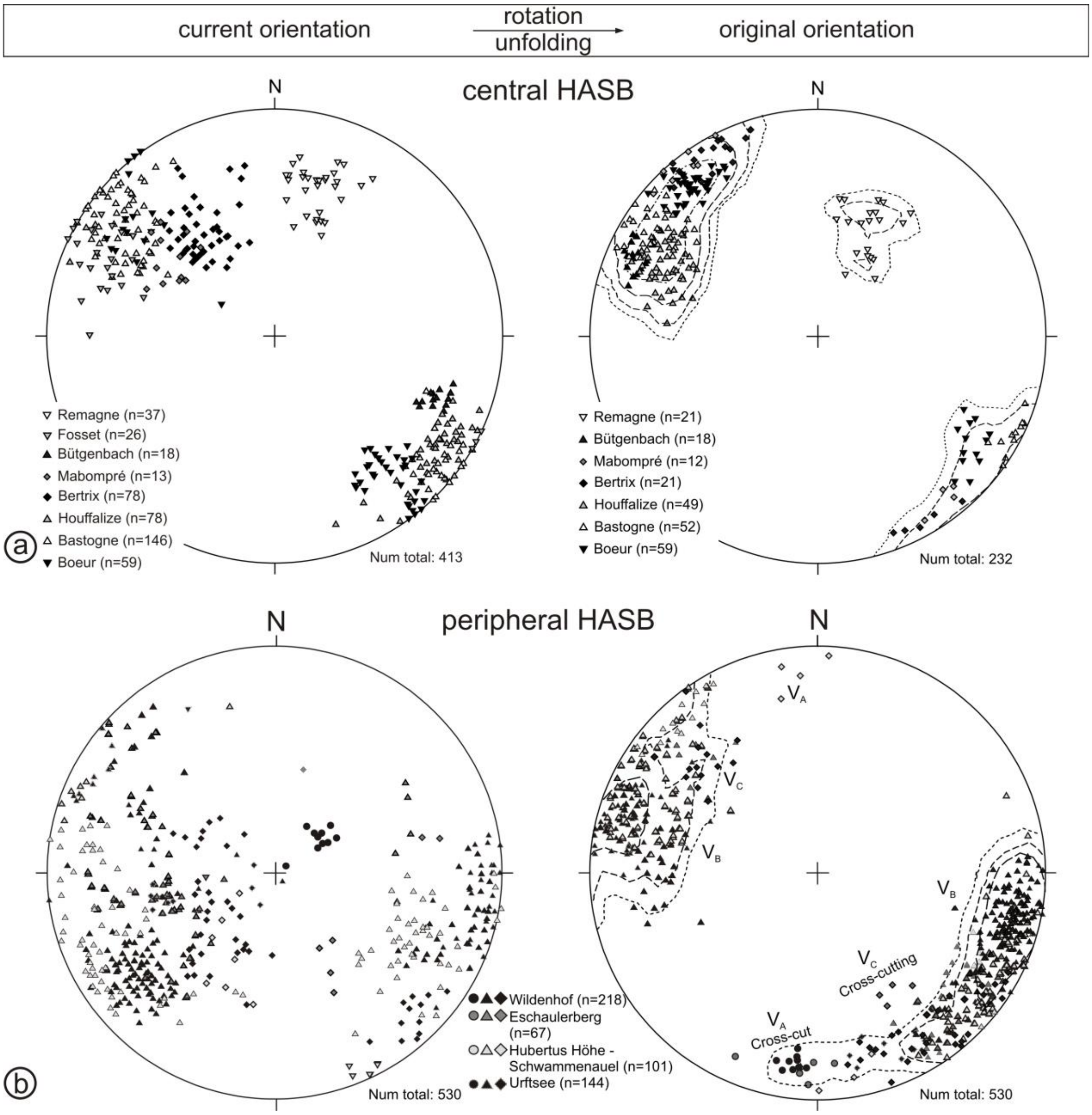

Figure 3.41: Lower-hemisphere, equal area stereographic projection of bedding-normal veins in their current and original unfolded orientation in the **(a)** central part of the High-Ardenne slate belt (cHASB) (data from Kenis 2004) and **(b)** peripheral part of the High-Ardenne slate belt. Modified after Van Noten & Sintubin (2010).

Subsequently in the pHASB, generation V_C developed, indicative of an ENE-WSW orientation of the stress field (Figure 3.41b). This stress-state evolution deduced from cross-cutting veins in the pHASB, might suggests that σ_2 equals σ_3 at a certain stage and that they switched locally during a short period in order to form the cross-cutting generation.

To conclude the different cross-cutting vein generations suggest that fracturing/veining in the pHASB occurred in a less consistent anisotropic stress field than in the cHASB and in different stages in the stress field evolution, which are not all preserved in the cHASB. Whether vein formation occurred simultaneously in both areas remains unclear and needs further research. Notwithstanding the differences between the areas, the presence of one consistent vein orientation in the whole High-Ardenne slate belt is representative of a consistent stress field at the time of this vein formation. This specific stress state consists of a vertical maximum principal stress $\sigma_{1,}$ a horizontal intermediate σ_2 oriented at about NW-SE in the cHASB and NW-SE to WNW-ESE in the pHASB, and a minimum principal stress σ_3 oriented NW-SE in the cHASB and NW-SE to WNW-ESE for the pHASB. This comparison is illustrated as Stage b on the evolutionary history in Figure 3.46.

3.5.2 Origin of bedding-parallel veins

3.5.2.1 State-of-the-art

In the past decades, the formation of bedding-parallel veins has caused considerable debate and as a result numerous different fracture and veining mechanisms have been proposed. Most authors agree that BPVs usually form in sedimentary basins with alternating lithologies, in which layer-normal uplift or layer-parallel slip, either due to folding or to thrusting, can easily occur. The principal issue in all these discussions is whether the veins developed prior (*e.g.* Fitches *et al.* 1986, 1990, Henderson *et al.* 1990), at the onset (*e.g.* Cosgrove 1993, Hilgers *et al.* 2006b) or contemporaneous to folding (*e.g.* Fowler 1996, Tanner 1989). The reader is referred specifically to Fowler (1996) and Hilgers *et al*. (2006b) for an overview on different models and further reading on the origin of bedding-parallel veins.

The controversy about distinguishing pre- from synfolding BPVs is similar to that of other pre- versus syndeformational structures, such as for example distinguishing synsedimentary folds from syntectonic folds (*e.g.* Debacker *et al.* 2006). Pre- and synfolding BPVs share common characteristics (Fowler & Winsor 1997) comprising multiple quartz laminae separated by thin pelitic inclusion seams, *i.e.* composite or laminated veins, as well as slickenlines with varying orientation on individual laminae. Both observations has been explained by flexural-slip related veining (Fowler & Winsor 1997, Horne & Culshaw 2001, Tanner 1989, 1990) or by bedding-parallel thrusting, whether or not prior to folding, related to high-angle reverse and low-angle thrust faulting (Boullier & Robert 1992, Cooke & Pollard 1997, Cox 1995, de Roo & Weber 1992, Jessell *et al.* 1994, Koehn & Passchier 2000, Wilson *et al.* 2009), in which successive quartz laminae of laminated veins suggest that opening and sealing of the veins are successive and recurrent features (Séjourné *et al.* 2005).

Related to this discussion, different configurations on the occurrence of the BPVs to the surrounding rocks have been discussed. Fitches *et al.* (1986) note from pre-folding BPVs, which formed by a combined process of gravitational sliding and hydraulic jacking, that the BPVs studied in the Welsh Basin (U.K.) mainly occur in homogeneous pelite or at the upper contact of a sandstone bed with overlying pelite. In this mechanism of hydraulic jacking bedding-normal uplift is caused by hydraulic fracturing resulting from lithostatic fluid overpressures. It is argued by Price and Cosgrove (1990) that such local sites of hydraulic fracturing form parallel to bedding interfaces with small bedding cohesion. At these locations a lens of fluid, termed as sills, will form along the bedding plane which jacks the bedding apart, reducing the bedding cohesion to zero. Subsequent thrusting may be accommodated by slip on these fluid sills (Teixell *et al.* 2000). Vein opening perpendicular to bedding at the interface of contrasting lithologies or intrabedded in fine-grained sequences has been defined as ‘beefs’ in which the fibrous infill of the veins, oriented orthogonal to the bedding-parallel vein wall, result from lithostatic fluid overpressures (Cobbold & Rodrigues 2007, Cosgrove 1993, Foxford *et al.* 2000, Rodrigues *et al.* 2009). These processes of uplift may be amplified by bedding-parallel flexural-slip if additional fluid flow occurs (Cosgrove 1993). In contrast, the most favoured site of flexural-slip veins is the lower contact of a sandstone bed with the underlying slate (Fowler & Winsor 1997, Tanner 1989).

In the Rhenish Massif, BPVs are reported to be related to local low-angle faulting and tend to occur intrabedded in slates, and interbedded near boundaries between rocks of contrasting competence (de Roo & Weber 1992, Weber 1980). Also the thickness of laminated veins has been correlated with the net slip along the veins. Because of their ability of BPVs to form thick veins, they are potentially interesting for the generation of economically interesting ore bodies (*e.g.* De Clercq *et al.* 2008, Dewaele *et al.* 2010, Foxford *et al.* 2000, Jia *et al.* 2000, Tunks *et al.* 2004). Flexural-slip veins are usually thin veins whereas sheared veins, either related to pre-folding slip or bedding-slip associated with faults, may increase in thickness up to several tens of centimetres (Fowler & Winsor 1997). These common features make it difficult to separate pre- from synfolding bedding-parallel veins. Moreover, the possibility exists that both models are mutually not exclusive and that a continuous evolution of pre-folding into flexural-slip synfolding veins may exist (Tanner 1990).

In order to distinguish pre- from synfolding veins, their microstructures should be analysed. In flexural-slip veins, the fracture opening trajectory can be distinguished from the orientation of small crystal fibres. In these veins, the step-like shear fibres are usually oriented orthogonal to the local fold hinges (Tanner, 1989). 'Beefs' resulting from bedding-normal uplift preserve a specific mineral fabric with vertical fibres tracking the opening trajectory (Cobbold & Rodrigues 2007, Cosgrove 1993, Rodrigues *et al.* 2009). BPVs formed by bedding-parallel thrusting are characterised by small, bedding-(sub)parallel inclusion trails and crack-seal bands, which both track the opening direction during vein formation and reflect the amount of displacement of sedimentary layers during layer-parallel slip. Shear veins or striped bedding-veins (Koehn & Passchier 2000) are formed by an amalgamation of overlapping dilational jogs in which vein growth occurs by fibrous crystal growth between adjacent shear planes. In these fibrous crystals, internal solid inclusion trails are oriented consistently and can be used as an indicator of oblique opening during layer-parallel shear (Jessell *et al.* 1994, Koehn & Passchier 2000, Vannucchi *et al.* 2008). Such striped bedding-veins thus have a strong anisotropic fabric that developed in a shear direction at high angle to the maximum compressive stress (Fagereng *et al.* 2010).

A lot of the models that are presented in literature concerning the origin of BPVs are based on the original microstructures. However, successive progressive deformation may partly destroy the original fabric, which complicates determining the origin of veining purely based on the microstructures. Furthermore, also the role of the fluid pressure varies significantly among the different models presented in literature. Especially the popular and often over-called hydraulic fracturing model has often been 'assumed' to be the driving mechanism for bedding-normal uplift, although the presence of fluid overpressures, necessary for hydraulic fracturing, has often not been determined by microthermometric analysis in these models.

It can be concluded from this state-of-the-art that a microstructural fabric analysis of BPVs, in which the deformation of microstructures has kept in mind to separate the original growth fabric from deformed microstructures, will provide crucial evidence on deducing how the bedding-parallel veins in the pHASB developed (see Chapter 4). Furthermore, combining this microstructural evidence with the role of the fluid pressure, derived from the detailed microthermometric analysis of fluid inclusions in vein quartz (see Chapter 5) will have a major advantage in constructing a new model on the formation of bedding-parallel veins. Furthermore, the importance of the stress state in the basin during vein formation has often been neglected. Therefore, combining stress-state changes with microstructural evidence and the magnitude of the fluid pressure (see Chapter 6) allows constructing an ultimate model which may form the base for a reconsideration of some of the models presented in literature.

3.5.2.2 Comparing the North Eifel BPVs to literature

Apart from a detailed microstructural analysis (Chapter 4), several macroscopic observations, explained and illustrated in detail in the different case studies at the Rursee, are already conclusive to the relative timing of the bedding-parallel veins with respect to other structural features. In the Rursee study area several types of bedding-parallel veins have been determined. Depending on their relation relatively to the surrounding sequences they are divided into interbedded and intrabedded BPVs. First of all, it is concluded that the thin, millimetre-size and single laminated BPVs, which are mostly present at the interface of a siltstone sequence with an overlying sandstone bed, are related to flexural-slip folding and are thus determined to be syntectonic features. From slickenline and slickenfibre analysis it has been shown that the veins have opposite shear senses towards the anticlinal hinges in opposite fold limbs and that the direction of layer-parallel slip is nearly orthogonal to the local fold hinges. The microstructural infill and composition of fluids, from which these flexural-slip veins formed, are not further dealt with in this work.

An early tectonic, pre- to early folding origin can be attributed to the majority of bedding-parallel veins that are exposed in the Rursee study area. Both thin, single fractured BPVs and thicker, up to 10 cm-thick, composite and complex laminated veins are observed. BPVs are continuously present around the folds without continuous thickness, an important observation incompatible with the flexural-slip mechanism. Four different configurations on the occurrence of the BPVs to the surrounding rocks have been observed (defined as case *i* to *iv* in the Wildenhof case study and confirmed in the Eschaulerberg and Hubertus Höhe - Schwammenauel case studies).

Case i) The overall part of the BPVs are situated below the competent units, interbedded between a siltstone and the overlying sandstone. These composite BPVs are detached from the overlying sandstone and have an irregular boundary with the underlying siltstone, which is characterised by numerous thin veins branching off from the quartz vein (Figure 3.13b and c). Owing to the irregular lower boundary of this BPV-type, its thickness varies considerable along its length. The vein walls are characterised by slickenlines which are uniform in trend on a single lamina, but vary slightly in orientation from lamina to lamina, evidencing bedding-parallel slip during quartz precipitation or between the emplacements of the different laminae (*e.g.* Figure 3.36). These slickenlines are often oriented at high angle to the local fold hinge line, but may also have a considerable variation in slip orientation along a single vein.

Case ii) BPVs situated above coarse-grained beds and below silty sequences, have similar composite characteristics as in the previous configuration and are also characterised by slickenlines, although local offshoots into the overlying layers have not been observed. Both the lower and upper vein boundaries are usually planar.

Case iii) Thin BPVs cross-cutting BNVs often occur intrabedded within the fine- to coarse-grained sandstone sequences. Absence of lateral displacement of the BNVs is indicative of a veining event in which this BPV-type opens perpendicular to bedding (cf. Figure 3.13d-h).

Case iv) Intrabedded BPVs in siltstone sequences frequently occur, sometimes characterised by a strong laminated nature. Host-rock inclusion fragments and host-rock inclusion lines separate internally the quartz laminae (Figure 3.13i; Figure 3.34f).

In the geometric analysis, different tentative vein mechanisms have been proposed for the formation of these four BPV configurations. A first proposed mechanism is applicable to the intrabedded BPVs occurring in competent units (cf. Figure 3.18a-f). In this model it has been postulated that the thin bedding-parallel quartz veins result from **bedding-normal uplift** of the layers, with absence of any lateral displacement, as evidenced by displaced bedding-normal veins orthogonal to bedding (Figure 3.42a). This mechanism might correspond to the so-called ‘beefs’, resulting from bedding-normal uplift in an isotropic rock at high fluid (over)pressures causing tensile hydraulic fracturing (cf. Cobbold & Rodrigues 2007), although bedding-normal fibres tracking the opening direction have not been observed macroscopically.

A second mechanism (cf. Figure 3.17), is related to the formation of the two types of interbedded composite BPVs and the intrabedded composite BPVs occurring in siltstone sequences. For all three configurations a mechanism can be attributed in which bedding-parallel slip related to **bedding-parallel thrusting** is responsible for the composite nature of the veins and for the multiple slickenline orientations on the different laminae (Figure 3.42b). This bedding-parallel slip is related to small-scale thrusts oriented at low angle to bedding, in which the competent units are duplicated giving rise to small-scale ramps (*e.g.* Eschaulerberg parasitic fold in Figure 3.25; duplicated sandstone in Figure 3.34h-i; Figure 3.42c). This evidence of thrusting can be confirmed by comparing these arguments to other cases in literature in which BPVs have been described. Evidence of thrusting at the onset of fold-and-cleavage development comprise: (i) BPVs with uniform vein thickness being folded and continuously present around fold hinges (cf. Cosgrove 1993, 1995b), an observation that can be made in the Eschaulerberg parasitic fold and in the box fold at Schwammenauel; (ii) the extreme variability of slip orientations in a single BPV, varying from orthogonal to parallel to the local fold hinge line, indicating that laminated veins formed during recurrent and successive slip (cf. Fitches *et al.* 1986, Fowler & Winsor 1997), an argument compatible to the variability in slip direction analysed on the composite BPV in the box fold (Figure 3.36); (iii) small-scale buckled veins folded within the regional folds (cf. Cosgrove 1995b, de Roo & Weber 1992), which has been confirmed by the buckled BPVs in the buckle folds in the north-dipping layers at Schwammenauel; (iv) cleavage fanning out against buckled BPVs and overprinting planar veins (Fowler & Winsor 1997).

To conclude, bedding-parallel quartz veins thus cross-cut, truncate and offset the bedding-normal veins, clearly indicating that both vein types formed during separate events, with the BPVs postdating the BNVs. From the macrostructural analysis it can be concluded that fracturing and sealing were successive and recurrent features during bedding-parallel veining. Hence, the formation of this vein type is associated with bedding-normal uplift prior to fold-and-cleavage development (*case iii*) or with a combination of bedding-normal uplift and bedding-parallel thrusting (*case i, ii and iv*) at the onset of folding. Theoretically, thrusting occurs at a specific stress state in which the maximum principal stress **σ_1 s**hould be at low angle to the vein walls (see Hilgers *et al.* 2006b). If such a stress state is applied to bedding-parallel thrusting studied in this work, then this implies a rotation of the principal stress axes after bedding-normal veining during which σ_1, now corresponding to the regional tectonic stress, reoriented from vertical towards horizontal. In this configuration, BPVs formed in an Andersonian stress regime in which $\sigma_1 \sim \sigma_T$ and σ_2 is now horizontal and σ_3 is vertical.

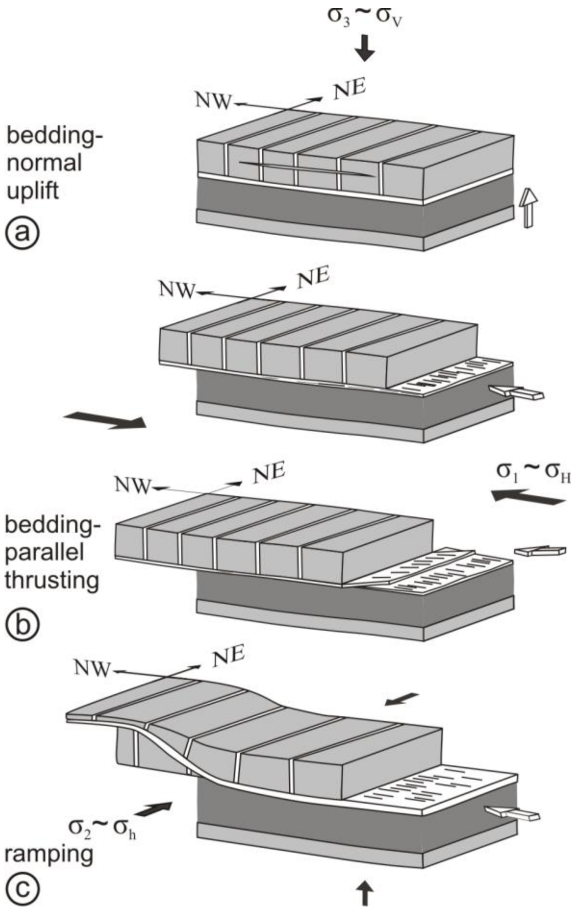

Figure 3.42: Different mechanisms for bedding-parallel veining based on geometric observations and correlated to literature. Bedding-parallel veins develop due to **(a)** bedding-normal uplift, **(b)** bedding-parallel thrusting in variable slip directions, **(c)** ramping or due to a combination of these mechanisms. For simplicity, the different cross-cutting bedding-normal veins have not been illustrated.

Initially after this rotation, σ_1 may be parallel to bedding allowing bedding-normal uplift. Afterwards, bedding must have been slightly tilted in order to allow shear stress on the bedding-parallel shear plane. This tilting is attributed to minor buckling at the onset of folding. In this configuration **$\sigma_1 \sim \sigma_T$** is still horizontal but is now oriented at **low angle to bedding**. For sake of simplicity, however, this low angle is not illustrated in the thrusting and ramping mechanism illustrated in Figure 3.42c or in other figures further in this work. In this light, bedding-parallel veins are the first brittle structures that reflect compression in the basin at the onset of the Variscan orogeny. The orientation of this tectonic stress component $\sigma_1 \sim \sigma_T$ can possibly be derived from the shear direction deduced from the geometric analysis of bedding-parallel veins. Analysis of slickenline orientations and fibre steps analysed on BPVs, displaced BNVs and thrust directions in small-scale ramps, indicates a mean **NNW- to NW-directed thrusting** (see Figure 3.25 and Figure 3.36). However, this direction can strongly vary locally, such as demonstrated by the varying slickenline orientations on different laminae in a BPV or by variable slickenline orientation laterally on a vein (*e.g.* composite BPV in the box fold at Schwammenauel).

It can furthermore be concluded that the models constructed for the bedding-parallel veins studied in the Rursee study area, are representative of bedding-parallel veining in Lower Devonian sequences in that part of the North Eifel in which mullions are absent. This assumption is based on additional observations in the Urftsee area, in which bedding-parallel veins occur in all four described configurations with respect to the surrounding host rock (*e.g.* Figure 3.43) and small-scale thrusts have been observed, either reflecting bedding-normal uplift or bedding-parallel thrusting.

Figure 3.43: Example of centimetre-thick interbedded bedding-parallel veins observed in the SE-dipping normal limb of zone 17 at the shores of the Urftsee. Pencil ~14 cm for scale. See Appendix A for localisation of zone 17 on a structural field map and corresponding orientation data.

3.5.2.3 Bedding-parallel veins versus mullions

The onset of Variscan shortening is expressed differently in the central part of the High-Ardenne slate belt. It was introduced in Chapter 1 that the coexistence of extensional features such as the regional (lensoid) bedding-normal veins and compressional features such as the cuspate-lobate geometry of the bedding interface, *i.e.* mullions, reflect a progressive deformation history from extension to compression (Kenis *et al.* 2002a, Urai *et al.* 2001). This deformation history represents a mixed brittle-plastic behaviour in which it has been demonstrated that the lensoid quartz veins formed above the brittle-ductile transition, whereas mullions are related to a deformation phase below this transition (Kenis 2004). Towards the periphery of the slate belt mullions are, however, absent. It is shown in this macrostructural analysis that shortening is exemplified differently and in a purely brittle behaviour in the pHASB. Bedding-parallel quartz veins developed in a specific stress state during which the least principal stress σ_3 was vertical. The advantages of studying bedding-parallel veins above mullions, is that the 3D nature of the state of stress can be estimated from these shear-related veins, whereas only stretch directions can be deduced from the mullion shape. For the above mentioned reasons it is fair to conclude that both bedding-parallel veins and mullions are the first manifestations of the compressional regime at the onset of Variscan contraction and can be assumed as each other equivalents respectively above and below the crustal brittle-ductile transition (see Stage c in Figure 3.46). However, the relative timing between mullion formation and bedding-parallel thrusting is unknown and can probably not be determined. Nevertheless, this comparison already shows how the onset of deformation is expressed differently at different structural levels in a slate belt that is subjected to orogenic shortening.

3.5.3 Variscan deformation & syntectonic features

The orientation analysis of bedding, cleavage, bedding-cleavage intersection lineation and fold hinge line in the three case studies demonstrates that the regional overall structural architecture is very consistent and displays second order, asymmetric to overturned, hectometre-scale folds with close interlimb angles and with a pronounced NW-verging asymmetry. The overturned folds have mostly rounded to angular fold hinges. Stereographic analysis of bedding shows that the folds are highly cylindrical (Figure 3.44a) in which three clusters can be recognised, representative of normal and overturned SE-dipping fold limbs in the overturned folds and normal SE- and NW-dipping fold limbs for the upright folds. The main tectonic foliation is a distinct pervasive cleavage of which the attitude remains constant throughout the study area (S_1~130/52). Whereas the incompetent rocks (*i.e.* pelite and siltstone) are characterised by a slaty cleavage, a weak or spaced cleavage exists in the competent sandstone beds. Stereographic analysis of cleavage indicates that cleavage is axial planar with respect to the folds (Figure 3.44b).

The bedding-cleavage intersection lineation is the most prominent linear feature and can be used as a tool to predict the orientation of the local fold hinge line. The intersection lineation varies from gently to steeply NNE-, NE- to east-plunging (Figure 3.44b). Due to irregular observed sedimentology related to the shallow depositional environment of the Upper Rurberg Unit and exemplified by small-scale gullies and large-scale point bars, bedding surfaces are often rather wavy, while the cleavage attitude remains constant through the area. Because of this, the bedding-cleavage intersection lineation may locally differ from outcrop to outcrop. Nevertheless this large variation, the mean intersection lineation (L_i~065/30) corresponds to the calculated β-axis (β~068/31), defined as the pole of the best fit through bedding (Figure 3.44a) illustrating the regional consistency of the plunge of the folds. The considerable variability of the bedding-cleavage intersection lineation can be explained by different phenomena. It is furthermore demonstrated that the regional folds plunge towards the NE. Because of this NE-plunging attitude, outcrops in the Hubertus-Höhe - Schwammenauel N section are situated at a higher structural and stratigraphic level than the outcrops in the Eschaulerberg and Wildenhof sections. Also, it is not possible to mutually link the alternating fold limbs studied between the different case studies in the Rursee area. The absence of interconnections shows that folds die out from the SW to the NE (see fold axes in Figure 3.1). It can be argued that these folds probably have a periclinal nature, with periclinal endings to the NE, in which fold hinges will slightly differ in orientation between the different sections studied. These differences will contribute to the variation in intersection lineation.

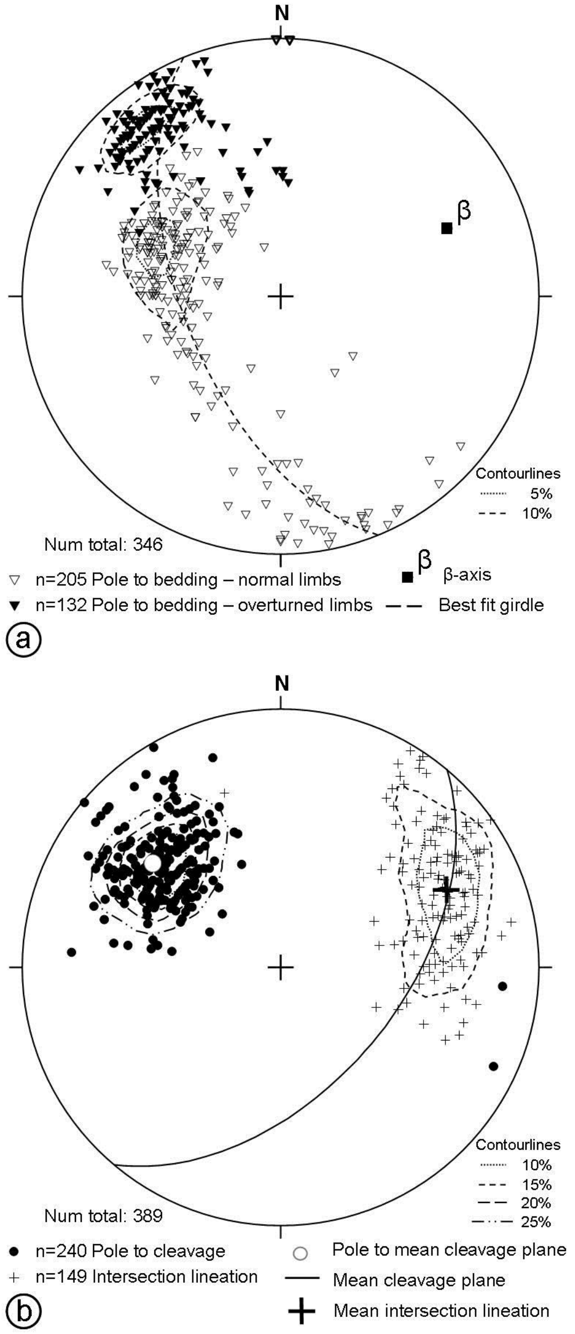

Figure 3.44: Lower-hemisphere, equal-area stereographic projection summarising the overall structural architecture of the Rursee area. **(a)** Poles to bedding. **(b)** Bedding-cleavage intersection lineation and poles to cleavage. Modified after Van Noten *et al.* (2008).

Locally at Schwammenauel N (zone 21) a peculiar bedding orientation has been observed. The kinematic analysis of this outcrop has shown that these layers can be interpreted as the flat hinge zone of an upright box fold in which small-scale buckle folds and buckled bedding-parallel veins are present, which are deformed due to the already tilted orientation of the layers at the time of the main Variscan contraction. It can be discussed when this tilting has occurred. A sedimentary origin has to be excluded as both bedding-normal and bedding-parallel veins are present and are deformed in the buckle folds. It is more likely that tilting results from the incipient development of a periclinal fold. In some configurations, unusual north-dipping bedding orientations can develop near the transition of the periclinal endings of an overturned fold limb with the adjacent normal SE-dipping fold limb (see Figure 3.45) (cf. Van Noten *et al.* 2008).

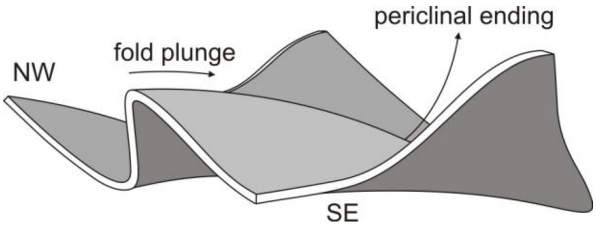

Figure 3.45: NE-plunging fold geometry of the Rursee area. North-dipping bedding orientations can develop near the transition of an periclinal ending of a NW-verging overturned fold with an adjacent normal SE-dipping limb.

The bedding-parallel veins have often been observed in small-scale ramps, such as for example in the Eschaulerberg parasitic fold (Figure 3.23). It is remarkable that this ramping is present in the fold hinge of this parasitic fold. It may be postulated that bedding-parallel thrusting, resulting in bedding-parallel veins, may have played a considerable role at the initiation of fold development in such way that these ramps influenced the location of fold hinges during progressive horizontal shortening due to their irregularity. Passchier & Trouw (2005) also reported that ramps associated with BPVs may develop at the incipient folding, rather than during flexural slip in maturing folds.

Small-scale tectonic features with associated quartz veining such as interboudin veins, out-of-syncline fault-related veins, sigmoidal tension gashes, filled hinge cracks, displaced or deformed bedding-normal veins and thin flexural-slip BPVs accompany folding and formed during the coaxial progressive deformation. Interboudin veins are formed due to extension of layers which are oriented parallel to cleavage, whereas tension gashes are related to shear movements during flexural-flow in the layer. Hinge cracks are originate from extension at the outer part of the competent layers during folding. These features are however only locally distributed and are related to small-scale deformation features. It is clear from the structural analysis that the regional veining event, expressed as bedding-normal and bedding-parallel veins, was widespread, while quartz veining seems to have occurred rather occasionally during the main contraction-dominated phase of the Variscan orogeny and is restricted to local deformation features related to folding and faulting.

Subsequently after the Variscan fold-and-cleavage development, many faults developed in the area. This is demonstrated by several different fault types with varying thickness. The large-scale faults, and the associated antithetic small-scale faults, are reverse faults with similar SE-dipping attitude as the axial planes of the overturned folds. A clear correlation of the beds at opposite sides of the reverse faults is often lacking. Small-scale low-angle thrust faults only occur locally as small-scale, interlimb displacement faults related to bedding-parallel vein formation. The relative timing of the large-scale reverse faults remains however enigmatic, either they developed synfolding, such as fault-bend-folding or fault-propagation-folding (*e.g.* Dittmar *et al.* 1994) or post-folding (break-thrust folding).

The clayey fault gouge in these reverse faults with variable width is free of any mineral precipitate that could indicate a deep burial as would be expected under the conditions of the Variscan Orogeny (Holland *et al.* 2006). Moreover, the porosity of the clay gouge is much higher than the porosity of the “overconsolidated” host rock, *i.e.* siltstones. Holland *et al.* (2006) suggested that deformation must have taken place in much shallower conditions than during the Variscan deformation and that at the time of faulting, the fault gouge was still deep enough to be isolated from surface weathering but shallow enough to avoid “cooking” of the fault gouge at deeper conditions. Hence, these fault zones were initiated as reverse faults during the main contraction-dominated phase of the Variscan orogeny, and may have been reactivated as normal faults in the late Variscan extensional regime during orogenic collapse (cf. Van Baelen 2010) or as normal faults during post-Variscan fault movements (cf. Holland *et al.* 2006).

3.5.4 Regional evolutionary history

Finally, to conclude this discussion, the different mechanisms proposed for the two different veining events in the northeastern, peripheral part of the High-Ardenne slate belt are compared relatively to the regional veining event and mullion formation in the central part of the High-Ardenne slate belt. This demonstrates how geodynamic constraints are expressed differently at the different structural levels of the Ardenne-Eifel basin that evolved during progressive Variscan deformation into the High-Ardenne slate belt. This summary is illustrated in Figure 3.46.

3.6 Synthesis

In order to frame the different vein types relatively with respect to structural features such as bedding, cleavage and folds, a pervasive structural geometric and kinematic analysis has been carried out on all vein systems that occur in the northeastern peripheral part of the High-Ardenne slate belt. It is demonstrated that two different vein types are oriented normal and parallel to bedding. The first vein type consists of several generations of bedding-normal veins that remain perpendicular to bedding around the folds, thereby clearly predating the main Variscan contraction and regional fold-and-cleavage development. The planar to lensoid veins are mostly restricted to competent sandstone layers (stratabound veins), although they sometimes continue into the adjacent incompetent layers (non-stratabound veins), refracting at the competent-incompetent interface similar to the cleavage. The specific orientation of the often fibrous quartz mineral infill of the veins and the absence of lateral displacement along the vein walls indicate that the bedding-normal veins are extension veins which developed in host-rock sequences that were still in a horizontal position at the time of vein formation. In this configuration, the maximum principal stress σ_1 was still vertical, corresponding with load of the overburden and the veins opened perpendicular to the least principal stress σ_3. Extension veins that formed prior to folding are particularly useful to reconstruct changes in palaeostress orientation at the time of vein formation. By numerous rotation exercises the veins were unfolded from their current position into their original vertical orientation in which the original alignment of the veins are indicative of the σ_1 - σ_2 plane of the stress field. It is deduced from the orientation of the different cross-cutting vein generations that the σ_1 - σ_2 orientation of the stress field originally evolved from a NE-SW to NNE-SSW orientation, in which a regionally consistent V_B generation developed, to a ENE-WSW orientation, in which generation V_C developed and has cross-cut the previous veins. It is suggested from this stress-state evolution of the pHASB that σ_2 equals σ_3 at a certain stage and that they switched locally during a short period in order to form the cross-cutting generation V_C. The consistent pre-folding orientation of the V_B bedding-normal vein generation in the North Eifel corresponds to the original NW-SE orientation of intermullion quartz veins in the central part of the High-Ardenne slate belt (Ardennes, Belgium) highlighting that this particular veining event occurred regionally in a basin that was still in extension at the latest stages of the burial.

Figure 3.46 (next page)**:** Comparison between the peripheral and central part of the High-Ardenne slate belt showing the evolutionary history from initial sedimentation to Variscan deformation (modified after Kenis *et al.* 2002a, Van Noten *et al.* 2008). (**Stage a**) Pragian to Lochkovian sedimentation. (**Stage b**) Differences in veining during the latest stages of burial. Evolution of several cross-cutting generations of BNVs in the pHASB contrary to one well-arranged, parallel vein generation in the cHASB. (**Stage c**) Initial Variscan shortening reflected by the formation of bedding-parallel veins (BPVs) in the pHASB owing to combined bedding-normal uplift and bedding-parallel thrusting. Slickenlines illustrate the different directions of thrusting and reflect a brittle deformation versus the mullion formation in the cHASB in a ductile way. Relative timing of both events is unclear. (**Stage d**) The contraction-dominated main phase of the Variscan Orogeny caused the formation of characteristic NW-verging overturned folds with associated SE-dipping cleavage in the pHASB and north-verging upright folds with associated south-dipping cleavage in the cHASB.

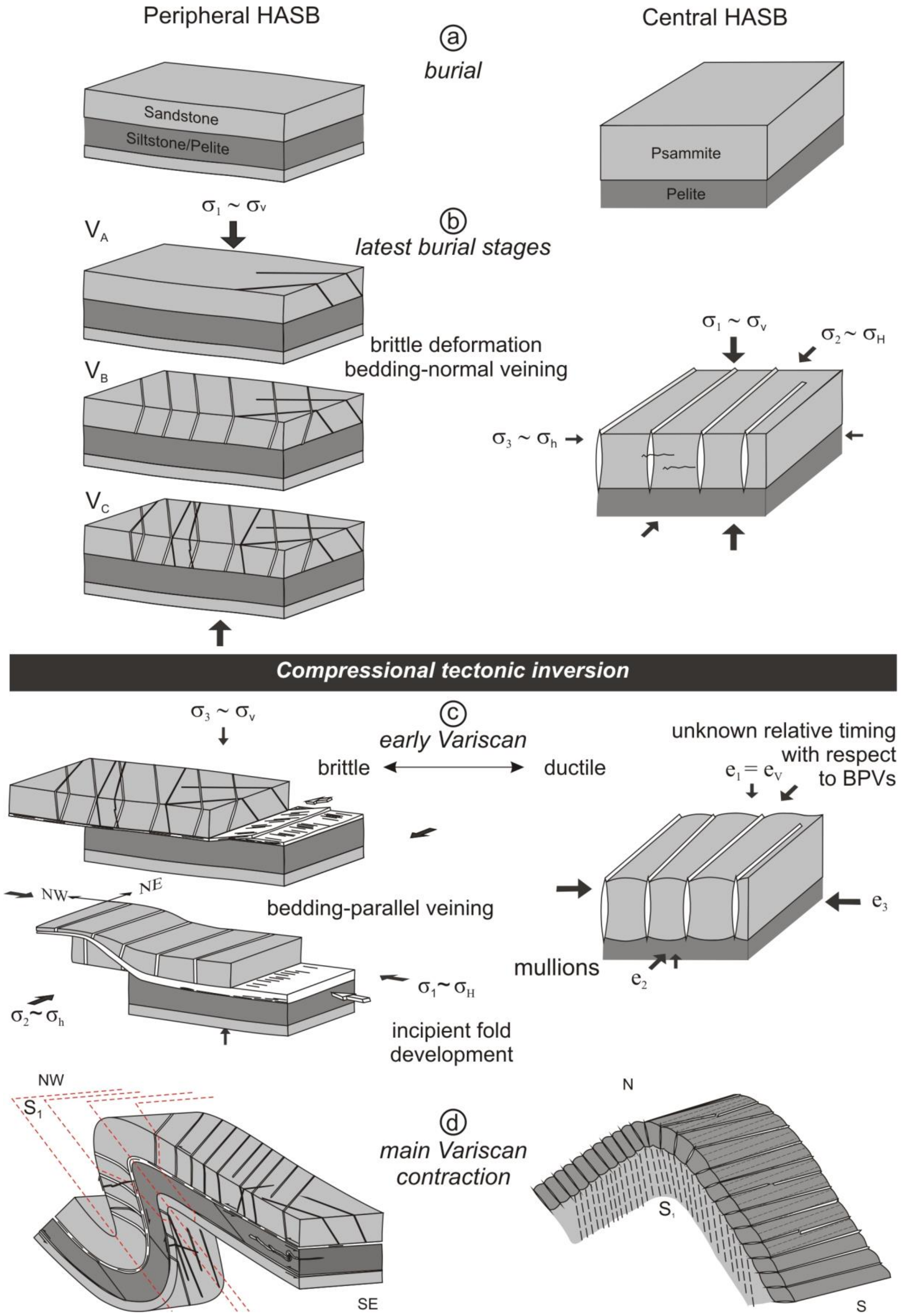
Peripheral HASB
Central HASB
ⓐ
burial
Sandstone
Siltstone/Pelite
Psammite
Pelite
$\sigma_1 \sim \sigma_v$
V_A
ⓑ
latest burial stages
brittle deformation
bedding-normal veining
V_B
$\sigma_1 \sim \sigma_v$
$\sigma_2 \sim \sigma_H$
$\sigma_3 \sim \sigma_h$
V_C
Compressional tectonic inversion
$\sigma_3 \sim \sigma_v$
ⓒ
early Variscan
brittle
ductile
unknown relative timing
with respect
to BPVs
$e_1 = e_V$
NW
NE
bedding-parallel veining
e_3
mullions
e_2
$\sigma_1 \sim \sigma_H$
$\sigma_2 \sim \sigma_h$
incipient fold
development
NW
S_1
ⓓ
main Variscan
contraction
SE
N
S_1
S

In the North Eifel, bedding-parallel quartz veins subsequently cross-cut, truncate and offset the bedding-normal veins and are continuously present around fold hinges. It is concluded from the macrostructural analysis that both veining events formed during separate phases preceding the regional fold-and-cleavage development. Bedding-parallel veins occur interbedded between two contrasting lithologies, as well as intrabedded in the competent and incompetent sequences. Macroscopically, the veins show a composite internal fabric consisting of several distinct generations of quartz laminae, often marked by slickenlines, intercalated with thin pelitic wall-rock inclusion seams. It is concluded that the bedding-parallel veins formed by several, whether or not alternating, mechanisms of bedding-normal uplift and bedding-parallel thrusting. The latter mechanism is evidenced by, NNW- to NW-directed, displacement of bedding-normal veins, small-scale ramps and numerous slickenlines on the different quartz laminae internally in the veins. It is interpreted that this vein type is the first brittle expression of the compressional stress regime affecting the siliciclastic metasediments of the North Eifel at the onset of Variscan shortening. In this configuration, the bedding-parallel veins demonstrate a particular stress-state in the basin at the time of vein formation in which the maximum principal stress σ_1 was oriented parallel to a presumably NW-SE-oriented tectonic compression σ_T and in which the minimum principal stress σ_3 corresponded to the vertical load of the overburden.

The succession of bedding-normal to bedding-parallel extension quartz veins thus materialises the transition from extension to compression at the onset of the Variscan orogeny and can be interpreted to have been formed during early orogenic compressional tectonic inversion. This inversion is expressed differently in the central part of the slate belt (Ardennes, Belgium) in which the psammites between the bedding-normal veins deformed in a ductile way into mullions.

Subsequently, during progressive Variscan contraction both vein types were passively folded within characteristic, NW-verging, upright to overturned folds of the North Eifel. Locally, deformation of bedding-normal veins or reactivation along the bedding-parallel veins may have taken place because of flexural-slip or flexural-flow folding. In contrast to both extensive veining events that characterise the tectonic inversion, quartz veining occurred rather occasionally during the main compression stage of the orogeny. Local vein emplacement only occurred for instance in the necks of boudinaged layers, as tension gashes in fold hinges or related to local faulting.

Although this evolutionary history already gives a tentative overview on how the veins developed, still many research questions remain unsolved and need to be unravelled in order to substantiate the constructed evolutionary model. Macroscopic observations, either on outcrop- or hand-scale, can only reveal the relative spatial and temporal relationship of the veins with respect to minor structures and fold and cleavage development.

To refine the vein opening mechanisms, further research has focused on a microstructural analysis of vein microstructures and is reported in the next chapter. This microstructural research allowed confirming if the veins are indeed extension veins and if it is justified to use them as a tool to reconstruct the palaeostress evolution (Chapter 4). Furthermore, as a macroscopical analysis of the veins does not provide information on the fluids from which the veins precipitated, it is important to also focus on a microthermometric analysis of the fluid inclusion of the vein quartz (Chapter 5) which eventually allows implementing the role of the pore-fluid pressure in the different proposed models for the two vein types (Chapter 6). However, to perform a microthermometric analysis properly, a detailed petrographic analysis of the fluid inclusions has been carried out first (Chapter 4).

CHAPTER 4 Microstructural fabric analysis

4.1 Introduction

In this chapter, the results of a detailed fabric analysis are presented to work out in more detail the evolutionary model constructed after the macroscopic geometric structural analysis. This allows characterising a paragenesis in vein infill for both bedding-normal and bedding-parallel veins and deducing the deformation mechanisms and conditions active after vein infill. To determine the state of stress in the upper crust at the time of bedding-normal quartz veining, more than 500 bedding-normal veins have been measured in the field during the macroscopic structural analysis and have been rotated to their original position in the orientation analysis (Chapter 3). Also dozens of examples of cross-cutting bedding-parallel quartz veins have been studied in the field. It is not possible and opportune to describe them all in this microscopic analysis. In order to avoid repetition, only those veins are described that are representative of a specific type of vein infill. Therefore, thin sections of representative vein samples were carefully selected and investigated by means of a petrographic microscope under both plane-polarised and cross-polarised light.

In the fabric description, mineralogy of the host-rock, vein fabric of mineral infill and microstructures, related to deformation, of bedding-normal and bedding-parallel vein quartz are discussed. Terminology used for the different fabrics and inclusions is explained in BOX III by referring to literature. A further subdivision into different vein types is mainly based on the microscopic vein fabric of both bedding-normal and bedding-parallel veins. On the one hand, the bedding-normal veins are subdivided into three different types depending on their width, *i.e.* hairline, centimetre and composite veins. Bedding-parallel veins, on the other hand, are subdivided depending on their relation with the surrounding host rock, *i.e.* thin intrabedded and thick interbedded veins. Furthermore, as a link to Chapter 5, in which temperature and pressure conditions of veining are reported, a comprehensive petrographic analysis of fluid inclusions is presented in this chapter to select those fluid-inclusion trails that are representative of vein growth and subsequently can be used for microthermometry. This petrographic analysis of fluid inclusions is carried out on doubly polished 150 µm thick wafers from oriented vein-quartz samples, which allows observing 3D orientations of fluid-inclusion planes, an advantage compared to the 2D fluid-inclusion trails seen in thin sections.

4.2 Mineralogy of the host rock

In the macrostructural analysis, the host-rock lithology adjacent to the veins was only determined roughly in the field. Both vein types are embedded in two lithologies: a fine- to coarse-grained sandstone and fine-grained siltstone. Bedding-normal stratabound quartz veins are restricted to the competent coarse-grained sandstone beds whereas non-stratabound veins always refract at the competent-incompetent interface, with their vein tips within the incompetent siltstones accompanying the sandstones. Bedding-parallel veins occur intrabedded in the sandstone or siltstone and interbedded at the interface of these lithologies.

As the mineralogy and the infill of the veins is studied in this chapter, it would also be interesting to refine the mineralogy found in the adjacent host rock in order to determine if the host-rock mineralogy corresponds to the one observed in the veins. Fracturing and veining are strongly dependent on the lithological properties and rock permeability. Therefore, the shape (sphericity and roundness) and the degree of sorting of the detritical grains have been estimated by using the image analysis software *JMicrovision* (Roduit 2008). Also the volume of quartz grains and quartz cement can be calculated in this program. Common grain sizes have been used for the description of the lithology. Additionally to the representative samples of the outcrops studied around the Rursee and Urftsee, also several representative samples of some outcrops in the central part of the High-Ardenne slate belt (cHASB) are described. The main reason to study the host rock is because later in this work (see Chapter 7) the vein spacing distribution observed in outcrops studied in the North Eifel are compared to the intermullion vein spacing in the cHASB.

The results show that the competent host-rock lithology in the Eifel area can be classified as a fine- to medium-grained quartzwacke, in which the quartz grains mostly are subrounded to subangular and moderately to well sorted (Figure 4.1a to h; Table 4.1). Almost all grains exist of quartz with a grain size varying between 50 µm and 350 µm. They are single detrital crystals with uniform interference colours showing that the quartz grains in the sandstone remained undeformed. The grains are cemented by quartz cement. In some samples, biotite grains have been observed (Figure 4.1e and f). Stretching and reorientation of the quartz grains due to compaction and deformation, such as described in the competent units of the Monschau Unit (Mukhopadhyay 1973, Spaeth 1969), have not been observed. Because of weathering, the rock has often a brownish to rusty aspect. The very fine-grained matrix between the quartz grains consists of minor amounts of elongated phyllosilicates, such as muscovite, biotite and chlorite. Sometimes mica (muscovite) is visible with the naked eye, however, too small amounts have been observed in thin section to define the competent host rock as a psammite. The incompetent host-rock lithology, defined as siltstone in the field, is a fine-laminated slate with a very well-developed continuous penetrative cleavage (Figure 4.1i). The siltstone is dominantly characterised by planar mica flakes, chlorites and small quartz grains (Figure 4.1j). Traces of feldspar have only been detected by XRD (cf. Holland *et al.* 2006). In the cleavage domains, micas are defined and are mostly aligned. In the clay-rich horizons between the cleavage domains, particles are too small to determine additional minerals that may be present.

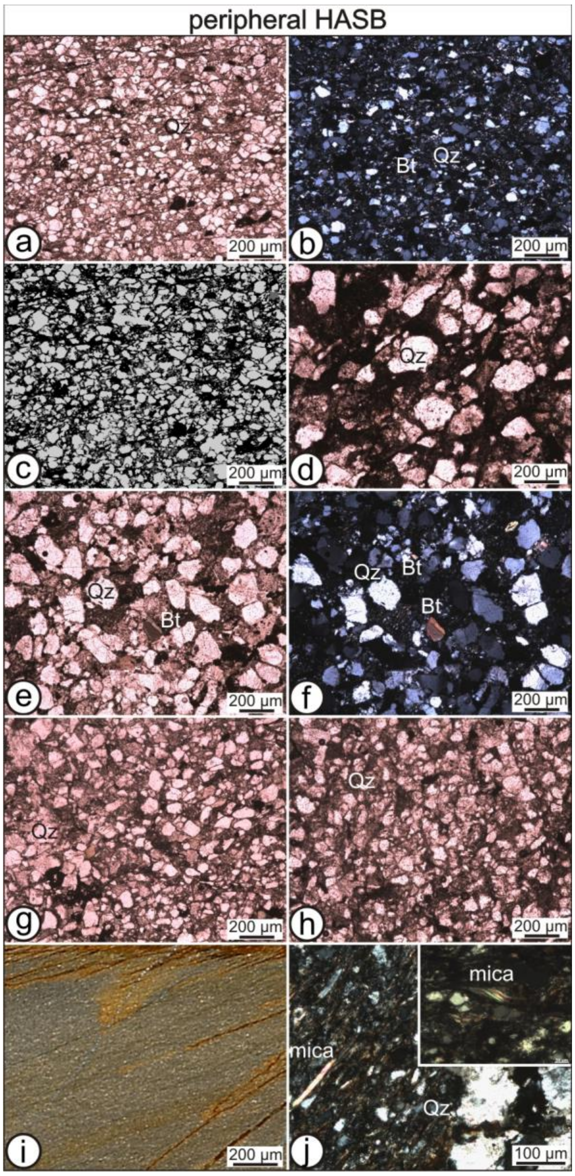

Figure 4.1: Representative microphotographs of the host rock of the different outcrops studied in the Rursee and Urftsee area. See Table 4.1 for the description of the samples. sdst: sandstone; Qz, quartz; Bt, biotite. **(a-c)** Fine-grained sandstone (Hubertus Höhe) in (a) plane polarised light, (b) under crossed polars and (c) *JMicrovision* (Roduit, 2008) used for estimating the percentage of quartz grains (light-grey: 42%) and quartz cement (dark grey: 16%). **(d)** Medium-grained sandstone (Wildenhof). **(e-f)** Medium-grained sandstone (Eschaulerberg) in (e) Plane polarised light and (f) under crossed polars. **(g)** Fine-grained sandstone (Schwammenauel). **(h)** Fine-grained sdst (Urftsee). **(i)** Siltstone with penetrative cleavage (Schwammenauel 72). **(j)** Siltstone with micas (mainly muscovite) in cleavage domains. The inlet shows a mica fish (Hubertus Höhe 77).

The host rock in the cHASB varies from fine-grained sandstone in the anchizone to quartzite in the epizone of the HASB (see studied samples in Table 4.1). The sandstone shows a fine-grained matrix, consisting of mainly quartz grains (Figure 4.2; Table 4.1) and minor amounts of feldspar, biotite, ilmenite and phyllosilicates of which muscovite and chlorite could be recognised. This mineralogy defines the competent units as psammites (Kenis 2004). In general, the quartz grains in the sandstone are mostly well sorted, subrounded to subangular and often show undulose extinction. They are altered by preferential dissolution and overgrown by quartz in strain fringes. Grain aggregates are frequently overgrown by phyllosilicates beards (Kenis *et al.* 2005a). Percentage of quartz grains and quartz cement corresponds to the sandstones in the pHASB. However, percentage of quartz grains in the quartzites is much more difficult to estimate as individual grains are difficult to recognise and are overgrown by the recrystallised quartz cement.

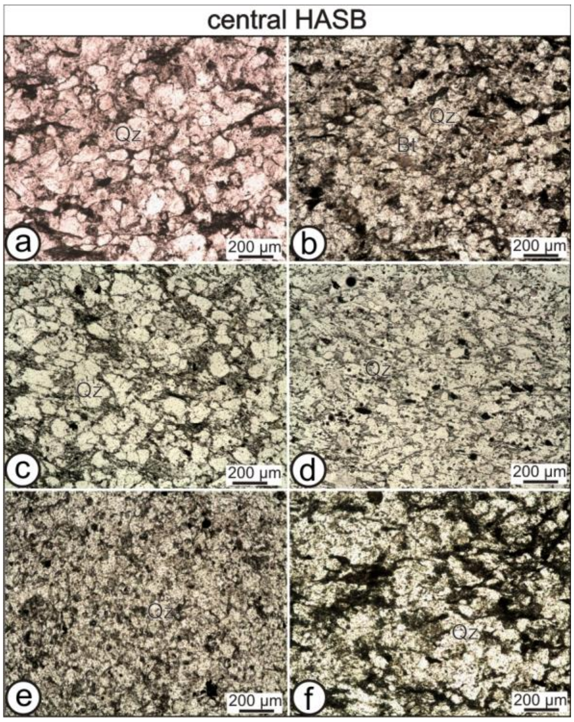

Figure 4.2: Representative microphotographs of the host rock of the different outcrops studied in the central part of the High-Ardenne slate belt as a comparison to the Rursee and Urftsee area. See Table 4.1 for description of the samples. **(a)** Medium-grained sandstone (Dedenborn). **(b)** Fine-grained sandstone (Boeur). **(c)** Quartzite (Bastogne Mardasson). **(d)** Quartzite (Remagne). **(e)** Quartzite (Bastogne Sur Les Roches). **(f)** Quartzite (Bertrix).

Table 4.1: Host rock and adjacent lithologies of the different outcrops studied compared to the host-rock lithologies of other areas in the North Eifel and the Ardennes. The image analysis software *JMicrovision* (Roduit, 2008) has been used for estimating the volume of quartz in each representative sample. An error of 5% has been estimated by regenerating the image and recalculating the volume of quartz in the sample. See Appendix B for sample localities. med-gr.: medium-grained; sdst, sandstone; slst, siltstone; pel, pelite; sphericity (Sph): low (LS), medium (MS), high (HS); roundness (Rnd): subangular (SA), subrounded (SR). See Appendix B for sample localities.

Locality	Data set	Formation / Unit	Sample	Layer lithology	% Qz grains	% Qz cement	% Qz	Sph	Rnd	Degree of sorting	Adjacent layer lithology
Rursee	Wildenhof 44a	Upper Rurberg	EI06VN08	med-gr. sdst	36	21	57	MS	SA	poorly	slst
Rursee	Eschaulerberg 64	Upper Rurberg	EI05VN34	med-gr. sdst	44	29	72	LS	SA	mod	slst
Rursee	Hubertus Höhe 72	Upper Rurberg	EI05VN36	fine-gr. sdst	42	16	59	HS	SR	well	pel
Rursee	Schwam. 93	Upper Rurberg	EI05VN43	fine-gr. sdst	46	19	64	HS	SR	well	slst
Urftsee	Zone 7	Heimbach	EI08VN26	fine-gr. sdst	37	25	62	HS	SR	well	slst
Eifel	Dedenborn	Middle Rurberg	EI05VN17	med-gr. sdst	51	29	80	HS	SA	mod	pel
Ardennes	Bütgenbach	Neufchâteau	BU05VN01	fine-gr.sdst	-	-	-	-	-	-	pel
Ardennes	Houffalize	Neufchâteau & Longlier	-	sandstone	-	-	-	-	-	-	pel
Ardennes	Boeur	Longlier	Boe 5	sandstone	49	22	71	MS	SA	well	pel
Ardennes	Bast. Coll.	Anlier	-	quartzite	-	-	-	-	-	-	slst/pel
Ardennes	Bast. SLR	Anlier	SLR 10	quartzite	46	28	73	HS	SR	well	slst
Ardennes	Bast. Mardasson	Anlier	BAMAR 8b	quartzite	59	25	84	HS	SA	well	slst
Ardennes	Rouette	Anlier	-	psammite	-	-	-	LS	SA	poorly	slst
Ardennes	Remagne	Oignies	Rem 3 A08	quartzite	51	29	79	MS	SR	well	pel
Ardennes	Bertrix	Saint-Hubert	Ber 8b	quartzite	35	30	65	HS	SR	mod	pel

4.3 Bedding-normal veins

4.3.1 Mineralogic composition of the veins

The bedding-normal veins (BNVs) studied in the Rursee almost exclusively consist of quartz. Different crystal shapes, such as fibrous, stretched, elongate-blocky and blocky, and several growth mechanisms have been recognised for the vein quartz. Also within the quartz grains, numerous fluid inclusions, deformation microstructures and host-rock inclusions have been observed. The overall part of the veins can thus be considered as monomineralic veins. In addition to quartz, sometimes chlorite occurs as mineral booklets (Figure 4.4k and Figure 4.5). In plane polarised light the chlorites have a greenish colour, whereas under crossed polars they change in colour, alternating between a bluish and a white colour. Chlorite fibres tracking the opening direction (*e.g.* Becker *et al.* in press) have not been observed. Chlorites only occur at the vein walls and never in the vein (Figure 4.4k and Figure 4.5i). Furthermore, calcite crystals have only been observed rarely in some BNVs from the Urftsee outcrops. During hot cathodoluminiscence petrography, the quartz grains in the competent host rock as well as the quartz minerals in the veins all have a similar dark blue luminescence. Differences in colour or fabric have not been observed.

4.3.2 Vein fabric

It is concluded from the different case studies that the bedding-normal veins are various in shape and thickness. **Hairline**, millimetre-thick veins have been observed in thin competent layers, closely alternating with narrow spaced fractures that have the same orientation as the hairline veins. The most observed bedding-normal veins are **centimetre**-thick veins that have an approximate mean thickness of ~1 cm and vary from a planar to a lensoid shape. Macroscopically, they consist of milky-white quartz without any host-rock inclusion lines or fragments visible with the naked eye or in thin section. Thick, several centimetre-thick, **composite** veins occur less frequently and are only observed in thicker competent layers. They consist of multiple quartz laminae intercalated with host-rock inclusion lines. In what follows, these three different vein types are discussed by studying their microstructures and growth mechanisms.

BOX III - Terminology of vein fabric and growth mechanisms

Early- to syntectonic calcite and quartz veins are common features in very low-grade to low-grade metamorphic terrains. It is well established that veins initiate as fractures and can evolve to many different fabrics with considerable size differences. It is not the intention to give a full overview on the geometry of veins, but rather to shortly quote the common terms. In this description the term grain is used to refer to the ‘crystal’ within the vein microstructure and does not refer to the ‘detrital grain’ such as in the host rock. Many veins are oriented at high angle to their opening direction and are therefore termed as **extension veins**. If a vein opens at a small angle to bedding, it is known as a **shear vein** (Ramsay & Huber 1983).

Extension veins have a very recognisable internal fabric that consists of aligned or repeated internal host-rock structures embedded in fibrous crystals. Ramsay (1980) originally defined that many extension veins form by accretionary processes involving the formation of a narrow fracture followed by fibrous infill of the fracture by crystalline material. This describes how extension veins are formed by the **crack-seal mechanism**. Veins attributed to this mechanism are commonly considered to form due to oscillations in fluid pressures and/or in bulk strain. Because of its widespread occurrence, this mechanism has been investigated and described in many studies (*e.g.* Boullier & Robert 1992, Cox 1987, de Roo & Weber 1992, Fisher & Brantley 1992, Hilgers & Tenthorey 2004, Laubach *et al.* 2004b, Reed & Laubach 2005, Renard *et al.* 2005, Wiltschko & Morse 2001). Unfortunately, through time, Ramsay’s crack-seal mechanism has evolved from a vein-forming mechanism into a vein fabric although it is still originally defined as a mechanism. Nevertheless, the original fabric by which Ramsay demonstrated the crack-seal mechanism has found its way in many textbooks on structural geology and is widely used.

BOX III (continued)

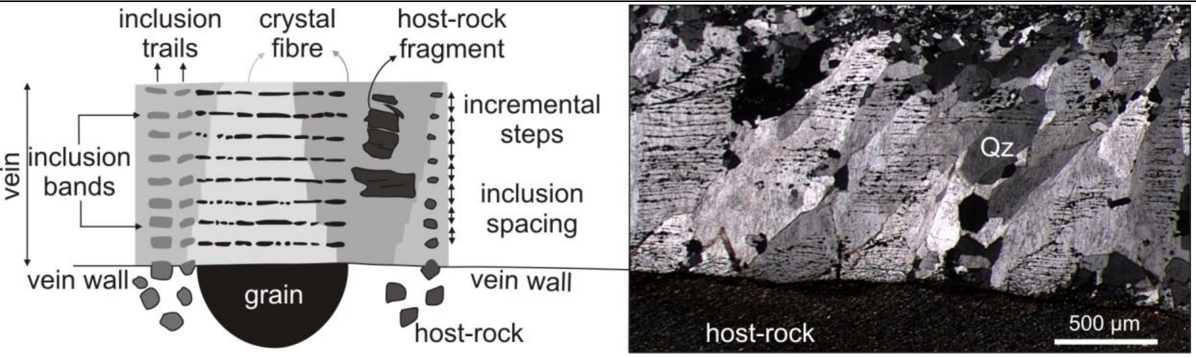

The overall result of the crack-seal mechanism is a succession of many small increments visualised by the alignment of host-rock inclusion trails and inclusion bands. **Inclusion trails** are interpreted to be series of aligned grain fragments that are oriented parallel to the displacement direction of the opening of the vein. They result from repetitive opening, the ‘*crack*’, and immediately infill of the crack, the ‘*seal*’. **Inclusion bands** are mostly dark seams that are arranged perpendicular to the displacement direction and nearly parallel to the vein wall.

They consist of aligned fragments of different grains present in the host rock, but can also exist of aligned fluid inclusions. Similar as inclusion trails, these inclusion bands reflect episodic vein opening as indicated by the inclusion spacing of the inclusion bands. Typical openings, as deduced from inclusion spacing, are generally in the order of several micrometres to tens of micrometres (Cox & Etheridge 1983, Cox 1987, Hilgers & Urai 2002, Renard *et al.* 2005, Wiltschko & Morse 2001, Xu 1997). The alignment of these inclusion trails and bands are better indicators of the opening of the vein, than the orientation of the **crystal fibres** that grow at high angle to the vein wall during the repeated phases of sealing (Urai *et al.* 1991). The grain boundary of these fibrous crystals has a typical saw-tooth crystal habit. Hilgers & Urai (2005), moreover, noted that the fabric of crystal fibres in crack-seal veins actually does not show a consistent aspect ratio and is thus not fibrous sensu stricto, but rather elongate or columnar.

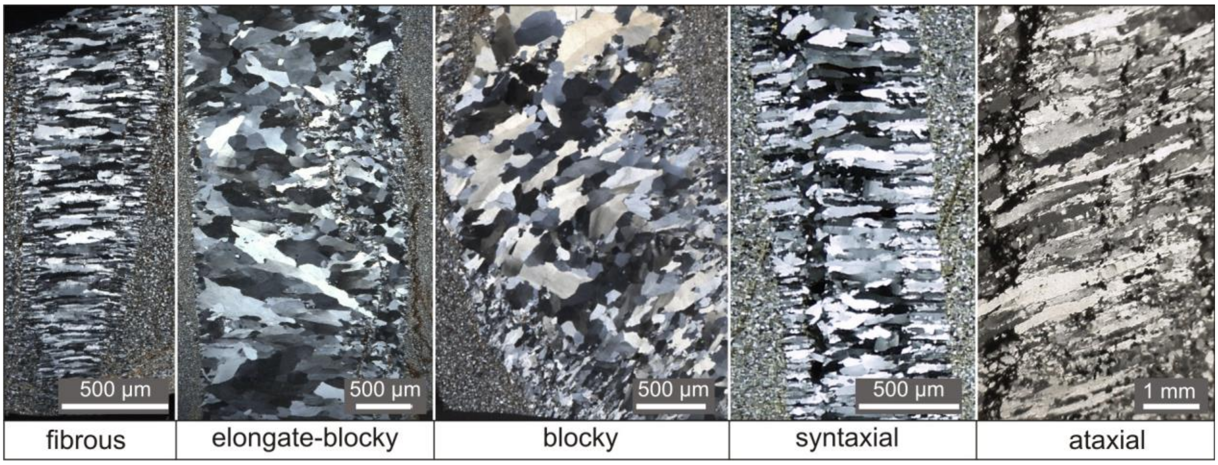

fibrous	elongate-blocky	blocky	syntaxial	ataxial

Veins that lack the typical repetitive pattern of inclusion bands and trails that indicate crystal growth by the crack-seal mechanism, are termed **fibrous veins** (Bons 2000, Means & Li 2001). They contain micrometre thin crystals that are continuous from vein wall to vein wall without changing in thickness and commonly show very high aspect ratios (length/width). They moreover maintain a continuous optical orientation along the fibrous **crystal elongation** and show no indication of growth competition (Cervantes & Wiltschko 2010, Means & Li 2001). The optical continuity of fibrous crystals can be interrupted in areas in which a particular fibre is irregular in shape. Whether the crystal elongation determines the relative motion of the opening of the vein or not, mainly depends on the roughness of initial fracture surface (Nollet *et al.* 2005a, Urai *et al.* 1991).

BOX III (continued)

Also, whether these specific fibrous or other fabrics develop, clearly depends on the relative opening rate of the fracture with respect to the fracture infill and the opening width of the fracture (Mügge 1928 in Hilgers *et al.* 2001).

Crystallographic controlled growth competition is typically observed in an **elongate-blocky** fabric (Bons 2000, Fisher & Brantley 1992). This microstructure is distinct from fibrous veins by its specific mineral habit that evolves from small crystals grown on ‘seed’ crystals at the vein wall, to elongate crystals with an aligned crystal elongation that have overgrown their neighbour crystals towards the centre of the vein. Such a fabric can eventually evolve into fully **blocky** in which all grains are equidimensional and randomly oriented. Veins often do not display one microstructure, but may contain several ones in which the crystals grow from one fabric into another (*e.g.* fibrous to elongate-blocky to blocky).

Furthermore, apart from the previously described common vein microstructures, following observations are indicative of the **vein growth morphology** and indicate a growth mechanism (Durney & Ramsay 1973). In an **antitaxial** vein, crystals grow from the centre of the vein towards the vein wall. The centre is marked by a **median line** defined by small equidimensional grains or fragments of the wall rock. The material that precipitates is often from a different composition than the minerals in the host rock which causes a discontinuity at the vein wall. Such vein growth has not been observed. A second growth mechanism concerns **syntaxial** veins, which are characterised by the reverse growth mechanism as antitaxial veins, namely from the vein wall towards the **median line** in the centre of the vein. The median line usually represents a thin fracture plane on which material is precipitated. Syntaxial veins can be symmetric or asymmetric. Contrary to the discontinuity at the vein wall in antitaxial veins, syntaxial veins comprised crystals that have grown **epitaxially** from the grains of the host rock. The major constituent in the veins is thus similar as the mineralogy of the host rock. In extreme cases crystals grow from one side of the vein to the other side only. Such veins are defined to have a **unitaxial** fabric and lack a median line (Fisher & Byrne 1990, Hilgers *et al.* 2001). In **ataxial** veins, fibrous crystals cross the vein from one vein wall to the other and are optically continuous, a specific fabric that is defined as **stretched** crystals. Ataxial veins also initiate as epitaxial overgrowths of grains from the vein wall (Hilgers & Urai 2002). It is interpreted that growth occurs by repetitive fracturing at different sites, in which they lack a localised growth surface such as on the median plane in syntaxial veins. Theoretically, if several growth mechanisms are combined in a vein, it is termed a composite vein (Passchier & Trouw 2005). However, in this work a **composite vein** refers to vein formation due to repetitive fracturing and sealing phases and comprise several quartz laminae intercalated with inclusion seams.

4.3.2.1 Hairline veins

Centimetre-thick layers often comprise closely spaced millimetre-thick healed microfractures that are defined as hairline veins. The vein walls of these healed microfractures, and those of non-mineralised fractures that occur parallel to the hairline veins in the same host-rock layer, have rough wall-rock morphology (Figure 4.3a and b). Fibrous quartz crystals in the hairline veins mostly span the entire millimetre vein thickness, characteristic of unitaxial mineral infill in which the crystal elongation tracks the vein opening direction perpendicular to the vein wall (Figure 4.3b, c and d). In medium-grained parts of the host rock, these crystal fibres are thicker than compared to the fine-grained parts (Figure 4.3c). Quartz fibres have grown epitaxially on grains from the wall rock, with a preserved optical continuity along the fibre length and connecting host-rock grains with a similar optical continuity (Figure 4.3d). Absence of a median line as growth surface and absence of host-rock inclusion bands indicate that fracturing rate was higher than the precipitation rate during vein growth. It is also obvious that the initial fracture has cut through the host-rock grains (Figure 4.3d), rather than fracturing around the grains, and that these trans-granular hairline veins are mostly characterised by a low tortuosity. This low tortuosity demonstrates that fracturing, and hence bedding-normal vein formation, is not affected by the grain-scale heterogeneity of the competent host rock. Sometimes buckled hairline veins are observed next to planar fractures and veins (Figure 4.3e and f). Internally, they consist of an elongate-blocky mineral infill, resulting from growth competition during crystal growth (Figure 4.3g). Crystals in this buckled part, show, moreover, similar characteristics than crystals in the planar part. This demonstrates that irregular opening is a fracture mechanism and is not caused due to further post-veining compaction or subsequent deformation. Sometimes bedding-parallel dissolution surfaces cross-cut the non-mineralised fractures and the planar to buckled hairline veins (*e.g.* Figure 4.3f and h), exemplifying that dissolution still occurred during bedding-normal veining. Other compaction features such as compaction halos (cf. Price & Cosgrove 1990, p. 421) indicative of deformation around (deformed) objects have not been observed.

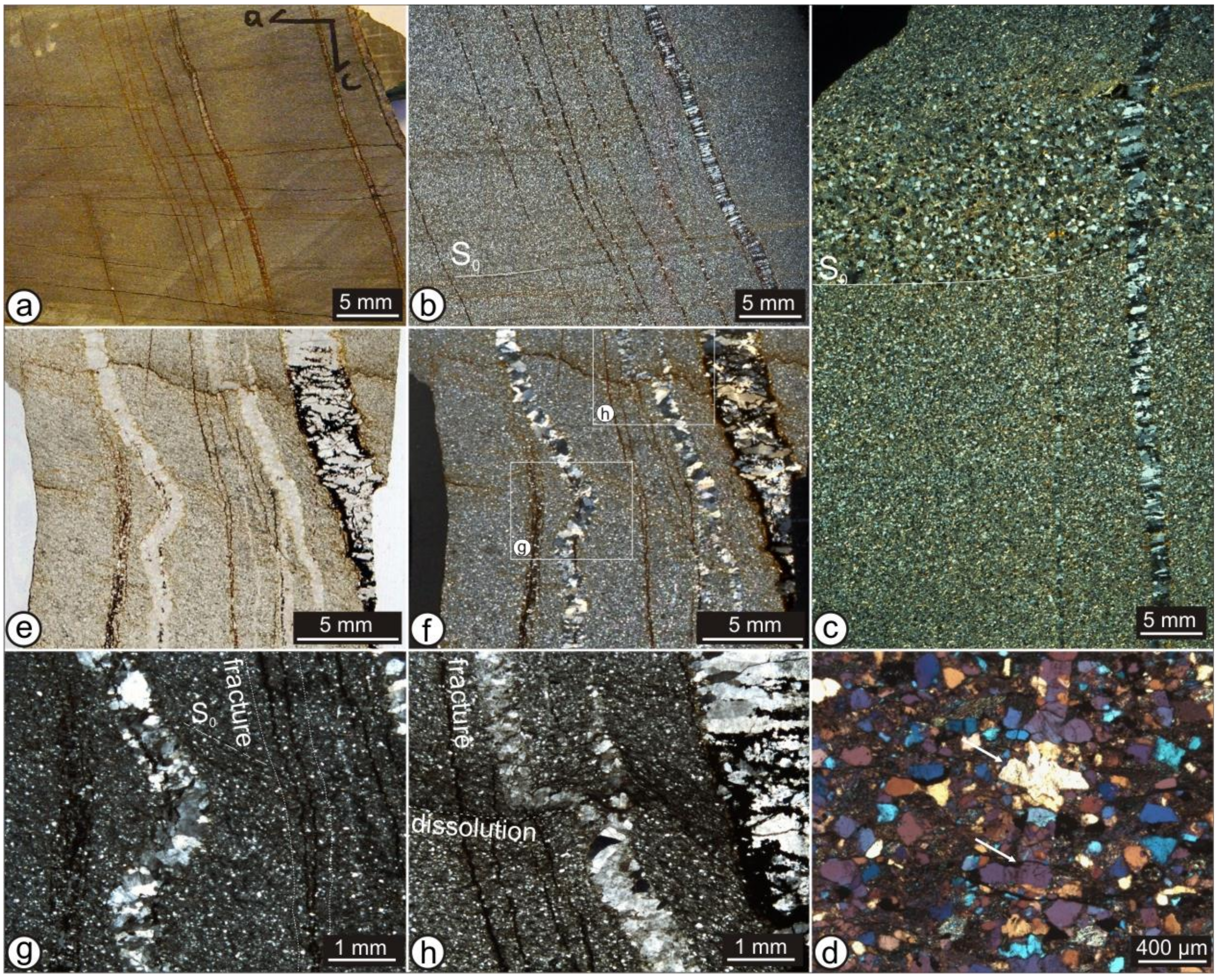

Figure 4.3: Habit and fabric in millimetre-thick hairline quartz veins. See Appendix B for sample localities. **(a-b)** Parallelism of fractures and hairline veins characterised by a fibrous infill (V_B generation; Wildenhof 10: see Figure 3.7f; EI07VN18). **(c)** Hairline vein with thicker quartz fibres in the medium-grained part than in the fine-grained part (Hubertus Höhe 72; EI07VN08). **(d)** Trans-granular hairline fracturing through host-rock grains (white arrows) indicative of absence of influence of the heterogeneity of the host rock. Fibres grow epitaxially on host-rock grains with identical optical continuity (Hubertus Höhe 68; EI05VN36). **(e-f)** Occurrence of planar fractures and planar to irregular hairline veins (Hubertus Höhe 77; EI05VN38). **(h)** Detail of (f) showing elongate-blocky to blocky infill in the planar and buckled parts of the hairline vein indicating opening at high angle to the vein wall. **(g)** Detail of (f) showing local dissolution of the buckled vein at a stylolitic surface.

4.3.2.2 Centimetre veins

The majority of the veins studied in the North Eifel are centimetre veins with a vein width of ~1cm. They show several important microstructural elements from which mechanism of vein growth can be deduced. First of all, irrespective of the vein generation from which the vein infill is studied (V_B or V_C in the different case studies), both syntaxial (Figure 4.4b and g) and ataxial (Figure 4.4e) crystal growth are recognised in these centimetre-thick veins. Syntaxial veins are observed in the planar V_B and cross-cutting V_C generation (Figure 4.4b). In syntaxial veins, it is observed that vein growth can consist of two phases: a first phase with a fibrous and a second phase with an elongate-blocky to blocky fabric (Figure 4.4b and g). Owing to the elongate-blocky infill, a median line is not present. In some veins, crystals evolve from elongate-blocky at the vein wall to blocky in the middle part of the vein, indicating that the fracture opening rate must have increased with respect to the growth rate of the crystals. A two-phase syntaxial infill has also been observed in lensoid centimetre veins (Figure 4.4j). In a specific section in which a cross-cutting relationship is observed in the bedding plane, fibrous crystals of V_C have grown epitaxially on the fibrous crystals of V_B and remain continuous in crystallographic orientation along the transition from V_B to V_C (Figure 4.4c and d). The angle of the deflected fibres mainly depends on the orientation of both veins (Figure 4.4c and d). The microstructural fabric of cross-cutting veins always confirms the cross-cutting relationship that was observed in the field (*e.g.* Figure 4.4a and b corresponding to Figure 3.13a).

The ataxial veins comprise stretched fibrous crystals that connect both vein walls with a continuous crystallographic orientation. Fibres have clearly grown epitaxially on the host-rock grains. Along the fibre elongation, the optical continuity of the stretched fibres is sometimes interrupted in particular areas in which a fibre is irregular in shape. In both syntaxial and ataxial veins, fibre contacts are smooth or serrated, *i.e.* saw-tooth fibre contacts (Figure 4.4h). Neighbouring fibres are sometimes characterised by briquette-like internal microstructures along the fibre contacts (Figure 4.4i), representative of small misfits during fibre growth (cf. Ramsay & Huber 1987, p. 248, Stowell *et al.* 1999). Fibres may widen towards the vein centre, allowing other fibres to develop. Another very characteristic feature of centimetre-thick veins is the repetitive pattern of crack-seal host-rock inclusion bands (Figure 4.4i) oriented parallel to the vein walls and perpendicular to the fibre elongation. Inclusion bands are continuous through several fibres, or are discontinuous and restricted to a single fibre (Figure 4.4i). Nevertheless, in both cases these host-rock fragments reflect episodic vein opening by the crack-seal mechanism and track vein opening trajectory perpendicular to the vein wall. Spacing of the host-rock inclusion bands is mostly ranges between 10 μm and 20 μm. Inclusion banding has been observed in syntaxial and ataxial veins.

Furthermore, when chlorites are observed within centimetre-thick veins, they always occur as chlorite booklets at the vein-wall interface and have nucleated on phyllosilicates in the vein wall (Figure 4.4k). The relationship of chlorite growth with respect to quartz growth is ambiguous in the veins.

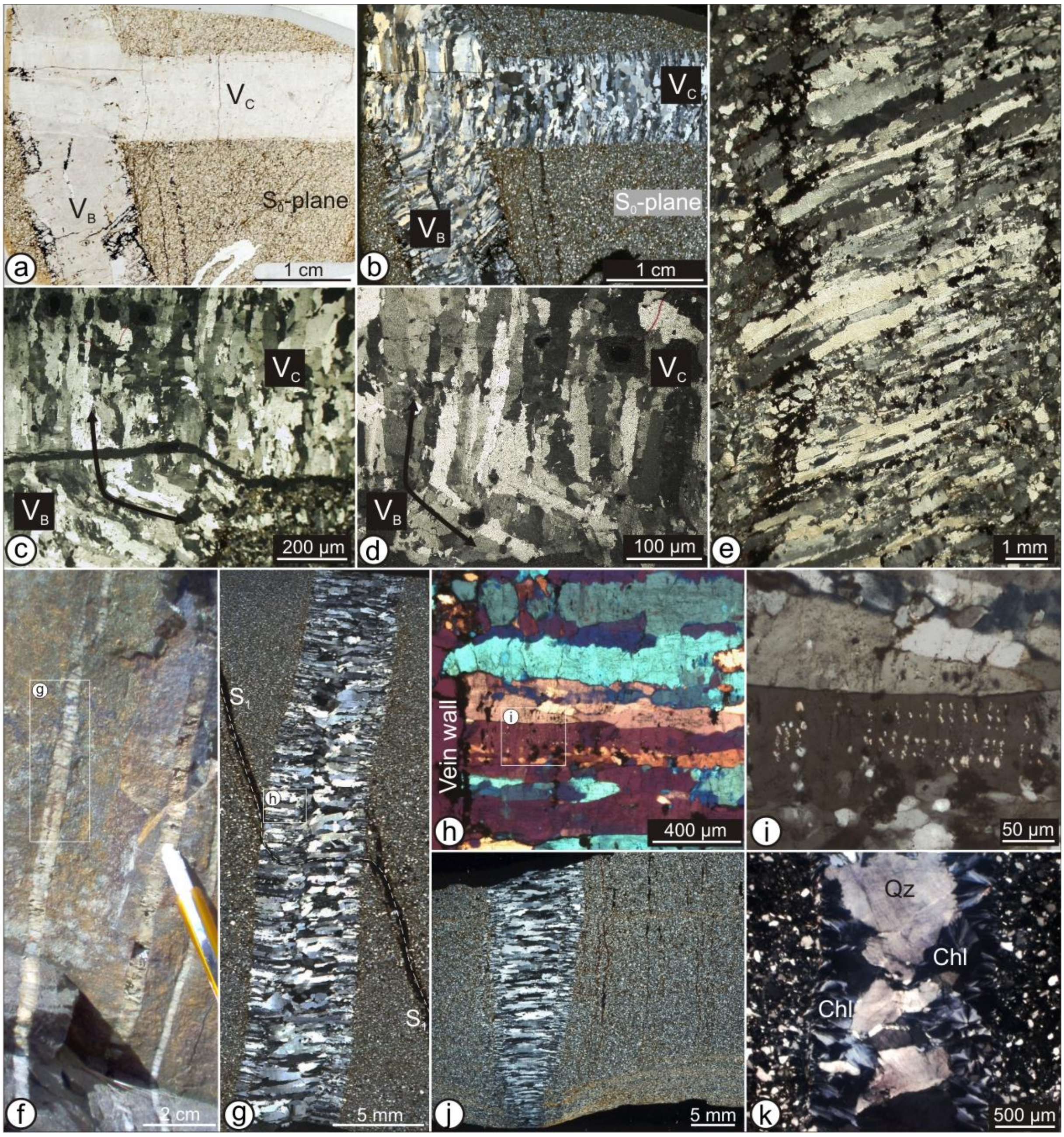

Figure 4.4: Habit and fabric of monomineralic centimetre-thick quartz veins. See Appendix B for sample localities. **(a-b)** Cross-cutting relationship between syntaxial veins V_B and V_C. V_B has a fibrous vein fabric, whereas V_C consists of a first fibrous and a second elongate-blocky microstructure (Wildenhof 27: see Figure 3.13a; EI06VN19). **(c-d)** Fibrous crystals in V_C that have grown epitaxially on fibrous crystals of V_B (black arrow) (Wildenhof 27; EI06VN19). **(e)** Fibrous crystal spanning the vein walls, ataxial vein growth (V_B; Wildenhof 44: see Figure 3.8b; EI06VN08). **(f-g)** Centimetre-thick vein showing syntaxial vein growth of a first phase with fibrous and a second phase with a elongate-blocky to blocky fabric in the centre of the vein. Cleavage refracts through the vein (Hubertus Höhe 68a; EI05VN34). **(h)** Fibrous fabric with serrated fibre edges and briquette-like microstructures (detail of g). **(i)** Discontinuous host-rock inclusion banding. Spacing of inclusion bands of 10 µm (detail of h). **(j)** Syntaxial, fibrous lensoid vein (EI07VN04; Hubertus Höhe 71: see Figure 3.32a). **(k)** Chlorite booklets at the vein wall, blocky quartz crystals in centre of the vein (en-echelon vein at Hubertus Höhe 74: see Figure 3.32f; EI05VN10).

4.3.2.3 Composite veins

Composite veins comprise all veins that have a thickness of one to several centimetre and that consist of several quartz laminae intercalated with macroscopically visible host-rock inclusion lines, giving the veins a dirty appearance. In thin section, these composite veins consist of several phases of vein infill, indicative of successive and recurrent vein opening. Several different types of composite veins have been observed. It was concluded from the macroscopic geometric analysis that if a non-stratabound vein exceeds the bedding plane of a layer, it refracts at the competent-incompetent interface. In a fibrous composite vein (Figure 4.5a) this refraction is exemplified by deformation of the fibrous infill in the siltstone whereas fibres in the competent part of the vein remain continuous in crystallographic orientation along the fibre length. The opening of the vein can moreover be deduced by the millimetre displacement of bedding at both vein walls, indicating an opening trajectory at high angle to the vein walls (Figure 4.5a). In other examples, composite veins may consist of elongate-blocky crystals at the vein wall, rapidly evolving to a fully blocky fabric in the centre of the vein (Figure 4.5b).

At the vein tip of thicker composite veins, often multiple strands of vein arrays occur, giving the vein a laminated appearance (Figure 4.5a and e). The fibrous infill of the middle part of the veins, as well as in the multiple vein tips illustrates a similar opening mechanism. However, a composite vein with an elongate-blocky fabric, in which crystals have preferentially grown on top of other neighbouring crystals, may occur next to a composite vein that is characterised by a fibrous infill (Figure 4.5e). In both cases, irrespective of the vein fabric, the opening of the vein is at high angle to the vein wall. The difference in fabric can be explained by differences in the fracture rate versus growth rate, rather than in different vein mechanisms. A fibrous infill is interpreted to have been formed during numerous fracture and sealing phases during which the growth velocity was faster than the fracturing velocity. This relationship is also the driving mechanism for the elongate-blocky veins, but occurs at a crystal growth velocity lower than compared to the fibrous vein (cf. Hilgers *et al.* 2001). Nevertheless these differences in ratio, both vein fabrics are representative of a syntaxial vein mechanism.

Composite veins comprise long inclusion lines subparallel to the vein wall, visible on a hand specimen (Figure 3.32b and c; Figure 4.5f) or in thin section (Figure 4.5g). These inclusion lines consist of micrometre-scale micas and other clayey aggregates. These inclusion lines are torn from the host-rock wall and form a growth surface for new quartz laminae in composite veins, irrespective if the vein is characterised by a fibrous (Figure 4.5f and g) or an elongate-blocky to blocky fabric (Figure 4.5h). Within the laminae, obliquely oriented fibres maintain a continuous crystallographic orientation along their elongation, showing that the obliquity is a growth feature and not a deformation feature formed during subsequent deformation. This fabric is also observed in the en-echelon vein at Hubertus Höhe in which the oblique fibre growth (Figure 4.5j) is in agreement with the macroscopic dextral shear observed in the field (Figure 3.32h and i). The en-echelon vein is moreover characterised by chlorite booklets abundantly present at the vein wall and at host-rock inclusion fragments and lines in the vein. In both cases chlorite has formed preferentially on the phyllosilicates present in the host-rock fragments or in the vein wall.

To conclude, the composite nature of the veins suggests that they formed due to numerous successive fracturing and sealing phases reflecting episodic vein growth in which the vein fill mainly depends on competition between the ratio of fracturing rate and precipitation rate. It may even be possible that composite veins initially grew separately as thin veins and became interconnected after successive phases. In many composite veins, the fibre elongation is oriented perpendicular to the median line and may have grown obliquely to the inclusion lines.

Figure 4.5: Habit and fabric of mainly monomineralic composite quartz veins. **(a)** Vein refraction at the competent-incompetent interface. Deformed crystals in the refracted part of the vein (Urftsee zone 7: see Figure 3.38c; EI08VN26). **(b)** Blocky fabric (Hubertus Höhe 73; EI07VN11). **(c)** Fibrous to elongate-blocky fabric. Large blocky crystals in the middle of the vein. Oblique crystal growth or oblique opening of the left vein (Wildenhof 09; EI05VN24). **(d-e)** Left: fibrous fabric in the middle part of the veins and in the vein tips. Right: typical elongate-blocky infill (Parasitic fold Wildenhof 30: see Figure 3.5b; EI09VN03). **(f-g)** Composite vein. Host-rock inclusion lines act as irregular median lines on which fibres initiate (Hubertus Höhe 75: see Figure 3.32b and c; EI07VN17). **(h)** Blocky vein infill with undulose extinction of the crystals (Hubertus Höhe 73; EI07VN11). **(i-j)** En-echelon vein with **(i)** blocky infill in the middle part of the vein and **(j)** oblique fibres at the vein tip conform to dextral vein opening deduced in the field. Chlorite (Chl) at the vein wall (Hubertus Höhe 74: see Figure 3.32f; (i) EI07VN01; (j) EI07VN13).

4.3.3 Microstructures in quartz

Although the different veins, subdivided in hairline, centimetre-thick and composite veins, are particularly useful to constrain the fracturing and sealing history of the host-rock, particular deformation microstructures in the crystals may obscure the original vein fabric. For the major part of the veins, the original fabric is preserved. Some, however, show recrystallisation that can be related to subsequent deformation. The microstructures are mainly related to the deformation of the grain boundary which locally led to reorientation of the crystal and possibly to the formations of new subgrains. Although it will be illustrated that deformation in the bedding-normal veins was limited, it must be said that the amount of deformation can be underestimated because deformation takes place in three dimensions and is only studied in a two dimensional thin sections. If the thin section is parallel to the deformation, it may not be deduced. The fibrous crystals in syntaxial and ataxial veins often have typical saw-tooth shaped grain boundaries and briquette-like internal microstructures (Figure 4.6a) (cf. Ramsay & Huber 1987, p. 248, Stowell *et al.* 1999). Since the insoluble particles are sometimes concentrated along the fibre margins and since the fibre margins resemble in shape to microstylolites (Figure 4.6b, c and d), it can be argued that the characteristic fibre-margin patterns are not only the result of misfits in orientation during quartz fibre growth, but also might evidence subsequent pressure-dissolution by diffuse mass transfer along the fibre margins (Blenkinsop 2000). This feature is described as intercrystal deformation which occurs during interpenetrating grain contacts between fibres of similar composition (Figure 4.6c and d). These grain contacts are sometimes marked by the presence of micas (Blenkinsop 2000, Smith 2005). In deformed fibrous veins, the grain boundaries between the fibre crystals are highly irregular and are marked by a dark, brown to black aspect (Figure 4.6d). It may be that these irregular surfaces enclose parts of the neighbouring grain in such way that one grain contains an incorporated subgrain with a similar interference colour as the neighbouring grain. This intercrystal deformation feature is visible both in thin section (Figure 4.6d) and in a thicker wafer, in which subgrains are surrounded by small cracks formed during later fracturing of the quartz grain (Figure 4.6e). If a subgrain is not fully incorporated in the neighbouring grain, but is situated at the interface of the grains, the subgrain has a slightly different extinction interference colour than the original grain (Figure 4.6f). Intragranular optically continuous crystals are visible in fibrous and blocky infill (*e.g.* Figure 4.6g). If intragranular deformation occurs within a vein with a fibrous or elongate-blocky to blocky fabric, it is displayed as undulose or sweeping extinction (Figure 4.6h) and deformation lamellae. Other higher strain-related planar microstructures have not been observed. Deformation lamellae occur as single sets of densely spaced planes representing small crystal defects that affect the whole crystal. They are oriented at high angle to perpendicular to the fibre edges (Figure 4.6i and j) irrespective of the orientation of the neighbouring grain (Figure 4.6k). Spanning the crystal edges, they slightly curve along their length, an observation typical for deformation lamellae that are related to orogenic deformation (Blenkinsop 2000). Deformation lamellae are oriented at high angle to the optical axis of the crystal in which they are enclosed in (cf. Vernooij *et al.* 2006). The different orientation of deformation lamellae of adjacent fibres shows that adjacent crystal grains in a fibrous fabric have different crystal orientations (Figure 4.6k).

4.3.4 Interpretation and discussion

In section 3.5.1, the different bedding-normal vein (BNV) generations are interpreted as extension veins that developed in a basin in which the layers were still in a horizontal position, with each generation as evidence of the stress field orientation prevalent during its formation. Petrographic analysis of the vein fill, summarised below, fully supports this hypothesis. The hairline bedding-normal veins (Figure 4.3) are not affected by grain-scale heterogeneity of the host-rock, as evidenced by transgranular microveins with low tortuosity. Small-scale irregular hairline veins occur next to planar hairline veins (Figure 4.3e-g) and are demonstrated to be related to a fracture mechanism and do not represent a post-veining deformation otherwise all the veins should be buckled.

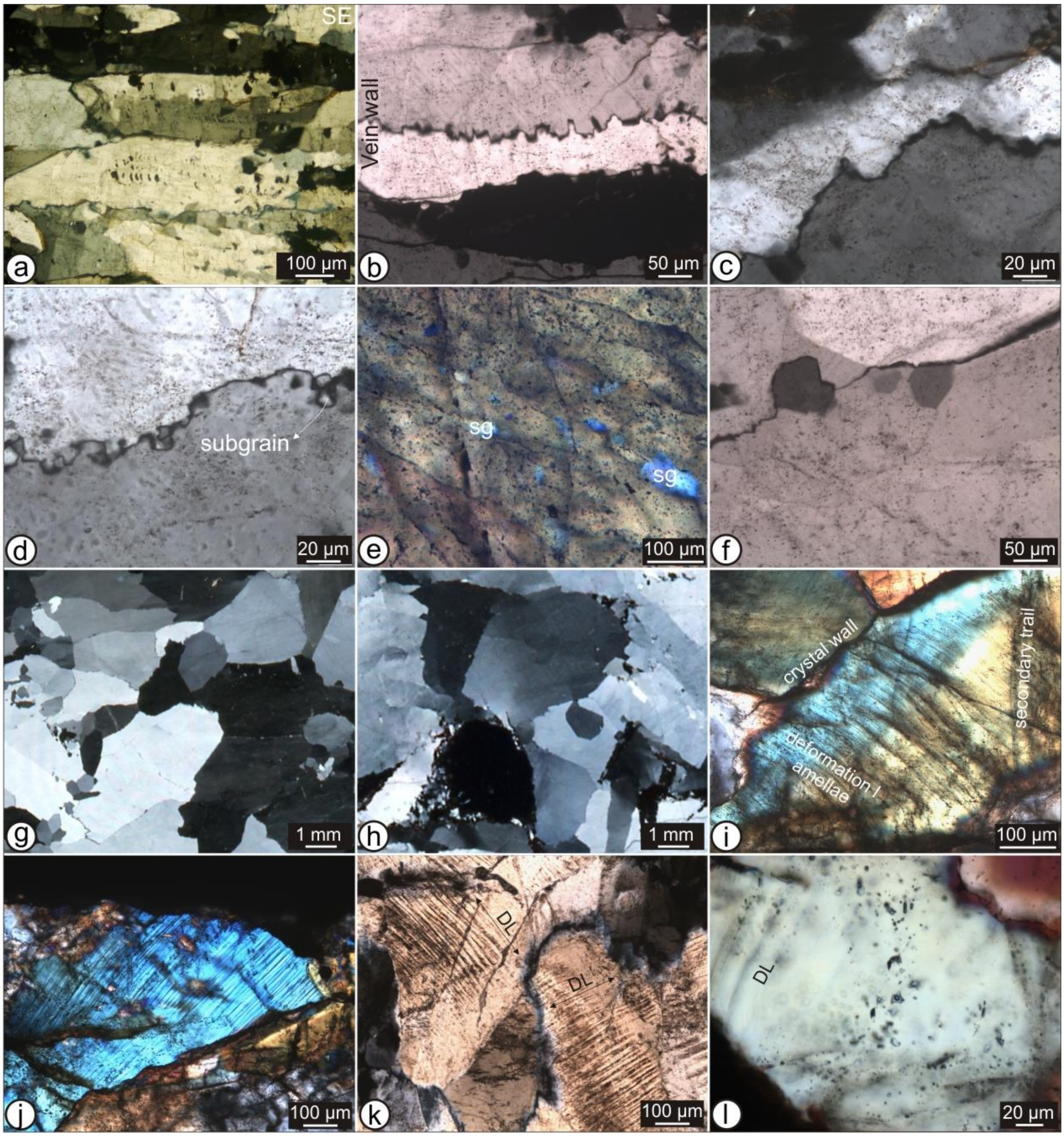

Figure 4.6: Inter- and intragranular deformation microstructures observed in bedding-normal veins. **(a)** Fibrous fabric characterised by typical, irregular sawtooth margins and briquette-like internal microstructural elements. Host-rock inclusion bands indicative of crack-seal (EI05VN34). **(b-c)** Inter-penetrating fibre contacts with insoluble particles (EI05VN36; EI07VN08). **(d)** Subgrain at the fibre contact misoriented with respect to the original grain (EI05VN36). **(e)** Quartz grains with irregular, diffuse, dark boundaries and subgrains with the same interference colour as the neighbouring grain, representative of bulging recrystallisation (EI05VN36). **(f)** Intragranular subgrains with higher interference colour than the original grain (wafer EI08VN12). **(g)** Undeformed blocky quartz grains (EI08VN08). **(h)** Sweeping extinction in blocky quartz grain (EI07VN11). **(i-k)** Deformation lamellae oriented at high angle to crystal wall, irrespective of the orientation of the neighbouring crystal (wafer EI06VN01). **(l)** Crystal imperfections such as deformation lamellae (DL) swept away the fluid inclusions in that area (wafer EI06VN07).

The fibrous crystals in hairline veins reflect opening of the veins in, whether or not several successive, tensile Mode I extension cracks. These above mentioned arguments support the evidence that the bedding-normal veins formed in a rock with an already significantly reduced porosity because of compaction at maximum burial conditions (see also Hilgers *et al.* 2006a). Moreover, the consistent orientation of the veins at high angle to bedding indicating a vertical maximum principal stress σ_1 at the time of vein formation (as suggested in section 3.5.1) contributed to this relative timing of the veins. Large compaction features such as compaction halos around the vein or vein buckling that would indicate a considerable volume decrease due to compaction have not been observed. This is indicative of an already significant reduced porosity at the time of vein formation and has been used as evidence in other sedimentary basins (*e.g.* Nollet *et al.* 2005b). Subsequent minor volume reduction is only locally observed as horizontal stylolitic planes dissolving buckled parts of a microvein (*e.g.* Figure 4.3h) or interpenetrating grain contacts at the fibre contacts of adjacent fibres demonstrating diffusive mass transfer (*e.g.* Figure 4.6d).

The vein fill of the centimetre and composite veins are used as indicator how the veins evolved from a hairline fabric to a more complex vein fill. The majority of the veins are centimetre veins with a fibrous to elongate-blocky fabric that have grown by a syntaxial or ataxial mechanism. In vein growth, the key parameter that controls the crystal morphology is the ratio of crystal growth velocity versus the fracturing or opening velocity (Figure 4.7), the width of the incremental opening and the roughness of the fracture wall (Hilgers *et al.* 2001, Nollet *et al.* 2005a, Urai *et al.* 1991). Following this theory, it can be argued that the syntaxial fibrous veins, whether or not reflecting several phases of infill (see Figure 4.4f and g), developed by repetitive fracturing and sealing phases in which the crystal precipitation was faster than fracture opening. This is supported by crack-seal structures distributed internally in the fibres and tracking the opening trajectory of the vein because of the rough wall morphology. The growth rate of the fibres must have been sufficiently fast enough to completely seal the entire fracture before the next crack event (Nollet *et al.* 2005a, Urai *et al.* 1991). It is thus fair to assume that centimetre and composite veins initiated as hairline veins, in which the crack-seal fabric track the opening trajectory during continuous vein growth. The inclusion bands within the fibres have common spacings of 10 μm to 20 μm, a spacing that corresponds to the lower limit described by various studies on inclusion banding (Cox & Etheridge 1983, Cox 1987, Hilgers & Urai 2002, Renard *et al.* 2005). Furthermore, the specific microstructures in extension veins often preserve the delicate vein wall geometry, suggesting that the fractures propagate at subcritical crack growth rate (Boullier & Robert 1992). In ataxial veins, some fibres also comprise host-rock inclusion bands that are continuous in a single fibre, but are discontinuous to adjacent fibres (Figure 4.4e). This is related to partial filling of the crack due to differential growth rates. Fast growing crystals that have reached the vein wall during vein growth comprise host-rock inclusion bands, whereas slowly growing crystals may not reach the vein wall until the next fracture opening and will thus not comprise any host-rock inclusions (Figure 4.7) (Fisher & Byrne 1990). Such discontinuous inclusion bands, indicative of the crack-seal mechanism (Passchier & Trouw 2005), indicate that ataxial veins show evidence of mineral accretion at the vein wall and did not develop because of delocalised fracturing and sealing (Hilgers & Urai 2002), such as constrained for ataxial veins without host-rock inclusions.

It is remarkable to observe inclusion banding in ataxial veins. Ataxial veins are assumed to form by delocalised fracturing and sealing in which the position of the growth surface changes through time (see references in BOX III). If host-rock fragments are absent within a fibre during ataxial crystal growth, it is impossible to form these crack-seal bands during delocalised fracturing because no host-rock grain is present. This implies that ataxial veins with host-rock inclusion bands show evidence of mineral accretion at the vein wall, rather that mineral accretion internally in the fibre such as expected for stretched crystals. Other ataxial veins without inclusion bands (Figure 4.4e) could still form by the described mechanism.

For veins with an elongate-blocky fabric, the precipitation rate occurs faster than the fracturing rate, although at slower growth velocity than in veins with a fibrous fabric

(Figure 4.7). This slower rate allows growth competition of neighbouring crystals during crystal growth. Whether the elongated fabric evolves into a complete blocky fabric depends on the fracturing rate and the width of the space created. If the velocity of fracturing exceeds the precipitation rate, then crystals grow in a seemingly free cavity and develop euhedral blocky crystals (Passchier & Trouw 2005). In the composite veins, a combination of fibrous and elongate-blocky crystals alternating with host-rock inclusion lines is observed. This indicates that these veins formed by a combination of growth mechanisms and that complete infill of the fracture cavity occurred several times. These inclusion lines are torn from the vein wall during multiple phases of fracturing and form a nucleation surface from which new crystals and new laminae, with a fibrous or elongate-blocky fabric, will develop.

Subsequent deformation of the veins has caused the development of microstructures indicative of different mechanisms. Microstructures in quartz are indicative of diffusive mass transfer (interpenetrating grain contacts), dynamic recrystallisation (bulging recrystallisation at the grain interface), recovery (undulose and sweeping extinction and subgrain formation) and brittle fracturing (deformation lamellae). There is a dominance of recovery which indicates low temperature deformation (Passchier & Trouw 2005), whereas bulging of the crystal walls is rarely observed and indicative of dynamic recrystallisation at slightly higher temperatures (Hirth & Tullis 1992) and high differential stress. Also deformation lamellae are often related to high strain rates and high differential stress during deformation (Van Baelen 2010, Vernooij & Langenhorst 2005). The microstructures in the veins can thus fully be attributed to post-veining deformation, presumably during the main Variscan contraction under higher differential stress.

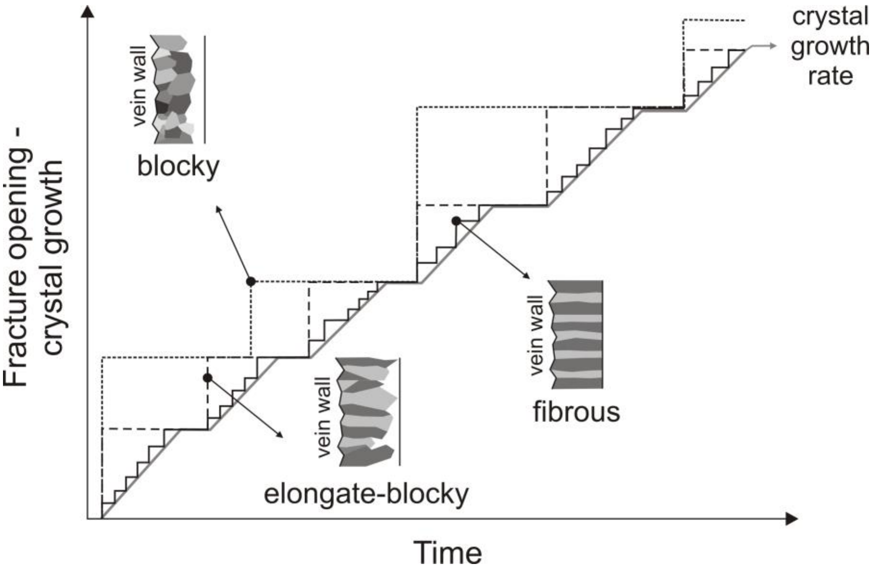

Figure 4.7: Schematic illustration on the different vein fabrics that develop due to differences between crystal growth versus fracture opening (modified after Hilgers *et al.* 2001, Passchier & Trouw 2005). Fibrous veins develop during fracture opening at small increments and immediate sealing. Fibre elongation tracks the vein opening. Elongate-blocky veins form during opening with larger increments due to increased fracture rate, but still at a lower rate than crystal growth. Elongate-blocky crystals form due to growth competition, in which the crystals are partly tracking the vein opening. Blocky veins grow when the opening rate exceeds the relative slow crystal growth, and are non-tracking.

4.4 Bedding-parallel veins

4.4.1 Vein composition

The bedding-parallel veins studied are mostly monomineral and exclusively composed of quartz. Based on the fabric analysis, numerous different crystal habits and a complex combination of growth mechanisms are observed. Quartz is often accompanied by host-rock inclusion bands and trails and numerous fluid-inclusion trails. During hot cathode-luminiscence petrography, the quartz grains in the different quartz laminae all have a similar dark blue luminescence. In addition to quartz, some BPVs contain chlorites that occur as greenish booklets in plane polarised light, and as blueish to white fanning booklets under crossed polars. The observed chlorites occur at the vein wall or closely related with host-rock fragments and host-rock inclusions incorporated in the BPVs (Figure 4.8b and d). Similar as to the chlorites in the bedding-normal veins, it remains questionable whether these chlorites are accompany quartz growth or did grow after veining. Furthermore, apart from chlorites, other phyllosilicates such as mica are observed in the host-rock fragments as well as in discrete planes in the BPVs. These discrete planes are interpreted as stylolites (see section 4.4.3).

4.4.2 Vein fabric

It section 3.5.2.2, several types of bedding-parallel veins were distinguished in the study area. This subdivision into several types is mainly based on the position of the veins with respect to the surrounding lithology. Thin intrabedded veins are veins that occur within a competent or incompetent host rock, whereas thick interbedded veins refer to BPVs that occur either at the incompetent-competent or competent-incompetent interface. Different tentative veining mechanisms have been proposed in the geometric analysis. For the intrabedded veins in siltstone sequences and interbedded BPVs, it was proposed that they result from bedding-parallel slip related to bedding-parallel thrusting causing the formation of composite veins (Figure 3.17). A second mechanism is proposed to be applicable to the intrabedded veins occurring in competent layers, where is postulated that BPVs result from bedding-normal uplift without any lateral displacement during vein growth (Figure 3.18a-f). It is the purpose of this fabric analysis to determine whether these two different mechanisms can be supported by the crystal growth in the vein fill.

4.4.2.1 Intrabedded veins

The first type of intrabedded veins that is discussed occurs as millimetre-thick BPVs in sandstone (*case iii* in Figure 3.18) or as centimetre-thick BPVs in siltstone sequences (*case iv* in Figure 3.17). These intrabedded BPVs are characterised by a milky-white appearance (see examples in Figure 3.13d-i from the Wildenhof section). These veins are not characterised by the laminated character of many of the BPVs, but are rather characterised by a large variability in quartz grain size, mainly dominated by a blocky quartz fabric. The following arguments support a vein growth from the base of the vein, *i.e.* the bottomside of the bedding-parallel fracture, towards its upper vein wall, *i.e.* the upperside of the fracture. Strictly spoken the vein is defined as a unitaxial vein (Figure 4.8a). At the bottom of the veins, elongate-blocky quartz grains that start to nucleate at host-rock grains of the wall rock rapidly evolve into a blocky fabric in the middle part of the vein. These blocky quartz grains can have sizes up to several millimetres. They developed up to the intervening host-rock inclusion seam in which they abruptly stop (Figure 4.8b). At this host-rock inclusion seam, very small quartz grains nucleated on this inclusion seam and again rapidly evolve into an elongate-blocky to blocky fabric in the upper part of the vein. At the upper vein wall, these blocky quartz grains again stopped growing. Locally, at the contact with the overlying medium-grained sandstone, sometimes chlorite booklets are present that have nucleated and developed on host-rock fragments or lines in the vein (Figure 4.8c and e). Internally in the blocky parts of the bedding-parallel vein, stylolites occur that are characterised by a dark brown rim along which insolubles occur (Figure 4.8c and d). Micas are mostly present at the vein wall (Figure 4.8e) and sometimes in the stylolites (see further Figure 4.11e).

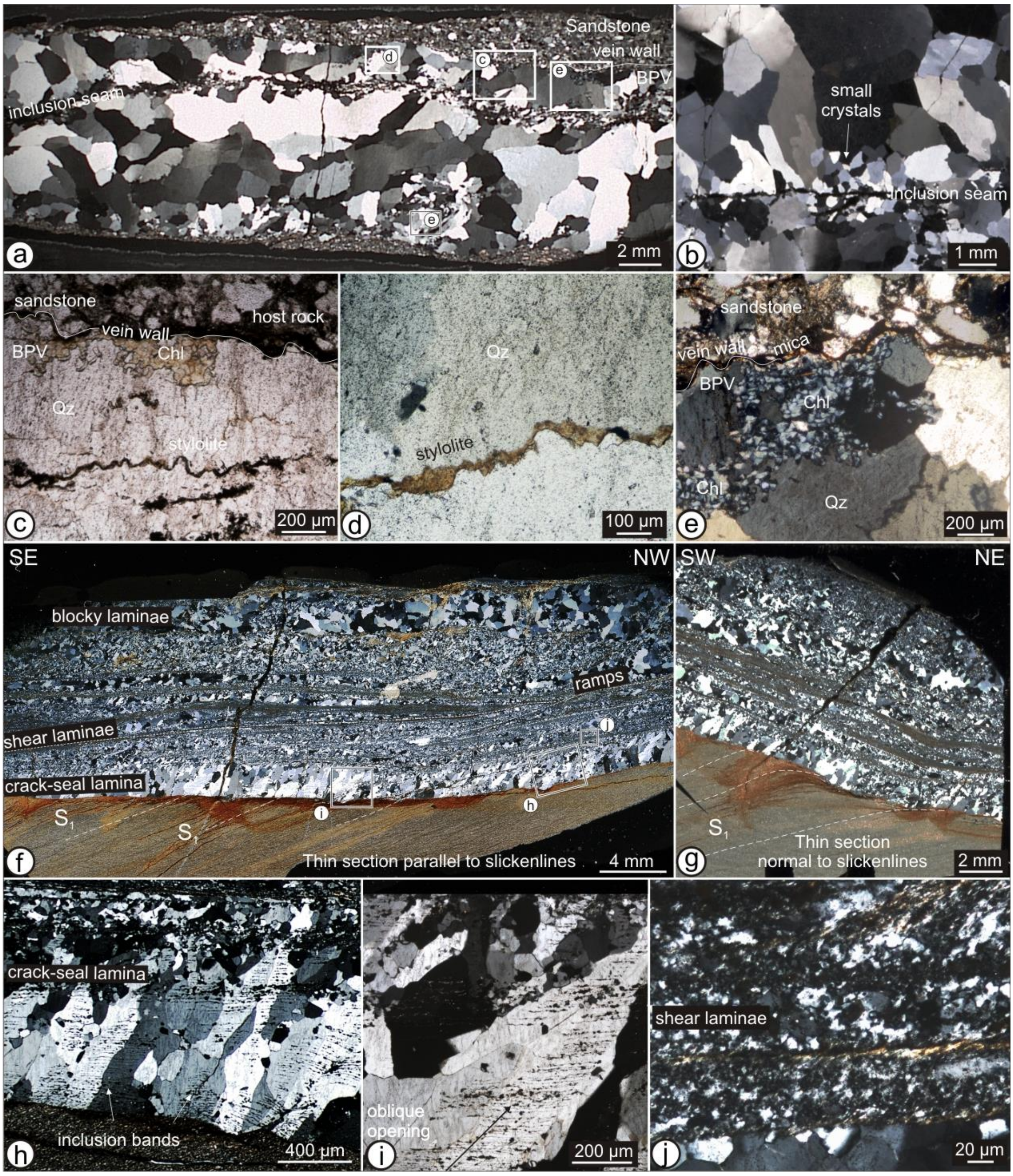

Figure 4.8: Microfabric of intrabedded bedding-parallel quartz veins. **(a)** Thin BPV in a sandstone showing an evolution from elongate-blocky at the vein wall to blocky in the middle part of the vein. This succession is repeated above the intervening host-rock inclusion seam (example from Wildenhof 27: see Figure 3.13d; EI09VN02). **(b)** Detail of a BPV in a siltstone showing small quartz crystals that nucleated on the host-rock inclusion seam (Wildenhof 42: see Figure 3.13i; EI06VN10). **(c)** Chlorite booklets present at the irregular vein wall. Bedding-parallel stylolites cross-cut the quartz grains. **(d)** Insolubles present in the stylolites. **(e)** Chlorite booklets at the vein wall are present between quartz grains. **(f)** Thin section cut parallel to the macroscopic slickenlines showing a thin laminated BPV in a siltstone sequence. Quartz laminae alternating with host-rock inclusion lines showing a pronounced top-to-the-NW bedding-parallel shear (example from Hubertus Höhe 73: see Figure 3.34f; EI07VN10). **(g)** Absence of shear in a thin section cut perpendicular to macroscopic slickenlines. **(h)** Crack-seal crystal fibres demonstrating oblique fibre growth and vein opening. **(i)** Discontinuous inclusion bands restricted to two fibrous crystals. (**j**) Detail of a shear laminae showing strong recrystallisation exemplified by bulging of the grain boundaries.

The mainly blocky vein fabric of the thin intrabedded BPVs supports crystal growth in a fracture (cavity), in which the fracture rate exceeds the crystal growth rate. Moreover, a transient high permeability must have existed in order to allow the formation of these large blocky crystals. This fracture (cavity) has completely sealed up the overlying fracture wall of the vein. When a new fracture is subsequently created, it tears a thin part of the host rock, currently present as a thin intervening irregular inclusion seam in the vein (see BOX II and BOX III for terminology of inclusion bands versus seams). Around this inclusion seam very small quartz crystals are observed. In the subsequent phase, these small crystals in this **blocky lamina** have nucleated on this surface and again grow in an open fracture, evolving from an elongate to a blocky crystal habit (Figure 4.8b) until this second phase is completely sealed. The absence of lateral displacement along the vein, for instance exemplified by an intrabedded BPV cross-cutting a bedding-normal vein in a sandstone unit (Figure 3.13e-h), is indicative of a **bedding-normal opening** of the vein, although the blocky vein fabric precludes to deduce the opening trajectory. The only possible solution to explain this vein growth is a mechanism that is able to keep this fracture open against the overburden pressure. This can be explained by the presence of lithostatic pore-fluid overpressures that created the initial fracture and remained present during crystal growth. However, it may be difficult to maintain lithostatic fluid pressure in a cavity during a long period. Therefore, small incorporated host-rock inclusion fragments might have formed bridges that kept the fractures open. Between these bridges, blocky quartz crystal growth might have occurred in a cavity in which the fluid-pressure state already decreased below lithostatic. Nevertheless, the vein fabric and macroscopic observations indicate that these thin intrabedded BPVs are clearly extension veins, interpreted to form at low differential stress (Etheridge 1983, Secor 1965).

The second type of intrabedded veins that is discussed concerns a centimetre-thick laminated vein observed in a siltstone sequence (see example in Figure 3.34f from the Hubertus Höhe section) which is representative of all the laminated intrabedded BPVs in siltstone sequences (*case iv*). Microscopically the vein is characterised of numerous quartz laminae consisting of very small crystal sizes, intercalated with numerous fine-grained host-rock inclusion lines and a single lamina with larger blocky crystals (upper part of the vein in Figure 4.8f). Similar to the BPV in Figure 4.8a, a vein growth from the lower vein wall to the upper vein wall is suggested. Furthermore, a pronounced shear direction is visible in thin sections that are cut through the veins, parallel to the macroscopic slickenlines on the vein wall (Figure 4.8f). This shear is absent in thin sections cut perpendicular to these slickenlines (Figure 4.8g). In the BPV, the bottomlying vein wall has a relatively flat morphology on which initially fibrous crystals nucleate. The fibres evolve along their crystal elongation into an elongate-blocky fabric. The fibres in this specific quartz lamina (**crack-seal lamina** in Figure 4.8f) are characterised by a repetitive pattern of numerous crack-seal inclusion bands which mimic the shape of the vein wall. These inclusion bands are oriented parallel to the vein wall, and oriented at high angle to the crystal elongation. They are laterally continuous along the vein thereby cross-cutting the quartz fibres (Figure 4.8h and i) and show an irregular spacing of 10 µm to 25 µm. It can be suggested that the spacing of these inclusion bands represents the opening and sealing of incremental fractures as they are continuously present in many fibres. The fibrous to elongated quartz crystals in which these solid inclusion bands are present, vary in orientation from subperpendicular to oblique to the vein wall. Both straight and slightly curved mineral fibres with sharp fibre-contacts, respectively oriented subperpendicular and oblique to the vein wall, appear in the vein. This oblique crystal orientation is indicative of an **oblique opening** as the fibrous to elongate crystals remain their crystallographic orientation along the crystal elongation. This oblique opening is furthermore shown by the oblique spacing of host-rock inclusion bands within a single fibre crystal (Figure 4.8i).

The orientation of the oblique fibres can locally be correlated with the NW-directed shear, indicated by the orientation of the slickenlines and slickenfibres on the bedding-parallel vein walls. Also, the uniform crystallographic orientation along the curved fibres and the absence of intragranular recrystallisation, deformation lamellae or undulose extinction in the fibres (Figure 4.8h and i) indicate oblique opening rather than post-veining shear. In this specific crack-seal lamina, it can be concluded that the precipitation rate was faster than the fracturing rate, as evidenced by the repetitive inclusion bands.

The overall part of the vein, however, consists of planar host-rock inclusion seams alternating with millimetre-thick laminae, in which assemblages of very small crystals of only a few µm occur (Figure 4.8j). These small quartz crystals show a strong variability in grain size and are intensely recrystallised compared to the crystals in for instance the blocky lamina at the upper part of the vein (Figure 4.8f). This recrystallisation is exemplified by bulging of the quartz grain boundaries, a common mechanism of dynamic recrystallisation on a grain scale at low temperature (Passchier & Trouw 2005) and high differential stress. These millimetre-thick laminae are interpreted to be shear-related laminae in which crystals small crystals grow and are recrystallised after vein emplacement. Contrary to the uniform thickness of the basal crack-seal lamina, these shear bands laterally fan out and are organised in small ramps (Figure 4.8a) corresponding to the NW-directed macroscopic shear deduced from the slickenfibres. Between the shear laminae, many laminae occur that are characterised by undeformed blocky quartz crystals, comparable to the blocky laminae observed in the intrabedded veins in the sandstone (Figure 4.8a).

It may be concluded from the fabric analysis of this type of intrabedded BPV that the pronounced bedding-parallel fabric and the localised deformation zones in the shear laminae are robust evidence of bedding-parallel shearing. During vein thickening, quartz initially precipitates in incremental steps of normal to oblique opening (crack-seal lamina) and subsequently as small crystals in the shear laminae. Deformation of the shear laminae took place during cataclasis and subsequent recrystallisation (see quartz microstructures in section 4.4.4 for explanation). The intervening blocky laminae may indicate intermediate crystal growth in an opening fracture, in a mechanism similar to the intrabedded veins in the competent unit. Alternating extensional features with shear-related features allow defining this specific type of BPV as an extension to extensional-shear vein which both form at low to relatively low differential stress (Etheridge 1983, Secor 1965).

4.4.2.2 Interbedded veins

Similar to the thin intrabedded bedding-parallel veins, the thicker interbedded BPVs can be subdivided in two different vein types, which can be recognised in the field. The first composite type is mainly quartz dominated (*e.g.* Figure 3.13a) and slickenlines and slickenfibres are absent on its vein wall. The second type is dominated by a laminated composition that is related to bedding-parallel shear as evidenced by various slickenlines and slickensides on different quartz laminae (*e.g.* Figure 3.29f and g). There is no tendency for both types to develop preferentially at the incompetent-competent or competent-incompetent interface.

The first type comprises several centimetre-thick composite BPVs that predominantly consist of blocky quartz crystals with variable crystal sizes, discontinuous host-rock inclusion seams and stylolites (Figure 4.9a and b). The stylolites will be discussed separately in section 4.4.3.

The different quartz laminae are characterised by a considerable grain size variability ranging from grains of a few µm to millimetre-size blocky grains. Only by combining several thin sections, a clear shear sense can be deduced. First of all, it is clear that the fine- and coarse-grained laminae are oriented subparallel to bedding and fan out towards the SE. This is visible by thickening of the vein towards the NW, and by small-scale **ramps** stepping up to the NW (Figure 4.9a). The fine-grained laminae at the base of the vein and those between the coarse-grained laminae have a more dark appearance and consist of both fine-grained blocky quartz crystals and grains which have recrystallised grain boundaries by bulging recrystallisation. These fine-grained laminae fan out towards the SE part of the vein. It is remarkable that the coarse-grained laminae, which are characterised by large blocky grains that have a milky-white appearance on the cut sample (Figure 4.9a), developed on these ramps, and are aligned inside the vein reflecting a top-to-the-NW shear.

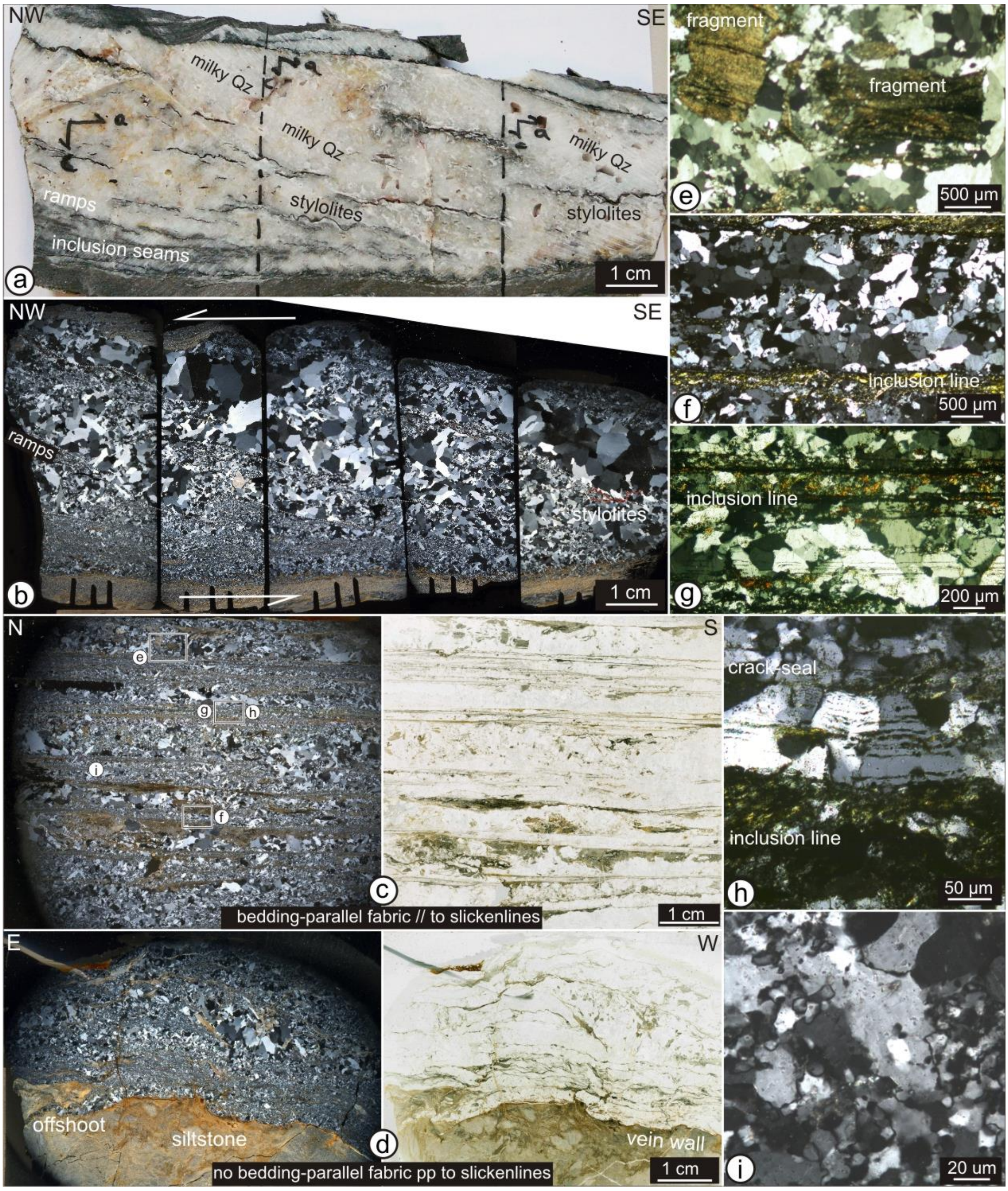

Figure 4.9: Microfabrics of composite and laminated interbedded bedding-parallel quartz veins. **(a-b)** Thick composite BPV with stylolites showing an alternation of shear laminae, characterised by very small quartz crystals, and coarse-grained laminae with large, undeformed blocky crystals. Alignment of blocky laminae (dashed lines) might indicate an oblique opening related to top-to-the-NW shear (Wildenhof 22; EI07VN22). **(c)** Pronounced bedding-parallel fabric in a thin section cut parallel to the macroscopic slickenlines on the vein wall (Schwammenauel 93, box fold: see Figure 3.29f; EI05VN40). **(d)** Less pronounced bedding-parallel fabric and absence of shear in a thin section oriented perpendicular to slickenlines (Schwammenauel 93, box fold: see Figure 3.29f; EI05VN39). **(e-i)** Details of (c). **(e)** Millimetre-size host-rock fragments incorporated in the shear laminae. **(f)** Host-rock inclusion line, consisting of mainly micas, intercalated between two quartz laminae with absence of shape preferred orientation of quartz grains. **(g)** Crack-seal host-rock inclusion banding reflecting bedding-normal opening of the vein. **(h)** Crack-seal inclusion bands in elongate-blocky crystals. Typical spacing of inclusion bands of 10µm. **(i)** Strong recrystallisation observed in the shear laminae, exemplified by bulging of the quartz grain boundaries.

Similar to the thin intrabedded BPVs, it can be argued that these fine-grained laminae reflect subparallel shear along small ramps (Figure 4.9b) in which small quartz grains grow and deform by cataclasis and recrystallise during subsequent deformation (see explanation in section 4.4.4). The coarse-grained laminae that are arranged in an oblique pattern fit in this kinematic history in such way that they represent phases in which a higher transient permeability was present allowing crystal growth with a blocky fabric. Unfortunately, the blocky crystal habit does not allow deducing an opening trajectory that could confirm this NW-directed shear.

The second type (Figure 4.9c and d) is strongly dominated by a laminated composite internal fabric consisting of several distinct generations of bedding-parallel quartz laminae with incorporated isolated fractured wall-rock fragments (Figure 4.9e) intercalated with planar wall-rock inclusion seams which vary from thin, millimetre-size slices parallel to the vein wall to fractured host-rock fragments. The vein walls of these veins are characterised by slickenlines which are uniform in trend on a single lamina, but slightly vary in orientation from lamina to lamina (*e.g.* BPV in box fold at Schwammenauel: Figure 3.36). It was proposed in section 3.5.2.2 that these veins result from bedding-parallel thrusting related to small ramps, during which several phases of quartz precipitation alternate with bedding-parallel slip. The microfabric of the vein can confirm this hypothesis. Similar to the sheared thin intrabedded BPVs, a pronounced bedding-parallel fabric is only observed in those thin sections which are cut parallel to the slickenlines, *i.e.* perpendicular to the vein (Figure 4.9c). In thin sections prepared perpendicular to slickenlines, in which a pronounced bedding-parallel fabric is absent, host-rock inclusion seams occur in an anastomosing pattern intercalated with ribbons of quartz laminae (Figure 4.9d). Local offshoots below the vein have a blocky infill (Figure 4.9d). This demonstrates that shear direction was preferential during vein growth.

Three types of microfabrics are observed within the laminated interbedded BPVs and are indicative of different phases of vein growth or vein deformation: crack-seal microstructures, curved mineral fibres and open-space filled blocky crystals. Repetitive crack and seal is defined by fibrous to elongate-blocky quartz crystals with a continuous crystallographic orientation in which host-rock inclusion bands occur. The inclusion bands are oriented parallel to the vein wall and perpendicular to the elongation of the quartz laminae. They are laterally continuous along the vein thereby cross-cutting the quartz fibres (Figure 4.9g). Inclusion bands are mostly irregularly spaced, ranging between 10 µm and 25 µm, and reflect the morphology of the original vein wall thereby representing the major opening direction of these **crack-seal laminae**. Within these laminae, both straight and curved mineral fibres with sharp fibre-contacts, respectively oriented perpendicular or subperpendicular to the vein wall or to the internal bedding-parallel seams, appear locally in the veins (Figure 4.9g and h). This oblique crystal orientation is indicative of growth competition of adjacent quartz crystals during crystallisation rather than an indication of an oblique opening (*e.g.* Cox 1987) as the inclusion bands are displaced perpendicular to the internal bedding. The open-space filling microstructures, *i.e.* elongate-blocky to blocky quartz crystals with a variability in grain size, are randomly distributed through the vein, but mainly occur within coarse-grained quartz lamina that are contained between thin host-rock inclusion seams (Figure 4.9f). The sometimes fully incorporated host-rock fragments contain thin bedding-parallel fractures and always occur in coarse-grained laminae (Figure 4.9e). They can take up considerable sizes up to several millimetres. Phyllosilicates are restricted to the host-rock inclusion seams and fragments and mimic the mineralogy of the under- or overlying siltstone. Finally, similar to the previous described BPVs, thin fine-grained **shear laminae** with strongly recrystallised grains occur interbedded in the coarse-grained laminae and host-rock inclusion lines (Figure 4.9i) and represent bedding-parallel shear restricted to these thin laminae.

To conclude, this type of laminated interbedded BPV resembles the laminated intrabedded BPVs in such way that alternating extensional and shear features co-occur within the vein. It is thus fair to define these laminated interbedded bedding-parallel veins as extension to extensional-shear veins, which are defined to form at low to relatively low differential stress respectively (Etheridge 1983, Secor 1965).

Finally, in order to give a conclusive answer to the question whether a bedding-parallel vein is composed differently at different positions with respect to the overlying rock, *i.e.* competent versus incompetent, the internal fabric of the folded BPV$_1$ at the Eschaulerberg parasitic fold is studied. It is described in section 3.3.3 that this interbedded vein changes from a configuration below coarse-grained sandstone in the synclinal hinge of the fold to an interbedded position above coarse-grained sandstone in the overturned SE-dipping limb (see Figure 3.23). First of all, it is clear that a shear component is present in those thin sections cut parallel to the slickenlines (Figure 4.10a and b) which is absent in thin sections perpendicular to the slickenlines (Figure 4.10c). Furthermore, several features in both parts of the BPV are supportive for a similar top-to-the-NNW shear during the complex development of this centimetre-thick BPV. Both parts of the vein comprise straight fibrous crystals which evolve to a curved crystal habit in which the crystallographic orientation remains constant along the curved crystal elongation. Although host-rock inclusion bands that could track the opening trajectory are absent, it can be argued that the dominant orientation of the oblique fibrous to elongate crystals to the NNW is a growth feature. The uniform crystallographic orientation along the curved fibres and the absence of recrystallisation, deformation lamellae or undulose extinction indicate simple shear during vein opening rather than post-veining shear. Also, several ramps are observed that step up towards the NNW. Moreover, sometimes elongate crystals have their crystal elongation oriented parallel to the SSE-side of a host-rock inclusion fragment, whereas at its NNW-side, the crystal elongation is oriented perpendicular to the host-rock inclusion fragment (see inclusion fragment in the NNW upper corner of Figure 4.10b and it surrounding crystals). Fine-grained shear laminae with recrystallised crystals occur at the upper part of both vein parts.

Eventually, it can be concluded that although the vein is folded, the complex fabric at both parts of the vein indicate a NNW-shear that corresponds to the shear direction derived from the slickenlines and slickenfibres on top of the vein (see Figure 3.25). Fibrous crystal infill is related to an increased precipitation rate with respect to the fracturing rate.

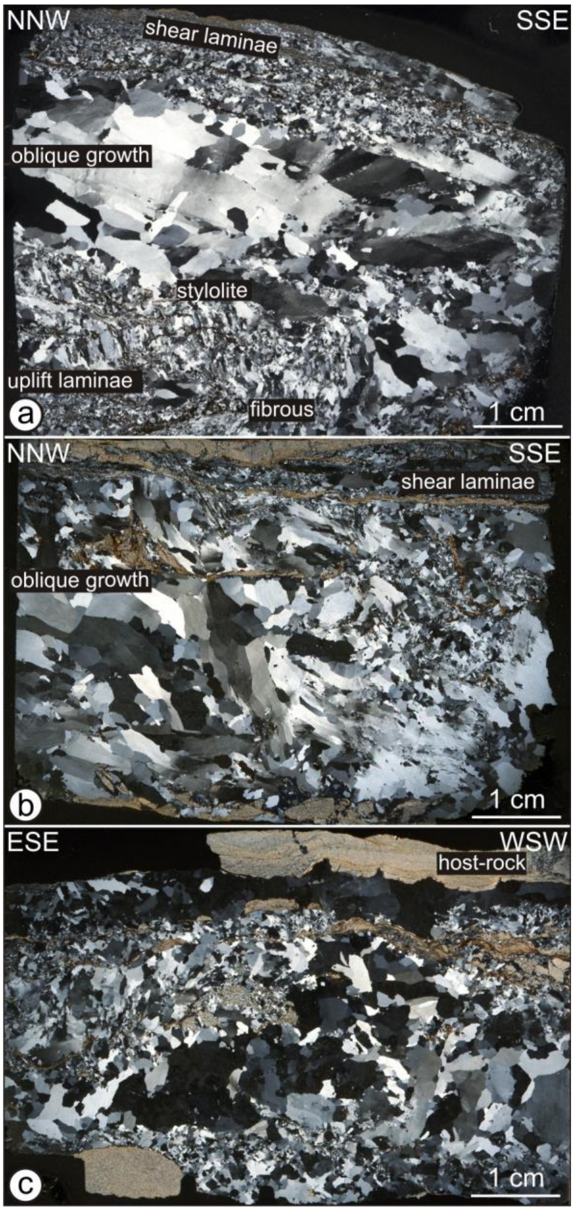

Figure 4.10: Composite bedding-parallel veins of the Eschaulerberg parasitic fold (see BPV$_1$ in Figure 3.23a and b). **(a)** BPV$_1$ of the overturned SE-dipping limb of the parasitic fold showing from bottom to top: fibrous bedding-normal laminae reflecting uplift, large elongate-blocky crystals reflecting oblique opening and shear laminae with micrometre-size crystals. Section parallel to slickenlines (EI08VN22). **(b)** BPV$_1$ of the normal SE-dipping limb of the parasitic fold showing centimetre-size elongated curved crystals with a consistent crystallographic orientation along their curvature indicating oblique opening (EI08VN25). **(c)** Thin section perpendicular to (b), and perpendicular to slickenlines, characterised by a less pronounced bedding-parallel fabric and absence of shear sense indicators (EI08VN22).

During subsequent infill, the fracture rate must have been increased with respect to the crystal rate as curved elongate-blocky crystals in the middle part of the vein are observed. Finally in a late stage, shear laminae developed, representing high-strain bedding-parallel shear during which small crystals grow and other crystals are cataclased. It is further concluded that if a vein is situated below an incompetent siltstone sequence, it may comprise more host-rock inclusion seams and fragments (Figure 4.10) than if it occurs interbedded below a sandstone (Figure 4.10b), simply because of the strength of the host rock, although, the internal fabric may not differ between both types. Consequently, laminated veins with clear planar host-rock inclusion lines and inclusion fragments will be mostly present below siltstone, whereas the composite BPVs are more favourite of a position below sandstone.

4.4.3 Stylolites in BPVs

Stylolites are serrated surfaces at which mineral material has been removed by pressure dissolution in a compressive state and are therefore used as a fabric to interpret them by means of maximum principal stress orientation. Stylolites in a rock or in a vein commonly develop at irregular particles that are characterised by a slightly higher permeability than compared to the rest of the rock body or vein. Continuous pressure-dissolution along these irregularities may develop a typical wavy pattern along which considerable dissolution has taken place. In veins, the formation of stylolites often result from fluid-assisted mass transfer processes (cf. Blenkinsop 2000) and are both temperature and pressure dependent.

Numerous bedding-parallel stylolites are present in the intrabedded and interbedded composite BPVs. They are absent, or they have not been observed in the laminated veins. On cut samples irregularly anastomosing patterns of laterally discontinuous stylolites are visible (Figure 4.11a). The clayey material within these stylolites is often completely eroded, leaving an empty stylolite behind (Figure 4.9a). In thin section, the stylolites are situated in the coarse-grained blocky laminae (Figure 4.8b-d), at the interface of different coarse-grained and fine-grained laminae, or at the contact with a host-rock inclusion seam (Figure 4.11f-h). Stylolites have a composite morphology consisting of a dark rim of insolubles, iron oxides (Figure 4.11b and c) and elongate micas (mainly muscovite, Figure 4.11d and e). Also chlorite booklets are often developed at these dissolved surfaces (Figure 4.11f).

In the blocky quartz laminae, stylolites are developed at irregularities at the contact of different quartz grains, which is evidenced by the different crystallographic of the grains above and below the stylolite (Figure 4.11d and e). They overprint primary crystal growth features (Figure 4.9b) and laterally fade out. If the irregular pattern of the stylolite is fully attributed to dissolution, then the amount of dissolution along these stylolites can be estimated. The height of the wavy pattern of a stylolite is assumed to be similar to the initial height before dissolution. By counting up the individual heights (h_1 to h_7 in Figure 4.11a) of different stylolites along an arbitrary chosen line through a vein, the total amount of dissolution can be estimated (Figure 4.11a). In this particular example, the total cumulative height of the stylolites measures 4.7 mm in a vein with a height (h_{tot}) of 32 mm. Hence, the original height of the vein would have been 36.7 mm. The ratio of 4.7 / 36.7 may indicate a (possibly overestimated) considerable amount of ~12% of dissolved material. This may indicate that a considerable amount of fluids must have been present in order to dissolve the quartz (solubility of quartz ~400 ppm at 250°C).

Stylolites also often intervene with the host-rock inclusion seams and fragments that are distributed internally in the BPVs, giving the inclusions an anastomosing irregular pattern (Figure 4.11g and h). These host-rock inclusions seem to be the irregularities necessary for the initiation of the dissolution. Such an anastomosing fabric developed at host-rock inclusions is defined as ‘stylolitised’ wall-rock seams (Fowler 1996). The anastomosing pattern of dissolution surfaces at the inclusion trails may, however, partly be related to the original fracture surface when the inclusion is teared from the wall rock and probably cannot fully be attributed to dissolution. In the majority of these examples, very small (~100 μm), undeformed quartz grains are present around the stylolitic surface and seem to have nucleated on the insolubles in the stylolite (Figure 4.8b; Figure 4.11g).

Stylolites characterised by composite morphologies and residual minerals, are common in BPVs and have been explained by various mechanisms (Cox 1995, de Roo & Weber 1992, Fisher & Byrne 1990, Fowler 1996, Jessell *et al.* 1994, Jia *et al.* 2000, Teixell *et al.* 2000; Koehn & Passchier 2000, Nicholson 1978, Wilson *et al.* 2009). Stylolites may form during bedding-parallel slip after vein emplacement (de Roo & Weber 1992), a process known as pressure-solution slip (Elliott 1976 in de Roo & Weber 1992). However, the stylolites observed in the composite BPVs, are quite irregular in shape, locally truncate larger crystals and are marked by residual minerals. These observations contrast with the rather planar pressure-dissolution slip, indicating that pressure-dissolution slip has not taken place in the BPVs after veins formation (cf. Jessell *et al.* 1994, Koehn & Passchier 2000). Therefore, it can be argued that dissolution already occurred during the development of the BPVs, rather than in a later stage.

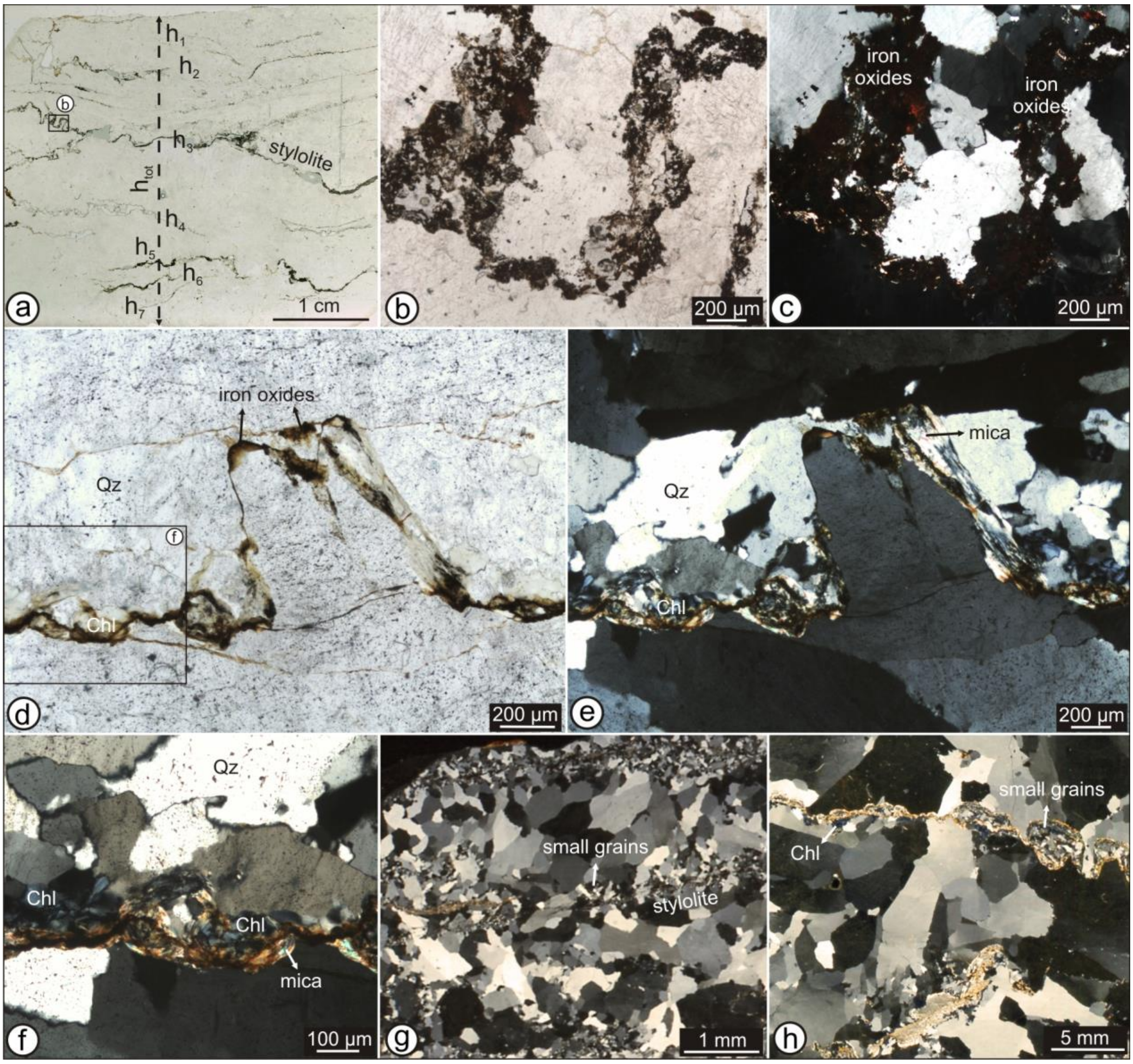

Figure 4.11: Microstructural petrography of stylolites in composite bedding-parallel veins. See Appendix B for sample localities. **(a)** Anastomosing bedding-parallel stylolites (EI05VN25). **(b-c)** Detail of (a) under (b) plane-polarised and (c) cross-polarised light showing insolubles and iron oxides. **(d)** Anastomosing stylolite with green chlorites (EI05VN44). **(e)** Similar sample as in (d) under cross-polarised light showing micas (mainly muscovite) and iron oxides in the stylolite. The blocky quartz grains have different crystallographic orientation above and below the stylolite. **(f)** Detail of (d) showing chlorite booklets that nucleated on the insolubles. **(g)** Two coarse-grained laminae with blocky grains separated by a stylolite which is characterised by small quartz grains (EI05VN25). **(h)** Small quartz crystals (grains) are present within the 'stylolitised' inclusion seam and on the inclusion fragment (EI05VN44).

The microstructural observations suggest that this pressure-dissolution took place along discrete planes, *e.g.* the porous host-rock inclusion seams, with local higher permeabilities along which fluids could pass and allowed transport of dissolved material. The dissolution is related to fluid-assisted mass transfer and presumably took place at the boundaries of quartz grains attached to the stylolites or at the host-rock inclusion seams. The dissolved material may have been precipitated immediately at the stylolite, which is exemplified by the presence of the very small crystals present at the stylolites and in the inclusion seams and fragments (Figure 4.8b; Figure 4.11g and h). Wilson *et al.* (2009) demonstrated that this process takes place commonly in extension and extensional-shear bedding-parallel veins. The consequences of these stylolites on the kinematic history will be discussed in section 4.4.5. Furthermore, the co-occurrence of stylolites, resulting from dissolution in an unsaturated fluid, with vein accumulation, resulting from a supersaturated fluid, might still be problematic to explain. Unfortunately, the discussion to solve this research problem is beyond the scope of this work.

4.4.4 Microstructures in quartz

Microstructures related to deformation have already briefly been illustrated in the fabric analysis of the BPVs. In the thicker coarse-grained blocky laminae, the majority of the blocky grains are undeformed quartz crystals with clear crystal contacts and without any evidence of intergranular deformation (see blocky lamina in Figure 4.12). Blocky grains sometimes coexist next to slightly deformed blocky crystals that show evidence of an internal crystal-plastic deformation, such as undulose extinction, and locally preserve deformation lamellae. This indicates that there must have been at least minor deformation after emplacement of the blocky grains. The minor deformation in the coarse-grained laminae strongly contrasts to the intense recrystallisation in the fine-grained shear laminae that consist of assemblages of very small crystals of only a few µm to crystals of several tens of µm (Figure 4.12). These shear laminae thus show a strong grain size variability. This can be mainly attributed to the strong recrystallisation which is mainly exemplified by bulging of the quartz grain boundaries (Figure 4.8j; Figure 4.9i; Figure 4.12). Bulging recrystallisation has been identified as the most important dynamic recrystallisation process in the shear laminae and is considered to be dominant during progressive deformation commencing at temperatures of 250°C at higher differential stress (Passchier & Trouw 2005).

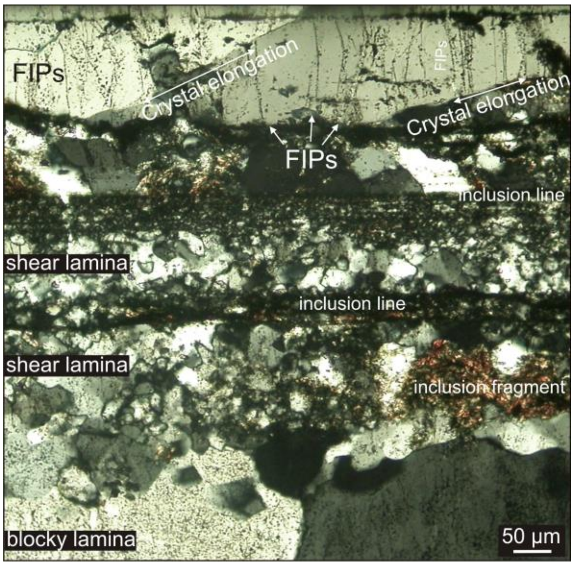

Figure 4.12: Quartz microstructures in a laminated bedding-parallel vein (EI05VN40). Undeformed crystals in the blocky lamina. Considerable grain size variability in shear laminae in which crystals are deformed by bulging recrystallisation. FIPs: fluid inclusion planes.

The occurrence of alternating small and large quartz crystals in laminated bedding-parallel veins has been used as evidence of cataclasis or brecciation of large quartz crystals during high strain-rate shear events (*e.g.* Cox 1995, de Roo & Weber 1992). The latter authors argue that after brecciation fast nucleation of small crystals could have occurred between the brecciated crystals causing a specific vein fabric with a strong variability in grain sizes. Unfortunately, brittle cataclasis of the large or small crystals in the BPVs has not directly been observed in the fabric analysis. Also, if cataclasis would have occurred during the formation of the BPVs studied, subsequent recrystallisation would have obscured the evidence.

Furthermore, shear is considered to be a relative fast process taking place at increased strain rates (*e.g.* Cox 1995, de Roo & Weber 1992), whereas recrystallisation occurs at relatively slow strain rate. The seemingly contrasting co-occurrence of these features in the shear laminae can be explained as follows: the formation of the bedding-parallel laminated veins is attributed to bedding-parallel thrusting at the onset of folding. Hence, it is likely that the formation of the shear laminae occurred along micrometre-size bedding-(sub)parallel thrusts and microramps (Figure 4.9b) at which cataclasis of quartz crystals must have taken place. As a result of cataclasis and nucleation of these small crystals, the quartz grains (de)formed along these microfractures would be characterised by numerous dislocations and defects in their crystal lattice. Subsequently, these lattice defects will act as a focus to subsequent deformation during the main phase of the Variscan contraction. As result, dynamic recrystallisation by bulging of the crystal walls occurred in the shear laminae, taking place at higher differential stress than during the formation of the extension to extensional-shear veins. In contrast, the large blocky crystals in the blocky laminae have grown in their preferred crystallographic orientation and contain hardly any dislocations or defects in their crystal lattice. Hence, they are resistant to deformation at higher differential stress and are undeformed. This is exemplified by the often clear and undeformed crystal contacts between the grains.

4.4.5 Interpretation and discussion

In section 3.5.2, two different veining mechanisms are proposed to be responsible for the formation of bedding-parallel veins. A first mechanism (Figure 3.42b and c) is related to the formation of interbedded BPVs, situated below and above competent sandstones, and the BPVs that occur intrabedded in siltstone sequences. For all three configurations a mechanism can be attributed in which bedding-parallel slip, related to bedding-parallel thrusting, is responsible for the composite nature of the veins. The latter mechanism is evidenced by, NNW- to NW-directed, displacement of bedding-normal veins, small-scale ramps and numerous slickenlines on the different quartz laminae internally in the veins. A second mechanism relates to the milky-white BPVs that occur intrabedded in competent units (Figure 3.42a) and in siltstones (Figure 3.13i). In this model it has been proposed that thin BPVs result from bedding-normal uplift of the layers, with absence of any lateral displacement.

It is shown in the microstructural analysis of the BPVs that these two mechanisms are supported by the internal fabric of the veins. The BPVs intrabedded in sandstone are composed of a fabric that consists of small elongate-blocky crystals at the lower vein wall which evolve to a dominantly blocky fabric up to the upper vein wall or to an intervening host-rock inclusion seam (Figure 4.8a). The absence of lateral displacement suggests that these are extension veins. This specific vein fabric is explained by crystal growth in a fracture cavity that remains open due to the opening rate exceeding the rate of crystal growth. This mechanism requires lithostatic pore-fluid overpressures to keep the cavity open against the overburden pressure allowing crystals to grow. Such bedding-parallel **extension veins** correspond to those that have formed in sedimentary basins in which the veins open parallel to the vertical minimum principal stress (*e.g.* Cosgrove 1993, Henderson *et al.* 1990, Jessell *et al.* 1994), although a bedding-normal fibrous fabric such as observed in the ‘beefs’ has not been observed (Cobbold & Rodrigues 2007, Rodrigues *et al.* 2009).

The microfabric of the typical laminated veins, characterised by numerous quartz laminae and host-rock inclusion seams (Figure 4.8f, Figure 4.9c), can be explained by bedding-normal uplift combined with bedding-parallel shear. First of all, crack-seal laminae, with spaced host-rock inclusion bands ranging between 10 μm and 25 μm, are typical in these laminated veins. The spacing of these inclusion bands reflects cyclic opening and sealing of incremental fractures that open perpendicular to subperpendicular to the vein wall. Crack-seal microstructures conform to those of Ramsay (1980) are common in laminated veins (Boullier & Robert 1992, de Roo & Weber 1992, Foxford *et al.* 2000) and an average spacing of 25 μm is representative of the “noisy” stress release fluctuations at the time of vein formation (Renard *et al.* 2005). This means that crack-seal spacing is related to variations in the local stress-state within the host-rock during fracturing (see Chapter 7 for the layer-scale stress state). Laminated veins are furthermore characterised by shear laminae that occur between planar host-rock inclusion seams and host-rock inclusion fragments which are incorporated in the veins. The considerable grain size variability in the shear laminae is indicative of localised shearing and subsequent recrystallisation of the crystals at higher differential stress during subsequent deformation. Owing to this robust evidence of bedding-parallel shearing, the laminated veins can be classified as **extensional-shear veins**.

These extensional to extensional-shear features exclude the possibility that the BPVs in the North Eifel are compressional shear veins, formed by an amalgamation of dilational jogs (*e.g.* Hilgers *et al.* 2006b, Koehn & Passchier 2000). In literature, shear veins related to bedding-parallel slip often comprise a very typical internal fabric in which oblique host-rock inclusion trails and subhorizontal crystal fibres track a lateral opening of the veins. The alignment of these inclusion trails have been used as shear sense indicators (Jessell *et al.* 1994, Koehn & Passchier 2000). Such a striped bedding-vein defines a specific stress state in which the maximum principal stress is at high angle to the vein (*e.g.* Fagereng *et al.* 2010), and high differential stresses are required (*e.g.* Teixell *et al.* 2000), a stress state however incompatible with the formation of BPVs in the North Eifel.

Bedding-parallel shear has also been observed in composite bedding-parallel veins that are characterised by alternating coarse-grained and fine-grained laminae (Figure 4.9b). In these veins, fine-grained recrystallised shear laminae occur in small ramps, indicative of a NW- to a NNW-directed shear. In the intermediate coarse-grained laminae, which grow on these ramps, grain size variability is a growth phenomenon that mainly is controlled by the ratio of the fracture opening rate versus the precipitation rate (Hilgers *et al.* 2001). Large blocky crystals may grow in an open fluid-filled void until the void collapses. Subsequently, either a new coarse-grained or a shear lamina subsequently may develop. The internal solid inclusion seams that are teared apart during fracturing form new surfaces on which crystals can grow during further vein thickening (Hilgers & Urai 2005). These multiple phases of opening and closing of a fluid-filled void at the time of vein formation can be linked to the earthquake cycle (Boullier & Robert 1992, Cox 1995) and to fluid-pressure cycling (cf. ‘fault-valving’) (Sibson 1990). In these models, veins precipitated from an overpressured fluid in the seismic periods while during the interseismic periods, the void collapsed in response to a decrease of the fluid pressure below lithostatic.

The phases of **bedding-normal collapse** can be interpreted to be the trigger of a transient compressive state during which anastomosing stylolites formed parallel to the quartz laminae in the BPVs. Stylolites in bedding-parallel veins often result from pressure-dissolution during fluid-assisted (diffuse) mass-transfer (Wilson *et al.* 2009). They preferentially developed at the contacts of quartz grains boundaries or at the contact with host-rock inclusion seams in which the porous structure of the host-rock provided the permeability to transport the dissolved material. The small grains present at the stylolites and at the host-rock seams may be the result of local precipitation of this dissolved material. Although the bedding-normal, uplift-related, extensional features evidence an overall stress state with a horizontal maximum principal stress ($\sigma_1 \sim \sigma_H$), such collapses occurred repeatedly and evidence compaction during transient seismic switches of σ_1 towards the vertical.

4.5 Fluid-inclusion petrography

Additional to the microfabric study of the veins, also a petrographic analysis of the fluid inclusions present in vein quartz has been performed. The study of fluid inclusions trapped in vein quartz is important as they are directly representative of the vein-forming fluids. From their study, the composition of the fluid from which the vein precipitated, as well as pressure and temperature (P-T) conditions at the time of precipitation can be derived by microthermometry (Chapter 5). However, to determine the P-T conditions properly, it is crucial to choose those fluid inclusions that are trapped during crystallisation and thus reflect the fluids during vein growth and not those inclusions that may have formed in late cracks, when the vein already completely sealed. Therefore a detailed petrographic analysis is needed.

Based on the timing of formation with respect to crystal growth, fluid inclusions are classically separated in three different groups (Roedder 1984, Shepherd *et al.* 1985). Primary inclusions are considered to be trapped during crystal growth when small crystal imperfections or irregularities in the crystal lattice are sealed off and allow the presence of small remnants of the vein-forming fluid. These primary inclusions are arranged in growth bands parallel to the crystal faces and mainly form in blocky crystals. Primary inclusions occurring in growth zones are absent in the selected samples representative of the bedding-normal veins (see Table 5.1 in Chapter 5). A second type comprises pseudosecondary fluid inclusions which are interpreted to represent fluids trapped in healed microcracks that formed during crystal growth. A third group of fluid inclusions concerns all secondary fluid inclusions that are trapped during fracturing and subsequent re-sealing of microcracks in a pre-existing crystal. If fluid inclusions are studied in 2D in a thin section, they often occur in trails. These trails, however, only provide a limited part of a 3D trapped fluid inclusion planes (FIPs). Studying fluid inclusions in 200 μm-thick wafers has the major advantage that the orientation of these 3D fluid-inclusion planes (FIPs) can be estimated and can be measured.

4.5.1 Bedding-normal veins

In the centimetre-thick and composite bedding-normal veins, pseudosecondary inclusion trails are ubiquitous in fibrous to elongate-blocky crystals. Pseudosecondary fluid inclusions are always oriented in trails at high angle or perpendicular to the crystal elongation in fibrous and stretched vein fills (Figure 4.13a-e). If the fibres for instance track an opening trajectory perpendicular to the vein wall, pseudosecondary trails are oriented parallel to the vein wall (Figure 4.13b and d). However, the microfabric analysis pointed out that sometimes fibres do not track the opening trajectory and are oriented oblique to the crystal wall. In these examples pseudosecondary fluid-inclusion trails may still be oriented perpendicular to the vein wall, but at high angle to the fibre elongation (Figure 4.13a). Trails are furthermore restricted to an individual fibre and change in orientation at the contact between two fibres (Figure 4.13e). If crack-seal inclusion bands are present in fibres, oriented perpendicular to the crystal elongation; the pseudosecondary inclusion trails in this fibre are parallel to the inclusion bands. Pseudosecondary inclusion trails thus correspond to intracrystal healed microcracks during crystal growth and also indicate that vein precipitation occurred by incremental crack-seal steps. The specific orientation of the pseudosecondary trails in BNVs; *i.e.* perpendicular to the fibrous crystal borders and parallel to the vein walls, and their repetitive pattern confirm the interpretations made in the fabric analysis (see section 4.3), indicating that the bedding-normal veins are extension veins, which originally grew in Mode I fractures. It may thus be interpreted that pseudosecondary fluid-inclusion trails have trapped a fluid from which the quartz precipitated and are therefore very useful to reconstruct the P-T conditions during veining. In the studied wafers of the bedding-normal veins, secondary inclusion trails are always oriented parallel to the outer vein walls (Figure 4.13b, f and i), but they are not necessarily oriented perpendicular to the crystal elongation (Figure 4.13g and h). The secondary trails are continuous through the different quartz crystals, *i.e.* transcrystal. In this configuration, the secondary fluid-inclusion trails correspond to the resealing of post-veining transcrystal microcracks. Although it is shown from the petrography that these trails have a secondary origin, their specific orientation parallel to the vein walls demonstrates that microcracks still developed after formation of the bedding-normal veins.

Fluid inclusions occur within quartz crystals that do not show any evidence of crystal deformation. In other crystals, the intersection of inclusion trails with crystal imperfections such as deformation lamellae (Figure 4.6l; Figure 4.13l) caused opening of the fluid inclusions and created a loss of fluid during deformation. Consequently, these recrystallised grains are swept-clean of any fluid inclusion (cf. O'Hara & Haak 1992). In order to measure fluid inclusions properly, such deformed crystals are avoided in the microthermometric study. In addition, if grain boundary migration such as bulging did occur during recrystallisation, fluid inclusions may be reduced in size or may have leaked during the grain boundary mobility (Schmatz & Urai 2010). In both cases, this will cause an increase in homogenisation temperature, indicating that measuring fluid inclusions at the grain boundary should be avoided for deducing original pressure and temperature conditions during veining.

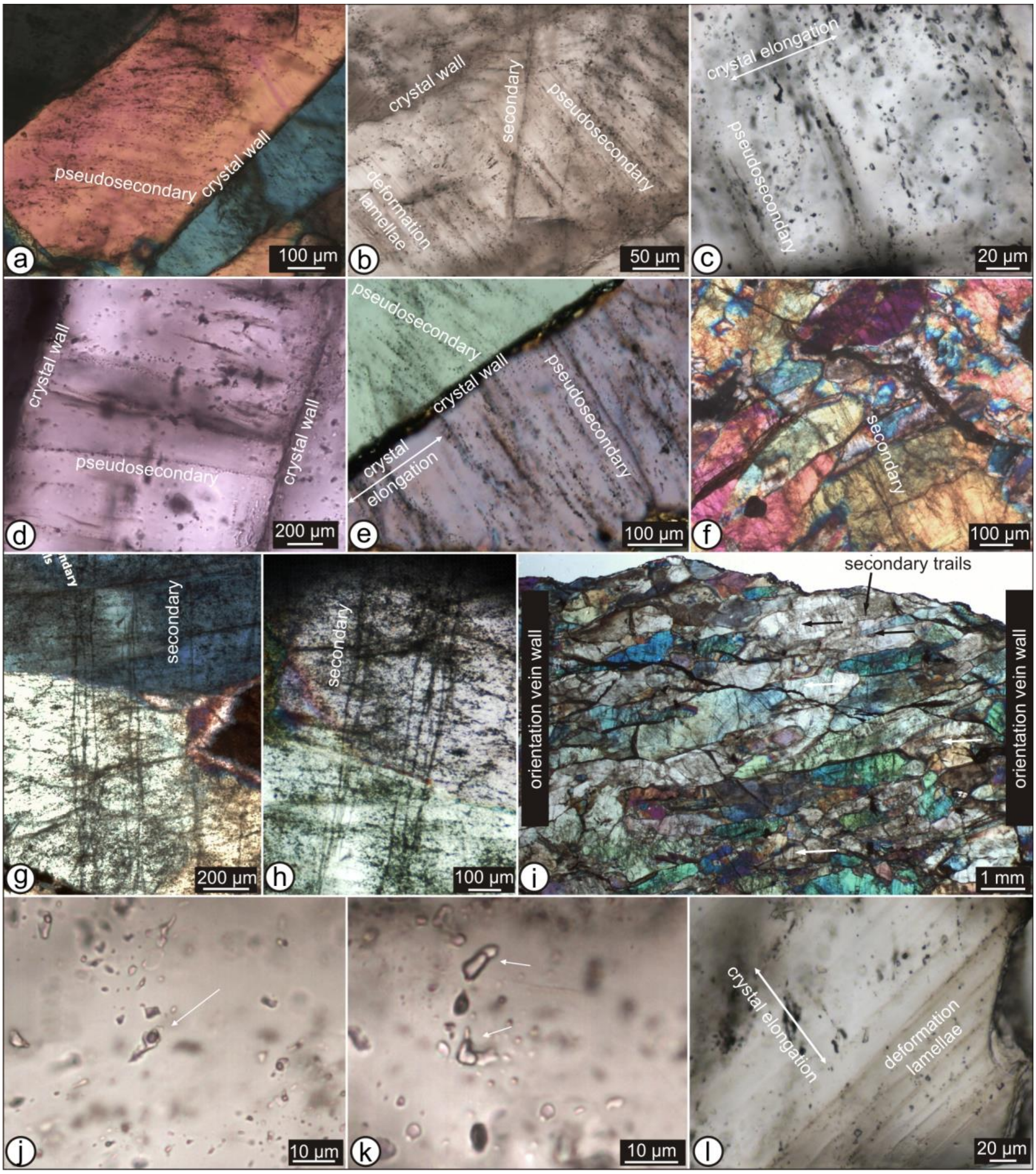

Figure 4.13: Microstructural petrography of fluid inclusions in bedding-normal veins. Examples studied on wafers. See Appendix B for sample localities. **(a-c)** Examples of intracrystal pseudosecondary fluid-inclusion planes oriented oblique or at high angle to the fibrous crystal walls (EI06VN07). **(d)** Pseudosecondary fluid-inclusion planes terminating at the crystal surface (EI06VN01). **(e)** Pseudosecondary fluid-inclusion planes remain at high angle to the crystal wall and to the crystal elongation irrespective of the orientation of the fibre crystal (EI06VN06). **(f-h)** Transcrystal secondary fluid-inclusion planes cross-cutting multiple fibres and oriented at high angle to the fibre orientation (EI06VN01). **(i)** Transcrystal secondary fluid-inclusion planes (arrows) oriented parallel to the macroscopic vein wall (EI06VN01). **(j-k)** Examples of re-equilibrated fluid inclusions that are avoided during microthermometry. **(j)** Leakage causing an increase in the vapour volume **(k)** Decrepitation causing an increase in the vapour volume. **(l)** Deformation lamellae causing leakage of fluids out of the fluid inclusion (EI06VN08).

At room temperature, both pseudosecondary and secondary fluid inclusions in the studied wafers consist of two phases; *i.e.* an aqueous liquid and aqueous vapour phase. The measured pseudosecondary inclusions have a consistent lenticular shape, with the long axis being smaller than 10 µm. The gas volume of the majority of the inclusions is ~15 % with the exception of some individual large inclusions, which show gas volumes up to ~35 %. Such large bubble sizes, however, are most probably related to re-equilibration of the fluid inclusion, attributed to leakage (Figure 4.13j and k). The secondary trails consist of alignment of very small spherical inclusions, often less than 5 µm with a gas bubble up to 20 % of the inclusion and are very difficult to measure. As previously described in the microstructural deformation of the veins, deformation lamellae are often present in fibrous veins. Because of the fact that they are oriented at high angle to the crystal elongation, and thus parallel to pseudo-secondary fluid-inclusion trails (Figure 4.13l), their formation has caused re-equilibration of the fluid inclusions in such way that either leakage or necking-down of the fluid inclusions occurred which results in higher homogenisation temperatures (cf. Kerrich 1976, Vernooij & Langenhorst 2005).

4.5.2 Bedding-parallel veins

In the bedding-parallel veins, only the undeformed crystals are of interest for defining primary or pseudosecondary inclusions that reflect the original composition and pressure-temperature conditions of the fluids from which the crystals in the bedding-parallel veins precipitated. The different types of bedding-parallel veins are characterised by an alternation of several different types of quartz laminae, *i.e.* blocky, crack-seal and shear laminae. Specific parts of the veins that are interesting to perform a fluid inclusion petrographical investigation are those laminae that contain undeformed quartz crystals.

In the coarse-grained laminae of the composite BPVs, blocky quartz grains do not show any recrystallisation fabric and show straight crystal margins. These grains form an ideal case to search for representative fluid inclusions. Although primary inclusions can develop parallel to growth zones in blocky quartz crystals (Roedder 1984), they have not been observed in the BPVs. Characteristically, only straight parallel trails and isolated inclusions are present in the blocky quartz-filled laminae. These planar trails are parallel to bedding (Figure 4.14a) and are interpreted to be pseudosecondary inclusion trails that have been trapped during incremental fracturing steps during blocky crystal growth. Isolated inclusions are abundant in these blocky grains, and sometimes show strong deformation as exemplified by a large gaseous vapour in the inclusion (Figure 4.14e). Although they could represent a primary growth feature (*e.g.* Kenis 2004), their origin is often unknown and they are not further studied.

Furthermore, also the crack-seal laminae, in which fibrous to elongate-blocky crystals occur (Figure 4.8h and i), are interesting for microthermometry. Pseudosecondary fluid-inclusion trails (*i.e.* fluid-inclusion planes, FIPs, see comment in section 4.5) are common in the fibrous to elongated crystals and are oriented at high angle to the crystal elongation (Figure 4.14b-d). They are interpreted as intragranular synkinematic trails reflecting fluid entrapment during vein precipitation and can thus be used to decipher the P-T conditions during quartz fibre growth. In the crack-seal bands, bedding-perpendicular columnar inclusion trails, oriented at high angle to the crystal elongation and cross-cutting fibrous crystal margins (Figure 4.14f), are interpreted to be secondary trails that correspond to post-veining transcrystal healed microcracks.

As indicated in the fabric analysis of the bedding-parallel veins (section 4.4.2), most crystals in the shear laminae show strong evidence of dynamic recrystallisation, taking place as bulging recrystallisation of the crystal borders after quartz growth (Figure 4.9i; Figure 4.14f). This recrystallisation has destroyed, stretched or leaked the fluid inclusions making them unsuitable for microthermometry. At room temperature, both pseudosecondary and secondary inclusions in the studied wafers consist of two phases, *i.e.* an aqueous liquid and aqueous vapour phase. The pseudosecondary inclusions vary in shape from lenticular to round and triangular, with sizes up to 15 µm and gas volumes of 15 %. Similar to the secondary inclusions in the BNVs, the secondary inclusions in the BPVs are rounded. They are usually very small (~5 µm) with consistent gas volumes (10 %).

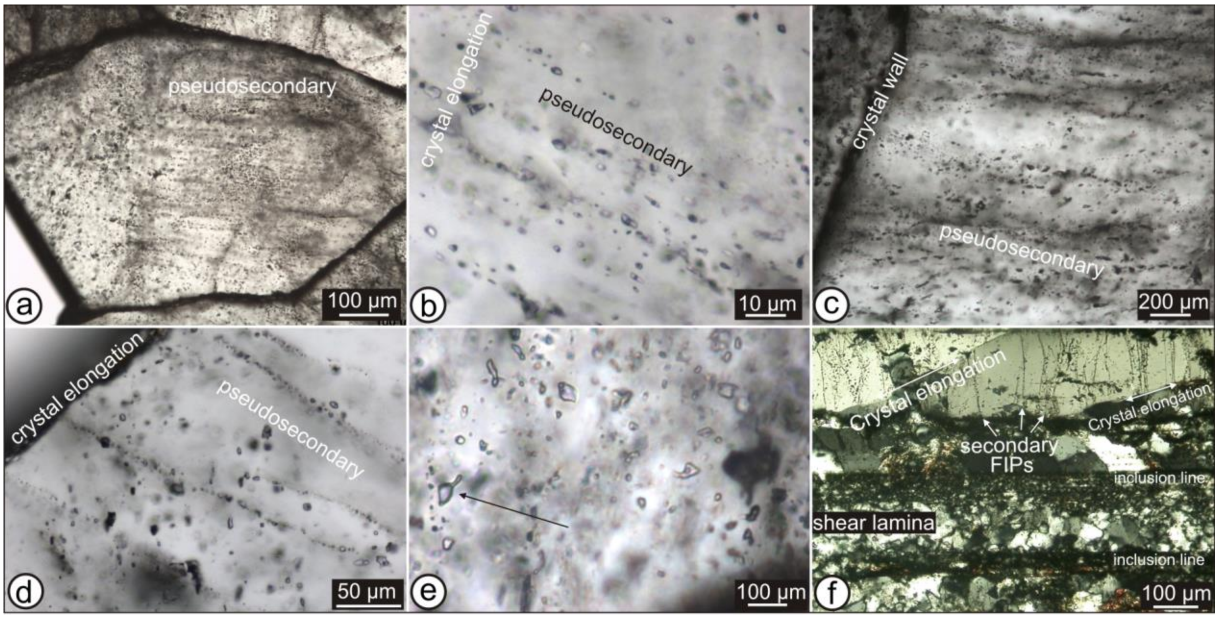

Figure 4.14: Fluid inclusion petrography in bedding-parallel veins. See Appendix B for sample localities. **(a)** Pseudosecondary fluid-inclusion trails in blocky quartz grains oriented parallel to bedding (EI08VN25). **(b)** Aligned pseudosecondary fluid-inclusion trails in fibrous crystal. Fluid inclusion sizes are less than 10µm (EI05VN25). **(c-d)** Pseudosecondary fluid-inclusion trails perpendicular to the fibrous crystal elongation (EI06VN10). **(e)** Re-equilibrated fluid inclusion (black arrow) evidenced by large gaseous bubble (EI05VN025). **(f) L**aminated bedding-parallel vein (EI05VN40). Vertical secondary fluid-inclusion planes (FIPs) cross-cutting the fibres in crack-seal lamina and oriented at high angle to fibre elongation. Measuring fluid inclusions in underlying shear laminae should be avoided because of recrystallisation.

4.5.3 Fluid inclusion planes as tectonic indicators

Microstructures given in literature that are useful to interpret them by means of maximum principal stress orientation, are for instance stylolites in limestone, deformation lamellae, calcite twins, planar microstructures and fluid-inclusion planes. The orientation of fluid-inclusion planes (often only seen as trials in thin sections) has been used in low-grade metamorphic environments as a microstructural marker to reconstruct the palaeostress evolution in the brittle crust, thereby often being parallel to the average maximum principal stress (σ_1) direction (Boullier & Robert 1992, Laubach 1989, Lespinasse 1999, Meere 1995a, Xu 1997). Especially pseudosecondary fluid inclusions in fibrous crystals are common in low metamorphic terrains and are very promising for a stress state reconstruction (Boullier & Robert 1992, O'Hara & Haak 1992, Stowell *et al.* 1999, Van Noten *et al.* 2009, 2011, Xu 1997).

For the bedding-normal veins studied, the specific orientation of the pseudosecondary planes is very consistent. Within the fibrous crystals, whether or not characterised by crack-seal inclusion bands, pseudosecondary inclusion planes are always oriented perpendicular to the crystal borders and (sub)parallel to the vein walls. Their repetitive pattern within the veins, moreover, indicate that the observed bedding-normal veins are extension veins, such as demonstrated by macrostructural and microstructural analysis, which originally grew by multiple phases of Mode I fracturing and subsequent healing in an already low-porous competent rock during the latest stage of burial. In this configuration, the orientation of fluid-inclusion planes indicates a maximum principal stress σ_1 that was still vertical corresponding to overburden loading in the basin, exemplified, for example, by dissolution features between the fibre crystals in an extension vein. These extension veins indicate an opening in the σ_1 - σ_2 plane parallel to σ_3.

The veins of the omnipresent generation V_B are thus aligned parallel to the intermediate principal stress σ_2 (Figure 4.15b) extending from the NNE to the SSW (Figure 4.15a).

Furthermore, although it is clearly demonstrated in the petrography that secondary fluid-inclusion planes have a secondary origin thereby cross-cutting multiple fibres, their specific consistent orientation parallel to the outer vein walls evidences that microcracks still developed after the opening and development of the extension veins. The vertical orientation of these secondary microcracks, however, demonstrates that they formed in a similar stress regime as the pseudosecondary inclusion trails (Figure 4.15b). These trails might thus contain similar fluids as the pseudosecondary trails.

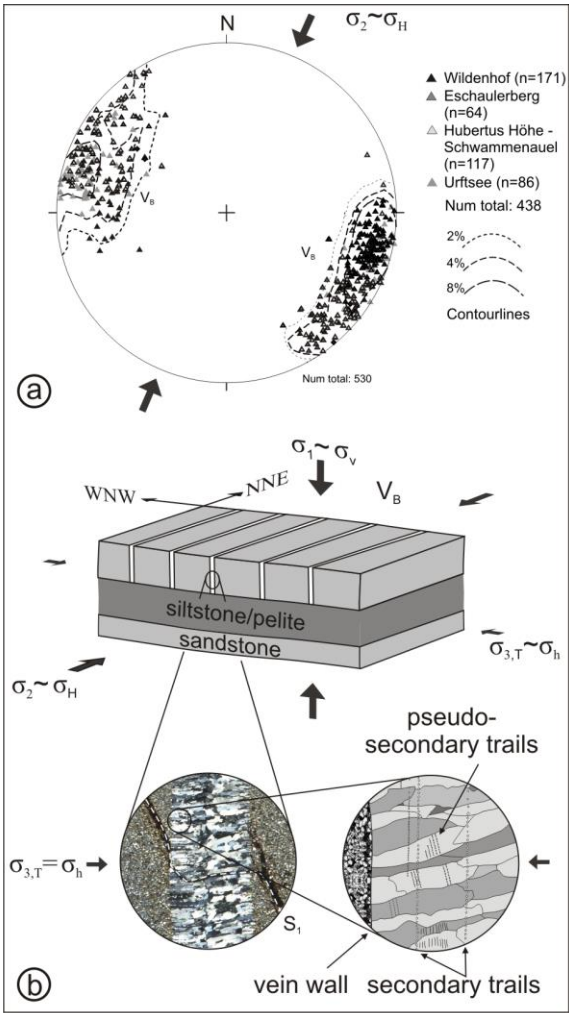

Figure 4.15: (a) Lower-hemisphere, equal-area stereographic projection showing the orientation of the consistent V_B bedding-normal quartz vein generation in its original unfolded orientation. **(b)** BNVs open in the $\sigma_1 - \sigma_2$ plane during extension induced by the vertical load of the overburden (σ_1) and an incipient tectonic stress (σ_t) which controls the regional vein alignment. Host-rock inclusion bands in the quartz fibres track a vein opening parallel to σ_3 and are oriented (sub)-perpendicular to the vein wall. They contain intracrystal pseudosecondary and transcrystal secondary fluid inclusions. σ_1, σ_2, σ_3 = maximum, intermediate, minimum principal stress respectively; σ_t = tectonic stress; σ_v, σ_H, σ_h = vertical, maximum horizontal and minimum horizontal (ESE-WNW) stress respectively.

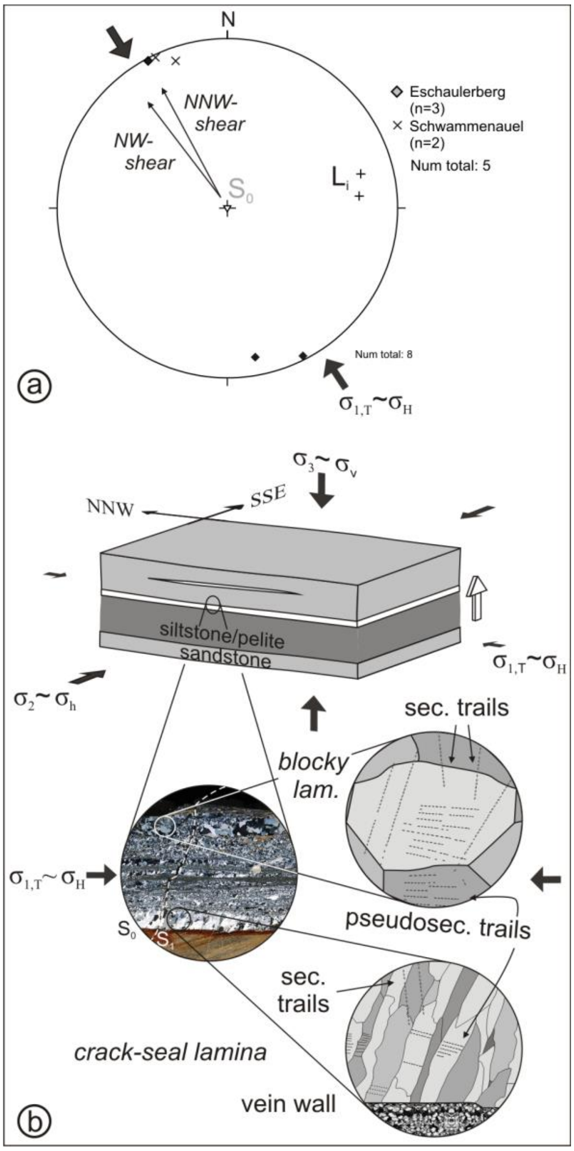

Figure 4.16: (a) Lower-hemisphere, equal-area stereographic projection showing the orientation of thrusting deduced from slickenfibres on bedding-parallel quartz veins in their original unfolded orientation. **(b)** BPVs open in the σ_1-σ_2 plane during compression. Pseudosecondary inclusion trails are subparallel in blocky crystals and are oriented at high angle to crystal margins in fibrous crystals. Secondary trails cross-cut the crystals and are subvertical. σ_1, σ_2, σ_3 = maximum, intermediate, minimum principal stress respectively; σ_T = tectonic stress; σ_v, σ_H, σ_h = vertical, maximum horizontal and minimum horizontal stress respectively.

Concerning the bedding-parallel veins studied, it has been demonstrated that these veins are defined as extension to extensional-shear veins. Consequently, pseudosecondary fluid-inclusion planes in the quartz crystals can be interpreted as Mode I cracks, *i.e.* tensile cracks that develop in the σ_1 - σ_2 plane, perpendicular to the vertical minimum principal stress σ_3, and are used as markers of the stress state during bedding-parallel veining (*e.g.* Boullier & Robert 1992). In the crack-seal laminae, pseudosecondary inclusion trails occur at high angle to the crystal elongation and were originally subhorizontal (Figure 4.16b). A similar orientation for pseudosecondary planes has been detected in the blocky grains in blocky laminae (Figure 4.16b). It is suggested that these planes thus reflect several phases of bedding-normal uplift in which microcracks open in trails in the crack-seal laminae perpendicular to the vertical minimum principal stress σ_3, or in which inclusions are trapped during crystal growth in blocky grains. It has to kept in mind that in BPVs in which shear laminae are observed, $\sigma_{1,T}$ was at low angle to bedding in order to allow shear stress on the bedding-parallel shear plane (see comment in section 3.5.2.2; Figure 3.42) and to allow oblique opening in the crack-seal laminae.

If trails are continuous through several grains and thereby cross-cutting the crystal margins, the trails are interpreted to be secondary and correspond to post-veining trans-crystal microcracks. A clear relationship between the orientation of secondary inclusion planes and bedding or the bedding-parallel vein wall, such as for the BNVs, could not be established. However, the secondary trails are often oriented perpendicular to the vein wall (Figure 4.16b) and might correspond to microcracks that developed during vertical shortening in periods of collapse that alternate with bedding-normal uplift (cf. Boullier & Robert 1992, Fisher & Byrne 1990, Henderson *et al.* 1990). Fluid inclusions in shear laminae are not investigated because of the strong recrystallisation that destroyed the originally trails reflecting the stress state during bedding-parallel thrusting.

At this stage, it is proposed that the orientation of the tectonic stress was oriented nearly parallel to the minimum principal stress ($\sigma_{3,T} \sim \sigma_h$; Figure 4.15) during bedding-normal veining and remained horizontal after the tectonic inversion during bedding-parallel veining ($\sigma_{1,T} \sim \sigma_H$; Figure 4.16b). It is appropriate to first demonstrate the role of the fluid pressure during both veining events before discussing the implications of the orientation of the tectonic stress. The latter implications will be discussed in Chapter 8.

4.6 Conclusions

A pervasive microstructural fabric analysis of both vein types has confirmed and refined the mechanisms that were proposed for the formation of successive quartz veins. It also allowed determining the microstructures in the veins that formed during subsequent deformation of the veins.

It can be concluded for the mainly mono-mineral bedding-normal veins, that vein formation occurred in a rock in which the porosity was already significantly reduced at maximum burial conditions. This is indicated by the low tortuosity of the veins and by the fact that hairline veins clearly cross-cut the sedimentary host-rock grains. Quartz commonly occurs as a fibrous to elongate-blocky fabric that has formed by an ataxial and syntaxial growth mechanism. A systematic vein fill related to a certain vein generation has not been deduced. Sometimes clear host-rock inclusion bands, oriented subparallel to the wall-rock, are torn from the vein walls during episodical opening of the vein by the crack-seal mechanism, marking former positions of the vein walls. These host-rock inclusions indicate that bedding-normal veins initiated as tensile Mode I fractures and that the rate of cementation was higher than the fracture rate. Fibrous crystals evolving to an elongate-blocky fabric indicates that either the fracture rate has increased or the precipitation rate has decreased. The veins may thicken to a composite fabric during numerous successive fracturing and sealing phases reflecting episodic vein growth during which crystal growth was dominated by the competition between fracturing rate and growth rate. The fibrous vein infill, the presence of crack-seal microstructures and the absence of lateral displacements are all indicative of a mechanism in which the BNVs developed as extension veins. If chlorite booklets occur, they are only present near both vein walls and evidence either a crystal growth together with the quartz or a late infill. A microstructural analysis of the orientation of pseudosecondary fluid inclusions confirmed a specific stress-state of the basin in which the veins propagated in the σ_1 - σ_2 plane, and opened parallel to σ_3. Vein-wall parallel microcracks, currently recorded as secondary inclusion trails, still developed after vein formation and under the same stress state as during vein growth.

Deformation microstructures in the veins, such as undulose extinction, deformation lamellae and bulging of the crystal walls, are indicative of relative low temperature deformation (~ 250°C) and only occur localised in the vein. They imply that limited deformation of the host crystals has taken place after veining, at higher differential stress than during the formation of extension veins. Primary microstructures such as fibrous crystals are often still present and were not destroyed afterwards. This indicates that the burial metamorphic conditions during which the veins were formed were not exceeded during subsequent progressive Variscan deformation.

Furthermore, it is concluded from fabric analysis of bedding-parallel veins that vertical opening occurred after the tectonic inversion. Two different vein mechanisms are distinguished. A first one comprises the intrabedded veins in competent units (*case iii*) that formed during several phases of bedding-normal uplift and collapse. As result of a fluid-filled open cavity, an elongate-blocky to blocky vein fabric developed during this mechanism. It can be concluded for this mechanism that these BPVs are extension veins. In the second mechanism, that involves all interbedded veins (*cases i and ii*) and the veins intrabedded in siltstone sequences (*case iv*), the vein fabric show a combination of bedding-normal uplift and bedding-parallel shearing during vein formation. Bedding-normal uplift is reflected by numerous crack-seal laminae in laminated BPVs, while it is reflected by coarse-grained blocky laminae in composite veins. In both laminated and composite BPVs, the shear laminae evidence phases of bedding-parallel thrusting during which quartz crystals (de)form during shear movements along microthrusts and afterwards recrystallise at higher differential stress during subsequent Variscan deformation.

Because of this pronounced bedding-parallel fabric, these veins can be classified as extensional-shear veins. It is concluded from the laminated or composite character of the bedding-parallel veins that they represent multiple phases of opening and closing of a fluid-filled void which may be linked to the earthquake cycle. It is proposed that veins precipitated from overpressured pore fluids at lithostatic values in the seismic periods while during the interseismic periods, the void collapsed in response to a decrease of the fluid pressure below lithostatic. This collapse is exemplified by stylolites in the BPVs oriented parallel to the quartz laminae and evidencing a fluid-assisted mass transfer. Such collapses occurred repeatedly and evidence compaction during transient seismic switches of σ_1 towards the vertical axis.

CHAPTER 5 Pressure-temperature conditions of vein formation

5.1 Introduction

In this chapter it is aimed to determine the pressure and temperature (P-T) conditions at the time of vein formation and hence at the time of fluid capture during crystal growth. The composition of the fluid from which the vein minerals precipitated and that have passed through the veins after veining, are deduced by a detailed microthermometric analysis of carefully selected fluid inclusions. In addition, Raman analysis of two representative samples is performed to check if the obtained results of the composition of the fluids by microthermometry can be confirmed. Both tools have often been used in various low-grade metamorphic terrains. Fluids in such low-grade metamorphic terrains, usually contain water with dissolved salts (*e.g.* mainly NaCl, KCl or $CaCl_2$), but can also comprise gaseous components of which CO_2, N_2 and CH_4 are very common (Shepherd *et al.* 1985). The deformation of the vein fabric and resulting destruction of fluid inclusions might hamper interpreting the results of microthermometry. This shows the importance of the detailed petrographic analysis of fluid inclusions in the previous chapter. Fluid-inclusion trails that have carefully been chosen and in which evidence of destruction is absent, are useful pressure and temperature markers. It has been demonstrated that several mechanisms are responsible for crystal growth in the bedding-normal and bedding-parallel veins. The bedding-normal veins (BNVs) mainly consist of a fibrous to elongate-blocky fabric in which pseudosecondary fluid-inclusion trails are trapped from the fluid that passed through the host rock and are captured during incremental steps of fracturing and crystal growth. The specific orientation at high angle to the fibre or elongate crystal wall illustrates that pseudosecondary inclusions are formed during incremental steps of crystal growth indicating a concomitant relationship. Transcrystal secondary inclusion trails are healed post-veining microcracks oriented parallel to the vein wall, but are demonstrated to be related to the similar stress state during which the pseudosecondary fluid inclusions in the bedding-normal veins formed.

Bedding-parallel veins (BPVs) formed by a combined mechanism of bedding-normal uplift and bedding-parallel shearing. As result of this mechanism, BPVs consist of a complex fabric in which finding the proper fluid inclusions that reflect the original P-T conditions and composition of the vein-forming fluids is strongly dependent on the understanding of the vein fabric. From the microfabric analysis it became clear that only fibrous and coarse-grained blocky laminae in composite BPVs and crack-seal laminae in laminated veins have the potential to contain proper original fluid inclusions. In the fine-grained laminae, crystals are mostly completely recrystallised so that the original fluid inclusions are destroyed. Primary inclusions are absent. Pseudosecondary trails are either found in fibrous crystals, oriented at high angle to the crystal wall, or in larger blocky grains in which they are oriented subhorizontal to the vein wall and hence subparallel to bedding. Secondary trails cross-cut the fibres and the blocky grains and are oriented normal to the bedding and the vein wall. They are synkinematic with the growth of the BPV and are interpreted to form during periods of bedding-normal collapse which allows forming bedding-normal transcrystal microcracks in a short transient extensional stress regime.

Microthermometry, however, only determines the fluid composition and the homogenisation temperature of fluid inclusions and does not directly provide the trapping temperature and pressure conditions of the vein. Fluid inclusions are interpreted to form from a single-phase homogeneous fluid at the time of vein formation. At room temperature, however, always two phases are observed in the samples: a liquid phase and a gaseous phase, seen as a bubble in the inclusions. To obtain the temperature of the homogeneous fluid from which the vein precipitated, the samples have been heated for determining the homogenisation temperature (T_h). Microthermometry only gives the possibility to draw isochores along a P-T path representing the range of P-T conditions at which the fluid inclusion formed. The T_h, however, underestimates the real trapping temperature (T_t) of the inclusion because the T_h is measured at the pressure conditions of the liquid-vapour curve. Hence, an independent geothermometer is needed to make a pressure correction for the T_h and to determine the true P-T conditions at depth during both veining events. In this work, the reflectance of vitrinite particles in the host rock is used a useful independent geothermometer.

Table 5.1: Samples from Wildenhof (Wild) measured during microthermometry and that are representative of bedding-normal and bedding-parallel veins. sdts, sandstone; slst, siltstone. See Appendix B for specific sample localities and Appendix C for detailed fluid inclusion results.

Sample nr	*Type*	*Gen.*	*Location*	*Host rock*
EI05VN27	BNV	V_B	Wild 36	sdst
EI06VN07	BNV	V_B	Wild 44	sdst
EI06VN08	BNV	V_B	Wild 44	sdst
EI06VN14	BNV	V_B	Wild 27	sdst
EI06VN16	BNV	V_B	Wild 42	sdst
EI06VN01	BNV	V_C	Wild 44	sdst
EI06VN09	BNV	V_C	Wild 39	sdst
EI08VN17	BNV		Wild 46a	vein in slst
EI08VN12	BNV		Urftsee zone 7	sdst
EI05VN25	BPV	composite	Wild 27	interbedded slst-sdst
EI05VN26	BPV	composite	Wild 27	interbedded slst-sdst
EI06VN10	BPV	composite	Wild 42	intrabedded slst

Importantly, it is preferred to elaborate the microthermometric results of one case study in detail in order to avoid lateral differences between the case studies that possibly may exist in fluid composition or in temperature conditions during fluid inclusion trapping. This allows constructing the proper pressure conditions needed for determining the ultimate stress-state evolution during both veining events. The Wildenhof section is a proper choice as several vein bedding-normal generations are present that are correlated regionally, and as the described bedding-parallel veins that occur in the study area are all present as well. One other sample from the Urftsee has been carefully studied to allow correlation. This justifies the choice of samples that are measured and interpreted (see Table 5.1). Only the composite BPVs are used for microthermometry as the quartz crystals in laminated BPVs have commonly very small sizes and are strongly recrystallised.

5.2 Microthermometry

5.2.1 Methodology

Microthermometric measurements on fluid inclusions were carried out on doubly polished 150 µm thick wafers from carefully selected and oriented vein-quartz samples. Detailed description of the preparation technique is given in Muchez *et al.* (1994). After petrographic analysis, fluid inclusions were analysed on a Linkam MDS-600 heating-cooling stage mounted on an Olympus BX51 microscope. Calibration was performed using synthetic, Syn Flinc^{Tm}, fluid inclusion standards and the stage was calibrated at -56.6°C, -21.2°C, -10.7°C, 0.0°C and 374.1°C using pure CO_2-, H_2O-NaCl-, H_2O-KCl- and H_2O-fluids respectively. The precision of the equipment used is within 0.2°C for melting temperatures, which has been determined by cycling heating-cooling sequences. Calibration of the equipment for high temperature at the lab of the *Geodynamics and Geofluids Research Group* indicates that the error for the homogenisation temperatures did not exceed 3°C. Quantification of gaseous components in the fluid inclusions was performed by laser Raman microspectroscopy at the *Royal Belgian Institute of Natural Sciences* (Brussels). Analyses have been made with a Senterra-Brüker laser Raman microspectrometer, which was mounted on an Olympus BX50 microscope. A 532 nm green confocal Ar^+ laser was used as excitation source, operating at 20 mW. Both short and long range objectives up to X100 magnification were used and an electronically cooled CCD camera allowed observation of the samples during analysis. The instrument was calibrated using NIST SRM 2242 (Choquette *et al.* 2007). Quantitative analyses of the different species present in the fluid inclusions are derived from the integrated peak intensities and the relative Raman scattering cross-sections, as described by Schrötter & Klöckner (1979) and Dubessy *et al.* (1989). Reproducibility and accuracy of the analyses are around 1 mol% and 5 mol% respectively (van den Kerkhof & Kisch 1993).

In microthermometry, the temperature of first melting (T_{fm}) can be determined by firstly freezing and subsequently heating the sample. Typical first melting temperature of the H_2O-NaCl system is around -21.2°C. From the measured T_{fm}, the main fluid composition of an inclusion can be estimated by comparison with the eutectic temperature of aqueous inclusions with different salts or salt mixes. In aqueous inclusions, the last temperature of melting (T_m (ice)) is characteristic of the fluid system salinity. Metastable melting of ice, *e.g.* due to the absence of a vapour bubble, has to be avoided. Furthermore, it is often very difficult to determine precisely the T_m (ice) due to the small size of the inclusions measured. In these small inclusions, it is often difficult to see the ice crystal under the microscope when approaching the final melting temperature, although 'cryptic' ice may still be present. To solve this problem, cyclic cooling and heating has been used, a method in which the inclusion is slowly heated at steps of 0.1°C, and subsequently rapidly cooled. This cycling allows the cryptic ice to grow as a large crystal, which can be observed better and which causes deformation of the gaseous bubble in the inclusion. The specific method of cycling has been termed sequential freezing and provides a very good solution to solve the problem that are involved with measuring small inclusions (cf. Haynes 1985).

The minimum trapping temperature, given by the homogenisation temperature (T_h) of the fluid inclusion, is measured for those inclusions that have an aqueous composition. Large inclusions are often deformed due to post-entrapment re-equilibration, *e.g.* stretching, leakage or decrepitation, which influences the T_h of the inclusions (Bodnar *et al.* 1989, Roedder 1984). Small inclusions are more resistant to re-equilibration and are therefore more suitable for microthermometry (Bodnar 2003, Vityk *et al.* 1994) and are used during the measurements (see size descriptions in the petrographic description of fluid inclusions in sections 4.5.1 and 4.5.2). A considerable effort has been put into the measurements of the pseudosecondary inclusion trails in order to have a proper statistic overview of the T_h. These measurements are performed on wafers in which melting temperatures (T_m (ice)) are not measured in order to avoid deformation and leakage of the inclusions during the increase of volume due to ice formation. This results in several tables in which only T_h measurements are reported. It is referred to Appendix C for the data corresponding to these T_h measurements.

5.2.2 Fluid composition

For both pseudosecondary and secondary fluid inclusions in the **BNVs,** first melting temperatures are clearly observed from -21°C, or higher, indicative of an aqueous H_2O-NaCl composition with an eutectic temperature of -21.2°C. Last melting temperatures (T_m (ice)) range between -5.1°C and -2.1°C (Table 5.2). This range in T_m (ice) corresponds to low salinities of **3.5 to 8 eq.wt.% NaCl** (Bodnar 1993). Pseudosecondary and secondary inclusions in **BPVs** also consist of an aqueous H_2O-NaCl composition. Their T_m (ice) ranges between -4.4°C and -2.4°C (Table 5.2), corresponding to low to moderate salinities of **4 to 7 eq.wt.% NaCl** (Bodnar 1993).

In the main part of the samples studied, gases are absent. However, in one sample (EI06VN07; generation V_B) CO_2-rich inclusions are detected after microthermometry. CO_2 occurs in two-phase, mixed aqueous-gaseous inclusions, characterised by a liquid phase and a small gaseous bubble, and one-phase gaseous inclusions. On the one hand, mixed two-phase CO_2-rich inclusions in this sample occur in trails that are situated near the vein wall in the sample (see Figure 5.1). One-phase gaseous inclusions, on the other hand, occur isolated in the sample (see inlet in Figure 5.1). The origin of both trails and isolated inclusions is, however, unknown. Inclusion I in Figure 5.1 might be related to a pseudosecondary trail parallel to the vein wall, but there are no real indicators to relate the other inclusions to pseudosecondary or secondary trails.

Table 5.2: Summary of the data of aqueous fluid inclusions in bedding-normal and bedding-parallel quartz veins of the Wildenhof section (Rursee) organised per sample. slst, siltstone; Sst, Sandstone; n, number of fluid inclusions measured; T_f, freezing temperature; $T_{m,}$ last melting temperature; T_h-range, homogenisation temperature. Peak homogenisation temperatures are organised in classes of 10°C and are shown in Figure 5.4. See Appendix C for detailed fluid inclusion data. Samples EI06VN01 and EI06VN09 are different samples of a similar BNV. Samples EI05VN25 and EI05VN26 are different samples of a similar BPV.

Bedding-normal veins H_2O-NaCl

Locality/Outcrop	*Sample*	*Host-rock lithology*	*T_f (°C)*	*T_m (°C)*	*Inclusion-type*	*n*	*T_h-range (°C)*
Rursee/Wildenhof 27	EI06VN14	sandstone	-47 to -35	-4.2 to -3.0	pseudosec.	38	115 to 232
					secondary	12	126 to 235
Rursee/Wildenhof 46a	EI08VN17	siltstone	-38 to -31	-5.1 to -2.8	pseudosec.	46	110 to 250
					secondary	12	120 to 248
Rursee/Wildenhof 36	EI05VN27	siltstone	-44 to -39	-3.6 to -3.0	pseudosec.	42	82 to 250
					secondary	5	125 to 182
Rursee/Wildenhof 42	EI06VN16	sandstone	-44 to -35	-3.9 to -2.6	pseudosec.	36	148 to 213
					secondary	6	148 to 240
Rursee/Wildenhof 44	EI06VN08	sandstone	-45 to -26	-3.8 to -2.7	pseudosec.	23	148 to 328
					secondary	21	93 to 322
Rursee/Wildenhof 44	EI06VN07	sandstone	-38 to -29	-4.4 to -2.6	pseudosec.	56	122 to 345
					secondary	5	115 to 280
Rursee/Wildenhof 44	EI06VN01 + 09	sandstone	-47 to -27	-3.8 to -2.1	pseudosec.	61	90 to 290
					secondary	11	121 to 218
					Total:	374	

Bedding-parallel veins H_2O-NaCl

Locality/Outcrop	*Sample*	*Host-rock lithology*	*T_f (°C)*	*T_m (°C)*	*Inclusion-type*	*n*	*T_h-range (°C)*
Rursee/Wildenhof 27	EI05VN25 + 26	Slst-Sst interface	-38 to -27	-4.4 to -2.4	pseudosec.	124	84 to 302
					secondary	11	117 to 300
Rursee/Wildenhof 42	EI06VN10	Slst-Sst interface	-39 to -31	-3.9 to -2.8	pseudosec.	49	80 to 192
					secondary	10	116 to 169
					Total:	194	

Table 5.3: Fluid inclusion data of sample (EI06VN07) in which two-phase aqueous-gaseous (aq-gas) and one-phase gaseous inclusions are found. The origin of the inclusions is unknown but it is indicated whether they occur isolated or in a trail. Size measurements are in μm (length / width). Inclusions in bold are indicated in Figure 5.1.

Incl.	Type		T_f	T_f	T_f	T_m	T_{fm}	T_m	Sal.	T_m	T_h	T_h	Size	Vol. %
nr	unknown		CO_2	ice	clath	CO_2	ice	ice		clath	CO_2	tot	(L / W)	bubble
A	aq-gas	isolated	-102.6	-34.6		-57.2		-2.9	4.7	11.5	10.0		3 / 2	10
C	aq-gas	isolated	-102.6	-36.6	-26.0	-61.4		-2.6	4.3	10.3	-6.0	< 280	13 / 4	40
E	aq-gas	trail	-95.6	-33.7	-27.7	-57.0	-21.8	-4.4	6.9	9.3	21.2		6 / 4	30
H	aq-gas	trail	-104.3		-23.7	-65.4		-1.8	3.0	10.6		212.4	5 / 4	20
I	aq-gas	trail	-100.1	-34.6	-26.1	-58.9		-2.6	4.3	10.1	15.6		6 / 5	10
M	aq-gas	trail	-103.6	-32.7		-57.3		-3.4	5.5	7.7			8 / 2	20
29	aq-gas	trail	-104.1	-34.9		-64.0	-22.3	-3.1	5.1	12.1	-9.2	198	5 / 5	30
Y	gaseous	isolated	-104.1			-64.4							6 / 3	100
Z	gaseous	isolated	-101.5			-60.2							8 / 4	100
28	gaseous	trail	-105.0			-63.6					-15.5	208	8 / 5	100
30	gaseous	trail	-105.1			-65.5					-48.5		6 / 6	100
31	gaseous	trail	-104.1			-65.0					-33.9	180	9 / 7	100

Table 5.4: Results of Raman analysis for aqueous-gaseous inclusions in sample EI06VN07 (BNV: Wildenhof 44) and sample EI05VN25 (BPV: Wildenhof 27). These samples are not representative of inclusions in other veins as only in sample EI06VN07 gaseous and aqueous-gaseous inclusions are detected by microthermometry.

Sample	Incl. nr	vein type	CO_2	N_2	CH_4
EI06VN07(2)	C	BNV_B	80%	0%	20%
EI05VN25	A2-15	BPV	70%	30%	0%

At room temperature, the aqueous-gaseous (aq-gas) inclusions have very small sizes (mostly smaller than 10 µm; see Table 5.3). They consist of two phases, *i.e.* an aqueous liquid phase and a gaseous vapour phase with varying bubble sizes between 10% and 40%. During cooling of the aqueous-gaseous inclusions, formation of clathrate occurs between -23.7°C and -27.7°C. Further cooling causes the solidification of water into ice between -32.7°C to -36.6°C. Finally, the liquid near the bubble freezes between -95.6°C and -104.3°C, a temperature range representative of the presence of CO_2. This indicates that a third liquid phase is present and that thus both two-phase and three-phase aqueous-gaseous inclusions occur, although only two phases are visible at room temperature. During subsequent heating, first, the solid CO_2 melts between -65.4°C and -57.0°C. First melting of the solid aqueous phase occurs between -22.3°C and -21,8°C indicative of a H_2O-NaCl composition.

Subsequent heating results in melting of ice, between -4.4°C and -1.8°C, and clathrate, between 7.7°C and 11.5°C (Table 5.3). The gaseous inclusions do only contain a vapour phase at room temperature, but during subsequent cooling a liquid rim appears that freezes between -101.5°C and -104.1°C. Further cooling did not reveal the presence of any other gases. By heating the sample, the solid phase melts between -65.5°C and -60.2°C.

The CO_2-rich inclusions homogenise at various temperatures. In the gaseous inclusions, homogenisation predominantly occurs to the liquid phase between -48.5°C and -15.5°C, whereas for the aqueous-gaseous inclusions partial homogenisation of the CO_2 takes place between -9.1°C and 21.2°C. Microthermometry of sample EI06VN07 clearly indicated the presence of another gaseous component in addition to CO_2 in the inclusions by the lowering of the melting temperature compared to the melting temperature of pure CO_2 at -56.6°C (see Table 5.3). Although this lower melting temperature indicates the presence of other gaseous component, the composition of these other gases cannot be determined by microthermometry.

Because of undefined gaseous components in some of the inclusions, additional Raman analysis is performed on a few samples to detect minor concentration of gaseous components in the dominant aqueous inclusions (Table 5.4). The results show that only a minor percentage of the measured inclusions (less than 10%) contain a gaseous component. The measured aqueous-gaseous fluid inclusion in sample EI06VN07 (inclusion C, Table 5.4, Figure 5.1) representative of the BNVs, contain 20% CH_4 of the gas component. Additional Raman analysis has also been performed on sample EI05VN25 (Table 5.4), representative of the BPVs. Although no evidence was found for the presence of gases during microthermometry, Raman analysis shows that the measured pseudosecondary inclusions contain N_2 in addition to CO_2, *i.e.* 30% of the gas component.

It may thus be concluded from the microthermometric results and Raman analysis that both BNVs and BPVs dominantly precipitated from an **aqueous H_2O-NaCl** fluid with a **low salinity**, which was occasionally accompanied by a minor amount of a CO_2-CH_4 and CO_2-N_2 during bedding-normal and bedding-parallel veining respectively.

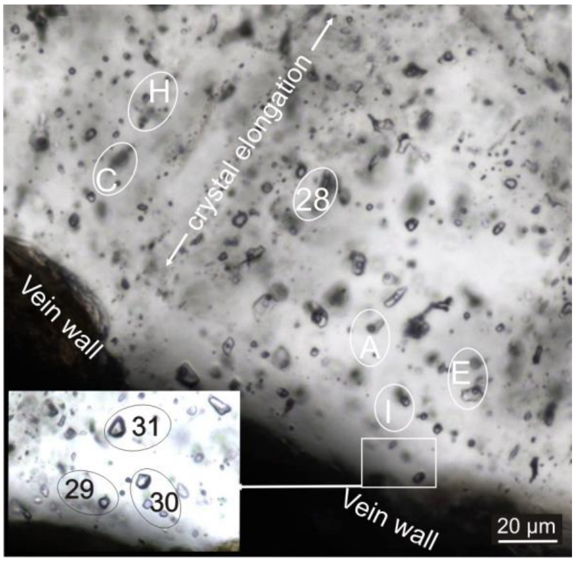

Figure 5.1: Detail of sample EI06VN07 showing two-phase aqueous-gaseous (A, C, E, H, I & 28) and one-phase gaseous (30 & 31) inclusions.

5.2.3 Homogenisation temperature

To interpret the results of the measured homogenisation temperatures of pseudosecondary and secondary inclusions, fluid inclusions organised within one fluid inclusion assemblage (FIA) should be compared. Conform the method of Goldstein & Reynolds (1994), fluid inclusions organised in a single FIA that are considered to be trapped together, *i.e.* inclusions in trails or in growth zones, should have a similar composition and a consistent homogenisation temperature if they did not re-equilibrate after entrapment. FIAs composed of inclusions with a constant liquid-to-vapour ratio might indicate that re-equilibration has not occurred (Bodnar 2003). In the BNVs and BPVs, inclusions in both pseudosecondary and secondary trails have been checked whether they comply with this criterion. Several pseudosecondary FIAs, however, yield inclusions with a T_h-range larger than 10°C (Figure 5.2). This indicates that the inclusions may have been subjected to post-entrapment re-equilibration such as i) stretching and leakage, causing an increased T_h, or ii) necking-down after a phase change, causing a change in T_h owing to phase separation of an original inclusion into several smaller inclusions in a changing temperature or pressure system (Bodnar 2003). In the latter situation, the inclusions in which a bubble formed after necking-down, homogenise at lower temperatures. Re-equilibration moreover depends on the individual inclusion size and shape and on the composition and structure of the host mineral (Bodnar *et al.* 1989, Bodnar 2003, Prezbindowski & Tapp 1991). Owing to re-equilibration and the small amount of measurable inclusions within a single FIA, data are represented per vein type and not per FIA (Table 5.2).

Although there might be a time span between pseudosecondary and secondary inclusion trapping in BNVs, both inclusion types trapped a fluid with a similar composition (Figure 5.3a) and T_h-range (Figure 5.4a and b). There are also no compositional differences between the pseudosecondary and secondary inclusions in the BPVs (Figure 5.3b).

Homogenisation of all measured inclusions from the Wildenhof section occurs to the liquid state. The frequency histogram of T_h-values of both pseudosecondary and secondary trails shows a large variation in T_h between 80°C and 350°C for the BNVs (Table 5.2; Figure 5.4a), without significant differences in T_h between both trail-types. The distribution of data can be classified as an asymmetrical, long-tailed distribution with skewness to higher temperatures. It is also remarkable that there are no differences in composition (Figure 5.3a), nor in homogenisation temperatures (Figure 5.4a) of fluid inclusions of the two measured cross-cutting generations V_B and V_C. A similar remark applies to the composition and T_h for pseudosecondary versus secondary inclusions.

The frequency histogram of pseudosecondary and secondary fluid inclusions of the BPVs (Table 5.2; Figure 5.4d) shows an asymmetrical distribution with a T_h-range between 80°C and 310°C, with the range of the secondary inclusions fully within the range of the pseudosecondary inclusions (Figure 5.4d). The inclusions in a quartz-vein sample that was taken in a BPV intrabedded in siltstone (EI06VN10) shows no difference in composition (Figure 5.3b), nor in homogenisation temperature (Figure 5.4c) compared to the inclusions in interbedded samples (EI05VN25+26).

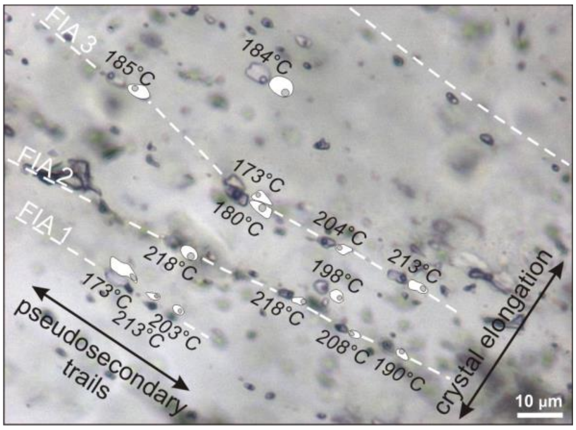

Figure 5.2: Photomicrograph of a bedding-parallel vein (EI05VN25) with pseudosecondary fluid inclusion assemblages (FIAs) oriented at high angle to the fibre crystal elongation. Each FIA contains fluid inclusions with a large range (> 30°C) in homogenisation temperatures.

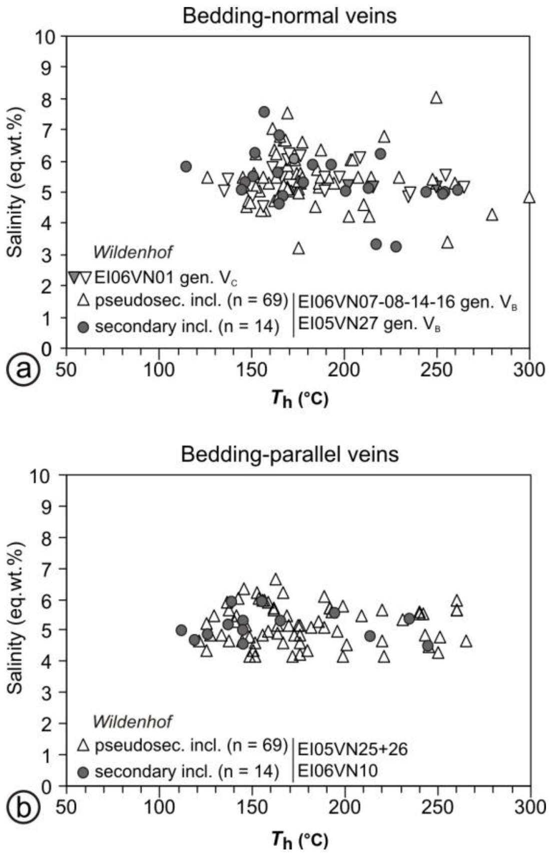

Figure 5.3 (above)**:** Homogenisation temperatures (T_h) versus salinity for all fluid inclusions in which a T_m(ice) could be measured. **(a)** Bedding-normal veins of both generations V_B and V_C. **(b)** Bedding-parallel veins. The wide T_h range in both diagrams can be attributed to cryptic post-entrapment fluid inclusion re-equilibration during formation and/or deformation of the veins. Compositional changes did not occur as both vein generations (V_B and V_C) and both vein types (BNV and BPV) plot in a similar salinity range.

Figure 5.4 (right)**:** Histograms of the homogenisation temperatures (T_h) of pseudosecondary and secondary fluid inclusions of samples from the Wildenhof section (See Appendix B for location of the samples). **(a)** Bedding-normal veins in the Wildenhof study area (Rursee) with peak T_h ranging between 140°C and 180°C. T_h of the two cross-cutting vein generations V_B and V_C, and of the irregular-shaped quartz vein intrabedded in slates has similar values. **(b)** Similar histogram as in (a) illustrating the similarity of T_h of pseudosecondary and secondary fluid inclusions. **(c)** Bedding-parallel veins in the Wildenhof section (Rursee) for which the T_h shows a plateau between 110°C and 160°C, showing slightly lower homogenisation temperatures than the BNVs in (a). **(d)** Similar histogram as (c) illustrating the similarity of T_h of pseudosecondary and secondary fluid inclusions in bedding-parallel veins. EI05VN25+26: interbedded BPV, EI06VN10: intrabedded BPV.

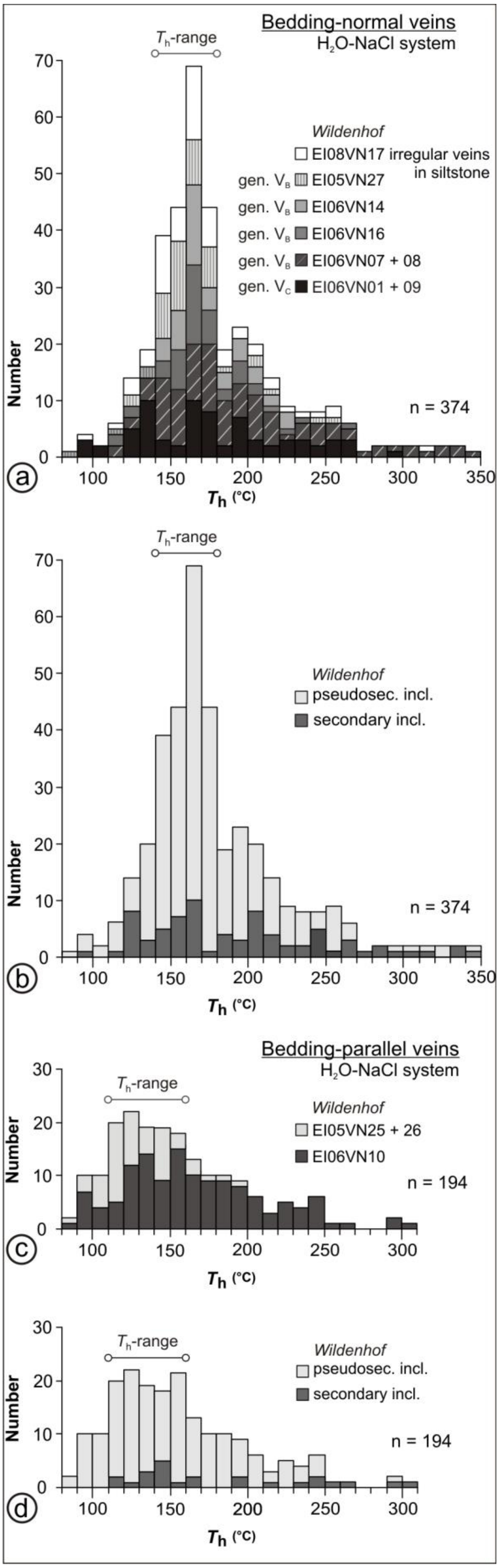

5.2.4 Re-equilibration of fluid inclusions

The wide range in T_h for both vein types can to a large extent be attributed to post-entrapment inclusion re-equilibration during deformation of the veins. Re-equilibration textures have been used to decipher the P-T history of the rock (Prezbindowski & Tapp 1991, Vityk *et al.* 1994, Vityk & Bodnar 1995). Decrepitated or clearly leaked inclusions in deformed crystals have been avoided during the measurements. The smaller inclusions may, however, also have been subjected to post-entrapment re-equilibration, although they do not show any re-equilibration textures that are visible during microscopic investigation. This cryptic re-equilibration (Vityk & Bodnar 1995) can only be deduced after microthermometry. The long-tailed distribution towards higher T_h-values (> 180°C; Figure 5.4a and b) can thus be interpreted as cryptic re-equilibration such as stretching of the inclusion walls (Bodnar *et al.* 1989). Although post-entrapment effects such as stretching, decrepitation and necking-down are more effective in softer minerals such as calcite, dolomite or barite (Evans 1995) than that they have an effect on quartz. It has been demonstrated by experimental research that stretching also occurs in quartz (Bodnar *et al.* 1989) due to internal overpressure of the inclusion thereby creating an increase in fluid volume and thus an increase in T_h. The lower T_h-values (< 140°C) can be attributed to necking-down after a phase change of an originally large, liquid-filled inclusion into smaller inclusions with lower T_h. This could have occurred without having noticed in the petrographic analysis.

Because of re-equilibration, a large range in T_h has been measured. Consequently, it is really important to determine the T_h-range that is representative of estimating the P-T conditions during veining. In literature it is not always clear which peak in the frequency histogram the investigators have chosen to determine the pressure conditions. In experimental work on fluid inclusions in quartz (cf. Vityk *et al.* 1995) one often chooses the T_h corresponding to the first large peak in the frequency distribution. In natural studies (*e.g.* Evans 1995), however, only the highest density inclusions, corresponding to the lowest T_h on the frequency histogram, are often used to provide a minimum estimate of the maximum density that prevailed during mineral growth. In this study, the lowest and highest T_h-values are interpreted to necking-down and cryptic re-equilibration of the fluid inclusions. Therefore the representative T_h-range of the highest frequencies (see various T_h-ranges in Figure 5.5) has been considered to be representative of the veining conditions during bedding-normal and bedding-parallel veining and has subsequently been used for calculating isochores which reflect the proper P-T conditions. The distribution of homogenisation data that thus likely reflects original P-T formation-conditions has a frequency peak of $\boldsymbol{T_h}$ between **140°C** and **180°C** for the **BNVs** (Figure 5.4a and b). Similar to the BNVs, the large range in T_h for the measured inclusions of the **BPVs** can be attributed to necking-down and cryptic re-equilibration. The distribution supports a frequency T_h-range between **110°C** and **160°C** (Figure 5.4c and d).

A similar range in T_h has been observed in the pseudosecondary fluid inclusions of a bedding-normal vein of the Urftsee study area (sample EI08VN12). Microthermometry reveals a T_h range between 170°C and 200°C with a frequency peak at 180°C and 190°C (Figure 5.5).

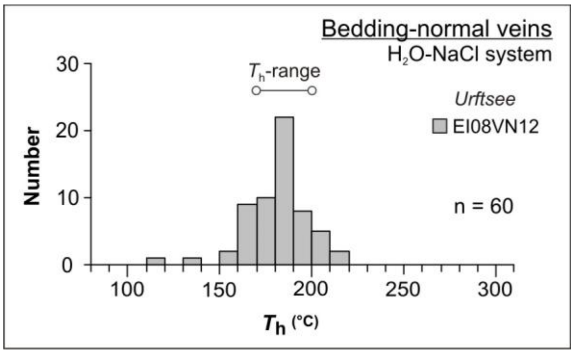

Figure 5.5: Histogram of homogenisation temperature of pseudosecondary fluid inclusions in a bedding-normal vein of the Urftsee study area (Urftsee zone 7, see Appendix A and B for location) showing a T_h-range of 170°C to 200°C with a frequency peak at 180°C.

5.3 Geothermometry

5.3.1 Isochores

The obtained homogenisation temperatures only represent the minimum temperature of the fluid trapped in the mineral. To obtain the trapping temperature (T_t) and eventually also the trapping pressure (P_t) during vein emplacement, a pressure correction should be made for the T_h. In order to estimate the trapping temperatures and pressures, isochores were constructed for the pseudosecondary fluid inclusions of both vein types, which are considered to represent P-T conditions during veining. These isochores represent a linear relationship between temperature and the internal pressure of a fluid inclusion, if the fluid remained at constant density during deformation and uplift, irrespective of the external pressure acting on the inclusion. The gradient of an isochore within a pressure-temperature graph depends on the salinity and the homogenisation temperature of the fluid inclusion measured (without a gaseous component) and can be calculated using the computer program FLINCOR (Brown 1989). The isochore calculations are based on a H_2O-NaCl system using the equation of Brown & Lamb (1989). Calculated isochores are plotted in a P-T diagram (see later Figure 5.8). This diagram is subsequently used to determine the maximum trapping pressure during veining by interpreting the intersection of the calculated isochores with either a regional geothermal gradient or with an independent geothermometer which defines the trapping temperature at maximum burial (cf. Shepherd *et al.* 1985).

Two sets of calculated isochores are presented: the first set (dashed lines in Figure 5.8), with density ranges between 0.92 g cm^{-3} and 0.98 g cm^{-3}, reflects the full T_h-range of the BNVs as determined on the frequency histogram (Figure 5.5a and b). The second set of isochores (full lines in Figure 5.8), with density ranges between 0.94 g cm^{-3} and 0.98 g cm^{-3}, corresponds to the T_h-range of the BPVs determined on the frequency histogram (Figure 5.5c and d).

5.3.2 Vitrinite reflectance (VR)

The method used for determining the trapping conditions is cross-cutting an independent geothermometer with the isochores of the fluid inclusions. Chlorite geothermometry, vitrinite reflectance, illite crystallinity and conodont alteration index have been used as possible geothermometers in the High-Ardenne slate belt (cf. Fielitz & Mansy 1999, Helsen 1995, Schroyen & Muchez 2000). Conodonts have not been observed in our samples of the Eifel area. Chlorites have been used successfully in low-grade metamorphic terrains as independent geothermometer (*e.g.* Sindern *et al.* 2007). However, previous geothermometric research on synkinematic chlorites in quartz veins, for instance by using the chlorite geothermometer of Vidal *et al.* (2005) on quartz veins in the Central Armorican Massif (Berwouts 2011), or on quartz veins in the central, epizonal part of the High-Ardenne slate belt (Kenis *et al.* 2002b, Verhaert 2001), pointed out that the variation in trapping temperature deduced from chlorite geothermometry is quite large (> 60°C), whereas the variation in trapping temperature derived by vitrinite reflectance data can be smaller and thus more precise if proper reflectance data are known (Bostick *et al.* 1979). Consequently, based on the availability of vitrinite reflectance data of the North Eifel in literature, vitrinite reflectance data are used as an independent geothermometer to derive the trapping temperature (cf. Van Noten *et al.* 2011).

5.3.2.1 VR as independent geothermometer

Vitrinite particles are very common in pelites and siltstones and they are particularly sensitive to temperature (Teichmüller 1987). The vitrinite reflectance, expressed in terms of average reflectance R_m or maximum reflectance R_{max}, defines the organic material maturity in the rock. Although this method is mostly used for coal rank stage determination and for deducing hydrocarbon presence in low temperature sedimentary basins, it can be used for low-grade metamorphic regions owing to the fact that the highest level of coalification, *i.e.* meta-anthracite, is congruent with the area of low-grade metamorphism (Kramm *et al.* 1985) or with the anchi- to epizone as determined by illite crystallinity (Frey & Robinson 1999, Teichmüller 1987). Vitrinite reflectance is thus a key method for identifying the thermal history of sediments in sedimentary basins and has often been used to evaluate the metamorphic grade of pelitic rock (e.g. Frey & Robinson 1999, Teichmüller 1987). The use of the thermal peak conditions derived from vitrinite reflectance studies in the host rock as geothermometer for the veins is valid since it has been demonstrated that the bedding-normal veins formed at maximum burial. Subsequently, successive bedding-parallel veins materialise the tectonic inversion to a compressional regime, and it is highly likely that the metamorphic conditions during maximum burial were still present at the onset of compression. It is furthermore demonstrated that maximum burial conditions are regionally consistent in the whole High-Ardenne slate belt (Fielitz 1997, Fielitz & Mansy 1999) (see also section 2.5). Moreover, metamorphic conditions are most probably in thermal equilibrium with the surrounding host rock (Kenis *et al.* 2000, 2005a, Muchez *et al.* 1995, Schroyen & Muchez 2000). Only at the Variscan front zone, thermal anomalies have been observed in Variscan veins (Lünenschloss *et al.* 2008, Sindern *et al.* 2007). Hence, this demonstrates that vitrinite reflectance data, recording the thermal peak conditions of the host rock surrounding the veins studied, can be used as a valid geothermometer for estimating the P-T conditions during vein growth.

5.3.2.2 VR in a very low-grade metamorphic terrain

Vitrinite reflectance data are ubiquitous in the very low-grade metamorphic terrain of the North Eifel. It has been a subject of research from the 50's, during which Teichmüller & Teichmüller (1952) have published the first results on a.o. vitrinite reflectance by studying Lower Devonian plant relicts. Further coalification studies during the decennia afterwards (starting from Teichmüller & Teichmüller 1979) increased the amount of data. Through these studies, it has been reported that the vitrinite reflectance isolines, *i.e.* lines of constant R_m and R_{max} values, roughly run parallel to bedding in most parts of the Rhenish Massif (Littke *et al.* 2000). In the North Eifel, the isolines decrease from the oldest rock at the Stavelot-Venn inlier, towards the youngest Emsian rocks in the SE. As the reflectance isolines run parallel to bedding, the maturation pattern is believed to be pre-orogenic and clearly represents the maturation of the buried sediments and not subsequent heating during the main orogenic contraction (Knapp 1980). Only locally, to the SE of the Urftsee area at Schleiden, an anomalous local increase in vitrinite reflectance has been reported (Ribbert & Vieth 2005), in which isolines run at low angle to the strike of bedding and the local fold axis. Published R_{max} values for the Upper Rurberg Unit range from 4.5 % (Vinzelberg 2002) to 5.44% (von Winterfeld 1994) and 5.5 % (Ribbert & Vieth 2005). A more general value of 5-6% has been reported for the Lower Devonian of the North Eifel (Fielitz & Mansy 1999, Oncken *et al.* 1999). Specific for the Wildenhof area an R_{max} value between 4.5 % and 5.5 % is thus representative of the vitrinite reflectance.

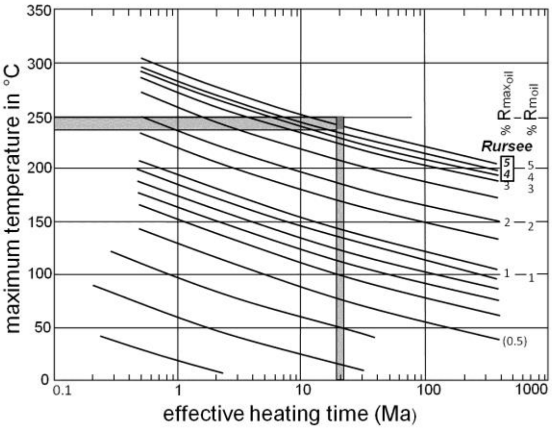

Figure 5.6: Conversion of vitrinite reflectance to burial temperatures after Bostick *et al.* (1979). Taking a 20 Ma heating time into account, a local vitrinite reflectance of 4.5 - 5.5 % R_{max}, representative of the vitrinite particles in the Rursee siltstones, corresponds to a maximum burial temperature of *c.* 235-250°C (grey area).

The relationship between vitrinite reflectance and temperature has been demonstrated by Hood *et al.* (1975) and Bostick *et al.* (1979) (see Figure 5.6). They show that the maximum temperature in a basin depends on the effective heating time of the basin, which is the time span during which the sediments were within 15°C of the basin's maximum burial (Hood *et al.* 1975), and that with increasing heating time the vitrinite reflectance increases. Because of this interaction, it is possible to relate a particular coalification degree to a specific temperature if the effective heating time of the basin is known. Such a specific temperature can thus be used as independent thermometer and to define the maximum derived temperature at the time of vein formation. For the sediments in the North Eifel a common effective heating time of 20 Ma has taken into account, a representative value that has been used in the frontzone of the Variscides and in the Campine basin (cf. Lünenschloss *et al.* 2008, Muchez *et al.* 1991) and that further will be elaborated in the construction of the burial model in section 5.3.3. Combining this effective heating time with the local vitrinite reflectance of 4.5 % to 5.5 % R_{max}, a maximum burial palaeo-temperature of *c.* 235-250°C is determined (Figure 5.6), based on the work of Bostick *et al.* (1979). Conversion of the vitrinite reflectance to burial temperature using the equation of Barker & Pawlewicz (1994), gives slightly higher temperatures (258°C to 273°C) than those predicted based on the work of Bostick *et al.* (1979), likely because the effective heating has not been taken into account in the equation of Barker & Pawlewicz (1994).

5.3.3 Geothermal gradient

Another independent geothermometer that is often used to determine trapping temperatures, is a geothermal gradient. The regional geothermal gradient, representative of the time of vein formation, can be used from literature, or can also be calculated by 1D burial modelling in which the stratigraphy of the sediments in the North Eifel (see lithostratigraphy in section 2.3) provides the input of the model. As the isolines of the vitrinite reflectance run parallel to bedding in most of the Rhenish Massif (Littke *et al.* 2000), the pseudowell concept can be applied in which the evolution of a hypothetic 1D borehole is reconstructed. It was chosen to work with the program 1D *Temis Suite well manager* (© Beicip-Franlab) at the *Institut Français du Pétrole* (IFP, France) for controlling if the derived temperatures by means of vitrinite reflectance are likely correct trapping temperatures. Firstly, it is checked if the temperature of 250°C is a realistic value. Secondly, the geothermal gradient corresponding to this temperature at maximum depth, is calculated. Afterwards this geothermal gradient is compared with values in literature.

The input parameters in the North Eifel basin model are the Palaeozoic stratigraphic successions deposited in the Ardenne-Eifel basin during burial (see lithostratigraphic table in Figure 2.4), the maturity of different rock units such as defined by vitrinite reflectance from literature (Heinen 1996, Ribbert & Vieth 2005, von Winterfeld 1994), the heat flow during Early Devonian rifting (60 mW/m^2 in the Eifel area according to Heinen 1996) and the estimation of the Moho depth before and after rifting (35 km and 20 km respectively; Heinen 1996).

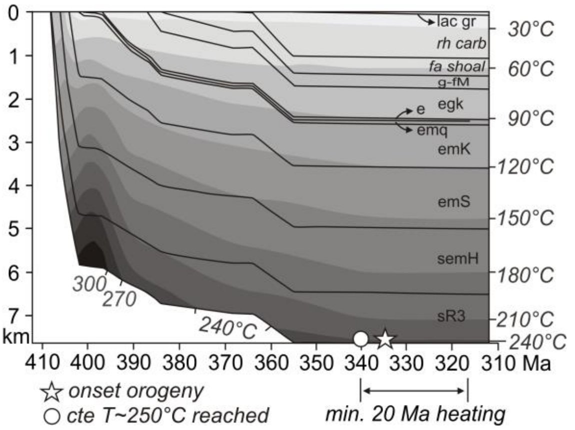

Figure 5.7: Constructed subsidence curve (depth versus time) for the Upper Rurberg Unit (Temis Suite © Beicip-Franlab). The predicted trapping temperature of 250°C by vitrinite reflectance at maximum depth of 7 km ± 0.1 km, corresponds to a mean geothermal gradient of 34°C km^{-1}. The initial high temperatures are related to an increased heat flow during rifting. Boundary conditions after Heinen 1996: palaeosurface temperature ~25°C, Moho depth: 35 km (rifting) and 20 km (after rifting). See Figure 2.4 for stratigraphical input and abbreviations of lithological units.

The result of this burial modelling (Figure 5.7) shows a subsidence curve in which temperatures increase rapidly during burial in the Early Devonian (~416 Ma to ~398 Ma). This increase in temperature is related to the rapid syn-rift subsidence that dominates the Early Devonian sedimentary infill of the Ardenne-Eifel basin (see Chapter 2). After the rapid infill, several units were deposited from the Middle to Late Devonian (~398 Ma to ~359 Ma) during which temperatures in the basin stabilise. The onset of Variscan Orogeny has been estimated to occur from ~335 Ma onwards (early Carboniferous) in the North

Eifel (Oncken *et al.* 1999). Afterwards the contraction-dominated main phase of the Variscan orogeny takes place. According to the model, maximum temperatures of 250°C are already reached prior to the onset of orogeny and rather constant after ~340 Ma. Subsequently the basin remained at this depth for at least 20 Ma, possibly 25 Ma. The model validates the effective heating time of 20 Ma that was taken into account for calculating the maximum burial temperature (Figure 5.6). It should be noticed that the effect of erosion is not modelled. Therefore a longer effective heating time may appear on the burial model. It is referred to Hilgers *et al.* (2006a) for a further continuation of the subsidence curve of the late- to post-Variscan development and subsequent erosion. Hence, the 1D burial model validates the 250°C which is predicted to be the trapping temperature of the veins at maximum burial. To reach temperatures of maximum 250°C in the Ardenne-Eifel basin, a mean geothermal gradient of ~34°C km^{-1} was calculated.

The calculated geothermal gradient can be correlated to various results in literature. For the anchizonal part of the High-Ardenne slate belt, illite crystallinity, conodont alteration index and vitrinite reflectance all point towards a regional geothermal gradient of 30-40°C km^{-1} present during burial of Lower Devonian strata in the Ardenne-Eifel Basin (Fielitz & Mansy 1999, Heinen 1996, Oncken *et al.* 1999). The regional geothermal gradient has been determined more accurately in the North Eifel by von Winterfeld (1994). He calculated values ranging between 33°C km^{-1} and 37°C km^{-1} representative of the Lower Palaeozoic deposits of the Stavelot-Venn Inlier and the unconformably overlying Lower Devonian deposits south of the basement inlier. A value that is similar to the calculated value of 34°C km^{-1} in the burial model. Values above 40°C km^{-1} have not been reported for the North Eifel during burial, neither for the succeeding Variscan Orogeny.

On the P-T diagram, the common range of 30°C km^{-1} to 40°C km^{-1} at both hydrostatic (30°C to 40°C for 10MPa^{-1} in Figure 5.8) and lithostatic (30°C to 40°C for 26.5 MPa^{-1} in Figure 5.8) pore-fluid pressures are shown. The range of the lithostatic geothermal gradient has a large overlap with the field defined by the intersection of the isochores and the independent geothermometer, indicating that the P-T trapping conditions during veining deduced from the vitrinite reflectance geothermometer and microthermometry are consistent.

5.3.4 Trapping conditions

In order to evaluate the range in pressure conditions during the two successive quartz veining events, it is now interesting, first, to determine the hydrostatic and lithostatic pore-fluid pressure at ~7 km, which is the maximum burial depth of the Lower Devonian host-rock studied, and second, to define the minimum and maximum trapping pressure (P_t) for both veining events and to compare these with the lithostatic and hydrostatic pore-fluid pressure.

Maximum **hydrostatic** pore-fluid **pressures** at ~7 km, which are determined from isochore calculations using a mean density of water (ρ) of 0.95 g cm^{-3}, are estimated to be **~67 MPa** at depth. The used water density of the low salinity liquid phase in the fluid inclusions are determined to be slightly lower than the value of 1.00 g cm^{-3} for water with zero salinity. These low densities (of the total inclusion) are the direct result of the low salinity, the low gas content and the high temperature at which the fluid was trapped.

A common density of the overburden rock of 2.65 g cm^{-3} corresponds to a maximum **lithostatic pressure** of **~185 MPa** at 7 km depth. Keeping into account an error of ±0.1 km on the total thickness of the deposits in the North Eifel (see section 2.3.5), the lithostatic pressure may range between 183 MPa and 188 MPa. Both hydrostatic and lithostatic pressures have been illustrated as straight curves in Figure 5.8. If the upper part of overburden would have slightly lower values of rock density because of the lower degree of compaction, the lithostatic value would be slightly overestimated.

The trapping temperature defined by the reflectance of vitrinite particles in the host rock, ranges between 235°C and 250°C and is illustrated as a gray column on the P-T diagram. The zone that is delimited by this trapping temperature and the calculated isochores, defines the specific fluid-pressure of each vein-type during fluid inclusion trapping and therefore defines the veining conditions. The results (Figure 5.8) show that the maximum T_t intersects with the maximum density of the

BNVs at **~190 MPa**, which is considered to correspond to a near-lithostatic pore-fluid pressure. For the **BPVs**, the intersection of the maximum T_t with the maximum density of the isochores calculated from microthermometric analysis of the pseudosecondary inclusions determines a value of **~205 MPa**, corresponding to supra-lithostatic pore-fluid pressures. This magnitude of overpressure lies above the range that is delimited by the error on the depth calculation of ±0.1 km, corresponding to a lithostatic pressure ranging between 183 MPa and 188 MPa. Hence, these intersections indicate that bedding-normal veining occurred at near-lithostatic fluid pressure, whereas pore-fluid pressures during bedding-parallel veining have risen up to lithostatic and supra-lithostatic. The absence of hydrostatic pore-fluid pressures during fluid inclusion trapping, and thus the absence of considerable fluid pressure fluctuations, can be demonstrated by the absence of overlap of the independent geothermometer with the isochores at hydrostatic geothermal gradients.

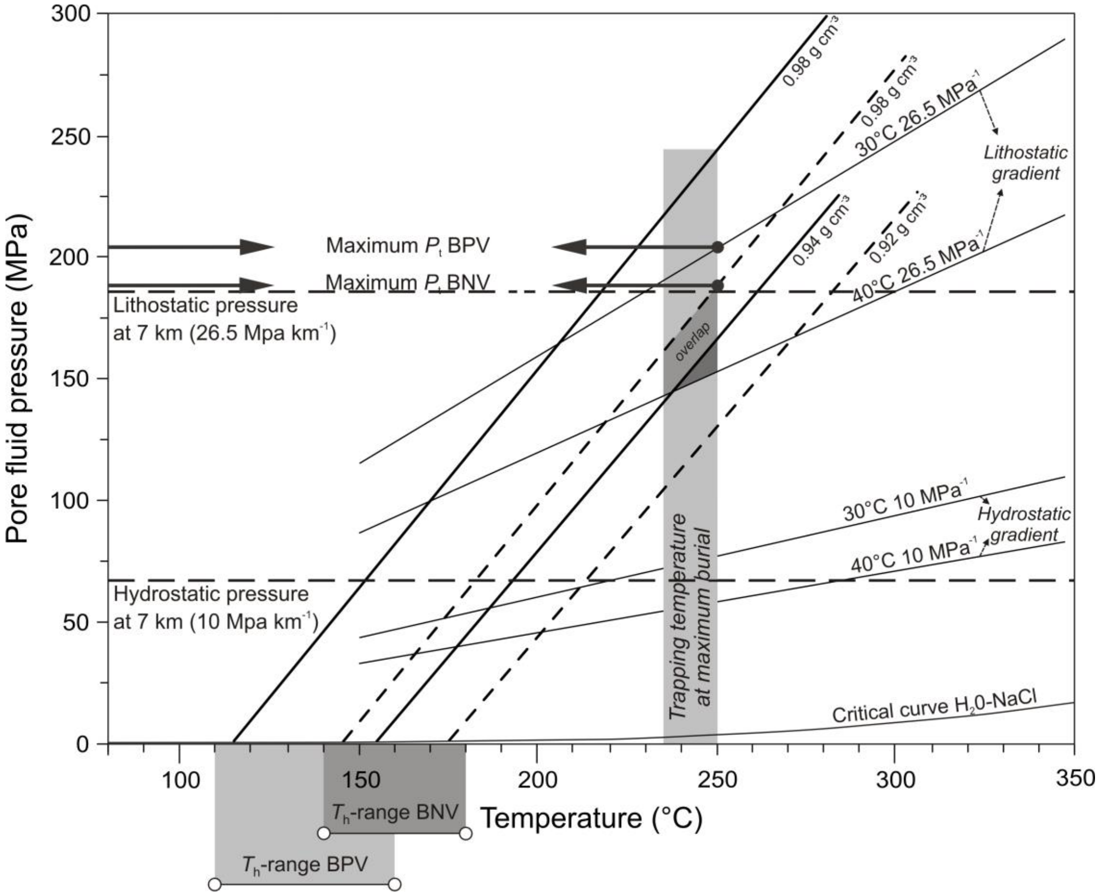

Figure 5.8: Pressure-temperature diagram showing trapping conditions of fluid inclusions in BNVs and BPVs of the Wildenhof section, representative of P-T conditions at maximum burial. Minimum and maximum isochores of each vein type were calculated on the basis of the T_h-range reported in Figure 5.4 and Table 5.2. Isochores of BNVs are represented in dashed lines and those of BPVs in full lines. The zone delimited by the range of the trapping temperature (235°C - 250°C) and calculated isochores evidences bedding-normal veining at near-lithostatic fluid pressure (up to ~190 MPa) and bedding-parallel veining at near-lithostatic to supra-lithostatic fluid pressure (up to ~205 MPa). Hydrostatic and lithostatic pore-fluid pressures at 7 km ± 0.1 km are calculated using water and overburden rock density (ρ) of 0.95 g cm^{-3} and 2.65 g cm^{-3} respectively. Modified after Van Noten *et al.* (2011).

5.4 Discussion

5.4.1 Fluid composition

It is aimed in this work, to determine the maximum trapping temperature and pressure of the fluids at the time of bedding-normal and bedding-parallel vein formation and not to illustrate the possible evolution of fluids that have circulated through the rock during the main phase of the Variscan deformation. If one would want to reconstruct this evolution, an additional intense fabric analysis of syntectonic veins and the microthermometric study of fluid inclusions in these veins should be performed. The results from such a research would contribute to the knowledge of the evolution and composition of fluids present during progressive deformation history. Such a fluid reconstruction, however, is not elaborated and lies beyond the scope of this work. The reader is referred to several microthermometric and geochemical studies performed on veins in the central, anchizonal to epizonal part of the central High-Ardenne slate belt (Darimont 1986, Darimont *et al.* 1988, Kenis *et al.* 2000, 2005a) or in the Lower Palaeozoic inliers (Schroyen & Muchez 2000).

The microthermometric results and Raman analysis of pseudosecondary and secondary inclusions imply that both BNVs and BPVs dominantly precipitated from a similar aqueous H_2O-NaCl fluid with a low salinity. Also gases such as CO_2, N_2 and CH_4 might have been present within these fluids, however, they are scarce and rarely observed within the fluid inclusions. The low proportion of other gases such as N_2 and CH_4 in addition to CO_2 have also been detected in intermullion veins in the anchizonal part of the High-Ardenne slate belt (Bütgenbach, Belgium, Kenis 2004) and are interpreted to be common in fluids that circulated through Lower Devonian rock. Kenis *et al.* (2002a) identified this type of fluid to be common in the Ardenne-Eifel basin. In high-grade rocks, commonly much more CO_2 is found in fluid inclusions than in very low to low-grade metamorphic environments (Roedder 1984). This is reflected by the strong decrease of the proportion of gases in fluid inclusions from the epizonal part of the High-Ardenne slate belt (from Bertrix to Bastogne) towards the anchizonal part (Darimont 1986, Kenis *et al.* 2005a), with a decrease in the anchizonal part from Bütgenbach towards the Rursee.

In literature, low to moderate salinity, aqueous H_2O-NaCl inclusions occurring in Devonian and Carboniferous sequences are frequently described as Variscan inclusions (Darimont 1986, Darimont *et al.* 1988, Kenis *et al.* 2000, Muchez *et al.* 2000, Schroyen & Muchez 2000). The salinity representative of the veins of the North Eifel corresponds to salinities of 0 to 5 eq.wt.% NaCl found in intermullion veins in the central, anchizonal part of the High-Ardenne slate (Kenis *et al.* 2005a). It has been demonstrated that this rather simple composition of the fluids changes into more mature and saline aqueous-gaseous fluids with moderate salinities up to 10 eq.wt.% NaCl towards the central, epizonal part of the slate belt (Kenis *et al.* 2002a, 2005a, Van Baelen 2010, Verhaert 2001) conform the increase in metamorphic grade. Also in other low-grade metamorphic slate belts, such as the Monts d'Arrée slate belt (Brittany, France), low salinity fluids are common (Berwouts *et al.* 2008, Berwouts 2011, van Noorden 2007). In the samples studied, the initial low salinity fluids, which most likely originated from marine seawater, are thus increased in salinity up to 4 to 8 eq.wt.% NaCl by interaction with the Lower Devonian sediments during progressive burial and increasing metamorphism, a process which takes place commonly during burial of sedimentary basins (Hanor 1994).

Several geochemical investigations on the quartz veins in the North Eifel have demonstrated that the host rock most likely acted as a source of the fluid that laterally migrated into the fractures (Breddin & Hellermann 1962, Fielitz & Mansy 1999, Fieremans 1982). This is also reflected by the minerals found in the veins, *i.e.* mainly quartz and chlorite, reflecting the host-rock mineralogy (quartz, chlorite, mica, and biotite). Also, dissolution features, such as stylolitic surfaces in the host rock and in the veins, diffuse mass transfer around fibres, and new precipitation, *i.e.* small crystal grains nucleating on inclusion seams in the vein, may be indicative of a lateral source in the vein-fillings. Such a lateral source would indicate diffusion as primary transport mechanism of the quartz on a very small scale near the vein. This can be supported by the lack of interconnection between the fractured sandstones. However, these assumptions should be supported by a detailed isotopic and geochemical analysis, a study that is currently lacking for the veins in the North Eifel. Nevertheless, it has been demonstrated in the High-Ardenne slate belt and in the Variscan frontzone, that the composition of the vein-filling fluid was buffered by the host rock (Kenis 2004, Kenis *et al.* 2005a, Muchez *et al.* 1995), in such way that fluid-rock interactions occurred in the vicinity of the veins and that fluids were in thermal and chemical equilibrium with the host rock (Kenis *et al.* 2000, Schroyen & Muchez 2000). Such a closed fluid system has been established to take place in other low-grade metamorphic terrains, especially in low permeability rocks in slate belts (Kerrich *et al.* 1978).

In summary, the spatial evolution of the fluids that circulated through the Lower Devonian rocks from the epizone towards the anchizone in the HASB is clearly related to the metamorphism and can be related to the maturation of sediments during burial. This clearly demonstrates that the metamorphism is burial-related.

5.4.2 Burial temperature

Some flaws may be present in the burial model. Firstly, in many sedimentary basins that are affected by a rapid synrift subsidence, a fast heating is commonly observed (Littke *et al.* 2000). This is shown by the increasing isotherms in the burial model (Figure 5.7). Subsequently, temperatures slightly cool during recovery after initial rifting. Most probably, the temperatures predicted during this initial heating (> 300°C) are too high for the basin. In the Eifel burial model of Hilgers *et al.* (2000, 2006a) initial temperatures do not exceed their final burial temperature (~270°C). Therefore only a final temperature of 250 °C (corresponding to the vitrinite reflectance) is used in this study. Secondly, an effective heating time of 20 Ma is determined for the timing during which the basin remained at its maximum burial. The determination of this heating time mainly depends on the moment in time chosen to reflect the last maximum burial. It should be noticed that the effect of compression and erosion is not modelled. Therefore, this heating time seems to be longer than 20 Ma on the burial model.

5.4.3 Lithostatic fluid overpressures

It has been demonstrated by microfabric analysis of bedding-normal vein quartz that the repetitive pattern of fibrous and elongate-blocky infill of the veins evidences an important cyclicity in fracturing and sealing phases during vein growth. Especially the numerous crack-seal inclusion bands in fibrous crystals illustrate that this cyclicity is controlled by the precipitation rate exceeding the fracturing rate. It is demonstrated by several studies that each fracturing phase during fibrous crystal growth is induced by repeated extensional fracturing at oscillating fluid pressures (Elburg *et al.* 2002, Petit *et al.* 1999, Ramsay 1980, Renard *et al.* 2005). In such cycles, high fluid pressures initiate the fracturing of the rock and immediately afterwards, fluid will be trapped at high fluid pressure. The formation of extension veins thus requires high fluid pressures (Etheridge 1983). This process corresponds to the formation of the bedding-normal veins, especially because the presence of near-lithostatic to lithostatic fluid pressures is indicated by the microthermometry and geothermometry. Consequently, both pseudosecondary and secondary trails, which respectively represent healed microcracks during crystal growth and cross-cutting transcrystal microcracks during successive fracturing, are trapped from these high pressured fluids.

Additionally, it can be discussed (*e.g.* Van Noten *et al.* 2009) whether or not the results illustrated in the P-T diagram (Figure 5.8) evidence cyclic phases of fluid pressure fluctuations during vein development, such as demonstrated for primary inclusions of intermullion veins in the central part of the High-Ardenne slate belt (Kenis *et al.* 2002a, Kenis 2004, Sintubin *et al.* 2000). The lowest isochore (dashed line in Figure 5.8) theoretically represents the minimum pressure during veining and intersects with the independent geothermometer at a value corresponding to a geothermal gradient above 40°C km^{-1}. Since this value does not correspond to the geothermal gradient that was discussed in section 5.3.3 and calculated by the burial modelling (Figure 5.7), it is fair to assume that the inclusions measured in the bedding-normal veins fully reflect the near-lithostatic to lithostatic fluid pressures of maximum

~190 MPa at the time of vein formation. The presence of hydrostatic fluid pressures is excluded because of the absence of overlap of the calculated isochores and the trapping temperature at the hydrostatic geothermal gradient. Therefore fluid-pressure fluctuations are restricted to values from supra-lithostatic to slightly below lithostatic (see Figure 5.8).

Based on macrostructural observations and microfabric analysis, a mechanism of bedding-normal uplift, sometimes combined with bedding-parallel shear, is proposed for the formation of the bedding-parallel veins studied. It has been suggested that bedding-normal uplift would require lithostatic fluid overpressures in order to keep the fracture/cavity open during precipitation. The pressure conditions derived from the pseudosecondary fluid inclusions in crack-seal laminae and coarse-grained blocky laminae, both representative of the bedding-normal uplift, fully supports this mechanism. Maximum pressure conditions are calculated to be ~205 MPa, indicated by the intersection of the minimum lithostatic gradient and the independent geothermometer (Figure 5.8). Crack-seal laminae clearly indicate that vein formation induced by lithostatic fluid overpressures is a cyclic process. Based on the applied pressure corrections by means of an independent geothermometer, the lower T_h-values for the bedding-parallel veins with respect to the T_h-values for the bedding-normal veins can thus be fully attributed to the pressure differences between both vein types at the time of vein formation. The blocky laminae, furthermore, evidence that the overall thickness of the BPVs is constructed during these phases of uplift during which a high transient permeability must have been present in order to allow blocky crystals to grow. These periods of overpressuring alternate with periods of collapse during which the fluid pressure suddenly drops and a transient vertical compression acts on the veins. This is indicated by stylolites representing dissolution along the BPVs, and also by the bedding-normal secondary fluid inclusions that indicate a short reorientation of the stress field from compression to a short extension, *i.e.* $\sigma_1 \sim \sigma_v$. The fractured host-rock fragments possibly result from this collapse. This dynamic process of uplift and collapse is cyclic as evidenced by the laminated structure of the veins. In the shear laminae, original quartz grains are formed during phases of collapse, whereas the intense dynamic recrystallisation of these new crystals directly occur during subsequent recovery of the fluid pressure increase that eventually will lead to a new phase of fracturing and opening of the veins (cf. Boullier & Robert 1992). Unfortunately it can not be determined if these lower pressures are present in the quartz grains in the shear laminae owing to the intense recrystallisation.

To conclude, it can be argued that this multiphase history of bedding-parallel vein formation can be linked to the earthquake cycle (Boullier & Robert 1992, Cox 1995, Sibson 2001) and to pressure cycling, *i.e.* ‘fault-valving’ (Sibson 1990). In the earthquake cycle, periods of lithostatic overpressuring correspond to the seismic events. Collapse of the fluid-filled fracture/cavity corresponds to the interseismic periods (Fisher & Byrne 1990, Henderson *et al.* 1990) and is characterised by a first rapid decrease of the fluid pressure slightly below lithostatic and a subsequent recovery of the pore-fluid pressure towards lithostatic and towards a new rupturing phase.

5.5 Conclusions

The microthermometric analysis of representative fluid inclusions in vein quartz of both bedding-normal and bedding-parallel veins has determined the pressure and temperature conditions during veining. Microthermometry reveals that both pseudosecondary and secondary trails of bedding-normal veins trapped from an aqueous (H_2O-NaCl) fluid with a low salinity (3.5-8 eq.wt.% NaCl). The inclusions all homogenise to the liquid state at temperatures ranging between 80°C and 350°C. This broad range can be attributed to necking-down and cryptic re-equilibration of the inclusions, which could only be deduced after microthermometry. The very low T_h values are explained by necking-down after phase change of originally large liquid-filled inclusions into smaller inclusions, whereas a high T_h occurs in inclusions that underwent re-equilibration such as by stretching of the inclusion walls. The homogenisation temperatures that correspond to the formation of bedding-normal veins show a homogenisation frequency peak between 140°C and 180°C. Pseudosecondary and secondary fluid inclusions in bedding-parallel veins precipitated from a similar H_2O-NaCl fluid with a low salinity (4-7 eq.wt.% NaCl) and yield homogenisation temperatures between 80°C and 310°C. Similar to the bedding-normal veins, this range is attributed to be an effect of cryptic re-equilibration of the fluid inclusions. The frequency distribution supports a T_h-range between 110°C and 160°C.

It is further assumed that veining occurred in thermal equilibrium with the host rock. Therefore, the trapping temperature and pressure of the fluid inclusions can be determined using published vitrinite reflectance data (at about 4.5% to 5.5 % R_{max}) of the host rock surrounding siltstone layers. By using this vitrinite reflectance range and taking an effective heating time of 20 Ma into account, a maximum trapping temperature of 235°C to 250°C can be derived. This offers an independent temperature for pressure correction of the trapped inclusions. Constructing a pressure - temperature graph eventually enables to determine the ultimate trapping conditions during which both vein types formed. Correlation of the calculated isochores, the trapping temperature and the calculated regional geothermal gradient of 34°C km^{-1} shows that pore-fluid overpressures of ~190 MPa are measured for the bedding-normal veins, slightly exceeding, but within error of a lithostatic pressure of *c.* 185 MPa. This reflects the pressure at a depth of 7 km ± 0.1 km. During subsequent bedding-parallel veining, the lithostatic pore-fluid pressure may even have exceeded the lithostatic pressure with a trapping pressure of ~205 MPa.

The trapping pressure conditions of both vein types fully support the cyclic fracturing and sealing mechanism invoked to explain the fibrous to elongate blocky infill during bedding-normal veining, no matter the hairline, centimetre or composite shape and thickness of the veins. The increase of the fluid pressure up to lithostatic, and possibly to supra-lithostatic fluid pressures, is fully responsible of the bedding-normal uplift as driving mechanism for the formation and thickening of bedding-parallel veins. These lithostatic fluid pressures allow a higher transient permeability within the rock. Subsequent bedding-parallel shearing occurred after fluid pressure collapse combined with formation of the shear laminae. During thrusting, small quartz grains are cataclased during bedding-parallel slip. The subsequent dynamical recrystallisation of the crystals in the shear laminae is attributed to higher differential stresses during the main phase of the Variscan contraction. It is further interpreted that bedding-normal uplift thus reflects seismic phases in an earthquake cycle, in which interseismic periods are characterised by bedding-normal collapse, followed by expulsion of fluids and restoration of the fluid pressure up to new rupturing.

CHAPTER 6 Stress-state evolution of the upper crust during tectonic inversion

6.1 Introduction

The geometry of bedding-normal veins, the fibrous to elongate-blocky vein infill and the presence of crack-seal microstructures all indicate that bedding-normal veins initiated as extension fractures and further developed as extension veins. This is clearly exemplified by the presence of single-fractured hairline microveins and by the presence of centimetre and thicker composite veins developed during successive fracturing and sealing phases (Chapter 4). Such as demonstrated by microthermometry and geothermometry (Chapter 5), the extension fractures initiated by high fluid pressures and specific microstructures preserve the delicate vein wall geometry in extension veins, suggesting that the fractures propagate slowly, presumably at subcritical crack growth rate (cf. Boullier & Robert 1992). Bedding-parallel veins are characterised by a pronounced bedding-parallel fabric in which crack-seal microstructures and repetitive quartz laminae are supportive for extension veins. The laminated character of the veins represents multiple phases of opening and closing of the fluid-filled void at the time of vein formation corresponding to bedding-normal uplift at supra-lithostatic fluid pressures. Also clear shear laminae are observed, which demonstrates that the BPVs can be classified as extension veins and extensional-shear veins.

Extension (Mode I) fractures are classically interpreted to form at low differential stress, *i.e.* less than four times the tensile strength (T) of the rock ($\sigma_1 - \sigma_3 < 4T$) (Secor 1965). Extensional-shear veins require slightly higher values of differential stress but smaller than 5.66 times the tensile strength of the host rock ($\sigma_1 - \sigma_3 < 5.66T$) (Secor 1965). Extension veins open parallel to the minimum principal stress σ_3 and propagate in the plane of the maximum (σ_1) and intermediate (σ_2) principal stress (Secor 1965). The alignment of fractures has therefore often been used in orogenic belts to determine the orientation of the palaeostress field at the time of fracturing (Cox *et al.* 2001, Gillespie *et al.* 2001, Laubach *et al.* 2004a). If veins, which initiated as extension fractures, are uniform in trend over a large area, then they can be used as such a palaeostress indicator (*e.g.* Boullier & Robert 1992, Cosgrove 2001, Gillespie *et al.* 2001, Mazzarini *et al.* 2010, Nollet *et al.* 2005b, Van Noten & Sintubin 2010). Different cross-cutting or successive vein generations are even more interesting because they have the potential (i) to serve as a tool to decipher changes in the overall stress regime during multiple phases of fracturing and (ii) to define the P-T conditions at which these stress changes occurred. On the one hand, different cross-cutting fracture and/or vein generations have been used in many studies to deduce local stress field rotation in a consistent remote stress regime (Crespi & Chan 1996, Jackson 1991, Laubach & Diaz-Tushman 2009, Stowell *et al.* 1999, Wiltschko *et al.* 2009). On the other hand, successive cross-cutting veins, *i.e.* vein types that are oriented differently with respect to bedding such as in this work, have often been used to determine a transition in regional stress regime from extension to compression or reverse (Boullier & Robert 1992, Hilgers *et al.* 2006b, Holland *et al.* 2009, Laubach & Diaz-Tushman 2009, Manning & Bird 1991, Van Noten *et al.* 2008, 2011). Cross-cutting vein types also occur in close relationship to faults in which they represent fluctuating fluid pressures during fault-valve activity and are related to short-lived local stress transitions in a consistent remote stress regime (Boullier & Robert 1992, Collettini *et al.* 2006, Muchez *et al.* 2000, Nielsen *et al.* 1998, Sibson 1995). Local cross-cutting vein sets may also occur in the presence of mechanical anisotropy (Fagereng *et al.* 2010, Healy 2009). In all these studies, transitions between regional stress regimes are defined as tectonic inversions or may take place as a short switch in a consistent stress field.

In the North Eifel, the transition from bedding-normal to bedding-parallel veins is interpreted to materialise the early Variscan tectonic inversion from the extensional to the compressional regime (see evolutionary history in section 3.5.4; Figure 3.46). In this model it is interpreted that the maximum principal stress changes from a vertical position in the extensional regime ($\sigma_1 \sim \sigma_v$) to a horizontal position in the compressional regime ($\sigma_1 \sim \sigma_H$). In the High-Ardenne slate belt, the compressional tectonic inversion is exemplified in a brittle way in upper crustal levels, *i.e.* transition from bedding-normal to bedding-parallel veins in the North Eifel, and in a ductile way in the middle crust (cf. Kenis 2004), *i.e.* transition of sandstones containing bedding-normal veins into mullions in the Ardennes (Figure 6.1). This clearly illustrates an important difference in the strength of the crust at different levels. The successive vein types in the North Eifel reflect a strong brittle upper crust, while the mullions in the Ardennes reflect a 'weak' middle crust (Kenis *et al.* 2005b).

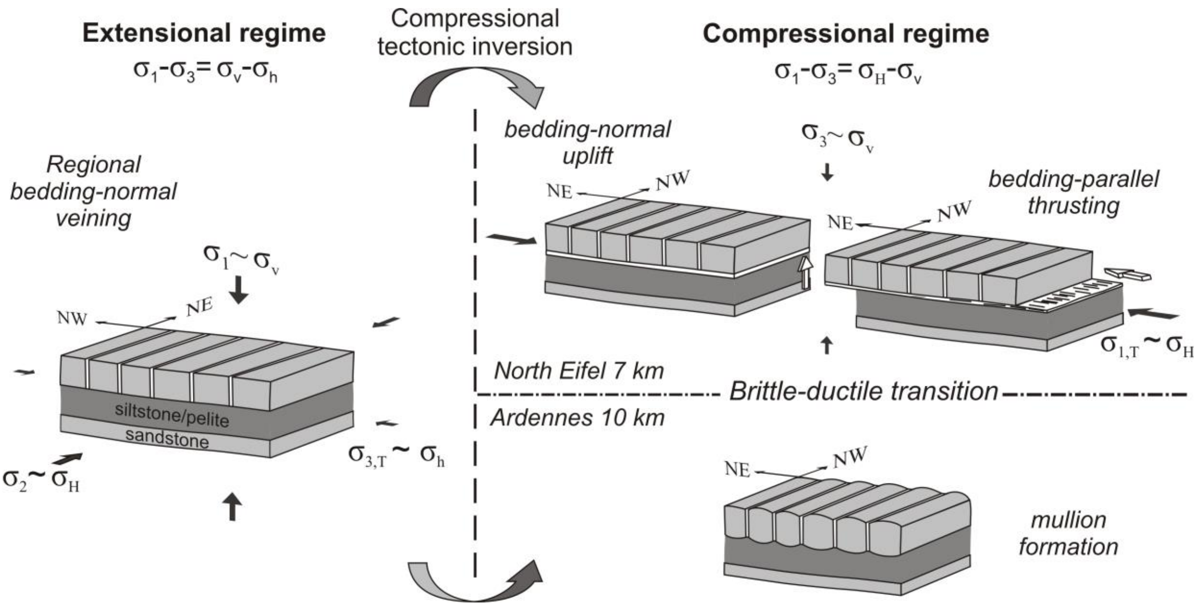

Figure 6.1: Bedding-normal veining, bedding-parallel veining and mullions exemplify the compressional tectonic inversion at different depths during compression of the Ardenne-Eifel. For simplicity, only the regional occurring bedding-normal veins (V_B at the Rursee) are illustrated.

Up to now, it is however unclear how both deformation features, *i.e.* the successive vein types and the mullions, relate to the timing of the actual switch from extension to compression. Although mullions reflect Variscan shortening after the compressional tectonic inversion, they are insufficient to deduce the changes in the stress state during orogenic shortening. As mullions are structures developed in a ductile way, they can only indicate stretching directions and thus cannot solve the research question how the successive vein types relate to the tectonic inversion. It is therefore aimed to unravel this question by quantifying and illustrating brittle failure by calculating the amount of differential stress that corresponds to the formation of extension bedding-normal and extension to extensional-shear bedding-parallel veins.

The conditions of brittle failure of an isotropic rock have classically been visualised in a Mohr-Coulomb diagram, relating the shear (τ) and the normal stress (σ_n) on a particular plane of failure with a particular orientation to the stress state (represented by the principal stresses). In such Mohr-Coulomb diagrams extension and extensional-shear failure is illustrated when the normal stress contacts the nonlinear Griffith criterion at negative, *i.e.* tensile, normal stresses (see Mohr circle reconstruction later in Chapter 8; Figure 8.7). Although Mohr-Coulomb diagrams provide an excellent way to illustrate both the relationship between stress magnitudes and differential stress, and show which type of fracture will develop (extension fracture, extensional-shear fracture or shear fracture) (Cosgrove 1995a, Cox *et al.* 2001), they are limited to illustrate a specific stress state at a specific moment to a particular depth. The evolution of the fluid pressure (P_f) during orogenic shortening can, however, only be illustrated by means of several Mohr circle reconstructions (*e.g.* Hilgers *et al.* 2006b, Wilson *et al.* 2009). Sibson (1998, 2000) introduced the concept of two-dimensional brittle failure mode (BFM) plots which allow a more dynamic and evolutionary analysis of brittle structures which is not possible in a classical Mohr-Coulomb diagram. In these BFM plots, the transition of Andersonian stress regimes at a certain depth is visualised by the change of differential stress versus the evolution of the pore-fluid factor (λ_v) and the effective vertical stress (σ_v'). They moreover illustrate the change in Andersonian stress orientations during tectonic inversion; a vertical σ_1 that switches to horizontal during compressional inversion, while σ_3 has an opposite reorientation from horizontal to vertical. BFM plots are useful to visualise parameters such as the tensile strength (T) of rock or the friction along faults (μ) which strongly influence the maximum overpressures that can be built up during tectonic inversion (Cox 2010). The layout of the BFM plots are, moreover, designed to illustrate contrasting failure conditions which may be expected from the transitions between two stress regimes (Sibson 2004).

Although these BFM plots are originally constructed to understand the development and evolution of fault systems with their associated vein types and are used in a wide range of tectonic settings, they might be very useful to define the timing of both vein phases in the North Eifel in terms of changing differential stresses during tectonic inversion. In order to do so, firstly the strength of the rock is discussed to allow the determination of the magnitude of differential stress. Secondly, the result of fluid pressure versus differential stress is plotted in a BFM plot, visualising the dynamic relationship between fluid pressure and differential stress during the orogenic shortening of a basin into a slate belt. This allows increasing our knowledge on fluid flow during these specific tectonic inversion periods.

6.2 Tensile strength of rock

As extension veins and fractures are defined to be dependent on the tensile strength (T) of rock, it is interesting to estimate the values of the tensile strength of the host rock in which bedding-normal and bedding-parallel veins developed. The tensile strength is a mechanical property of the rock that has been tested by indirect measurements in laboratory experiments (*e.g.* Brazilian tests, ring test, bending test, etc.) (Etheridge 1983). Published laboratory experiments of the tensile strength of rock yield values between 1 and 10 MPa for sedimentary rocks and up to 20 MPa or even more for crystalline rocks (Lockner 1995, Singh 1989). Most rock types, however, have a tensile strength below 12 MPa and the strength even decreases if the rock has undergone regional metamorphism (Etheridge 1983). In these laboratory tests rock samples are usually dry and not heated, specific conditions that are not fully representative of the wet and hot conditions at depth in the Earth's crust in which the rock is fractured. By measuring dry samples, the tensile strength is often overestimated. A reasonable value for metamorphic rock strength would thus be between 5 and 10 MPa (Etheridge 1983).

Furthermore, these experiments are often performed on isotropic rock bodies which show similar tensile strengths in all directions. Many sedimentary rocks have anisotropic strength characteristics such as lamination, bedding or foliation which influences the tensile strength. Also, for example, the Young's modulus parallel to bedding is often greater than perpendicular to bedding. In some tests, these mechanical rock properties are taken into account during testing the strength of rock at various angles to its anisotropy. Theoretically, the tensile strength of rock in the direction perpendicular to bedding is smaller than the tensile strength parallel to bedding (Cosgrove 1995a). Experimental compressive Brazilian tests on laminated sandstones (Figure 6.2), show that failure stress and also fracture length are considerably affected by the layer orientation at the time of fracturing (Tavallali & Vervoort 2010). Other laboratory experiments on laminated sandstones report values of 10 MPa for bedding-parallel tensile strength and 7.66 MPa for bedding-normal tensile strength (Chenevert & Gatlin 1965). At existing planes such as bedding contacts between a rock with contrasting competence, the tensile strength will be even less (Mandl 2005) (Figure 6.2). Hence, a lower differential stress but a higher fluid pressure is needed to induce fracturing parallel to bedding (Cox & Paterson 1989, Sibson & Scott 1998).

Given the fact that the type of fracturing is determined by the tensile strength of rock, the differential stress which is needed to form extension veins ($\sigma_1 - \sigma_3 < 4T$) must have been different in the extensional and compressional regime because of the orientation of the principal stress relative to the orientation of the anisotropy, *i.e.* bedding. For $\sigma_1 - \sigma_3 < 4T$, values of differential stress during bedding-normal and bedding-parallel tensile fracturing must have been below ~40 MPa and ~30 MPa respectively. Extensional-shear veins require slightly higher differential stresses ($\sigma_1 - \sigma_3 < 5.66T$) corresponding to values below approximately ~43 MPa.

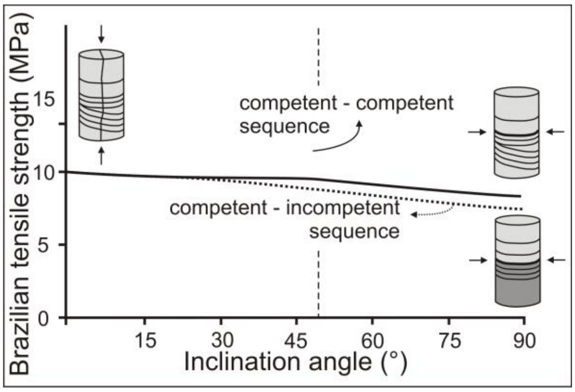

Figure 6.2: Variation in rock tensile strength as function of the inclination angle of the anisotropy of the sample during Brazilians tests. Interpretation of data from Tavallali & Vervoort (2010) and Mandl (2005) illustrating the differences in strength during bedding-normal and bedding-parallel veining. The decrease in strength after a critical angle (dashed line) is attributed to tests in which samples fail into shear.

6.3 Construction of a brittle failure mode plot

The presentation of the changes in fluid pressure versus the differential stress and vertical effective stress in Sibson's brittle failure mode (BFM) plot has proven to be very useful in the dynamic understanding of how these features relate to faulting and transient changes in stress fields during fault valving (*e.g.* Cox 2010, Sibson 1998, 2003, 2004). Although these BFM plots are originally constructed to understand the development and evolution of fault systems with their associated vein types in a wide range of tectonic settings, they are also applicable to define the timing of fracturing and mineralisation (Cox 2010). Consequently, they are very suitable for interpreting both veining events that occurred during tectonic inversion affecting the Ardenne-Eifel basin.

In the BFM plot, the fluid-pressure (P_f) evolution is plotted versus the differential stress ($\sigma_1 - \sigma_3$) and vertical effective stress ($\sigma'_v = \sigma_v - P_f$) (Figure 6.3). The different brittle failure modes, *i.e.* extensional (ext), extensional-shear (es) and compressional (cs) failure, are defined by the tensile strength in such way that: es < 4T; 4T < ext < 5.66T and cs > 5.66T respectively. Sibson (1998) calculated how the changing differential stress in these modes should change as function of the vertical effective stress σ_v' and the tensile strength T at a consistent coefficient of static friction for intact rock (μ_i ~0.75). This resulted in the following equations for intact rock in the extensional regime:

(es) $4T > \sigma_1 - \sigma_3 = \sigma'_v + T$

(ext) $5.66T > \sigma_1 - \sigma_3 = -4T \pm 4(T^2 + T\sigma'_v)^{-1/2}$

(cs) $5.66T < \sigma_1 - \sigma_3 = 2.083T + 0.75\sigma'_v$

while for the compressional regime it is:

(es) $\sigma_v = \sigma_3$ and $\sigma'_v = -T$

(ext) $5.66T > \sigma_1 - \sigma_3 = 4T \pm 4(T^2 + T\sigma'_v)^{1/2}$

(cs) $5.66T < \sigma_1 - \sigma_3 = 8.33T + 3\sigma'_v$

By using these BFM plots it is important to keep in mind that Andersonian stress regimes are assumed, defining that in each stress regime one of the principal stresses corresponds to the vertical (Anderson 1951). Furthermore, rock tensile strengths of 10 MPa and ~7.66 MPa are used for the extensional and compressional tectonic regime respectively. The relationship between $\sigma_1 - \sigma_3$ and σ_v' in the extensional and compressional regime has been calculated using the equations of Sibson (1998, 2004) but is adapted to reflect the veining conditions at 7 km ± 0.1 km depth. The result of these modes is plotted as a solid line in Figure 6.3 and defines the maximum sustainable overpressure for a given differential stress. The lithostatic and hydrostatic pressure are expressed by the pore-fluid factor λ_v ($\lambda_v = P_f/\sigma_v$) in which λ_v with a value slightly below 0.4 corresponds to hydrostatic at a pore-fluid pressure of ~67 MPa and λ_v~1.0 to lithostatic at a pore-fluid pressure of ~185 MPa (Figure 6.3). Supra-lithostatic fluid pressures have a pore-fluid factor of

λ_v ~1.0 to λ_v~1.1. Changing the value of the static friction μ_i has only minor influences on the position of the solid line in the BFM plot. Maximum differential stress for extensional-shear failure is modelled as 5.66T for μ_i~0.75 and decreases to ~4T for μ_i~0.1 (Cox 2010). Using a value of μ_i~0.1 would lower the solid line in the BFM plot to a position just above the lithostatic pressure. However, many crustal rocks have a static friction coefficient between $0.5 < \mu_i < 1$ (Sibson 2004) with an average value of μ_i ~0.75. Using this value is thus appropriate for estimating the failure conditions during which the successive veins are formed.

Subsequently, the pressure conditions, resulting from the microthermometric analysis (Figure 5.8) are plotted on the BFM plot. It was determined that during bedding-normal veining (BNV) maximum pore-fluid pressures of 190 MPa were reached whereas during bedding-parallel veining fluid pressure may even have exceeded the lithostatic pressure up to a maximum of ~205 MPa (grey areas in Figure 6.3). The lower values of the conditions during which BNVs and BPVs can be formed, are delimited by the brittle modes of extension and extensional-shear failure respectively and correspond to minimum fluid pressures of ~153 MPa and ~193 MPa. These lower limits resemble the lower limits of P-T conditions derived on the P-T diagram (Figure 5.8).

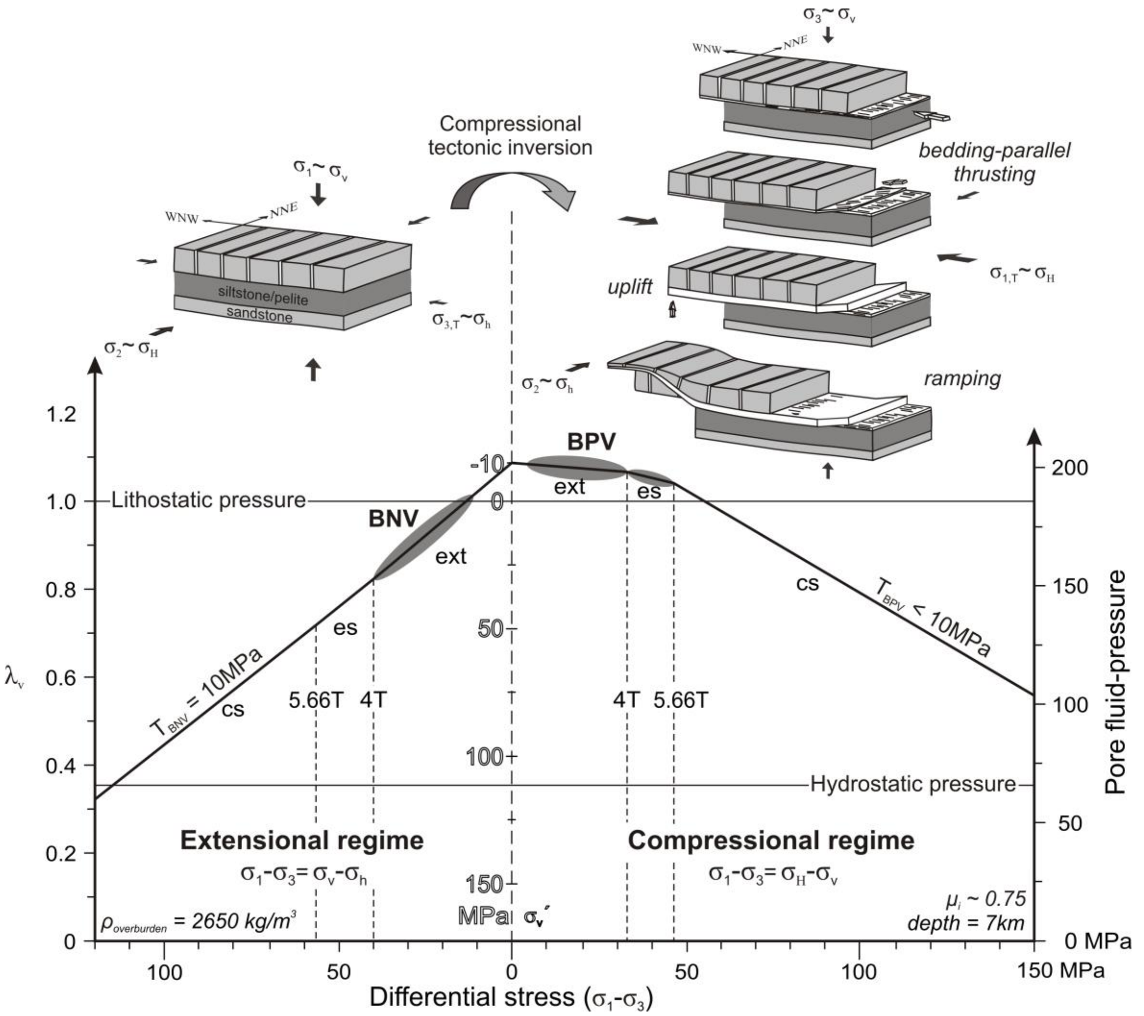

Figure 6.3: Brittle failure mode plot (Sibson 1998) of differential stress (σ_1-σ_3) versus pore-fluid factor ($\lambda_v = P_f / \sigma_v$), vertical effective stress ($\sigma'_v = \sigma_v - P_f$) and pore-fluid pressure (P_f) calculated for successive quartz veins of the Wildenhof section (Rursee) defining the pressure conditions (grey areas) for vein emplacement during Variscan compressional tectonic inversion. Extensional (ext) and extensional-shear (es) failure are defined by σ_1-$\sigma_3 < 4T$ and σ_1-$\sigma_3 < 5.66T$ respectively (Secor 1965). Note the differences in magnitude of the tensile strength T before and after inversion. Stress-state changes demonstrate that bedding-normal veining (BNV) occurred at near-lithostatic fluid pressures and was succeeded after the tectonic inversion by bedding-parallel veining (BPV) occurring at near- to supra-lithostatic fluid pressures. After Van Noten *et al.* (2011).

6.4 Implications

The solid line in Figure 6.3 represents the stress-state evolution from extension to compression during tectonic inversion and illustrates the maximum pressure conditions that are sustainable during this evolutionary history. A specific stress state that exceeds this line does not exist. It has been demonstrated in Chapter 5 that it is likely that only high, near- to supra-lithostatic fluid pressures are captured in the fluid inclusions in the vein. However, it is has been demonstrated by the microstructural analysis that fluid pressure changes must have been present between the different episodes of veining. Consequently, to show the real evolution of the stress-state and fluid-pressure changes during veining, possibly trajectories have been constructed to illustrate the formation of both veining events (grey lines in Figure 6.4). In these trajectories, representative for the successive vein types in the Eifel region, is it assumed that the differential stress changes continuously through the deformation cycle. With respect to the stress-state changes in the Ardenne-Eifel basin at the onset of Variscan orogeny, this assumption indicates that the differential stress in the trajectories decreases towards the tectonic inversion between the extensional and compressional regime, and increases after inversion during subsequent Variscan compression. For the sake of simplicity, the different steps in differential stress are exaggerated in the illustrating the different trajectories in Figure 6.4.

In the extensional regime, each trajectory must commence at a sufficient low differential stress (< 4T) to allow the initiation of extension fractures. The fluctuating line of **trajectory A** reflects episodical vein growth such as expected during the development of (crack-seal) extension veins. Initial failure will eventually occur when trajectory A hits the solid line a first time (shown by the star in Figure 6.4). As most veins have a fibrous or elongate fabric, the initial fracture will seal before a next fracturing phase occurs. After sealing of the fracture, a new fracture can only develop when the fluid pressure will be sufficient high enough to overcome the tensile strength of the vein. If the differential stress decreases towards the tectonic switch, subsequent fracturing may occur at a higher fluid pressure than compared to the initial fracture. The fracture will seal before the next fracture develops. After fracturing, sealing will again occur. Eventually the formation of bedding-normal veins can be explained by cyclic fracturing and sealing phases. These cyclic phases are illustrated on the BFM plot (Figure 6.4) by small fluid pressure drops, *i.e.* vertical lines illustrating the sealing phases, and recovery of the fluid pressure during subsequent decreasing differential stress. Thick composite veins are formed by several successive fracturing and sealing cycles whereas thin veins are formed by less fracturing cycles, illustrated as **trajectory B**.

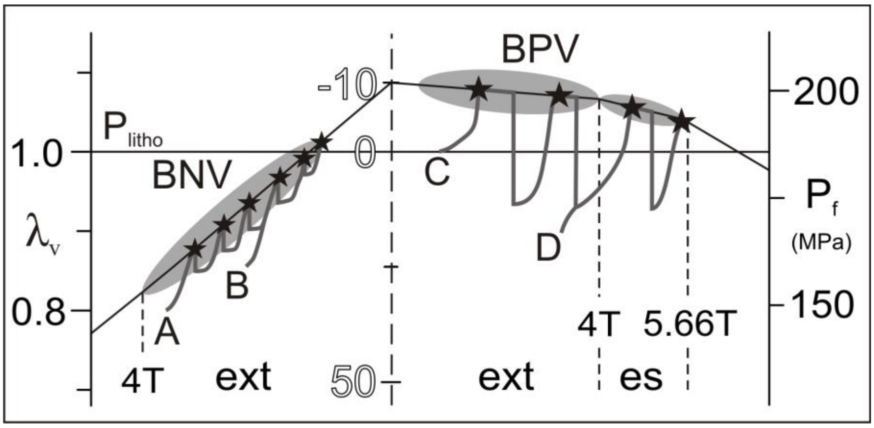

Figure 6.4: Detail of the brittle failure mode plot in Figure 6.3 illustrating different possible trajectories (grey lines) during which bedding-normal and bedding-parallel veins could have been formed. Decreasing differential stress in the different steps of trajectories A and B and increasing differential stress in the different steps of the trajectories C and D are exaggerated to be able to illustrate cyclic vein growth. See text for discussion and explanation of trajectories A to D. ext: extensional failure; es: extensional-shear failure.

Because of the laminated character of the BPVs, resulting from numerous phases of bedding-normal uplift and bedding-parallel shear, it can be argued that vein growth after the tectonic inversion is not a continuous process, but results from cyclic phases. Similar to the BNVs, each trajectory must start at low differential stress to allow the formation of extension fractures (starting point C or D). Subsequently, after nucleation of the fracture at (supra-)lithostatic fluid pressure (see the star in each trajectory in Figure 6.4), growth and opening of the extension fracture delimits further rising of pore pressure and allows infill of the veins during increasing differential stress. This is illustrated by **trajectory C** that moves parallel to the solid line at supra-lithostatic fluid pressure. As an open fracture, generated by supra-lithostatic fluid pressures, cannot be maintained continuously, sudden rapid fluid-pressure drops (vertical attitude of the trajectories) will occur. These pressure drops causes vertical collapse of the vein and give rise to a transient vertical shortening in a stress field in which σ_1 shortly switches towards vertical. At this moment a transient local extensional stress field exists in a remote compressional stress field. These phases of collapse might be caused by dissipation and escape of the fluid laterally in the bedding-parallel fracture and hence the decrease of the fluid pressure below lithostatic. The specific geometry of the thin bedding-parallel veins suggests that bedding-parallel fracturing occurred by small increments and that the fluid pressure drops are accompanied by only small volume changes. This explains why the pore pressure never drops significantly below lithostatic in the different trajectories in the BFM plot (Figure 6.4) and can rapidly regain its original high pressure. Also fluid pressure fluctuations from supra-lithostatic to considerable lower values are not deduced in the P-T diagram in Figure 5.8. Subsequently after the pressure drops, bedding-normal uplift and new vein growth will occur again after recovery of the fluid pressure.

Trajectory C describes how the intrabedded veins in sandstone (*case iii*) or the crack-seal laminae and blocky laminae in the interbedded veins (*case i, ii and iv*) develop. The increasing differential stress, accompanied by continuing interseismic recovery and seismic rupturing, will eventually drive the stress state towards extensional-shear failure mode. In this failure mode, bedding-normal or oblique dilation first occurs, when the trajectory hits the solid line. During fluid pressure drop, shear failure causes brittle deformation of the present quartz grains along incremental microthrusts. A BPV evolving along trajectory C will first develop crack-seal or blocky quartz laminae and afterwards shear laminae, or a combination of both. A vein that commence at **trajectory D** may develop only shear laminae.

To conclude, a brittle failure mode plot allows thus defining the conditions during which extensional veining can occur in a basin that evolves from extension to compression during tectonic inversion (Sibson 1998). It can be interpreted that fluid pressures increased rapidly during decreasing differential stress until it is small enough to allow the initiation of Mode I extension fractures, interpreted to represent the onset of bedding-normal veining. Subsequent successive fracturing and sealing phases at low differential stress caused fracture infill, vein formation and vein thickening of the BNVs of various thicknesses, exemplified by hairline, centimetre and composite veins. After the tectonic switch, *i.e.* the switch from $\sigma_1 \sim \sigma_v$ to $\sigma_1 \sim \sigma_H$, supra-lithostatic overpressures at low differential stress caused uplift of the overburden. This is reflected in the BPVs by various incremental opening microstructures in quartz crystals. During increasing differential stress in the compressional regime, extensional-shear fractures have been developed at supra-lithostatic fluid pressures, such as suggested by microthermometry. The BFM plot moreover illustrates that the maximum sustainable overpressure is the highest during the tectonic switch and is easier to maintain in compressional tectonic regimes at relatively low values of differential stress (< 5.66 T), rather than in the extensional regime at low values of differential stress (cf. Sibson 2004). Both veining events illustrate that during a compressional tectonic inversion a considerable transient permeability enhancement takes place in which flow could preferentially take place along the alignment of the veins in the σ_2 direction. Furthermore, veining is mostly related to the competent units. Impermeable layers, such as the siltstone surrounding these competent units, can compartmentalise the pore-fluid system during burial, allowing the pore-fluid pressure to rise within the sandstone without any vertical connectivity between the compartmentalised competent units. With respect to compartmentalisation, the overpressures that accompany the tectonic inversions are restricted to the individual competent strata. As bedding-normal veining occurred regionally, it can be concluded that the Ardenne-Eifel basin was composed of fossil intrastratum high-pressure compartments.

6.5 Conclusions

Plotting the derived pressure conditions in a brittle failure mode plot demonstrates how successive vein types that are induced by near-to (supra-)lithostatic fluid overpressures are important to determine the changes in the stress regimes during early tectonic, compressional tectonic inversion. These brittle failure mode plots are furthermore very useful to reconstruct the evolutionary history of vein infill in terms of fluid pressure evolution and differential stress changes clarifying the stress state in the basin. At the time of bedding-normal veining at low differential stress, near-lithostatic fluid pressures were present in the Ardenne-Eifel basin at the latest stages of the extensional regime. After the early Variscan tectonic inversion, bedding-parallel vein emplacement indicates that (supra-)lithostatic fluid pressures were generated which can only be maintained atlow to intermediate values of differential stress during the earliest stages of the compressional stress regime. An estimation of the tensile strength of rock furthermore shows that BPVs developed at lower differential stress in the compressional regime rather than that extension veins formed in the extensional regime, because of the orientation of the anisotropy (bedding) relative to the principal stresses.

This kinematic history of two successive vein types reflects brittle deformation at high fluid pressures during the compressional tectonic inversion in a strong upper crust at the onset of the Variscan Orogeny. It is concluded that both the fluid pressure and differential stress changes play a crucial role in increasing the permeability during orogeny. Fluid redistribution preferentially occurs parallel to σ_2 during tectonic inversion, as demonstrated by the percolation of fluids normal to bedding, in the extensional regime, to parallel to bedding in the compressional regime. This fluid redistribution was widespread and should have occurred regionally in the upper crustal levels of the overpressured Ardenne-Eifel basin at the onset of Variscan orogeny. The regional aspect of fluid redistribution strongly contrast with more localised fluid flow that occurs along faults or fault systems caused by fault-valving.

CHAPTER 7 Regional vein spacing as indicator for layer-scale stress state

7.1 Introduction

The succession from bedding-normal to bedding-parallel veins reflects the regional stress-state evolution during compressional, early Variscan tectonic inversion affecting the Ardenne-Eifel basin. Within this kinematic history, bedding-normal veining represents a regional consistent fracturing event induced by near-lithostatic fluid overpressures at low differential stress. Although the regional stress-state evolution is known, it is interesting to investigate how stress is distributed at the scale of a single layer during extension in order to gain a detailed insight in the fracture and initial vein development. This stress state at layer scale can be deduced by comparing the spatial relationship of stratabound bedding-normal veins with the thickness of the competent layer that comprises the veins (cf. Stowell *et al.* 1999). For this investigation (after Van Noten & Sintubin 2010), only the centimetre veins are used.

It is investigated if the repetitive spacing of the late burial quartz veins in the High-Ardenne slate belt, both in the pHASB (Germany) as well as in the cHASB (Belgium) is proportional to the layer thickness and if the observed spacing can be explained by one of the numerously published geomechanical models which are developed to predict fracture patterns in naturally fractured reservoirs. In order to do so, firstly, some representative geomechanical models of fracture and vein spacing are discussed. Secondly, the spacing of planar veins and the aspect ratios of fractured blocks in thin (< 1m) siliciclastic multilayer sequences from the different case studies in the geometric analysis (see Chapter 3) are compared with: (i) field examples of vein spacing in boudinaged layers; (ii) published fracture distributions for a range of lithologies; (iii) the spacing of lensoid veins in shortened sequences, *i.e.* mullions, in the central part of the slate belt. This could show if vein spacing is consistent in the regional bedding-normal vein arrays. It is interesting to examine the distribution of these stratabound veins to gain insight into a time-integrated history of compartmentalised fluid redistribution during low-grade metamorphism and to understand the initial development of veins (Manning 1994, Stowell *et al.* 1999). Such as demonstrated in previous chapters, working on veins rather than on fractures has moreover the advantage that the role of fluid pressure can be implemented in the interpretation of the results, whereas this is often neglected in fracture models. Variations in the magnitude of the layer-scale compressive stress are often reflected by the spacing of crack-seal host-rock inclusion bands in veins and may already demonstrate the importance of the fluid pressure (Renard *et al.* 2005). Eventually, this vein spacing analysis can therefore serve as an analogue for fracture patterns in the subsurface.

7.1.1 Fracture development

Knowledge of the geometry of fracture and vein networks is essential in subsurface research (*e.g.* oil reservoir research, mining geology). Discontinuities such as fractures, faults and veins are potential sites for fluid transport and have important implications for the hydraulic properties of rock (André-Mayer & Sausse 2007, Clark *et al.* 1995). Spatial fracture distribution has been studied in numerous papers commonly using statistical methods in search of the best fit between actual or numerical data sets and theoretical distribution laws. This theoretical approach not only provides a simplified image of the fracture set, but also enables a numerical definition (Huang & Angelier 1989). Most fracture distributions, however, are not applicable to the spatial distribution of veins (Gillespie *et al.* 2001, Peacock 2004). Although veins initially are similar mechanically as fractures (*e.g.* Thomas & Pollard 1993), there are important geometric, scaling and genetic differences and they should be considered separately (Gillespie *et al.* 2001).

It is widely accepted that extensional fracture spacing is mainly controlled by lithological parameters of the host rock and layer thickness. There is a large literature on the relationship between fracture spacing (*S*) and layer thickness (*T*) in which the mechanics of fracture spacing has been described by both field observations (Engelder *et al.* 1997, Gillespie *et al.* 1999, 2001, Hobbs 1967, Huang & Angelier 1989, Ladeira & Price 1981, Narr & Suppe 1991, Van Noten & Sintubin 2010) and geomechanical or numerical modelling (Bai & Pollard 2000a, 2000b, de Joussineau & Petit 2007, Fischer *et al.* 1995, Ji & Saruwatari 1998, Ji *et al.* 1998, Li & Yang 2007, Mandal *et al.* 1994, Olson 2004, Schöpfer *et al.* in press, Wu & Pollard 1995). Both linear as non-linear relationships between fracture spacing (*S*) and layer thickness (*T*) have been described. Throughout these studies, spacing is explained from a mechanical point of view without considering the role of pore fluid pressure, although it is commonly accepted that high fluid pressures in combination with tectonic extension can induce opening fractures (Ladeira & Price 1981, Secor 1965, Simpson 2000). Recent experimental results show that fracture spacing decreases progressively with increasing strain perpendicular to the fracture in such way that new fractures form between earlier fractures, with increasing bedding-plane friction and with overburden pressure (cf. Schöpfer *et al.* in press). During extension, the fractures are flanked by 'stress shadows' (Hobbs 1967, Lachenbruch 1961) in which new fractures are unlikely to form. The size of the stress shadow is directly proportional to the length of the fracture, *i.e.* the layer thickness (Pollard & Segall 1987). In layered sequences, these fractures are usually prevented from further growth at the interface between competent and incompetent beds (Cooke *et al.* 2006, Engelder *et al.* 1997, Wu & Pollard 1995). The final stage of fracture development is reached when no more 'freedom' exists for nucleating new fractures between pre-existing ones and this stage is referred to as the 'saturation level' by Narr & Suppe (1991). Recent modelling showed that the crack-normal stress between closely spaced fractures actually becomes compressive at certain fracture spacing so no more tensile fractures can form (Bai & Pollard 2000b, de Joussineau & Petit 2007). This result dictates that at the saturation level, the opening of pre-existing fractures is preferred over nucleation of new additional fractures with increasing extensional strain (André-Mayer & Sausse 2007, Olson 2004). Bai & Pollard (2000a) defined a critical *S*/*T* ratio of 0.976 which gives a lower limit for fractures driven by extension in a material without significant flaws and defines the conditions of fracture saturation. This critical value increases non-linearly with increasing ratio of the Young's modulus of the fractured layer with respect to that of the neighbouring layers, with increasing Poisson's ratio of the fractured layer, and with increasing magnitude of the overburden stress (Bai & Pollard 2000b). However, the effects of the elastic constants on the critical value are minor.

Spacing to thickness ratios less than the critical value have often been seen in outcrop. The concept of fracture saturation may break down if a local stress field exists due to the presence of flaws between adjacent fractures, or due to a local mechanism such as high fluid pressures, which can overcome the compressive stress at the stage of fracture saturation in such way that new fractures are nucleated in the vicinity of pre-existing fractures (Simpson 2000). This contrasts with a large body of work in which the nucleation of nearby fractures is prohibited at the stage of fracture saturation and the role of high fluid pressures has therefore been underexplored. These closely spaced infilling fractures are, moreover, more likely to initiate near the interfaces than in the middle of the layer.

Besides lithological parameters, fracture spacing is also dependent on the degree of pre-existing rock deformation (Harris *et al.* 1960) and the interference of adjacent competent layers (Bai & Pollard 1999, Ladeira & Price 1981). The effect of the layer thickness variations may overshadow other variables, such as strain level, strain anisotropy and the subcritical crack index, which also influence fracture spacing. Experimental modelling (Olson 1993, 2004) has shown that the subcritical crack index controls the degree of fracture organisation and depends on the rock's microstructure (grain mineralogy, grain size, cement type, porosity) and the chemical environment (Atkinson 1984). Moderate values of subcritical index (*e.g.* sandstones) result in more regularly fracture spacing that is roughly proportional to the mechanical layer thickness, whereas higher values (*e.g.* in carbonates) predict the occurrence of fracture swarms or widely spaced fracture clusters (Olson 2004, Rijken 2005). The subcritical index thus determines if a stress shadow and resulting regularly spaced fractures can develop.

7.1.2 Vein spacing

Clear examples of vein spacing distributions in literature are scarce. They have been described in limestones (Gillespie *et al.* 2001), or in pelites, in which veins for instance can occur in en-echelon arrays (Fisher *et al.* 1995) or axial planar (Simpson 2000). Gillespie *et al*. (1999) and Foxford *et al*. (2000) give a detailed description of vein spacing for a range of lithologies. A fundamental distinction in spacing is apparent between stratabound vein arrays, veins confined to competent rock in multilayer sequences, and non-stratabound vein arrays, in which veins occur in homogeneous rock. Veins often show well defined spacing statistics for a specific host-rock lithology, but comparing different studies remains difficult due to the regional variability of rock properties. Putz-Perrier & Sanderson (2008) statistically describe the decrease of vein spacing near faults and faulted blocks. Stowell *et al*. (1999) characterise a spacing distribution of veins cross-cutting folds and cleavage, caused by a late orogenic uplift. They specifically discuss the distribution of late-orogenic veins in deformed multilayer sequences. Although the results of both case studies are applicable for the spacing of syntectonic veins, they cannot be compared to the Ardenne-Eifel case in which veining is the result of a regional early tectonic deformation event predating the main Variscan fold-and-cleavage development. Vein spacing distributions are thus difficult to compare since, in addition to the vein-hosting lithology, the timing of fracturing influences vein spacing. Furthermore the different ways of how data may be represented in graphs can strongly influence the interpretation of results and complicates comparing case studies. Nevertheless the difficulty of comparing different vein-spacing studies, it is still worthy to present new data from the interesting studied area.

7.2 Factors influencing vein spacing

In order to investigate the effect of the layer thickness to vein spacing and to compare it properly with published fracture distributions, possible parameters can be determined in the field and which could influence the spatial distribution are excluded. Following parameters have an influence to the spacing pattern and are well described in literature (Figure 7.1).

Firstly, fracture and vein spacing strongly depends on the lithological properties and on rock permeability. To avoid the influence of lithology and permeability on the spacing distribution, only the spacing of veins is measured which are confined to competent sandstones (pHASB) and quartzites (cHASB) from the slate belt. It is not considered to measure vein spacing in other lithologies. Material properties of sandstone need to be constant in an area to demonstrate the true effect of the layer thickness. This is extremely difficult as there is a substantial rock property change (change of subcritical crack index) (Olson *et al.* 2002) from initial composition through diagenesis and metamorphism. Bedding-normal veins, however, are not affected by grain-scale mechanical heterogeneity of the host rock, as evidenced by transgranular microveins with low tortuosity (Figure 4.3) and by absence of compaction features associated with the veins, indicating that the veins formed in an already low-porous rock at maximum burial. So the material properties solely depend on the initial composition of the host rock and not on the grain/cement ratio. A change in subcritical crack index of sandstone will thus determine the variability in fracture spacing. This change in crack index between the cHASB and pHASB, however, will be rather small as both areas contain sandstones which are deposited in a shallow marine, deltaic to tidal environment with an identical mineral source. Correlating the percentage of quartz (grains and cement; Table 4.1; Figure 4.1; Figure 4.2) with experimental tests on a wide range of sandstones (Rijken 2005), supports intermediate subcritical crack indices between 50 and 60, which are indicative of regular spacing proportional to bed thickness (Olson *et al.* 2002, Rijken 2005) with a minor regional spacing variability.

Secondly, because the influence of the layer thickness is investigated, measurements of vein spacing in outcrops with an irregular bedding surface or with varying layer thickness are not taken into account. After all, vein spacing is strongly variable within a single competent layer which shows an irregular bed continuity (Figure 7.1a), and this influences the correlation of layer thickness and vein spacing. Thirdly, besides lithology and layer thickness another parameter known to influence fracture spacing is the degree of deformation experienced by rock prior to fracturing (Harris *et al.* 1960). Yet, the variation in spacing due to the deformation of rock will in no way mask the fundamental variation of fracture spacing exhibited due to layer thickness and lithology (Ladeira & Price 1981). As studied in the geometric analysis, several vein generations in the pHASB mutually cross-cut (Figure 7.1b). In a rock that is already characterised by the presence of veins, their anisotropy will change the host-rock properties in such way that new fractures or veins will be influenced by the presence of the oldest generation (Caputo & Hancock 1999). To avoid this anisotropy, only the spacing of the oldest generation is used for the vein spacing distribution. Finally, the influence of the thickness of adjacent incompetent units bounding the fractured layer plays also a minor role in fracture/vein spacing (Bai & Pollard 1999, Cooke *et al.* 2006, Fisher *et al.* 1995, Ladeira & Price 1981). In outcrops in which competent layers are omnipresent, fractures will 'jump' from one layer to the other, which makes it very difficult to determine the effect of a single layer thickness to the spacing pattern. Moreover, when two competent layers are only separated by a thin incompetent layer, with the interlayer by convention smaller than 5 centimetre (Ladeira & Price 1981), fractures are more closely spaced than if they are separated by a thick incompetent layer (Ji *et al.* 1998). Bai & Pollard (1999), moreover, calculated that if adjacent incompetent layers are 1.5 times thicker than the competent layer, then the fractured layer does not have any influence of nearby competent layers and the adjacent incompetent layers can be treated as an infinitely thick. Similar observations have been made in our study area (Figs. 5c and d). Therefore all measurements in competent beds which are surrounded by thin incompetent beds are neglected in order to avoid the influence of adjacent competent beds.

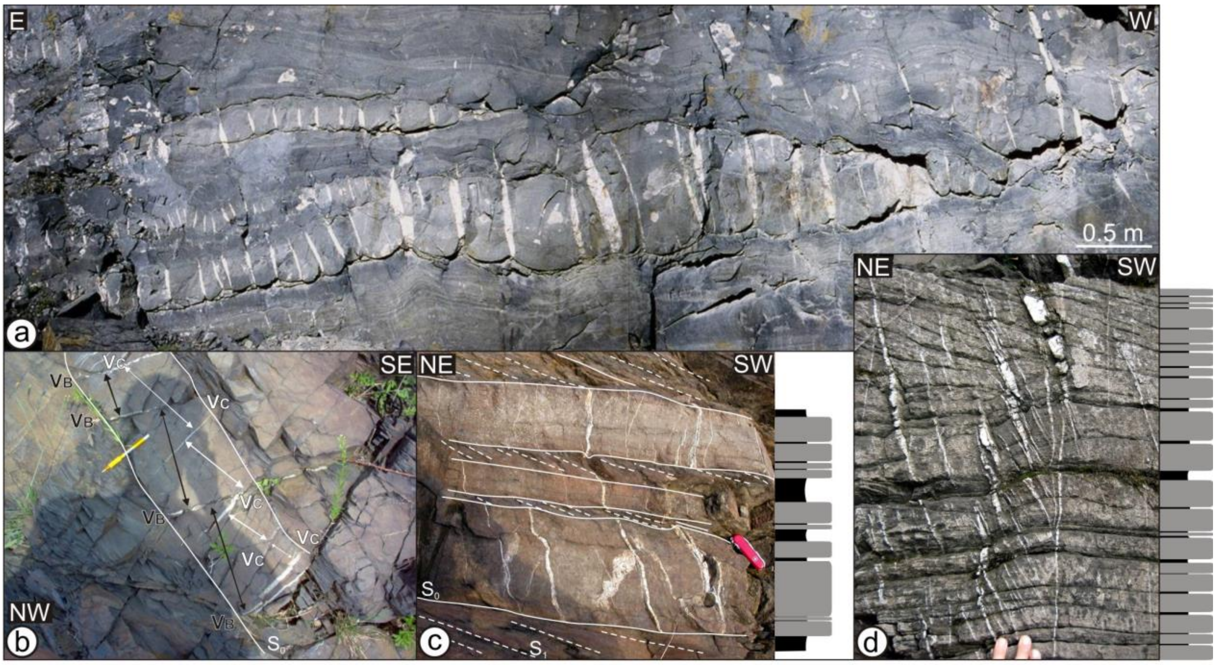

Figure 7.1: Parameters influencing vein spacing. **(a)** Variability in intermullion vein spacing due to irregular layer thickness. Upper left: veins are equally spaced in a layer with a uniform thickness (cHASB, Bastogne Mardasson, Belgium). **(b)** The presence of the regional consistent vein generation V_B influences the spacing pattern (white arrows) of the cross-cutting V_C vein generation (pHASB, Wildenhof zone 9, pencil ~15 cm). **(c)** Variability in vein spacing in heterogeneous sandstone due to the interference of adjacent competent layers. The veins refract at the competent - incompetent interface and are oriented oblique to bedding as a result of flexural-slip folding (pHASB, Wildenhof zone 8; knife ~10 cm). **(d)** Veins cross-cutting multiple competent layers, which are separated by thin incompetent units (pHASB, Urftsee zone 17; fingernails ~1.4 cm).

7.3 Vein spacing distribution throughout the HASB

7.3.1 Aspect ratio

Besides describing the absolute vein spacing as a function of the layer thickness, the aspect ratio of each segment is given (Figure 7.2). This ratio represents the ratio of the layer thickness relative to the median spacing of the veins (which is a better and more stable estimator of the centre of the spacing population than the arithmetic mean) and is referred to as the fracture spacing ratio (*FSR*) by Gross (1993). The *FSR* is useful to compare spacing patterns of different outcrops and has been used in the past to determine if boudinage can be invoked as a mechanism for veining (Kenis *et al.* 2002a). Aspect ratios in the HASB (Figure 7.2) vary between 0.5 and 21 in the cHASB and between 0.7 and 6 in the pHASB. A small percentage of the aspect ratios are lower than 1, with mean values of these low aspect ratios of 0.7 in the cHASB and 0.8 in the pHASB. The aspect ratios of rectangular boudins (*i.e.* those boudins considered to develop by tensile fracturing of brittle layers at right angles to layering) are commonly less than 0.55 (Ghosh & Sengupta 1999, Mandal *et al.* 2000, Price & Cosgrove 1990, Van Baelen & Sintubin 2008). The difference in aspect ratios of the veins in the slate belt with respect to the low ratios of rectangular boudins clearly shows that boudinage was not the mechanism for veining and is not responsible for the regular spacing pattern.

Despite the widely used *FSR*, its inverse is often used in geomechanical modelling. Based on this *S*/*T* ratio in the HASB (see mean *S*/*T* in Table 7.1 and Table 7.2), vein spacing in the HASB can mostly be classified into Range III of Bai and Pollard (2000b), *i.e.* the regime in which spacings have ratios less than the critical value of 0.976. This indicates that the veins developed at distances closer than those predicted for fracture saturation and that it is reasonable to seek other mechanisms to overcome the stress transition around fractures at the stage of fracture saturation.

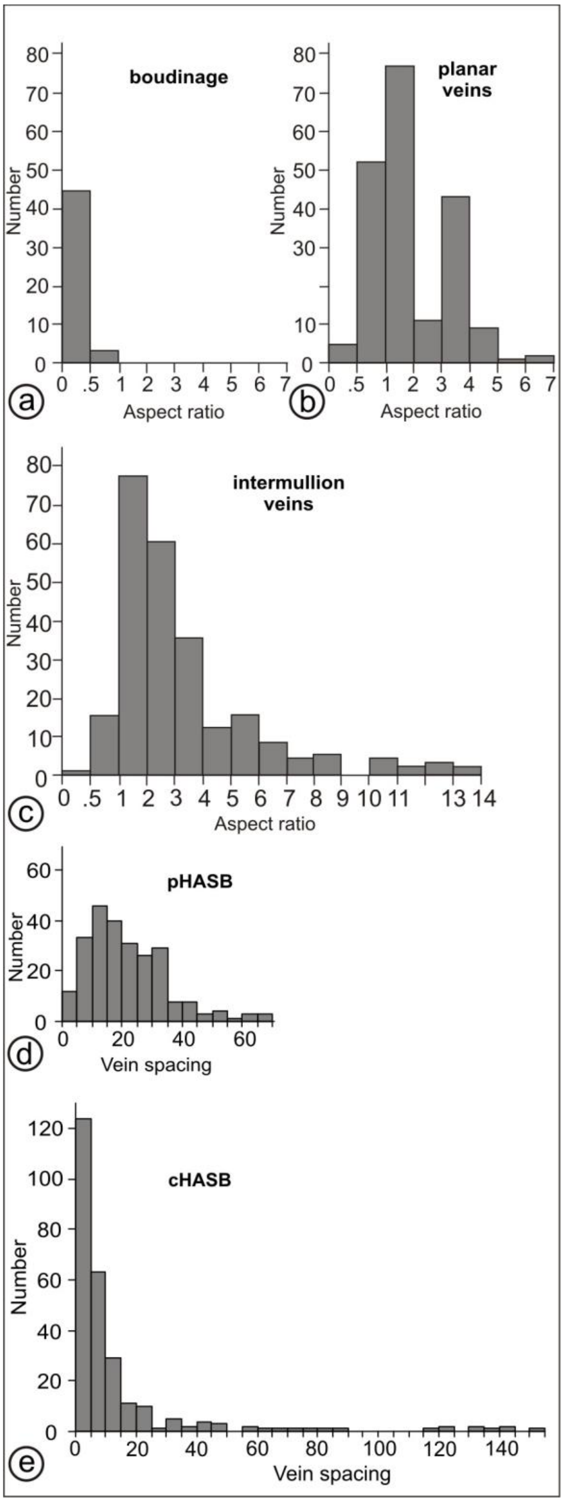

Figure 7.2: Block aspect ratios reflecting vein spacing in **(a)** boudinaged layers (examples from Price & Cosgrove 1990, Van Baelen & Sintubin 2008), **(b)** 'undeformed' segments in the Rursee/Urftsee area and **(c)** mullions, cHASB. **(d-e)** Histograms showing the vein spacing frequency in the pHASB and cHASB.

7.3.2 Coefficient of variation

There are a lot of analytical methods to characterise the spatial distribution of veins; the standard deviation (σ) represents the quality of the measurements; the lower σ is, the more representative the median will be. This largely depends on the amount of measurements (n) taken. A more suitable measure is the coefficient of variation (C_v): the ratio of the standard deviation (σ) to the mean spacing (S) ($C_v = \sigma / S$). The C_v characterises the variability in a dataset from anticlustered to clustered and has been used developed to determine the spatial distribution of modelled fault populations (Gillespie 2003), but also works for opening mode fractures and veins (André-Mayer & Sausse 2007, Foxford *et al.* 2000, Gillespie *et al.* 1999, 2001). Gillespie *et al.* (1999) calculated that for $C_v > 1$: veins are clustered, *i.e.* power-law, for $C_v = 1$: veins are randomly distributed; for $C_v < 1$: vein spacings are anticlustered or periodic, and for $C_v = 0$: veins are equally spaced. Fracture saturation is therefore characterised by $C_v < 1$. A modified coefficient of variance (C_v^*)

$$C_v^* = C_v\,((n+1)/(n-1))^{1/2}$$

needs sometimes to be calculated due to the small amount of measurements (n) taken along a fractured bed (Gillespie 2003). This modified value C_v^* has been calculated in Table 7.1 and Table 7.2, but only causes a minor change in the estimated C_v and does not influence the interpretation. At the pHASB and the cHASB, the vein arrays have low values of C_v ranging between 0.09 to 0.55 and 0.01 to 0.70 with an average C_v of 0.29 and 0.27 respectively. This indicates anticlustered, periodic spacing distributions in the whole HASB and although spacings sometimes seem to be varied, they appear to have some regularity in outcrop. Characteristic regularly spaced vein clusters are typical for stratabound vein arrays in sandstones (Foxford *et al.* 2000, Gillespie *et al.* 2001). The histograms (Figure 7.2d and e), moreover, show a normal to power-law vein spacing population in the pHASB and the cHASB respectively.

Table 7.1: Summary of vein spacing data from the North Eifel (pHASB). Mean original vein strike represents vein orientation prior to folding, convention used: dip direction/dip; Min, minimum spacing; Mean, arithmetic average; Max, maximum spacing; σ, standard deviation; Cv, coefficient of variation of all veins in the measured bed; Cv*, modified version of Cv. Mean S/T determined by average of spacing/thickness ratio.

Locality/ Dataset	Mean original vein strike	Line length (cm)	Nr of values (n)	Thick-ness (*T*)	Min	Median (*S*)	Mean	Max	σ	C_v	C_v*	Mean *S/T*
Rursee / Wildenhof 45a	282/78	26	8	3	1	3	3.13	4	0.99	0.32	0.36	0.88
Rursee / Wildenhof 45b	280/70	64	5	7	10	13	12.8	16	2.77	0.22	0.27	1.76
Rursee / Wildenhof 39a	276/73	84	6	10	7	12	14	28	7.72	0.55	0.65	1.13
Rursee / Wildenhof 46b	285/74	25	3	12	10	12	12.3	15	2.52	0.2	0.29	1.00
Rursee / Wildenhof 5	310/89	85	6	17	9	13.5	14.2	21	5.12	0.36	0.43	0.75
Rursee / Wildenhof 50	286/76	203	8	18	12	24	25.4	34	6.84	0.27	0.31	1.28
Rursee / Wildenhof 39b	276/73	58	5	23	7	12	11.6	18	4.72	0.41	0.50	0.44
Rursee / Wildenhof 44b	282/77	536	24	28	12	22	22.3	35	6.53	0.29	0.30	0.73
Rursee / Wildenhof 40	293/77	410	15	28	21	25	27.3	35	5.19	0.19	0.20	0.95
Rursee / Wildenhof 44a	284/76	539	23	35	10	23	23.4	44	8.95	0.38	0.40	0.58
Rursee / Wildenhof 46a	285/74	98	3	44	30	30	32.7	38	4.62	0.14	0.20	0.73
Rursee / Wildenhof 19b	089/60	460	11	56	31	38	41.8	62	11.69	0.28	0.31	0.70
Rursee / Wildenhof 42	273/74	573	11	93.5	20	53	52.2	70	14.27	0.27	0.30	0.50
Rursee / Schwam. 94	254/88	29	4	22	6	8	7.3	9	1.50	0.21	0.27	0.32
Rursee / Schwam. 93	254/88	75	3	60.5	12	31	25	32	11.27	0.45	0.64	0.34
Rursee / Hub. Höhe 71	337/85	65	10	9	3	6.5	6.5	10	2.37	0.36	0.40	0.58
Rursee / Hub. Höhe 71	106/76	42	6	15	5	6.25	6.9	13	3.17	0.46	0.54	0.40
Rursee / Hub. Höhe 72	140/83	84	6	31	9	15	14	18	3.90	0.28	0.33	0.42
Rursee / Hub. Höhe 72	108/78	177	4	52	12	20.5	21.7	31	6.38	0.29	0.38	0.39
Rursee / Hub. Höhe 72	109/62	133	8	55	21	35	33.3	40	9.71	0.29	0.33	0.56
Rursee / Hub. Höhe 72	114/82	117	5	72	17	26	25.4	31	5.32	0.21	0.26	0.31
Rursee / Eschauler 64	294/65	294	13	75	10	25	22.6	33	7.50	0.33	0.36	0.30
Urftsee / Urftsee 27b	108/83	57	7	9	7	8	8.1	10	1.21	0.15	0.17	0.95
Urftsee / Urftsee 27b	105/77	26	3	12	12	12	12.7	14	1.15	0.09	0.13	1.05
Urftsee / Urftsee 27b	292/78	265	24	13	7	11	11	17	2.66	0.24	0.25	0.80
Urftsee / Urftsee 27a	109/71	237	14	16	12	17.5	16.9	22	3.02	0.18	0.19	1.10
Urftsee / Urftsee 28b	105/87	152	7	31	11	22	21.7	33	7.30	0.34	0.39	0.57
Urftsee / Urftsee 6	330/77	185	5	60	20	43	37	45	10.93	0.3	0.36	0.56
		Total measurements:	*247*						*Mean C_v:*	*0.29*	*0.34*	*0.72*

Table 7.2: Summary of intermullion vein spacing data from the Ardennes (cHASB). Bast, Bastogne; Mard, Mardasson; Coll., Collignon; SLR, Sur Les Roches. Mean original vein strike represents vein orientation prior to folding, convention used: dip direction/dip; Min, minimum spacing; Mean, arithmetic average; Max, maximum spacing; σ, standard deviation; C_v, coefficient of variation of all veins in the specified layer; C_v^*, modified version of C_v; Mean *S*/*T* constructed by average of spacing/thickness ratio. *% of sh.*, percentage of shortening calculated from line length balancing of mullion. *data from Kenis *et al.* (2004, 2005b). Mean S/T determined by average of spacing/thickness ratio.

Locality / Data set	Mean original vein strike	Line length (cm)	Nr of values (*n*)	Thick-ness (*T*)	Min	Median (*S*)	Mean	Max	*σ*	C_v	C_v*	Mean *S/T*	% of sh.
Eifel / Dedenborn	346/52	278	14	28	16	21	19.9	24	3.18	0.16	0.17	0.75	29.7
Ardennes / Bütgen.	112/77	12	8	2.1	0.9	1	1.5	2.2	0.45	0.3	0.34	0.64	
Ardennes / Bütgen.	112/77	24	5	7	4.3	4	4.5	5	0.4	0.09	0.11	0.59	
Ardennes / Bütgen.	112/77	937	16	86	41	57	58.6	88	14.07	0.24	0.26	0.63	11.8
Ardennes / Houffalize	114/64	12	7	6	1	1	1.6	2	0.53	0.32	0.37	0.13	
Ardennes / Houffalize	114/64	163	26	10	2	6	6.2	11	4.35	*0.7*	0.72	0.24	
Ardennes / Houffalize	114/64	36	6	11	3	7	5.9	8	2.2	0.37	0.44	0.47	
Ardennes / Houffalize	114/64	27	3	13	7	9	9	11	2	0.22	0.31	0.67	
Ardennes / Boeur	140/75	13	13	2	0.8	1	1	1.5	0.32	0.32	0.35	0.5	
Ardennes / Boeur	140/75	9	6	4	0.8	1	1.3	2	0.4	0.31	0.37	0.31	
Ardennes / Boeur	304/72	10	8	5	1	1	1.3	2	0.4	0.31	0.35	0.24	28.4*
Ardennes / Boeur	140/75	153	26	7	2.3	6	5.9	10	1.95	0.33	0.35	0.7	20.4*
Ardennes / Boeur	140/75	36	7	9	2.5	5	5.2	9	2.27	0.45	0.52	0.56	
Ardennes / Bast. Coll.	121/62	12	6	1.3	1.1	1	1.9	2.6	0.61	0.41	0.48	1.12	
Ardennes / Bast. SLR	149/78	6	7	1.5	0.5	0.65	0.8	1.6	0.35	0.46	0.53	0.48	
Ard. / Bast. Mard.	125/81	3	3	2.1	0.5	1.1	1.1	2	0.21	0.19	0.27	0.5	
Ard. / Bast. Mard.	125/81	21	10	3.5	1.1	1.7	1.7	2.4	0.37	0.22	0.24	0.5	28.0*
Ard. / Bast Mard.	125/81	16	6	5	4	2.7	2.6	3.8	0.96	0.37	0.44	0.49	23.1*
Ardennes / Bast. Coll.	121/61	7	4	5	1	1.7	1.6	2.1	0.46	0.29	0.37	0.28	
Ardennes / Bast. SLR	149/78	102	8	26.5	14	12	12.8	16	2.42	0.19	0.21	0.47	
Ardennes / Bast. Coll	121/61	142	4	40	33	34.5	35.5	40	3.11	0.09	0.11	0.85	
Ardennes / Bast. SLR	149/78	186	6	50	24	32.5	31	36	4.29	0.14	0.16	0.61	
Ardennes / Bast. SLR	149/78	130	3	92	40	43	43.3	48	1.53	0.04	0.05	0.47	32.3*
Ardennes / Bast. SLR	149/78	203	4	100	40	45	42	45	15.02	0.36	0.46	0.48	29.5*
Ardennes / Bast. SLR	149/78	270	5	110	65	55	55	65	4.24	0.08	0.09	0.59	25.4*
Ardennes / Rouette	142/82	38	9	9	3.5	6	5.5	7.2	2.23	0.41	0.45	0.67	27.6*
Ardennes / Rouette	142/82	51	3	26	10	17	16.7	17	0.58	0.03	0.05	0.65	31.0*
Ardennes / Remagne	207/44	7	5	3	1	1	1.3	1.8	0.37	0.29	0.36	0.37	
Ardennes / Remagne	207/44	15	9	8	1.2	1	1.6	2.8	0.6	0.37	0.41	0.23	
Ardennes / Bertrix	148/85	20	3	15	5	5	6.7	10	2.89	0.43	0.61	0.4	19.8*
Ardennes / Bertrix	148/85	38	7	17	5	6	6.9	13	2.79	0.4	0.47	0.36	
Ardennes / Bertrix	148/85	88	12	23	4	9	7.3	10	2.43	0.33	0.36	0.28	
Ardennes / Bertrix	148/85	35	4	26	8	8	8.6	14	3.77	0.44	0.56	0.3	26.4*
Ardennes / Bertrix	148/85	58	7	34	5	9	8.3	10	2.01	0.24	0.28	0.23	
Ardennes / Bertrix	148/85	164	14	70	12	17	16.4	20	4.4	0.27	0.29	0.15	
Ardennes / Bertrix	148/85	228	4	200	50	57	55.3	58	1.98	0.04	0.05	0.29	
Ardennes / Bertrix	148/85	195	3	229	60	68	67.5	75	8.66	0.13	0.18	0.29	
Ardennes / Bertrix	148/85	399	3	250	108	108	108.3	109	0.58	0.01	0.01	0.52	
Ardennes / Bertrix	148/85	500	4	500	80	125	119.6	130	23.65	0.2	0.26	0.27	
Ardennes / Bertrix	148/85	780	6	800	89	137.5	130	155	22.17	0.17	0.2	0.16	
		Total measurements:	*304*						*Mean C_v:*	*0.27*	*0.32*	*0.46*	

7.3.3 Influence of layer thickness

The term 'spacing' is used for the distance between two neighbouring, parallel veins and is measured perpendicular to the vein walls. Vein spacing was measured between stratabound veins cross-cutting the competent bed and hence terminating at the competent-incompetent interface. Hairline veins or microveins with thin apertures (~1mm), which are sometimes present between the vein arrays, are ignored, although they are also formed due to fracturing. Median vein spacing to layer thickness relationship in thin (< 1 m; Figure 7.3 and Figure 7.4) as well as in thick layers (> 1 m; Figure 7.5) is shown. The range of spacing along a single bed is indicated by minimum and maximum error bars and the data are represented both on a linear scale, so that the relationship between spacing and thickness may readily be seen (Figure 7.4a-d), and on log-log axes (Figure 7.5e and f) in order to obviate the problem related to the irresolvable data near the origin.

The following features are characteristic:

(i) Vein spacing increases with increasing layer thickness;

(ii) In the realm of thin layers (< 40 cm) a linear relationship can be assumed for an individual outcrop. There is, however, a small variation between different outcrop localities in the pHASB: veins show for example a wider spacing in the Urftsee outcrop than in the Hubertus Höhe outcrop, although quartz content of the host rock (Table 7.1) and thus subcritical crack index in both localities is nearly the same. This variation in spacing between different outcrops is smaller in the cHASB;

(iii) The assumed linear relationship in thin layers becomes non-linear in thicker layers (> 100 cm) and tends to evolve towards a maximum value (Figure 7.5) indicating that the layer thickness is decreasing importance in controlling vein spacing. Variation in vein density along a single bed (expressed by the error bars in Figure 7.5) increases towards thicker units. This increasing relationship, however, could be a sampling artefact; large veins in thick units are only observed in two quarries in the cHASB (Bastogne and Bertrix;). With thicker beds and wider spacings, the number of veins sampled is smaller than for thin layers with narrow spacings. Therefore, these results have to be carefully interpreted due to undersampling in thick layers and a lack of comparable units in the pHASB. Extrapolation of the results to larger scales using fractal statistics may be possible, but probably may be flawed because the mechanics of vein formation may be governed by different dominant processes at larger scales (Cowie *et al.* 1996).

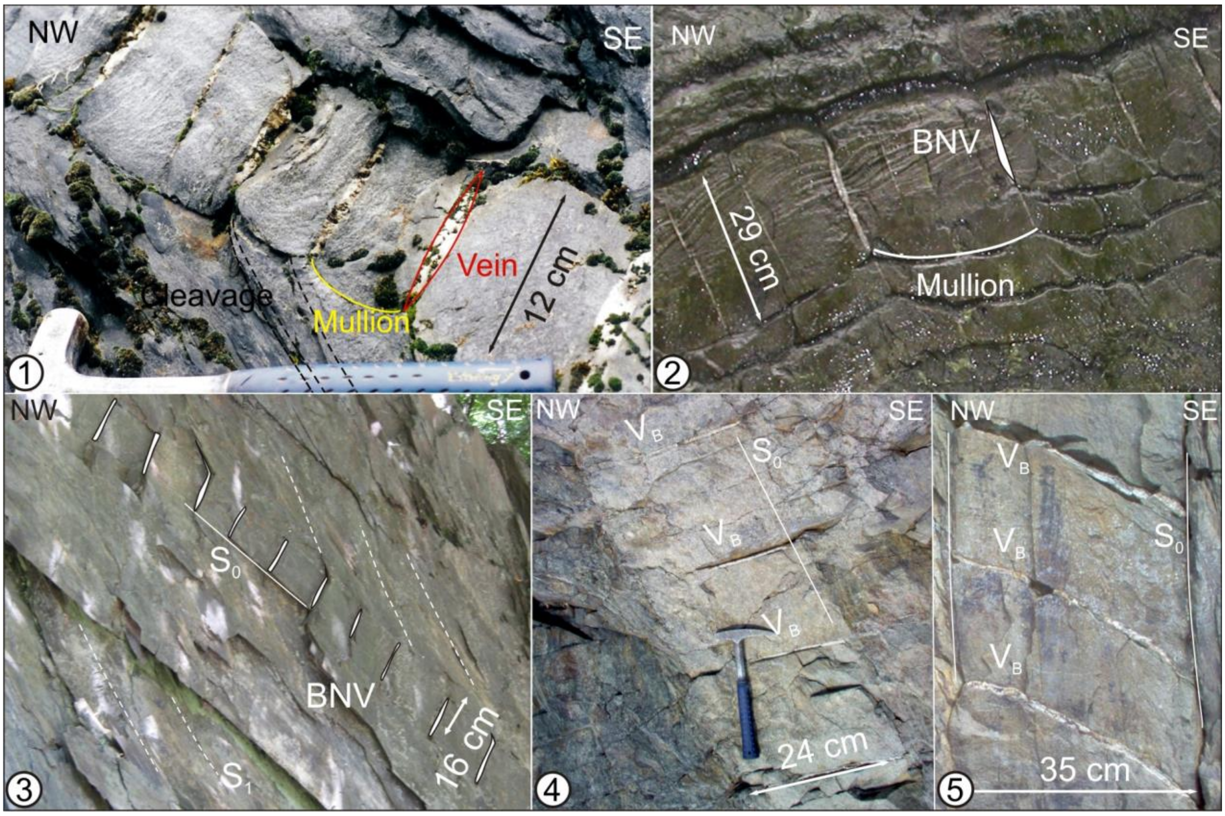

Figure 7.3: Examples of **(1-2)** intermullion vein spacing from the cHASB (1: Boeur after Kenis 2004, 2. Flamierge) and **(3-5)** spacing of planar veins in the pHASB (3: Urftsee zone 7, 4-5: Wildenhof zone 9). Numbers 1-5 correspond to the numbers in Figure 7.4a and b.

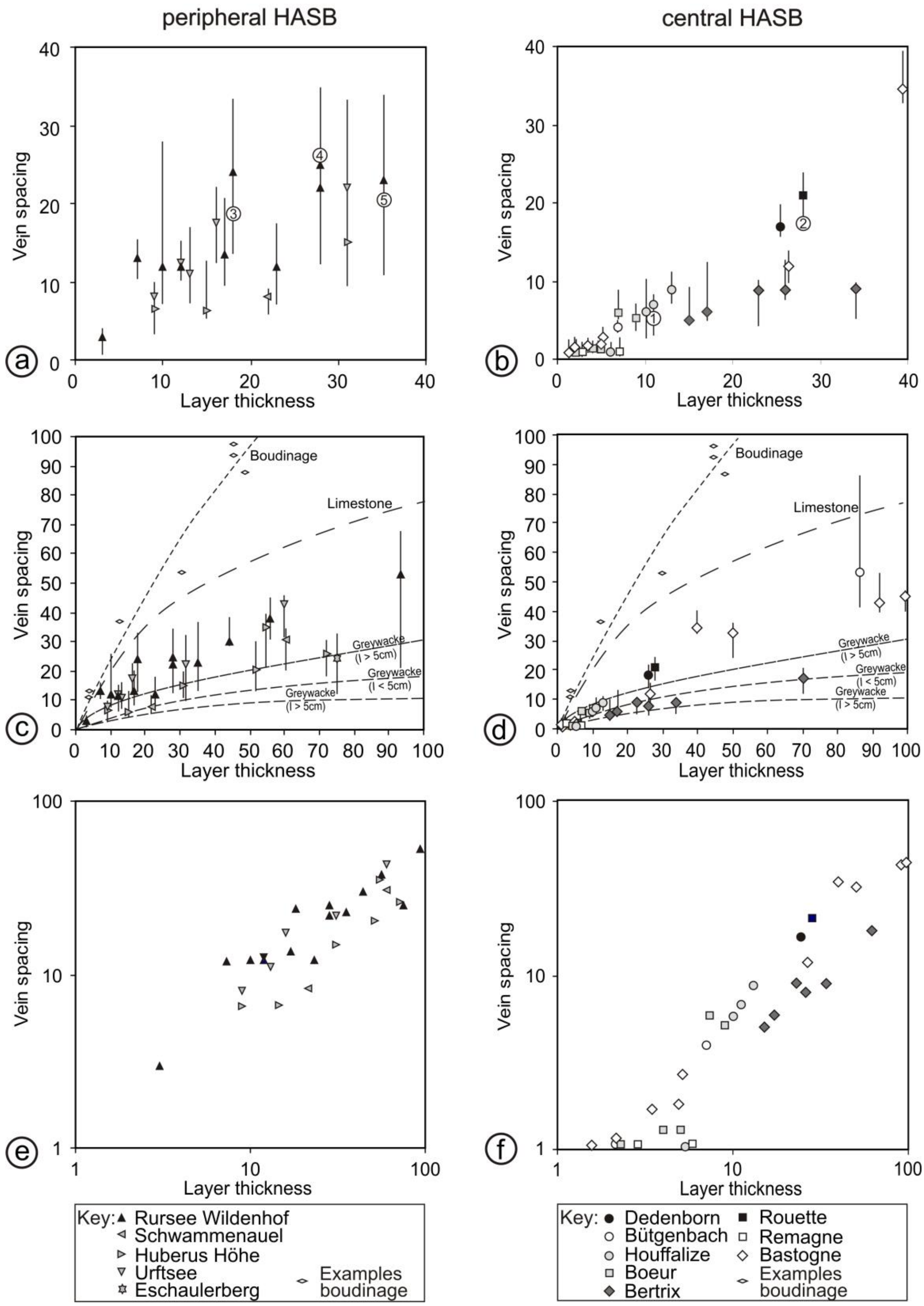

Figure 7.4: Vein spacing (in cm) versus layer thickness (in cm) relationship for veins from the pHASB in **(a)** thin and in **(c)** thicker siliciclastic multilayer sequences taking into account the spatial distribution **(b and d)** for intermullion veins in the cHASB. The numbers in circles refer to the examples shown in Figure 7.3. **(c - d)** Vein spacing is also compared to published fracture spacing in greywackes (examples from the U.K. and Portugal) and in limestone (Ladeira & Price, 1981). Examples of boudinaged layers are from Price & Cosgrove (1990) and Van Baelen & Sintubin (2008). **(e - f)** Vein spacing versus layer thickness data presented on a log-log scale, showing a power-law *S*/*T* relationship (modified after Van Noten & Sintubin 2010).

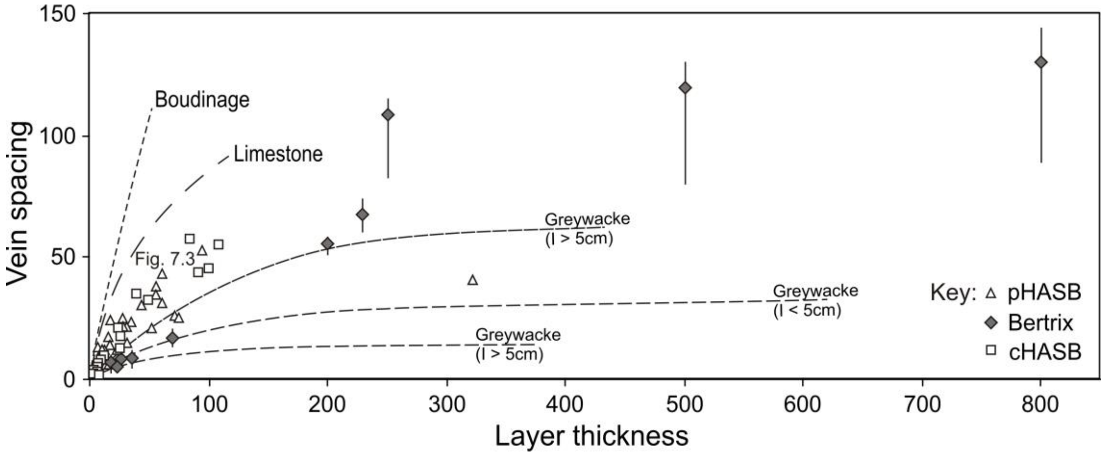

Figure 7.5: Relationship between vein spacing (in cm) and layer thickness (in cm) for quartz veins in thick metasedimentary multilayer sequences (data from Bertrix; cHASB), compared to the relationship between fracture spacing and layer thickness (data from Ladeira & Price, 1981). Axes not to scale (modified after Van Noten & Sintubin 2010).

7.3.4 Restoration of mullion shortening

For a given layer thickness smaller than 40 cm, intermullion veins in the cHASB are closer spaced than planar veins in the pHASB. This is represented by smaller S/T-values in Table 7.3 and in Figure 7.4b. As mullions are compression features developed due to early Variscan layer-parallel shortening, it would be interesting comparing the original spacing to layer thickness ratio (S_0/T_0) with the S/T ratio in the pHASB, in order to show consistency of vein spacing in the slate belt. Based on field observations, incipient layer-parallel shortening mainly varies between 19% and 33% (Kenis *et al.* 2005b), without any correlation with the metamorphic grade in the HASB. The percentage of layer-parallel shortening (see Figure 7.6 and Table 7.3) has been calculated by converting the area of host rock between two veins to a rectangle with thickness equal to 95% of the length of the vein with a quartz strain of 5% to correct for deformation of the vein, thereby assuming no volume change has taken place during shortening (Kenis *et al.* 2004, 2005b). In order to estimate S_0/T_0, a small number of mullions of different localities in the cHASB were reconstructed into their initial shape (Table 7.3). Firstly bedding length is measured between the vein tips along the lobate bedding to estimate the initial spacing of the veins (S_0). Secondly, the original layer thickness (T_0) was deduced by measuring the distance between the vein tips minus 5% shortening to correct elongation of the vein during mullion formation. This restoration of mullion shortening causes an increase of the S_0/T_0 ratio, with spacings into the realm of the vein spacing measured in the pHASB (Figure 7.6), with even wider spaced veins for a small amount of outcrops. Due to the small amount of measurements, no interpretations can be made on the variation of vein spacing in function of the metamorphic grade or on variability of the host-rock parameters between the cHASB and the pHASB. One also has to keep in mind that the S_0/T_0 ratio in the pHASB was most probably also higher than the present measured S/T ratio due to – macroscopically not observable – Variscan layer-parallel shortening at the onset of cleavage development. The amount of shortening in sandstones during cleavage development is, however, not known.

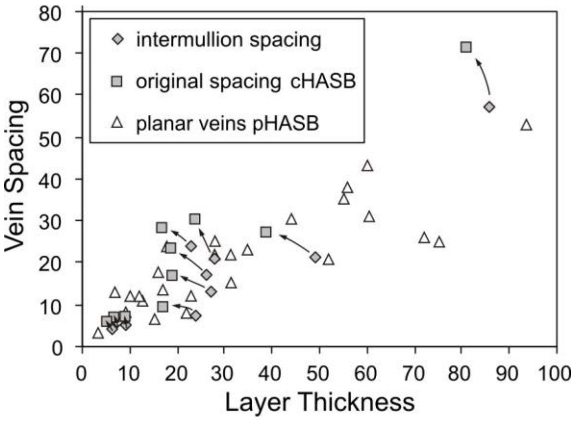

Figure 7.6: S/T- versus S_0/T_0 -relationship of intermullion veins from some examples in the Ardennes, compared to S/T-relationship of planar veins from the Eifel.

Table 7.3: Restoration of the degree of mullion shortening by means of methods explained in the text. The ratio of original vein spacing (S_0) versus initial layer thickness (T_0) increases after restoration. Entries in bold correspond to data which are rather exceptional in the slate belt. * data from Kenis *et al.* (2004; 2005b).

Locality	Data set	Median (S)	Thickness (T)	S / T	% of shortening	S_0	T_0	S_0 / T_0
Eifel	Dedenborn	21	28	0.75	29.7	29.9	23.8	1.26
Ardennes	Bütgenbach	57	86	0.63	**11.8**	71.0	81.0	0.86
Ardennes	Boeur	6	7	0.70	20.4*	5.7	5.7	1.00
Ardennes	Boeur	5	9	0.56	25.7	6.7	9.2	0.73
Ardennes	Boeur	13	27	0.48	22.0*	16.5	19.1	0.87
Ardennes	Bastogne Mardasson	21	49	0.48	26.9	26.8	39.0	0.68
Ardennes	Bastogne Mardasson	24	23	1.05	**14.2**	28.0	17.2	1.60
Ardennes	Rouette	6	9	0.67	27.6*	6.7	6.9	0.97
Ardennes	Rouette	17	26	0.65	31,0*	23.3	18.6	1.25
Ardennes	Bertrix	7	24	0.30	25.5*	9.4	17.2	0.57

7.4 Discussion

Comparing the vein spacing to layer thickness relationship with various fracture distributions serves as a useful indicator of the processes which may have been responsible for controlling the observed regular vein spacing in the High-Ardenne slate belt. Vein spacing increases linearly with layer thickness in thin sedimentary sequences (< 40 cm), but tends to increase non-linearly in thick layers. The pattern looks similar to published fracture spacings (*e.g.* Ladeira & Price 1981, Mandal *et al.* 1994) with the minor difference that veins are wider spaced than fractures in thick layers. The resemblance of vein spacing with fracture spacing could imply that initial vein development in an unfractured rock occurs in a similar way to fracture development.

Bai & Pollard (cf. 2000b) have demonstrated that regularly spaced fractures form at the stage of fracture saturation. The low coefficient of variation ($C_v < 1$) calculated for our examples indicates that saturation could have been reached during initial vein development. Some of the S/T- and calculated S_0/T_0 ratios are, however, below the critical value for fracture saturation supporting a mechanism to overcome the compressive stress state around saturated fractures. This has been explained by pre-existing flaws which cut through the compressive region existing between the saturated fractures (*e.g.* Bai & Pollard 2000b) or by hydraulic fracturing (*e.g.* Ladeira & Price 1981). The presence of pre-existing flaws is very difficult to determine and largely depends on the heterogeneity of the rock. High pore fluid pressures are recorded both in regularly as in closely spaced veins, indicating that these high pressures can account for vein nucleation rather than that they control vein spacing. The regular spacing pattern may thus suggest that initial veins are ‘aware’ of adjacent veins during the initial development (Figure 7.7a and b) and that the process of spacing is still favoured by stress distributions around fractures. Despite a lack of constraints on the timing of the initial veins relative to each other, the spacing pattern suggests that a rock can be saturated by the presence of initial veins. This saturation is in contrast with the crack-jump model of Caputo & Hancock (1999) who state that once vein formation has commenced, the local stress conditions around incipient veins are fully restored due to sealing of the host rock, with new cracks being ‘unaware’ of the existence of any pre-existing ones. They moreover argue that the factors leading to a layer becoming saturated by the presence of fractures do not apply for veins if the vein filling is more resistant to tension than the host rock. The presence of crack-seal host-rock inclusion bands in the veins, however, evidences that new fractures will form in the quartz crystals of the initial (syntaxial or ataxial) veins rather than that they will form in the adjacent host rock. Successive fracturing and sealing phases therefore result in vein thickening (Figure 7.7c).

In the pHASB, only the first generation V_B shows a clear, regularly distribution pattern. The absence of any regular spacing pattern in cross-cutting generations (Figure 7.7d) indicates that it is only possible to create a stage of saturation in an unfractured rock and not in an already deformed rock.

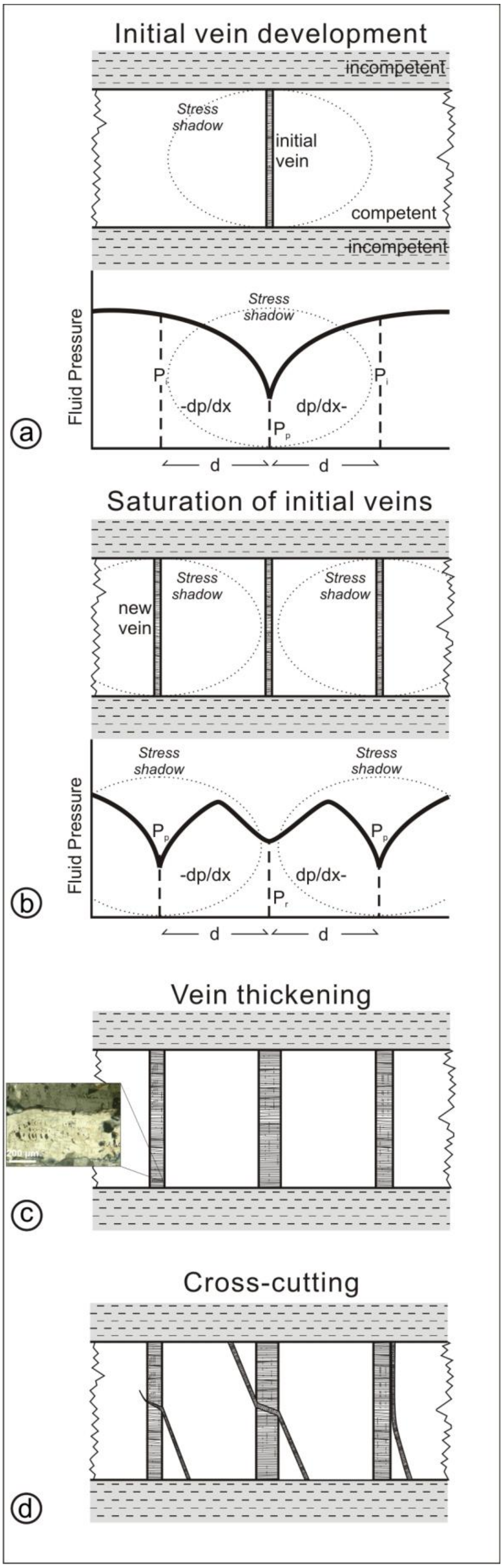

Figure 7.7 (left)**:** Simplified conceptual sketch of bedding-normal vein development in the Eifel area, based on the comparison of vein spacing with fracture spacing (cf. Ladeira and Price, 1981). The time increments between the different steps are unknown. **(a)** Early/initial vein development in an unfractured rock. Locally around the initial vein a lateral fluid pressure drop creates a stress shadow which inhibits the creation of new veins. d: distance between fractures; dp/dx: fluid pressure gradient; P_i: unaffected fluid pressure; P_p: decreased fluid pressure. **(b)** Only at a certain distance of the initial vein, the fluid pressure will be sufficiently high enough to create new veins. Repetitive steps of (a) and (b) creates a rock saturated by the presence of initial veins. P_f: recovering fluid pressure. **(c)** In a saturated rock, veins will thicken by the crack-seal mechanism rather than forming new veins during continuous extension. **(d)** Due to changes in the stress field, new vein generations are influenced in their growth by the earliest generation.

7.5 Conclusions

In this chapter it is demonstrated by means of a comparative field-based study that in thin isolated sandstone layers (< 40 cm), veins have a typical spacing pattern which increases linearly with increasing bed thickness. The assumed linear relationship in thin layers becomes non-linear and less dependent of the layer thickness towards thicker units (> 40 cm) and tends to saturate at a maximum vein spacing (~1 m) independent of bed thickness for beds thicker than 2 m.

The spacing pattern observed in the vein examples of the Ardenne-Eifel region (Belgium, Germany) shows similarities with fracture spacing distributions, supporting the idea that individual veins inhibit the formation of new adjacent veins at a certain distance during initial development and that the rock can be saturated by the presence of initial veins, although this may be in contrast with the previously published crack-jump model. It has been demonstrated by a detailed microthermometric study (Chapter 5) that high fluid pressures are responsible for vein initiation and repetitive growth of the veins. This gives an explanation for vein initiation, but the spacing pattern of the veins might probably be attributed to the local, intrastratum stress state around initial fractures indicating a close interaction between fluid overpressures and the local small-scale stress state.

At the stage of saturation, in which new veins are prohibited to grow, high fluid pressures can overcome the compressive stresses between the saturated initial veins causing irregularly spaced veins at a smaller distance than those predicted at fracture saturation. The presence of crack-seal microstructures in the bedding-normal veins, furthermore, indicate that at the stage of fracture saturation, it will be easier to fracture the vein quartz of the initial vein than to fracture the adjacent host rock because of strength difference between quartz and intact rock. This implies that during subsequent extension, the thickness of the initial veins will increase by the process of crack-sealing, rather than new veins forming near pre-existing ones.

Whether a single consistent set of veins, such as the V_B veins in the pHASB and the intermullion veins in the cHASB, or subsequent cross-cutting vein generations (V_C in the cHASB) will develop, with only the first generation (V_B) regularly spaced, depends largely on the consistency of the regional stress field. When the far field stress field rotates, irrespective on the mechanism that causes this rotation, the earliest veins will become unfavourably oriented to allow further (crack-seal) growth of the veins. Instead, new (cross-cutting) veins may form that reflect the new stress field but that will be influenced in their growth by the already existing veins and hence are prohibited to form regularly spaced patterns.

CHAPTER 8 3D complexity of stress-state changes during tectonic inversion

8.1 Introduction

The constructed stress-state evolution of the upper crust, as defined by the successive vein types in the North Eifel, shows an import coupling between fluid-assisted deformation during the early Carboniferous tectonic inversion affecting the Ardenne-Eifel basin at the onset of the Variscan orogeny. Owing to low differential stress during tectonic inversion, it is demonstrated in this work that near- to supra-lithostatic fluid overpressures are captured in extension or in extensional-shear veins that accompany the tectonic inversion. As illustrated on the brittle failure mode (BFM) plot (Figure 6.3) and shown by theoretical studies (Sibson 1998, 2000, 2004), fluid overpressures are likely to develop during the transition from extension to compression and are easier to maintain at low differential stress in the compressional regime than in the extensional regime. The stress-state derived from macro- and microstructural analysis moreover shows that there is an important influence of the 3rd dimension as demonstrated by the orientation of the veins (Figure 6.3). However, the way these three principal stresses change in three dimensions during the tectonic inversion has not been explained in this work. Furthermore, although it is clear the veins are closely related in time to the actual switch between stress regimes, the influence of the tectonic stress σ_T in this kinematic history has not been elaborated. Therefore, possible stress-state evolutions are analysed in this discussion to illustrate the complexity of 3D stress transitions during compressive tectonic inversion. abbreviations that are further used in this discussion are summarised in Table 8.1.

Table 8.1: Abbreviations used in the stress-state reconstructions

T	tensile strength	σ_1	maximum principal stress component
P_f	pore-fluid pressure	σ_2	intermediate principal stress component
σ'	effective stress	σ_3	minimum principal stress component
σ_v	vertical principal stress component	$\sigma_{1,T}$	maximum principal stress component
σ_T	tectonic principal stress component		increased by the tectonic stress component
σ_H	maximum horizontal principal stress component	$\sigma_{2,T}$	intermediate principal stress component increased by the tectonic stress component
σ_h	minimum horizontal principal stress component	$\sigma_{3,T}$	minimum principal stress component increased by the tectonic stress component

8.1.1 Problem definition

The tectonic switch, which is illustrated on the brittle mode by the zero differential stress line (Figure 8.1), reflects the specific stress state at which the maximum principal stress σ_1 equals the minimum principal stress σ_3 so that $\sigma_1 - \sigma_3 = 0$, without considering the role of the intermediate principal stress σ_2. This specific stress state of a zero differential stress during the tectonic switch can only be reached in a state of isotropic pressure, *i.e.* $\sigma_1 = \sigma_2 = \sigma_3$. Although isotropic stresses are reported in thick shaly sequences (*e.g.* Gale *et al.* 2007), the chances that a stress state equals a pure pressure state in multilayer sequences such as the Lower Devonian deposits, is, however, questionable (*e.g.* Healy 2009). Because of the assumption of an isotropic stress, the stress-state evolution illustrated in the BFM plots is actually an oversimplification of the true three-dimensional stress-state evolution in the Earth’s crust. In more realistic anisotropic stress conditions, the transition from extensional to compressional might be more complex than classically illustrated in BFM plots owing to the fact that a triaxial stress state might remain present during inversion. It is mentioned by Sibson (1998) that failure curves for an intermediate strike-slip regime ($\sigma_2 \sim \sigma_v$) lie anywhere at the zero differential stress line between the extensional and compressional regime, depending on the value of σ_2 with respect to σ_1 and σ_3. To date, however, this intermediate regime has been ignored in any tectonic inversion model.

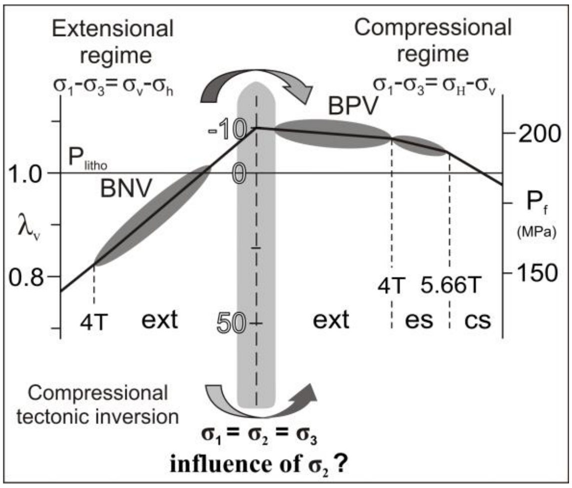

Figure 8.1: Problem definition: a brittle failure mode plot is useful to define the timing of veining with respect to the tectonic switch between stress regimes, but oversimplifies the true 3D stresses by assuming isotropic stress conditions. At the switch point, it is assumed that $\sigma_1 = \sigma_3$ without considering the influence of σ_2.

8.1.2 Successive veins as palaeostress indicators

Since the stress-state during the formation of the late burial, bedding-normal veins and the formation of the successive early tectonic, bedding-parallel quartz veins is known (Figure 6.3), their orientation and growth direction can be used as end-members in the stress-state reconstructions. The orientation data necessary to understand the stress-state reconstructions are first shortly summarised.

The regionally occurring bedding-normal veins are interpreted to be extension veins that formed in the extensional regime at the latest stages of the burial. If rotated to their original pre-folding orientation, they are more or less consistent in orientation across the whole High-Ardenne slate belt (Figure 8.2). The veins originally range from NE-SW in the SW and central part of the High-Ardenne slate belt (Bertrix, Bastogne, Mabompré, Boeur) to NNE-SSW in the peripheral part of the slate belt (Houffalize, Bütgenbach, Urftsee, Rursee). This structural change is probably related to a post-veining oroclinal bending of the slate belt during the main Variscan contraction because of the presence of a rigid basement in the north, *i.e.* the Brabant parautochthon (Fielitz 1992, Mansy *et al.* 1999). Notwithstanding this post-veining oroclinal bending, the regional stress state was consistent over a large area and the bedding-normal extension veins can be used as a regional palaeostress indicator for the stress state during the extensional regime at the time of vein formation. The orientation of the principal stress axes is derived from the distribution of extension veins that open parallel to σ_3 and align in the σ_1 - σ_2 plane. Veins are thus formed in a consistent anisotropic stress field, characterised by a vertical σ_1, corresponding to the overburden stress σ_v, and two well-defined horizontal principal stresses (σ_H and σ_h), reflecting a triaxial stress state during bedding-normal veining.

Bedding-normal veining is followed by bedding-parallel veining in the upper structural levels of the pHASB after the tectonic inversion. During inversion σ_3 changes towards vertical ($\sim\sigma_v$), whereas σ_H now corresponds to σ_1 reflecting regional shortening in the compressional regime (Figure 6.3). Similar to the bedding-normal veins, the extension bedding-parallel quartz veins are the brittle expression of the σ_1 - σ_2 plane (cf. Secor 1965), opening parallel to σ_3, and can be used as a palaeostress indicator. A difference between the three principal stress axes is present in the compressional regime, with bedding as an important anisotropy. Macro- and micro-structural analysis of the shear laminae in the microfabric of the bedding-parallel veins and NW-SE-trending slickensides on their vein walls are used to indicate that shortening occurred in an overall NW-SE compression at the onset of folding. Bedding-parallel veining is followed by the formation of NW-verging folds and a SE-dipping axial planar cleavage during Variscan fold-and-cleavage development in the North Eifel. In fact, similar to the North Eifel, the major part of the Rhenish Massif is characterised by a strong NW-directed vergence that reflects an overall NW-SE compression during the main phase of the Variscan contraction (Weber 1981).

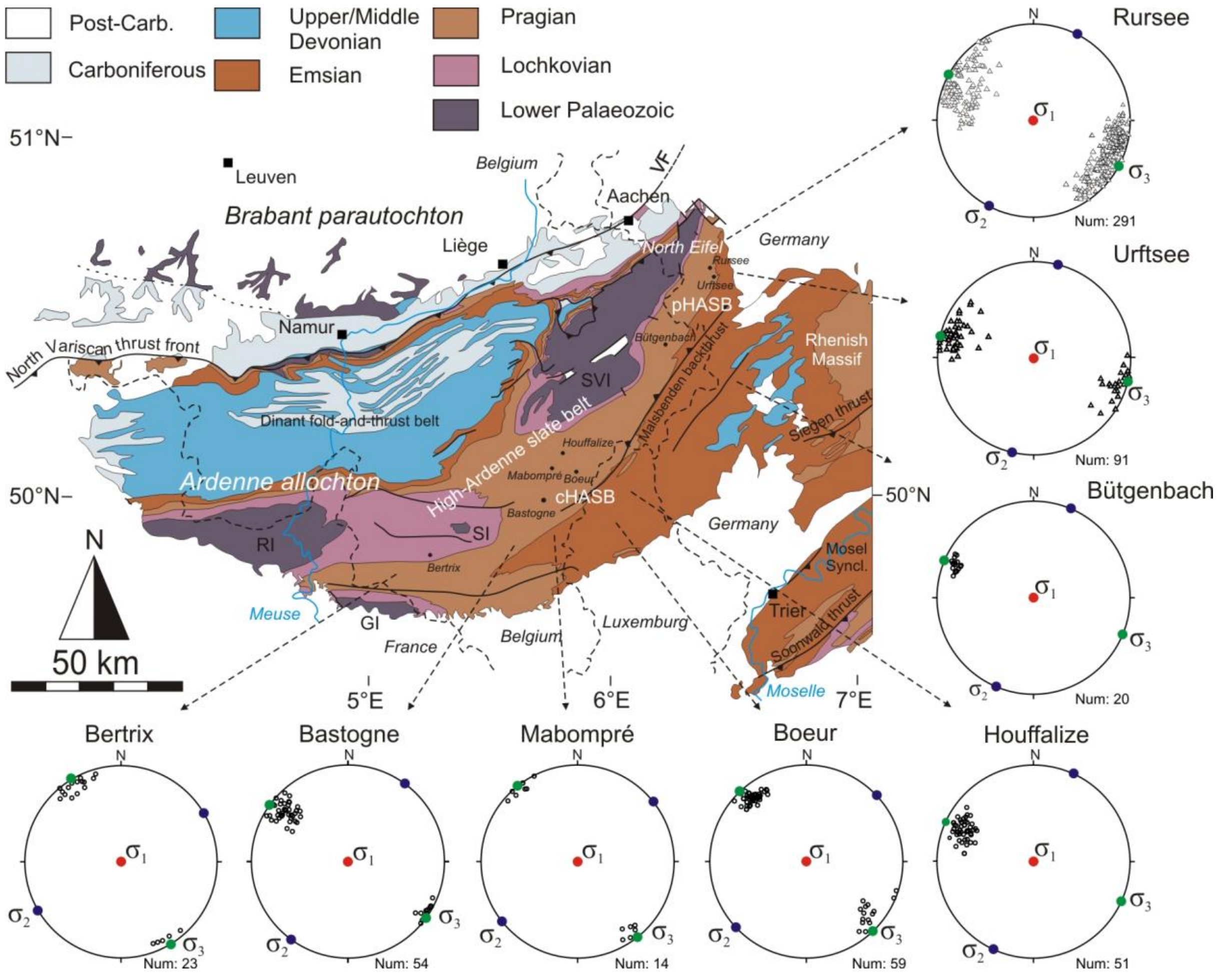

Figure 8.2: Structural map and palaeostress analysis of bedding-normal quartz veins in the High-Ardenne slate belt (Belgium, Germany). The lower-hemisphere, equal-area stereographic projection show the original orientation of the veins prior to folding and reflect a consistent extensional stress-field at the time of vein formation (modified after Van Noten *et al.* accepted).

8.2 Basic assumptions

Although the state of stress at the time of vein formation is well understood, to date the actual switch between two stress regimes has only been approached from a crust with isotropic stress conditions. From the consistent vein orientation in the extensional regime and the bedding anisotropy in the compressional regime, it is, however, already clear that mostly anisotropic stress conditions are present in the Earth's crust. To illustrate the complexity of 3D stress transitions in a triaxial stress state, three different scenarios (Figure 8.3) are constructed in which a basin with a certain predefined sedimentary geometry experiences a compressional tectonic inversion induced by a continuous increasing horizontal tectonic stress. In a first scenario (Figure 8.4) a tectonically relaxed basin, that is able to extend to all directions without any predefined horizontal principal stress component, is shortened. The second scenario starts from an extensional basin that has an NE-SW-directed sedimentary basin elongation and extends perpendicular to σ_3 (Figure 8.5). In the third scenario, an extensional basin with a NE-SW-directed extension and a NW-SE elongation is shortened (Figure 8.6).

In each scenario, the stress-state evolution in the basin is investigated by changing the orientation of the consistent tectonic stress component causing shortening from NW-SE to a NE-SW direction. The three different scenarios (Figure 8.3) are exemplified by means of 3D stress-state graphics, with the longest axis representing σ_1, the intermediate axis σ_2 and the shortest axis σ_3. The Mohr-Coulomb diagrams corresponding to each specific stress-state are illustrated next to the graphics during the stress-state evolution (see Figure 8.4, Figure 8.5 and Figure 8.6).

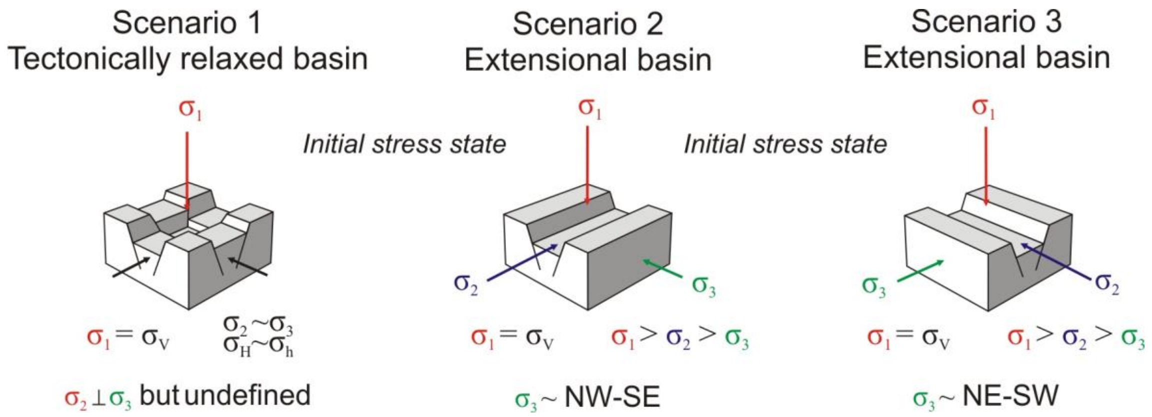

Figure 8.3: Simplified presentation of different basins as a starting point for the stress reconstructions. (**Scenario 1**) Tectonically relaxed basin extending to all directions. (**Scenario 2**) Extensional basin with a NE-SW extension. (**Scenario 3**) Extensional basin with a NE-SW extension, mirror image of scenario 2.

The starting point for constructing these three different scenarios is based on the following questions:

(i) How does a continuous increasing horizontal tectonic stress σ_T influence the orientation of extension veins?

(ii) Does the initial basin geometry influence the orientation of extension veins?

(iii) Do veins with a regionally consistent orientation only form in one specific stress regime, or can they occur in several different stress regimes?

(iv) What is the effect of the intermediate principal stress σ_2 during inversion?

In order to evaluate the different scenarios during tectonic inversion, the following constraints are assumed:

Constant σ_v during tectonic inversion

The 3D stress-state reconstructions are constructed in such way that σ_V is assumed to have a constant magnitude, corresponding to σ_1 in the extensional regime prior to tectonic inversion and σ_3 in the compressional regime after tectonic inversion. This constraint implies that the thickness of the overburden does not drastically change and no additional overburden is added to the basin during tectonic inversion. Also no erosion is assumed. This is a realistic assumption since it was demonstrated that the tectonic inversion takes place at the maximum burial, during the 20 Ma effective heating time (see Figure 5.7). Moreover, the assumption of a constant vertical principal stress is valid owing to the limited compressibility of rocks both at maximum burial and during initial tectonic compression (*i.e.* the timing of bedding-normal and bedding-parallel veining respectively). This constraint furthermore implies that the Poisson's ratio (ν) of the fractured sandstones; *i.e.* $\nu \sim 0.25$: a common value for sandstone, remains constant during inversion.

Horizontal σ_T

The tectonic inversion is induced by a horizontal tectonic principal stress component σ_T that is consistent in orientation during the onset of orogeny. It is assumed to be parallel to one of the two horizontal principal stresses, σ_H or σ_h, and increases in magnitude from extension to compression. If the tectonic stress component σ_T is parallel to the minimum, intermediate or maximum principal stress it is indicated as $\sigma_{3,T}$, $\sigma_{2,T}$ or $\sigma_{1,T}$ respectively (see Table 8.1). If the increasing horizontal σ_T is parallel to the maximum principal stress (σ_H), then the minimum principal stress (σ_h), will indirectly increase due to the compressibility of the host rock (Mandl 2000) but at a lower rate than the increasing σ_H. This assumption also implies that in the extensional regime a tectonic principal stress can already be present, although the basin is still in extension.

$\sigma_1 > \sigma_2 > \sigma_3$ and $\sigma_H > \sigma_h$

The basic assumption is that both veining events in the case study reflect 'Andersonian' stress regimes with one vertical principal stress σ_V and the other two principal stresses in the horizontal plane, parallel to the Earth's surface, and with the minimum horizontal stress σ_h being smaller than the maximum horizontal principal stress σ_H (Anderson 1951). In an Andersonian stress regime, the three principal stresses are defined as $\sigma_1 > \sigma_2 > \sigma_3$. This implies that if σ_3 increases because of the consistent tectonic stress component σ_T, that is oriented parallel to σ_3, $\sigma_{3,T}$ can become so large that it will pass σ_2 in such a way that $\sigma_{3,T}$ becomes $\sigma_{2,T}$ and σ_2 turns into σ_3. A similar transition can also occur between σ_2 and σ_1 if the tectonic principal stress σ_T influences σ_2. In the different Mohr-Coulomb diagrams that illustrate the different stress-states, this change between two principal stresses is illustrated by a *switch point*, in which the magnitude of both principal stresses is equal and both stress states coincide. Two different kinds of tectonic stress transitions can thus occur; one between σ_3 and σ_2 and one between σ_2 and σ_1. However it will be shown that apparently no switch can occur immediately between σ_3 and σ_1, unless equality is reached between all three principal stresses at a certain point in time at isotropic stress conditions (cf. Cosgrove 1995a).

Principal stresses

All stresses tend to be compressional in the Earth's crust and true tensile stresses are uncommon at larger depths (Cosgrove 1995a). In the different scenarios principal stresses are used to illustrate the stress changes during tectonic inversion. During the whole evolution of inversion, it is assumed that fracturing can take place continuously by reducing the effective stresses ($\sigma' = \sigma - P_f$) by a fluid pressure (P_f) that will overcome σ_3, which tends to be compressional. Differential stresses are thereby inferred to be low enough to allow extension fracturing. This constraint allows evaluating vein formation during each different stage.

Vein rotation

Although a slight reorientation of the original vein orientation has been observed from the SW (NE-SW; Bertrix) to the NE (NNE-SSW; Rursee) of the High-Ardenne slate belt (see Figure 8.2), the orientation of the veins is kept constant for simplicity of the constructed stress models. If veins form, they are assumed to be NE-SW. This simplified model allows predicting during which specific moments the NE-SW bedding-normal vein type can be formed during inversion.

8.3 Stress-state reconstructions

8.3.1 Scenario 1: Tectonically relaxed basin

In a first scenario, the stress-state reconstruction starts with a tectonically relaxed sedimentary basin in the extensional regime (Figure 8.4). The boundary conditions of a tectonically relaxed basin are such that the maximum principal stress corresponds to the vertical stress ($\sigma_1 \sim \sigma_v$) and that there is no distinction between the two horizontal principal stresses ($\sigma_2 = \sigma_3$ or $\sigma_H = \sigma_h$) (see Cosgrove 1997, 2001). This equality is illustrated by a switch point in the Mohr-Coulomb diagram with a stress magnitude substantially smaller than $\sigma_1 \sim \sigma_v$. In a tectonically relaxed basin, σ_V and σ_H are related by common constraints of the rock in such way that $\sigma_H = \sigma_V/(m-1)$ in which m is the reciprocal of the Poisson ratio ν (Price 1966). A tectonic stress component σ_T is assumed to be absent during subsidence in the tectonically relaxed basin (**stage 1**). If extension veining would occur due to elevated fluid pressures in stage 1, there would be a tendency to form vertical veins, but not in a certain direction. Theoretically, if the veins are close enough to interfere, polygonal vein arrays would develop at this specific stress state in which $\sigma_v > \sigma_H = \sigma_h$ at low differential stress smaller than 4T (Cosgrove 1995a, 1997).

As soon as a positive tectonic stress component σ_T starts to increase in the basin at the onset of orogeny (**stage 2**), σ_H and σ_h is defined as result of σ_T influencing one of the horizontal principal stresses. It depends on the NW-SE (1a in Figure 8.4) or NE-SW (1b in Figure 8.4) orientation of σ_T in which direction the maximum horizontal stress $\sigma_H \sim \sigma_{2,T}$ will develop. Concomitant with the increase of $\sigma_{2,T}$, $\sigma_3 \sim \sigma_h$ increases, but at a lower rate depending on the limited compressibility of the host rock. Eventually, the initial increase of σ_T results in a decrease of the differential stress $\sigma_1 - \sigma_3$, which is illustrated by a decreased diameter of the Mohr circle in stage 2 with respect to stage 1. Owing to the protracted compression and increasing σ_T, $\sigma_{2,T}$ will approach the magnitude of $\sigma_1 \sim \sigma_V$. When the σ_1 and σ_2 are subsequently equal in magnitude, a major tectonic inversion will occur during which $\sigma_{2,T}$ becomes $\sigma_{1,T} \sim \sigma_H$, while σ_1 turns into $\sigma_2 \sim \sigma_v$. The tectonic transition at this point implies a transition between two stress regimes, changing from an extensional regime into a ‘wrench’ tectonic regime, with σ_2 as the vertical principal stress. In the Mohr-Coulomb diagram, this major tectonic inversion between the two stress regimes is illustrated by a switch point between σ_2 and σ_1 at the magnitude of σ_v. At this switch point of inversion, the minimum principal stress σ_3 remains substantially smaller than the intermediate and maximum principal stress, so that a differential stress remains present during this first major inversion and no isotropic stress condition is reached.

Subsequently in **stage 3**, after this first major tectonic inversion, $\sigma_{1,T} \sim \sigma_H$ passes the magnitude of σ_v and keeps increasing with increasing σ_T. Similar to stage 2, $\sigma_3 \sim \sigma_h$ increases concomitant with $\sigma_{1,T} \sim \sigma_H$, but at a lower rate owing to the compressibility effect of the host rock, and approaches the magnitude of σ_2. As result of the compressibility effect, the differential stress ($\sigma_1 - \sigma_3$) increases again, as illustrated by an increase in magnitude of the Mohr circle in stage 3. This already shows that a differential stress state of zero is never reached during progressive compression but that a residual differential stress at a value substantially smaller than 4T remains present. A second major tectonic inversion occurs when eventually also $\sigma_3 \sim \sigma_h$ exceeds $\sigma_2 \sim \sigma_v$. This transition is illustrated as a switch point in which the intermediate and minimum principal stresses change in such way that σ_v becomes σ_3 and a σ_2 becomes σ_h.

This second switch point implies a tectonic inversion from a ‘wrench’ tectonic regime into a compressional tectonic regime, which occurs during increasing differential stress. Finally, in the compressional regime (**stage 4**), the differential stress increases as long as the tectonic stress component σ_T does not stagnate and $\sigma_{1,T}$ keeps increasing. Eventually, the tectonic inversion from extension to compression of a tectonically relaxed basin in scenario 1 results in a triaxial stress state with three well defined principal stresses.

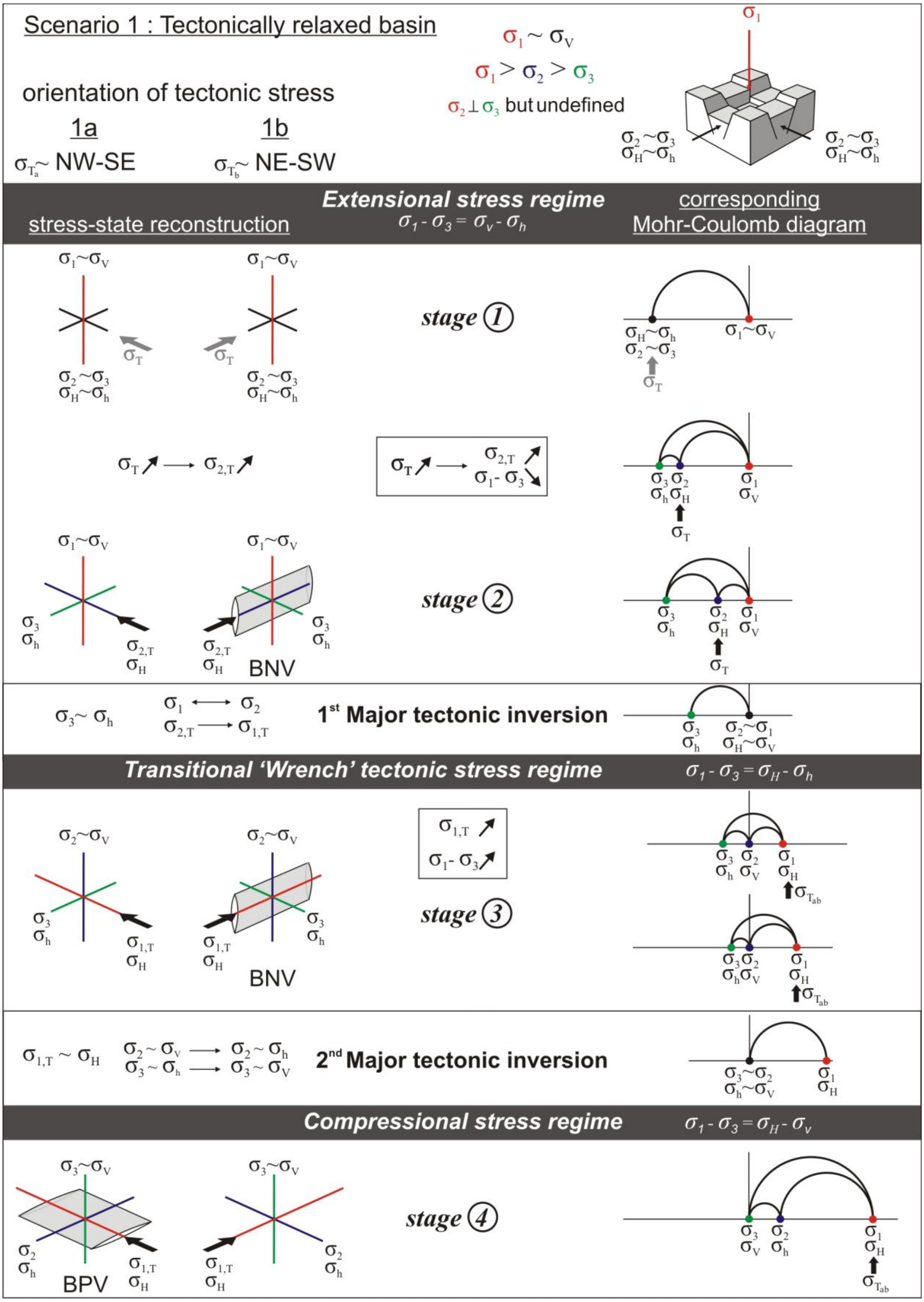

Figure 8.4: Scenario 1 illustrating the 3D stress-state changes and corresponding Mohr circles of a tectonically relaxed basin that is shortened by a consistent oriented tectonic stress at the onset of orogeny and during compressional tectonic inversion. See text for discussion. In the four stages σ_1-σ_3 < 4T. BNV: bedding-normal quartz veins. BPV: bedding-parallel quartz veins. The vertical line in the Mohr circles corresponds to σ_v.

8.3.2 Scenario 2: Extensional basin with predefined $\sigma_3 \sim$ NW-SE

In a second scenario, it is examined what the effect of an increasing tectonic stress component applied on an extensional basin with a predefined structural orientation owing to the preceding regional extension during sedimentary basin development. This scenario reflects a more general case in which the two horizontal stresses are different. The elongation of the basin is parallel to the intermediate principal stress σ_2 and the basin opens parallel to σ_3 in a NW-SE direction (Fig. 4b). The basin is shortened in two options in which the tectonic stress component σ_T varies from orthogonal (*i.e.* $\sigma_{Ta} \sim$ NW-SE; 2a in Figure 8.5) to parallel (*i.e.* $\sigma_{Tb} \sim$ NE-SW; 2b in Figure 8.5) to the predefined structural elongation of the basin. The initial stress state prior to inversion is displayed in the Mohr-Coulomb diagram, by a universal triaxial stress state with σ_1 corresponding to σ_v. The initial starting point is equal for the two options, however, as soon as the tectonic stress component σ_T starts to increase (**stage 1**), the resulting stress state will be different for both options. When σ_{Ta} increases in a NW-SE-directed contraction (**stage 2**, option 2a), $\sigma_{3,T} \sim \sigma_h$ and $\sigma_2 \sim \sigma_H$ will both increase, although with a different rate because of the compressibility effect of the host rock. Because of this different rate, $\sigma_{3,Ta} \sim \sigma_h$ will first approach σ_2 and will afterwards become equal in magnitude as $\sigma_2 \sim \sigma_H$. This equality is exemplified by a switch point in the Mohr-Coulomb diagram, in which $\sigma_{3,T}$ switches into $\sigma_{2,T}$ and σ_2 becomes $\sigma_3 \sim \sigma_h$. This minor horizontal switch has no influence on the overall extensional stress regimes because σ_1 remains vertical and σ_2 and σ_3 remain in the horizontal plane corresponding to the two different horizontal principal stresses. If an increasing σ_{Tb} in a NE-SW-direction is applied on the predefined basin (**stage 2**, option 2b), however, then the previously described minor tectonic switch between the minimum and intermediate principal stress will not occur between stage 1 and stage 2 because σ_{Tb} immediately influences the initial σ_2. In this option 2b, $\sigma_{2,T}$ subsequently approaches σ_1 in stage 2, at a faster rate than the increase of σ_3 so that a minor horizontal switch between both principal stresses can never occur in the horizontal plane. Despite the differences between options 2a and 2b in the extensional regime, eventually a major tectonic inversion occurs in both options (Figure 8.5). At the switch point, $\sigma_{2,T}$ equals σ_1 and during subsequent progressive compression they will mutually change into a stress state in which $\sigma_2 \sim \sigma_V$ and σ_1 becomes $\sigma_{1,T} \sim \sigma_H$. This specific stress state has also been recognised during the tectonic inversion of a tectonically relaxed basin (scenario 1) and corresponds to a ‘wrench’ tectonic stress regime. In both options 2a and 2b, a residual differential stress remains present during this first major tectonic inversion because of the difference between σ_1 and σ_3. Although the stress state at the inversion is illustrated in one specific Mohr-Coulomb diagram for both options (Figure 8.4), there could be a substantial difference in differential stress between both options, with a lower differential stress state when σ_{Ta} first starts to work on σ_3 (option 2a) than if σ_{Tb} works on σ_2 (option 2b).

(s**tage 3**) After the first major tectonic inversion, $\sigma_{1,T} \sim \sigma_H$ keeps increasing and because of the compressibility effect of the host rock in the horizontal plane, $\sigma_3 \sim \sigma_h$ approaches $\sigma_2 \sim \sigma_v$. This leads to a second major tectonic inversion of the ‘wrench’ tectonic regime into the compressional tectonic regime (**stage 4**) during which σ_3 eventually turns towards the vertical axis after the switch point and $\sigma_{1,T}$ and σ_2 are now both situated in the horizontal plane, such as expected in the compressional stress regime. However, because of the orientation of the initial tectonic stress component σ_{Ta} or σ_{Tb}, the eventual structural grain of the deformed basin is oriented differently in both options.

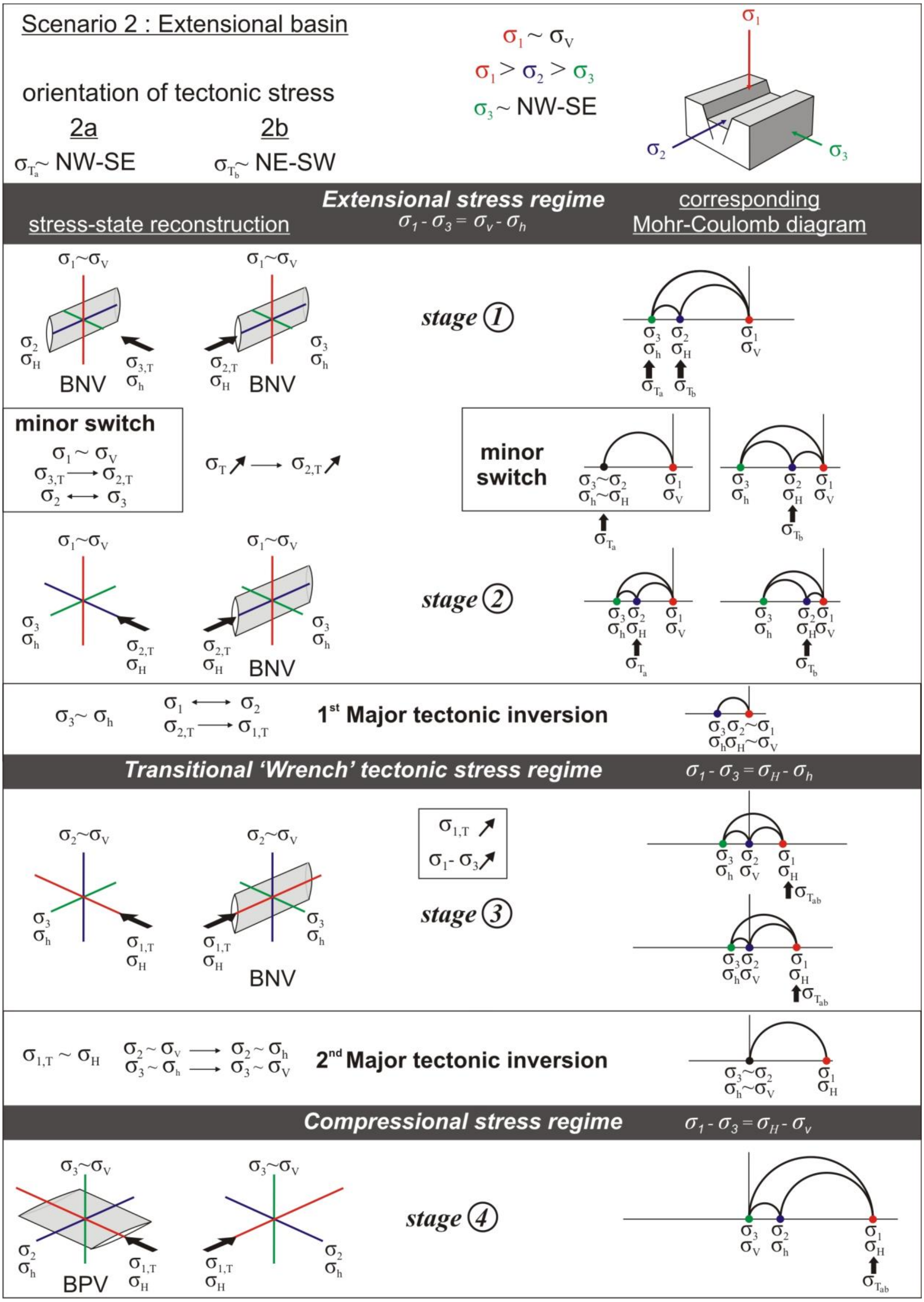

Figure 8.5: Scenario 2 illustrating the 3D stress-state changes and corresponding Mohr circles of an extensional basin with a predefined σ_3 oriented NW-SE that is shortened by a consistent oriented tectonic stress at the onset of orogeny and during compressional tectonic inversion. See text for discussion. In the four stages σ_1-σ_3 < 4T. BNV: bedding-normal quartz veins. BPV: bedding-parallel quartz veins. The vertical line in the Mohr circles corresponds to σ_V.

)

8.3.3 Scenario 3: Extensional basin with predefined σ_3 ~ NE-SW

The third scenario displays the effect of a stress component that is applied on an extensional basin with a predefined structural orientation in which the elongation of the basin (σ_2) is now oriented in a NW-SE direction and the basin opens parallel to σ_3 in a NE-SW-direction (Figure 8.6). Similar to the second scenario, two options are investigated in which a consistent positive tectonic stress component is applied on the predefined basin in a NW-SE-direction (σ_{Ta}; option 3a) and in a NE-SW-direction (σ_{Tb}; option 3b).

The initial starting point (**stage 1**) is again equal for the two options; with σ_1 corresponding to the vertical and two predefined horizontal intermediate and minimum principal stresses. When σ_T starts to increase, no minor tectonic switch will occur in option 3a if the applied tectonic stress $\sigma_{T,a}$ immediately works on $\sigma_{2,T}$ (**stage 2**) and subsequently approaches $\sigma_1 \sim \sigma_v$ at the end of stage 2 (option 3a in Figure 8.6). However, when a tectonic stress component $\sigma_{T,b}$ increases parallel to σ_3 (option 3b in Figure 8.6), a minor tectonic switch will occur because $\sigma_{3,T} \sim \sigma_h$ approaches $\sigma_2 \sim \sigma_H$ faster than σ_2 will approach $\sigma_1 \sim \sigma_v$. At the switch point of this minor tectonic inversion (Figure 8.6), $\sigma_{3,T}$ will change into $\sigma_{2,T}$, and σ_2 changes into $\sigma_3 \sim \sigma_h$ at constant $\sigma_1 \sim \sigma_v$. After this minor inversion in the horizontal plane, the differential stress further decreases because of increasing σ_{Ta} and σ_{Tb}, leading to the first major tectonic inversion at the end of stage 2.

Similar to scenario 2, $\sigma_{2,T}$ equals σ_1 at the switch point and during subsequent progressive compression they will mutually change at the point in which $\sigma_{2,T}$ turns towards the vertical σ_v and σ_1 becomes $\sigma_{1,T} \sim \sigma_H$. This stress state is indicative of a ‘wrench’ tectonic stress regime, in which extensional extensional fracturing can occur at low differential stress > 0.

With increasing differential stress in **stage 3**, σ_3 approaches $\sigma_2 \sim \sigma_V$, which leads to the second major tectonic inversion during which σ_3 switches towards the vertical σ_v, corresponding to the compressional regime (**stage 4**).

8.4 Fracturing and vein formation

The stress-state evolution of a shortened sedimentary basin during compressional tectonic inversion, which is demonstrated by means of three different scenarios, yield several possibilities during which the two successive quartz vein types in the North Eifel can be formed. Concerning the timing of bedding-normal veining, the different stages during which the NE-SW bedding-normal extension veins (BNVs) can be formed are illustrated by means of the veins drawn in the three corresponding figures. The bedding-parallel veins (BPV) are drawn in the compressional regime if they reflect the observed NW-SE shear.

Starting from a relaxed basin (scenario 1), the only possibility to form the observed NE-SW BNVs, is if a NE-SW σ_T decreases the differential stress during progressive compression until extensional fracturing is allowed (Figure 8.5; stage 2; option 1b). Veining can occur prior to the first major tectonic inversion in the extensional regime, as well as after the major tectonic inversion, in the transitional ‘wrench’ tectonic regime, owing to the fact that σ_3 remains constant during the first major inversion (stage 3; option 1b; Figure 8.4). Subsequently, bedding-parallel veins with pronounced NW-SE fabric can only be formed in the compressional regime during consistent NW-SE-directed compression (stage 4; option 1a; Figure 8.4).

In an extensional basin with predefined NW-SE-oriented σ_3 (scenario 2), bedding-normal veins can be formed in several phases during progressive compression. Initially in stage 1 of both options 2a and 2b (Figure 8.5), the NW-SE extension of the basin is the solely determining factor that NE-SW BNVs can be formed, under the circumstance that a NW-SE or NE-SW tectonic compression decreases the differential stress until extensional fracturing is allowed. After the predicted minor tectonic switch of σ_2 and σ_3 during progressive compression, the stress field is, however, misoriented to allow veining (stage 2; option 2a; Figure 8.5). In option 2b, no minor switch occurs because the tectonic stress component σ_{Tb} is oriented parallel to σ_2, resulting in a stress field that remains constant during stages 1 and 2.

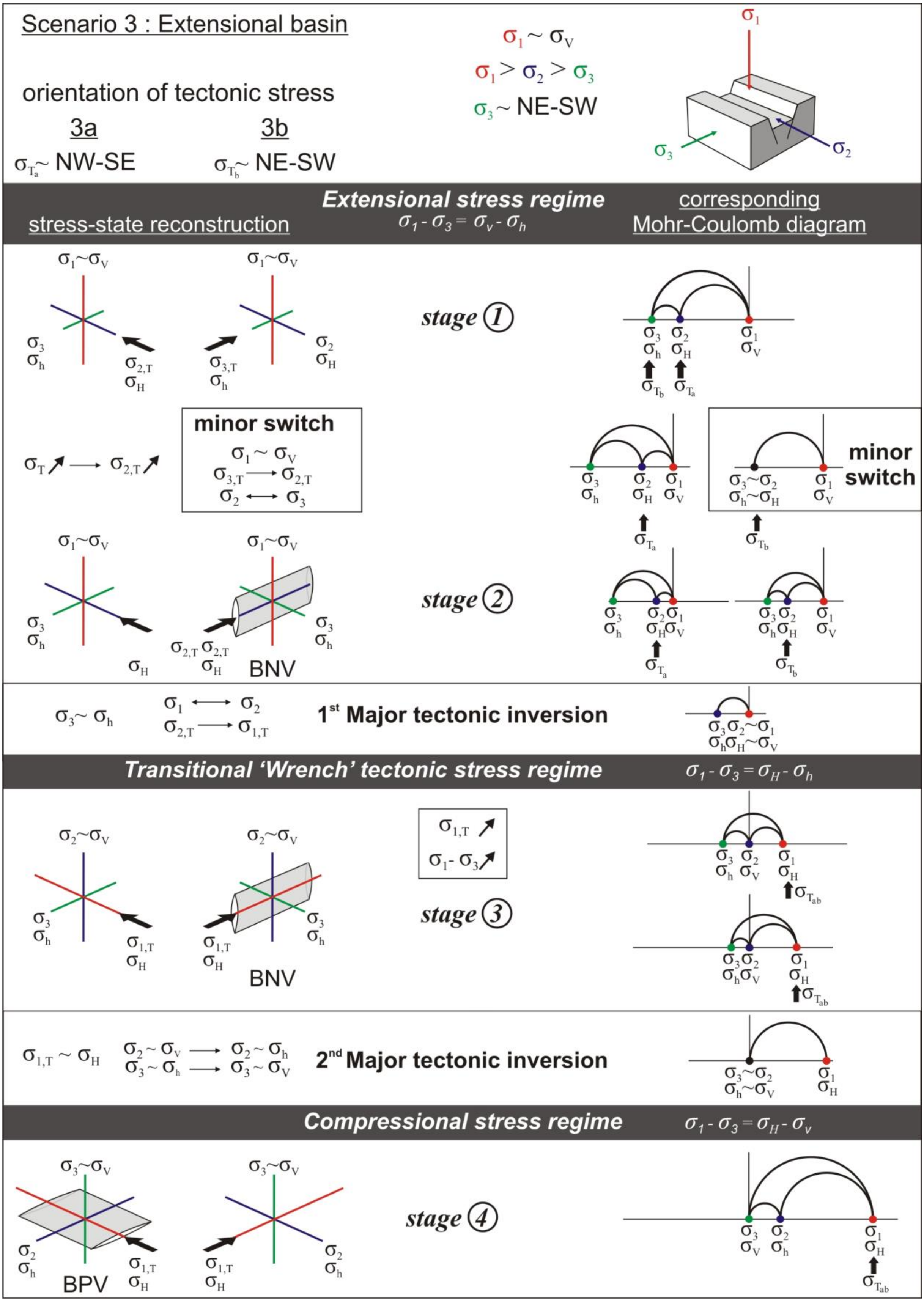

Figure 8.6: Scenario 3 illustrating the 3D stress-state changes and corresponding Mohr circles of an extensional basin with a predefined σ_3 oriented NE-SW that is shortened by a consistent oriented tectonic stress at the onset of orogeny and during compressional tectonic inversion. See text for discussion. In the four stages σ_1-σ_3 < 4T. BNV: bedding-normal quartz veins. BPV: bedding-parallel quartz veins. The vertical line in the Mohr circles corresponds to σ_v.

For similar reasons as in scenario 1, NE-SW veins can still be formed after the first major tectonic inversion in the transitional 'wrench' tectonic regime owing to the consistent σ_3 during inversion. Subsequently, the bedding-parallel veins are only formed in option 2a, reflecting NW-SE oriented compression.

Compression of a sedimentary basin in which the predefined σ_3 is NE-SW oriented (scenario 3), NE-SW veins can only be formed in stage 2, after the minor horizontal tectonic switch during NE-SW-directed contraction of σ_{Tb} (Figure 8.6). Similar to the other two scenarios, veins can be formed both prior as well as after the major tectonic inversion to a transitional 'wrench' tectonic regime. Similar to the other scenarios, the subsequent bedding-parallel veins with a NW-SE fabric are formed in the compressional regime after the second tectonic inversion, owing to a NW-SE-oriented σ_{Ta} (stage 4; option 3a; Figure 8.6).

All three different scenarios considered, only option 2a (Figure 8.5) complies with the observations in the High-Ardenne slate belt, demonstrating how the regional NE-SW BNVs first developed and local BPVs with a NW-SE oriented internal fabric are subsequently formed in the North Eifel. In this option, the model starts from an extensional basin that has a predefined structural NE-SW orientation, owing to the geodynamic context of the Ardenne-Eifel basin on the northern passive margin of the Rhenohercynian basin (Figure 2.2; Figure 8.2). This particular basin configuration is corroborated by the identification of major basin-bounding NE-SW normal fault systems indicated by stratigraphical mapping (see Lacquement 2001, Mansy *et al.* 1999). During extension of the basin, in which the load of the overburden corresponds to σ_1 in the basin, there is already a tectonic stress component in a NW-SE direction, parallel to σ_3, that causes an increase in the magnitude of σ_3 and consequently a decrease in differential stress, leading to regionally consistent NE-SW extensional fracturing. This model furthermore implies that no veins are formed after the minor tectonic switch and in the transitional 'wrench' tectonic regime because of misorientation of the stress regime. It is important to highlight the importance of this minor tectonic switch in the evolutionary history of the Ardenne-Eifel basin, in particular with respect to the ENE-WSW oriented cross-cutting veins V_C in the North Eifel (Figure 3.44d). At the moment of the minor tectonic switch σ_2 equals $\sigma_{3,T}$ (Figure 8.5), which allows fracturing and vein formation in no particular orientation. The fact that V_C can be correlated in the different case studies at the Rursee, however, implies that a particular stress-state was present at the time of V_C formation, during which the growth of these veins was influenced by the anisotropy of V_B. It is therefore likely that the ENE-WSW stress-state corresponding to the formation of V_C occurs just before the tectonic minor switch and that a minor tectonic inversion does not necessary represent one specific point in time, but rather a period in time during which there are no large differences between σ_2 and $\sigma_{3,T}$. The suggestion from the macrostructural geometric analysis (see Chapter 3) that σ_2 equals σ_3 at a certain stage and that they switched locally to form the cross-cutting generation, is demonstrated by this stress-state reconstruction and can fully be attributed to the increasing tectonic stress σ_T after the formation of V_B.

The proper configuration in option 2a, allows developing a stress-state reconstruction by means of several Mohr-Coulomb diagrams that illustrate successive fracturing and vein formation during the compressional tectonic inversion. It is defined by microthermometry that maximum fluid overpressures of *c.* 190 MPa and *c.* 205 MPa are reached during bedding-normal and bedding-parallel extension veining respectively. The magnitude of the constant burial-related σ_v that corresponds to the load of the overburden at a depth of ~7 km ± 0.1 km, reflects a lithostatic pressure of *c.* 185 MPa, which is kept constant in the Mohr circle reconstructions (Figure 8.7). During bedding-normal veining, the value of σ_h relates to σ_v in such way that:

$$\sigma_h = \sigma_v \left(\nu\,(1-\nu)^{-1}\right) + \sigma_T \qquad (8.1)$$

(Cosgrove 1995a, Cox *et al.* 2001)

with a common Poisson ratio of $\nu \sim 0.25$ for sandstone (Mandl 2000).

In a tectonically relaxed basin, in which $\sigma_T = 0$, this equation corresponds to $\sigma_h \sim 62$ MPa. However, it is defined that the basin had a predefined geometry with extension oriented NW-SE, parallel to $\sigma_3 \sim \sigma_h$, indicating that the magnitude of $\sigma_3 \sim \sigma_h$ of the basin in extension must thus have been below $\sigma_h \sim 62$ MPa.

In such a configuration, the differential stress $\sigma_1 - \sigma_3$ that corresponds to $\sigma_v - \sigma_h$, is ~123 MPa (Figure 8.7a). This value is too large to allow the formation of extension fractures developing at $\sigma_1 - \sigma_3 < 4T \sim 40$ MPa with $T \sim 10$ MPa (see section 6.2). Therefore, σ_T, acting on $\sigma_{3,T}$ (option 2a; stage 1; Figure 8.5) must at least increase up to 83 MPa in order to decrease the differential stress until the stress configuration of $\sigma_1 - \sigma_{3,T} < 40$ MPa is fulfilled (Figure 8.7b). At this stage, a P_f of *c.*190 MPa is able to overcome the tensile strength of rock, allowing the formation of bedding-normal veins against the action of total pressure. This is illustrated by the fluid pressure that pushes the Mohr into the tensile domain (Figure 8.7b). Note that the stress-state evolution from Figure 8.7a to Figure 8.7b is a static reconstruction, whereas in reality this is a dynamic process in which σ_T increases together with P_f.

Subsequently, after the minor switch of $\sigma_{3,T}$ into $\sigma_{2,T}$, the first major tectonic inversion occurs (Figure 8.7c). At this point, a residual differential stress remains present, at an estimated value of approximately $\sigma_1 - \sigma_3 \sim T$. After this stage, differential stress increases again in the transitional ‘wrench’ tectonic regime until the second tectonic inversion takes place at a differential stress above T but below a substantial value of 4T (Figure 8.7d). After the reorientation of the principal stresses in the compressional regime, fracturing and vein formation takes place at a value of $\sigma_1 - \sigma_3 < \sim 30$ MPa for extensional failure (Figure 8.7e) and slightly increases to $\sigma_1 - \sigma_3 < \sim 43$ MPa during subsequent extensional-shear failure (Figure 8.7f). Extensional failure takes thus place at lower differential stress in the compressional regime than compared to the extensional regime because of the lower tensile strength owing to the bedding anisotropy ($T < 10$ MPa) during compression. Because of $\sigma_1 - \sigma_3 = \sigma_H - \sigma_v$ and of equation 8.1, modified for σ_H, σ_T is allowed to rise up to values of σ_T ~155 MPa during extensional failure and σ_T ~167 MPa during extensional-shear failure in the compressional regime.

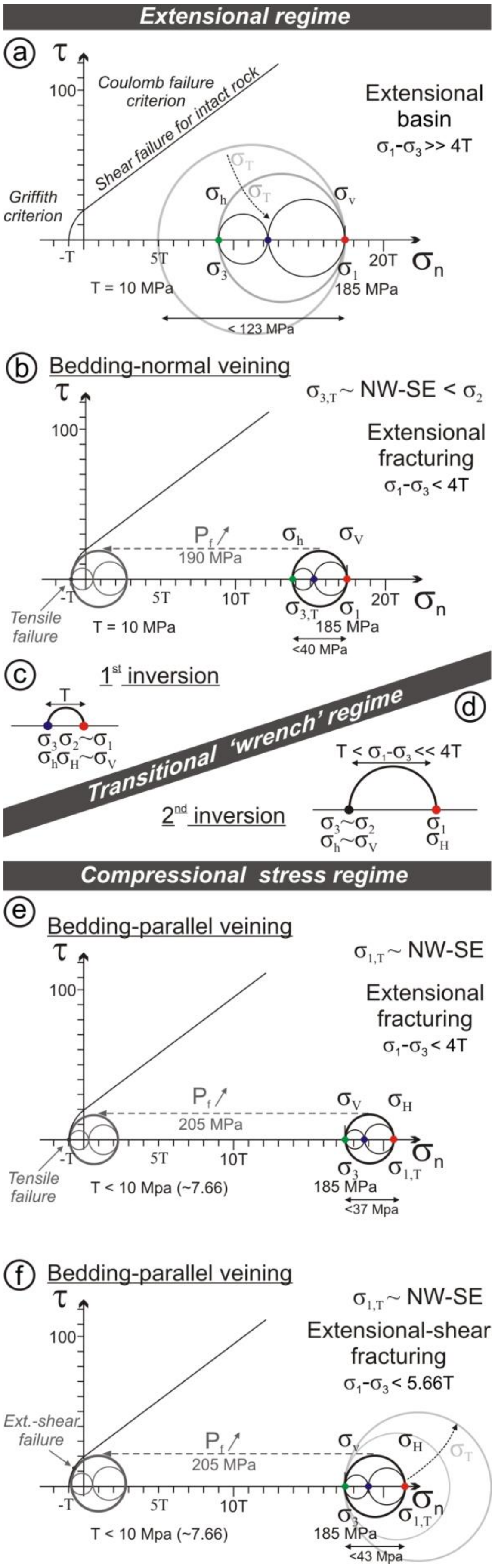

Figure 8.7 (right)**:** Stress-state Mohr circle reconstruction of the upper structural levels of the Ardenne-Eifel basin (North Eifel) during formation of successive vein types. Stages **(a)** to **(f)** reflect the different stages of failure. See text for discussion and Table 8.1 for abbreviations.

At this stage, the (supra-)lithostatic fluid pressure of P_f at *c.* 205 MPa overcomes the tensile strength of the rock and allows the shift of the Mohr circle to the tensile domain, allowing failure when the Mohr circle hits the failure envelope. Furthermore, note that in a Mohr-Coulomb diagram, supra-lithostatic failure is not illustrated as the Mohr circle cannot pass the Griffith criterion. Subsequently, σ_T increases during further contraction in the compressional regime (grey circle in Figure 8.7f). A further Mohr circle reconstruction is prohibited as subsequently folds and cleavage developed, defining a plastic deformation which cannot be illustrated in a brittle failure diagram.

8.5 General implications

Apart from the regional implications of vein formation, the different stress state reconstruction presented in the three scenarios imply that if a basin is subjected to a tectonic compression, always two or three tectonic switches are necessary to explain the complex 3D tectonic inversion from an extensional regime to a compressional regime. It solely depends on the orientation of σ_T with respect to σ_3 of the extensional sedimentary basin, whether or not a minor horizontal tectonic switch between σ_2 and σ_3 occurs prior to the first major tectonic inversion. Furthermore no matter what orientation of the basin geometry or the orientation of tectonic shortening is, a **transitional 'wrench' tectonic regime** should always occur between extension and compression in a shortened basin that is affected by a tectonic inversion at low differential stress induced by the orientation of an increasing tectonic stress component. Although one should expect strike-slip in such a stress configuration (Anderson 1951), brittle features exemplifying this intermediate stage has to date never been observed, or they are not preserved in a shortened basin that has been subjected to a compressional tectonic inversion. This is possibly due to (very) low differential stresses that remain present during inversion, or due to the anisotropy of tectonic features such as veins that formed in a previous phase. In the High-Ardenne slate belt, it is unlikely that the original NE-SW veins are reactivated in the 'wrench' tectonic regime because of the NE-SW misorientation of the veins with respect to the expected NW-SE strike-slip.

Despite the fact that Sibson (1998, 2004) already mentioned that the 'wrench' tectonic regime has an intermediate value bounded by the compressional and extensional regime criteria (*i.e.* at the zero differential stress line in Figure 8.1), the presence of a transitional 'wrench' tectonic regime between the extensional and compressional regime has to date not been visualised in a brittle failure mode plot. However, the stress-state reconstruction in this work emphasises that, depending on the value of the intermediate principal stress, a whole range of possibilities are present during tectonic inversion. Therefore, one should take into account both the presence of an intermediate 'wrench' tectonic regime and the 3D complexity of a tectonic switch in the construction of the brittle failure mode plots. Tectonic inversions between stress regimes should not be considered as a single switch point, but should be subdivided in a double tectonic switch with a short-lived intermediate 'wrench' tectonic regime.

Importantly, the stress-state reconstructions also show that there is a need for a strict definition of an isotropic stress state. It is proposed that one should define a stress state of $\sigma_H = \sigma_h = \sigma_v$ as isotropic and not a stress state in which all stresses are in a small range of each other, *i.e.* $\sigma_H \sim \sigma_h \sim \sigma_v$, in which $\sigma_1 - \sigma_3 << 4T$ and $P_f >> \sigma_3$ or even $P_f > \sigma_3$. This allows defining both major tectonic inversions and the transitional 'wrench' tectonic regime during a tectonic inversion.

With respect to the time-scale during which tectonic inversion may take place, there is evidence that the speed of such transition in stress regime may occur relatively fast and that it may not be possible to generate the structures related to the 'wrench' tectonic regime. For example, transition from active extension to active contraction has been determined to occur within 1 Ma (*e.g.* Schneider *et al.* 1996). Knowing these time constraints for the Ardenne-Eifel basin would help considering if structures related to the short-lived 'wrench' tectonic regime could be found. However, the degree of overpressuring is affected by the speed of the transition between stress regimes (Sibson 1995). The presence of regional intrastratum overpressured compartments at lithostatic values in the Ardenne-Eifel basin already indicates that overpressuring took place during at least several Ma (but definitely less than the 20 Ma effective heating time) reflecting a relative slow tectonic inversion of the Ardenne-Eifel basin compared to recent settings.

8.6 Conclusions

Although brittle failure mode plots are very useful to visualise the fluid pressure and stress-state evolution during tectonic inversion, they oversimplify the true anisotropic stress conditions in the upper crust that are present during the tectonic inversion of a sedimentary basin at low differential stress. The bedding-normal and bedding-parallel quartz veins, formed during an extensional and compressional regime respectively and materialise the early Variscan tectonic inversion affecting the Ardenne-Eifel basin. Their geometries clearly demonstrate the stress state in the basin. Using these vein types as end-members, a 3D stress-state reconstruction of a compressional tectonic inversion has been carried out in order to determine the stress-field orientation during compressional tectonic inversion. These reconstructions are developed by applying a consistent tectonic stress component to a basin with a predefined structural geometry orientation. By changing both the initial sedimentary basin geometry and the direction of the tectonic compression, several scenarios are developed.

The results show that only one specific scenario can explain the vein occurrences observed in the North Eifel. In the proper model, the occurrence of the NE-SW bedding-normal extension veins can only be explained by a NW-SE directed tectonic stress component σ_T, oriented parallel to the opening direction (σ_3) of the extensional Ardenne-Eifel basin, reducing the differential stress substantially in order to allow the formation of extension veins. Bedding-parallel veins with a NW-SE internal fabric, can subsequently only be formed under the same NE-SW-directed compression. Although bedding-normal veins still developed in a basin that was affected by extension, it is clear that the initial increasing tectonic stress has affected the basin and that the bedding-normal veins are considered to be the first manifestations of the Variscan tectonic compression (cf. Van Noten *et al.* 2007, accepted).

More generally, these stress-state reconstructions predict that if an increasing positive tectonic stress component starts to compress a sedimentary basin at constant vertical principal stress (= overburden pressure), always two or three tectonic stress switches are necessary to explain the inversion from extension to compression, depending on the orientation of σ_T with respect to the extension direction of the basin. If σ_T is oriented parallel to σ_3, a first minor stress switch occurs in the horizontal plane between σ_3 and σ_2. This minor switch is, however, absent if a tectonic stress component increases in a tectonically relaxed basin or if it increases parallel to the elongation of the basin (*i.e.* σ_2). During further progressive compression, however, no matter what orientation of basin geometry, or the direction of the tectonic stress component, in all the different scenarios an intermediate transitional ‘wrench’ tectonic stress regime is predicted between the extensional and compressional regime. To date no evidence has been found in particular brittle features that could reflect this transitional stage in a shortened basin that has been subjected to a tectonic inversion at low differential stresses. Eventually, these reconstructions illustrate that if a basin experiences a tectonic inversion under triaxial, anisotropic stress conditions, stress transitions are more complex than classically represented. Ideally, the predicted intermediate ‘wrench’ tectonic regime should be implemented in brittle failure mode plots, either in a third dimension or in separate brittle failure mode plots that illustrate the differences of σ_1 and σ_3 with σ_2.

CHAPTER 9 Conclusions & perspectives

9.1 Incipient shortening of a sedimentary basin

The Lower Devonian rapid syn-rift infill of the passive margin of the developing Rhenohercynian Ocean resulted in kilometre-thick siliciclastic deposits in the Ardenne-Eifel basin, which are currently exposed as multilayer sequences in the High-Ardenne slate belt (Belgium, France, Luxemburg and Germany). These multilayers are dominated by incompetent pelite and siltstone intercalated with competent psammite, sandstone and quartzites, reflecting the deltaic, shallow marine depositional infill of the Ardenne-Eifel basin. Sediments diachronously young from Lochkovian in the southwestern central part of the High-Ardenne slate belt to Pragian in the northeastern peripheral part of the High-Ardenne slate belt, reflecting the deepest (~10 km of sediments) and a more shallow part (~7 km of sediments) of the Ardenne-Eifel basin, respectively. The competent units are regionally characterised by the occurrence of bedding-normal quartz veins that reflect incipient shortening of the Ardenne-Eifel basin at the onset of Variscan orogeny. In the cHASB (Belgium and Germany), the competent-incompetent interface of the units commonly shows a cuspate-lobate geometry, defined as mullions, reflecting a ductile deformation of the middle crust at the onset of shortening (cf. Kenis 2004). In the pHASB (North Eifel, Germany), however, shortening is expressed differently as indicated by bedding-parallel quartz veins reflecting brittle deformation of a strong upper crust. In order to characterise this brittle behaviour in the upper crust and to investigate how slate belts develop differently in mid- to upper crustal levels, a detailed combined structural and microthermometric analysis of fluid inclusions has been performed on these successive quartz vein occurrences that occur in numerous outcrops around the Rursee and Urftsee water reservoirs in the North Eifel (Germany).

Planar to lensoid bedding-normal quartz veins, mostly restricted to competent fine- to medium-grained sandstones, *i.e.* stratabound veins, are the first structural features that characterise the sequences. Also continuous non-stratabound veins sometimes occur, refracting at the layer boundary of the competent unit with the adjacent incompetent siltstone in a similar way to cleavage. Bedding-normal veins are determined to reflect vein formation prior to the regional fold-and-cleavage development. This is exemplified by veins that remain at high angle to bedding around fold hinges and by clear vein deformation in the fold limbs. Stratabound veins are often curved in the sandstone in a direction in agreement with flexural-flow folding within competent units. The non-stratabound veins are displaced at the competent-incompetent interface reflecting bedding-parallel displacement attributed to flexural-slip folding. Millimetre, hairline veins cross-cut the siliciclastic grains and demonstrate that fracturing and vein formation occurred in a host rock in which the porosity was already significantly reduced due to burial compaction and cementation. Moreover, the limited compressibility of the competent host rock allows determining that bedding-normal veins formed during the latest stages of the burial.

The majority of the mainly mono-mineral quartz veins are centimetre-thick veins in which quartz has grown epitaxially on the host-rock grains. Vein infill is mainly characterised by a fibrous and elongate-blocky fabric that formed by ataxial and syntaxial growth mechanisms. Fibrous crystals and crack-seal host-rock inclusion bands indicate that vein formation occurred by repetitive fracturing and sealing phases in which competition between precipitation rate and fracture rate dominated the crystal habit. Some veins have grown to composite veins during numerous fracturing and sealing phases reflecting episodical vein growth during which thin host-rock inclusion lines were incorporated in the veins and formed new surfaces on which crystals have nucleated and further grown. Furthermore, the specific alignment of pseudosecondary fluid-inclusion planes, oriented at high angle to the elongation of the quartz crystals, proves that bedding-normal veins developed as extension veins at low differential stress and repeatedly fractured by incremental Mode I cracks. The specific orientation of fluid-inclusion planes has been particularly useful as microstructural marker to reconstruct the stress state in the basin at the time of vein formation in the extensional regime. They show that veins open in incremental steps perpendicular to the minimum principal stress σ_3, which roughly defines the extension of the Ardenne-Eifel basin, and propagate in the plane of the maximum principal stress σ_1 and the intermediate principal stress σ_2. This further defines the stress state present in the extensional regime in which the magnitude of σ_1 is determined by the load of the overburden σ_v, and σ_2 indicates the elongation of the basin. In this configuration, maximum and minimum horizontal stresses were still smaller that the vertical stress. Subsequent healed microcracks, observed as secondary fluid-inclusion planes oriented parallel to the vein wall, still developed after vein growth. They show that fracturing continued after vein formation in a similar stress regime as during the formation of pseudosecondary fluid inclusions. This specific elongate-blocky and fibrous crystal habit, whether or not incorporated with crack-seal host-rock inclusion bands, evidences the presence of overpressured fluids that are responsible to overcome the rock strength at low differential stress (Cosgrove 1995a). Microthermometry of pseudosecondary and secondary inclusions, both reflecting the stress state in the basin, confirms this hypothesis and shows that fluid pressure is able to increase to near-lithostatic values, corresponding to maximum burial conditions. In this configuration the fluid pressure exceeded the magnitude of the minimum principal stress in order to allow fracturing, *i.e.* $P_f > \sigma_3$. Microthermometry and Raman analysis of pseudosecondary and secondary inclusions furthermore imply that the bedding-normal veins dominantly precipitated from an aqueous H_2O-NaCl fluid with a low salinity. Also gases such as CO_2 and CH_4 might have been present within these fluids, however, they are rarely observed within the fluid inclusions.

Two dominant bedding-normal vein generations are observed. A third and oldest bedding-normal generation V_A occurs only locally. The first dominant generation V_B, can be correlated with the intermullion bedding-normal veins in the cHASB. Based on a regional palaeostress analysis, it is concluded that extension in the basin was predominantly NW-SE, as demonstrated by the original orientation of the veins prior to folding in both the cHASB and pHASB. The slight rotation of the veins in the North Eifel to NNE-SSW is attributed to post-veining orogenic bending of the veins during subsequent Variscan contraction. It is furthermore established that in thin sedimentary sequences, the spacing of the veins correlate to the thickness of the host-rock layer. This is a regional phenomenon and is attributed to the saturation of initial veins that occur during initial fracturing. Veins that cross-cut the regional bedding-normal veins occur only locally in the North Eifel. These cross-cutting veins V_c exemplify a specific stress state in the extensional regime during which σ_2 and σ_3 are nearly the same, causing the formation of cross-cutting extension veins.

It is established that the onset of Variscan shortening in the North Eifel is exemplified by the presence of bedding-parallel quartz veins that cross-cut, truncate and offset the bedding-normal veins. They are defined to be the first brittle structures that formed in the compressional stress regime prior to the fold-and-cleavage development. In this respect, the transition of bedding-normal veins into bedding-parallel veins reflects the early Variscan compressional tectonic inversion, taking place in the early Carboniferous prior to the main Variscan contraction.

With exception of intrabedded veins in sandstones, the relative position of bedding-parallel veins with respect to the surrounding host rock has no influence on the bedding-parallel fracturing mechanism. Either laminated veins developed that reflect bedding-normal uplift combined with bedding-parallel shear, or composite veins in which shear deformation is reflected in the microstructures of small-scale quartz laminae. Both laminated and composite veins show an alternation of quartz laminae with host-rock inclusion seams and, fractured, host-rock fragments. On the one hand, vein growth and vein thickening in the laminated veins is dominated by a specific fabric, in which the spacing of inclusion bands in crack-seal quartz laminae track dilation of the veins, either oriented normal or oblique to the vein wall. In the composite veins, on the other hand, quartz laminae with a mainly blocky fabric demonstrate how opening and thickening of the veins is dominated by crystal growth in an open fracture. A (supra-)lithostatic fluid pressure is the only mechanism that is able to keep such bedding-parallel fractures open, acting against the overburden pressure. This mechanism and the (supra-)lithostatic fluid pressure is inferred by microthermometry of pseudosecondary fluid inclusions that occur at high angle to the crystal elongation in the crack-seal laminae and subparallel to the vein wall in the blocky laminae. Microthermometry and Raman analysis of pseudosecondary inclusions indicate that the bedding-parallel veins precipitated from a similar aqueous H_2O-NaCl fluid with a low salinity as the bedding-normal veins. Gases such as CO_2 and N_2 might have been present, however, they are rarely observed within the fluid inclusions. The specific orientation of pseudosecondary inclusions and micro-structural observations such as crack-seal host-rock inclusion bands are indicative of the stress state in the basin in the compressional regime after tectonic inversion. It is demonstrated that σ_1 corresponds to the maximum horizontal tectonic principal stress σ_T and that σ_3 corresponds to the load of the overburden and thus to σ_v.

The blocky laminae in the laminated and composite bedding-parallel veins are intercalated with thin shear laminae in which quartz grains are recrystallised dynamically, mostly exemplified by bulging of the crystal walls. The rather undeformed blocky laminae indicate that recrystallisation is restricted to the shear laminae in which originally cataclased crystals deformed at higher differential stress during the main phase of the Variscan contraction. Because of this combination of extensional and shear-related features, bedding-parallel veins are defined to be extension and extensional-shear veins that developed at (supra-)lithostatic fluid pressures at low differential stress during a complex, multiphased development. Bedding-parallel veining thus resulted from a cyclic process in which vein growth predominantly occurs at supra-lithostatic fluid pressures and shear occurs after a sudden fluid-pressure decrease and subsequent recovery. These fluid pressure drops are accompanied by transient stress transitions in which σ_1 reoriented towards the vertical, allowing the formation of bedding-parallel stylolites.

9.2 Lithostatic overpressures and the Variscan orogeny

In this work it has been demonstrated how incipient shortening affects a sedimentary basin that is subjected to orogenic contraction. Owing to the occurrence of high fluid pressures at the moment of bedding-normal veining, the Lower Devonian Ardenne-Eifel basin is considered as an exposed 340 million-year-old reservoir (Hilgers *et al.* 2006a, Kenis & Sintubin 2007). One of the objectives of this research was to estimate the dimension of this naturally fractured, overpressured basin. The presence of overpressures in the central part of the High-Ardenne slate belt has been demonstrated by several studies (Kenis *et al.* 2002a, 2005a, Kenis 2004, Urai *et al.* 2001) in which is shown that that bedding-normal veining, related to these overpressures, occurred regionally. In this work it is further demonstrated that the bedding-normal veins can be correlated to the North Eifel in which veining is still a result of overpressuring, taking place at near-lithostatic fluid pressures. This indicates that the dimensions of such an overpressured reservoir can be correlated laterally over an area of more than 100 km. Not only the lateral extent of this overpressured reservoir is important, also the vertical compartmentalisation can be estimated. Near-lithostatic overpressuring took place at the time of bedding-normal veining in a sequence of at least 3 km thick, from mid-crustal conditions at ~10 km in the central part of the High-Ardenne slate belt, to upper crustal conditions at ~7 km in the peripheral part of the High-Ardenne slate belt. These near-lithostatic overpressures were present in intrastratum compartments in the competent units and incompetent units surrounding these compartments formed the perfect seal allowing pore-fluid pressures to rise until fracturing.

Furthermore, this research has also established an estimation of the timing during which overpressuring took place. Although bedding-normal veins formed in a basin that was still in extension, bedding-normal veins are considered to be the first manifestations of the Variscan orogeny. By means of several stress-state reconstructions, it is demonstrated that an initial increasing tectonic stress σ_T at the onset of the Variscan orogeny, parallel to σ_3, can be invoked as the driving mechanism to decrease the differential stress at the latest stages of the burial and to generate overpressures which are necessary to form vertical extension veins. The initial tectonic stress may be considered as the driving force for the stagnating extension at the end of the extensional regime. After the compressional tectonic inversion, bedding-parallel veins formed because the presence of (supra-)lithostatic pore-fluid fluids allowed bedding-normal uplift. The tectonic stress, now considered to be parallel to σ_1 in the basin, causes shear-related vein formation at high fluid pressures prior to the main contraction of the Variscan orogeny. The fact that both bedding-normal and bedding-parallel veins are related to lithostatic overpressuring supports the assumption that this magnitude of overpressuring took place during the whole tectonic inversion.

With respect to seismogenesis, bedding-parallel vein formation in the compressional regime can be related to the earthquake cycle in which rupturing occurs both in the seismic periods during bedding-normal uplift and in the interseismic periods immediately after the fluid pressure drop during shear-related lateral movements. Absence of movements correlate to subsequent recovery of fluid pressure until overpressuring re-occurs and the cycle restarts.

With respect to the processes active in the crust, high fluid pressures are predicted at the base of the seismogenic crust and play a role in seismogenesis (*e.g.* Miller *et al.* 2004, Terekawa *et al.* 2010). This seismicity is often expressed by slow-slip events (*e.g.* low frequency earthquakes). The added value of this work to this research question is limited: the two vein types that formed by hydrofracturing at lithostatic fluid pressures, may materialise structures which have to be looked for in high fluid-pressure fields during low slip-events at the base of the seismogenic crust.

To conclude, the naturally fractured Ardenne-Eifel basin at the onset of Variscan orogeny can serve as an analogue to the present upper crust by its extent of lithostatic overpressuring, but more importantly by showing that a tectonic inversion from extension to compression is the crucial timing during which lithostatic overpressures can be sustained.

9.3 Importance of tectonic inversions

In the High-Ardenne slate belt quartz veining occurred extensively and regionally during incipient shortening of the Lower Devonian sequences and is related to overpressuring, before and after the compressional tectonic inversion. In contrast to these two important veining phases at the onset of orogeny, quartz veining seems to have occurred rather occasionally during the main compressional stage of the Variscan orogeny. In the North Eifel syntectonic veining is restricted to local deformation features that are related to folding, *e.g.* local boudinage and flexural slip veins, and to local fluid release accompanying faulting. Also in the central part of the High-Ardenne slate belt and in the Lower Palaeozoic inliers (*e.g.* Van Baelen & Sintubin 2008), syntectonic quartz veining related to the Variscan fold-and-cleavage development seems rather limited. However, in the latest stages of the Variscan orogeny, extensive veining seems to resume (Van Baelen 2010). It has been proven by several microthermometric analyses that temperature conditions during the positive tectonic inversion (*e.g.* Kenis *et al.* 2005a, Schroyen & Muchez 2000, Van Noten *et al.* 2011), the main Variscan contraction (Fielitz & Mansy 1999) and during the Variscan destabilisation after negative tectonic inversion (Van Baelen 2010) remained constant. This implies that no significant subsidence or uplift of the shortened Ardenne-Eifel basin occurred during the Variscan orogeny and that the magnitude of the vertical principal stress remained constant during both positive and negative Variscan tectonic inversion.

The late Variscan, negative (extensional) tectonic inversion is evidenced locally in the cHASB (Bertrix, Herbeumont) by discordant quartz veins that cross-cut the south-dipping Variscan cleavage and that underwent a shape modification during progressive shearing reflecting the late Variscan destabilisation of the Variscan Orogen (Van Baelen 2010). These subvertical veins have been demonstrated to initiate as extension veins at conditions of low differential stress and have subsequently been deformed, either as a vein or as an open cavity due to increasing differential stress related to further extension within an extensional regime. These parental cracks are very interesting because they occur over the entire Belgian part of the Eifel depression, showing that this extensional destabilisation is regional and corresponds to the negative tectonic inversion (Van Baelen 2010). The presence of high fluid pressures could not be demonstrated conclusively but the rare fibrous infill of these extension veins suggests that opening occurred at a fluid pressure exceeding the minimum principal stress.

The results of this work and that of Van Baelen (2010), clearly demonstrate that these tectonic inversions turn out to be key moments in the deformation cycles during which a considerable permeability enhancement occurs that is related to major changes in the overall stress regime. During compressional tectonic inversion, (near-lithostatic) overpressures will be generated in the extensional regime and are able to rise to supra-lithostatic after the tectonic switch in the compressional regime in which they are maximum sustainable at low differential stress (Sibson 1998, 2000, 2004). This evolution is reflected by the bedding-normal and bedding-parallel veins in the pHASB and furthermore shows that high fluid-pressures are easier to maintain during the compressional tectonic inversion at the onset of orogeny than during the subsequent main contractional deformation stage of orogeny. The reverse path occurs at a negative inversion. At the end of the compressional regime, elevated fluid pressures are again developed at low differential stress, which cannot be sustained in the subsequent extensional regime after inversion, giving rise to a release of fluids, as exemplified by the extension veins in the cHASB. Both studies highlight the importance of tectonic inversions and corroborates with the importance of the interaction between fluid flow, fluid pressure changes and changes in the tectonic stress field.

Finally, as a zero differential stress state is not necessarily expected during inversion, the 3D complexity of a tectonic inversion contributes to this permeability enhancement. It is demonstrated by means of different stress-state reconstructions that, apart from the tectonic stress σ_T, also the intermediate principal stress σ_2 plays an important role in anisotropic stress conditions. In a compressional inversion, but probably also in a negative inversion, a transitional 'wrench' tectonic regime is always predicted, in which σ_2 is defined to correspond to the overburden stress. Also in this transient configuration the permeability will basically increase in the σ_1-σ_2 plane, corresponding to the same permeability in the extensional regime. Eventually the application of these 3D stress transitions under triaxial stress conditions may have a wide range of implications with respect to the evolution of dynamic permeability during orogenic shortening.

9.4 Perspectives

Well-studied areas such as the frontal part of the central European Variscides (*i.e.* the northern front of the Rhenohercynian fold-and-thrust belt; Belgium, Germany) and several Central African orogenic belts (more specifically the Kibara orogenic belt and the Copperbelt; DRC, Rwanda, Uganda, Zambia) are important areas for the study of fluid flow and mineralisation and are studied intensely in several research projects of the *Geodynamics and Geofluids Research Group* at the Katholieke Universiteit Leuven. Historical and mineralogical studies have been carried out concerning the structural reconstruction of these orogenic belts and large-scale fluid migration as a source for economically interesting ore deposits (*e.g.* Muchez *et al.* 2010). In these studies the general relationship between regional tectonics, large-scale fluid flow and mineralisation has been investigated. Despite this great interest in tectonics and fluid flow, the interaction between changes in stress regimes, fluid pressure and fluid migration has to date not been investigated in detail. However, Sibson (2004) and Cox (2010) theoretically demonstrated that this interaction is important for the genesis of ore deposits. Since this study and the study by Van Baelen (2010) demonstrated that fluid permeability is enhanced during tectonic inversion, irrespective of the kind of inversion, and that supra-lithostatic fluid overpressures will be sustained in the compressional regime, further research could focus on these tectonic inversion periods, as they might be of great importance for the genesis of ore deposits.

The tectonic inversion models (both 2D and 3D) predict that overpressures form during changes in stress regimes. These models are, however, barely consistent with geological structures. Although the barren successive bedding-normal and bedding-parallel quartz veins in the pHASB have been very suitable to develop and refine these models, it would be interesting for further research to test these inversion models for different settings in other parts of the world, primarily because the extent to which fluid redistribution occurs during the intimate relationship between stress changes and fluid pressures at low differential stress is unknown. Further research could be performed in different steps. Firstly, a validation and verification of the theoretically derived complexity of 3D stress-state changes during tectonic inversion could be made by a numerical modelling approach. Secondly, based on the results of the numerical models, the structural-controlled tectonic inversion model could be applied in other geodynamic settings, with special focus on economic mineral deposits.

The Fault Analysis Group (FAG) at the University College Dublin (UCD) has in the recent years demonstrated that Discrete Element Method (DEM) codes (Cundall & Hart 1992), and in particular PFC2D and PFC3D (‘Particular Flow Code’; Itasca Consulting Group Inc.) are very promising methods for reproducing the formation of joints in multilayers and the growth of faults in 2D and 3D (*e.g.* Imber *et al.* 2004, 2006, Schöpfer *et al.* in press). The DEM approach employed in these studies would be suitable for the generation of a 3D numerical model for predicting the brittle structures associated with tectonic inversion. Firstly, fracture formation could be investigated in three different discontinue numerical models, each reflecting the different predicted stress states during inversion (*i.e.* the extensional regime, transitional wrench regime and compressional regime) (Van Noten *et al.* accepted) under appropriate boundary conditions and within heterogeneous multilayers with different strength distributions. The fracture patterns generated in these models can be validated in the ‘simple’ case of compressional tectonic inversion, as manifested in the Ardenne-Eifel region and demonstrated in this work. The output of this modelling would permit investigation of the impact of changing rock mechanical properties (tensile strength, Young’s modulus, Poisson’s ratio, etc.) on the orientation of fractures during the 3D stress-state changes arising from inversion. Such an investigation is important as these rock parameters define the magnitude of the horizontal and vertical principal stress (Mandl 2000), but also define the maximum overpressures that can be sustained during inversion (Sibson 2004). In a second phase, numerical models could be constructed for more ‘complex’ cases by implementing an additional anisotropy, such as a cleavage pattern, that will be reactivated during extensional tectonic inversion to form, as represented by discordant veins in the High-Ardenne slate belt (Van Baelen 2010).

Furthermore, based on the results of the numerical modelling and the gained expertise build during the investigation of the successive vein types in this work, the inversion model could be tested during field-based studies of other vein systems. In search of such vein systems, one has to seek for analogues of the structures predicted in the numerical models. Investigations that report multiple cross-cutting types of (mineralised) veins which provide a basis for palaeostress analysis and highlight changes in stress regimes, or those that document the presence of high to lithostatic pore-fluid pressures within veins, can serve as potentially interesting field areas to test and refine the tectonic inversion model. Not only vein systems in low-grade metamorphic areas are promising, but also vein types that reflect short stress transitions, *e.g.* above the emplacement of pluton bodies (*e.g.* Manning & Bird 1991).

Apart from the search for new potential study areas, well-studied areas within the ore deposit research at the *Geodynamics and Geofluids Research Group* at the Katholieke Universiteit Leuven, could provide useful constraints for the integration and refinement of the kinematic inversion model. One of these petrographical and geochemical well-studied areas are the stratiform Cu-Co deposits in the Neoproterozoic Katanga Supergroup at Nkana in the Zambian part of the Copperbelt (Brems *et al.* 2009, Muchez *et al.* 2010). Here, high-grade deposits resulted from multiple mineralisation and remobilisation phases in several vein generations, *i.e.* bedding-parallel veins, cross-cutting veins, and late tectonic, massive veins. A (micro)structural study of vein-filling minerals in these bedding-parallel veins will provide constraints on their coupled fluid-pressure and stress-state evolution, and the extent to which they comply with the criteria for compressional tectonic inversion that are determined in this work. The opening direction of bedding-parallel veins, whether they are opened by shear or by uplift induced by high fluid pressures, is an essential feature for the validation of the inversion model. One should specifically focus on the infillings of the other veins, which permit definition of the opening directions inferred from fibrous or elongated crystals, the orientation of fluid-inclusion planes or mineral growth features in the vein. Furthermore, as the cross-cutting and massive veins are late tectonic features, it can be verified if they are related to the extensional tectonic inversion (Brems *et al.* 2009).

A similar approach can be performed for the tin- and tungsten vein-type mineral deposits in bedding-parallel and cross-cutting hydrothermal quartz veins in the Central African Palaeo-Mesoproterozoic Kibara orogenic belt (Rwanda). De Clercq *et al.* (2008) and Dewaele *et al.* (2010) recently studied the origin and evolution of the Sn-W-mineralising fluids during ore emplacement in different successive vein types. If the relationship between structural features (*e.g.* cleavage, folds, faults, lineations, etc.) and the veins is studied both in the field and the laboratory, also these vein types are very promising to test the inversion model.

Ultimately, such a combined research can establish the importance of the redistribution of (mineralising) fluids during tectonic inversion by means of combined numerical modelling-, field- and (micro)structural research. The main goal would be the development of an inversion model irrespective of any field area, that has been calibrated by numerical modelling and which can be used for different settings in other parts of the world. Such a general model, in which the 3D aspects of a theoretical inversion model are fine-tuned, would eventually indicate to which extent fluid redistribution during inversion actually controls the formation of ore bodies.

APPENDIX A Urftsee structural data

The data below are the result of a mapping exercise in 2008. Goal of this mapping was to check consistency of the different vein generations that have been studied in the Rursee study area. A detailed structural field map, the geometric analysis of bedding, cleavage and bedding-cleavage intersection lineation illustrated in lower-hemisphere, equal-area stereographic projection are presented. All the data are summarised in a table. The selected outcrop, of which the geometry and the veins have been discussed in section 3.5.1, is situated in zone 7. The outcrops are situated between the *Vogelsang Sattel* in the SE and *Vogelsang Mulde* in the NW, *i.e.* a local culmination and depression corresponding to a larger scale (first order) anticline and syncline respectively (see Figure 2.3).

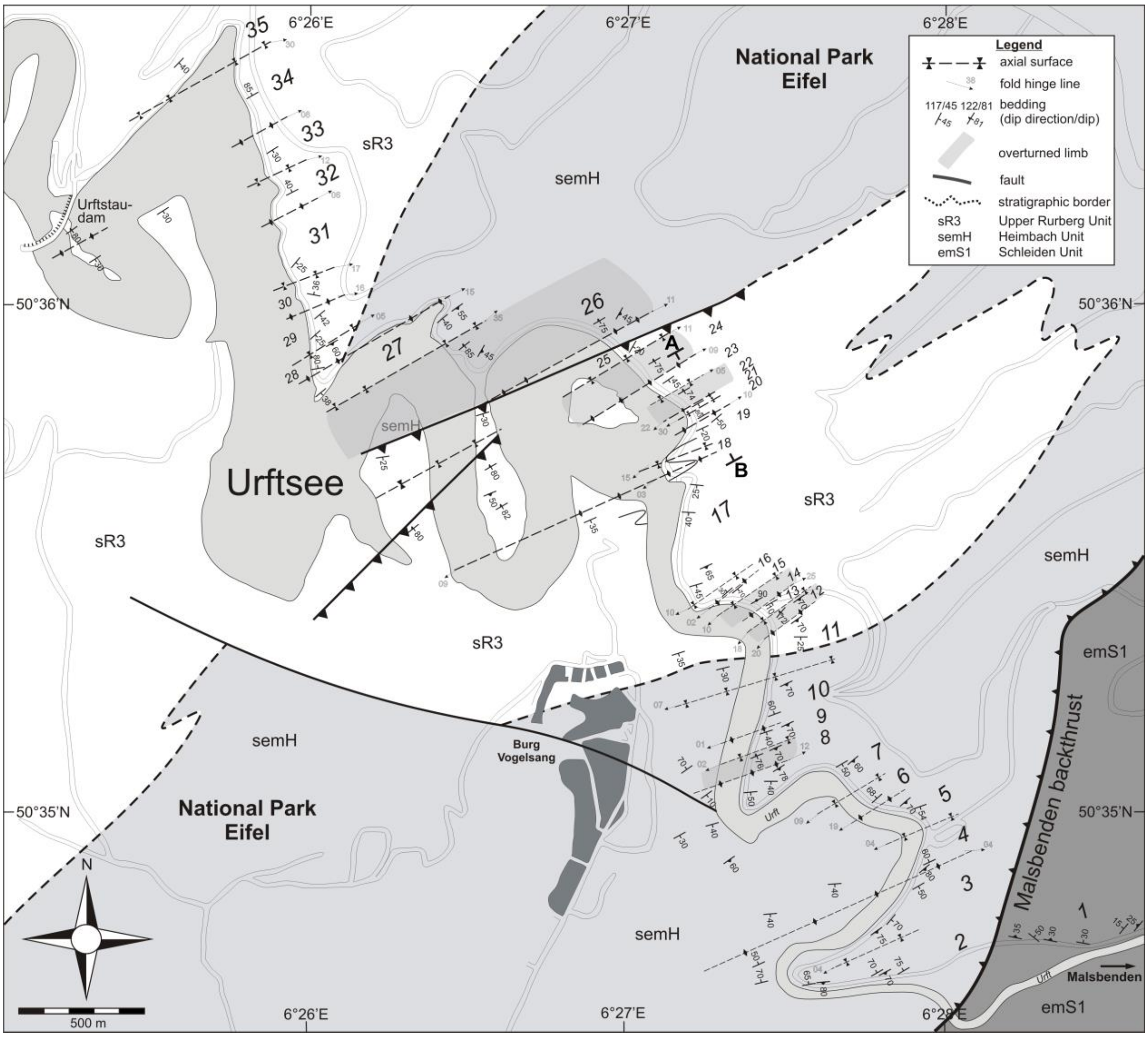

Figure A1: Structural map of the outcrops along the Urft river from Malsbenden in the SE to the Urftsee dam in the NW. The outcrops in the SE are situated on a higher stratigraphic and structural level. The stratigraphic separation between the Upper Rurberg, Heimbach and Schleiden Units are adapted from Ribbert (1994). See table A1 for the specific field data of zone 1 to zone 35.

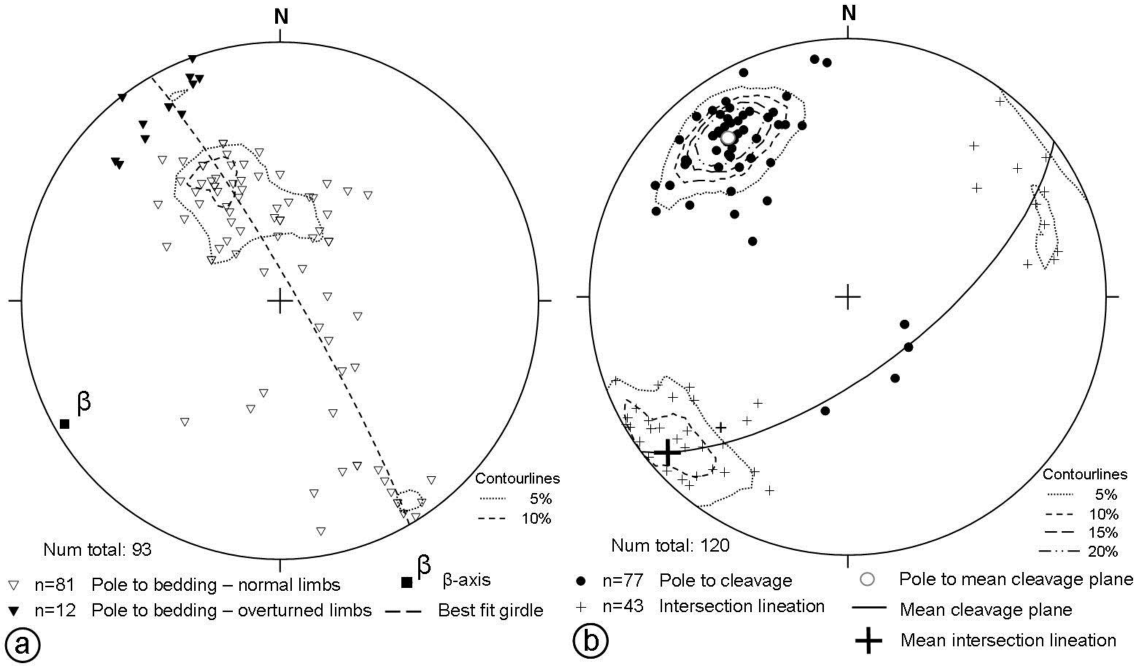

Figure A2: Lower-hemisphere, equal-area stereographic projection of measured structures at Malsbenden - Urftsee cross-section. **(a)** poles to bedding; **(b)** bedding-cleavage intersection lineation and poles to cleavage.

The overall structural architecture of the area north of the Malsbenden backthrust (see Figure A1) is very consistent but differs from the structural architecture of the Rursee area. This area displays first order, asymmetric upright hectometre-scale folds with open interlimb angles and with a NW-verging asymmetry. The overturned folds have rounded to angular fold hinges. Contrary to the Rursee structural architecture, overturned fold limbs, and thus overturned folds barely occur. The stereographic analysis of bedding (Figure A2) shows that the folds are cylindrical. Only one separate cluster, representative of normal fold limbs with a normal structural polarity (S_0~323/53), can be recognised. The cleavage (S_1~143/71), axial planar to the upright folds, dips more steeply than cleavage in the Rursee area (S_1~166/55), corroborating with the upright fold style in the Urftsee area versus the overturned fold style in the Rursee area. These differences in fold style between both areas might be attributed to tilting of the Malsbenden backthrust affecting the Urftsee area.

South of the Urftsee area, the Malsbenden backthrust occurs; a red coloured metre-wide disruptive fault zone west of the little town Malsbenden. In this zone (see zone 1 in Table A1), a north-dipping cleavage in strongly south-verging folds is apparent. Veins have not been studied in this area. Knapp (1980) reports that this 500 m wide zone, in which these south-verging folds occur, characterises the footwall of the backthrust. This south-vergence is not recognised further to the south.

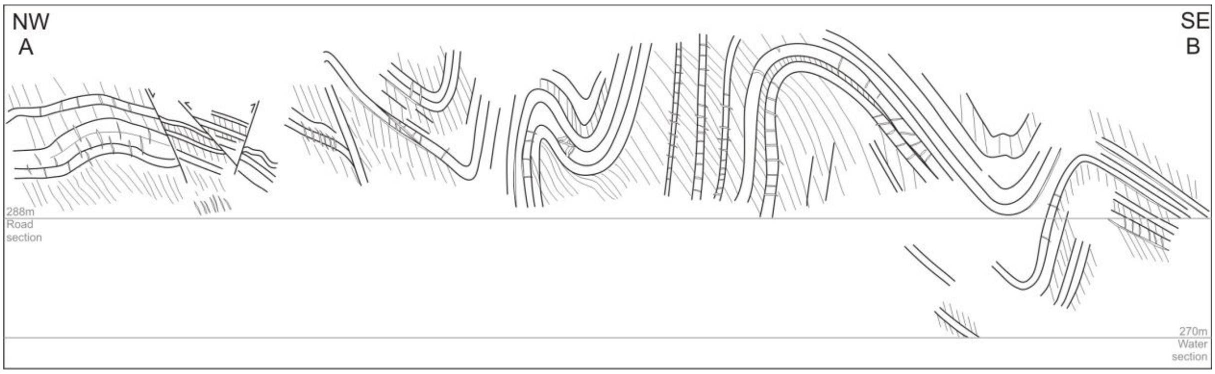

Figure A3: Cross-section A-B (see Figure A1 for location) showing the characteristic upright fold style of the Urftsee area. Bedding-normal veins remain at high angle to bedding around the folds. Cross-section approximately 500 m wide.

Table A1: Bedding and cleavage data of the investigated zones at the Malsbenden and Urftsee outcrops. See Urftsee structural map for localisation of the fold limbs (zone 1 to 35). The number of measurements is given in brackets. Grey zones represent the data specific for an overturned limb. - : not observed or suspicious data.

Outcrop	**Bedding (S_0)**	**β - axis of bedding**	**Cleavage (S_1)**	**S_0/S_1 L_i (measured)**	**S_0/S_1 L_i (merged)**
*Zone **1** : Above MB thrust*	001/23 (4)	321/18	321/23 (6)	226/13 (1)	341/21 (10)
*Zone **2***	332/72 (6)	050/31	150/68 (10)	246/11 (3)	062/12 (16)
*Zone **3***	155/52 (2)	-	140/65 (2)	227/15 (1)	210/36 (4)
*Zone **4***	335/60 (1)	-	160/65 (2)	053/19 (1)	062/04 (2)
*Zone **5***	158/44 (7)	160/44	150/68 (5)	231/34 (2)	235/12 (13)
*Zone **6***	150/42 (1)	-	140/70 (1)	038/05 (1)	225/13 (2)
Zone 7	Best fit girdle:				
Fold train with mullions	042/68 (31)	222/22	138/68 (19)	224/18 (9)	218/24 (50)
*Zone **8***	155/74 (2)	-	153/72 (2)	224/20 (1)	-
*Zone **9***	162/38 (2)	-	163/70 (1)	242/08 (1)	242/08 (3)
*Zone **10***	340/60 (1)	-	155/70 (1)	064/20 (1)	067/05 (2)
*Zone **11***	150/25 (1)	-	146/70 (1)	235/02 (1)	235/02 (2)
*Zone **12***	130/72 (1)	-	144/70 (1)	219/38 (1)	219/18 (2)
*Zone **13***	*SE-dipping*	-	-	-	-
*Zone **14***	154/90 (3)	-	147/67 (3)	238/10 (2)	064/16 (6)
*Zone **15***	150/10 (1)	-	140/70 (1)	239/02 (1)	239/02 (2)
*Zone **16***	319/30 (1)	-	142/69 (1)	231/01 (1)	231/01 (2)
*Zone **17***	164/37 (16)	-	148/65 (1)	230/15 (1)	233/15 (17)
*Zone **18***	325/85 (1)	-	148/65 (1)	221/07 (3)	235/05 (2)
*Zone **19***	146/52 (6)	-	138/67 (3)	230/15 (1)	219/21 (9)
*Zone **20***	325/80 (2)	-	146/65 (1)	240/30 (1)	235/02 (3)
*Zone **21***	*NW-dipping*	-	-	230/20 (1)	-
*Zone **22***	150/75 (1)	-	142/70 (1)	222/20 (1)	081/53 (2)
*Zone **23***	136/29 (3)	068/12	135/70 (2)	-	225/01 (5)
*Zone **17-23***	Best fit girdle:		Mean value:	Mean value:	Mean value:
Fold train	052/78 (29)	232/12	142/67 (9)	229/16 (8)	228/14 (38)
*Zone **24***	150/75 (1)	-	120/60 (2)	-	068/23 (3)
*Zone **25***	120/20 (1)	-	120/65 (1)	-	-
*Zone **26***	151/79 (3)	-	129/48 (3)	061/27 (2)	067/27 (6)
*Zone **27***	140/38 (3)	-	145/60 (2)	078/18 (1)	057/05 (5)
*Zone **28***	340/80 (2)	-	150/60 (1)	245/20 (1)	068/13 (3)
*Zone **29***	138/25 (1)	-	126/45 (1)	-	053/02 (2)
*Zone **30***	015/36 (1)	-	150/60 (2)	080/20 (1)	072/21 (3)
*Zone **31***	130/25 (3)	-	142/65 (2)	220/05 (1)	057/09 (5)
*Zone **32***	335/40 (1)	-	160/60 (1)	040/25 (1)	248/03 (2)
*Zone **33***	*SE-dipping*	-	-	-	-
*Zone **34***	330/85 (2)	-	140/55 (2)	-	058/12 (4)
*Zone **35***	115/40 (1)	-	140/60 (1)	080/30 (1)	070/31 (2)
*Zone **2 - 35***	Best fit girdle:		Mean value:	Mean value:	Mean value:
Urftsee fold train	058/81 (93)	238/09	143/71 (77)	229/15 (43)	233/09 (189)

APPENDIX B Sample list & water level Rursee

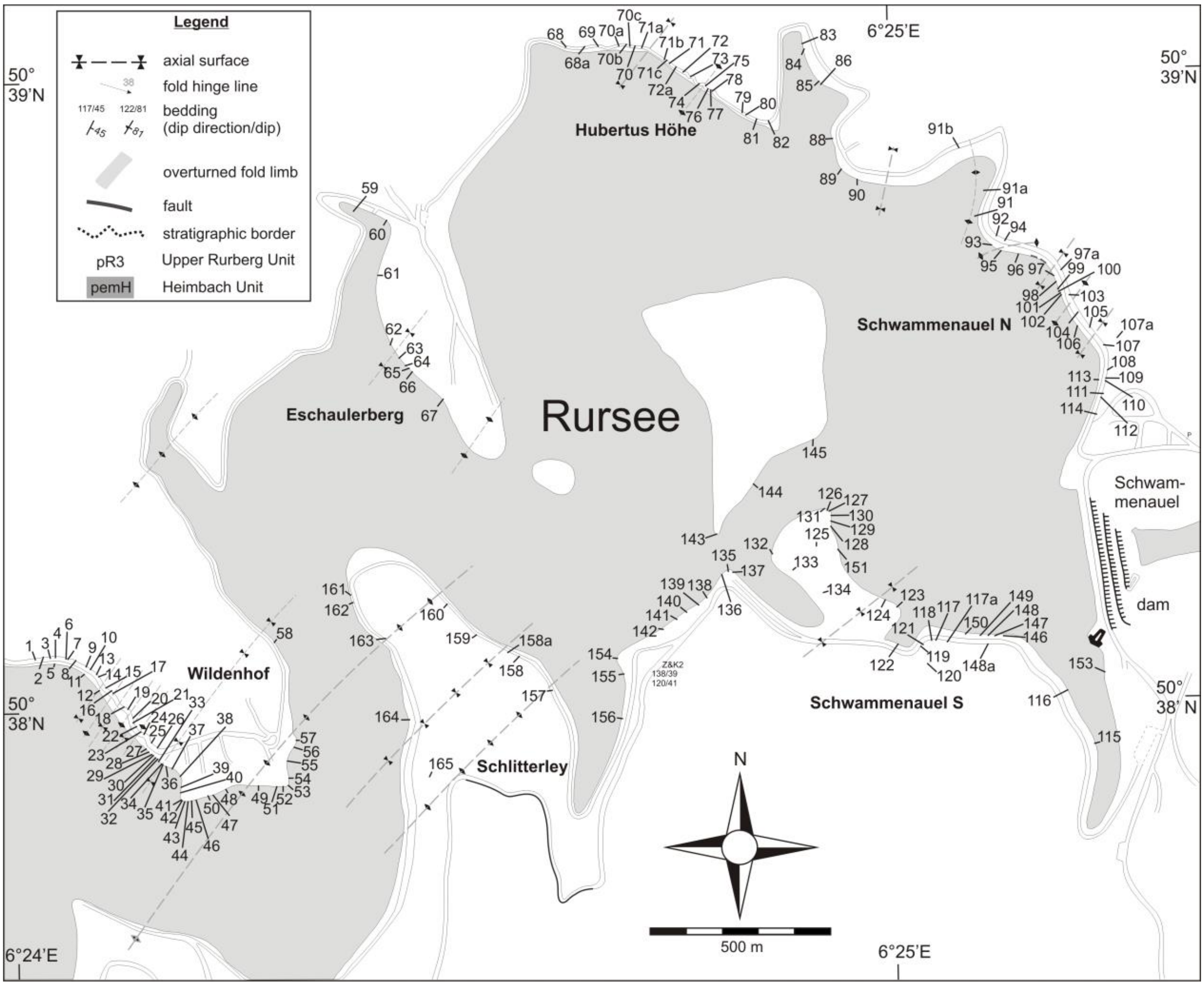

Figure B1: Sample locations indicated by field numbers starting from Wildenhof counting up clockwise to Schlitterley. The sample data corresponding to the field numbers are listed in Table B1.

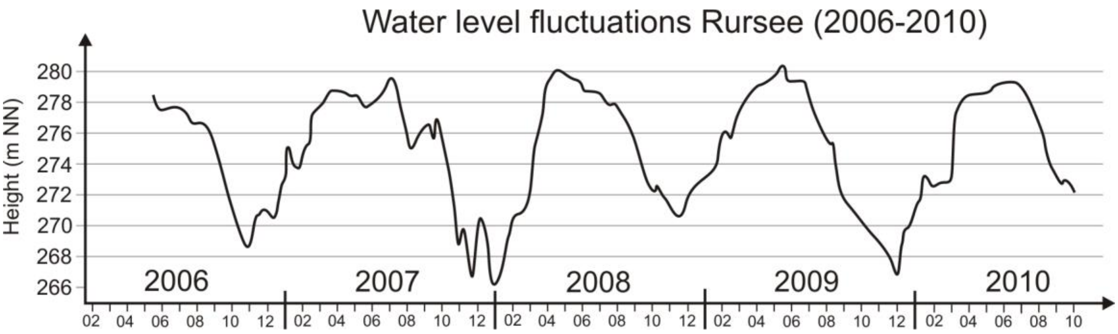

Figure B2: Water level fluctuations of the Rursee. Autumn and Winter are the best periods to have maximum outcrop capacity. NN: Normalnull: German zero sea level point. Data from *WasserVerband Eifel-Rur* (*WVER*). *http://www.wver.de*

Table B1: Sample list corresponding to the sample numbers. Samples, thin sections and wafers can be obtained at request by contacting the *Geodynamics and Geofluids Research Group*, *K.U.Leuven.* **W**: wafer available; **SL**: thin section available; **Orientation**: orientation of the sample, measured parallel to bedding (S_0) or parallel to the vein wall (V); BNV: bedding-normal vein; BPV: bedding-parallel vein; n.o.: no orientation; **Outcrop**: outcrop numbers referring to the numbers on the Rursee sample map in Figure B1; **Comments**: short description of the lithology surrounding the vein or additional comments on the sample location or the sample.

W	SL	Sample nr	Orientation		Outcrop	Comments	W	SL	Sample nr	Orientation		Outcrop	Comments
	SL	EI05VN04	085/35	S_0~BPV	Wild 24	sl 150/12	W	SL	EI06VN16		V~BNV	Wild 42	V_B
	SL	EI05VN05	072/70	V~BNV	Wild 24			SL	EI06VN17	240/15	V~BNV	Wild 18b	cross-cuttings
	SL	EI05VN06	310/85	V~BNV	Wild 24			SL	EI06VN18	115/35	S_0~BPV	Wild 31	offshoots
		EI05VN07	075/35	S_0~BPV	Wild 27	sl 125/25		SL	EI06VN19	150/80	S_0~BNV	Wild 50	
W	SL	EI05VN08	n.o.	Fault	Wild 31	dilational jog		SL	EI07VN01	070/85	V~BNV	HH 74a	
	SL	EI05VN09	070/80	V~BNV	HH 74	sdst		SL	EI07VN02	290/58	V~BNV	HH 70	
	SL	EI05VN10	070/85	V~BNV	HH 74	sdst		SL	EI07VN03	068/32	V~BNV	HH 70	
	SL	EI05VN11	145/65	S_0~BPV	HH 71b	sl 210/55 - slst		SL	EI07VN04	155/70	S_0~BNV	HH 71	lensoid
	SL	EI05VN23	214/62	V~BNV	Wild 06			SL	EI07VN05	035/28	V~BNV	HH 71	lensoid
	SL	EI05VN24	115/24	S_0~BNV	Wild 09			SL	EI07VN06	n.o.		HH 71	lensoid
W	SL	EI05VN25	296/40	S_0~BPV	Wild 27	interbedded		SL	EI07VN07	020/25	V~BNV	HH 71	lensoid
W	SL	EI05VN26	280/10	S_0~BPV	Wild 27	interbedded		SL	EI07VN08	060/81	V~BNV	HH 72	hairline
W	SL	EI05VN27	100/60	V~BNV	Wild 36			SL	EI07VN09	078/70	V~BNV	HH 73	
	SL	EI05VN28	135/73	S_0~BPV	Wild 41	sl 058/12	W	SL	EI07VN10	156/72	S_0~BPV	HH 73	slst
		EI05VN29	138/76	S_0~BPV	Wild 41	sl 192/60		SL	EI07VN11	059/80	V~BNV	HH 73	
		EI05VN30	124/60	V~BNV	Wild 57				EI07VN12	076/86	V~BNV	HH 74	en-echelon
	SL	EI05VN31	064/32	V~BNV	Esch 64			SL	EI07VN13	148/74	V~BNV	HH 74	en-echelon
	SL	EI05VN32	154/61	S_0~BNV	Esch 66	sl 202/50			EI07VN14	090/30	S_0~BPV	HH 75	
	SL	EI05VN33	054/36	S_0~BNV	Esch 67				EI07VN15	n.o.		HH 75	
	SL	EI05VN34	150/61	S_0~BNV	HH 68			SL	EI07VN16	n.o.		HH 75	
	SL	EI05VN35	151/65	S_0~BNV	HH 69			SL	EI07VN17	270/85	V~BNV	HH 75	
	SL	EI05VN36	107/78	V~BNV	HH 68a			SL	EI07VN18	294/65	V~BNV	Wild 10	
	SL	EI05VN37	129/45	V~BNV	HH 70c	hairline veins		SL	EI07VN19	282/85	V~BNV	Wild 09	
	SL	EI05VN38	107/40	S_0~BNV	HH 70c				EI07VN20	n.o.		Wild 11	
	SL	EI05VN39	359/76	S_0~BPV	Sch N 93	sl 088/32		SL	EI07VN21	113/54	S_0~BPV	Wild 22	
W	SL	EI05VN40	002/74	S_0~BPV	Sch N 93	sl 082/30		SL	EI07VN22	113/54	S_0~BPV	Wild 22	
	SL	EI05VN41	089/56	V~BNV	Sch N 93	Box fold	W	SL	EI08VN01	160/80	S_0~BPV	Urft 05	fault related
	SL	EI05VN42	064/30	S_0~BPV	Sch N 96	Box fold		SL	EI08VN02	130/72	S_0~BPV	Urft 24	fault related
	SL	EI05VN43	198/27	V~BNV	Sch N 108	sl 315/77			EI08VN04	283/85	V~BNV	Urft 27	
						sl 284/60			EI08VN05	276/76	V~BNV	Urft 27	
	SL	EI05VN44	143/28	S_0~BPV	Sch N 106				EI08VN06	114/85	S_1~BNV	Urft 27	
	SL	EI05VN45	121/29	S_0~BPV	Sch N 106			SL	EI08VN07	115/55	S_1~BNV	Urft 27	fold hinge vein
	SL	EI05VN46	344/86	S_0~BPV	Sch S 124	sl 315/77		SL	EI08VN08	115/55	S_1~BNV	Urft 27	fold hinge vein
		EI05VN47	140/46	V~BNV	Sch S 131	cross-cuttings	W	SL	EI08VN09	161/37	S_0~BPV	Urft 25	
	SL	EI05VN48	049/28	S_0~BPV	Sch S 153	fault related			EI08VN10	161/37	S_0~BPV	Urft 25b	
	SL	EI05VN49	131/74	S_0~BPV	Sch S 153				EI08VN11	162/40	S_0~BPV	Urft 25b	sl 182/32
	SL	EI05VN50	n.o.	-	Sch S 153	cross-cuttings	W	SL	EI08VN12	200/40	S_0~BNV	Urft 21	
W	SL	EI06VN01	134/75	V_C~BNV	Wild 44	V_C			EI08VN13	140/48	S_0~BPV	Wild 45	sl 216/58
W	SL	EI06VN02	050/70	V_B~BNV	Wild 44	V_B			EI08VN14	140/48	S_0~BPV	Wild 45	sl 216/58
		EI06VN03	265/60	V~BNV	Sch N 93			SL	EI08VN15	200/80	V~BNV	Wild 46a	slst
		EI06VN04	315/78	V~BNV	Schlit 160			SL	EI08VN16	200/80	V~BNV	Wild 46a	slst
		EI06VN05	078/66	V~BNV	Schlit 165		W	SL	EI08VN17	020/85	V~BNV	Wild 46a	slst
		EI06VN06	038/48	V_C~BNV	Wild 44	V_C			EI08VN18	140/70	S_0~BPV	Wild 43	thin BPV
W	SL	EI06VN07	054/60	V_B~BNV	Wild 44	V_B	W		EI08VN19	140/70	S_0~BPV	Wild 43	thin BPV
W	SL	EI06VN08	050/60	V_B~BNV	Wild 44	en-echelon			EI08VN20	140/70	S_0~BPV	Wild 43	thin BPV
W	SL	EI06VN09	130/75	S_0~BNV_C	Wild 39	V_B			EI08VN21a	140/70	S_0~BPV	Wild 43	thin BPV
W	SL	EI06VN10	135/60	S_0~BNV	Wild 42	V_B	W	SL	EI08VN22	158/80	S_0~BPV	Esch 67b	parasitic fold SE-limb
	SL	EI06VN11	120/54	S_0~BNV	Wild 36	V_B			EI08VN23	305/30	S_0~BPV	Esch 67b	parasitic fold NW-limb
		EI06VN063a	122/35	S_0~BNV	Wild 26	V_B			EI08VN24	305/30	S_0~BPV	Esch 67b	parasitic fold NW-limb
		EI06VN12	120/55	V~BNV	Wild 36	V_B	W	SL	EI08VN25	155/30	S_0~BPV	Esch 67b	parasitic fold SE-limb
		EI06VN13	298/70	V~BNV	Wild 27	composite	W	SL	EI08VN26	n.o.		Urft 27	vein refraction
W	SL	EI06VN14	305/60	V~BNV	Wild 27	cross-cuttings		SL	EI09VN01	140/40	S_0~BPV	Wild 23	fault vein
		EI06VN15	324/65	V~BNV	Wild 06				EI09VN02	111/35	S_0~BPV	Wild 27	cross-cuttings
		EI06VN16	280/65	V~BNV	Wild 10			SL	EI09VN03	118/51	V~BNV	Wild 30	parasitic fold

APPENDIX C Fluid inclusion data

Bedding-normal veins

Sample EI05VN27 - Wildenhof outcrop nr 36 - generation V_B

Sample Wafer	*Incl. Nr*	*T_f ice*	*T_m ice*	*Salinity*	*T_h tot*	*Type*	*Size (L / W) (µm)*	*Vol %*
EI05VN27	1				138	isolated		
EI05VN27	2				146	Isolated		
EI05VN27	3				142	isolated		
EI05VN27	4				125	isolated		
EI05VN27	5				161	isolated		
EI05VN27	6	-44.2	-45.1	5.74	115	isolated		
EI05VN27	7				154	isolated		
EI05VN27	8				173	isolated		
EI05VN27	9	-44.0	-44.9	5.43	163	sec.		
EI05VN27	10				122	sec.		
EI05VN27	11				172	sec.		
EI05VN27	12				142	sec.		
EI05VN27	13				141	sec.		
EI05VN27	14				160	sec.		
EI05VN27	15				139	sec.		
EI05VN27	16				182	sec.		
EI05VN27	17				82	pseudosec.		
EI05VN27	18				170	pseudosec.		
EI05VN27	19				160	pseudosec.		
EI05VN27	20				210	pseudosec.		
EI05VN27	21				167	pseudosec.		
EI05VN27	22				159	pseudosec.		
EI05VN27	23				157	pseudosec.		
EI05VN27	24				150	pseudosec.		
EI05VN27	25				150	pseudosec.		
EI05VN27	26	-42.6	-43.4	5.28	> 250	pseudosec.		
EI05VN27	27				160	pseudosec.		
EI05VN27	28				150	pseudosec.		
EI05VN27	29				148	pseudosec.		
EI05VN27	30	-44.2	-45.1	0.49	145	pseudosec.		
EI05VN27	31				152	pseudosec.		
EI05VN27	32				145	pseudosec.		
EI05VN27	33				179	pseudosec.		
EI05VN27	34				167	pseudosec.		
EI05VN27	35				209	pseudosec.		
EI05VN27	36				155	pseudosec.		
EI05VN27	37				175	pseudosec.		
EI05VN27	38				204	pseudosec.		
EI05VN27	39				155	pseudosec.		
EI05VN27	40	-44.2	-45.1	5.43	>> 230	pseudosec.		
EI05VN27	41				168	sec.		
EI05VN27	42				149	sec.		
EI05VN27	43				> 230	sec.		
EI05VN27	44				159	sec.		
EI05VN27	45	-44.7	-45.6	5.28	179	sec.		
EI05VN27	46				155	sec.		
EI05VN27	47				179	sec.		
EI05VN27	48	-44.1	-45.0	5.13	>> 250	sec.		
EI05VN27	49	-39.9	-40.7	5.43	151	sec.		

Sample EI06VN08 - Wildenhof outcrop nr 44 - generation V_B

Sample Wafer	*Incl. Nr*	*T_f ice*	*T_m ice*	*Salinity*	*T_h tot*	*Type*	*Size (L / W) (µm)*	*Vol %*
EI06VN08 (1)	1	-39.1	-0.9	1.51	148	isolated	11 / 10	10
EI06VN08 (1)	2	-39.1	-2.2	3.62	204	sec.	7 / 3	10
EI06VN08 (1)	3	-38.7	-1.8	2.99	130	sec.	6 / 2	10
EI06VN08 (1)	4	-30.3	-1.2	2.01	245	sec.	5 / 2	10
EI06VN08 (1)	5	-30.4	-1.3	2.28	269	sec.	7 / 3	20
EI06VN08 (1)	6	-29.6	-1.1	1.95	> 300	sec.	7 / 3	30
EI06VN08 (1)	7	-29.1	-1.1	1.95	> 350	sec.	9 / 4	50
EI06VN08 (1)	9	-28.8	-		93	sec.	-	10
EI06VN08 (1)	10	-31.3			123	sec.	13 / 2	10
EI06VN08 (1)	11		-1.9	3.25	194	sec.	8 / 3	10
EI06VN08 (1)	12		-2.1	3.57	-	sec.	10 / 4	20
EI06VN08 (1)	13	-41.1	-1.1	1.95	-	sec.	7 / 4	30
EI06VN08 (3)	14	-32.5	-1.3	2.28	-	isolated	11 / 7	10
EI06VN08 (3)	15	-42.7	-3.0	4.94	247	pseudosec.	6 / 4	20
EI06VN08 (3)	16	-44.1	-3.8	6.09	208	pseudosec.	9 / 2	10
EI06VN08 (3)	17	-42.8	-2.0	3.41	> 350	pseudosec.	9 / 8	20
EI06VN08 (3)	18	-30.2			-	pseudosec.	18 / 16	10
EI06VN08 (3)	19		-3.0	4.94	320	pseudosec.	9 / 2	10
EI06VN08 (3)	20		-3.4	5.52	255	pseudosec.	6 / 2	15
EI06VN08 (3)	21	-42.3	-2.5	4.18	213	pseudosec.	8 / 3	10
EI06VN08 (3)	22	-32.4			> 300	pseudosec.	7 / 6	30
EI06VN08 (3)	23	-44.1	-1.9	3.25	290	pseudosec.	5 / 3	20
EI06VN08 (2)	24	-36.8	-3.2	5.23	-	sec.	7 / 3	10
EI06VN08 (2)	25	-34.4	-3.3	5.38	248	sec.	8 / 6	20
EI06VN08 (2)	25b				252	sec.	9 / 3	10
EI06VN08 (2)	26	-26.0	-2.3	3.10	-	sec.	8 / 6	15
EI06VN08 (2)	27	-28.2	-0.3	0.60	289	sec.	4.5 / 4.5	10
EI06VN08 (2)	28	-28.3	-0.4	0.77	245	sec.	6 / 4	10
EI06VN08 (2)	29	-28.0	-0.4	0.77	-	sec.	5 / 2	30
EI06VN08 (2)	30	-28.9	-1.6	2.77	305	sec.	6 / 4	25
EI06VN08 (2)	31	-28.0	-0.7	1.28	328	sec.	5 / 2	40
EI06VN08 (2)	32	-27.4	-3.3	5.01	-	sec.	5 / 3	10
EI06VN08 (2)	33	-38.0	-5.3	-10.58	-	sec.	8 / 2	10
EI06VN08 (2)	34		-0.9	1.62	319	sec.	6 / 4	40
EI06VN08 (3)	35	-40.3	-0.6	0.97	280	sec.	5 / 3	40
EI06VN08 (3)	36	-	-1.3	2.31	275	sec.	3.5 / 3	20
EI06VN08 (3)	38	-34.6	-3.1	5.12	216	pseudosec.	4.5 / 3	15
EI06VN08 (3)	39	-32.7	-3.0	4.97	202	pseudosec.	3 / 3	10
EI06VN08 (3)	40	-35.2	-3.0	4.97	190	pseudosec.	3 / 2.5	15
EI06VN08 (3)	41	-34.8	-1.8	3.12	234	sec.	6 / 3.5	10
EI06VN08 (3)	42	-35.4	-3.3	5.45	178	isolated	10 / 6	10
EI06VN08 (3)	43	-	-3.2	5.15	265	sec.	3 / 2	15
EI06VN08 (3)	44	-	-3.1	5.01	262	sec.	3 / 2.5	20
EI06VN08 (3)	45	-	-1.1	1.85	203	sec.	3 / 2	10
EI06VN08 (3)	47	-33.7	-2.8	4.56	211	isolated	5 / 4	35
EI06VN08 (J)	7	-26.5	-3.1	5.08	214	pseudosec		
EI06VN08 (J)	8	-28.4	-		176	sec.		
EI06VN08 (J)	9	-	-		162	sec.		
EI06VN08 (J)	11	-32.0	-2.1	3.57	149	isolated		
EI06VN08 (J)	12	-33.3	-2.2	3.73	228	isolated		
EI06VN08 (J)	13	33.4	-2.9	4.79	>>300	isolated		
EI06VN08 (J)	14	-41.2	-2.5	4.19	203	isolated		
EI06VN08 (J)	15	-33.3	-3.1	5.08	175	isolated		
EI06VN08 (J)	16	-34.3	-2.9	4.79	235	pseudosec.		
EI06VN08 (J)	17	-32.6	-3.0	4.93	236	pseudosec.		
EI06VN08 (J)	18	-32.8	-2.2	3.73	176	pseudosec.		
EI06VN08 (J)	19	-34.3	-2.9	4.79	150	pseudosec.		
EI06VN08 (G)	20	-33.0	-3.1	5.08	169	pseudosec.		
EI06VN08 (G)	21	-32.9	-2.7	4.49	156	pseudosec.		
EI06VN08 (G)	22	-33.7	-3.0	4.93	255	pseudosec.		
EI06VN08 (G)	23	-33.4	-3.0	4.93	176	pseudosec.		

Sample EI06VN07 - Wildenhof outcrop nr 44 - generation V_B

Incl. Nr	T_f CO_2	T_f ice	T_f clath	T_m CO_2	T_m ice	Salinity	T_m clath	T_h CO2	T_h tot	Type	Size (L / W) (µm)	Vol %
A	-102.6	-34.6		-61.2	-2.9	4.72	11.5	10.0		aq-gas. iso.	2.8 / 2.0	10
B		-30.6			-1.1	1.85			114.8	sec.		< 10
C	-102.6	-36.6	-26.0	-61.4	-2.6	4.27	10.3	-6.0	< 280	aq-gas. iso.	13 / 4	40
	-104.5	-38.5	-24.3		-1.1	1.85	11.8			aq-gas. iso.		
D1	-97.7			-56.9	-1.2	2.02			-	sec.		10
D2									203.6	sec.		10
E	-95.6	-33.7	-27.7	-57.0	-4.4	6.88	9.3	21.2	-	trail	6.2 / 4.3	30
F1		-35.0			-3.1	5.02			-	sec.	7 / 5.6	10
F2									167.3	sec.		
G1		-32.4							131.8	sec.		10
G2		-32.5					11.8		282.1	isolated		10
H	-104.3		-23.7	-65.4	-1.8	3.00	10.6		212.4	trail	5 / 4	20
I	-100.1	-34.6	-26.1	-58.9	-2.6	4.27	10.1	15.6		trail	6 / 4.5	10
J			-27.5	-58.6	-3.5	5.61	9.3			pseudosec.		20
K		-34.3		-58.4	-0.6	1.00	9.3			pseudosec.		20
L			-27.9		-3.9	6.18			338.9	pseudosec.		40
M	-103.6	-32.7		-57.3	-3.4	5.47	7.7			trail	8 / 2	20
N		-32.4			-1.5	2.51			122.4	pseudosec.		20
O		-29.5			-3.0	4.87	9.0		> 340	pseudosec.	3 / 2	20
P		-35.8			-3.0	4.87			253.7	pseudosec.	2.5 / 2.4	20
Q		-38.6	-26.4		-4.0	6.32	11.2		345.7	pseudosec.	8 / 4	15
R		-37.1			-3.5	5.61				pseudosec.	6 / 2	10
S		-34.0	-26.5		-3.5	5.61				pseudosec.	8 / 3	10
T										unknown		35
U		-38.9			-3.8	6.04	11.4			unknown		20
V		-33.9			-3.5	5.61			331.0	unknown	5 / 4	20
W		-35.7			-3.1	5.02				unknown	7 / 2	10
X		-38.7	-29.5		-3.7	5.90				sec.	7 / 2.3	10
Y	-104.1			-64.4						isolated	6 / 3	
Z	-101.5			-60.2						Isolated		
27	-98.0			-58.1	-3.9	6.18				Isolated	4 / 2	
28	-105.0			-63.6				-15.5		trail		
29	-104.1	-34.9		-64.0			12.1	-9.2		trail	5 / 5	
30	-105.1			-65.5				-48.5	Liq.	trail	6 / 6	
31	-104.1			-65.0				-33.9	Liq.	trail	9 / 7	
A		-32.65			-3.1	5.12			169	pseudosec.	8 / 7	10
B		-34.63			-3.3	5.41			188	pseudosec.	10 / 5	15
C		-34.33			-3.3	5.41			192	pseudosec.	6.5 / 4	10
D		-33.24			-3.1	5.12			146	pseudosec.	6 / 4	10
E		-32.45			-3.1	5.12			152	pseudosec.	7 / 3	15
F		-32.85			-3.0	4.97			154	pseudosec.	6 / 5	10
G		-34.93			-3.4	5.56			177	pseudosec.	5 / 5	10
H		-33.44			-3.4	5.56			151	pseudosec.	5 / 3	
I		-32.75			-2.8	4.68			162	pseudosec.	13 / 7	15
J		-34.73			-3.2	5.27			159	pseudosec.	11 / 9	
1		-34.3			-3.1	5.12			>>	isolated	12 / 10	20
2		-35.5			-3.1	5.12			187	isolated	7 / 6	10
3		-33.4			-3.2	5.26			177	isolated	6 / 4	10
4		-35.5			-3.3	5.41			215	isolated	6 / 5	10
5		-34.0			-3.3	5.41			208	isolated	7 / 4	10
6		-31.0			-2.7	4.52			185	isolated	6 / 4	10
7		-34.8			-3.2	5.26			195	isolated	6 / 4	10
8		-35.3			-3.5	5.70			186	isolated	4 / 2.5	20
9		-32.3			-3.6	5.84			184	isolated	9 / 8	10
10		-35.3			-				190	isolated	6 / 3	10
11		-34.2			-3.4	5.55			170	isolated	4 / 3	10
12		-35.5			-3.0	4.97			-	isolated	5 / 3.5	15
13		-34.0			-3.4	5.55			174	isolated	4.5 / 3.5	10
14		-32.5			-1.7	2.97			-	isolated	6.5 / 4	40
15		-32.6			-2.9	4.82			164	pseudosec.	7 / 6	10
16		-33.0			-2.8	4.67			148	pseudosec.	4.5 / 4	10
17		-31.3			-2.7	4.52			147	pseudosec.	6 / 3	10
18		-34.6			-3.3	5.41			156	pseudosec.	9 / 3	10
20		-34.7			-3.3	5.41			145	pseudosec.	10 / 7	10
21		-33.7			-3.0	4.97			171	pseudosec.	11 / 4	10
22		-34.3			-3.2	5.26			187	pseudosec.	5 / 3	10
23		-32.6			-2.6	4.37			157	pseudosec.	7.5 / 4	10
24		-33.0			-2.6	4.37			155	pseudosec.	13 / 8	10

Sample EI06VN07 - Wildenhof outcrop nr 44 - generation V_B (pseudosecondary inclusions)

Incl. Nr	T_f ice	T_m ice	Salinity	T_h tot
1				130
2				178
3				172
4				162
5				165
6				148
7				161
8				154
9				148
10				183
11				149
12				189
13				149
14				141
15				139
16				161
17				110
18				187
19				202
20				160
21				169
22				183
23				143
24				151
25				138
26				179
27	-43	-3.4	5.15	160
28				152
29				161
30				160
31	-44.8	-3.8	6.12	165
32	-44.8	-3.9	6.33	158
33				141
34				148
35				198
36				202
37				137
38				136

Sample EI06VN14 - Wildenhof outcrop nr 27 - generation V_B

Sample Wafer	Incl. Nr	T_f ice	T_m ice	Salinity	T_h tot	Type	Size (L / W) (µm)	Vol %
EI06VN14 (1)	1				212	pseudosec.		
EI06VN14 (1)	2				118	pseudosec.		
EI06VN14 (1)	3				175	pseudosec.		
EI06VN14 (1)	4				126	pseudosec.		
EI06VN14 (1)	5				115	pseudosec.		
EI06VN14 (1)	6				189	pseudosec.		
EI06VN14 (1)	7				220	pseudosec.		
EI06VN14 (1)	8				225	pseudosec.		
EI06VN14 (1)	9				215	pseudosec.		
EI06VN14 (1)	10				169	pseudosec.		
EI06VN14 (1)	11				199	pseudosec.		
EI06VN14 (1)	12				198	pseudosec.		
EI06VN14 (1)	13				155	pseudosec.		
EI06VN14 (1)	14				204	pseudosec.		
EI06VN14 (1)	15				189	pseudosec.		
EI06VN14 (1)	16				163	pseudosec.		
EI06VN14 (1)	17				209	pseudosec.		
EI06VN14 (4)	18				176	pseudosec.		
EI06VN14 (4)	19				161	pseudosec.		
EI06VN14 (4)	20	-46.0			197	pseudosec.		
EI06VN14 (4)	21		-3.9	6.33	162	pseudosec.		
EI06VN14 (4)	22				152	pseudosec.		
EI06VN14 (4)	23				149	pseudosec.		
EI06VN14 (4)	24	-47.2	-4.1	6.63	167	pseudosec.		
EI06VN14 (4)	25				147	pseudosec.		
EI06VN14 (4)	26				143	pseudosec.		
EI06VN14 (4)	27				176	pseudosec.		
EI06VN14 (4)	28				188	pseudosec.		
EI06VN14 (4)	29	-46.2	-4.1	6.63	168	pseudosec.		
EI06VN14 (4)	30				163	pseudosec.		
EI06VN14 (4)	31				161	pseudosec.		
EI06VN14 (4)	32				160	pseudosec.		
EI06VN14 (4)	33	-47.1	-4.2	6.77	222	pseudosec.		
EI06VN14 (4)	34	-46.0	-4.1	6.63	-	pseudosec.		
EI06VN14 (5)	35				205	sec.		
EI06VN14 (5)	36				235	sec.		
EI06VN14 (5)	37				152	sec.		
EI06VN14 (5)	38				164	sec.		
EI06VN14 (5)	39				172	isolated		
EI06VN14 (5)	40				155	isolated		
EI06VN14 (5)	41				158	isolated		
EI06VN14 (5)	42				166	isolated		
EI06VN14 (5)	43				162	isolated		
EI06VN14 (5)	44				>>250	isolated		
EI06VN14 (5)	45				168	pseudosec.		
EI06VN14 (5)	46				149	pseudosec.		
EI06VN14 (5)	47				156	pseudosec.		
EI06VN14 (5)	48	-48.1	-1.1	1.88	192	pseudosec.		
EI06VN14 (5)	49				124	pseudosec.		

Sample EI06VN16 - Wildenhof outcrop nr 42 - generation V_B

Sample Wafer	Incl. Nr	T_f ice	T_m ice	Salinity	T_h tot	Type	Size (L / W) (μm)	Vol %
EI06VN16 A	1				149	pseudosec.		
EI06VN16 A	2					pseudosec.		
EI06VN16 A	3		-3.9	6.27		pseudosec.		20
EI06VN16 A	4				163	pseudosec.		
EI06VN16 A	5		-2.6	4.29	>>	pseudosec.		80
EI06VN16 A	6		-3.7	5.97	183	pseudosec.		30
EI06VN16 A	7		-3.9	6.27	198	pseudosec.		20
EI06VN16 A	8		-3.6	5.82		pseudosec.		
EI06VN16 A	9		-3.8	6.12	173	pseudosec.		10
EI06VN16 A	10		-3.6	5.82	155	pseudosec.		10
EI06VN16 A	11		-3.8	6.12	187	pseudosec.		20
EI06VN16 A	12		-3.8	6.12	161	pseudosec.		20
EI06VN16 A	13				148	pseudosec.		
EI06VN16 A	14		-3.6	5.82	225	pseudosec.		30
EI06VN16 A	15		-3.8	6.12	240	pseudosec.		20
EI06VN16 A	16		-3.9	6.27	245	pseudosec.		30
EI06VN16 A	17				148	pseudosec.		
EI06VN16 A	18				162	pseudosec.		
EI06VN16 A	19				164	pseudosec.		
EI06VN16 A	20				158	pseudosec.		
EI06VN16 A	21				203	pseudosec.		
EI06VN16 A	22				197	pseudosec.		
EI06VN16 A	23				163	pseudosec.		
EI06VN16 E	24				165	pseudosec.		
EI06VN16 E	25				178	pseudosec.		
EI06VN16 E	26				175	pseudosec.		
EI06VN16 E	27				157	pseudosec.		
EI06VN16 E	28				213	pseudosec.		
EI06VN16 E	29				168	pseudosec.		
EI06VN16 E	30				175	pseudosec.		
EI06VN16 E	31				153	pseudosec.		
EI06VN16 E	32				198	pseudosec.		
EI06VN16 E	33				>>	pseudosec.		
EI06VN16 E	34				196	pseudosec.		
EI06VN16 E	35				163	pseudosec.		
EI06VN16 E	36				204	pseudosec.		
EI06VN16 E	37				163	isolated		
EI06VN16 E	38				151	isolated		
EI06VN16 E	39				153	isolated		
EI06VN16 E	40				167	isolated		
EI06VN16 E	41				173	isolated		
EI06VN16 E	42				168	isolated		
EI06VN16 E	43				165	isolated		
EI06VN16 E	44				179	isolated		
EI06VN16 E	45				163	isolated		
EI06VN16 E	46				160	isolated		
EI06VN16 E	47				158	isolated		

Sample EI06VN09 - Wildenhof outcrop nr 39 - generation V_C (pseudosecondary inclusions)

Sample	Incl. Nr	T_f ice	T_m ice	T_h tot
EI06VN09	7			96
	8			125
	9			268
	10			195
	11			226
	12			248
	13			265
	14			120
	15			148
	16			153
EI06VN09	17			180
	18			260
	19			136
	20			228
	21			238
	22			240
	23			132
	24			129
	25			174

Sample EI06VN01 - Wildenhof outcrop nr 44 - generation V_C

Sample Wafer	*Incl. Nr*	*T_f ice*	*T_m ice*	*Salinity*	*T_h tot*	*Type*	*Size (L / W) (µm)*	*Vol %*
EI06VN01 b-5	1	-34.6	-0.7	1.30	143	pseudosec.	7 / 3	10
EI06VN01 b-5	2	-35.7	-1.0	1.81	105	pseudosec.	10 / 3	10
EI06VN01 b-5	3	-37.0	-0.9	1.64	90	pseudosec.	5 / 2	10
EI06VN01 b-5	4	-35.6	-0.8	1.47	99	pseudosec.	6 / 1.5	10
EI06VN01 b-5	5	-40.1	-		107	pseudosec.	5 / 2	10
EI06VN01 b-5	7	-38.8	-1.4	2.46	135	pseudosec.	3 / 2	10
EI06VN01 b-5	8	-32.5	-0.5	0.96	-	pseudosec.	7.5 / 4	10
EI06VN01 b-5	9	-47.0	-		138	pseudosec.	7 /2	10
EI06VN01 b-5	10	-35.8	-0.7	1.30	137	pseudosec.	9 / 4	10
EI06VN01 b-5	11	-37.2	-1.1	1.97	134	pseudosec.	6.5 / 3	10
EI06VN01 b-5	12	-31.7	-3.3	5.38	137	pseudosec.	11 / 2.5	10
EI06VN01 b-1-2	1	-32.4	-0.9	1.64	213	sec.	2.5 / 2.5	10
EI06VN01 b-1-2	4	-28.5	-0.7	1.30	152	sec.	3.5 / 3.5	10
EI06VN01 b-3	6	-29.1	-0.8	1.47	136	pseudosec.	8 / 4	10
EI06VN01 b-3	7	-28.0	-0.7	1.30	256	pseudosec.	8 / 5	10
EI06VN01 b-3	9	-39.1	-0.6	1.13	230	pseudosec.	2 / 2	10
EI06VN01 b-3	10	-40.3	-0.7	1.30	198	pseudosec.	7 /4	10
EI06VN01 b-3	11	-33.5	-0.8	1.47	180	pseudosec.	6 / 3	10
EI06VN01 a (d)	1	-36.3	-3.8	5.73	>>	pseudosec.	7 / 5	20
EI06VN01 a (d)	2	-33.7	-3.7	5.59	173	pseudosec.	3 / 3	15
EI06VN01 a (d)	3	-34.6	-3.6	5.44	169	Isolated	5 / 4	10
EI06VN01 a (d)	4	-36.2	-3.7	5.59	171	Isolated	3 / 3	10
EI06VN01 a (d)	5	-37.3	-3.6	5.44	194	Isolated	4 / 2	10
EI06VN01 a (d)	6	-33.0	-3.4	5.15	164	isolated	4 / 3.5	10
EI06VN01 a (d)	7	-39.4	-0.4	0.19	203	isolated	8 / 4	10
EI06VN01 a (d)	8	-	-3.2	4.86	>260	pseudosec.	5 / 3	10
EI06VN01 a (d)	9	-35.3	-3.8	5.73	177	pseudosec.	7 / 3	10
EI06VN01 a (d)	10	-33.4	-3.3	5.01	198	pseudosec.	3.5 / 3	10
EI06VN01 a (d)	11	-38.8	-		173	pseudosec.	4 / 2.5	10
EI06VN01 a (d)	12	-35.9	-3.4	5.15	165	pseudosec.	3.5 / 2	15
EI06VN01 a (d)	13	-33.2	-0.4	0.19	239	isolated	8 / 3	95
EI06VN01 a (a1)	14	-	-1.2	1.30	169	sec.	8 / 3	10
EI06VN01 a (a1)	17	-28.3	-		172	sec.	7.5 / 4.5	10
EI06VN01 a (a2)	19	-33.2	-2.8	3.88	165	sec.	6 / 3	10
EI06VN01 a (a2)	20	-35.3	-		164	sec.	6 / 3	10
EI06VN01 a (a2)	21	-32.8	-3.1	4.34	145	sec.	2 / 2.5	5
EI06VN01 a (a2)	22	-37.7	-1.5	1.80	121	sec.	2.5 / 1.5	5
EI06VN01 a (a2)	23	-32.8	-		122	sec.	2.5 / 1.5	10
EI06VN01 a (a2)	24	-	-2.3	3.10	218	sec.	3.5 / 3.2	15
EI06VN01 a (a2)	25	-32.7	-2.2	2.94	-	sec.	4 / 2.5	10
EI06VN01 a (a2)	27	-32.9	-2.1	2.78	165	isolated	4 / 3	10
EI06VN01 a (a2)	28	-32.8	-		198	isolated	8 / 3	15
EI06VN01 a (a2)	29a	-33.5	-		290	isolated	4 / 4	10
EI06VN01 a (a2)	29b	-	-		192	isolated	3 / 3	10
EI06VN01 a (a2)	30	-	-3.3	4.65	176	isolated	4.5 / 3	15
EI06VN01 a (a2)	31	-34.4	-3.1	4.34	135	isolated	4 / 3	15
EI06VN01 a (a2)	32	-34.8	-3.7	5.24	-	isolated	3.5 / 3	15
EI06VN01 a (a2)	33	-	-		205	sec.	4 / 2.5	20
EI06VN01 a (b)	34	-34.9	-1.8	2.29	205	isolated	4 / 2	10
EI06VN01 a (b)	35	-36.0	-		169	isolated	3 / 2	20
EI06VN01 a (b)	36	-28.2	-		228	isolated	6 / 3.5	20
EI06VN01 a (b)	37	-36.2	-3.4	4.79	190	isolated	8 / 4	15
EI06VN01 a (b)	38	-35.3	-3.2	4.50	167	isolated	4 / 2	5
EI06VN01 a (b)	40	-35.0	-2.4	3.26	256	isolated	3.5 / 2	25
EI06VN01 a (b)	41	-30.5	-		135	isolated	5 / 3	10
EI06VN01 a (b)	42	-	-		171	pseudosec.	4 / 2.5	10
EI06VN01 a (b)	43	-35.4	-3.6	5.09	161	pseudosec.	5 / 3	10

Sample EI08VN17 - Wildenhof outcrop nr 46a - veins in slates (unknown fluid inclusion type)

Incl. Nr	*T_f ice*	*T_m ice*	*Salinity*	*T_h tot*
1		-5.1	8.00	250
2		-2.9	4.80	310
3	-37.3	-0.4	0.70	
4		-		212
5	-31.9	-2.8	4.65	149
6	-33.0	-		120
7		-		
8		-3.9	6.30	
9		-3.5	5.71	
10		-2.7	4.49	
11		-		
				230
12	-37.9	-3.7	6.01	204
13	-37.8	-3.9	6.30	188
14	-37.0	-3.8	6.16	220
15	-37.8	-3.7	6.01	205
16				162
				164
				175
				250
17	-37.0	-3.7	6.01	169
18	-37.0	-3.8	6.16	170
				155
19	-37.0	-3.2	5.26	147
20	-38.4	-3.3	5.41	126
21	-35.0	-3.8	6.16	163
22	-36.0	-3.8	6.16	152
23				110
24				167
25				148
26				140
27				138

Incl. Nr	*T_f ice*	*T_m ice*	*Salinity*	*T_h tot*
28				179
29				157
30				145
31				160
32				162
33				138
34				159
35				163
36				192
37				198
38				129
39				135
40				172
41				155
42				145
43				248
44				140
45				218
46	-36.0	-4.2	6.74	165
47				170
48	-37.5	-4.1	6.59	178
49				177
50				163
51				158
52				168
53				148
54				183
55				145
56	-38.1	-4.3	7.02	161
57				143
58				184
59				162

Sample EI08VN12 - Urftsee zone 7 (pseudosecondary inclusions)

Incl. Nr	*T_f ice*	*T_m ice*	*Salinity*	*T_h tot*
1	-33.0	-3.5	5.71	189
2	-34.0	-2.6	4.38	188
3				181
4	-33.0	-2.6	4.38	175
5	-36.0	-2.9	4.85	179
6	-32.0	-2.9	4.85	188
7		-2.5	4.22	175
8				198
				202
9	-45.2	-3.5	5.77	191
10		-3.6	5.92	186
				163
11		-3.2	5.31	165
12		-3.5	5.77	172
13		-3.7	6.07	168
14		-3.5	5.77	138
15				160
16				202
17		-3.4	5.62	203
18		-3.5	5.77	190
19				165
20		-3.7	6.07	207
21				194
22				199
23				198
24	-33.0			115
25	-44.2	-3.0	5.00	150
26		-3.2	5.31	169
27				185

Incl. Nr	*T_f ice*	*T_m ice*	*Salinity*	*T_h tot*
28		-2.2	3.74	169
29	-42.1	-3.1	5.16	182
30				175
32				183
33				182
34	-40.3	-3.0	5.00	190
35		-2.6	4.38	177
36		-2.0	3.41	187
37		-2.7	4.53	159
38	-43.5	-3.1	5.16	182
39				170
40	-42.1	-3.1	5.16	173
41		-3.2	5.31	183
42		-2.8	4.69	185
43		-2.4	4.06	181
44				178
45		-2.7	4.53	211
46		-3.5	5.77	198
47		-2.1	3.57	188
48				197
49	-37.9	-4.4	7.09	172
50		-2.1	3.57	180
51		-2.9	4.85	189
52		-2.7	4.53	188
53		-2.9	4.85	162
54		-3.3	5.46	188
55		-2.9	4.85	186
56				165
57				186

Bedding-parallel veins

Sample EI05VN25 - Wildenhof outcrop nr 27 - Interbedded vein

Sample Wafer	*Incl. Nr*	*T_f ice*	*T_m ice*	*Salinity*	*T_h tot*	*Type*	*Size (L / W) (µm)*	*Vol %*
EI05VN25 A1	1	-33.2	-0.2	0.35	107	pseudosec.		10
EI05VN25 A1	2	-33.2	-1.9	3.23	129	pseudosec.		10
EI05VN25 A1	3	-32.3	-2.5	4.18	176	pseudosec.		15
EI05VN25 A1	4	-35.2	-0.7	1.22	99	pseudosec.		5
EI05VN25 A1	5	-34.1	-0.2	0.35	95	pseudosec.		10
EI05VN25 A1	6	333.5	-0.8	1.40	120	pseudosec.		10
EI05VN25 A1	6b	-	-	0.00	126	pseudosec.		10
EI05VN25 A1	7	-31.1	-3.0	4.96	196	pseudosec.		10
EI05VN25 A1	8	-34.1	-2.9	4.80	176	pseudosec.		10
EI05VN25 A1	9	-36.1	-2.6	4.34	180	pseudosec.		20
EI05VN25 A1	10	-33.4	-1.1	1.91	132	pseudosec.		15
EI05VN25 A1	11	-33.1	-0.9	1.57	138	pseudosec.		30
EI05VN25 A1	12	-36.3	-3.3	5.41	>> 300	pseudosec.		25
EI05VN25 A1	13	-35.0	-2.7	4.49	201	pseudosec.		25
EI05VN25 A1	14	-	-	-		pseudosec.		0
EI05VN25 A1	15	-34.3	-2.9	4.80	>>>	pseudosec.		80
EI05VN25 A1	16	-33.4	-3.2	5.26	293	pseudosec.		20
EI05VN25 A1	17	-32.1	-0.2	0.35	96	pseudosec.		10
EI05VN25 A1	17b	-	-	-	112	pseudosec.		10
EI05VN25 A1	18	-37.1	-2.9	4.80	155	pseudosec.		10
EI05VN25 A1	19	-32.9	-2.8	4.65	220	pseudosec.		30
EI05VN25 A1	20	-32.1	-2.8	4.65	265	pseudosec.		30
EI05VN25 A1	21	-33.3	-2.8	4.65	144	pseudosec.		10
EI05VN25 A1	22	-33.1	-2.6	4.34	150	pseudosec.		10
EI05VN25 A1	22b	-	-	0.00	162	pseudosec.		15
EI05VN25 A1	23	-34.1	-3.2	5.26	165	pseudosec.		15
EI05VN25 A1	24	-33.0	-0.5	0.88	-	pseudosec.		30
EI05VN25 A1	25	-33.5	-2.9	4.80	243	pseudosec.		30
EI05VN25 A1	26	-31.1	-	0.00	>> 300	pseudosec.		15
EI05VN25 B1	27	-28.7	-0.1	0.18	117	sec.		10
EI05VN25 B1	28	-35.4	-2.3	3.87	153	sec.		15
EI05VN25 B1	29	-35.1	-3.1	5.11	137	sec.		10
EI05VN25 B1	30	-35.1	-3.4	5.56	>> 300	sec.		30
EI05VN25 B2	31	-37.6	-4.0	6.45	>> 300	sec.		25
EI05VN25 B2	32	-35.0	-3.3	5.41	168	sec.		10
EI05VN25 B2	33	-33.6	-3.4	5.56	193	pseudosec.		10
EI05VN25 B2	34	-34.5	-3.3	5.41	209	pseudosec.		10
EI05VN25 B2	35	-34.4	-3.4	5.56	240	pseudosec.		25
EI05VN25 B2	36	-35.1	-3.5	5.71	192	pseudosec.		10
EI05VN25 B2	37	-35.7	-4.0	6.45	162	pseudosec.		10
EI05VN25 B2	38	-36.3	-	-	>>>	pseudosec.		10
EI05VN25 B2	39	-35.1	-3.1	5.11	163	pseudosec.		10
EI05VN25 B2	40	-33.5	-3.0	4.96	158	pseudosec.		15
EI05VN25 B2	41	-32.7	-2.7	4.49	145	pseudosec.		10
EI05VN25 B2	42	-33.9	-3.1	5.11	175	sec.		10
EI05VN25 B2	43	-34.2	-3.1	5.11	174	sec.		10
EI05VN25 B2	44	-34.0	-1.5	2.57	132	sec.		10

Sample EI05VN25 - Wildenhof outcrop nr 27 - Interbedded vein

Incl. Nr	*T_f ice*	*T_m ice*	*Salinity*	*T_h tot*
1				128
2				169
3				240
4				193
5				151
6				128
7				131
8				138
9				171
10				139
11				125
12				178
13				230
14	-35.3	-3.52	5.74	199
15				180
16				128
17				106
18	-32.3	-3.72	6.04	189
19	-34	-3.62	5.89	158
20				143

Incl. Nr	*T_f ice*	*T_m ice*	*Salinity*	*T_h tot*
21				131
22				136
23				111
24				131
25				141
26				159
27				96
28				108
29				131
30				208
31				152
32				131
33				129
34				168
35				131
36				84
37				110
38				122
39				110
40				205

Incl. Nr	T_f ice	T_m ice	Salinity	T_h tot
41				215
42				230
43				220
44				184
45				151
46				300
47				120
48				98
49				160
50				235

Incl. Nr	T_f ice	T_m ice	Salinity	T_h tot
51				188
52				179
53				161
54				156
55				159
56				98
57				104
58				124
59				95

Sample EI05VN26 - Wildenhof outcrop nr 27 - Interbedded vein

Sample Wafer	Incl. Nr	T_f ice	T_m ice	Salinity	T_h tot	Type	Size (L / W) (µm)	Vol %
EI05VN26a (1)	1	-36.34	-1.86	3.17	291	pseudosec.	4.5 / 2.5	20
EI05VN26a (1)	2	-36.04	-3.65	5.93	155	pseudosec.	12 / 6	10
EI05VN26a (1)	2b	-37.73			208	pseudosec.		
EI05VN26a (1)	3		-3.85	6.22		pseudosec.	3 / 3	25
EI05VN26a (2)	4	-24.65	-			pseudosec.	8 / 5	35
EI05VN26a (2)	5	-34.36	-3.65	5.93	> 260	pseudosec.	5 / 2	10
EI05VN26a (2)	6		-2.76	4.58	166	pseudosec.	6 / 2	10
EI05VN26a (2)	7	-34.36	-			pseudosec.	4 / 4	20
EI05VN26a (2)	8	-38.32	-2.86	4.73		pseudosec.	11 / 4	10
EI05VN26a (2)	9	-34.36	-3.85	6.22	>>	pseudosec.	6 / 3	55
EI05VN26a (2)	10	-33.17	-3.05	5.04	189	pseudosec.	5 / 3	10
EI05VN26a (5)	11	-32.08	-2.46	4.12	148	sec.	5 / 3	10
EI05VN26a (5)	12	-33.57	-2.76	4.58	176	sec.	9 / 9	15
EI05VN26a (5)	13	-33.86	-2.86	4.73	251	pseudosec.	4 / 3	10
EI05VN26a (5)	14		-3.35	5.49	242	pseudosec.	5 / 2	15
EI05VN26a (5)	15	-37.03	-3.25	5.34	231	pseudosec.	4 / 2	10
EI05VN26a (5)	16	-33.96	-3.45	5.64	137	pseudosec.	8 / 3.5	10
EI05VN26a (5)	17	-34.06	-3.45	5.64	220	pseudosec.	7 / 4	10
EI05VN26a (5)	18	-33.37	-		157	pseudosec.	10 / 3	10
EI05VN26a (5)	19		-			pseudosec.	5 / 2	10
EI05VN26a (5)	20	-34.36	-3.45	5.64	>>	pseudosec.	5 / 3	10
EI05VN26a (5)	21	-33.76	-2.46	4.12	> 260	pseudosec.	4 / 2.5	35
EI05VN26a (5)	22	-34.36	-2.36	3.96	171	pseudosec.	5 / 4	10
EI05VN26a (5)	23	-34.26	-		192	pseudosec.	5 / 2	10
EI05VN26a (5)	24	-42.98	-2.76	4.58	156	pseudosec.	4 / 3	5
EI05VN26a (5)	25	-33.96	-		151	pseudosec.	5 / 2.5	10
EI05VN26a (5)	26	-35.25	-3.45	5.64	165	pseudosec.	7 / 3	10
EI05VN26a (5)	27	-33.37	-2.86	4.73	> 260	sec.	6 / 3	15
EI05VN26a (5)	28	-35.75	-3.45	5.64	148	sec.	5 / 2	10
EI05VN26a (5)	29	-35.15	-3.15	5.19	161	sec.	4.5 / 2	20
EI05VN26a (5)	30	-35.75	-3.65	5.93	125	sec.	4 / 1.5	15
EI05VN26a (5)	31	-33.67	-		156	sec.	4 / 3	10
EI05VN26a (5)	32	-34.26	-2.46	4.12		sec.	7 / 4	15
EI05VN26a (5)	33	-36.04	-2.86	4.73	199	sec.	7 / 2	10
EI05VN26a (5)	34		-2.26	3.80	214	sec.	5 / 3	20
EI05VN26a (5)	35	-34.56	-		205	pseudosec.	6 / 4	10
EI05VN26a (5)	36	-33.76	-2.46	4.12	226	pseudosec.	9 / 5	15
EI05VN26a (5)	37		-		221	pseudosec.	11 / 4	15
EI05VN26a (5)	38	-34.95	-2.46	4.12		sec.	4 / 3	10
EI05VN26a (5)	39	-32.18	-		151	sec.	5 / 3	10
EI05VN26a (5)	40	-35.25	-			sec.	7 / 3	10
EI05VN26a (5)	41a		-3.25	5.34	185	pseudosec.	6 / 6	10
EI05VN26a (5)	41b	-34.36	-3.35	5.49	235	pseudosec.	4 / 3.5	10
EI05VN26a (5)	42	-33.17	-3.05	5.04	195	pseudosec.	4 / 2	20
EI05VN26a (5)	43	-33.37	-2.95	4.89	182	pseudosec.	8 / 3	10
EI05VN26a (5)	44a		-		163	pseudosec.	4.5 / 2	10
EI05VN26a (5)	44b		-		151	pseudosec.	5 / 3	10
EI05VN26a (5)	44c	-33.86	-		215	pseudosec.	4 / 4	10
EI05VN26a (5)	45	-34.66	-			pseudosec.	14 / 4	30
EI05VN26a (5)	46	-33.57	-2.56	4.27		pseudosec.	6 / 3	15
EI05VN26a (5)	47	-37.03	-3.35	5.49	> 250	pseudosec.	6 / 3	20
EI05VN26a (5)	48	-35.15	-		240	pseudosec.	9 / 3	10
EI05VN26a (5)	49	-33.27	-2.66	4.43		pseudosec.	9 / 6	20
EI05VN26a (5)	50	-33.27	-		> 245	pseudosec.	4 / 2	20
EI05VN26a (5)	51				180	pseudosec.	7 / 2	10

Sample EI06VN10 - Wildenhof outcrop nr 42 - Intrabedded vein (slates)

Sample Wafer	*Incl. Nr*	*T_f ice*	*T_m ice*	*Salinity*	*T_h tot*	*Type*	*Size (L / W) (µm)*	*Vol %*
EI06VN10 (A)	1	-33.4	-1.7	2.90	128	pseudosec.		10
EI06VN10 (A)	2	-32.4	-0.7	1.22	114	pseudosec.		10
EI06VN10 (A)	3	-31.9	-1.7	2.90	134	pseudosec.		15
EI06VN10 (A)	4	-32.5	-0.7	1.22	112	pseudosec.		10
EI06VN10 (A)	5	-36.6	-2.1	3.55	113	pseudosec.		10
EI06VN10 (A)	6	-37.9	-1.6	2.74	118	pseudosec.		15
EI06VN10 (A)	7	-34.1	-2.8	4.65	121	pseudosec.		15
EI06VN10 (A)	8	-34.7	-0.4	0.70	116	pseudosec.		10
EI06VN10 (A)	9	-34.7	-0.5	0.88	129	pseudosec.		10
EI06VN10 (A)	10	-34.5	-1.9	3.23	140	pseudosec.		15
EI06VN10 (A)	11	-33.8	-3.1	5.11	169	pseudosec.		10
EI06VN10 (A)	12	-32.7	-2.9	4.80	126	pseudosec.		10
EI06VN10 (A)	13	-33.5	-2.9	4.80	133	pseudosec.		10
EI06VN10 (A)	14	-33.7	-1.9	3.23	119	pseudosec.		15
EI06VN10 (A)	15	-34.1	-1.1	1.91	117	pseudosec.		10
EI06VN10 (A)	16	-	-	-	80	pseudosec.		5
EI06VN10 (A)	17	-32.1	-1.5	2.57	123	pseudosec.		10
EI06VN10 (A)	18	-34.0	-2.6	4.34	125	pseudosec.		10
EI06VN10 (A)	19	-33.5	-3.5	5.71	161	pseudosec.		10
EI06VN10 (A)	20	-34.7	-2.8	4.65	137	pseudosec.		10
EI06VN10 (A)	21	-32.7	-3.6	5.86	150	pseudosec.		10
EI06VN10 (A)	22	-32.9	-	-	-	pseudosec.		10
EI06VN10 (A)	23	-36.2	-	-	104	pseudosec.		10
EI06VN10 (A)	24	-32.0	-0.8	1.40	114	pseudosec.		10
EI06VN10 (A)	25	-33.6	-0.5	0.88	110	pseudosec.		10
EI06VN10 (A)	26	-31.7	-1.2	2.07	122	pseudosec.		10
EI06VN10 (A)	27	-32.9	-0.5	0.88	105	pseudosec.		10
EI06VN10 (A)	28	-33.5	-	-	96	pseudosec.		10
EI06VN10 (A)	29	-32.7	-	-	105	pseudosec.		10
EI06VN10 (A)	30	-	-	-	-	pseudosec.		10
EI06VN10 (A)	31	-33.5	-1.0	1.74	104	pseudosec.		10
EI06VN10 (A)	32	-33.9	-0.3	0.53	106	pseudosec.		10
EI06VN10 (A)	33	-	-	-	98	pseudosec.		10
EI06VN10 (A)	34	-34.0	-0.4	0.70	148	pseudosec.		10
EI06VN10 (A)	34a	-	-	-	117	pseudosec.		10
EI06VN10 (A)	35	-34.0	-0.4	0.70	105	pseudosec.		10
EI06VN10 (A)	36	-33.5	-3.3	5.41	129	pseudosec.		10
EI06VN10 (A)	37	-32.0	-1.0	1.74	115	isolated		10
EI06VN10 (A)	38	-35.2	-0.6	1.05	118	isolated		15
EI06VN10 (A)	39	-33.0	-1.6	2.74	120	isolated		10
EI06VN10 (A)	40	-32.7	-	-	-	pseudosec.		15
EI06VN10 (A)	41	-34.5	-3.3	5.41	141	isolated		10
EI06VN10 (A)	42	-32.3	-2.9	4.80	172	pseudosec.		20
EI06VN10 (A)	43	-32.2	-2.9	4.80	127	pseudosec.		10
EI06VN10 (A)	44	-31.7	-3.0	4.96	112	pseudosec.		25
EI06VN10 (A)	45	-31.8	-3.0	4.96	145	pseudosec.		10
EI06VN10 (A2)	46	-33.2	-1.7	2.90	115	pseudosec.		10
EI06VN10 (A2)	47	-39.5	-1.0	1.74	144	pseudosec.		10
EI06VN10 (A2)	48	-34.6	-2.8	4.65	119	pseudosec.		10
EI06VN10 (A2)	49	-34.8	-3.2	5.26	145	pseudosec.		10
EI06VN10 (A2)	50	-	-	-	99	pseudosec.		10
EI06VN10 (A2)	51	-34.2	-3.2	5.26	186	pseudosec.		20
EI06VN10 (A2)	52	-35.5	-3.1	5.11	146	pseudosec.		10
EI06VN10 (A2)	53	-35.9	-3.6	5.86	139	pseudosec.		10
EI06VN10 (A2)	54	-34.9	-3.7	6.01	142	pseudosec.		10
EI06VN10 (B)	55	-34.7	-3.7	6.01	153	pseudosec.		10
EI06VN10 (B)	56	-35.1	-3.5	5.71	192	pseudosec.		10
EI06VN10 (B)	57	-34.1	-0.8	1.40	-	sec.		10
EI06VN10 (B)	58	-36.0	-3.9	6.30	145	sec.		10
EI06VN10 (B)	59	-35.4	-3.8	6.16	152	sec.		15
EI06VN10 (B)	60	-35.6	-1.6	2.74	-	pseudosec.		15
EI06VN10 (B)	61	-37.2	-3.8	6.16	166	pseudosec.		20
EI06VN10 (B)	62	-38.4	-3.5	5.71	-	pseudosec.		30
EI06VN10 (B)	63	-36.7	-3.2	5.26	140	pseudosec.		30
EI06VN10 (B)	64	-35.7	-3.6	5.86	136	pseudosec.		10

References

Ahrendt, H., Clauer, N., Hunziker, J.C. & Weber, K. 1983. Migration of Folding and Metamorphism in the Rheinisches Schiefergebirge deduced from K-Ar and Rb-Sr Age Determinations. In: *Intracontinental Fold Belts. Case Studies in the Variscan Belt of Europe and the Damara Belt in Namibia* (edited by Martin, H. & Eder, F.W.), Heidelberg, Springer, 323-338.

Anderson, E.M. 1951. *The dynamics of Faulting and Dyke Formation with Application to Britain*. Oliver and Boyd, Edinburgh, 206p.

André-Mayer, A.-S. & Sausse, J. 2007. Thickness and spatial distribution of veins in a porphyry copper deposit, Rosia Poieni, Romania. *Journal of Structural Geology* **29**, 1695-1708.

Asselberghs, E. 1946. L'Eodévonien de l'Ardenne et des régions voisines. *Mémoires de l'Institut géologique de l'Université de Louvain* **14**, 1-598.

Asselberghs, E., Henke, W., Schriel, W. & Wünstorf, W. 1936. Über eine gemeinsame Exkursion durch die Siegener Schichten des Rheinischen Schiefergebirges und der Ardennen. *Jahrbuch der preußischen geologischen Landesanstalt* **56**, 324-370.

Atkinson, B.K. 1984. Subcritical crack growth in geological materials. *Journal of Geophysical Research* **89**, 4077-4114.

Bai, T. & Pollard, D.D. 1999. Spacing of fractures in a multilayer at fracture saturation. *International Journal of Fracture* **100**, 23-28.

Bai, T. & Pollard, D.D. 2000a. Closely spaced fractures in layered rocks: initiation mechanism and propagation kinematics. *Journal of Structural Geology* **22**, 1409-1425.

Bai, T. & Pollard, D.D. 2000b. Fracture spacing in layered rocks: a new explanation based on the stress transition. *Journal of Structural Geology* **22**, 43-57.

Barker, C.E. & Pawlewicz, M.J. 1994. Calculation of vitrinite reflectance from thermal histories and peak temperatures. A comparison of methods. In: *Vitrinite Reflectance as a Maturity Parameter* (edited by Mukhopadhyay, P.K. & Dow, W.G.). *ACS Symposium series* **570**, 216-229.

Bassett, M.G. 1985. Towards a "common language" in stratigraphy. *Episodes* **8**, 87-92.

Baum, F. 1955. Tektonische untersuchungen am westrand der Eifeler nord-süd-zone zwischen Untermaubach und Heimbach. *Geologische Rundschau* **44**, 148-167.

Berwouts, I. 2011. *Reconstruction of fluid system evolution in a wrench tectonic setting. Implications for the geodynamic history of Central Armorica, Brittany, France*. Aardkundige mededelingen 26, 251p.

Berwouts, I., Van Noorden, M., Muchez, Ph., Boyce, A.J. & Sintubin, M. 2008. Inferring intermediate-scale fluid flow in a heterogeneous metasedimentary multilayer sequence during progressive deformation: evidence from the Monts d'Arrée slate belt (Brittany, France). *Geofluids* **8**, 143-158.

Beugnies, A. 1986. Le métamorphisme de l'aire anticlinale de l'Ardenne. *Hercynica* **2**, 17-33.

Blenkinsop, T. 2000. *Deformation Microstructures and Mechanisms in Minerals and Rocks*. Kluwer Academic Publishers, Dordrecht, The Netherlands.

Blundell, D.J. 2002. The timing and location of major ore deposits in an evolving orogen: the geodynamic context. *Geological Society, London, Special Publications* **204**, 1-12.

Bodnar, R.J. 1993. Revised equation and table for determining the freezing point depression of H_2O-NaCl solutions. *Geochimica et Cosmochimica Acta* **57**, 683-684.

Bodnar, R.J. 2003. Reequilibration of fluid inclusions. In: *Fluid Inclusions: Analysis and Interpretation* (edited by Samson, I., Anderson, A. & Marshall, D.). *Mineralogical Association of Canada, Short Course* **32**, 213-231.

Bodnar, R.J., Binns, P.R. & Hall, D.L. 1989. Synthetic fluid inclusions. VI. Quantitative evaluation of the decrepitation behavior of fluid inclusions in quartz at one atmosphere confining pressure. *Journal of Metamorphic Geology* **7**, 229-242.

Bons, P.D. 2000. The formation of veins and their microstructures. In: *Stress, Strain and Structure. A volume in honour of W.D. Means* (edited by Jessell, M.W. & Urai, J.L.). *Journal of the Virtual Explorer* **2**.

Bons, P.D. 2001. The formation of large quartz veins by rapid ascent of fluids in mobile hydrofractures. *Tectonophysics* **336**, 1-17.

Bostick, N., Cashman, S., McCulloh, T. & Waddell, C. 1979. Gradients of vitrinite reflectance and present temperature in the Los Angeles and Ventura Basins, California. In: *Low Temperature Metamorphism of Kerogen and Clay Minerals* (edited by Oltz, D.F.). *Society of Economic Paleontologists and Mineralogists*, Los Angeles, 65-96.

Boullier, A.-M. & Robert, F. 1992. Palaeoseismic events recorded in Archaean gold-quartz vein networks, Val d'Or, Abitibi, Quebec, Canada. *Journal of Structural Geology* **14**, 161-179.

Boullier, A.M., France-Lanord, C., Dubessy, J. & Champenois, M. 1991. Linked fluid and tectonic evolution in the High Himalaya Mountains (Nepal). *Contributions to Mineralogy and Petrology* **107**, 358-372.

Bradley, J.S. & Powley, D.E. 1994. Pressure compartments in sedimentary basins: a review. In: *Basin compartments and seals* (edited by Ortoleva, P.). *AAPG Memoir* **61**, 3-26.

Breddin, H. 1930. Milchquarzgänge des Rheinischen Schiefergebirges, einen Nebenerscheinung der Druckschieferung. *Geologische Rundschau* **21**, 367-388.

Breddin, H. 1963. Über die neue "Geologische Karte der nördlichen Eifel 1:100 000 (Hochschulumgebungskarte Aachen)" des Geologischen Landesamtes von Nordrhein-Westfalen. *Geologische Mitteilungen* **3**, 139-142.

Breddin, H. & Hellermann, E. 1962. Petrogene Mineralgänge im Palaözoikum der Nordeifel und ihre Beziehungen zur inneren Deformation der Gesteine. *Geologische Mitteilungen* **2**, 197-224.

Brems, D., Muchez, Ph., Sikazwe, O. & Mukumba, W. 2009. Metallogenesis of the Nkana copper-cobalt South Orebody, Zambia. *Journal of African Earth Sciences* **55**, 185-196.

Brown, E.B. 1989. FLINCOR: a microcomputer program for the reduction and investigation of fluid inclusion data. *American Mineralogist* **74**, 1390-1393.

Brown, P.E. & Lamb, W.M. 1989. P-V-T properties of fluids in the system $H_2O \pm CO_2 \pm NaCl$: New graphical presentations and implications for fluid inclusion studies. *Geochimica et Cosmochimica Acta* **53**, 1209-1221.

Bultynck, P., Coen-Aubert, M. & Godefroid, J. 2000. Summary of the state of correlation in the Devonian of the Ardennes (Belgium-NE France) resulting from the decisions of the SDS. *Courier Forschungsinstitut Senckenberg* **225**, 91-114.

Bultynck, P. & Dejonghe, L. 2001. Devonian lithostratigraphic units (Belgium). *Geologica Belgica* **4**, 39-69.

Caputo, R. & Hancock, P.L. 1999. Crack-jump mechanism and its implications for stress cyclicity during extension fracturing. *Journal of Geodynamics* **27**, 45-60.

Cervantes, P. & Wiltschko, D.V. 2010. Tip to midpoint observations on syntectonic veins, Ouachita orogen, Arkansas: Trading space for time. *Journal of Structural Geology* **32**, 1085-1100.

Chenevert, M.E. & Gatlin, C. 1965. Mechanical anisotropies of laminated sedimentary rocks. *Society of Petroleum Engineers* **5**, 67-77.

Choquette, S.J., Etz, E.S., Hurst, W.S., Blackburn, D.H. & Leigh, S.D. 2007. Relative intensity correction of Raman spectrometers: NIST SRMs 2241 through 2243 for 785 nm, 532 nm, and 488 nm/514.5 nm excitation. *Applied Spectroscopy* **61**, 117-129.

Clark, M.B., Brantley, S.L. & Fisher, D.M. 1995. Power-law vein-thickness distributions and positive feedback in vein growth. *Geology* **23**, 975-978.

Cobbold, P.R. & Rodrigues, N. 2007. Seepage forces, important factors in the formation of horizontal fractures and bedding-parallel fibrous veins ('beef' and 'cone-in-cone'). *Geofluids* **7**, 313-322.

Collettini, C., De Paola, N. & Goulty, N.R. 2006. Switches in the minimum compressive stress direction induced by overpressure beneath a low-permeability fault zone. *Terra Nova* **18**, 224-231.

Cooke, M.L. & Pollard, D.D. 1997. Bedding-plane slip in initial stages of fault-related folding. *Journal of Structural Geology* **3-4**, 567-581.

Cooke, M.L., Simo, J.A., Underwood, C.A. & Rijken, P. 2006. Mechanical stratigraphic controls on fracture patterns within carbonates and implications for groundwater flow. *Sedimentary Geology* **184**, 225-239.

Cooper, M.A., Williams, G.D., de Graciansky, P.C., Murphy, R.W., Needham, T., de Paor, D., Stoneley, R., Todd, S.P., Turner, J.P. & Ziegler, P.A. 1989. Inversion tectonics - a discussion. In: *Inversion Tectonics* (edited by Cooper, M.A. & Williams, G.D.). *Geological Society, London, Special Publications* **44**, 335-347.

Cosgrove, J.W. 1993. The interplay between fluids, folds and thrusts during the deformation of a sedimentary succession. *Journal of Structural Geology* **15**, 491-500.

Cosgrove, J.W. 1995a. The expression of hydraulic fracturing in rocks and sediments. In: *Fractography: fracture topography as a tool in fracture mechanics and stress analysis* (edited by Ameen, M.S.). *Geological Society, London, Special Publications* **92**, 187-196.

Cosgrove, J.W. 1995b. The interplay between fluids, folds and thrusts during the deformation of a sedimentary succession: Discussion. *Journal of Structural Geology* **10**, 1478-1480.

Cosgrove, J.W. 1997. Hydraulic fractures and their implications regarding the state of stress in a sedimentary sequence during burial. In: *Evolution of Geological Structures in Micro- to Macro-scales* (edited by Sengupta, S.). *Chapman & Hall*, London, 11-25.

Cosgrove, J.W. 2001. Hydraulic fracturing during the formation and deformation of a basin: A factor in the dewatering of low-permeability sediments. *AAPG Bulletin* **85**, 737-748.

Cowie, P.A., Knipe, R.J. & Main, I.G. 1996. Introduction to the special issue. Scaling laws for fault and fracture populations - analyses and applications. *Journal of Structural Geology* **18**, v-vi.

Cox, S.F. 1987. Antitaxial crack-seal vein microstructures and their relationship to displacement paths. *Journal of Structural Geology* **9**, 779-787.

Cox, S.F. 1995. Faulting processes at high fluid pressures: An example of fault valve behavior from the Wattle Gully Fault, Victoria, Australia. *Journal of Geophysical Research* **100**, 12 841 - 12 859.

Cox, S.F. 2010. The application of failure mode diagrams for exploring the roles of fluid pressure and stress states in controlling styles of fracture-controlled permeability enhancement in fault and shear zones. *Geofluids* **10**, 217-233.

Cox, S.F. & Etheridge, M.A. 1983. Crack-seal fibre growth mechanisms and their significance in the development of oriented layer silicate microstructures. *Tectonophysics* **92**, 147-170.

Cox, S.F., Knackstedt, M.A. & Braun, J. 2001. Principles of Structural Control on Permeability and Fluid Flow in Hydrothermal Systems. In: *Structural Controls on Ore Genesis*. *Reviews in Economic Geology*. *Society of Economic Geology* **14**, Boulder, 1-24.

Cox, S.F. & Paterson, L. 1989. Tensile fracture of heterogeneous solids with distributed breaking strengths. *Physical Review B* **40**.

Cox, S.F., Sun, S.S., Etheridge, M.A., Wall, V.J. & Potter, T.F. 1995. Structural and geochemical controls on the development of turbidite-hosted gold quartz vein deposits, Wattle Gully mine, central Victoria, Australia. *Economic Geology* **90**, 1722- 1746.

Crespi, J.M. & Chan, Y.-C. 1996. Vein reactivation and complex vein intersection geometries in the Taconic Slate Belt. *Journal of Structural Geology* **18**, 933-939.

Crispini, L. & Frezzotti, M.-L. 1998. Fluid inclusion evidence for progressive folding during decompression in metasediments of the Voltri Group (Western Alps, Italy). *Journal of Structural Geology* **20**, 1733-1746.

Cundall, P.A. & Hart, R.D. 1992. Numerical Modelling of discontinua. *Engineering Computations* **9**, 101-113.

Darimont, A. 1986. Les inclusions fluides de quartz filoniens d'Ardenne. *Annales de la Société géologique de Belgique* **109**, 587-601.

Darimont, A., Burke, E.A.J. & Touret, J.L.R. 1988. Nitrogen-rich metamorphic fluids in devonian metasediments from Bastogne, Belgium. *Bulletin de Minéralogie* **111**, 321-330.

De Clercq, F., Muchez, Ph., Dewaele, S. & Boyce, A.J. 2008. The tungsten mineralisation at Nyakabingo and Gifurwe (Rwanda): Preliminary results. *Geologica Belgica* **11**, 251-258.

de Joussineau, G. & Petit, J.-P. 2007. Can tensile stress develop in fractured multilayers under compressive strain conditions? *Tectonophysics* **432**, 51-62.

de Roo, J.A. & Weber, K. 1992. Laminated veins and hydrothermal breccia as markers of low-angle faulting, Rhenish Massif, Germany. *Tectonophysics* **208**, 413-430.

Debacker, T.N., Dewaele, S., Sintubin, M., Verniers, J., Muchez, Ph. & Boven, A. 2005. Timing and duration of the progressive deformation of the Brabant Massif, Belgium. *Geologica Belgica* **8**, 20-34.

Debacker, T.N., Dumon, M. & Matthys, A. 2009. Interpreting fold and fault geometries from within the lateral to oblique parts of slumps: A case study from the Anglo-Brabant Deformation Belt (Belgium). *Journal of Structural Geology* **31**, 1525-1539.

Debacker, T.N., van Noorden, M. & Sintubin, M. 2006. Distinguishing syn-cleavage folds from pre-cleavage folds to which cleavage is virtually axial planar: examples from the Cambrian core of the Lower Palaeozoic Anglo-Brabant Deformation Belt (Belgium). *Journal of Structural Geology* **28**, 1123-1138.

DEKORP. 1991. Results of the DEKORP 1 (BELCORP-DEKORP) deep seismic reflection studies in the western part of the Rhenish Massif. *Geophysical Journal International* **106**, 203-227.

Dewaele, S., De Clercq, F., Muchez, Ph., Schneider, J., Burgess, R., Boyce, A.J. & Fernandez-Alonso, M. 2010. Geology of the cassiterite mineralisation in the Rutongo area, Rwanda (Central Africa): Current state of knowledge. *Geologica Belgica* **13**, 91-112.

Dittmar, D., Meyer, W., Oncken, O., Schievenbusch, T., Walter, R. & von Winterfeld, C. 1994. Strain partitioning across a fold and thrust belt: the Rhenish Massif, Mid-European Variscides. *Journal of Structural Geology* **16**, 1335-1352.

Dubessy, J., Poty, B. & Ramboz, C. 1989. Advances in C-O-H-N-S fluid geochemistry based on micro-Raman spectrometric analyses on fluid inclusions. *European Journal of Mineralogy* **1**, 517-534.

Durney, D.W. & Ramsay, J.G. 1973. Incremental strains measured by syntectonic crystal growths. In: *Gravity and Tectonics* (edited by de Jong, K.A. & Scholten, R.), Wiley, New York, 67-96.

Duyster, J. 2000. StereoNett Version 2.46. Ruhr Universität, Bochum, Germany.

Elburg, M.A., Bons, P.D., Foden, J. & Passchier, C.W. 2002. The origin of fibrous veins: constraints from geochemistry. In: *Deformation Mechanisms, Rheology and Tectonics: Current Status and Future Perspectives* (edited by De Meer, S., Drury, M.R., de Bresser, J.H.P. & Pennock, G.). *Geological Society, London, Special Publications* **200**, 103-118.

Engelder, T., Gross, M.R. & Pinkerton, P. 1997. An Analysis of Joint Development in Thick Sandstone Beds of the Elk Basin anticline, Montana-Wyoming. In: *Fractured Reservoirs: Characterization and Modeling* (edited by Hoak, T., Klawitter, A. & Blomquist, P.). *Rocky Mountain Association of Geologists 1997 Guidebook*, Denver, Colorado, 1-18.

Etheridge, M.A. 1983. Differential stress magnitudes during regional deformation and metamorphism: Upper bound imposed by tensile fracturing. *Geology* **11**, 231-234.

Etheridge, M.A., Wall, V.J. & Cox, S.F. 1984. High fluid pressures during regional metamorphism and deformation: implications for mass transport and deformation mechanisms. *Journal of Geophysical Research* **89**, 4344-4358.

Evans, M.A. 1995. Fluid inclusions in veins from the Middle Devonian shales: A record of deformation conditions and fluid evolution in the Appalachian Plateau.

Geological Society of America Bulletin **107**, 327-339.

Fagereng, A., Remitti, F. & Sibson, R.H. 2010. Shear veins observed within anisotropic fabric at high angles to the maximum compressive stress. *Nature Geoscience* **3**, 482-485.

Fielitz, W. 1987. Schieferung und Ausmass der Innendeformation der paläozoischen Gesteine am Südost-Rand des Stavelot-Venn-Antiklinoriums in der Nordeifel (Rheinisches Schiefergebirge). Unpublished Ph.D. thesis, RWTH Aachen.

Fielitz, W. 1992. Variscan transpressive inversion in the northwestern central Rhenohercynian belt of western Germany. *Journal of Structural Geology* **14**, 547-563.

Fielitz, W. 1995. Epizonal to lower mesozonal diastathermal metamorphism in the Ardennes (Rhenohercynian belt of western central Europe). *Terra Nostra* **95**, 95.

Fielitz, W. 1997. Inversion tectonics and diastathermal metamorphism in the Serpont Massif area of the Variscan Ardenne (Belgium). *Aardkundige Mededelingen* **8**, 79-82.

Fielitz, W. & Mansy, J.-L. 1999. Pre- and synorogenic burial metamorphism in the Ardenne and neighbouring areas (Rhenohercynian zone, central European Variscides). *Tectonophysics* **309**, 227-256.

Fieremans, M. 1982. Sedimentologie, tektoniek en metamorfose van het Gedinniaan langs de zuidrand van het Massief van Stavelot, PhD Thesis, Katholieke Universiteit Leuven, 166p.

Fischer, M.P., Gross, M.R., Engelder, T. & Greenfield, R.J. 1995. Finite-element analysis of the stress distribution around a pressurized crack in a layered elastic medium: implications for the spacing of fluid-driven joints in bedded sedimentary rock. *Tectonophysics* **247**, 49-64.

Fisher, D.M. & Brantley, S.L. 1992. Models of quartz overgrowth and vein formation: deformation and episodic fluid flow in an ancient subduction zone. *Journal of Geophysical Research* **97**, 20043-20061.

Fisher, D.M., Brantley, S.L., Everett, M. & Dzvonik, J. 1995. Cyclic fluid flow through a regionally extensive fracture network within the Kodiak accretionary prism. *Journal of Geophysical Research* **100**, 12881-12894.

Fisher, D.M. & Byrne, T. 1990. The character and distribution of mineralized fractures in the Kodiak Formation, Alaska: Implications for fluid flow in an underthrust sequence. *Journal of Geophysical Research* **95**, 9069-9080.

Fitches, W.R., Cave, R., Craig, J. & Maltman, A.J. 1986. Early veins as evidence of detachment in the Lower Palaeozoic rocks of the Welsh Basin. *Journal of Structural Geology* **8**, 607-620.

Fitches, W.R., Cave, R., Craig, J. & Maltman, A.J. 1990. The flexural-slip mechanism: Discussion. *Journal of Structural Geology* **12**, 1081-1087.

Fowler, T.J. 1996. Flexural-slip generated bedding-parallel veins from central Victoria, Australia. *Journal of Structural Geology* **18**, 1399-1415.

Fowler, T.J. & Winsor, C.N. 1997. Characteristics and occurrence of bedding-parallel slip surfaces and laminated veins in chevron folds from the Bendigo-Castlemaine goldfields: implications for flexural-slip folding. *Journal of Structural Geology* **19**, 799-815.

Foxford, K.A., Nicholson, R., Polya, D.A. & Hebblethwaite, R.P.B. 2000. Extensional failure and hydraulic valving at Minas da Panasqueira, Portugal: evidence from vein spatial distributions, displacements and geometries. *Journal of Structural Geology* **22**, 1065-1086.

Franke, W. 2000. The mid-European segment of the Variscides: tectonostratigraphic units, terrane boundaries and plate tectonic evolution. In: *Orogenic processes: Quantification and modelling in the Variscan Belt* (edited by Franke, W., Haak, V., Oncken, O. & Tanner, D.). *Geological Society, London, Special Publications* **179**, 35-61.

Fransolet, A.-M. 1978. Données nouvelles sur l'ottrélite d'Ottré, Belgique. *Bulletin Minéralogique* **101**, 548-557.

Frey, M. & Robinson, D. 1999. *Low-grade metamorphism*. Blackwell Science, Oxford.

Furtak, H. 1965. Die Tektonik der unterdevonischen Gesteinsfolgen in deutsch-belgisch-luxemburgischen Grenzgebiet. Unpublished Ph.D. thesis, RWTH Aachen.

Gale, J.F.W., Reed, R.M. & Holder, J. 2007. Natural fractures in the Barnett Shale and their importance for hydraulic fracture treatments. *AAPG Bulletin* **91**, 603-622.

Garcia-Castellanos, D., Cloetingh, S. & Van Balen, R. 2000. Modelling the Middle Pleistocene uplift in the Ardennes-Rhenish Massif: thermo-mechanical weakening under the Eifel? *Global and Planetary Change* **27**, 39-52.

Geukens, F. 1999. Notes accompagnant une révision de la carte structurale du Massif de Stavelot. *Aardkundige Mededelingen* **9**, 183-199.

Ghosh, S.K. & Sengupta, S. 1999. Boudinage and composite boudinage in superposed deformations and syntectonic migmatization. *Journal of Structural Geology* **21**, 97-110.

Gillespie, P. 2003. Comment on "The geometric and statistical evolution of normal fault systems: an experimental study of the effects of mechanical layer thickness on scaling laws" by R.V. Ackermann, R.W. Schlische and M.O. Withjack. *Journal of Structural Geology* **25**, 819-822.

Gillespie, P.A., Johnston, J.D., Loriga, M.A., McCaffrey, K.J.W., Walsh, J.J. & Watterson, J. 1999. Influence of layering on vein systematics in line samples. In: *Fractures, Fluid Flow and Mineralisation* (edited by McCaffrey, K.J.W., Lonergan, L. & Wilkinson, J.J.). *Geological Society, London, Special Publications* **155**, 35-56.

Gillespie, P.A., Walsh, J.J., Watterson, J., Bonson, C.G. & Manzocchi, T. 2001. Scaling relationships of joint and vein arrays from The Burren, Co. Clare, Ireland. *Journal of Structural Geology* **23**, 183-201.

Glen, R.A., Hancock, P.L. & Whittaker, A. 2005. Basin inversion by distributed deformation: the southern margin of the Bristol Channel Basin, England. *Journal of Structural Geology* **27**, 2113-2134.

Goemaere, E. & Dejonghe, L. 2005. Paleoenvironment reconstruction of the Mirwart Formation (Pragian) in the Lambert quarry (Flamierge, Ardenne, Belgium). *Geologica Belgica* **8**, 37-52.

Goldstein, R.H. & Reynolds, T.J. 1994. Systematics of fluid inclusions in diagenetic minerals. In: *Society for Sedimentary Geology, Short Course 31. 199 p.*

Goscombe, B.D., Passchier, C.W. & Hand, M. 2004. Boudinage classification: end-member boudin types and modified boudin structures. *Journal of Structural Geology* **26**, 739-763.

Gross, M.R. 1993. The origin and spacing of cross joints: examples from the Monterey Formation, Santa Barbara Coastline, California. *Journal of Structural Geology* **15**, 737-751.

Han, G., Yans, J., Goudalier, M., Lacquement, F., Corfield, R.M., Mansy, J.-L., Boulvain, F. & Préat, A. 2003. Recognition and implication of tectonic loading-influences reheating in the northern Variscan front (Belgium and northern France), based on illite Kübler index and oxygen isotope study. *International Journal of Earth Sciences (Geologische Rundschau)* **92**, 348-363.

Hance, L., Ghysel, P., Laloux, M., Dejonghe, L. & Mansy, J.-L. 1999. Influence of a heterogeneous lithostructural layering on orogenic deformation of the Variscan Front Zone (eastern Belgium). *Tectonophysics* **309**, 161-177.

Hanor, J.S. 1994. Origin of saline fluids in sedimentary basins. *Geological Society, London, Special Publications* **78**, 151-174.

Harris, J.F., Taylor, G.L. & Walper, J.L. 1960. Relation of deformational fractures in sedimentary rocks to regional and local structures. *American Association of Petroleum Geologists, Bulletin* **44**, 1853-1873.

Haynes, F.M. 1985. Determination of fluid inclusion compositions by sequential freezing. *Economic Geology* **80**, 1436-1439.

Hayward, A.B. & Graham, R.H. 1989. Some geometrical characteristics of inversion. In: *Inversion Tectonics* (edited by Cooper, M.A. & Williams, G.D.). *Geological Society, London, Special Publications* **44**, 17-39.

Healy, D. 2009. Anisotropy, pore fluid pressure and low angle normal faults. *Journal of Structural Geology* **31**, 561-574.

Heinen, V. 1996. *Simulation der präorogen devonisch-unterkarbonischen Bechenuntwicklung und Krustenstruktur im Linksrheinischen Schiefergebirge*. Aachen geowissenschaftliche Beiträge **15**, RWTH Aachen. 161p.

Helsen, S. 1995. Burial history of Palaeozoic strata in Belgium as revealed by conodont colour alteration data and thickness distributions. *Geologische Rundschau* **84**, 738-747.

Henderson, J.R., Henderson, M.N. & Wright, T.O. 1990. Water-sill hypothesis for the origin of certain veins in the Meguma Group, Nova Scotia, Canada. *Geology* **18**, 654-657.

Henk, A. 1999. Did the Variscides collapse or were they torn apart?: A quantitative evaluation of the driving forces for postconvergent extension in central Europe. *Tectonics* **18**, 774-792.

Hilgers, C., Bücker, C. & Urai, J.L. 2006a. Fossil overpressures compartments? A case study from the Eifel area and some general aspects. In: *Symposium "Tektonik, Struktur- und Kristallingeologie"* (edited by Phillipp, S., Leiss, B., Vollbrecht, A., Tanner, D. & Gudmundsson, A.). *Universitätsdrucke Göttingen* **11**, Göttingen, Germany, 87-89.

Hilgers, C., Bücker, C., Urai, J.L., Littke, R., Post, A., van der Zee, W. & Kraus, J. 2000. Field study of an exhumed lower Devonian high pressure reservoir. *Geophysical Research Abstracts* **2**, 47.

Hilgers, C., Kirschner, D.L., Breton, J.-P. & Urai, J.L. 2006b. Fracture sealing and fluid overpressures in limestones of the Jabal Akhdar dome, Oman mountains. *Geofluids* **6**, 168-184.

Hilgers, C., Koehn, D., Bons, P.D. & Urai, J.L. 2001. Development of crystal morphology during unitaxial growth in a progressively widening vein: II. Numerical simulations of the evolution of antitaxial fibrous veins. *Journal of Structural Geology* **23**, 873-885.

Hilgers, C., Nollet, S., Schoenherr, J. & Urai, J.L. 2006c. Paleo-overpressure formation and dissipation in reservoir rocks. *OIL GAS European Magazine* **122**, 68-73.

Hilgers, C. & Tenthorey, E. 2004. Fracture sealing of quartzite under a temperature gradient: experimental results. *Terra Nova* **16**, 173-178.

Hilgers, C. & Urai, J.L. 2002. Microstructural observations on natural syntectonic fibrous veins: implications for the growth process. *Tectonophysics* **352**, 257-274.

Hilgers, C. & Urai, J.L. 2005. On the arrangement of solid inclusions in fibrous veins and the role of the crack-seal mechanism. *Journal of Structural Geology* **27**, 481-494.

Hillis, R.R. 2003. Pore pressure/stress coupling and its implications for rock failure. In: *Subsurface Sediment Mobilization* (edited by Van Rensbergen, P., Hillis, R.R., Maltman, A.J. & Morley, C.K.). *Geological Society, London, Special Publications* **216**, 359-368.

Hirth, G. & Tullis, J. 1992. Dislocation creep regimes in quartz aggregates. *Journal of Structural Geology* **14**, 145-159.

Hobbs, D.W. 1967. The formation of tension joints in sedimentary rocks: an explanation. *Geological Magazine* **104**, 550-556.

Hoffmann, K. 1961. Die Tektonik am Südrand des Hohen Venns. *Neues Jahrbuch für Geologie und Paläontologie, Abhandlungen* **111**, 341-367.

Holcombe, R.J. 2004. GEOrient Version 9.2. University of Queensland, Queensland, Australia.

Holder, M.T. & Leveridge, B.E. 1986. Correlation of the Rhenohercynian Variscides. *Journal of the Geological Society, London* **143**, 141-147.

Holland, M., Urai, J.L., Muchez, Ph. & Willemse, E.J.M. 2009. Evolution of fractures in a highly dynamic thermal, hydraulic, and mechanical system – (I) Field observations in Mesozoic Carbonates, Jabal Shams, Oman Mountains. *GeoArabia* **14**, 57-110.

Holland, M., Urai, J.L., van der Zee, W., Stanjek, H. & Konstanty, J. 2006. Fault gouge evolution in highly overconsolidated claystones. *Journal of Structural Geology* **28**, 323-332.

Hood, A., Gutjar, C.C.M. & Heacock, R.L. 1975. Organic metamorphism and the generation of petroleum. *American Association of Petroleum Geologists, Bulletin* **59**, 986-996.

Horne, R. & Culshaw, N. 2001. Flexural-slip folding in the Meguma Group, Nova Scotia, Canada. *Journal of Structural Geology* **23**, 1631-1652.

Huang, Q. & Angelier, J. 1989. Fracture spacing and its relation to bed thickness. *Geological Magazine* **126**, 335-362.

Imber, J., Tuckwell, G.W., Childs, C., Walsh, J.J., Manzocchi, T., Heath, A.E., Bonson, C.G. & Strand, J. 2004. Three-dimensional distinct element modelling of relay growth and breaching along normal faults. *Journal of Structural Geology* **26**, 1897-1911.

Jackson, R.R. 1991. Vein arrays and their relationship to transpression during fold development in the Culm Basin, central south-west England. *Proceedings of the Ussher Society* **7**, 356-362.

Jessell, M.W., Willman, C.E. & Gray, D.R. 1994. Bedding parallel veins and their relationship to folding. *Journal of Structural Geology* **16**, 753-767.

Ji, S. & Saruwatari, K. 1998. A revised model for the relationship between joint spacing and layer thickness. *Journal of Structural Geology* **20**, 1495-1508.

Ji, S., Zhu, Z. & Wang, Z. 1998. Relationship between joint spacing and bed thickness in sedimentary rocks; effects of interbed slip **135**, 637-655.

Jia, Y., Li, X. & Kerrich, R. 2000. A Fluid Inclusion Study of Au-Bearing Quartz Vein Systems in the Central and North Deborah Deposits of the Bendigo Gold Field, Central Victoria, Australia. *Economic geology* **95**, 467-494.

Johnston, J.D. & McCaffrey, K.J.W. 1996. Fractal geometries of vein systems and the variation of scaling relationships with mechanism. *Journal of Structural Geology* **18**, 349-358.

Jongmans, D. & Cosgrove, J.W. 1993. Observations structurales dans la région de Bastogne. *Annales de la Société géologique de Belgique* **116**, 129-136.

Kenis, I. 2004. *Brittle-Ductile Deformation Behaviour in the Middle Crust as Exemplified by Mullions (Former "Boudins") in the High-Ardenne Slate Belt, Belgium*. Aardkundige mededelingen 14, Leuven University Press.

Kenis, I., Muchez, Ph., Sintubin, M., Mansy, J.-L. & Lacquement, F. 2000. The use of a combined structural, stable isotopic and fluid inclusion study to constrain the kinematic history at the northern Variscan front zone (Bettrechies, France). *Journal of Structural Geology* **22**, 598-602.

Kenis, I., Muchez, Ph., Verhaert, G., Boyce, A.J. & Sintubin, M. 2005a. Fluid evolution during burial and Variscan deformation in the Lower Devonian rocks of the High-Ardenne slate belt (Belgium): sources and causes of high-salinity and C-O-H-N fluids. *Contributions to Mineralogy and Petrology* **150**, 102-118.

Kenis, I. & Sintubin, M. 2007. About boudins and mullions in the Ardenne-Eifel area (Belgium, Germany). *Geologica Belgica* **10**, 79-91.

Kenis, I., Sintubin, M., Muchez, Ph. & Burke, E.A.J. 2002a. The "boudinage" question in the High-Ardenne Slate Belt (Belgium): a combined structural and fluid-inclusion approach. *Tectonophysics* **348**, 93-110.

Kenis, I., Sintubin, M., Muchez, Ph., Urai, J.L., Verhaert, G. & van der Zee, W. 2002b. "Boudins" in the High-Ardenne slate belt (Belgium): The state of the art. In: *Contributions to the Geology of Belgium and Northwest Europe* (edited by Degryse, P. & Sintubin, M.). *Leuven University Press*, Leuven, 169-172.

Kenis, I., Urai, J.L., van der Zee, W., Hilgers, C. & Sintubin, M. 2005b. Rheology of fine-grained siliciclastic rocks in the middle crust - evidence from structural and numerical analysis. *Earth and Planetary Science Letters* **233**, 351-360.

Kenis, I., Urai, J.L., van der Zee, W. & Sintubin, M. 2004. Mullions in the High-Ardenne Slate Belt (Belgium): numerical model and parameter sensitivity analysis. *Journal of Structural Geology* **26**, 1677-1692.

Kerrich, R. 1976. Some effects of tectonic recrystallisation on fluid inclusions in vein quartz. *Contributions to Mineralogy and Petrology* **59**, 195-202.

Kerrich, R., Beckinsdale, R. & Shackleton, N. 1978. The physical and hydrothermal regime of tectonic vein systems: Evidence from stable isotope and fluid inclusion studies. *Neues Jahrbuch für Mineralogie - Abhandlungen* **131**, 225-239.

Kisters, A.F.M. 2005. Controls of gold-quartz vein formation during regional folding in amphibolite-facies, marble-dominated metasediments of the Navachab Gold Mine in the Pan-African Damara Belt, Namibia. *South African Journal of Geology* **108**, 365-380.

Knapp, G. 1962. Der varistische Gebirgsbau im Bereich der Oleftalsperre (Eifel). *Geologische Jahrbuch* **79**, 399-422.

Knapp, G. 1980. Erläuterungen zur Geologischen Karte der nördlichen Eifel 1 : 100000, Krefeld.

Koehn, D. & Passchier, C.W. 2000. Shear sense indicators in striped bedding-veins. *Journal of Structural Geology* **22**, 1141-1151.

Kramm, U. & Buhl, D. 1985. U-Pb zircon dating of the Hill tonalite, Venn-Stavelot-Massif, Ardennes. *N. Jb. Geol. Paläont. Abh.* **171**, 329-337.

Kramm, U., Spaeth, G. & Wolf, M. 1985. Variscan metamorphism in the NE Stavelot-Venn Massif, Ardennes: a new approach to the question of regional dynamothermal or contact metamorphism. *Neues Jahrbuch für Geologie und Paläontologie - Abhandlungen* **171**, 311-327.

Kukla, P., Walter, R. & Becker, S. 2008. A geological traverse through the North Eifel. In: *Geo 2008 Excursion Guide. "Resources and Risks in the Earth System"*. Deutsche Gesellschaft für Geowissenschaften (DGG), Aachen.

Lachenbruch, A.H. 1961. Depth and spacing of tension cracks. *Journal of Geophysical Research* **66**, 4273-4292.

Lacquement, F. 2001. *L'Ardenne Varisque. Déformation progressive d'un prisme sédimentaire pré-structuré, de l'affleurement au modèle de chaîne*. Société Géologique du Nord, 29, Lille.

Ladeira, F.L. & Price, N.J. 1981. Relationship between fracture spacing and bed thickness. *Journal of Structural Geology* **13**, 179-183.

Laubach, S.E. 1989. Paleostress directions from the preferred orientation of closed microfractures (fluid-inclusion planes) in sandstone, East Texas basin, U.S.A. *Journal of Structural Geology* **11**, 603-611.

Laubach, S.E. & Diaz-Tushman, K. 2009. Laurentian palaeostress trajectories and ephemeral fracture permeability, Cambrian Eriboll Formation sandstones west of the Moine Thrust Zone, NW Scotland. *Journal of the Geological Society, London* **166**, 349-362.

Laubach, S.E., Eichhubl, P., Hilgers, C. & Lander, R.H. 2010. Structural diagenesis. *Journal of Structural Geology* **32**, 1866-1872.

Laubach, S.E., Olson, J.E. & Gale, J.F.W. 2004a. Are open fractures necessarily aligned with maximum horizontal stresses? *Earth and Planetary Science Letters* **222**, 191-195.

Laubach, S.E., Reed, R.M., Olson, J.E., Lander, R.H. & Bonnell, L.M. 2004b. Coevaluation of crack-seal texture and fracture porosity in sedimentary rocks: cathodoluminiscence observations of regional fractures. *Journal of Structural Geology* **26**, 967-982.

Lespinasse, M. 1999. Are fluid inclusion planes useful in structural geology? *Journal of Structural Geology* **21**, 1237-1243.

Li, Y. & Yang, C. 2007. On fracture saturation in layered rocks. *International Journal of Rock Mechanics and Mining Sciences* **44**, 936-941.

Littke, R., Buker, C., Hertle, M., Karg, H., Stroetmann-Heinen, V. & Oncken, O. 2000. Heat flow evolution, subsidence and erosion in the Rheno-Hercynian orogenic wedge of central Europe **179**, 231-255.

Lockner, D.A. 1995. Rock failure. In: *Rock Physics and Phase Relations: A Handbook of Physical constants* (edited by Ahrens, T.A.). *American Geophysical Union*, Washington, D.C., pp. 127-147.

Lohest, M., Stainier, X. & Fourmarier, P. 1908. Compte rendu de la session extraordinaire de la Société Géologique de Belgique, tenue à Eupen et à Bastogne les 29, 30 et 31 août et le 1, 2 et 3 septembre 1908. *Annales de la Société géologique de Belgique* **35**, B351-B434.

Lünenschloss, B., Bayer, U. & Muchez, Ph. 1997. Coalification anomalies induced by fluid flow at the Variscan thrust front: a numerical model of the palaeotemperature field. *Geologie en Mijnbouw* **76**, 271-275.

Lünenschloss, B., Muchez, Ph. & Bayer, U. 2008. Late-Variscan fluid migration at the Variscan thrust front of Eastern Belgium: numerical modelling of the palaeothermal and fluid flow field. *International Journal of Earth Sciences* **97**, 1201-1212.

Mamtani, M.A., Mukherji, A. & Chaudhuri, A.K. 2007. Microstructures in a banded iron formation (Gua mine, India). *Geological Magazine* **144**, 271-287.

Mandal, N., Chakraborty, C. & Samanta, S.K. 2000. Boudinage in multilayered rocks under layer-normal compression: a theoretical analysis. *Journal of Structural Geology* **22**, 373-382.

Mandal, N., Deb, S.K. & Khan, D. 1994. Evidence for a non-linear relationship between fracture spacing and layer thickness. *Journal of Structural Geology* **16**, 1275-1281.

Mandl, G. 2000. *Faulting in brittle rocks. An introduction to the mechanics of tectonic faults*. Springer-Verlag Berlin, Heidelberg.

Mandl, G. 2005. *Rock Joints: The Mechanical Genesis*. Springer-Verlag, Berlin.

Manning, C.E. 1994. Fractal clustering of metamorphic veins. *Geology* **22**, 335-338.

Manning, C.E. & Bird, D.K. 1991. Porosity evolution and fluid flow in the basalts of the Skaergaard magma-hydrothermal system, East Greenland. *American Journal of Science* **291**, 201-257.

Mansy, J.-L. & Lacquement, F. 2003. Le Paléozoïque du Nord de la France et de la Belgique. *Géologues* **133-134**, 7-24.

Mansy, J.L., Everaerts, M. & De Vos, W. 1999. Structural analysis of the adjacent Acadian and Variscan fold belts in Belgium and northern France from geophysical and geological evidence. *Tectonophysics* **309**, 99-116.

Matte, P. 1991. Accretional history and crustal evolution of the Variscan belt in Western Europe. *Tectonophysics* **196**, 309-337.

Matte, P. 2001. Tectonic review of the Armorica microplate. *Terra Nova* **13**, 122-128.

Mazzarini, F., Isola, I., Ruggieri, G. & Boschi, C. 2010. Fluid circulation in the upper brittle crust: Thickness distribution, hydraulic transmissivity fluid inclusion and isotopic data of veins hosted in the Oligocene sandstones of the Macigno Formation in southern Tuscany, Italy. *Tectonophysics* **493**, 118-138.

Means, W.D. & Li, T. 2001. A laboratory simulation of fibrous veins: some first observations. *Journal of Structural Geology* **23**, 857-863.

Meere, P.A. 1995a. High and low density fluids in a quartz vein from the Irish Variscides. *Journal of Structural Geology* **17**, 435-446.

Meere, P.A. 1995b. Sub-greenschist facies metamorphism from the Variscides of SW Ireland an early syn-extensional peak thermal event. *Journal of the Geological Society* **152**, 511-521.

Meere, P.A. & Banks, D.A. 1997. Upper crustal fluid migration: an example from the Variscides of SW Ireland. *Journal of the Geological Society, London* **154**, 957-985.

Meilliez, F., André, L., Blieck, A., Fielitz, W., Goffette, O., Hance, L., Khatir, A., Mansy, J.-L., Overlau, O. & Verniers, J. 1991. Ardenne -Brabant. *Sci. Geol. Bull.* **44**, 3-29.

Meilliez, F. & Mansy, J.-L. 1990. Déformation pelliculaire différenciée dans une série lithologique hétérogène: le Dévono-Carbonifère de l'Ardenne. *Bulletin de la Société géologique de France* **6**, 177-188.

Meyer, W. & Stets, J. 1980. Zur Paläogeographie von Unter- und Mitteldevon im westlichen und zentralen Rheinischen Schiefergebirge. *Zeitschrift der Deutschen Geologischen Gesellschaft für Geowissenschaften* **131**, 725-751.

Meyer, W. & Stets, J. 2002. Pleistocene to Recent tectonics in the Rhenish Massif (Germany). *Geologie en Mijnbouw* **81**, 217-221.

Micklethwaite, S., Sheldon, H.A. & Baker, T. 2010. Active fault and shear processes and their implications for mineral deposit formation and discovery. *Journal of Structural Geology* **32**, 151-165.

Miller, S.A., Collettini, C., Chiaraluce, L., Cocco, M., Barchi, M. & Kaus, B.J.P. 2004. Aftershocks driven by a high-pressure CO2 source at depth. *Nature* **427**, 724-727.

Mitra, S. 2002. Fold-Accomodation Faults. *AAPG Bulletin* **86**, 671-693.

Muchez, Ph., Boven, J., Bouckaert, J., Leplat, P., Viaene, W. & Wolf, M. 1991. Illite crystallinity in the Carboniferous of the Campine-Brabant Basin (Belgium) and its relationship to organic maturity indicators. *Neues Jahrbuch für Geologie und Paläontologie - Abhandlungen* **182**, 117-131.

Muchez, Ph., Brems, D., Clara, E., De Cleyn, A., Lammens, L., Boyce, A., De Muynck, D., Mukumba, W. & Sikazwe, O. 2010. Evolution of Cu-Co mineralizing fluids at Nkana Mine, Central African Copperbelt, Zambia. *Journal of African Earth Sciences* **58**, 457-474.

Muchez, Ph., Marshall, J.D., Touret, J.L.R. & Viaene, W.A. 1994. Origin and migration of paleofluids in the Upper Visean of the Campine basin, northern Belgium. *Sedimentology* **41**, 133-145.

Muchez, Ph., Sintubin, M. & Swennen, R. 2000. Origin and migration pattern of palaeofluids during orogeny: discussion on the Variscides of Belgium and northern France. *Journal of Geochemical Exploration* **69-70**, 47-51.

Muchez, Ph., Slobodnik, M., Viaene, W. & Keppens, E. 1995. Geochemical constraints on the origin and migration of palaeofluids at the northern margin of the Variscan foreland, southern Belgium. *Sedimentary Geology* **96**, 191-200.

Muchez , P., Zhang, Y., Dejonghe, L., Viaene , W. & Keppens, E. 1998. Evolution of palaeofluids at the Variscan thrust front in eastern Belgium. *Geologische Rundschau* **87**, 373-380.

Mukhopadhyay, D. 1973. Strain measurements from deformed quartz grains in the slaty rocks from the Ardennes and the northern Eifel. *Tectonophysics* **16**, 279-296.

Narr, W. & Suppe, J. 1991. Joint spacing in sedimentary rocks. *Journal of Structural Geology* **13**, 1037-1048.

Nicholson, R. 1978. Folding and pressure solution in a laminated calcite-quartz vein from the Silurian slates of the Llangollen region of N Wales. *Geological Magazine* **115**, 47-54.

Nielsen, P., Swennen, R., Muchez, Ph. & Keppens, E. 1998. Origin of Dinatian zebra dolomites south of the Brabant-Wales Massif, Belgium. *Sedimentology* **45**, 727-743.

Nollet, S., Urai, J.L., Bons, P.D. & Hilgers, C. 2005a. Numerical simulations of polycrystal growth in veins. *Journal of Structural Geology* **27**, 217-230.

Nollet, S., Urai, J.L., Bons, P.D. & Hilgers, C. 2005b. Sealing of fluid pathways in overpressure cells: a case study from the Buntsandstein in the Lower Saxony Basin (NW Germany). *International Journal Earth Sciences (Geologische Rundschau)* **94**, 1039-1055.

O'Hara, K. & Haak, A. 1992. A fluid inclusion study of fluid pressure and salinity variations in the footwall of the Rector Branch thrust, North Carolina, U.S.A. *Journal of Structural Geology* **14**, 579-589.

Oliver, W.A. & Chlupáč, I. 1991. Defining the Devonian: 1979-89. *Lethaia* **24**, 119-122.

Olson, J.E. 1993. Joint pattern development - Effects of subcritical crack growth and mechanical crack interaction. *Journal of Geophysical Research* **98**, 12251-12265.

Olson, J.E. 2004. Predicting fracture swarms - the influence of subcritical crack growth and the crack-tip process zone on joint spacing in rock. In: *The initiation, propagation and arrest of joints and other fractures* (edited by Cosgrove, J.W. & Engelder, T.). *Geological Society, London, Special Publications* **231**, 73-88.

Olson, J.E., Holder, J. & Rijken, P. 2002. Quantifying the Fracture Mechanics Properties of Rock for Fractures Reservoir Characterisation. In: *SPE/ISRM Rock Mechanics Conference*, Irving, Texas, pp. 20-23.

Oncken, O., Plesch, A., Weber, J., Ricken, W. & Schrader, S. 2000. Passive margin detachment during arc-continent collision (Central European Variscides). In: *Orogenic Processes: Quantification and Modelling in the Variscan Belt* (edited by Franke, W., Haak, V., Oncken, O. & Tanner, D.). *Geological Society, London, Special Publications* **179**, 199-216.

Oncken, O., von Winterfeld, C.H. & Dittmar, U. 1999. Accretion of a rifted passive margin: The Late Paleozoic Rhenohercynian fold and thrust belt (Middle European Variscides). *Tectonics* **18**, 75-91.

Paproth, E., Dreesen, R. & Thorez, J. 1986. Famennian paleogeography and event stratigraphy of northwestern Europe. *Annales de la Société géologique de Belgique* **109**, 175-186.

Passchier, C.W. & Trouw, R.A.J. 2005. *Microtectonics*. Springer-Verlag, Berlin.

Peacock, D.C.P. 2004. Differences between veins and joints using the example of the Jurassic limestones of Somerset. In: *The initiation, propagation and arrest of joints and other fractures.* (edited by Cosgrove, J.W. & Engelder, T.). *Geological Society, London, Special Publications* **231**, 209-221.

Petit, J.-P., Wibberley, C.A.J. & Ruiz, G. 1999. 'Crack-seal', slip: a new fault valve mechanism? *Journal of Structural Geology* **21**, 1199-1207.

Pharaoh, T.C. 1999. Palaeozoic terranes and their lithospheric boundaries within the Trans-European Suture Zone (TESZ): a review. *Tectonophysics* **314**, 17-41.

Piecha, M. 2002. A considerable hiatus at the Frasnian/Famennian boundary in the Rhenish shelf region of northwest Germany. *Palaeogeography, Palaeoclimatology, Palaeoecology* **181**, 195-211.

Pilger, A. & Schmidt, W. 1957. Die Mullion-Structuren in der Nord-Eifel. *Abhandlungen des Hessischen Landesamtes für Bodenforschung* **20**, 1-53.

Pio Lucente, F., De Gori, P., Margheriti, L., Piccinini, D., Di Bona, M., Chiarabba, C. & Piana Agostinetti, N. 2010. Temporal variation of seismic velocity and anisotropy before the 2009 MW 6.3 L'Aquila earthquake, Italy. *Geology* **38**, 1015-1018.

Plesch, A. & Oncken, O. 1999. Orogenic wedge growth during collision - constraints on mechanics of a fossil wedge from its kinematic record (Rhenohercynian FTB, Central Europe). *Tectonophysics* **309**, 117-139.

Pollard, D.D. & Segall, P. 1987. Theoretical displacements and stresses near fractures in rock: with applications to faults, joints, veins, dikes, and solution surfaces. In: *Fracture mechanics of rock* (edited by Atkinson, B.K.). *Academic Press*, London, 277-349.

Prezbindowski, D.R. & Tapp, J.B. 1991. Dynamics of fluid inclusion alteration in sedimentary rocks: a review and discussion. *Organic Geochemistry* **17**, 131-142.

Price, N.J. 1966. *Fault and Joint development in Brittle and Semi-Brittle Rock*. Pergamon Press, Oxford. 176p.

Price, N.J. & Cosgrove, J.W. 1990. *Analysis of geological structures.* Cambridge University Press, Cambridge.

Putz-Perrier, M.W. & Sanderson, D.J. 2008. Spatial distribution of brittle strain in layered sequences. *Journal of Structural Geology* **30**, 50-64.

Ramsay, J.G. 1967. *Folding and fracturing of rocks*, New York: McGraw-Hill.

Ramsay, J.G. 1980. The crack-seal mechanism of rock deformation. *Nature* **284**, 135-139.

Ramsay, J.G. & Huber, M.I. 1983. *The techniques of modern structural geology. Volume 1: strain analysis*. Academic Press, London.

Ramsay, J.G. & Huber, M.I. 1987. *The techniques of modern structural geology. Volume 2: folds and fractures*. Academic Press, London.

Reed, R.M. & Laubach, S.E. 2005. Integrated SEM-based cathodoluminiscence imaging and fluid inclusion analysis of crack-seal quartz cement in sandstone macrofractures. In: *Salt Lake City Annual Meeting*. Geological society of Amerika **37**, Salt Lake City, 235.

Renard, F., Andréani, M., Boullier, A.-M. & Labaume, P. 2005. Crack-seal patterns: records of uncorrelated stress release variations in crustal rocks. In: *Deformation Mechanisms, Rheology and Tectonics: from Minerals to the Lithosphere* (edited by Gapais, D., Brun, J.P. & Cobbold, P.R.). *Geological Society, London, Special Publications* **243**, 67-79.

Ribbert, K.-H. 1992. Geologische Karte von Nordrhein-Westfalen; Erläuterungen Blatt C5502 Aachen. Geologisches Landesamt Nordrhein-Westfalen, Krefeld.

Ribbert, K.-H. 1994. Geologische Karte von Nordrhein-Westfalen; Erläuterungen Blatt 5404 Schleiden. Geologische Landesamt Nordrhein-Westfalen.

Ribbert, K.-H. 2007. Rurberg-Formation. In Litholex [Online-Datenbank]. Hannover: BGR. Last Updated 06.06.2007 [cited 14.12.2010]. Record No. 7016046. Available from: http://www.bgr.bund.de/litholex.

Ribbert, K.-H. & Vieth, A. 2005. Coalification analysis as a tool for regional geology in the Northern Eifel (Rhenish Massif, Germany). *International Journal of Coal Geology* **62**, 61-70.

Richter, D.K. 1967. Aachen und Umgebung: Nordeifel und Umgebung. *Sammlung geologischer Führer* **48**.

Richter, D.K. 1985. Aachen und Umgebung. Nordeifel und Nordardennen mit Vorland. *Sammlung Geologischer Führer* **48**.

Rijken, P. 2005. Modeling naturally fractured reservoirs: from experimental rock mechanics to flow simulation. Unpublished Ph.D. thesis, University of Texas at Austin.

Rodrigues, N., Cobbold, P.R., Loseth, H. & Ruffet, G. 2009. Widespread bedding-parallel veins of fibrous calcite ('beef') in a mature source rock (Vaca Muerta Fm, Neuquen Basin, Argentina): evidence for overpressure and horizontal compression. *Journal of the Geological Society* **166**, 695-709.

Roduit, N. 2008. JMicroVision: Image analysis toolbox for measuring and quantifying components of high-definition images. Version 1.2.7. http://www.jmicrovision.com (accessed October 2008).

Roedder, E. 1984. Fluid inclusions (edited by Ribbe, P.H.). *Reviews in Mineralogy* **12**, Mineralogical Society of America, Washington, 644 p.

Savage. 2010. The role of fluids in earthquake generation in the 2009 Mw 6.3 L'Aquila, Italy, earthquake and its foreshocks *Geology* **38**, 1055-1056.

Sawyer, E.W. & Robin, P.-Y.F. 1986. The subsolidus segregation of layer-parallel quartz-feldspar veins in greenschist to upper amphibolite facies metasediments. *Journal of metamorphic Geology* **4**, 237-260.

Schmatz, J. & Urai, J.L. 2010. The interaction of fluid inclusions and migrating grain boundaries in a rock analogue: deformation and annealing of polycrystalline camphor–ethanol mixtures. *Journal of Metamorphic Geology* **28**, 1-18.

Schmidt, W. 1956. Die paläogeographische entwickelung des linksrheinischen Schiefergebirges vom Kambrium bis Obercarbon. *Zeitschrift der Deutschen Geologischen Gesellschaft Band* **103**, 151-177.

Schmidt, W. & Schröder, E. 1962. Erläuterungen zur Geologische Ubersichtskarte der nördlichen Eifel 1:100.000. Geologisches Landesamt Nordrhein-Westfalen, Krefeld, 110 pp.

Schneider, C.L., Hummon, C., Yeats, R.S. & Huftile, G.L. 1996. Structural evolution of the northern Los Angeles basin, California, based on growth strata. *Tectonics* **15**, 341-355.

Schöpfer, M.P.J., Arslan, A., Walsh, J.J. & Childs, C. in press. Reconciliation of contrasting theories for fracture spacing in layered rocks. *Journal of Structural Geology*.

Schöpfer, M.P.J., Childs, C. & Walsh, J.J. 2006. Localisation of normal faults in multilayer sequences. *Journal of Structural Geology* **28**, 816-833.

Schrötter, H.W. & Klöckner, H.W. 1979. Raman scattering cross-sections in gases and liquids. In: *Raman Spectroscopy of Gases and Liquids* (edited by Weber, A.). *Springer-Verlag*, Berlin, 123-166.

Schroyen, K. & Muchez, Ph. 2000. Evolution of metamorphic fluids at the Variscan fold-and-thrust belt in eastern Belgium. *Sedimentary Geology* **131**, 163-180.

Schultz, B., Audren, C. & Triboulet, C. 2002. Oxygen isotope record of fluid-rock-SiO_2 interaction during Variscan progressive deformation and quartz veining in the meta-volcanosediments of Belle-Ile (Southern Brittany). *Journal of Structural Geology* **24**, 1281-1297.

Secor, D.T. 1965. Role of fluid pressure in jointing. *American Journal of Sciences* **263**, 633-646.

Séjourné, S., Malo, M., Savard, M.M. & Kirkwood, D. 2005. Multiple origin and regional significance of bedding parallel veins in a fold and thrust belt: The example of a carbonate slice along the Appalachian structural front. *Tectonophysics* **407**, 189-209.

Servais, T. & Sintubin, M. 2009. Avalonia, Armorica, Perunica: terranes, microcontinents, microplates or palaeobiogeographical provinces? *Geological Society, London, Special Publications* **325**, 103-115.

Shepherd, T.J., Rankin, A.H. & Alderton, D.H.M. 1985. *A practical guide to Fluid inclusion Studies*. Blackie, London.

Sibson, R. 1983. Continental fault structure and the shallow earthquake source. *Journal of the Geological Society, London* **140**, 741-767.

Sibson, R.H. 1990. Conditions for fault-valve behaviour **54**, 15-28.

Sibson, R.H. 1995. Selective fault reactivation during basin inversion: potential for fluid redistribution through fault-valve action. *Geological Society, London, Special Publications* **88**, 3-19.

Sibson, R.H. 1996. Structural permeability of fluid-driven fault-fracture meshes. *Journal of Structural Geology* **18**, 1031-1042.

Sibson, R.H. 1998. Brittle failure mode plots for compressional and extensional tectonic regimes. *Journal of Structural Geology* **20**, 655-660.

Sibson, R.H. 2000. Tectonic controls on maximum sustainable overpressure: fluid redistribution from stress transition. *Journal of Geochemical Exploration* **69-70**, 471-475.

Sibson, R.H. 2001. Seismogenic Framework for Hydrothermal Transport and Ore Deposition. *Society of Economic Geologists Reviews* **14**, 25-50.

Sibson, R.H. 2003. Brittle-failure controls on maximum sustainable overpressure in different tectonic regimes. *AAPG Bulletin* **87**, 901-908.

Sibson, R.H. 2004. Controls on maximum fluid overpressure definitions conditions for mesozonal mineralisation. *Journal of Structural Geology* **26**, 1127-1136.

Sibson, R.H. & Scott, K. 1998. Stress/faults controls on the containment and release of overpressured fluids: Examples from gold-quartz vein systems in Juneau, Alaska; Victoria, Australia and Otago, New Zealand. *Ore Geology Reviews* **13**, 293-306.

Simpson, G.D.H. 2000. Synmetamorphic vein spacing distributions: characterisation and origin of a distribution of veins from NW Sardinia, Italy. *Journal of Structural Geology* **22**, 335-348.

Sindern, S., Stanjek, H., Hilgers, C. & Etoundi, Y. 2007. Short-term hydrothermal effect on the 'crystallinities' of illite and chlorite in the footwall of the Aachen-Faille du Midi thrust fault - first results of the RWTH-1drilling project. *Clays and Clay Minerals* **55**, 200-212.

Singh, M.M. 1989. Strength of rock. In: *Physical Properties of Rocks and Minerals. Vol. II-2* (edited by Touloukian, Y.S., Judd, W.R. & Roy, R.F.). *Hemisphere Publications*, New York, NY, 83-122

Sintubin, M. 2008. Photograph of the month: Boudin centennial. *Journal of Structural Geology* **30**, 1315-1316.

Sintubin, M., Debacker, T.N. & Van Baelen, H. 2009. Early Palaeozoic orogenic events north of the Rheic suture (Brabant, Ardenne): A review. *Comptes Rendus Geosciences* **341**, 156-173.

Sintubin, M., Kenis, I., Schroyen, K., Muchez, Ph. & Burke, E. 2000. "Boudinage" in the High-Ardenne slate Belt (Belgium), reconsidered from the perspective of the "interboudin" veins. *Journal of Geochemical Exploration* **69-70**, 511-516.

Sintubin, M. & Mathijs, J. 1998. Structural implications of the geometry of the western margin of the Lower Paleozoic Stavelot Massif in the Ninglinspo area (Nonceveux, Belgium). *Aardkundige Mededelingen* **9**, 97-110.

Sippli, G. 1981. Ausbildung und Verbreitung von K-Boudins (Mullions) in der westlichen Nordeifel und Überlegungen zu ihrer Entstehung, Diplom Thesis, RWTH Aachen.

Smith, J.V. 2005. Textures recording transient porosity in synkinematic quartz veins, South Coast, New South Wales, Australia. *Journal of Structural Geology* **27**, 357-370.

Smith, R.B. 1977. Formation of folds, boudinage, and mullions in non-Newtonian materials. *Bulletin Geological Society of America* **88**, 312-320.

Spaeth, G. 1969. Das Deformationsbild planolinear geschieferten Grauwacken aus dem Unterdevon am SE-rand des Hohes Venns (Rheinische Schiefrgebirge). *Geologische Mitteilungen* **8**, 309-326.

Spaeth, G. 1979. Neuere Beobachtungen und Vorstellungen zur Variszischen Tektonik der westlichen Nordeifel (Rheinisches Schiefergebirge). *Zeitung der Deutschen Geologischen Gesellschaft* **130**, 107-121.

Spaeth, G. 1986. Boudins und Mullions in devonischen Schichtfolgen der Nordeifel und Ardennen; Erscheinungsbild, Entstehung und Umformung. *Nachrichten - Deutsche Geologische Gesellschaft* **35**, 74-75.

Steemans, P. 1989. Paléogéographie du bassin ardennais au cours de l'Eodévonien. *Annales de la Société Géologique de Belgique* **112**, 103-119.

Stets, J. & Schafer, A. 2002. *Depositional Environments in the Lower Devonian Siliciclastics of the Rhenohercynian Basin (Rheinisches Schiefergebirge, W-Germany). Case study and a model*. Contributions to Sedimentary Geology **22**. E. Schweizerbart.

Stets, J. & Schafer, A. 2009. The Siegenian delta: land-sea transitions at the northern margin of the Rhenohercynian Basin. *Geological Society, London, Special Publications* **314**, 37-72.

Stowell, J.F.W., Watson, A.P. & Hudson, N.F.C. 1999. Geometry and populations systematics of a quartz vein set, Holy Island, Anglesey, North Wales. In: *Fractures, Fluid Flow and Mineralisation* (edited by McCaffrey, K.J.W., Lonergan, L. & Wilkinson, J.J.). *Geological Society, London, Special Publications* **155**, 17-33.

Swarbrick, R.E. & Osborne, M.J. 1998. Mechanisms that generate abnormal pressures: an overview. In: *Abnormal pressures in hydrocarbon environments* (edited by Law, B.E., Ulmishek, G.F. & Slavin, V.I.). *AAPG Memoir* **70**, 13-34.

Tanner, G.P.W. 1989. The flexural-slip mechanism. *Journal of Structural Geology* **11**, 635-655.

Tanner, G.P.W. 1990. The flexural-slip mechanism: Reply. *Journal of Structural Geology* **12**, 1085-1087.

Tavallali, A. & Vervoort, A. 2010. Effect of layer orientation on the failure of layered sandstone under Brazilian test conditions. *International Journal of Rock Mechanics and Mining Sciences* **47**, 313-322.

Teichmüller, M. 1987. Organic material and very low-grade metamorphism. In: *Low Temperature Metamorphism* (edited by Frey, M.). *Blackie and Son*, London, 114-161.

Teichmüller, M. & Teichmüller, R. 1952. Zur Fazies und Metamorphose der "Kohlen" im Devon des Rheinischen Schiefergebirges. *Zeitschrift der Deutschen Geologischen Gesellschaft Band* **103**, 219-232.

Teichmüller, M. & Teichmüller, R. 1979. Ein Inkohlungsprofil der linksrheinischen Geotraverse von Schleiden nach Aachen und die Inkohlung der Nord-Süd-Zone der Eifel. *Fortschritt Geologie Rheinland und Westfalen* **27**, 323-355.

Teixell, A., Durney, D.W. & Arboleya, M.-L. 2000. Stress and fluid control on décollement within competent limestone. Journal of Structural Geology 22, 349-371.

Terekawa, T., Zoporowski, A., Galvan, B. & Miller, S.A. 2010. High-pressure fluid at hypocentral depths in the L'Aquila region inferred from earthquake focal mechanisms. *Geology* **38**, 995-998.

Thomas, A.L. & Pollard, D.D. 1993. The geometry of echelon fractures in rock: implications from laboratory and numerical experiments. *Journal of Structural Geology* **15**, 323-334.

Treagus, S.H. 1983. A theory of finite strain variation through constrasting layers, and its bearing on cleavage refraction. *Journal of Structural Geology* **5**, 351-368.

Tunks, A.J., Selley, D., Rogers, J.R. & Brabham, G. 2004. Vein mineralization at the Damang Gold Mine, Ghana: controls on mineralization. *Journal of Structural Geology* **26**, 1257-1273.

Twiss, R.J. & Moores, E.M. 1992. *Structural Geology*. W.H. Freeman and Company, New York.

Urai, J.L., Spaeth, G., van der Zee, W. & Hilgers, C. 2001. Evolution of Mullion (formerly Boudin) structures in the Variscan of the Ardennes and Eifel. *Journal of the Virtual Explorer* **3**, 1-15.

Urai, J.L., Williams, P.F. & van Roermond, H.L.M. 1991. Kinematics of crystal growth in syntectonic fibrous veins. *Journal of Structural Geology* **13**, 823-836.

Van Baelen, H. 2010. *Dynamics of a progressive vein development during the late-orogenic mixed brittle-ductile destabilisation of a slate belt. Examples of the High-Ardenne slate belt (Herbeumont, Belgium)*. Aardkundige mededelingen 24, 221p.

Van Baelen, H. & Sintubin, M. 2008. Kinematic consequences of an angular unconformity in simple shear: An example from the southern border of the Lower Palaeozoic Rocroi inlier (Naux, France). *Bulletin de la Société géologique de France* **179**, 73-87.

van den Kerkhof, A.M. & Kisch, H.J. 1993. CH_4-rich inclusions from quartz veins in the Valley-and-Ridge Province and the anthracite fields of the Pennsylvania Appalachians; reply. *American Mineralogist* **78**, 220-224.

van der Pluijm, B.A. & Marshak, S. 1997. *Earth Structure. An introduction to structural geology and tectonics*. WCB/McGraw-Hill.

Van Grootel, G., Verniers, J., Geerkens, B., Laduron, D., Verhaeren, M., Hertogen, J. & De Vos, W. 1997. Timing of subsidence-related magmatism, foreland basis development, metamorfism and inversion in the Anglo-Brabant fold belt. *Geological Magazine* **134**, 607-616.

van Noorden, M. 2007. New insights into early Variscan geodynamics in the Armorican massif : evidences of contraction-dominated deformation and incipient strain partitioning in the palaeozoic of the Monts d'Arrée, Brittany, France, PhD thesis, Katholieke Universiteit Leuven, 193 pp.

Van Noten, K., Berwouts, I., Muchez, Ph. & Sintubin, M. 2009. Evidence of pressure fluctuations recorded in crack-seal veins in low-grade metamorphic siliciclastic metasediments, Late Palaeozoic

Rhenohercynian fold-and-thrust belt (Germany). *Journal of Geochemical Exploration* **101**, 106.

Van Noten, K., Hilgers, C., Urai, J.L. & Sintubin, M. 2008. Late burial to early tectonic quartz veins in the periphery of the High-Ardenne slate belt (Rursee, North Eifel, Germany). *Geologica Belgica* **11**, 179-198.

Van Noten, K., Kenis, I., Hilgers, C., Urai, J.L. & Sintubin, M. 2007. Early vein generations in the High-Ardenne slate belt (Belgium, Germany): the earliest manifestations of the Variscan orogeny? In: *Mechanics of Variscan Orogeny: a modern view on orogenic research.* Géologie de la France **2**, Orléans, France, 170.

Van Noten, K., Muchez, Ph. & Sintubin, M. 2011. Stress-state evolution of the brittle upper crust during compressional tectonic inversion as defined by successive quartz vein types (High-Ardenne slate belt, Germany). *Journal of the Geological Society, London* **168**, 407-422.

Van Noten, K. & Sintubin, M. 2010. Linear to non-linear relationship between vein spacing and layer thickness in centimetre- to decimetre-scale siliciclastic multilayers from the High-Ardenne slate belt (Belgium, Germany). *Journal of Structural Geology* **32**, 377-391.

Van Noten, K., Van Baelen, H. & Sintubin, M. accepted. The complexity of 3D stress-state changes during compressional tectonic inversion at the onset of orogeny. In: *Faulting, Fracturing, and Igneous Intrusion in the Earth's crust* (edited by Healy, D.). *Geological Society, London, Special Publications*.

Van Ruth, P., Hillis, R.R., Tingate, P. & Swarbrick, R.E. 2003. The origin of overpressure in 'old' sedimentary basins: an example from the Cooper Basin, Australia. *Geofluids* **3**, 125-131.

Vanbrabant, Y. & Dejonghe, L. 2006. Structural analysis of narrow reworked boudings and influence of sedimentary successions during a two-stage deformation sequence (Ardenne-Eifel region, Belgium-Germany). *Memoirs of the Geological Survey of Belgium* **53**, 43p.

Vannucchi, P., Remitti, F. & Bettelli, G. 2008. Geological record of fluid flow and seismogenesis along an erosive subducting plate boundary. *Nature* **451**, 699-703.

Verhaert, G. 2001. Kwartsaders en dubbelzijdige mullions in de lochkoviaanmetasedimenten in de Hoge-Ardennenleisteengordel (groeve La Flèche, Bertrix, België). Unpublished Master thesis, Katholieke Universiteit Leuven.

Vermilye, J.M. & Scholz, C.H. 1995. Relation between vein length and aperture. *Journal of Structural Geology* **17**, 423-434.

Verniers, J., Herbosch, A., Vanguestaine, M., Geukens, F., Delcambre, B., Pingot, J.-L., Belanger, I., Hennebert, M., Debacker, T.N., Sintubin, M. & De Vos, W. 2001. Cambrian-Ordovician-Silurian lithostratigraphic units (Belgium). In: *Guide to a revised lithostratigraphic scale of Belgium* (edited by Bultynck, P. & Dejonghe, L.). *Geologica Belgica* **4**, 5-38.

Verniers, J., Pharaoh, T.C., André, L., Debacker, T.N., De Vos, W., Everaerts, M., Herbosch, A., Samuelsson, J., Sintubin, M. & Vecoli, M. 2002. The Cambrian to mid Devonian basin development and deformation history of eastern Avalonia, east of the Midlands Microcraton: new data and a review. In: *Palaeozoic Amalgamation of Central Europe* (edited by Winchester, J.A., Pharaoh, T.C. & Verniers, J.). *Geological Society, London, Special Publications* **201**, 49-93.

Vernooij, M.G.C., den Brok, B. & Kunze, K. 2006. Development of crystallographic preferred orientations by nucleation and growth of new grains in experimentally deformed quartz single crystals. *Tectonophysics* **427**, 35-53.

Vernooij, M.G.C. & Langenhorst, F. 2005. Experimental reproduction of tectonic deformation lamellae in quartz and comparison to shock-induced planar deformation features. *Meteoritics & Planetary Science* **40**, 1353-1361.

Vidal, O., Parra, T. & Vieillard, P. 2005. Thermodynamic properties of the Tschermak solid solution in Fe-chlorite: Application to natural examples and possible role of oxidation. *American Mineralogist* **90**, 347-358.

Vinzelberg, G. 2002. Kartierung devonischer Einheiten nördlich des Rursees unter besonderer Berücksichtigung der

Vitrinitreflexion. Unpublished Mapping thesis, RWTH Aachen.

Vityk, M.O., Bodnar, J.R. & Dudok, I.V. 1995. Natural and synthetic re-equilibration textures of fluid inclusions in quartz (Marmarosh Diamonds): Evidence for refilling under conditions of compressive loading. *European Journal of Mineralogy* **7**.

Vityk, M.O. & Bodnar, R.J. 1995. Textural evolution of synthtic fluid inclusions in quartz during reequilibration, with applications to tectonic reconstruction. *Contributions to Mineralogy and Petrology* **121**, 301-323.

Vityk, M.O., Bodnar, R.J. & Schmidt, C.S. 1994. Fluid inclusions as tectonothermobarometers: Relation between pressure-temperature history and reequilibration morphology during crustal thickening. *Geology* **22**, 731-734.

von Winterfeld, C.-H. 1994. *Variszische Deckentektonik und devonische Beckengeometrie der Nord-Eifel - Ein quantitatives Modell (Profilbilanzierung und Strain-Analyse im Linksrheinischen Schiefergebirge).* Aachener Geowissenschaftliche Beiträge **2**, RWTH Aachen. 319p.

von Winterfeld, C. & Walter, R. 1993. Die variszische Deformationsfront des nordwestlichen Rheinischen Schiefergebirges - Ein bilanziertes geologisches Tiefenprofil über die Nordeifel. *N. Jb. Geol. Paläont. Mh.* **5**, 305-320.

Wagner, T. & Boyce, A.J. 2003. Sulphur isotope geochemistry of black shale-hosted antimony mineralization, Arnsberg, northern Rhenish Massif, Germany: implications for late-stage fluid flow during the Variscan orogeny. *Journal of the Geological Society* **160**, 299-308.

Walter, R. 1992. *Geologie von Mitteleuropa*. E. Schweizerbart'sche Verlagsbuchhandlung, Stuttgard.

Wangen, M. 2000. Communication between overpressured compartments. *Geofluids* **1**, 273-287.

Weber, K. 1980. Anzeichen abnormal hoher Porenlösungsdrucke am Beginn der Faltung im Rheinischen Schiefergebirge. *Zeitschrift der Deutschen Geologischen Gesellschaft für Geowissenschaften* **131**, 605 - 625.

Weber, K. 1981. The structural development of the Rheinische Schiefergebirge. In: *The Variscan Orogen in Europe* (edited by Zwart, H.J. & Dornsiepen, U.F.). *Geologie en Mijnbouw* **60**, 149-159.

Williams, G.D., Powell, C.M. & Cooper, M.A. 1989. Geometry and kinematics of inversion tectonics. In: *Inversion Tectonics* (edited by Cooper, M.A. & Williams, G.D.). *Geological Society, London, Special Publications* **44**, 3-15.

Wilson, C., Robinson, J. & Dugdale, A. 2009. Quartz vein fabrics coupled to elevated fluid pressures in the Stawell gold deposit, south-eastern Australia. *Mineralium Deposita* **44**, 245-263.

Wiltschko, D.V., Lambert, G.R. & Lamb, W. 2009. Conditions during syntectonic vein formation in the footwall of the Absaroka Thrust Fault, Idaho-Wyoming-Utah fold and thrust belt. *Journal of Structural Geology* **31**, 1039-1057.

Wiltschko, D.V. & Morse, J.W. 2001. Crystallization pressure versus "crack seal" as the mechanism for banded veins. *Geology* **29**, 79-82.

Woodcock, N.H., Soper, N.J. & Strachan, R.A. 2007. A Rheic cause for the Acadian deformation in Europe. *Journal of the Geological Society, London* **164**, 1023-1036.

Wu, H. & Pollard, D.D. 1995. An experimental study of the relationship between joint spacing and layer thickness. *Journal of Structural Geology* **17**, 887-905.

Wünstorf, W. 1931. Über das Unterdevon auf dem Südflügel des Venn-Sattels. *Sitzung Berliner Preußische geologische Landesanstalt* **6**, 157-168.

Wünstorf, W. 1932. Die Siegenerschichten bei Monschau. *Jahrbuch Preußische geologische Landesanstalt* **52**, 251-256.

Wünstorf, W. 1936. Bericht über die Begehung des Unterdevons der Nordeifel. *Jahrbuch Preußische geologisches Landesanstalt* **56**, 326-329.

Wünstorf, W. 1943. Erläuterungen zu den Blättern 5303 Rötgen - Eupen, 5304 Nideggen. Geologische Karte Deutsche Reich, Berlin, 76 p.

Xu, G. 1997. Fluid inclusions in crack-seal veins at Dugald River, Mount Isa Inlier: implications for palaeostress states and deformation conditions during orogenesis.

Journal of Structural Geology **19**, 1359-1368.

Yilmaz, P.O., Norton, I.O., Leary, D. & Chuchla, R.J. 1996. Tectonic evolution and paleogeography of Europe. In: *Peri-Tethys Memoir 2: Structure and Prospects of Alpine Basins and Forelands* (edited by Ziegler, P.A. & Horvath, F.). *Mémoires du Muséum du Muséum National d'Histoire Naturelle*, Paris, 48-60.

Ziegler, P.A. 1990. *Geological atlas of Western and Central Europe*. Shell internationale Petroleum Maatschappij, 2nd ed., 239p.

Zier, U. & Kuhl, I. 1999. Structural Mapping Of The Rursee Area. Unpublished Mapping thesis, RWTH Aachen.

About the Author

Koen Van Noten was born on Monday, February 2nd, 1981 in Antwerp, Belgium. At the present, he lives in Deurne and is married with Kim Van Gheluwe. They are currently expecting their first child. Already in his childhood, Koen was fascinated by rocks and mountain ranges during numerous hikes in the Austrian Alps with his parents, brother and sister. After graduating from High School, he started studying Geology at the Ghent University in 1999. He obtained the degree of Licentiate in Geology in 2004 after performing a thesis under guidance of Prof. dr. Jacques Verniers. Being triggered by geological research after graduation, he started his PhD-research at the Katholieke Universiteit Leuven in January 2005, under supervision of Prof. dr. Manuel Sintubin and Prof. dr. Philippe Muchez. At this university, he is currently responsible for teaching students during field work and in practical courses. He enjoys being in the field, which he beliefs forms the base of good structural research. On May 3rd 2011, the author will defend his PhD-research at the Katholieke Universiteit Leuven.

Education & Professional activities

2005 – 2011	Research & Teaching Assistant at the Geology Division, KULeuven PhD in Structural Geology: *"Stress-state evolution of the brittle upper crust during early Variscan tectonic inversion as defined by successive quartz vein types in the High-Ardenne slate belt, Germany"* Supervised by Prof. dr. Manuel Sintubin & Prof. dr. Philippe Muchez, Geodynamics and Geofluids Research Group, Department of Earth and Environmental Sciences, Katholieke Universiteit Leuven
2002 – 2004	Licentiate/Masters degree in Geology - *Magna cum Laude* Master Thesis: *"Lithostratigraphy and biostratigraphy with chitinozoa from the Ordovician type area of the Bornival Formation, Sennette Valley (Brabant Massif)"* Supervised by Prof. dr. Jacques Verniers, Research Unit Palaeontology, Department of Geology and Soil Sciences, Universiteit Gent
1999 – 2002	Candidate/Bachelors degree in Geology Department of Geology and Soil Sciences, Universiteit Gent
1997 – 1999	Sciences - Mathematics, Sint-Anna College, Antwerpen
1993 – 1997	Latin - Mathematics, Sint-Anna College, Antwerpen

Grants & Scientific Awards

27.01.2011	Second Place in **Midland Valley's Student Structural Prize** competition for his paper contribution on the tectonic inversion of the High-Ardenne slate belt (Van Noten *et al.* 2011) *Awarded by Midland Valley Company, January 2011, Glasgow, U.K.*
08.09.2010	Badleys Industry Sponsored Travel Grant, Travel bursary for attending the Anderson Stress Conference, Glasgow University, U.K.
01.09.2010	Grant for participation at a Congress abroad, Fond voor Wetenschappelijk Onderzoek (FWO), Grant for attending the Anderson Stress Conference, Glasgow University, U.K.
08.01.2009	The **Mike Coward Award** of best Post-Graduate Talk at the Tectonic Studies Group Annual Meeting, Keele University, U.K. *Awarded by the TSG committee, January 2009, Keele, U.K.*

Courses Taught as Teaching Assistant

Practical Exercises Geology
1st Ba Geology, Chemistry, Biochemistry & Biotechnology, Geography: Determining minerals, rocks and fossils, crystallography and interpretation of geological maps.

Field Excursions Geology
1st Ba Geology/Geography: Organisation of one-day and three-day field trips to the south of Belgium and Luxemburg/Germany, respectively, with focus on sedimentology, stratigraphy, structural geology and Quaternary Eifel volcanism

Introduction into Geological Mapping (Aywaille-Stavelot area)
3th Ba Geology: Initiation in geological mapping

Exercises and Field trips Structural Geology
3th Ba Geology: Interpretation of geological maps, creation of cross-sections, stereographic projection, all applied to the geology of Belgium

Field trip Soft-sediment deformation
1st & 2nd Ma Geology: guidance of field trip on soft-sediment analysis in the Brabant Massif (Sennette Valley) & Namur Synclinorium (Namur citadel)

Exercises Geological Mapping
1st & 2nd Ma Geology: assistance of students during their individual geological mapping assignment

Additional activities
Creator of plate tectonic puzzles for children (2005; together with Hervé Van Baelen & Peter Stassen)
Instructor during the LERU kids University week/Science 4 fun week (Leuven 2005-’06-‘07’-’08-’09)
Instructor during the LERU kids University final event at the Sci-fun roadshow (Brussels 2005)
Instructor during the ‘Vlaamse Wetenschapsfeest: slotshow’ (Ghent 2006, Mechelen 2008)
Introduction into Geology for high school students (Ninglinspo Valley, Belgium; 2007-’08-‘09)
Instructor Geology during the ‘Wetenschapskamp’ (Leuven 2007-’08-‘09-’10)
Ombudsman of the Bachelor degree (2007-’08-‘09).

List of Publications

Publications in International Journals with Reading Committee

Van Noten, K., Van Baelen, H. & Sintubin, M. accepted. The complexity of 3D stress-state changes during compressional tectonic inversion at the onset of orogeny. In: *Faulting, Fracturing and Igneous intrusion in the Earth's crust* (edited by Dave Healy). *Geological Society, London, Special Publications 367, 51-69.*

Van Noten, K., Muchez, Ph. & Sintubin, M., 2011. Stress-state evolution of the brittle upper crust during compressional tectonic inversion as defined by successive quartz vein types (High-Ardenne slate belt, Germany). *Journal of the Geological Society, London* **168**(2), 407-422

Van Noten, K. & Sintubin, M. 2010. Linear to non-linear relationship between vein spacing and layer thickness in centimetre- to decimetre-scale siliciclastic multilayers from the High-Ardenne slate belt (Belgium, Germany). *Journal of Structural Geology* **32**, 377-391.

Van Noten, K., Berwouts, I., Muchez, Ph. & Sintubin, M. 2009. Evidence of pressure fluctuations recorded in crack-seal veins in low-grademetamorphic siliciclastic metasediments, Late Palaeozoic Rhenohercynian fold-and-thrust belt (Germany). *Journal of Geochemical Exploration* **101**(1), 106.

Van Noten, K., Hilgers, C., Urai, J. L. & Sintubin, M. 2008. Late burial to early tectonic quartz veins in the periphery of the High-Ardenne slate belt (Rursee, North Eifel, Germany). *Geologica Belgica* **11**(3-4), 179-198.

Vanmeirhaeghe, J., Storme, A., **Van Noten, K.**, Van Grootel, G. & Verniers, J. 2005. Chitinozoan biozonation and new lithostratigraphical data in the Upper Ordovician of the Fauquez and Asquempont areas (Brabant Massif, Belgium). *Geologica Belgica* **8**(4), 145-159.

Published abstracts in Proceedings or abstracts in abstract books of International Conferences

Van Noten, K., Van Baelen, H., Berwouts, I. Muchez, Ph., Sintubin, M. 2011. Quartz Microstructures, the Key to Unravel Orogenic History. Abstract book of conference: Interrelationships between deformation and metamorphism, 23-26 May 2011, Granada, Spain - *Poster presentation*

Van Noten, K., Van Baelen, H. & Sintubin M. 2011. 3D Stress-State Evolution during Tectonic Inversion. Abstract book of the Tectonic Studies Group Annual Meeting, 5-8 January 2011, Durham, U.K. - *Poster presentation*

Sintubin, M., Adriaens, R., Ronchi, B., Vandewijngaerde, W., Berwouts, I., De Clercq, F., D’Haenens, S., Moermans, G., Vanhove, D. & **Van Noten, K.** 2011. Integrating field courses in the undergraduate geology curriculum at the K.U.Leuven (Belgium) using Google Earth. Abstract book of the GSSA Penrose Conference, Google Earth: Visualizing the Possibilities for Geoscience Education and Research. 4-8 January 2011, Mountain View, U.S.A. - *Co-author poster presentation*

Van Noten, K., Van Baelen H., Muchez, Ph. & Sintubin M. 2010. Stress-state evolution of the crust during extensional and compressional tectonic inversion as documented by quartz veins. Abstract book of the Anderson Conference: Stress controls on faulting, fracturing and igneous intrusion in the Earth's crust, 6-8 September 2010, Glasgow, U.K. - *Oral presentation*

Sintubin, M., Van Baelen, H., **Van Noten, K.** & Muchez, Ph. 2010. Mixed brittle-plastic deformation behaviour at the base of the seismogenic zone as documented by quartz veins (High-Ardenne slate belt, Belgium, Germany). Abstract book of the Gordon Research Conference, Transient and transitional behaviour in rock deformation: Moving away from steady-state, August 8-13, 2010, Tilton, NH, USA - *Co-author poster presentation*

Van Noten, K. 2010. Veins in the High-Ardenne slate belt: useful tools to define early and late orogenic failure. Studiedag: Tectonics and Structural Geology in Belgium. Koninklijke Vlaamse academie voor Wetenschappen en Kunsten (KVAB), 14 Mai 2010, Brussels, Belgium - *Invited oral presentation*

Sintubin, M., Van Baelen, H., **Van Noten, K.** & Muchez, Ph. 2010. Mixed brittle-plastic deformation behaviour in a slate belt. Examples from the High-Ardenne slate belt (Belgium, Germany). *Geophysical Research Abstracts* **12**, 1836. Session TS3.1 Deformation processes, EGU, 2-7 April 2010, Vienna, Austria - *Co-author poster presentation*

Van Noten, K., Muchez., Ph. & Sintubin, M. 2010. The stress state in the brittle upper crust during early Variscan tectonic inversion and its influence on high-pressure compartments. Abstract book of the Tectonic Studies Group Annual Meeting, 6-8 January 2010, Birmingham, U.K. - *Oral presentation*

Van Noten, K., Muchez, Ph. & Sintubin, M. 2009. Early veining in the Ardenne-Eifel basin (Rursee - Urftsee, Germany): Evidence of tectonic inversion in an overpressured sedimentary basin at the onset of the Variscan Orogeny. Abstract book of the Third International Conference Geologica Belgica, 14-15 September 2009, Ghent, Belgium - *Oral presentation*

Van Noten, K., Berwouts, I., Muchez, Ph. & Sintubin, M. 2009. Evidence of pressure fluctuations recorded in crack-seal veins in low-grade metamorphic siliciclastic metasediments, Late Palaeozoic Rhenohercynian fold-and-thrust belt (Germany). *Journal of Geochemical Exploration* **101**(1), 106. Geofluids, 15-17 April 2009, University of Adelaide, Adelaide, South-Australia - *Poster presentation*

Van Noten, K. & Sintubin, M. 2009. Spatial distribution of quartz veins in alternating siliciclastic sequences and its relationship to bed thickness. Abstract book of the Tectonic Studies Group Annual Meeting, 7-8 January 2009, Keele University, U.K. - *Oral presentation*

Van Noten, K., Hilgers, C., Urai, J. L. & Sintubin, M. 2008. The record of a tectonic inversion in the Lower Devonian Ardenne-Eifel basin (Belgium, Germany): a switch from bedding-normal to bedding-parallel quartz veins. Abstract book of the Tectonic Studies Group Annual Meeting, 8-10 January 2008, La Roche-en-Ardenne, Belgium - *Oral presentation*

Van Noten, K., Kenis, I., Hilgers, C., Urai, J. L. & Sintubin, M. 2007. Early vein generations in the High-Ardenne slate belt (Belgium, Germany): the earliest manifestations of the Variscan orogeny? In: *Mechanics of Variscan Orogeny: a modern view on orogenic research*. Géologie de la France **2**, 170, 13-15 September 2007, Orléans, France - *Oral presentation*

Van Noten, K., Sintubin, M., Hilgers, C. & Urai, J. L. 2007. On the formation of bedding-perpendicular and bedding-parallel quartz veins in the Variscan fold-and-thrust belt: late burial or early tectonic? Abstract book of the Tectonic Studies Group Annual Meeting, 4-6 January 2007, University of Glasgow, Glasgow, U.K. - *Poster presentation*

Van Noten, K., Kenis, I., Sintubin, M. & Urai, J. L. 2007. Quartz veining in the High-Ardenne slate belt. New evidences from the Rursee area, North Eifel, Germany. *Geologica Belgica* **10**(3-4), 218. Geologica Belgica International Meeting, 7-8 September 2006, Liège, Belgium - *Oral presentation*

Coenen, B., Debacker, T.N., **Van Noten, K.** & Verniers, J. 2007. Lateral variations of deformation style in virtually coaxially deformed sequences: the example of the upper Silurian of the inclined shiplift at Ronquières, southern Brabant Massif (Belgium). *Geologica Belgica* **10**(3-4), 188-189. Abstract book of the Geologica Belgica International Meeting, 7-8 September 2006, Liège, Belgium - *Co-author oral presentation*

Van Noten, K., Kenis, I., Sintubin, M. & Urai, J.L. 2006. Structural morphology and quartz veining in the periphery of the High-Ardenne slate belt, Rursee, North-Eifel, Germany. Abstract book of the Tectonic Studies Group Annual Meeting, 4-6 January 2006, University of Manchester, Manchester, U.K. - *Oral presentation*

Vanmeirhaeghe, J., Storme, A., **Van Noten, K.**, Van Grootel, G. & Verniers, J. 2004. Local chitinozoan biozonation of the Upper Ordovician of the Fauquez area (Brabant Massif, Belgium). Abstract book of the Avalonia-Moesia conference/workshop: Early Palaeozoic orogens in the Trans-European Suture Zone?, Ghent/Ronse, 41-42. - *Co-author oral presentation*

Vanmeirhaeghe, J., **Van Noten, K.**, Van Grootel, G. & Verniers, J. 2004. Chitinozoans from the Upper Ordovician of the Fauquez area (Brabant Massif, Belgium). In: International Symposium on Early Palaeogeography and Palaeoclimate (edited by Munnecke, A., Servais, T. & Schulbert, C.). Erlanger Geologische Abhandlungen, Sonderband 5, Erlangen, Germany, 71-72. - *Co-author oral presentation*